UNIVERSIDADE FEDERAL DE JUIZ DE FORA

DEPARTAMENTO DE FÍSICA

DOUTORADO EM FÍSICA

**Theoretical characterization of graphene and other 2D materials**

**SAIF ULLAH**

JUIZ DE FORA

JANUARY 22, 2020

UNIVERSIDADE
FEDERAL DE JUIZ DE FORA

UNIVERSIDADE FEDERAL DE JUIZ DE FORA

DOUTORADO EM FÍSICA

**Theoretical characterization of graphene and other 2D materials**

**SAIF ULLAH**

JUIZ DE FORA

DEPARTAMENTO DE FÍSICA

JANUARY 22, 2020

**Theoretical characterization of graphene and other 2D materials**

**SAIF ULLAH**

Tese submetida à banca examinadora, para conclusão do Curso de DOUTORADO EM FÍSICA,como parte dos requisitos necessários para a obtenção do título de Doutor.
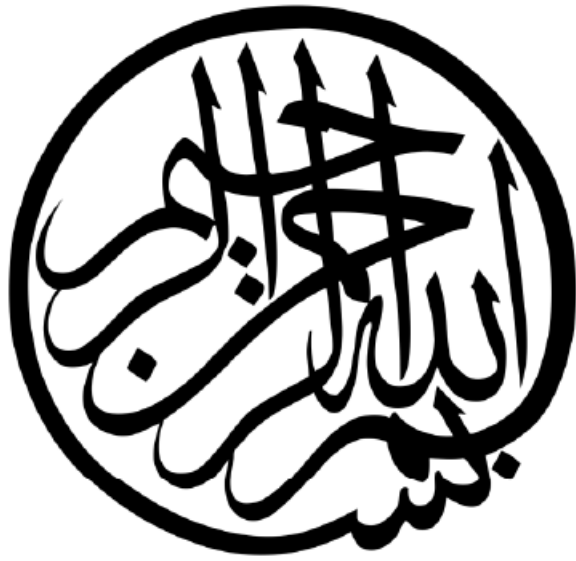
Aprovado em: 22/01/2020

Por:

_____

Orientador: Prof. Dr. Fernando Sato

_____

Prof. Dr. Pedro Alves da Silva Autreto

_____

Prof. Dr. Erix Alexander Milán Garcés

_____

Prof. Dr. Valdemir Aeneas Ludwig

_____

Prof. Dr. Daniel Vasconcelos Pazzini Massote

**(In the name of Allah, the Most Gracious, the Ever Merciful)**


"Read in the name of your Lord"

Al-Qur'an (96:1)


Al-Alaq

# Dedication

Dedicated to my

Mother, Mothers, Family, and Friends,

Without whom I am nothing.

And to all of those who work for the benefits of humankind.

# Declaration

This thesis includes several published papers from various publishers and for that reason, special permission was taken from the relevant publishers despite the fact that most publishers allow you to use your published work in your thesis. I'm extremely grateful to them.

All the papers are properly cited and full credit is given to all the used articles in this thesis.

Full credit should be given to the corresponding article(s) in case of using any part of this thesis.

# Acknowledgements

"Read, in the name of your Lord who created. Created man from a clinging substance. Read, your Lord is the Noblest and most Generous, Who taught by the pen. Who taught man what he did not know." (Qur'an, 96:1-5).

First and foremost, I'm exceedingly thankful to Allah Almighty for blessing me with everything I might not deserve and especially bringing that day in my life which is humongous for my family.

I wish to express my sincere appreciation to my supervisor, Professor Fernando Sato, who gave me free-hand to work and, consequently, a fruitful outcome appeared in the form of more than 20 research articles. I remember quite vividly when on the very first day of my Ph.D., Sato told me "you need to work independently and I want 5 papers". In a couple of months when I wrote my first article and informed him about that, his reaction was worth watching. From that day, I was given a free-hand of doing whatever I want to do. However, he kept on changing my research goal and every time he used to add 5 more articles to that. He did not make me feel even once that he is my boss rather we were friends from the very beginning. Thank you very much for providing me this opportunity and believing in me.

I'm unable to find suitable words to thank Professor Pablo A. Denis, my teacher, colleague, friend, and family. You have a great part in trimming and modifications in my personality. Without your help, motivation, and guidance, I would not be able to reach the point I'm standing now. You made me distinguished from my peers. Thanks for providing me every support I needed and above all, thanks for treating me like your family. I devilishly enjoyed the moments I spent there in Uruguay where I found that my host is as hospitable as a Pakistani in general and a Pashtun in particular. I still feel the taste of that pizza made by your great mother. I see my own parents in them. I look forward to seeing you soon in Hunza. Finally, I would like to say that your lab is way too cold and, furthermore, too many white Toblerone is not good for health.

I'm extremely thankful to two of my collaborators and best friends, Professor Rodrigo B. Capaz and Professor Marcos G. Menezes, from whom I learned a lot. Whenever I have any kind of problem, I just ask via email or WhatsApp and in a few moments, I get my answers. There is an unexplainable joy working with so dynamic, knowledgeable, and friendly people. Rodrigo, thanks for making your presence possible in our workshops even on the short notices. Rodrigo and Marcos, thank you for your valuable time and support.

I would like to pay my deepest gratitude to my family, oh my God! What a family I got. My Ph.D. happened because of my mother, the biggest reason for my higher studies.

I and all my siblings got lucky for having the unconditional love of six "mothers", no one can even think how lucky we are. I'm literally unable to write anything about them as there are no such words in any dictionary that can justify their indubitable love. I'm thankful to my father for not appreciating anything which keeps me motivated for doing better and better. My father is a perfectionist and he really knows "something about everything and everything about something". I'll continue my hard work and I hope that one day I'll hear the golden words "good job" from my father. Thank you very much for providing every possible resource and thanks for being a best buddy (most of the time) and inspiring Dad rather than a bossy father. My father is like my lighthouse who always stand firm in troubled seas and raging water. I seek my path in your shine. I'm grateful to my elder brother Asad, who is more like a friend, for taking care (of the financial requirement) of the family. I'm thankful to my sisters for being strong and making me even stronger. Fozia, I learned how to stay calm even in the worst phases of life. Nasima, you are a great sister and friend and I would say you are an "iron-lady". Ghazala, I learned from you that "life is too short to be taken seriously". Nida, thanks for teaching me "it's never too late". Ayaz, thanks for taking care of the Family. Maria, thank you very much for your prayers. You are always there for me.

I got lucky in the "department" of friends that I always get friends larger than life. I would like to thank Vahid for being such an amazing friend. João, you are like a brother, I wish I would become as kind as you. Hamid and Josiel, you did not make me feel that I'm away from family. Max, you are a great colleague and friend. Geissy, Isis, Thamiris, you are a great company. Ana, thanks for such a good time. Deliane, I'm really grateful for having you as a friend and your free-of-cost advises regarding my dental health. Erix and Yuli, you took care of me like a family and according to Stefano, you are my grandparents. Thanks for making Pakistani food for me almost every week. I'm literally thankful to each and everyone, including students and professors, in the department of physics. Finally, I wish to thank all the people whose assistance (directly or indirectly) was a milestone in the completion of this project.

"A father gives his child nothing better than a good education".

Prophet Muhammad (S.A.W)

# Resumo

Nesta tese, estudamos diversos aspectos do grafeno e outros materiais 2D por meio de cálculos de primeiros princípios baseados na Teoria do Funcional da Densidade (DFT em inglês). Inicialmente, propomos dois modelos de dopagem em grafeno para a abertura de gaps de forma eficiente. Além disso, estudamos pela primeira vez dopantes triplos em grafeno, o que é útil para o desenho de propriedades eletrônicas e para o aumento de sua reatividade química.

Em uma segunda frente, estudamos a possibilidade de se utilizar grafeno mono-dopado e bi-dopado como ânodo em baterias baseadas em metais alcalinos (lítio, sódio e potássio). Além disso, descobrimos que o fosteto de boro hexagonal ($h$BP) e o arseneto de boro hexagonal ($h$BAs) possuem excelentes propriedades eletroquímicas que são desejáveis em ânodos eficientes. Verificamos que todos os sistemas propostos apresentam uma ampla capacidade de armazenamento em comparação com outros ânodos conhecidos.

Em outra frente, investigamos detalhadamente as propriedades estruturais, térmicas, dinâmicas, eletrônicas e ópticas de monocamadas de $h$BX (X = P, As), monocamada $Be_3N_2$, e o boroxino ($B_3O_3$), um material que apresenta buracos em sua estrutura cristalina. Tais investigações representam um enriquecimento importante à família de materiais 2D.

Além disso, estudamos a estabilidade e as propriedades optoeletrônicas de diversas hetero-estruturas de van-der-Walls (vdW), incluindo multicamadas de $h$BP, $h$BAs e combinações, onde verificamos uma grande tunabilidade. Consideramos ainda diferentes heteroestruturas baseadas em $SiC_3$ e $h$BN de forma a investigar o potencial do $SiC_3$ como um substituto para o grafeno em dispositivos nanoeletrônicos. Verificamos que a aplicação de um campo elétrico externo nessas heteroestruturas leva à abertura de um gap com maior magnitude e tunabilidade em comparação aos gaps encontrados em heteroestruturas baseadas em grafeno e $h$BN.

Finalmente, investigamos os efeitos de uma dopagem substitucional na monocamada de $h$BN. Observamos que a estrutura de níveis de energia induzidos pela impureza dentro do gap é bem exótica, apresentando uma forte dependência com a posição de sub-rede ocupada pela impureza e com o seu comportamento como doadora ou aceitadora. Por exemplo, quando uma impureza aceitadora substitui um átomo de nitrogênio, observa-se uma forte interação entre os vales, resultando em um estado fundamental não-degenerado. Por outro lado, quando uma impureza aceitadora substitui um átomo de boro, verifica-se

uma fraca interação entre vales e um estado fundamental quase duplamente degenerado. Observamos ainda que impurezas doadoras se comportam de forma similar.

## Abstract

In this thesis, various aspects of graphene and other 2D materials were studied by means of first-principles density functional theory (DFT) calculations. Initially, we propose two types of doping models in graphene for efficient band gap opening. In addition, we study triple dopants in graphene for the first time which is useful for the designing of the electronic properties and increasing the chemical reactivity of graphene.

We also design several mono-doped and dual-doped graphene as potential anode materials for alkali-based (lithium, sodium, and potassium) batteries. Moreover, it is found that hexagonal boron phosphide ($h$BP) and hexagonal boron arsenide ($h$BAs) possess excellent electrochemical properties that are desirable for efficient anode materials. All of these proposed systems offer large storage capacities in comparison with the other famous anode materials.

In addition, we report monolayer BX (X=P, As) derivatives, monolayer beryllium-nitride ($Be_3N_2$), and 2D holey boroxine ($B_3O_3$). In detail, the structural, thermal, dynamical, mechanical, electronic, and optical properties were systematically investigated and carefully examined. These theoretical investigations considerably upgrade the family of 2D materials.

We inspect the stability and the electronic and optical properties of various vdW-heterostructures including ($h$BP), ($h$BAs), and their derivatives which offer tunable optoelectronic properties. Additionally, we consider $SiC_3$-$h$BN (vdW-heterostructure, and encapsulated $SiC_3$ in $h$BN) as a potential replacement for graphene in nanoelectronics. Furthermore, the external electric field provides a great tunability of the gaps which is somewhat missing (or weaker) in the graphene-$h$BN bilayer.

Finally, we investigate the effect of substitutional doping in single layer $h$BN. The induced impurity level structure is quite exotic and strongly dependent on the sublattice position and its behavior as a donor or an acceptor. For example, for an acceptor replacing a nitrogen atom, a strong intervalley interaction is observed with a strong valley and spin splitting. Conversely, when a boron atom is replaced with an acceptor, a much weaker intervalley interaction is observed with near-valley-degenerate levels. The behavior of the donor impurities is found to be the same.

**Key-words**: DFT; Graphene; 2D Materials and vdW heterostructures; Alkali-based batteries; Defects.

# Resumen

En esta tesis se estudian diferentes aspectos del grafeno y otros materiales bidimensionales por medio de cálculos teóricos. Inicialmente, se proponen dos tipos de dopado de grafeno. El primero, llamado dopado hexagonal, es muy efectivo para abrir un band gap, con una mínima concentración de dopante. En segundo involucra la introducción de tres dopantes en forma simultánea, que también es útil para manipular las propiedades electrónicas del grafeno además de aumentar su reactividad química con respecto al grafeno puro.

También proponemos grafeno dopado como ánodo para baterías de litio, potasio o sodio. Además del grafeno consideramos otros materiales bidimensionales para diseñar ánodos. En este sentido, seleccionamos fosfuro de boro hexagonal ($h$BP) y arsenuro de boro hexagonal ($h$BAs). Todos estos materiales propuestos ofrecen gran capacidad de almacenamiento em comparación com otros anodos mas populares.

Se estudiaron las propiedades electrónicas de materiales bidimensionales diferentes al grafeno como el BP, el BAs y sus derivados, que ofrecen excelentes propiedades ópticas. Adicionalmente, se estudiaron heteroestructuras de siligraphene $SiC_3$ y nitruro de boro hexagonal $h$BN como materiales que pueden ser utilizados en lugar del grafeno en nanoe- lectrónica. Además, consideramos $SiC_3$-$h$BN (vdW-heterostructure, and encapsulated $SiC_3$ in $h$BN) como reemplazante del grafeno en nanoelectrónica. Interesantemente, gracias al uso de un campo eléctrico es posible modular el gap en la heteroestructura tricapa, algo difícil para el bicapa.

Finalmente, se estudiaron las propiedades electrónicas de $h$BN dopado.Observamos que la estructura de los niveles de energía inducida por la impureza dentro de gap es bastante exótica, presentando una fuerte dependencia de la posición de subred ocupada por la impureza y su comportamiento como donante o aceptor. Por ejemplo, cuando una impureza de aceptación reemplaza un átomo de nitrógeno, existe una fuerte interacción entre los valles, lo que resulta en un estado fundamental no degenerado. Por otro lado, cuando una impureza que acepta reemplaza un átomo de boro, hay una interacción débil entre los valles y un estado fundamental casi doblemente degenerado. También observamos que las impurezas donantes se comportan de manera similar.

**Palabras-clave**: teoría de los funcionales de la densidad; grafeno; Heteroestructuras de Van der Waals; Baterías alcalinas.

# LIST OF FIGURES

# LIST OF ABBREVIATIONS

**BSCCO** *Bismuth strontium calcium copper oxide*

**2D** *Two-dimensional*

**VBM** *Valence band maximum*

**CBM** *Conduction band maximum*

**FETs** *Field-effect-transistors*

**LIBs** *Lithium-ion batteries*

**SIBs** *Sodium-ion batteries*

**KIBs** *Potassium-ion batteries*

**hBN** *hexagonal boron nitride*

**hBP** *hexagonal boron phosphide*

**hBAs** *hexagonal boron arsenide*

**vdW** *Van der Waals*

**DFT** *Density functional theory*

**DFT-D** *Dispersion corrected density functional theory*

**CNTs** *Carbon nanotubes*

**ORR** *Oxygen reduction reaction*

**HER** *Hydrogen evolution reaction*

**DDG** *Dual-doped graphene*

**TDG** *Triple-doped graphene*

**DZP** *Double-zeta with polarization*

**LCAO** *Linear combination of atomic orbitals*

**NC** *Norm-conserving*

**PPs** *Pseudopotentials*

**TM** *Troullier-Martins*

**LDA** *Local density approximation*

**GGA** *Generalized-gradient approximation*

**PAW** *Projected augmented wave*

**SSSP** *Standard solid-state pseudopotentials*

**OCV** *open-circuit voltage*

**DOS** *Density of states*

**AIMD** *Ab-initio molecular dynamics*

**ELF** *Electron localization function*

**STM** *Scanning tunneling microscopy*

**DFPT** *Density functional perturbation theory*

**UV** *Ultra-violet*

**TB** *Tight-binding*

**EM** *Effective-mass*

**IIE** *Interlayer interaction energy*

Part I

Introduction and Literature Review

# 1 INTRODUCTION

The entire organic chemistry is based on carbon (C), which is the raw material for any kind of life on planet earth (at least). The extraordinary importance is given by nature to C also reflects in its position in periodic table where C is leading both the conventional semiconductors, silicon (Si) and germanium (Ge). The nature of C-C bond is so pliable that there is a (possibility of a) vast range of C-based structures with substantial diversity in the physical properties. That being said, these physical properties are largely associated with the dimensionality of the C-based structures. When C atoms are organized in a strict two-dimensional (2D) flat disk with sp2 hybridization in a honeycomb hexagonal crystal lattice, the resultant structure is called graphene or more precisely, monolayer graphene. Graphene is not only important due to its significant role in understanding other allotropes of C but is also the basic building block or unitcell of these allotropes with different dimensions. That being said, the stacking of graphene in layers form will result in 3D graphite, whereas, the rolling of graphene sheet along a particular direction, to make it a hollow tube or a bangle, will result in 1D carbon nano-tube (CNT). In addition to this, by introducing pentagons in graphene sheet and by wrapping around that sheet will cause the formation of a spherical molecule known as fullerene or bucky-ball, a 0D dimensional allotrope of C. All these different allotropes of C can be viewed in Figure 1.
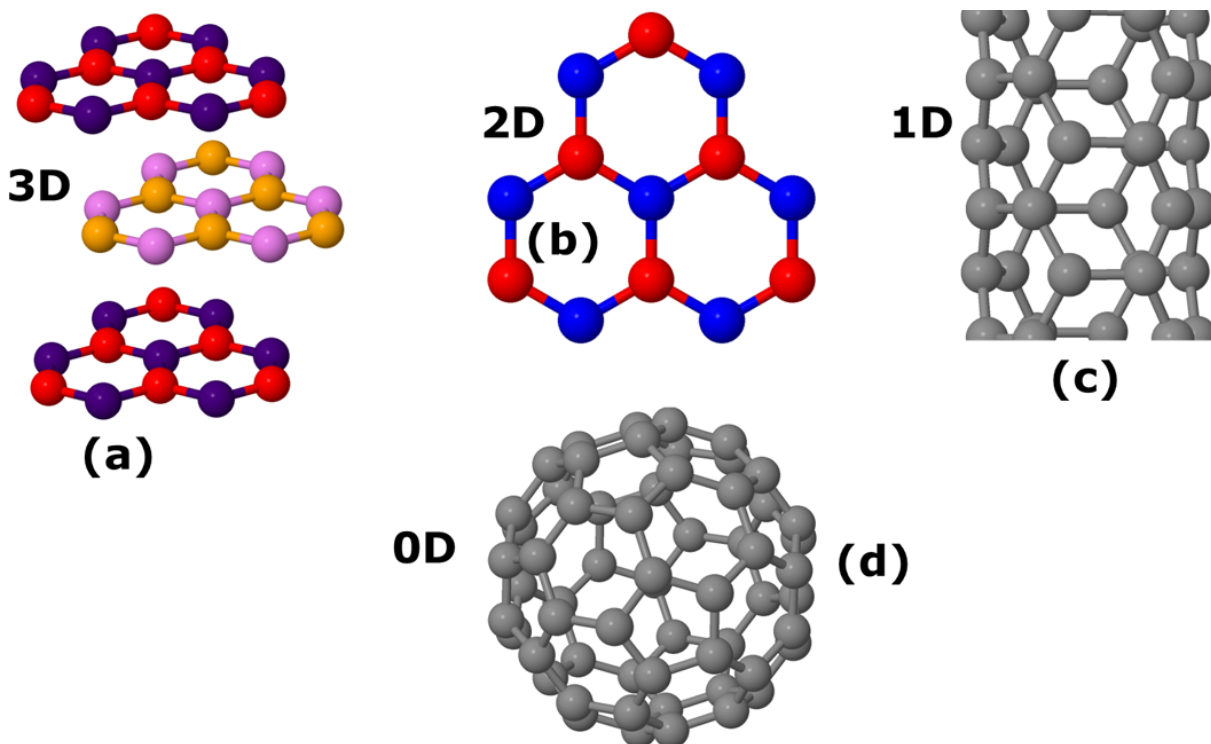


Figure 1 – Various allotropes of C (a) 3D graphite, (b) 2D graphene, (c) 1D nanotube, and (d) 0D fullerene or buckyball [1].

The isolation of monolayer graphene can be dated to time of invention of graphite pencils or the use of graphite as a writing medium (gadget) [5]. Having said that, writing with a graphite-pencil actually produces flakes of graphite and somewhere in those flakes, one might already have produced a single layer of graphite or graphene. However, it is not known that when a single layer was isolated from the bulk graphite due to the absence of such powerful tools that can penetrate into the carbon dust produced by the graphite pencil and look for the monolayer (or a few-layer) graphene.

## 1.1 Story of monolayer graphene

The story of a single layer of graphite (graphene) begins in 1947 when Wallace studied for the first time, with the help of the tight-binding method, the then called single layer of graphite, now known as graphene [6]. The existence of a strictly 2D material was already questioned by Landau and Peierls theoretically [7, 8]. In their theory, it was concluded that 2D materials would be thermodynamically unstable and, therefore, could not exist or sustain. The reason for this instability was given that at any finite temperature, the displacement of atoms will become equivalent to their interatomic separations due to the divergent participation of thermal fluctuations. Later on, this confirmation was reported in the form a whole set of experimentation carried out by Mermin [9]. This is in line with the fact that a decrease in the thickness of a material will cause an abrupt decay in the melting temperature and, therefore, at a thickness of a few dozens of atomic layers, the material becomes unstable [10, 11]. Consequently, the 2D structures were considered as an essential slice of the 3D bulk structures achieved by the epitaxial growth on single-crystals of somewhat matched crystal lattices. That being said, the existence of 2D materials in the absence of such a 3D support was not expected until 2004. In 2004, Geim and Novoselov, by "breaking the spell" synthesized (exfoliated) and reported a single isolated layer of graphite (or graphene) [12]. They used a quite simple method of micromechanical cleavage (scotch tape method) to isolate graphene from the bulk graphite as the non-covalently bonded layers (or sheets) in graphite are glued together by weak van der Waals (vdW) interactions. This can be understood by peeling off the skin of graphite down to atomic level. Such crystals (graphene, monolayer hexagonal boron nitride (hBN), and the half-layer BSCCO) can be acquired in various ways, such as deposition on a non-crystalline substrate, as suspended membranes, and in liquid suspension [13].

## 1.2 Structural properties

As mentioned above that C has a quite unique place in the periodic table and it comes at number 6 which means that C atoms are having 6 electrons as shown in Figure

2a [2]. As can be seen, the electrons around the nucleus of a C atom are arranged in three orbitals ($1s$, $2s$, $2p$) in which the two electrons in the first orbital ($1s$) are considered as core electrons, whereas, the rest of the four electrons in the two outer shells are deemed as valence electrons. One can think of these electrons in the arrangement of $1s^2 2s^2 2p_x^1 2P_y^1 2p_z^0$, as given in Figure 2b. The energy levels $2p_x$ and $2p_y$ are equivalent to that of $2p_z$ but for simplicity, the $2p_z$ level is shown without an electron. The flexibility of C-C bonding (as mentioned earlier) is the result of the electronic arrangement which can make $sp$, $sp^2$, and $sp^3$ hybridized-bonding. In the case of $sp^2$ hybridization, a C atom shares three of its electrons with the neighboring three C atoms forming a covalent bond which results in a hexagonal honeycomb network of C atoms named as monolayer graphene. These $sp^2$ hybridized orbitals which are made of $2s$, $2p_x$, and $2p_y$ form strong in-plane $\sigma$ bonds with the bond length of 1.42 Å which is shorter than the C-C bond in $sp^3$ hybridized diamond. The excellent mechanical properties of graphene are a consequence of this short $\sigma$ bonding, keeping in mind the Young's modulus and tensile strength of 1 TPa and 130.5 GPa, respectively [14]. There are two nonequivalent C atoms 1.42 Å apart in the unitcell of graphene with a lattice constant of 2.46 Å. One can think of the unitcell as two triangles mingled together as shown in Figure 2c. Due to the presence of 4 valence electrons, three of them are responsible for an in-plane $\sigma$ bonding, whereas the fourth one is in charge of creating an out of plane (perpendicular to the plane of graphene) $\pi$ bond and associated with each of the C atoms (see Figure 2(d)). In addition, this makes half-filled $\pi$-$\pi$* bands which is the consequence of the extraordinary electronic properties of graphene.

## 1.3 Electronic band structure

In the above section, it is mentioned that due to the single electron left after making three in-plane sigma bonds, an out of plane $2p_z$ orbital is formed which connects with the neighboring C atoms through covalent bonding, results in the realization of a $\pi$ band. This half-filled $\pi$-$\pi$* band is the basis for the unusual electronic structure and exceptional electronic properties of graphene. The first report on the electronic structure of single layer of graphite is dated back to 1947 when Wallace reported the exceptional semimetallic behavior with the help of the tight-binding method [6]. There are two primitive lattice vectors when C atoms are arranged in a honeycomb hexagonal lattice as shown in Figure 3a [3]. One can write these vectors as:

$$\vec{a}_1 = \left(\frac{a}{2}\right)(3, \sqrt{3}) \text{ and } \vec{a}_2 = \left(\frac{a}{2}\right)(3, -\sqrt{3}) \tag{1.1}$$

where a is the C-C bond length in graphene and is equal to 1.42 Å. The reciprocal lattice vectors can be expressed as:
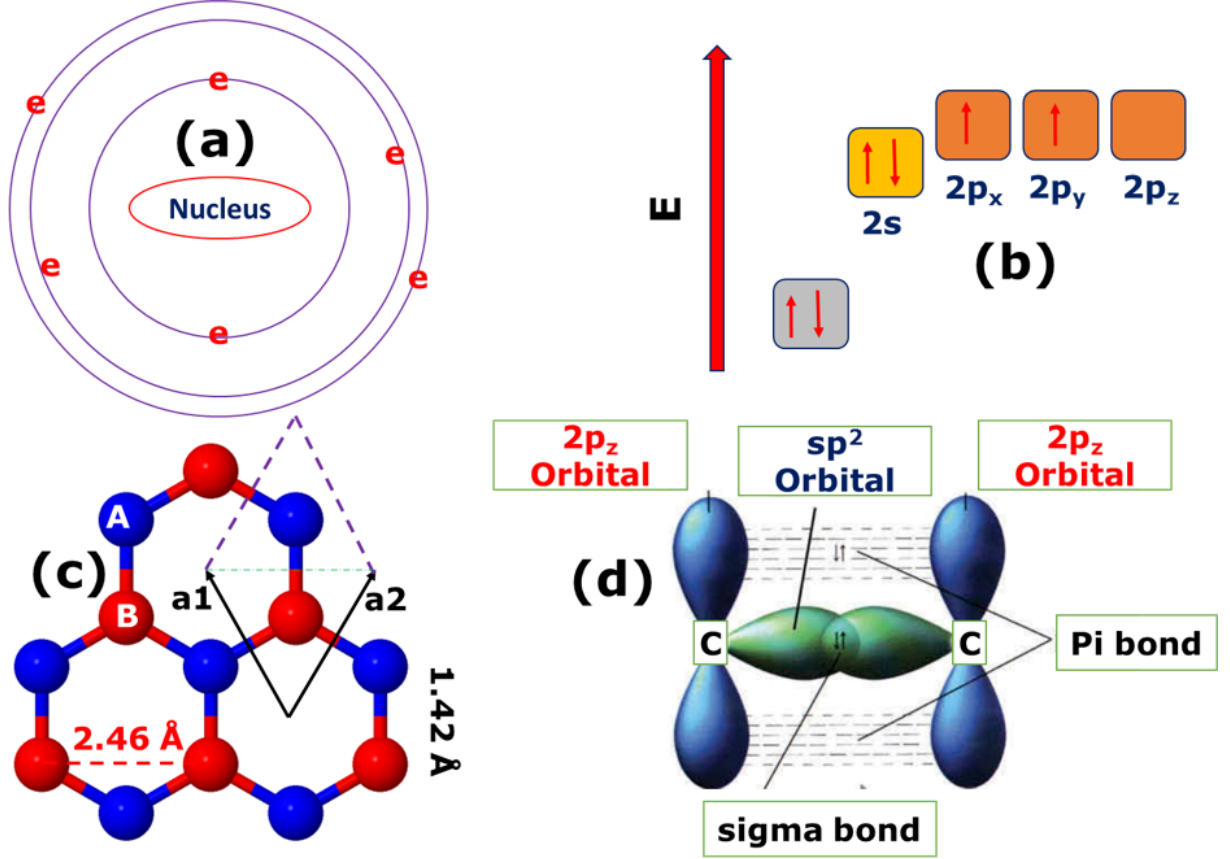
Figure 2 – Representation of the atomic structure of C (a). Energy levels of electrons in C. The hexagonal honeycomb lattice of graphene where sublattice sites A and B are shown along with the lattice vectors **a1** and **a2** (c). The formation of $\sigma$ and $\pi$ bonds as a result of $sp^2$ hybridization (d) [2].

$$\vec{b_1} = \left(\frac{2\pi}{3a}\right)(1, \sqrt{3}) \text{ and } \vec{b_2} = \left(\frac{2\pi}{3a}\right)(1, -\sqrt{3}) \tag{1.2}$$

The edges of the Brillouin zone of graphene denoted by $K$, and $K'$ are of significant interest which carry interesting physics and are called Dirac points where valence band minimum (VBM) and conduction band maximum (CBM) meets and form a Dirac cone.

As we know from the definition of kinetic energy:

$$E = \frac{mv^2}{2} = \frac{(mv)^2}{2m} = \frac{p^2}{2m} \tag{1.3}$$

where $p$, $v$, $m$, and $E$ are momentum, speed, mass, and energy, respectively. This means that the energy-momentum ($E_K$) relation is quadratic and should be parabolic. However, in graphene, we see a linear $E_K$ dispersion relation which is:

$$E = vp \tag{1.4}$$
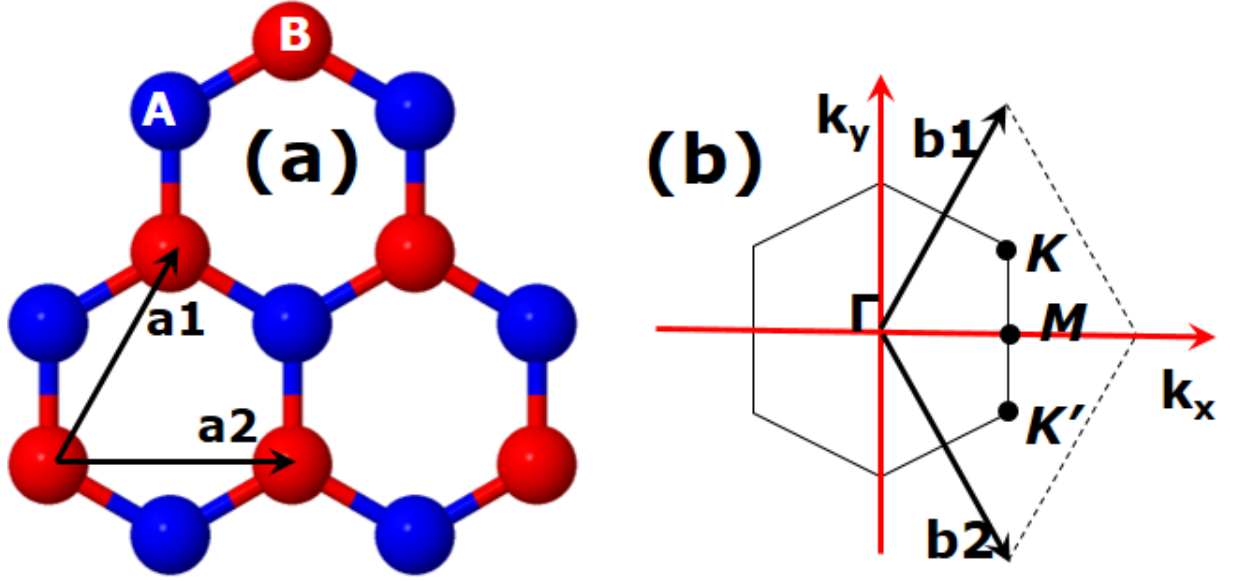
Figure 3 – (a) hexagonal honeycomb crystal structure of graphene with the primitive lattice vectors **a1** and **a2**. (b) The corresponding Brillouin zone with $K$ and $K'$ where Dirac cone is located [3].

And for comparison with light:

$$E = h\nu = \frac{hc}{\lambda} \tag{1.5}$$

Also, we know that de Broglie wavelength is:

$$p = \frac{h}{\lambda} \tag{1.6}$$

So,

$$E = cp \tag{1.7}$$

which means that E is proportional to p. Consequently, this is comparable to particle of light rather than the massive particle as $E = cp$, where $c$ is the speed of light. This means that graphene is not only a semimetal or a zero bandgap semiconductor but also exhibits some exciting physics including the relativistic effect with the charge carrier being massless. In Figure 4, the full band structure of graphene is shown. Further details can be found in earlier reviews [3, 15].

## 1.4 Graphene in nanoelectronics

The advancement of existing technology is related to the discovery of new materials or the modification of the existing materials. For that reason, it is obvious to see if
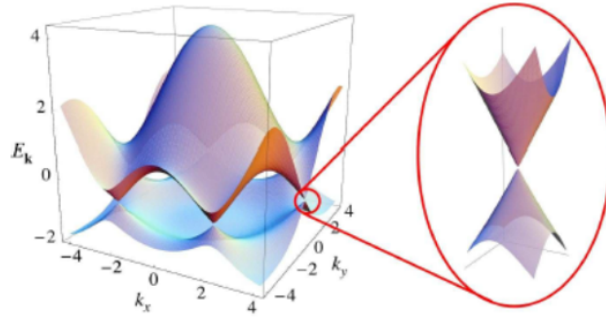
Figure 4 – Electronic band structure of a single layer of graphite (graphene). The zoom-in part of the Dirac cone is also presented [3].

graphene can be a potential candidate to revolutionize the electronics industry. Graphene has certainly an edge over the rival materials by virtue of its remarkable properties and prospective applications [12, 16–19]. The behavior of electron and hole motion in a semiconductor is usually studied by doping it with a foreign impurity. However, at the Dirac point in graphene, electrons change into holes and contrariwise. In addition, the energy-momentum dispersion relation in an ordinary semiconductor is parabolic (quadratic relation), whereas, in graphene, we see a linear dispersion. This unusual linear dispersion gives rise to the exceptional electronic properties of graphene. The incredible charge carrier mobility, which is 2-3 times higher than the counter semiconducting materials, is as high as 2 X $10^5$ cm$^2$/Vs [20, 20]. Furthermore, at exceedingly low (even at zero) carrier concentration, graphene still offers a finite conductivity [17, 21]. Another advantage of using graphene in nanoelectronics is the atom-thick size of graphene which is critical for the small-sized (and lighter) electronic devices. That being said, the computational power of nowadays smartphones are much larger than the combined computational power of the moon-mission which occupied the space of a big room, when NASA in 1969, sent the first-men on moon [22]. Besides, this computational power comes in much more sophisticated devices where all the information is at your finger-tips and, additionally, the (wider) availability to most human beings.

The unique electronic structure of graphene, which is responsible for the exceptional electronic properties at the same time makes it difficult to be used directly in nanoelectronic devices, such as field-effect-transistors (FETs). As mentioned, the VBM and the CBM meets at the Dirac point leaving graphene as a zero bandgap semiconductor. Now, it is well-known that a sizeable gap is crucial to control the on/off ratio of a FET. Consequently, the zero-gap character of graphene is a restriction in utilizing it in nanoelectronics. However, there are several solutions that can adequately address this hurdle. These include the confinement of electrons by employing the superstructures of graphene, deposition of graphene on various substrate, adsorption of atoms or molecules, and the substitutional doping. These methods are discussed in chapter 2.

## 1.5  **Alkali-based secondary batteries**

We are heavily counting on fossil fuels in order to meet our day-to-day energy expenses. In this context, the basic and fundamental question which bang our mind is whether fossil fuels do have an ending or not? If yes, then how long will it take to run out of all the available resources? Since the growth in the World population has a direct impact on the consumption of energy resources and, consequently, the energy demand will be doubled by 2050. In addition, the pollution caused by $CO_2$ and various other greenhouse gases which are produced as a consequence of the use of fossil fuels, are of significant concern. Thus to avoid the disturbance in eco-system, minimize climate change, and prevent thermal pollution, looking for other energy resources as alternatives, which are renewable and environmental-friendly, become critical and of utmost importance. Some of these alternatives are the energy storage, which includes supercapacitors and batteries, and conversion, which comprises of fuel-, and solar-cells. Besides, the broader application scope of the secondary batteries (rechargeable batteries) makes it one of the interesting fields in energy storage and conversion. Due to some interesting features, such as high energy density, long cycle life, and favorable size, lithium-ion batteries (LIBs) have proven its worth after the first-ever pioneering launch in 1991, thanks to SONY [23–25]. Nowadays, LIBs are utilized in smartphones, laptop computers, and camcorders, just to name a few. In such batteries, the positive electrode (or cathode) material is $LiCoO_2$, whereas, the negative electrode (or anode) material is graphite [26]. There are two main issues with that sort of arrangement, one with the graphite and another with the Li itself. That being said, graphite offers only an inadequate storage capacity of 372 mAh/g for Li, which is not suitable for practical applications, such as in hybrid electric cars [24, 27]. Since there is not enough availability of Li and according to demand and supply rule, the price of Li will be touching the sky [28]. Consequently, the replacement to Li becomes critical. Luckily, by virtue of their similar electrochemical systems, sodium-ion batteries (SIBs) and potassium-ion batteries (KIBs) become the center of attention because of much greater availability and non-toxicity [29–31]. However, the larger sizes of Na and K in comparison with Li make their intercalation quite difficult and for that reason, graphite offers an insufficient storage capacity of just 35 mAh/g for Na [32]. In that scenario, it becomes crucial to modify the current anode material or replace it with new materials.

## 1.6  **Other 2D materials**

The breakthrough experiment was not only limited to graphene but it led the foundation of a new class of materials. Several hundred materials have already joined the 2D family and it is still expanding [33]. Many of them share the same story as that of

graphene being a part of the 3D network (layered materials), whereas, some of them are a segment of the nonlayered parent materials. The 2D framework of various transition metal dichalcogenides, which consist of one (transition) metal and two chalcogen atoms, become quite a hot topic from the past decade or so [34, 35]. Moreover, by virtue of their significant potential applications in spintronics, nanoelectronics, optoelectronics, III-V compounds have proved their worth and are the sizzling research topics both in academics and in industries. Among them, the most popular is hexagonal boron nitride, the monolayer of which was synthesized just after the isolation of graphene, consist of boron (B) and nitrogen (N) which are the neighbors to C atom [36]. In addition to this, there are several other isoelectronic 2D materials that are yet to be synthesized but the growing attention from researchers already making them hot materials. They possess several interesting properties, such as sizeable and flexible band gaps, smaller effective mass values, excellent mobilities touching to the limit of graphene, etc. Those materials are BX (X= P, As, Sb), which have the potential to be used in nanoelectronics, optoelectronics, and in energy storage devices [37].

## 1.7 Van der Waals heterostructures

Let's take the case of TMDCs which offer a variety of flexible electronic properties themselves. That being said, we have superconducting $NbSe_2$, quantum spin-Hall insulator $WTe_2$, semiconductor $MoS_2$, etc [38, 39]. These materials can be combined with the wide gap semiconductor (or insulator) $h$BN, and of course, the semimetallic graphene to tailor the electronic properties to the desired level. All of the aforementioned materials are layered materials that are bonded through vdW interactions and interestingly, the 2D structures bear quite different properties in comparison with their 3D counterparts. By combining various materials with different properties in stacked configurations provide tremendous opportunities to design a vast number of materials with diverse properties. In fact, vdW heterostructures have become a sub-family of the 2D materials.

## 1.8 Defects

It is quite natural for any kind of material to have some defects as the defects-free system is hard to realize in real World. The nature of these defects can be intrinsic, which includes vacancies, anti-sites, interstitial, etc, or impurities [40]. The latter is present automatically while growing or synthesizing a material and can also be integrated manually. In order to tailor the optoelectronic properties of a material, the donor and acceptor states play a key role, which can be achieved by doping. As these wave-function act as recombination centers and thus critical for solar cells and light-emitting diode applications.

For example, in a classic semiconductor (bulk *h*BN), the replacement of a N atom with a C atom is a typical case, which induces prominent changes in photoluminescence and absorption spectra by the introduction of an extra peak (around 4 eV) associated with the transition between the impurity level and conduction band [41, 42]. In fact, a different picture is seen in a 2D material, such as monolayer *h*BN, in comparison with the bulk counterpart. In the monolayer, it is expected that the binding energies (of impurity levels) and valley splitting would be much larger (in comparison with the bulk counterparts) due to the nonhomogeneous and weaker screening. Thus, it is crucial to study in-depth nature of those impurity levels introduced inside the gap in *h*BN and related semiconductors.

## 1.9 Theoretical framework

In this work, we mostly rely on the first-principles density functional theory (DFT) method, which is one of the most efficient and popular quantum mechanical models, to study various properties of different 2D materials associated with electronic structure calculations. As any system of interacting particles consists of positively charged nuclei and negatively charged electrons. In order to enable Schrödinger equation to solve many-body problem, several approximations are needed. As nuclei are very heavier in comparison with the electrons and, additionally, the behavior of valence electrons is not similar to that of core electrons, hence, can be treated differently. It should be noted that DFT calculations are based on first-principles (or ab-initio) which are beneficial in electronic structure calculations as atomic species and reasonable initial atomic positions should be provided without the use of any (adjustable) empirical parameters. A concise detail of the formalism, starting from the basic Schrödinger equation to the practical implementation of DFT, is given in chapter 3.

## 1.10 Publications

I published the following papers during my Ph.D.

1. **Saif Ullah**, Pablo A. Denis, Marcos G. Menezes, Fernando Sato: *Tunable and sizeable band gaps in $SiC_3$/hBN vdW heterostructures: A potential replacement for graphene in future nanoelectronics. Submitted*

2. **Saif Ullah**, Pablo A. Denis, Fernando Sato: *Theoretical investigation of various aspects of two dimensional holey boroxine, B3O3.* RSC Advances 09/**2019**; 9: 37526-37536., DOI: 10.1039/C9RA07338H

3. **Saif Ullah**, Fernando Sato, Marcos G. Menezes, Rodrigo B. Capaz: *Exotic impurity-induced states in single-layer h-BN: The role of sublattice structure and intervalley interactions.* Physical Review B 08/**2019**; 100 (8): 85427

4. **Saif Ullah**, Pablo A. Denis, Fernando Sato: *Non-trivial band gaps and charge transfer in Janus-like functionalized bilayer boron arsenide.* Computational Materials Science 08/**2019**; 170:109186., DOI:10.1016/j.commatsci.**2019**.109186

5. **Saif Ullah**, Pablo A. Denis, Marcos G. Menezes, Fernando Sato: *Tunable optoelectronic properties in h-BP/h-BAs bilayers: The effect of an external electrical field.* Applied Surface Science 07/**2019**; 493., DOI:10.1016/j.apsusc.**2019**.07.030

6. **Saif Ullah**, Pablo A. Denis, Fernando Sato: *Monolayer boron-arsenide as a perfect anode for alkali-based batteries with large storage capacities and fast mobilities.* International Journal of Quantum Chemistry 05/**2019**;, DOI:10.1002/qua.25975

7. **Saif Ullah**, Pablo A. Denis, Fernando Sato: *Coupled Cluster Investigation of the interaction of Beryllium, Magnesium, and Calcium with Pyridine: Implications for the Adsorption on Nitrogen-Doped Graphene.* Computational and Theoretical Chemistry 02/**2019**; 1150., DOI:10.1016/j.comptc.**2019**.01.015

8. **Saif Ullah**, Pablo A. Denis, Fernando Sato: *Adsorption and diffusion of alkali-atoms (Li, Na, and K) on BeN dual doped graphene.* International Journal of Quantum Chemistry 01/**2019**;, DOI:10.1002/qua.25900

9. **Saif Ullah**, Pablo Andres Denis, Rodrigo B. Capaz, Fernando Sato: *Theoretical characterization of hexagonal 2D Be3N2 monolayer.* New Journal of Chemistry 01/**2019**; 43(7)., DOI:10.1039/C8NJ05600E

10. **Saif Ullah**, Pablo A. Denis, Fernando Sato: *Hydrogenation and Fluorination of 2D Boron Phosphide and Boron Arsenide: A Density Functional Theory Investigation.* 12/**2018**; 3(12):16416-16423., DOI:10.1021/acsomega.8b02605

11. **Saif Ullah**, Pablo A. Denis, Fernando Sato: *Hexagonal boron phosphide as a potential anode nominee for alkali-based batteries: A multi-flavor DFT study.* Applied Surface Science 12/**2018**; 471., DOI:10.1016/j.apsusc.**2018**.12.020

12. **Saif Ullah**, Pablo A Denis, Fernando Sato: *Unusual Enhancement of the Adsorption Energies of Sodium and Potassium in Sulfur-Nitrogen and Silicon-Boron Codoped Graphene.* 11/**2018**; 3(11):15821-15828., DOI:10.1021/acsomega.8b02500

13. **Saif Ullah**, Pablo A. Denis, Fernando Sato: *Coupled Cluster and Density Functional Investigation of the Neutral Sodium-Benzene and Potassium-Benzene Complexes.* Chemical Physics Letters 06/**2018**; 706., DOI:10.1016/j.cplett.**2018**.06.028

14. **Saif Ullah**, Pablo A. Denis, Fernando Sato: *Adsorption of Sodium on Doped Graphene: A vdW-DFT study.* Current Graphene Science **2018**; 2(1), 35-44; DOI:10.2174/2452273202666180517101215

15. **Saif Ullah**, Pablo Andres Denis, Fernando Sato: *First-principles study of the dual doped graphene: Towards the promising anode materials for Li/Na-ion batteries.* New Journal of Chemistry 05/**2018**; 42(13)., DOI:10.1039/C8NJ01098F

16. **Saif Ullah**, Pablo A Denis, Fernando Sato: *Beryllium doped graphene as an efficient anode material for lithium-ion batteries with significantly huge capacity: A DFT study.* DOI:10.1016/j.apmt.**2017**.08.013

17. **Saif Ullah**, Pablo A. Denis, Fernando Sato: *Triple-Doped Monolayer Graphene with Boron, Nitrogen, Aluminum, Silicon, Phosphorus, and Sulfur.* ChemPhysChem 06/**2017**; 18(14)., DOI:10.1002/cphc.**2017**00699

18. **Saif Ullah**, Akhtar Hussain, Fernando Sato: *Rectangular and hexagonal doping of graphene with B, N, and O: a DFT study* †. RSC Advances 03/**2017**; 7(26):16064., DOI:10.1039/c6ra28837e

### 1.11   **Other publications**

19. Santunu Ghosh, **Saif Ullah**, João P.A. de Mendonça, Luciano G. Moura, Marcos G. Menezes, Leonã S. Flôres, Tiago S. Pacheco, Luiz F.C. de Oliveira, Fernando Sato, Sukarno O. Ferreira: Electronic properties and vibrational spectra of (NH4)2M"(SO4)2•6H2O (M" = Ni, Cu) Tutton's salt: DFT and experimental study. DOI:10.1016/j.saa.**2019**.04.023

20. Santunu Ghosh, Alessandro H Lima, S Flôres, Tiago S Pacheco, Ananias A Barbosa, **Saif Ullah**, P A De Mendonça, F C Oliveira, Welber G Quirino: Growth and characterization of ammonium nickel-copper sulfate hexahydrate: A new crystal of Tutton's salt family for the application in solar-blind technology. Optical Materials 09/**2018**; 85:425-437., DOI:10.1016/j.optmat.**2018**.09.004

21. Eduily B. V. Freire, João Paulo A. de Mendonça, **Saif Ullah**, Geórgia M. A. Junqueira, Fernando Sato: Exploring the effect of substitutional doping on the electronic properties of graphene oxide. Journal of Materials Science 05/**2018**; 53(35)., DOI:10.1007/s10853-018-2076-z

22. Akhtar Hussain, **Saif Ullah**, M. Arshad Farhan, Muhammad Adnan Saqlain, Fernando Sato: Structural, electronic, and magnetic properties of non-planar doping of BeO in graphene: A DFT study. New Journal of Chemistry 08/**2017**; 41(19)., DOI:10.1039/C7NJ00328E

23. Akhtar Hussain, **Saif Ullah**, M. Arshad Farhan: Fine tuning of band-gap of graphene by atomic and molecular doping: A density functional theory study. RSC Advances 05/**2016**; 6(61)., DOI:10.1039/C6RA04782C

24. **Saif Ullah**, Akhtar Hussain, WaqarAdil Syed, Muhammad Adnan Saqlain, Idrees Ahmad, Ortwin Leenaerts, Altaf Karim: Band-gap tuning of graphene by Be doping and Be, B co-doping: A DFT study. RSC Advances 06/**2015**; 5(69):55762., DOI:10.1039/c5ra08061d

## 1.12  **Thesis organization**

This thesis is divided into the following parts.

- Chapter 1 provides a background, introduction, and problem statement.

- Chapter 2 covers the necessary literature review.

- Chapter 3 deals with the theoretical background and technical aspects.

- Chapter 4 contains the electronic properties of doped graphene.

- Chapter 5 deals with the electrochemical properties of doped graphene

- Chapter 6 covers electrochemical properties of 2D materials beyond graphene

- Chapter 7 includes theoretical characterization of other 2D materials

- Chapter 8 includes vdW heterostructures

- Chapter 9 contains defects

- Chapter 10 covers main highlights

## 2 Literature review

### 2.1 Electronic properties of doped graphene

As mentioned in the first chapter that the main hurdle in using graphene in nanoelectronics is the absence of a bandgap around the Dirac point and, furthermore, the opening of a sizeable gap is crucial. This shortcoming can be addressed in a variety of ways. One way is the synthesis of graphene superstructures, such as nanoribbons [43, 44], quantum dots [45, 46], and nanomeshes [47, 48]. In all these superstructures, bandgaps can be introduced due to the quantum confinement effect. However, control over the sizes of these structures is a difficult assignment. Another way of inducing a bandgap in graphene is the decoration of graphene surface with suitable atoms or molecules. This includes the (physical) adsorption of atoms (or molecules) or the chemical functionalization of graphene (mostly with H and F) [49–52]. In addition, the most efficient technique is the substitutional doping of graphene with the integration of foreign impurities. Since C belongs to group IV so it can be doped with group III (B) and group V (N) impurities to achieve $p$-type and $n$-type doping, respectively. In addition, it is easier to replace a C atom with B or N as they are the neighbors and are of (nearly) the similar size to that of C. Panchakarla *et al.* reported the synthesis of B and N doped graphene [53]. It is shown that B and N doping introduced $p$- and $n$-type doping in graphene, respectively [54]. Moreover, the linear dispersion of Dirac cones is preserved up to a greater extent. In addition, the replacement of a C atom with an O atom can induce a bandgap of 0.50 eV. The F impurity caused a magnetic moment of 0.71 $\mu_B$. Additionally, all these dopants settled well in the planar structure of graphene except F dopant. Besides, the systemic doping of B and N in graphene plane is reported by Rani and Jindal [55]. The authors reported that the value of bandgap opening depends on the relative positions of B (or N) atoms in the structure of graphene. Furthermore, the doping of Be, which is the second neighbor of C and belongs to group II, induced $p$-type doping in graphene [56]. Additionally, Be doping was found to be more efficient than B doping in terms of opening the gap around the Dirac point. Nonetheless, it was also articulated that impurity atoms should not only be integrated on the same sub-lattice sites in graphene but they should also be employed at specific configuration (hexagonal doping) in order to open a maximum bandgap. Besides the integration of $2p$ elements, the incorporation of $3p$ elements has also been widely studied. Among them, the synthesis of P- and S-doped graphene is quite common and there are numerous studies reporting the integration of P and S in graphene [57–67]. In addition, there are various experimental and theoretical studies on the doping of Si in graphene [57, 58, 68–72]. The synthesis of aluminabenzene is also reported earlier [73]. It is shown that P and S impurity can create a sizeable bandgap in

graphene. Apart from that, the replacement of C with bigger atoms (4p element) is also reported. To that end, graphene and carbon nanotubes (CNTs) doped with Se and Ge were synthesized and further explored for the oxygen reduction reaction (ORR) [74, 75]. Moreover, the electronic properties and chemical reactivity of graphene doped with Ga, Ge, As, and Se was systematically calculated theoretically [76]. These doped graphene systems provide flexible electronic properties with bandgap ranging from a few meV to a few eV. There are experimental reports on the doping of transition metals, such as Mn, Fe, Co, and Ni, in graphene [77–79]. These dopants can significantly enhance the electrocatalytic and magnetic properties of graphene. Nevertheless, much bigger atoms (Uranium and Thorium) can also be doped in graphene plane [80]. The experiments suggest that these impurities can alter the electrocatalytic activity of graphene and show excellent performance in ORR and hydrogen peroxide reduction. Besides, the individual integration of impurity atoms in graphene, another fascinating way to tune the properties of graphene is the simultaneous doping of two hetero-species. The most common type is the addition of B and N to the graphene geometry which can turn out be a promising material in terms of electronic and catalytic properties [81, 82]. In addition, it is predicted that Be-B codoped graphene systems have excellent electronic properties [56]. The electronic properties of graphene can also be engineered by employing Be and N at the same time [83]. Furthermore, two types of molecular doping, planar and non-planar doping, have also been explored [83, 84]. Besides, 2p elements can concomitantly be doped with 3p elements in the base of graphene. There can be various combinations among which P-N, S-N, and P-O are the most famous arrangements [85–87]. P-N dual doped graphene (DDG) is prepared experimentally which shows promising electrocatalytic properties and is beneficial for hydrogen evolution reaction HER [88–90]. Besides, it was reported that P-N DDG is a favorable anode material for lithium-ion batteries [90]. An efficient way of obtaining S-N DDG is articulated in which the concentration of both S and N can be fine-tuned [91–95]. S-N DDG is also found to be an exceptional material for ORR. More interestingly, the formation energy calculations suggest that DDG is quite easier to synthesize in comparison with the mono doped graphene. This idea of single and dual doping is extended to investigate triple doping in graphene.

## 2.2 Electrochemical properties of graphene and 2D materials beyond graphene

Fossil fuels, on one hand, run our World as these are by far the primary source of energy but on the other hand, the use of fossil fuels results in the formation of $CO_2$ and various other greenhouse gasses. The picture becomes worse when we look at the pace in which human population is increasing keeping in mind that fossil fuels have a limit and are not renewable and, therefore, won't last forever. Consequently, the exploration of

other energy resources becomes critical and rechargeable battery technology is one of them. Thanks to SONY for taking the necessary and important step of commercializing the first-ever Li-ion battery in 1991 which has become an integral part of human life. For that reason, the 2019 Nobel Prize in Chemistry is awarded to Goodenough, Whittingham, and Yoshino for the development of Li-ion battery technology [96]. Though Li-ion batteries have revolutionized our lives yet there is a big room for further improvement. One shortcoming is associated with the anode material (graphite) used in Li-ion battery which has a capacity limited to 372 mAh/g [23, 24, 97]. Another issue is the Li itself as the Li resources are quite limited and in the near future, Li will be as precious as gold [28]. The latter issue can be resolved by the replacement of Li with Na or K since they offer the same electrochemical properties [29–31, 98–101]. In addition, both Na and K can be found in pretty much abundance in nature. However, the intercalation of Na/K is the main issue by virtue of their bigger sizes (in comparison with Li). Consequently, the Na storage capacity of graphite is as low as 35 mAh/g [32]. In this scenario, it is of utmost importance to explore anode materials with somewhat higher storage capacities for Li, Na, and K. To address this issue, various doped graphene systems have been proposed. It is shown that using B- or N-doped graphene can seriously increase the storage capacity for Li [102]. In addition, Li adsorption on graphene at various concentrations is studied [103]. The authors increased the Li concentration from 1% to 50 % to examine the adsorption behavior. The adsorption and diffusion mechanism of Li on pristine, B-, and N-doped graphene was studied with help of DFT calculations [104]. It is found that the presence of B impurity can largely increase the adsorption strength of Li on graphene. Moreover, N-doped graphene was found to be better than B-doped graphene with a smaller energy barrier. In another study, it is confirmed that 6Li atoms can be adsorbed around a 6ring C unit in graphene [105]. Fan *et al.* theoretically analyzed the adsorption of Li on pristine and (vacancy) defective graphene [106]. Furthermore, it was shown that Li diffusion can significantly be speeded up with the introduction of vacancies. Moreover, first-principles calculations demonstrated that the use of two B atoms in a 6x6 supercell of graphene can increase the storage capacity for Li [107]. The authors also check the favorability of dopant sites for B and N. They tested the doping on *ortho*, *meta*, and *para* positions. Denis *et al.* reported the adsorption of Li on various mono- and dual-doped graphene [108]. It was observed that the S-N DDG offers the strongest interaction for Li. Furthermore, Na adsorption is investigated by the help of DFT study on graphene and graphene oxide [109]. A well-documented investigation on Na-ion batteries is reported in the literature [29]. Ling and Mizuno reported an efficient anode material consisting of B-doped graphene for Na-ion batteries [110]. Their DFT computations revealed a high storage capacity with 0.44 V open-circuit voltage. Moreover, the reported B-doped graphene can be considered as B

and C alloy due to a high degree of B doping. With the help of theoretical calculations, adsorption and diffusion mechanism of Na is investigated on pristine, defective, and B doped graphene [111]. A systematic study of Na intercalation and ionic mobility on B- and N-doped graphene is reported by Yao *et al.* with the help of DFT calculations [112]. A detailed experimental study on the Na interactions with graphene is documented [113]. In a recent (experimental+theoretical) study, it is found that S-N DDG is a better choice for SIBs [114]. Additionally, the authors argued that the protrusion caused by S atom is far efficient than making holes in graphene. With the help of theoretical calculations, the interaction of alkali and alkaline earth metals on graphene was investigated and, furthermore, reported that why graphite (and other materials) have a small capacity for Na [115].

There are several other materials that can be used as anode materials for alkali-based batteries. For example, graphenylene, which is an allotrope of C, can possibly serve as an anode [116]. It was shown that Li-ions can favorably be adsorbed in comparison with graphene. The reported storage capacity was about 1100 mAh/g. However, in some cases, the energy barrier was a bit high (0.99 eV). Wang *et al.* reported the synthesis of a new material, chlorine substituted graphdiyne, which consists of sp- and $sp^2$-hybridized C atoms and, furthermore, investigated to be favorable for Li storage [117]. Wang *et al.* proposed another 2D allotrope of C atoms which was named as net W and the possible experimental synthesis of this material was discussed by Xu *et al.* and, furthermore, Yu *et al.* predicted that net W has the potential to be a competitive anode material for Li storage [118–120]. The Li storage capacity of $MoS_2$ is 600 mAh/g and, additionally, it is shown that the storage capacity of the nanostructured $MoS_2$ is higher than the bulk counterpart [121–124]. Another 2D material of atomic thickness, $Bi_2MoO_6$, was synthesized by Zhen and coworkers which is found to be excellent material for Li storage [125]. Several monolayers including GeS, GeSe, SnS, and SnSe were proposed as anodes for LIBs with the storage capacities of 256, 178, 89, and 136 mAh/g, respectively [126]. Wan *et al.* demonstrated that $Ti_2C$ can be used as an anode material for Li storage [127]. In addition, Peeters and coworkers reported low energy barriers and high storage capacities of Li, Na, and K on $Mo_2C$ [128]. Various silicon allotropes were considered as anode materials for LIBs and SIBs [129]. Using DFT calculations, $Na_2Mn_3O_7$ is proposed for SIBs [130]. In short, several materials have been explored as anode materials for SIBs, such as phosphorene, $CrS_2$, GeS, $MoS_2$, $TiS_2$, $VS_2$, $NbS_2$, $ZrS_2$, $CoTe_2$, and $NiTe_2$, etc [131–136].

## 2.3   **Other 2D materials**

The discovery of graphene is not only related to the synthesis of just one material but it was the beginning of a new era. In the past decade or so, a significant number

of 2D materials have been synthesized or their existence is theoretically predicted [33]. The investigation of new materials and the advancement of technologies have a direct dependence on each other as these new materials make considerable advancement to the existing technologies which, in turn, will result in the cultivation of new materials and vice versa. Due to the lack of a sizeable bandgap in graphene, it is desirable to design 2D materials with a finite gap that can be utilized in electronic devices. The vast variety of 2D materials comes with a wide diversity in electronic properties. That being said, silicene and germanene share the same Dirac-like character as that of graphene [137, 138]. Phosphorene has a sizeable bandgap and thus suitable for its application in nanoelectronics [139, 140]. There are other 2D materials called MXenes which offer quite flexible electronic properties ranging from semiconductors to metals [141–143]. Several reviews have been documented on these 2D materials [144, 145]. The wide gap semiconductor $h$BN is not a good choice to be employed in FETs but there exist other materials from the same family with bandgap values lie in between $h$BN and graphene [36]. These materials are $h$BP and $h$BAs which have bandgaps appropriate for their use in electronic devices [146]. Furthermore, their charge carrier mobilities are of the similar order to that of graphene [37].

## 2.4  Van der Waals Heterostructures

The isolation of graphene created a great hype for several years and within a decade, numerous other 2D materials were reported. These 2D materials are just one layer among the many layers of the bulk parent crystal which are glued together by weak vdW forces. In that context, one can design a material by putting up different monolayers in a stacked form called vdW heterostructure. The diversity in the electronic properties of 2D materials provides the possibility of designing a material of interest. For example, from the wide gap insulator $h$BN to a semiconducting $MoS_2$ and a semimetallic graphene, metallic and superconducting $NbSe_2$, ferromagnetic $CrI_3$ to the quantum spin-Hall insulator $WTe_2$ provides countless possibilities of designing new vdW heterostructures [3, 141, 147–153]. Among them, graphene/$h$BN vdW heterostructure is the most common example [154–156]. Consequently, a gap around the Dirac point can be induced in graphene without significant degradation in the carrier mobility. Such vdW heterostructures have additional advantage of preventing of graphene plasmons from scattering [157]. In addition, hybridized plasmonic modes can also be achieved [158]. Moreover, it is shown that encapsulated monolayer $TiSe_2$ (in 1T phase) in $h$BN can increase the superconducting transition temperature (from 0K to 3K) [159]. In a recent experimental investigation, it was observed that encapsulated graphene in $h$BN can preserve the high mobility which is desirable for its use in FETs [160]. There are several review articles covering this topic [38, 39, 161].

## 2.5 **Defects**

Monolayer hexagonal boron nitride ($h$BN) was one of the monolayers synthesized just after the isolation of graphene. It is a wide gap insulator with a bandgap of 7 eV. As discussed, substitutional doping is the classic technique to alter the optoelectronic properties of the materials. The doping of $h$BN with C (at B and N sites), and O (at N site) is reported and the impurities existence is confirmed by the help of transmission electron microscopy [162]. Ajayan and coworkers also confirmed the C dopants in $h$BN framework [163]. In another study, C impurities were substituted at B and N sites with the help of electron-beam irradiation [164]. It was shown that the $h$BN electronic properties were significantly tuned. In addition, deep impurity levels inside the gap of $h$BN due to C doping were reported [165–168]. Moreover, Be impurities (at B sites) are implanted by thermal annealing method in $h$BN [169].

Part II

Methodology

## 3  Computational background

This chapter deals with the method of electronic structure calculations used in the development of research presented in this thesis. It is quite a difficult task to address each and everything used in the calculation of electronic structure based on first-principles density functional theory (DFT) but the indispensable aspects will briefly be described. Electronic structure calculations have a key role in describing the physical and chemical properties of materials. Since the behavior of electrons is responsible (up to a great extent) for most of the properties of a system, it is critical to model the electronic structure calculation method quite accurately. Having said that, DFT does not have empirical parameters, rather it is based on the quantum theory and, therefore, exact in nature, and needed some fundamental information as a starting point, provided the atomic number of the ingredients (atoms) and some initial guess of the geometry of interest. The beauty of DFT comes from the replacement of many-body problem of interacting electrons, which is quite complex, with an equivalent single electron problem moving in an effective potential. The use of DFT to predict the structural, electronic, magnetic and dynamical properties are a routine now. The success of DFT was already acknowledged by the ascription of the Nobel Prize in Chemistry in 1998 [170]. The formalism of DFT is given below.

### 3.1  Electronic structure calculation

In quantum mechanics, Schrödinger's wave equation is used to tackle the electronic structure or any other quantum mechanical problem.

$$\hat{H}\Psi = E\Psi \tag{3.1}$$

For many-body problem, this equation 3.1 will take the form

$$\hat{H}\Psi_i \left( \vec{r}_1, \vec{r}_2, \ldots, \vec{r}_n, \vec{R}_1, \vec{R}_2, \ldots, \vec{R}_N \right) = E\Psi_i \left( \vec{r}_1, \vec{r}_2, \ldots, \vec{r}_n, \vec{R}_1, \vec{R}_2, \ldots, \vec{R}_N \right), \tag{3.2}$$

where $\hat{H}$ and $\Psi_i$ are the Hamiltonian operator and the *ith* state wave-function of the system, respectively. Additionally, the $\Psi_i$ contain all the information related to the system and the $\Psi$ is dependent on the $3N$ spatial coordinates. The term $E$ is the total energy of the interacting particles.

The description of a solid, in reality, is the accumulation of electrons, which are negatively charged and lighter, and nuclei which are positively charged and considered as quite heavier in comparison with electrons. Moreover, the charge carries by a nucleus is denoted by

*Z.e*, where *Z* denotes the atomic number and *e* is used for the representation of electron charge. That being said, *N* nuclei will bear a problem of *N+ZN* interacting particles. For many-body problem, eq. 3.2 (Hamiltonian) will take the form of

$$\hat{H}_{tot} = \hat{T}_e\left(\vec{r}_i\right) + \hat{T}_N\left(\vec{R}_\lambda\right) + \hat{V}_{ee}\left(\vec{r}_i, \vec{r}_j\right) + \hat{V}_{NN}\left(\vec{R}_\lambda, \vec{R}_\sigma\right) + \hat{V}_{eN}\left(\vec{r}_i, \vec{R}_\lambda\right), \quad (3.3)$$

where $\hat{T}_N$ and $\hat{T}_e$ represent the kinetic energy operators for positively charged nuclei and negatively charged electrons, respectively. A system being consist of electrons and nuclei has coulombic interactions among electron-electron, nucleus-nucleus, and electron-nucleus which are given by the last three terms of eq. 3.3.

By taking all the terms of eq. 3.3 into account, only then the interaction behavior of a system can be described and understood. The complexity of electron-electron and nucleus-nucleus interactions forbids the solution of this Hamiltonian to be solved by the stationary Schrödinger wave equation even with the help of a superfast computer, given that any system is composed of a large number of atoms. Consequently, it is crucial to remedy the Schrödinger wave equation in such a way that enables it to address many-body problems and calculate electronic structure. The electrons in an atom can be divided into two sub-classes on the basis of their (orbital) energy. The valence electrons, which are the outer-shell electrons, usually interact with other electrons and are mostly responsible for various chemical aspects (reactions, etc). On the other hand, core electrons are the inner-shell (completely occupied orbitals) electrons, close to the nucleus and, therefore, do not usually take part in chemical interactions. In addition, the core electrons along with the nuclei make an ion-core. This allows us to separate or detach the valence electrons from the core ones. The next step in simplifying the many-body Hamiltonian is the use of Born-Oppenheimer approximation [171].

## 3.2 Born-Oppenheimer approximation

By virtue of enormous mass difference between the electrons and nuclei, their speed is also remarkably different than each other. Since the motion of electrons is extremely faster (several times) than the motion of nuclei, it is safe to treat the nuclei as an immobile charge particle. As a result, the term $\hat{T}_N\left(\vec{R}_\lambda\right)$ in eq. 3.3, which is the kinetic energy of nuclei, vanishes for being treating the nuclei as a stationary particle. The nucleus-nucleus potential energy term ($\hat{V}_{NN}\left(\vec{R}_\lambda, \vec{R}_\sigma\right)$) turn down to a constant and eq. 3.3 is simplified to electron kinetic energy term, electron-electron and electron-nucleus potential energy terms. The electron-nucleus potential energy term can also be regarded as the external potential ($\hat{V}_{eN} = \hat{V}_{ext}$).

After the substitutions, eq. 3.3 becomes

$$\hat{H}_{tot} = \hat{T}_e + \hat{V}_{ee} + \hat{V}_{ext} \tag{3.4}$$

Taking these terms in atomic units ($= \hbar = e^2 = 1$) and are given below:

$$\hat{T}_e = -\frac{1}{2}\sum_i \vec{\nabla}_i^2, \quad \hat{V}_{ee} = \frac{1}{2}\sum_{i \neq j} \frac{1}{|\vec{r}_i - \vec{r}_j|}, \quad and \; \hat{V}_{ext} = -\sum_{i,j} \frac{Z_\lambda}{\left|\vec{r}_i - \vec{R}_\lambda\right|}$$

Here, the coordinates of $i$ and $j$ electrons are represented by $\vec{r}_i$ and $\vec{r}_j$, respectively. The nucleus charge is represented by $Z_\lambda$ at a position $\vec{R}_\lambda$. It must be noted that both the kinetic energy of the electron and the potential energy of electron-electron interaction terms have a sole electron-dependence. All the information related to the nuclei and their positions are incorporated in $\hat{V}_{ext}$. The Hamiltonian is simplified up to a greater amount by the Born-Oppenheimer approximation, however, the solution of Hamiltonian is way too difficult.

## 3.3 Independent-electron approximation

As stated, one of the biggest hurdles in solving the Schrödinger wave equation is the electron-electron interaction and for that reason, this complexity should be avoided by any means. In independent-electron approximation, the complex electron-electron interaction is neglected which might sound odd but for instance, this approximation treats a helium atom as two ions that do not interact with each other, given that each of the ions consists of a single electron which shares the same nucleus. Also, for single-electron system, the periodic potential as a consequence of electron-electron interaction in Schrödinger wave equation is:

$$[T_e + V(r)]\Psi_k(r) = \varepsilon(k)\Psi_k(r) \tag{3.5}$$

Here, the $r$ and subscript $k$ represent electron position and wave-vector, respectively.

## 3.4 Hartree approximation

The product of single-particle wave-functions is equal to the many-electron wave-function as proposed by Hartree in 1920s [172]. The many-electron wave-function can be expressed as: $\Psi(r_1, r_2, \ldots, r_n) = \Psi_1(r_1)\Psi_2(r_2), \ldots, \Psi_n(r_n)$. This means that Schrödinger wave equation can be solved for many-electron by Hartree approximation in the form of $\Psi(r_1 s_1, r_2 s_2, \ldots, r_n s_n)$. This potential introduces a new potential by partitioning the electron potential $V_e$ from the ion potential $V_{ion}$. The impact of electric field of one electron on another and taking the allotment to negative charges into account to all the other electrons can be expressed as:

$$\rho_i(r) = -e\sum_i |\Psi_i(r)|^2 \tag{3.6}$$

The subscript $i$ will prevent the electrons for correlation as electrons follow the Pauli Exclusion Principle. The electron potential, with the substitution of charge density, can take the form:

$$V_e = e^2 \sum_i \int dr' |\Psi_i(r')|^2 \frac{1}{|r - r'|} \tag{3.7}$$

This equation 3.7 along with the ion-ion interaction potential ($V_{ion}$) when substituted in eq. 3.5, we get the Hartree equation.

$$\varepsilon_i \Psi_i(r) = [T_e + V_{ion}(r) + V_e(r)] \Psi_i(r) \tag{3.8}$$

The shortcomings of Hartree approximation, which narrates the effect of the electric field of one electron on others, is addressed in Hartree-Fock approximation.

## 3.5  Hartree-Fock approximation

Hartree approximation does not take the anti-symmetry of electron wave-function into consideration. This issue was addressed by Fock where a particle exchange was included. This modification is done by the inclusion of an exchange term to the Hartree equation and is based on independent-electron approximation. The new equation is known as Hartree-Fock approximation. In addition, the independent-electron approximation is given by the one-electron Hamiltonian.

$$H_{app} = \sum_{i=1}^{n} [T_e + V(r_i)] \tag{3.9}$$

The single-electron potential energy in the proximity of nuclei is $V(r_i)$. Finally, $n$ represents the total number of electrons. The solution of the Schrödinger wave equation is the product of one-electron states.

$$\Psi(x_1, x_2, \ldots, x_n) = \Psi_1(x_1) \Psi_2(x_2) \ldots \Psi_n(x_n) \tag{3.10}$$

The term is the Schrödinger equation's eigenstates of one-electron. These eigenstates do not correlate since the particles do not interact with each other for being considering them independent of each other. Additionally, the position of $r_1$ (orbital coordinate) and $s_1$ (spin) both are incorporated in the term $x_1$. This can be written as:

$$x_1 = (r_i, s_i) \tag{3.11}$$

Also, the probability density of finding or locating electrons in orbital coordinates is given by:

$$\rho(x_1, x_2, \ldots, x_n) = |\Psi_1(x_1)|^2 |\Psi_2(x_2)|^2 \ldots |\Psi_n(x_n)|^2 \tag{3.12}$$

Eq. 3.12 is just the product of non-correlated probability densities (of one-electron). A determinant (first introduced by Slater) is used to satisfy the Pauli Exclusion Principle and hence, eq. 3.10 becomes:

$$\Psi\left(x_1, x_2, \ldots, x_n\right) = \frac{1}{\sqrt{N!}} Det\left[\Psi\left(x_1\right), \Psi\left(x_2\right) \ldots \Psi\left(x_n\right)\right] \qquad (3.13)$$

For electron with the same spin, Slater determinant is helpful in obtaining the exchange term $-\frac{1}{2}\sum_j \int d^3r' \Psi_j^*\left(r'\right)\Psi_i\left(r'\right)\frac{1}{|r-r'|}\Psi_j\left(r\right)$. With the introduction of this term, Hartree equation becomes Hartree-Fock approximation which can be written as:

$$\varepsilon_i\Psi_r = \left[T_e + V_{ion}\left(r\right) + V_e\right]\Psi_i\left(r\right) - \frac{1}{2}\sum_j \int d^3r' \Psi_j^*\left(r'\right)\Psi_i\left(r'\right)\frac{1}{|r-r'|}\Psi_j\left(r\right) \qquad (3.14)$$

For ground-state energy calculations of atoms, this method works quite well. However, due to the absence of electrons correlation (coulombic repulsion), Hartree-Fock approximation gives unsatisfactory results. Despite its success in molecular calculations, it faces serious problems and complications when treating solid, especially metals where density of states (DOS) (in particular) cannot be computed with Hartree-Fock approximation.

Luckily, to overcome these issues, another method known as density functional theory (DFT) was introduced with a different line of action in comparison with the Hartree-Fock approximation. DFT is exact is nature but the practical implementation, however, requires a number of approximations, especially for exchange-correlation potential.

## 3.6 **Density Functional Theory**

Due to the complexity of the Hartree-Fock method as discussed above, another method of solving the Schrödinger equation is proposed which works different than the former method. This method is called Density Functional Theory (DFT) and is regarded as one of the efficient, versatile, powerful, and popular quantum mechanical models used for the calculations of electronic structure. The electronic properties (structure) of many-electron systems are calculated from the ground-state charge density by an ab-initio method as proposed by Hohenberg, Kohn, and Sham. DFT gives quite comparable outcomes to that of experimental results.

Actually, the DFT of quantum systems can be dated back to 1927 as proposed by Thomas and Fermi [173, 174]. Though their approach demonstrates the working principle of DFT, their approximation cannot be applied to the modern-day electronic structure calculations, since it is not adequately precise. They proposed a method where the kinetic energy is a functional of the electron density by taking electron-electron interaction into consideration through mean-field potential, in analogy with the methods proposed by Hartree and Hartree-Fock. Since the exchange-correlation was neglected in their method,

it was Dirac who proposed the local approximation for exchange, a method still in practice today but without significant improvement of the method [175]. The modern-day DFT formulation was proposed and developed by Hohenberg, Kohn, and Sham. In this method, the particle density is used as a basic variable with the ability to describe any kind of many-electron system. In other words, a unique functional, $\rho(\overrightarrow{r})$, of single-electron density (of ground state) which contains all the necessary information related to the system and, consequently, the properties of interacting-particle system can be depicted. DFT bifurcates the total energy of many-body interactions into kinetic energy term, coulombic interaction of electron-nuclei, and exchange-correlation term. In this formalism, density is taken as a function of three variables (Cartesian coordinates) which solves the *3N* problem. The formalism of DFT is given below.

### 3.6.1 Formalism

#### 3.6.1.1 Hohenberg-Kohn Theorems

The foundation of DFT is the two uncomplicated theorems which were proposed by Hohenberg and Kohn in 1964 [176]. These theorems simplify the Hamiltonian by introducing an external potential as a replacement of all the complex interactions and using the electronic density (given that ground state energy as a functional) rather than the wave-functions. These theorems are:

**Theorem 1:** The ground-state electron density $(\rho_0)$ is a unique functional which determines the external potential $V_{ext}(\overrightarrow{r})$.

**Proof 1:** Let us take two potentials $V_{ext}(\overrightarrow{r})$ and $V'_{ext}(\overrightarrow{r})$ in such a way that $V_{ext}(\overrightarrow{r}) - V'_{ext}(\overrightarrow{r}) \neq Constant$. The corresponding Hamiltonians of $V_{ext}(\overrightarrow{r})$ and $V'_{ext}(\overrightarrow{r})$ will be $\hat{H}_{ext}(\overrightarrow{r})$ and $\hat{H}'_{ext}(\overrightarrow{r})$, respectively. These, in turn, will produce $\Psi_{ext}(\overrightarrow{r})$ and $\Psi'_{ext}(\overrightarrow{r})$ wave-functions. Now the ground state has the least of energy as per variational principle, so:

$$E = \left\langle \Psi \,\middle|\, \hat{H} \,\middle|\, \Psi \right\rangle < \left\langle \Psi' \,\middle|\, \hat{H} \,\middle|\, \Psi' \right\rangle \tag{3.15}$$

For two Hamiltonians with similar ground-state densities, the inequality is held by taking into consideration the ground-state as a non-degenerate. So we have:

$$\left\langle \Psi' \,\middle|\, \hat{H} \,\middle|\, \Psi' \right\rangle = \left\langle \Psi' \,\middle|\, \hat{H}' \,\middle|\, \Psi' \right\rangle + \int \left[ V_{ext}(\overrightarrow{r}) - V'_{ext}(\overrightarrow{r}) \right] n_0(\overrightarrow{r}) \, d\overrightarrow{r} \tag{3.16}$$

By interchanging the tags in eq. 3.15

$$\left\langle \Psi \,\middle|\, \hat{H}' \,\middle|\, \Psi \right\rangle = \left\langle \Psi \,\middle|\, \hat{H} \,\middle|\, \Psi \right\rangle + \int \left[ V'_{ext}(\overrightarrow{r}) - V_{ext}(\overrightarrow{r}) \right] \tag{3.17}$$

Let's add eq. 3.15 and 3.16, we get

$$E + E' < E' + E \tag{3.18}$$

This is a clear case of controversy.

**Theorem 2:** The ground state total energy functional $E_{V_{ext}}[\rho_0]$ is the global minimum at the ground-state electron density ($\rho_0$) in any external potential $V_{ext}$.

$$E[\rho_0] \leq E[\rho] \tag{3.19}$$

**Proof 2:** The potential can uniquely describe the ground state wave-function and the external potential can be determined by the density and in this way, energy turns out to be the functional of density.

$$E[\rho_0] = T[\rho_0] + E_{int}[\rho_0] + \int V_{ext}(\vec{r})\,\rho_0(\vec{r}) + E_{//} \equiv F[\rho_0] + \int V_{ext}(\vec{r})\,\rho_0(\vec{r}) + E_{//} \tag{3.20}$$

As for any system, potential energy and kinetic energy is dealt in a similar way and, $F[\rho_0]$ therefore, becomes a global (universal) functional.

As the ground-state energy is obtained from the ground-state density $\rho_0(\vec{r})$, so

$$E = E[\rho_0] = \left\langle \Psi \left| \hat{H} \right| \Psi \right\rangle \tag{3.21}$$

As per variational principle, a higher density $\rho'(\vec{r})$ will determine higher energy (excited-state).

$$E = E[\rho_0] = \left\langle \Psi \left| \hat{H} \right| \Psi \right\rangle < \left\langle \Psi' \left| \hat{H} \right| \Psi' \right\rangle = E' \tag{3.22}$$

The calculation of ground-state total energy can be done by minimizing the total energy $E_{V_{ext}}[\rho]$ with respect to $\rho_0(\vec{r})$, given that $\rho_0(\vec{r})$ acts as a functional of total energy. The ground state density is obtained by the minimization of energy with accurate density.

### 3.6.1.2 The Kohn-Sham equation

The Hohenberg-Kohn theorems provide the possibility of using the ground-state electron density to compute the (physical) properties of a system, however, these theorems lack the information of calculating the ground-state electron density. The solution to this problem is provided by the Kohn-Sham equation [177]. The correlation energy is described as a fragment of total energy and for that reason, the total energy ($E = T + V$) can be rewritten as:

$$E_{V_{ext}}[\rho] = T_0[\rho] + V_H[\rho] + V_{xc}[\rho] + V_{ext}[\rho] \tag{3.23}$$

In equation 3.23, $T_0$, $V_H$, and $V_{xc}$ are the representation of kinetic energy, Hartree potential, and exchange-correlation functional, respectively. The corresponding Hamiltonian can be expressed as: $\hat{H}_{KS} = \hat{T}_0 + \hat{V}_H + \hat{V}_{xc} + \hat{V}_{ext}$, is called Kohn-Sham Hamiltonian. The functional derivative of the exact ground state density gives exchange-correlation potential ($\hat{V}_{xc} = \frac{\delta E_{xc}[\rho]}{\delta \rho}$).

Finally, we can write the Kohn-Sham equation as:

$$\hat{H}_{KS}\phi_i = \varepsilon_i\phi_i \tag{3.24}$$

Where, $\phi_i$, and $\varepsilon_i$ represent single-particle wavefunction, and inhomogeneous energy, respectively. The $\phi_i$ satisfy $\sum_{i=1}\phi_i^*\phi_i = \rho$. Although Kohn-Sham method is exact in describing the properties of ground state many-electron systems, the practical implementation of Kohn-Sham method requires some approximations as the exchange-correlation functional is not known. In this context, further approximations are needed.

### 3.6.2  **Local Density Approximation**

One of the most common and extensively used exchange-correlation functional is the local density approximation (LDA) [176, 177]. The exchange-correlation energy is equated and compared to the homogeneous electron gas (which changes at a slow pace) and have a dependence only on the electron density.

$$E_{xc}^{LDA}[\rho] = \int \rho\left(\overrightarrow{r}\right)\epsilon_{xc}^{homo}\rho\left(\overrightarrow{r}\right)d^3\left(\overrightarrow{r}\right) \tag{3.25}$$

In the above equation 3.25, $\epsilon_{xc}^{homo}$ shows the exchange-correlation energy density. As the name suggests, LDA should be used for the cases with uniform density, however, it also describes the realistic systems with great accuracy. Besides, if there are swift fluctuations in the electron density (as in the case of molecular systems or strongly correlated systems), the performance of LDA is gravely degraded.

### 3.6.3  **Generalized Gradient Approximation**

The shortcomings of LDA can be cured with several other approximations and among them, generalized gradient approximation (GGA) is one of the famous and widely utilized approximations [178, 179]. In this approximation, the exchange-correlation is dependent on the electron density, as well as its gradient ($|\nabla\rho\left(\overrightarrow{r}\right)|$).

$$E_{xc}^{GGA}[\rho\left(\overrightarrow{r}\right)] = \int \rho\left(\overrightarrow{r}\right)\epsilon_{xc}\left(\rho\left(\overrightarrow{r}\right),\nabla\rho\left(\overrightarrow{r}\right)\right)d^3\left(\overrightarrow{r}\right). \tag{3.26}$$

The use of GGA has certain advantages over LDA in various cases, such as structural properties and lattice parameters, and binding energy, etc. However, GGA also fails in strongly correlated systems and non-covalent interaction. Besides, both these local and semi-local approximations underestimate the band gaps. There is a vast range of other functionals that can be used according to the desired problem and accuracy. In case of strongly correlated systems, the band gaps can be corrected by introducing a coulombic term (an additional parameter) $U$ to the Hamiltonian, which is called the Hubbard model (DFT+$U$) [180]. In addition to this, there are many hybrid functionals as

well in which a fraction from Hartree-Fock (exact exchange) is added to GGA (or LDA) exchange-correlation. These class of functionals significantly improve the performance and the resultant band gap opening is comparable to the experimental ones. However, these functionals utilize a significant amount of computational resources.

## 3.7  **Dispersion corrected DFT**

It is a well established fact that the vdW force does exist and nowadays is the center of attention than ever before despite the fact that it was first introduced in 1873 [181]. It is a natural force that can be found anywhere but its complex demonstration and its dependency on environment are the challenging questions that need to be addressed [182]. These different systems and environments include surfaces, soft-matters, DNA, supramolecular binding, dynamic properties of water, and surface reactions. Although the (weak) attraction of intermolecular forces among molecules can be described by the vdW forces, which consist of dipole-dipole forces (polar molecules) and London dispersion forces (between atom and non-polar molecule), the practical implementation in DFT is way too complicated. The inclusion in DFT is given below, whereas the theoretical and conceptual background can be found in a nice review article [183].

The isolation of graphene has led to a momentous interest in layered materials and adsorption of atoms or molecules on these layered materials or surfaces. The absence of dispersion in weakly bonded systems causes a substantial reduction in the performance of local or semi-local DFT. For all such non-covalent interactions, the DFT energies can be corrected by adding a semi-empirical Grimme's dispersion term (DFT+D2 or DFT+D3) [184–186]. Nevertheless, Wu and Yang already tried an empirical term to correct the DFT energies [187]. The Grimme's DFT+D can be written as:

$$E_{tot} = E_{DFT} + E_{disp} \tag{3.27}$$

where, $E_{disp}$ is the part responsible for the vdW forces. Moreover, this term contains many adaptable parameters.

$$E_{disp} = -\frac{s_6}{2} \sum_{i \neq j} \frac{C_6^{ij}}{R_6^{ij}} f_{damp}(R_{ij}) \tag{3.28}$$

For each pair of atoms $(i, j)$, we have a $(C_6^{ij})$ dispersion coefficient.

$$C_6^{ij} = \sqrt{C_6^i C_6^j} \tag{3.29}$$

The $f_{damp}$ which represents a damping term can be expressed as:

$$f_{damp}(R) = \frac{1}{1 + e^{-d(R/R_r - 1)}} \tag{3.30}$$

The divergence at any small $R_{ij}$ of the $E_{disp}$ is prevented by these adjustable parameters.

In addition, there are several non-local van der Waals (vdW) density functional which can be used.

## 3.8 Non-local vdW-DF

The idea discussed above is just the addition of a dispersive term to the local or a semi-local functional. In 2004, Dion *et al.* designed a separate and freestanding non-local vdW-DF functional [188]. The exchange-correlation term in vdW-DF can be expressed as:

$$E_{xc}\left[n\left(r\right)\right] = E_x^{GGA}\left[n\left(r\right)\right] + E_c^{LDA}\left[n\left(r\right)\right] + E_c^{nl}[n\left(r\right)] \tag{3.31}$$

The last term in eq. 3.31 in the simplest form, which is the vdW-DF correlation energy part, can be expressed as:

$$E_c^{nl}\left[n\left(r\right)\right] = \frac{\hbar}{2}\int dr \int dr' n\left(r\right)\Phi\left(r,r'\right)n(r') \tag{3.32}$$

In eq. 3.32, the kernel $\Phi\left(r,r'\right)$, which is a general function, not only dependent on $r - r'$ but on the densities $n\left(r\right)$, $n(r')$ as well.

Unlike the Grimme DFT+D scheme, where an empirical parameter is presented, the vdW-DF by Dion *et al.* is considered as an ab-initio approach as the dispersion is taken into account without the use of any empirical parameter. In the original vdW-DF (sometimes called vdW-DF1) by Dion *et al.*, the exchange is adopted from the revPBE functional where the binding energies have a strong dependence on the equilibrium distances. This very first version of vdW-DF is improved by many researchers and now we have a vast variety of vdW-DF functionals. That platter includes vdW-DF2 [189], optPBE-vdW [190], optB88-vdW [191], VV10 [192], rVV10 [193], vdW-DF-C09 [194], and vdW-DF-cx [195], just to name a few. The details can be found in the corresponding references.

## 3.9 Plane-wave, Bloch's theorem, and the basis set

Crystal is the name of the periodically repeating (infinitely) basis (or units) which means that infinite number of electrons should be treated for the resolution of the corresponding wavefunctions. This, in turn, demands the basis sets to be infinite to tackle all the wavefunctions. Consequently, this gives rise to difficulties for the simulation codes and, therefore, needed further approximations to make things practically feasible for DFT codes. One approach is the use of Bloch's theorem which states that the solution of Kohn-Sham equation can be expressed as the product of a plane-wave along with a function $u$ which is the periodicity of the cell (or crystal).

$$\Psi_i\left(k;r\right) = u_{i,k}(r)e^{ik.r} \tag{3.33}$$

This means that the **k** vectors are restricted to the primitive cell (of the reciprocal lattice) in the first Brillouin zone due to the crystal periodicity. Practically, the sampling of the Brillouin zone is done by a finite number of k-points. For this purpose, the Monkhorst-Pack scheme is usually utilized [196]. Furthermore, the supercell approach enables us to carry out calculations even for the non-periodic systems (such as atoms, molecules, and clusters) or systems having impurities or defects.

For the expansion of wavefunctions, the electron basis set is defined for the solution of the Kohn-Sham equation. The wavefunction is actually the linear combination of the basis functions. There are several varieties of the bases functions including plane-waves (PW), linear combination of atomic orbitals (LCAO), linear combination of Gaussian (type) orbitals (LCGO), and Muffin-Tin orbitals, etc [197–203]. The PW method is used in VASP, QE, and ABINIT, etc, whereas, SIESTA is based on LCAO method.

## 3.10  Pseudopotentials and the SIESTA method

A major portion of this thesis is established by using the Spanish Initiative for Electronic Simulations with Thousands of Atoms (SIESTA) and for which some basic approximations are necessary for the practical implementation.

When it comes to the chemical properties (chemical bonding, etc) of a material, it is an established fact that valence electrons do play a vital role with almost negligible involvement from the core electrons. This is due to the strong localization of the wavefunctions of the core electrons around the nucleus. In this thesis, electronic properties are studied which are associated with the valence electrons and for this purpose, the core electrons can safely be separated from the valence ones. This can be done by the pseudopotential method in which the core electrons are replaced by an effective potential acting on the outer or valence electrons. Except for minimizing the number of electrons, this method also transmutes the nodal wavefunction into a smooth one. Consequently, computational cost is significantly reduced [204].

For the expansion of Kohn-Sham orbitals, SIESTA uses pseudo-atomic (numerical) orbitals as basis sets.

$$\Psi_i\left(r\right) = \sum_\mu c_{i\mu}\chi_\mu\left(r\right), \tag{3.34}$$

where $c_{i\mu}$ and $\chi_\mu\left(r\right)$ are coefficients and bases functions, respectively. In addition, the term $\mu$ represents various functions in the basis set.

These basis functions in SIESTA are strictly localized numerical atomic orbitals which means that beyond a certain distance (radius) from the nucleus, these reaches quickly to zero. The atomic orbitals which are the product of spherical harmonic and the numerical

radial function can be expressed as:

$$\chi_\mu\left(r\right) \equiv \chi_{jnlm}\left(r\right) = R_{jnl}\left(r\right).Y_{lm}(\theta,\varphi), \qquad (3.35)$$

where $n$, $l$, and $m$ are principle, angular, and azimuthal quantum numbers, respectively. Finally, $j$ represents the valence states basis sets for a given set of $n$ and $l$.

An infinite large basis is required for accurate description of Kohn-Sham orbitals which sounds unrealistic when it comes to the practical implementation. This can be done by achieving adequately converged results at the cost of possible minimum orbitals. There are many options available and one has the liberty to use it according to the choice and demand. The default basis set in SIESTA is the double-zeta with polarization function (DZP). This means that for each occupied state of the free atom, two orbitals are used, the angular shape of which are same with a different radial function. Additionally, the polarization orbital is a higher angular momentum ($l_p=l+1$). That being said, for treating a hydrogen atom, two orbitals are used having s symmetry but different radial function (with the additional shell of *2p* orbitals). Further details can be obtained from SIESTA's manual and the relevant papers [205].

## 3.11 Technical aspects of computational details

A DFT code is crucial for solving the Kohn-Sham equations. We use a variety of different codes. As mentioned earlier, SIESTA is a LCAO code that uses atomic-orbitals as basis sets and pseudopotentials (PPs) [206,207]. We use norm-conserving (NC) Troullier-Martins (TM) PPs [208]. The mesh cutoff value is selected to be 200 Ry which gives well-converged binding energies. Most of the calculations (in SIESTA) were performed within the vdW-DF framework [188]. In addition, we also make use of LDA, GGA, and a hybrid of GGA-LDA. It should be noted that this hybrid is not in the true sense as this does not account for Hartree-Fock exchange. The split-norm is selected to be 0.15. Even the low radial confinement does not guarantee that the interaction energies calculated with SIESTA will be free of basis set superposition error (BSSE). This issue can be tackled by using the counterpoise correction as suggested by Boys and Bernardi [209]. Consequently, with the help of this correction, we get comparable interaction energies to that of the plane-wave and all-electron codes [210]. Finally, we build our own PPs using the atom program which can be used with SIESTA [211]. Additionally, all the generated PPs were tested with the known systems and other DFT codes.

We also use VASP code [1] which comes with the tested PPs [212–214]. In VASP, the projected augmented wave (PAW) method is used with the aid of PPs [199]. For the

---

[1] We are extremely thankful to Prof. Pablo A. Denis for providing and assisting with the DFT codes along with the computational facilities.

expansion of wavefunctions, a kinetic energy cut-off of 500 eV is used. In addition, most of the calculations (using any code) were cross-checked with the all-electron Gaussian code[1] [215].

Finally, we also make use of another plane-wave and PPs based open-source quantum espresso (QE) DFT package [216, 217]. There are a generous number of libraries for PPs which can be used according to the choice and depending on the problem. The Hamann, Schluter, Chiang, and Vanderbilt (HSCV) library consists of NC PPs which require a kinetic energy cut-off of 130 Ry for the expansion of wavefunctions [218]. For Charge density, the (required) corresponding cut-off is 520 Ry. The Optimized Norm-Conserving Vanderbilt (ONCV) library is a set of NC PPs with scalar relativistic corrections [219]. These PPs are quite accurate and efficient by virtue of lower values of cut-off of planewaves (60 Ry) and charge densities (240 Ry). This library can actually be regarded as the modified version of HSCV library. In addition, the Garrity, Bennett, Rabe, and Vanderbilt (GBRV) PPs library contains ultrasoft PPs that give converged results even with cut-off of 40 Ry and 200 Ry for wavefunctions and charge densities, respectively [220, 221]. Furthermore, many PP libraries were checked to scrutinize the best PP for each element in the periodic table by virtue phonon frequencies, stresses, and cohesive energies leading to a standard solid-state pseudopotentials (SSSP) library [222, 223]. This library includes the best guesses. The atomic code of QE is also utilized for the construction of PPs from the PSlibrary [224]. Further information about PP libraries is here [225].

Part III

Results and Discussions

## 4 Electronic properties of doped graphene

The practical implementation of graphene in nanoelectronic devices is forbidden due to the absence of a sizeable bandgap around the Dirac point and for that reason, bandgap engineering of graphene is crucial. Various techniques can be employed to overcome that hurdle among which substitutional doping is considered an effective way. First-principles density functional theory calculations were performed to investigate the doping of boron (B), nitrogen (N), and oxygen (O) in graphene. We select two types of doping models namely rectangular doping and hexagonal doping. The concentration of these dopants was systematically increased from 1 to 4 atoms in a 4x4 supercell of graphene. It is found that p- and n-type doping is achieved by integrating B, N and O atoms, respectively. It was known that injecting impurity atoms on the same sub-lattice site in graphene causes a maximum bandgap opening [55]. However, we show that this is not the only criterion. In both of our models, dopants are incorporated at the same sub-lattice sites but the resultant bandgaps are quite different. By incorporating the maximum number of dopants at rectangular sites, we get 0.55, 0.55, and 1.03 eV bandgap opening for B, N, and O, respectively. The gaps, however, are quite larger when dopants were integrated on hexagonal sites. The calculated bandgaps were 0.70 eV for B (and N) and 1.68 eV for O. Furthermore, it should be noted that when three O atoms at hexagonal sites were replaced, the calculated bandgap (1.15 eV) was larger than the doping of four O atoms at rectangular sites. Consequently, a larger bandgap opening can be achieved at the cost of minimal doping which preserves the cohesive strength of graphene up to a great extent. It is found that N doping causes a smaller reduction in the cohesive energy of graphene. On the other hand, a higher reduction in the cohesive energy is noted for O doping. This can be attributed to relatively different sizes of the dopants. Additionally, the size of N is somewhat comparable to that of C. Also, the cohesive energy of hexagonal doping of three O atoms is -8.83 eV/atom, which is quite better than the cohesive energy of rectangular doping of four atoms (-8.60 eV/atom). For a higher concentration of B and N doping at hexagonal sites, we also report magnetic moment. All these outcomes show that graphene should be doped at hexagonal sites for maximum bandgap opening and minimum reduction in cohesive energy. This paper is published in RSC Advances (RSC Adv., 2017,7, 16064-16068) [226] and is given in appendix A.1.

As mentioned earlier, doping is quite a classic and efficient way to tune the electronic properties of a material. In addition, there are several studies regarding the mono- and dual-doping of graphene with heteroatoms. These involve the second-, third-, and even fourth-row elements as dopants. In addition, numerous studies on the simultaneous integration of two different atoms in the graphene (dual doped graphene) plane have
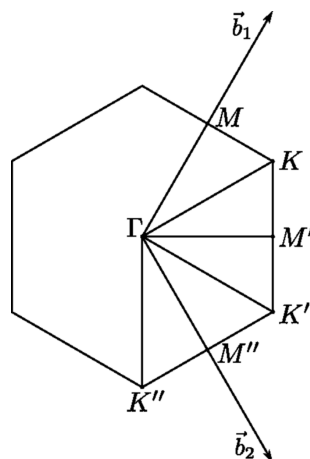
Figure 5 – High symmetry points in the first brillouin zone for the calculation of band structures of triple doped graphene [4].

also been well documented [85–95]. Furthermore, it is shown that dual doping is quite fascinating and efficient than the monodoping in terms of fine-tuning the physicochemical properties of graphene [88–90]. The electronic properties of DDG were found to be very different than the monodoped counterpart. In addition, DDG systems bear excellent catalytic properties and have extensively been utilized in oxygen reduction reactions. Most importantly, by virtue of formation energy calculations, it is reported that the experimental synthesis of DDG systems is easier in comparison with the monodoping. Since there is no report on triple doping in graphene so, we carried out a systematic study regarding the integration of three dopants at the same time in graphene to observe various properties. A huge number of possibilities exist for triple doping but we stick to the more meaningful combinations. In this context, we select two elements, B and N, from the 2p block and one element from the 3p block to investigate triple doped graphene (TDG). From the later block, we select Al, Si, P, and S. These dopants can be accommodated in graphene in a number of ways and we almost checked as many possibilities as we could. In the first place, we keep all the dopants in the same hexagon. Secondly, we keep B and N bonded and change the position of the 3p element within the graphene supercell. Finally, we separate all the dopants in various positions. In this way, we get 19 doping patterns for each sort of arrangements and 76 different structures were optimized. According to the total energy calculations, we find that the patterns in which the dopants are bonded are the most favorable one in all the cases. In fact, BNX (X=3p elements) pattern is preferred except for the S, where NBS pattern is found to be the most favored one. The formation energy calculations suggest that the synthesis of TDG systems would be easier than the dual- and mono-doped counterparts. In addition, a slight reduction was noted in the cohesive energies of TDG systems in comparison with the pristine graphene. The electronic band structure is calculated with the high symmetry points as shown in Figure

5. Furthermore, electronic properties were modified and in many cases, the bandgaps were reduced when compared to the DDG. In addition, the Dirac-like shape of the conduction band minima and valence band maxima that was destroyed in DDG now restored in TDG. Of the interest are the chemical reactivity of these systems. To that end, a hydrogen atom is attached on both sides of the dopants (except for the 3p element where only one side is considered) and neighboring C atoms. It is calculated that the reactivity has significantly increased due to the triple doping in graphene. While the reactivity of pristine graphene is just limited to -16.7 kcal/mol, the reactivity of TDG can be as high as -76 kcal/mol. Consequently, TDG systems have possible applications in catalytic reactions and furthermore suitable for the utilization in nanoelectronics. It is, therefore, expected that these materials will soon be synthesized experimentally. This article was highlighted on the front cover of ChemPhysChem (ChemPhysChem 18 (14), 1864-1873, 2017) [227].

# Triple-Doped Monolayer Graphene with Boron, Nitrogen, Aluminum, Silicon, Phosphorus, and Sulfur

Saif Ullah,[b] Pablo A. Denis,*[a] and Fernando Sato[b]

The structure, stability, electronic properties and chemical reactivity of X/B/N triple-doped graphene (TDG) systems (X = Al, Si, P, S) are investigated by means of periodic density functional calculations. In the studied TDGs the dopant atoms prefer to be bonded to one another instead of separated. In general, the XNB pattern is preferred, with the exception of sulfur, which favors the SBN motif. The introduction of a third dopant results in a negligible decrease of the cohesive energies with respect to the dual-doped graphene (DDG) counterparts. Thus, it is expect that these systems can be prepared soon. For SiNB TDG, the introduction of the B dopant reduces the gap opening at the K point and restores the Dirac cones that are destroyed in SiN DDG. On the contrary, for PNB TDG, the bandgap is increased with respect to PN DDG, probably because the introduction of B weakens the PN bonding, and thus the electronic structure is rather similar to that of P-doped graphene. Finally, with regard to the reactivity of the TDGs, for AlNB, PNB, and SNB the carbon atoms are more reactive than in their AlN, PN, and SN DDG counterparts. On the contrary, the reactivity of SiNB is lower than that of SiN DDG. Therefore, to increase the reactivity of graphene, Al, P, and S should be combined with BN motifs.

## 1. Introduction

By using a rational bottom-up approach, great advances were made during the last few years in synthesizing one- and two-dimensional graphene derivatives. Highlights include armchair ribbons with desired widths,[1] boron-doped ribbons with the boron atoms in *para* disposition,[2–3] sulfur-doped armchair ribbons,[4] and graphene ribbons with OBO[5] and NBN[6] structural motifs. The methods available to produce heteroatom-doped graphene ribbons and sheets offer almost unlimited possibilities to accommodate the dopants. Reviews describing all of the methods for their production have been published.[7–9] Among the 2p elements, B-[10–12] and N-doped[10–13] graphene can be produced in large quantities and with defined structures. For the 3p elements, the preparation of S-[14–21] and P-doped[14,15,22–25] graphene is routine, while Si-doped graphene has been observed experimentally and studied theoretically.[4–15,26–29] However, Al-doped graphene still remains elusive,[14,15,30,31] despite the recent synthesis of aluminabenzene.[32] Of the 4p elements, Se-[33] and Ge-doped[34] graphene sheets and carbon nanotubes have been prepared and their properties predicted by first-principles calculations.[35] Moreover, heavier elements such as transition metals[36–38] and acti-

nides[39] have also been embedded in the graphene framework. Recently, the simultaneous introduction of two types of dopants has been reported and found to be a more efficient approach than monodoping to fine-tune the physicochemical properties of graphene. PN,[40–42] SN,[41–51] BeB,[52] and BeN[53] dual-doped graphene (DDG) shows outstanding catalytic and electronic properties. These findings have also been extended to dual-doped carbon nanomaterials containing Ge and N dopants,[34] which showed enhanced performance for the oxygen reduction reaction, as suggested earlier by theoretical calculations.[54]

Previous studies indicated that DDGs have exceptional catalytic properties,[48,49] as the introduction of the dopants increase the reactivity of graphene up to fivefold. In addition, we found that DDGs have unique electronic properties, because their bandgaps are unexpectedly smaller than those of their monodoped counterparts. To extend our previous investigations of mono- and dual-doped graphene systems, we investigated triple-doped graphene (TDG) systems. Given that the number of possibilities for the introduction of three dopants is very large, we restricted our investigation to three dopants: boron, nitrogen, and one 3p element (Al, Si, P, or S). Our results indicated that the synthesis of these materials is not forbidden from a thermodynamic standpoint and further revealed that the introduction of a third dopant augments the reactivity of the carbon atoms compared to DDG systems. The electronic properties of the most stable TDG systems revealed that in general the introduction of a third dopant does not increase the bandgap opening, and in some cases it even restores the Dirac points. Finally, and more importantly, our results demonstrate that dopants prefer to be agglomerated and bonded among themselves. We expect that this work can trigger new

[a] *Dr. P. A. Denis*
*Computational Nanotechnology, DETEMA*
*Facultad de Química, UDELAR, CC 1157*
*11800 Montevideo (Uruguay)*
*Fax: (+ 58) 9229241906*
*E-mail: pablod@fq.edu.uy*

[b] *S. Ullah, Prof. F. Sato*
*Departamento de Física, Instituto de Ciências Exatas*
*Campus Universitário, Universidade Federal de Juiz de Fora*
*Juiz de Fora, MG 36036-900 (Brazil)*

The ORCID identification number(s) for the author(s) of this article can be found under https://doi.org/10.1002/cphc.201700278.

experimental investigations pursuing the synthesis of these fascinating 2D materials.

## 2. Methods Section

We studied TDG by means of spin-polarized VDW-DF,[55] M06-L,[56] and HSEH1PBE[57] periodic density functional calculations. We employed $N \times N$ unit cells of graphene ($N = 4$–8). Three C atoms were replaced by three dopant atoms with the restriction of including only one 3p dopant (Al, Si, P, or S) and two 2p dopants (B and N). The M06-L and HSEH1PBE calculations were carried out with Gaussian 09,[58] and the VDW-DF calculations were run with the aid of SIESTA.[59,60] For the Gaussian-based calculations, the 6-31G* basis set was selected,[61] and in all cases we utilized the ultrafine grid. The unit cells were sampled for 3000 k-points. For the most stable structures, we performed calculations with a larger basis set, namely, 6-311G*, because the smaller basis set gave unrealistic charges (see below).

For the VDW-DF calculations the double-zeta basis set with polarization functions (DZP) was selected, and the orbital-confining cutoff was fixed to 0.01 Ry. The split norm used was 0.15. The interaction between ionic cores and valence electrons was described by the Troullier–Martins norm-conserving pseudopotentials.[62] The Mesh cutoff was fixed to 200 Ry, which gave converged binding energies within 0.02 eV. The lattice parameters were optimized along the $a$ and $b$ directions, but the $c$ axis was kept frozen at 20 Å. Unit cells were sampled by using a Monkhorst–Pack k-point sampling scheme of $40 \times 40 \times 1$ k-points. Band structures in the first Brillouin zone were calculated along the Γ–M–K–Γ–M′–K′–Γ–M″–K″–Γ path, recently employed by us to study DDG.[50–51] Geometry optimizations were pursued by using the conjugate gradient algorithm until all residual forces were smaller than 0.01 eV Å$^{-1}$.

## 3. Results and Discussion

### 3.1. Structural Characterization of X/B/N (X = Al, Si, P, S) Triple-Doped Monolayer Graphene

The number of possibilities to accommodate three dopants in $N \times N$ ($N = 4$–8) unit cells of graphene is tremendously large. For this reason, we adopted the following procedure to cover as many different scenarios as possible. Considering our previous works on DDG, in which the dopants showed a clear preference for agglomeration, we first investigated the structures in a $5 \times 5$ unit cell formed by placing the three dopants in the same hexagon. In a second step, we kept the 2p dopants bonded and moved the 3p dopant over the neighboring hexagons, and finally we completely separated the three dopants. Using this procedure, we investigated a total of 19 structures for each X/B/N (X = Al, Si, P, S) TDG. The structures and relative energies of Al/N/B, Si/N/B, P/N/B, and S/B/N TDGs are presented in Figures 1–4.

Although the ordering of the relative energies is not the same for the four families of TDG studied, there are general patterns. In line with our previous findings on DDG,[48–51] the most stable structures are those having all three dopants bonded with each other. For Al, Si, and P, the X-N-B bonding pattern is preferred, while for S the S-B-N pattern is favored, and the S-N-B structure is 0.50 eV less stable at the VDW-DF/DZP level of theory. The reason for the different bonding observed for S/B/N TDG (S-B-N instead of S-N-B) can be traced back to the fact that in SN DDG the S and N dopants are not bonded, despite the fact that S and N replace the C atoms of a C=C bond.[48–51] Thus, the introduction of B forces unstable
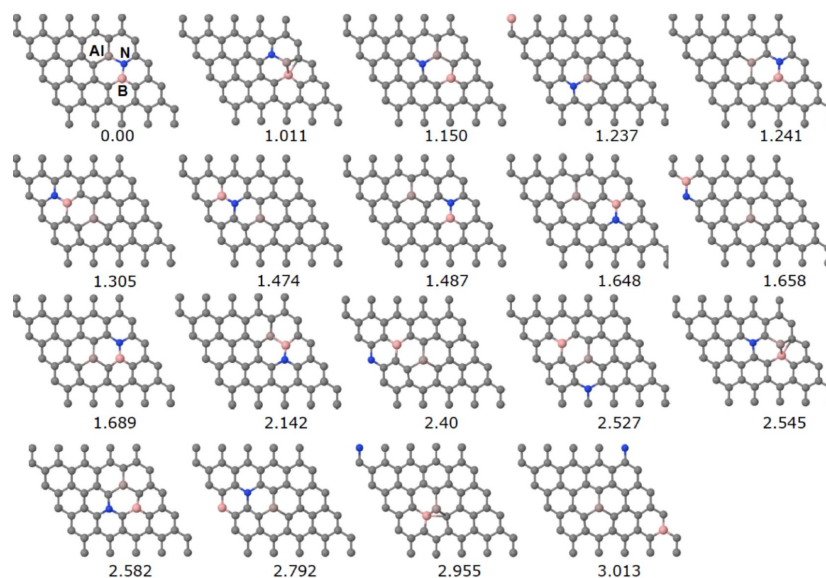


Figure 1. Relative energies [eV] determined for the Al/N/B TDG systems at the VDW-DF/DZP level of theory.
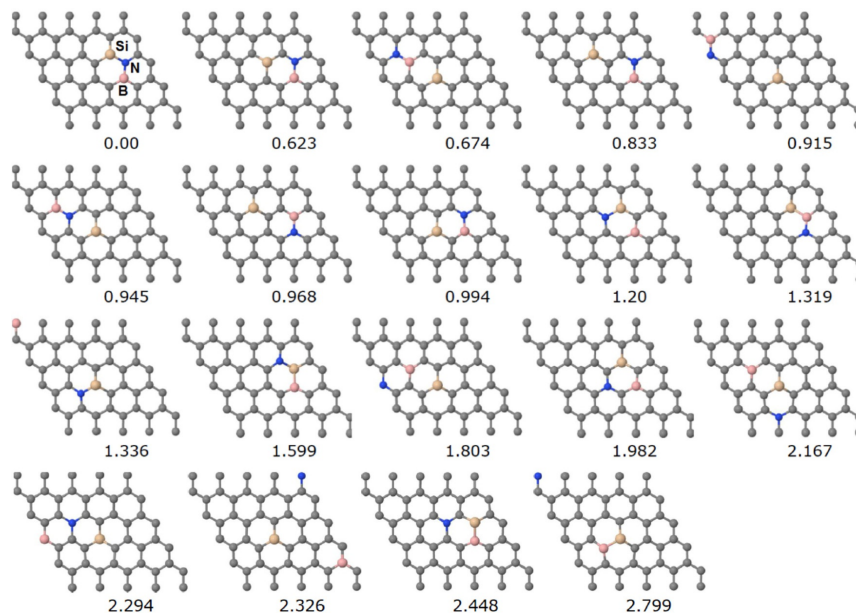
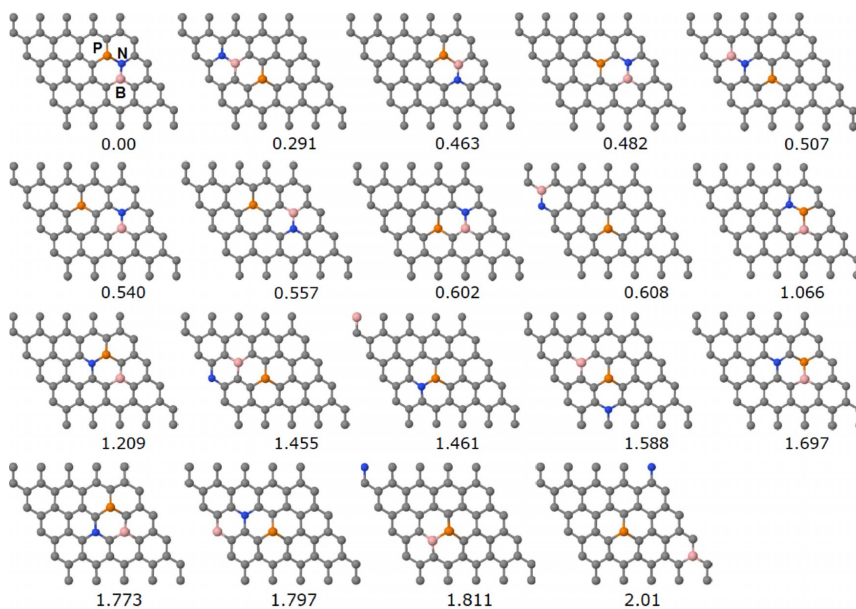**Figure 2.** Relative energies [eV] determined for the Si/N/B TDGs at the VDW-DF/DZP level of theory.



**Figure 3.** Relative energies [eV] determined for the P/N/B TDGs, at the VDW-DF/DZP level of theory.
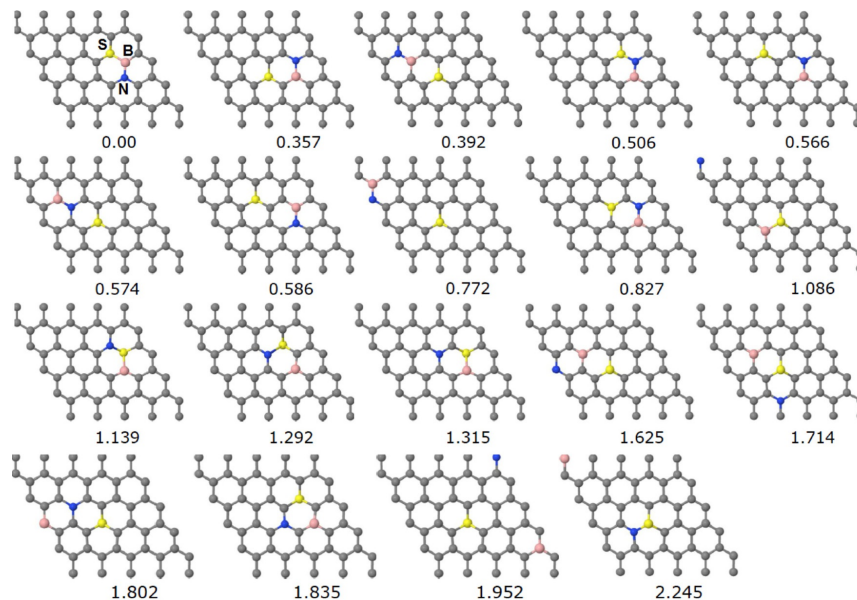
**Figure 4.** Relative energies [eV] determined for the S/N/B TDGs, at the VDW-DF/DZP level of theory.

bonding between S and N, as can be seen in Figure 4. For almost all the systems studied the B and N dopants prefer to be bonded in the most stable structures. As expected, the Al/N/B combination of dopants was the exception to this trend, because Al and B both belong to the same group in the periodic table, and thus can form an AlN bond, which can compete with the BN bonding.

For Al/N/B and Si/N/B TDGs, the energy difference between the first and second most stable structures is 1.01 and 0.62 eV, respectively, at the VDW-DF/DZP level of theory. However, for P/N/B and S/N/B TDGs the second most stable structure is 0.29 and 0.36 eV higher in energy, respectively, at the VDW-DF/DZP level of theory. To support the results obtained with SIESTA, we investigated the relative energies of all structures employing the M06-L density functional. In all cases, the results obtained with the latter functional were in agreement with those obtained at the VDW-DF/DZP level of theory, as the structures with the heteroatoms bonded with each other were the most stable. In fact, for PNB and SBN TDGs the relative energies of the second most stable structures (compared with the most stable ones) were 0.37 and 0.45 eV, respectively, while for AlNB and SiNB they were 1.40 and 0.79 eV, respectively, at the M06-L/6-31G* level of theory. Therefore, the particular stability of the systems with bonded dopants is confirmed at both levels of theory employed.

### 3.2. Formation and Cohesive Energies of X/B/N (X=Al, Si, P, S) Triple-Doped Monolayer Graphene

The formation energies (FEs) of the TDG systems were calculated as $FE_{XYZ\text{-}TDG} = E_{XYZ\text{-}TDG} + 3\mu_C - \mu_X - \mu_Y - \mu_Z - E_{graphene}$. We used the atomic forms of all dopants for chemical potentials $\mu$, whereas the chemical potential of carbon was calculated as the cohesive energy per atom of graphene. Table 1 lists the calculated FEs. Comparison of the FEs of the TDGs with those corre-

**Table 1.** Formation energies [eV] computed for 5×5 mono-, dual-, and triple-doped monolayer graphene at the M06-L/6-31G* level of theory.

| System | FE | $FE_X + FE_Y + FE_Z$ | $\Delta1^{[a]}$ | $FE_{XY} + FE_Z$ | $\Delta2^{[b]}$ |
|---|---|---|---|---|---|
| AlNB | −10.63 | −5.97 | 4.66 | −9.02 | 1.61 |
| SiNB | −12.92 | −9.10 | 3.82 | −10.83 | 2.09 |
| PNB | −12.03 | −8.64 | 3.39 | −10.15 | 1.88 |
| SBN | −10.61 | −7.16 | 3.45 | −8.88 | 1.73 |
| AlN | −3.97 | | | | |
| SiN | −5.78 | | | | |
| PN | −5.01 | | | | |
| SB | −5.38 | | | | |
| Al | 2.58 | | | | |
| Si | −0.55 | | | | |
| P | −0.09 | | | | |
| S | 1.39 | | | | |
| B | −5.05 | | | | |
| N | −3.50 | | | | |

[a] $\Delta1 = FE_{XYZ} - (FE_X + FE_Y + FE_Z)$. [b] $\Delta2 = FE_{XYZ} - (E_{XY} + E_Z)$

sponding to the sum of the FEs of the monodoped systems (Δ1 in Table 1) clearly shows that it is much easier to introduce three dopants that interact among themselves, instead of having the dopants completely separated. This finding is independent of the chemical potentials employed, as we have shown previously.[50] Considering the sum of the FEs of a DDG and that of a monodoped graphene (Δ2 in Table 1) reveals that in all the cases it is more favorable to dope a graphene sheet with three dopants rather than with a combination of dual-doped and monodoped graphene (Δ2 is positive in all cases).

The cohesive energies (CE) are gathered in Table 2. Comparison of the CEs calculated for TDGs and DDGs reveals that the introduction of a third dopant causes a small change in the CE per atom. In effect, the CE of a TDG is reduced by 0.022 eV on average with respect to a DDG. This value is smaller

**Table 3.** Bandgaps [eV] computed for $N \times N$ triple-doped monolayer graphene at the M06-L/6-31G*, HSEH1PBE/6-31G*, and VDW-DF/DZP levels of theory.

|  | AlNB[b] | SiNB | PNB | SBN | AlN | SiN | PN | SB |
|---|---|---|---|---|---|---|---|---|
|  | | | | M06-L | | | | |
| 4×4 | 0.57/0.16[c] | 0.13[c] | 0.91/0.60[a,c] | 0.43[c] | 0.17 | 0.45/0.10 | 0.54 | 0.49/0.54 |
| 5×5 | 0.45/0.42 | 0.06 | 0.69/0.48[c] | 0.39[c] | 0.13 | 0.38/0.05 | 0.37 | 0.37/0.40 |
| 6×6 | 0.12/M | 0.11 | 0.23/0.07[c] | 0.11[c] | 0.09 | 0.06/0.03 | 0.08 | 0.02/0.05 |
| 7×7 | 0.27/0.07[c] | 0.17 | 0.40/0.34[c] | 0.24[c] | 0.08 | 0.22/0.05 | 0.20 | 0.23/0.23 |
| 8×8 | 0.22/0.21[c] | 0.02 | 0.34/0.29[c] | 0.22[c] | 0.07 | 0.18/0.08 | 0.17 | 0.19/0.19 |
|  | | | | HSEH1PBE | | | | |
| 5×5 | 0.69/0.68 | 0.19 | 0.94/0.67[c] | 0.61[c] | 0.20 | 0.50/0.06 | 0.45 | 0.54/0.59 |
|  | | | | VDW-DF | | | | |
| 5×5 | metal | 0.08 | 0.62/0.45[c] | 0.35[c] | 0.08 | 0.32/0.14 | 0.33 | 0.52/0.52 |

[a] 0.91/0.60 corresponds to a 0.91 eV gap for spin up and a 0.60 eV gap for spin down. [b] The magnetic moment in the M06-L and HSEH1PBE calculations was 1 μB, and that in the VDW-DF/DZP calculations was zero. If the magnetic moment is fixed to 1 μB at the VDW-DF/DZP level of theory, the gap calculated is similar to the M06-L/DZP value. [c] Indirect gap.

**Table 2.** Cohesive energies [eV/atom] computed for TDG.

|  | VDW-DF/DZP | M06-L/6-31G* |
|---|---|---|
| graphene | −7.335 | −7.626 |
| AlNB | −7.116 | −7.381 |
| SiNB | −7.159 | −7.427 |
| PNB | −7.141 | −7.409 |
| SBN | −7.105 | −7.381 |
| AlN | | −7.400 |
| SiN | | −7.435 |
| PN | | −7.421 |
| SB | | −7.429 |
| Al | | −7.422 |
| Si | | −7.484 |
| P | | −7.475 |
| S | | −7.446 |
| B | | −7.574 |
| N | | −7.544 |

than the average reduction observed for DDGs compared with monodoped graphene (0.035 eV). This decline in CE for DDG becomes more prominent when compared to B- and N-doped graphene (0.052 and 0.067 eV, respectively). Therefore, from a thermodynamic standpoint the TDG systems appear to be stable.

### 3.3. Electronic Properties of X/B/N (X = Al, Si, P, S) Triple-Doped Monolayer Graphene

Two of the systems studied showed a clear preference for a nonmagnetic ground state (SiNB and SBN TDG), which is not surprising, because the electron count is even. PNB TDG has a magnetic moment of 0.91 μB, while that of AlNB TDG is zero, at the VDW-DF/DZP level of theory. The bandgaps computed for different concentrations of dopants are listed in Table 3. When a boron atom is added to AlN DDG, the bandgap is increased at the M06-L/6-31G* level of theory. However, if the VDW-DF method is used to study AlNB a different scenario is observed, and the system is found to be a metal (M), as can be

appreciated in Figure 5, because of the lack of magnetic moment at this level of theory. The different results observed between the two density functionals are due to the fact that the M06-L calculations were performed with a fixed magnetic moment of 1 μB.
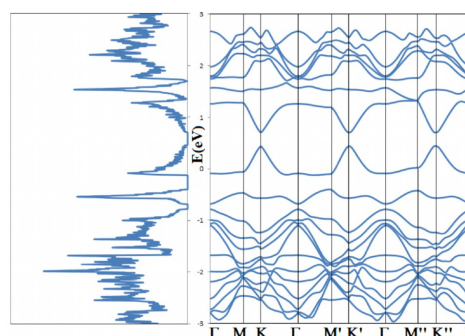


**Figure 5.** DOS and band structure determined for 5×5 AlNB TDG at the VDW-DF/DZP level of theory. Only the spin-up case is shown, because the spin-down case is identical, as the spin-polarized calculation indicated that $Q = 0$ μB.

In line with our previous findings for DDG, that is, decreasing gaps with increasing number of dopants, the bandgap of SiNB TDG is smaller than that calculated for SiN DDG. Moreover, we do not observed a smooth decay of the bandgaps of SiNB TDG with increasing unit-cell size. For example, the bandgap computed for the 5×5 unit cell is 0.11 eV smaller than that calculated for a 7×7 SiNB-doped unit cell. The band structure and density of states of SiNB TDG are shown in Figure 6. The introduction of a B atom reconstructs the Dirac cones at the K point, since they were strongly modified for the spin-up channel in SiN. For PNB TDG the introduction of a B atom in PN DDG increases the bandgap and causes a smooth
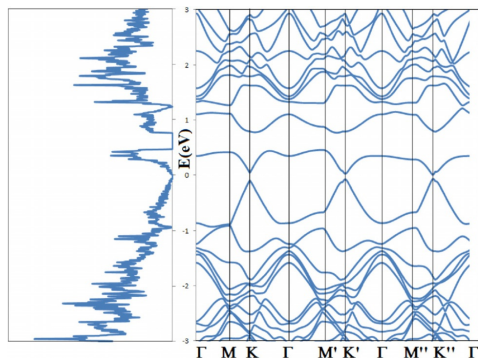
**Figure 6.** DOS and band structure determined for 5×5 SiNB TDG at the VDW-DF/DZP level of theory.



**Figure 7.** DOS and band structure determined for 5×5 PNB TDG at the VDW-DF/DZP level of theory. a) Spin up. b) Spin down.

decay of the bandgap with increasing size of the unit cell. The 6×6 unit cell is the only exception due to the particular folding of the K and Γ points of the $3N\times3N$ unit cells. Unfortunately, the gaps computed for PNB TDG are indirect, but the largest among the systems studied. The latter finding could have been predicted, because phosphorus opens the largest gaps for dual and monodoped graphene systems among the 3p dopants. The density of states and band structure of PNB TDG are shown in Figure 7, and the band structure of SBN TDG is shown in Figure 8. The differences between the gaps computed for SBN and SB are small. In general the gaps are larger for SBN TGD with the exception of the 4×4 unit cell, for which the gap of SBN TDG is 0.06–0.11 eV smaller.

Finally, to gain further insight into the electronic structure of the TGD systems, we studied the partial density of states (pDOS) of SBN and PNB TDG (Figure 9). In the case of PNB, the main contribution to the DOS is from the C atoms. Strong hybridization between C 2p, N 2p, and P 3p and comparatively weak hybridization with B 2p orbitals can be seen at the valence band maximum. B 2p and N 2p (along with C 2p) are responsible for the DOS at the conduction band minimum. The prominent contribution from P 3p in the conduction band appears at an energy of 1.6 and 1.7 eV for spin up and down, respectively.

As for SBN TGD, once again, the C 2p is greatly responsible for the DOS. The 3p orbitals of S are hybridized with the C 2p orbitals near the Fermi level in the valence band, with a contribution of B 2p in the range from −0.4 to −0.6 eV. The B 2p and N 2p are hybridized with C 2p and contribute to the conduction band near the Fermi level. Additionally, the 2p orbitals of B and N and the 3p orbital of S are strongly hybridized with C 2p at 1 eV.

### 3.4. Chemical Reactivity of X/B/N (X = Al, Si, P, S) Triple-Doped Monolayer Graphene

To investigate the effect of heteroatom doping on the chemical reactivity of graphene, we employed the hydrogenation re-
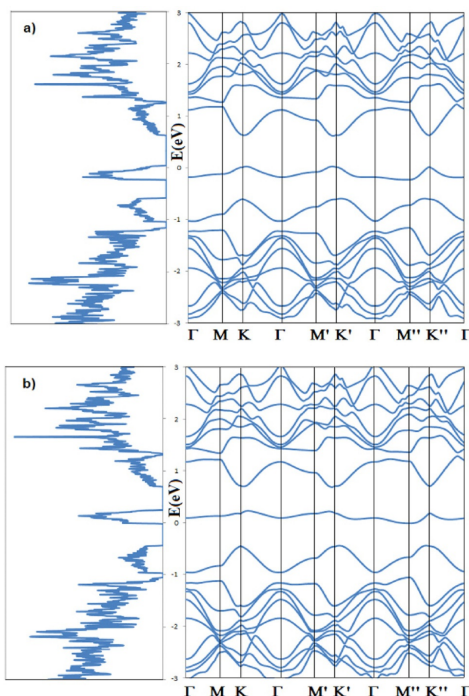


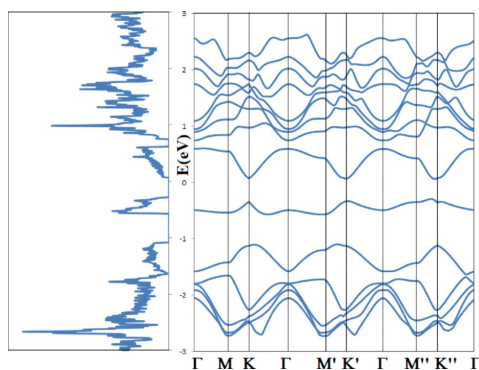**Figure 8.** DOS and band structure determined for 5×5 SBN TDG at the VDW-DF/DZP level of theory.

action. To that end, we added one hydrogen atom to the heteroatoms and to the ten carbon atoms surrounding these dopants. In this way, a total of 13 centers were considered, and the addition of H was performed on both sides of the sheet for each center, except for the 3p dopant. Note that the two
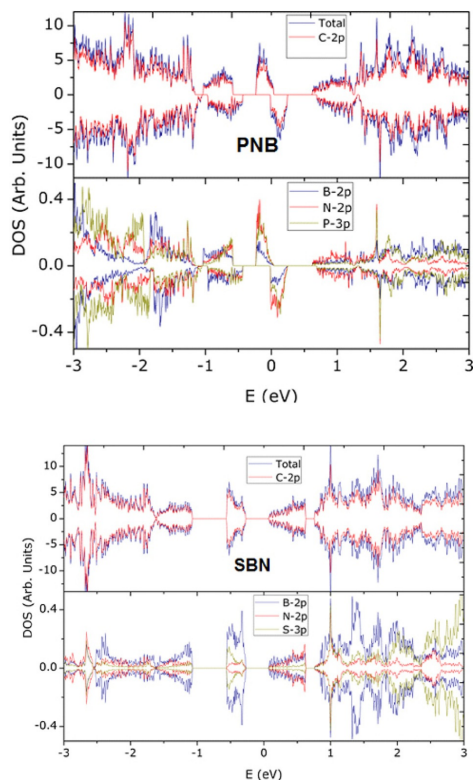
61

**Figure 9.** Partial DOS determined for 5×5 PNB and SBN TDG at the VDW-DF/DZP level of theory.



**Figure 10.** BEs [kcal mol⁻¹] computed for the addition of hydrogen to different sites of AlNB TDG at the M06-L/6-31G* level of theory. Bottom value in italics corresponds to the BE determined when hydrogen is attached on the side of the sheet from which the heteroatom protrudes, and the value above indicates the BE computed when the hydrogenation occurs on the side of the sheet from which the heteroatom does not protrude.



**Figure 11.** BEs [kcal mol⁻¹] computed for the addition of hydrogen to different sites of SiNB triple doped graphene, at the M06-L/6-31G* level of theory. Bottom value in italics corresponds to the binding energy determined when hydrogen is attached on the side of the sheet that the heteroatom protrudes while the value above indicates the binding energy computed when the hydrogenation occurs on the side of the sheet that the heteroatom does not protrude.

sides of the doped sheet are not equivalent, because the 3p heteroatom cannot fit in the graphene plane and thus protrudes to one side. The reaction energies are shown in Figures 10–13 for AlNB, SiNB, PNB, and SBN TDG, respectively. In the case of AlNB, SiNB, and PNB, the most reactive site is the 3p heteroatom, which has an X—H binding energy (BE) for hydrogenation of −71.0, −76.0, and −57.4 kcal mol⁻¹, respectively, at the M06-L/6-31G* level of theory. The BE for the addition of one H atom to perfect graphene is −16.7 kcal mol⁻¹.[49] The sulfur atom is very unreactive in SBN TDG, as the S—H BE is only −6.6 kcal mol⁻¹. However, the C5 site (see Figure 13) has the largest BE of −70.2 kcal mol⁻¹ when the hydrogen atoms is added to this carbon atom and below the plane of the heteroatom. This finding is in line with the reactivities observed for the C atoms directly bonded to 3p dopants. C4 and C5 have the highest BE among the four TDG systems. In general, the N atoms exhibit modest reactivity, and SBN TDG is the system that has the weakest N—H bond. Interestingly, for SBN TDG the boron atom is very reactive, too, with a B—H BE of −62.3 kcal mol⁻¹. If we consider the average BE, the most reactive TDG system is AlNB, with a value of −42.2 for the addition

of H on the side from which the Al dopant protrudes. The average BEs computed for SiNB, PNB, and SBN TDG are 32.2, 34.0, and 31.9 kcal mol⁻¹, respectively. When the addition is performed on the plane opposite to the protrusion of the 3p heteroatoms, the average BE becomes smaller, with values of −38.4, −27.7, −32.0, and −21.8 kcal mol⁻¹, for AlNB, SiNB, PNB, and SBN, respectively.

Finally, it is interesting to compare the hydrogenation of the TGD systems with that of the corresponding DDGs AlN, SiN, PN, and SB [49]. In the case of AlN, the reactivity of the 3p dopant remains unaltered after B addition, since the Al—H BE is −71.0 kcal mol⁻¹. The C4 and C5 atoms bonded to Al in AlNB became more reactive than the C atoms bonded to Al in AlN
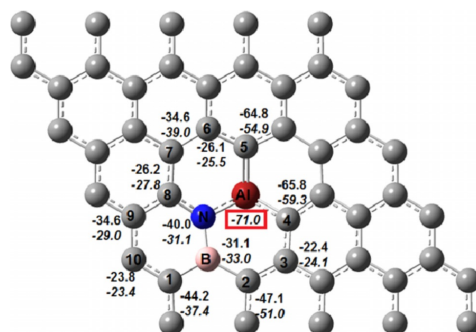
62

**Figure 12.** BEs [kcal mol$^{-1}$] computed for the addition of hydrogen to different sites of PNB TDG at the M06-L/6-31G* level of theory. Bottom values in italics correspond to the BE determined when hydrogen is attached on the side of the sheet from which the heteroatom protrudes, and the value above indicates the BE computed when the hydrogenation occurs on the side of the sheet from which the heteroatom does not protrude.
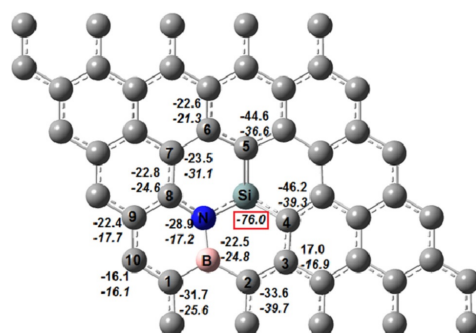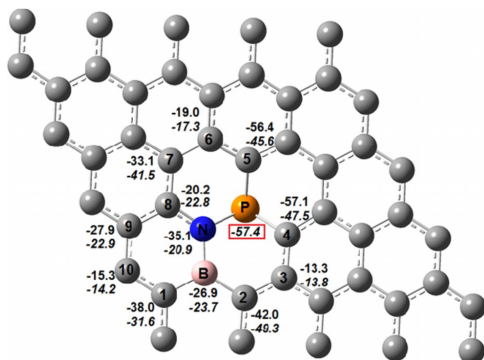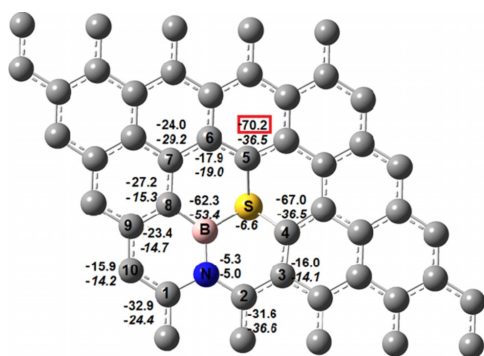


**Figure 13.** BEs [kcal mol$^{-1}$] computed for the addition of hydrogen to different sites of SBN TDG at the M06-L/6-31G* level of theory. Bottom values in italics correspond to the BE determined when hydrogen is attached on the side of the sheet from which the heteroatom protrudes, and the value above indicates the binding energy computed when the hydrogenation occurs on the side of the sheet from which the heteroatom does not protrude.

DDG by 7.0 kcal mol$^{-1}$ [49]. Thus, the introduction of the B dopant enhances the reactivity of C atoms to which it is not directly bonded, probably due to the charge transferred from the B atoms to the C atoms. The Mulliken charges of C4 and C5 in AlNB are the most negative: $-0.42$ and $-0.51$ e, respectively, at the M06-L/6-311G* level of theory. With regards to SiNB TDG, the Si—H BE is 9.4 kcal mol$^{-1}$ lower than that computed for SiN DDG. Similarly, the C4 and C5 atoms of SiNB TDG have a C—H BE that is 6–8 kcal mol$^{-1}$ lower than that of SiN DDG. Therefore, in the case of SiNB, the addition of B does not enhance reactivity. As for PNB TDG, we observed a similar be-

havior to AlNB, that is, substitution with a B atom increases the reactivity with respect to PN DDG. The P—H BEs are $-57.4$ and $-33.4$ kcal mol$^{-1}$ for PNB- and PN-doped graphene, respectively. For C4 and C5 the enhancement of the C—H BE is also pronounced with respect to PN DDG, about 11–12 kcal mol$^{-1}$. Finally, for SBN TDG the C4 and C5 atoms experience a dramatic increase of the C—H BEs. In SB DDG, the C—H BE of the C atoms bonded to S is 59.0 kcal mol$^{-1}$, while in SBN TDG the C—H BEs are $-70.2$ and $-67.0$ kcal mol$^{-1}$ for C5 and C4, respectively. The high reactivity of the C5 and C4 atoms is again associated with a large negative charge of $-0.55$ e at the M06-L/6-311G* level of theory. The B atom has similar B—H BEs of $-62.3$ and $-63.5$ kcal mol$^{-1}$ in SBN- and SB-doped graphene, respectively.

In summary, we have observed that for three systems AlNB, PNB and SBN that the introduction of the third dopant is a useful method to increase the reactivity of the carbon atoms near the substitution site with respect to pristine and dual-doped graphene. SiNB was the sole exception to this behavior.

## 4. Conclusions

By means of first-principles calculations we have investigated the structure, stability, electronic properties, and chemical reactivity of X/B/N TDGs with X = Al, Si, P, N. The following are considered to be the most important findings of this work:

1. For the TDG systems studied the dopants prefer to be bonded to one another instead of separated. In general, the XNB pattern is preferred, with the exception of sulfur, which favors the SBN pattern.
2. The introduction of a third dopant results in a small decrease ($< 0.3$ eV per atom) of the cohesive energies with respect to their DDG counterparts.
3. For SiNB TGD we observed that the introduction of the B dopant restored the Dirac cones that were lost for SiN DDG, and the gap opening at the K point was reduced. On the contrary, for PNB TDG, the bandgap was increased with respect to PN DDG, probably because of the introduction of B, since the PN bonding and electronic structure are rather similar to that of P-doped graphene. For a $5 \times 5$ unit cell, the computed bandgap for PNB TDG was 0.94/0.67 eV (spin up/spin down).
4. For AlNB, PNB, and SBN TDG the reactivities of the carbon atoms were increased with respect to their dual-doped counterparts AlN, PN, and SN. Conversely, for SiNB, the reactivity was lower than for SiN DDG. Therefore, to increase the catalytic properties of graphene, Al, P, and S should be combined with BN motifs.

## Conflict of interest

The authors declare no conflict of interest.

**Keywords:** density functional calculations · doping · electronic structure · graphene · main group elements

[1] Y.-C. Chen, D. G. de Oteyza, Z. Pedramrazi, C. Chen, F. R. Fischer, M. F. Crommie, *ACS Nano* **2013**, *7*, 6123.

[2] R. R. Cloke, T. Marangoni, G. D. Nguyen, T. Joshi, D. J. Rizzo, C. Bronner, T. Cao, S. G. Louie, M. F. Crommie, F. R. Fischer, *J. Am. Chem. Soc.* **2015**, *137*, 8872 – 8875.

[3] E. Carbonell-Sanromà, P. Brandimarte, R. Balog, M. Corso, S. Kawai, A. Garcia-Lekue, S. Saito, S. Yamaguchi, E. Meyer, D. Sanchez-Portal, J. I. Pascual, *Nano Lett.* **2017**, *17*, 50 – 56.

[4] G. D. Nguyen, F. M. Toma, T. Cao, Z. Pedramrazi, C. Chen, D. J. Rizzo, T. Joshi, C. Bronner, Y.-C. Chen, M. Favaro, S. G. Louie, F. R. Fischer, M. F. Crommie, *J. Phys. Chem. C* **2016**, *120*, 2684 – 2687.

[5] X.-Y. Wang, X.-C. Wang, A. Narita, M. Wagner, X.-Y. Cao, X. Feng, K. Müllen, *J. Am. Chem. Soc.* **2016**, *138*, 12783 – 12786.

[6] X. Wang, F. Zhang, K. S. Schellhammer, P. Machata, F. Ortmann, G. Cuniberti, Y. Fu, J. Hunger, R. Tang, A. A. Popov, R. Berger, K. Mullen, X. Feng, *J. Am. Chem. Soc.* **2016**, *138*, 11606 – 11615.

[7] X. Wang, G. Sun, P. Routh, D. H. Kim, W. Huang, *Chem. Soc. Rev.* **2014**, *43*, 7067 – 7098.

[8] H. Terrones, R. Lv, M. Terrones, M. S. Dresselhaus, *Rep. Prog. Phys.* **2012**, *75*, 062501.

[9] a) A. Ambrosi, C. K. Chua, N. M. Latiff, A. H. Loo, C. H. A. Wong, A. Y. S. Eng, A. Bonanni, M. Pumera, *Chem. Soc. Rev.* **2016**, *45*, 2458 – 2493; b) H. L. Poh, M. Pumera, *ChemElectroChem* **2015**, *2*, 190 – 199; c) E. Otyepková, P. Lazar, K. Čépe, O. Tomanec, M. Otyepka, *Appl. Mater. Today* **2016**, *5*, 142.

[10] L. Wang, Z. Sofer, P. Simek, I. Tomandl, M. Pumera, *J. Phys. Chem. C* **2013**, *117*, 23251 – 23257.

[11] N. Al-Aqtash, I. Vasiliev, *J. Phys. Chem. C* **2011**, *115*, 18500 – 18510.

[12] A. Laref, A. Ahmed, S. Binomran, S. J. Luo, *Carbon* **2015**, *81*, 179 – 192.

[13] a) R. Lv, Q. Li, A. R. Botello-Mendez, T. Hayashi, B. Wang, A. Berkdemir, Q. Hao, A. L. Elias, E. Cruz-Silva, H. R. Gutierrez, Y. A. Kim, H. Muramatsu, J. Zhu, M. Endo, H. Terrones, J.-C. Charlier, M. Pan, M. Terrones, *Sci. Rep.* **2012**, *2*, 586; b) T. V. Vineesh, M. A. Nazrulla, S. Krishnamoorthy, T. N. Narayanan, S. Alwarappan, *Appl. Mater. Today* **2015**, *1*, 74 – 79; c) P. Hu, D. Meng, G. Ren, R. Yan, X. Peng, *Appl. Mater. Today* **2016**, *5*, 1 – 8.

[14] P. A. Denis, *Chem. Phys. Lett.* **2010**, *492*, 251 – 257.

[15] P. A. Denis, *Chem. Phys. Lett.* **2011**, *508*, 95 – 101.

[16] a) J. Zhang, J. Li, Z. Wang, X. Wang, W. Feng, W. Zheng, W. Cao, P. Hu, *Chem. Mater.* **2014**, *26*, 2460 – 2466; b) C. Goyenola, C. C. Lai, L. A. Naslund, L. Hultman, J. Rosen, G. K. Gueorguiev, *J. Phys. Chem. C* **2016**, *120*, 9527 – 9534.

[17] S. Yang, L. Zhi, K. Tang, X. Feng, J. Maier, K. Müllen, *Adv. Funct. Mater.* **2012**, *22*, 3634 – 3640.

[18] H. Gao, Z. Liu, L. Song, W. Guo, W. Gao, L. Ci, A. Rao, W. Quan, R. Vajtai, P. M. Ajayan, *Nanotechnology* **2012**, *23*, 275605.

[19] Z. Wang, P. Li, Y. Chen, J. He, W. Zhang, O. G. Schmidt, Y. Li, *Nanoscale* **2014**, *6*, 7281 – 7287.

[20] H. L. Poh, P. Šimek, Z. Sofer, M. Pumera, *ACS Nano* **2013**, *7*, 5262 – 5272.

[21] J. Dai, J. Yuan, *J. Phys. Condens. Matter* **2010**, *22*, 225501.

[22] G. K. Gueorguiev, A. Furlan, Z. Czigany, S. Stafstrom, L. Hultman, *Chem. Phys. Lett.* **2011**, *501*, 400 – 403.

[23] H. L. Poh, Z. Sofer, M. Novacek, M. Pumera, *Chem. Eur. J.* **2014**, *20*, 4284 – 4291.

[24] F. Niu, L.-M. Tao, Y.-C. Deng, Q.-H. Wang, W.-G. Song, *New J. Chem.* **2014**, *38*, 2269 – 2272.

[25] D. Gonzalez Larrude, Y. Garcia-Basabe, F. , Jr., Lazaro Freire, M. L. M. Rocco, *RSC Adv.* **2015**, *5*, 74189 – 74197.

[26] W. Zhou, M. D. Kapetanakis, M. P. Prange, S. T. Pantelides, S. J. Pennycook, J.-C. Idrobo, *Phys. Rev. Lett.* **2012**, *109*, 206803.

[27] Q. M. Ramasse, C. R. Seabourne, D.-M. Kepaptsoglou, R. Zan, U. Bangert, A. J. Scott, *Nano Lett.* **2013**, *13*, 4989 – 4995.

[28] P. A. Denis, *Chem. Phys. Lett.* **2017**, *672*, 70 – 79.

[29] M. Houmad, H. Zaari, A. Benyoussef, A. El Kenz, H. Ez-Zahraouy, *Carbon* **2015**, *94*, 1021 – 1027.

[30] A. Fukushima, A. Sawairi, K. Doi, M. Senami, L. Chen, H. Cheng, *J. Phys. Soc. Jpn.* **2011**, *80*, 074705.

[31] Z. M. Ao, J. Yang, S. Li, Q. Jiang, *Chem. Phys. Lett.* **2008**, *461*, 276 – 279.

[32] T. Nakamura, K. Suzuki, M. Yamashita, *J. Am. Chem. Soc.* **2014**, *136*, 9276 – 9279.

[33] Z. Jin, H. Nie, Z. Yang, J. Zhang, Z. Liu, X. Xu, S. Huang, *Nanoscale* **2012**, *4*, 6455 – 6460.

[34] X. She, Q. Li, N. Ma, J. Sun, D. Jing, C. Chen, L. Yang, D. Yang, *ACS Appl. Mater. Interfaces* **2016**, *8*, 10383 – 10391.

[35] P. A. Denis, *ChemPhysChem* **2014**, *15*, 3994 – 4000.

[36] R. J. Toh, H. L. Poh, Z. Sofer, M. Pumera, *Chem. Asian J.* **2013**, *8*, 1295 – 1300.

[37] J. Zhao, Q. Deng, A. Bachmatiuk, G. Sandeep, A. Popov, J. Eckert, M. H. Rümmeli, *Science* **2014**, *343*, 1228 – 1232.

[38] A. W. Robertson, B. Montanari, K. He, J. Kim, C. S. Allen, Y. A. Wu, J. Olivier, J. Neethling, N. Harrison, A. I. Kirkland, J. H. Warner, *Nano Lett.* **2013**, *13*, 1468 – 1475.

[39] Z. Sofer, O. Jankovský, P. Šimek, K. Klímová, A. Macková, M. Pumera, *ACS Nano* **2014**, *8*, 7106 – 7114.

[40] E. Cruz-Silva, F. López-Urías, E. Muñoz-Sandoval, B. G. Sumpter, H. Terrones, J. C. Charlier, V. Meunier, M. Terrones, *ACS Nano* **2009**, *3*,1913 – 1921.

[41] Y. Zheng, Y. Jiao, L. H. Li, T. Xing, Y. Chen, M. Jaroniec, S. Z. Qiao, *ACS Nano* **2014**, *8*, 5290 – 5296.

[42] X. Ma, G. Ning, C. Xu, J. Gao, *ACS Appl. Mater. Interfaces* **2014**, *6*, 14415 – 14422.

[43] J. P. Paraknowitsch, B. Wienert, Y. Zhang, A. Thomas, *Chem. Eur. J.* **2012**, *18*, 15416 – 15423.

[44] J. M. You, M. S. Ahmed, H. S. Han, J. Choe, Z. Ustundag, S. Jeon, *J. Power Sources* **2015**, *275*, 73 – 79.

[45] W. Kiciński, M. Norek, A. Dziura, M. Polański, *Microporous Mesoporous Mater.* **2016**, *225*, 198 – 209.

[46] B. Feng, J. Xie, C. Dong, S. Zhang, G. Cao, X. Zhao, *RSC Adv.* **2014**, *4*, 17902 – 17907.

[47] X. Ma, G. Ning, Y. Sun, Y. Pu, J. Gao, *Carbon* **2014**, *79*, 310 – 320.

[48] P. A. Denis, C. P. Huelmo, F. Iribarne, *Comput. Theor. Chem.* **2014**, *1049*, 13 – 19.

[49] P. A. Denis, C. P. Huelmo, *Carbon* **2015**, *87*, 106 – 115.

[50] P. A. Denis, C. P. Huelmo, A. S. Martins, *J. Phys. Chem. C* **2016**, *120*, 7103 – 7112.

[51] P. A. Denis, F. Iribarne, *Phys. Chem. Chem. Phys.* **2016**, *18*, 24693 – 24703.

[52] S. Ullah, A. Hussain, W. Syed, M. A. Saqlain, I. Ahmad, O. Leenaerts, A. Karim, *RSC Adv.* **2015**, *5*, 55762 – 55773.

[53] A. Hussain, S. Ullah, M. A. Farhan, *RSC Adv.* **2016**, *6*, 55990 – 56003.

[54] P. A. Denis, F. Iribarne, *Chem. Phys. Lett.* **2016**, *658*, 152.

[55] M. Dion, H. Rydberg, E. Schroder, D. C. Langreth, B. I. Lundqvist, *Phys. Rev. Lett.* **2004**, *92*, 246401.

[56] Y. Zhao, D. G. Truhlar, *J. Chem. Phys.* **2006**, *125*, 194101.

[57] J. Heyd, G. E. Scuseria, *J. Chem. Phys.* **2004**, *120*, 7274 – 7280.

[58] Gaussian 09 (Revision A1), M. J. Frisch, G. W. Trucks, H. B. Schlegel, G. E. Scuseria, M. A. Robb, J. R. Cheeseman, G. Scalmani, V. Barone, B. Mennucci, G. A. Petersson, H. Nakatsuji, M. Caricato, X. Li, H. P. Hratchian, A. F. Izmaylov, J. Bloino, G. Zheng, J. L. Sonnenberg, M. Hada, M. Ehara, K. Toyota, R. Fukuda, J. Hasegawa, M. Ishida, T. Nakajima, Y. Honda, O. Kitao, H. Nakai, T. Vreven, J. A. Montgomery, Jr., J. E. Peralta, F. Ogliaro, M. Bearpark, J. J. Heyd, E. Brothers, K. N. Kudin, V. N. Staroverov, R. Kobayashi, J. Normand, K. Raghavachari, A. Rendell, J. C. Burant, S. S. Iyengar, J. Tomasi, M. Cossi, N. Rega, J. M. Millam, M. Klene, J. E. Knox, J. B. Cross, V. Bakken, C. Adamo, J. Jaramillo, R. Gomperts, R. E. Stratmann, O. Yazyev, A. J. Austin, R. Cammi, C. Pomelli, J. W. Ochterski, R. L. Martin, K. Morokuma, V. G. Zakrzewski, G. A. Voth, P. Salvador, J. J. Dannenberg,

64

65

**ChemPubSoc**
Europe

**CHEMPHYSCHEM**
Articles

S. Dapprich, A. D. Daniels, O. Farkas, J. B. Foresman, J. V. Ortiz, J. Cioslowski, D. J. Fox, Gaussian, Inc., Wallingford, CT, **2009**.

[59] P. Ordejón, E. Aratacho, J. M. Soler, *Phys. Rev. B* **1996**, *53*, R10441.

[60] J. M. Soler, E. Artacho, J. D. Gale, A. Garcia, J. Junquera, P. Ordejon, D. Sanchez-Portal, *J. Phys. Condens. Matter* **2002**, *14*, 2745.

[61] W. Hehre, L. Radom, P. v. R. Schleyer, J. A. Pople, *Ab Initio Molecular Orbital Theory,* Wiley, New York, **1986**.

[62] N. Troullier, J. L. Martins, *Phys. Rev. B* **1991**, *43*, 1993.

65

## 5 Electrochemical properties of doped graphene

Humankind is facing several issues in which a key issue is the energy storage and conversion. For energy requirements, there is a substantial dependency on fossil fuels which can be used one-time (non-renewable) and their resources are limited which means that ultimately there will be an ending of the fossil fuels. Additionally, the consumption of fossil fuels is immensely responsible for the production of several hazardous greenhouse gases including $CO_2$. In this regard, the substitution of fossil fuels with environmental-friendly and renewable resources becomes crucial. One of the substitutes is the rechargeable secondary batteries. Among them, lithium-ion batteries (LIBs) are the most famous and in practical use. As discussed briefly earlier, the anode material in LIBs, which is graphite, has issues regarding the storage capacity which is just 372 mAh/g [23, 24, 97]. If we only rely on LIBs, then there is a fear of running out of Li resources, which will exponentially increase the price of LIBs [28]. Another approach is the replacement of LIBs with SIBs and KIBs [29–31, 98–101]. However, this seems impractical as the Na storage capacity of using graphite as an anode is just 35 mAh/g [32]. These make the replacement of LIBs with SIBs/KIBs and the discovery of an efficient anode material critical and demanding. To tackle these issues, we propose mono- and dual-doped graphene. Before investigating the real problem, we first checked the accuracy of our methodology. To that end, we performed benchmarking calculations on benzene alkali complexes by using many of the available DFT functionals, especially most of the vdW-DF functionals [228]. It is found that the vdW-DF1 functional as implemented in SIESTA code is the best choice and, furthermore, many of the versatile vdW-DF functionals tend to overestimate the binding. Therefore, it is of immense importance to take care when using vdW-DF functionals in the investigation of alkali and graphene-based- or graphene-like-materials. In addition, we also benchmarked the interaction of alkaline atoms with pyridine and, furthermore, discussed its implication for the adsorption on nitrogen doped graphene [229]. This methodology was further applied to study the interaction of alkali atoms with doped graphene. In the first place, we study the adsorption of Li and Na on Be-doped graphene. It is found that the introduction of a single Be atom inside the graphene plane can cause a significant improvement in the adsorption of Li/Na. That being said, the adsorption energy of Li/Na is increased from -1.11/-0.67 eV/atom to -2.53/-2.04 eV/atom due to a single Be atom doping in a 5x5 supercell of graphene. Furthermore, it is quite likely for alkali atoms to make cluster on the surface of graphene, the introduction of one Be atom can easily capture 16 Li and 10 Na atoms, thus causing a great improvement in the storage capacity. The theoretical storage capacity of Be doped graphene for Li and Na was found to be 2303.3 and 1005.6 mAh/g, respectively. These calculated storage capacities were 6.19 times

and 28.71 times to that of graphite for Li and Na storage, respectively. In addition, we find that the alkali adsorption also alters the electronic structure of graphene to metallic one which is another key aspect in alkali-based batteries. These huge rises in the storage capacities of Be doped graphene along with several other interesting properties suggest that Be doped graphene can be a possible and extremely efficient anode material for alkali-based batteries. These results are published in (APMT 9, 333-340, 2017, and CGS 2, 35-44, 2018) [230, 231] and are given in Appendix B.1 and B.2.

In the next step, we explore some DDG systems among which Be-B DDG is further considered as a possible anode material for alkali-based batteries. The integration of Be and B were done at the *ortho*, *meta*, and *para* dispositions. It is found that the *ortho* and *para* dispositions were very close in energy. In addition, at ortho disposition, the Be and B atoms were not bonded which is similar to the case of S-N DDG reported earlier [87]. We also check the stability of DDG, in various configurations, with the help of ab-initio molecular dynamics simulations which show that these structures are quite stable even at 600 K temperature. Additionally, the Be-B DDG systems were found to be metallic ensuring better electronic conductivities which are critical in alkali-based batteries. We also compute the adsorption energy of one Li/Na atom adsorbed on Be-B DDG to compare the results with that of pristine graphene. We see a monumental increment in the adsorption energy of Li/Na. The adsorption energy of Li/Na can be as high as -3.44/-2.92 eV/atom. This means almost 3 and 4.35 times enhancement in the adsorption of Li and Na, respectively. The concentration of alkali contents was increased systematically by carefully analyzing the changes in the adsorption energy. We find that Be-B DDG can easily hold nine ions on each side (18 on both sides). Interestingly, we get exceptional storage capacities of 2334 mAh/g and 1012 mAh/g for Li and Na, respectively. The calculated storage capacities are 6.3/28.91 times larger than the Li/Na storage capacities of graphite. This article was published in (New J. Chem., 2018,42, 10842-10851) [232] and is given in Appendix B.3.

Additionally, the adsorption of alkali atoms (Li, Na, and K) on BeN DDG was analyzed. As Be-N dual doping favors the *ortho* disposition, therefore, this pattern is considered for the adsorption of alkali atoms. In this type of configuration, the dopants are contributing to the four hexagons for which two are connected with Be-N, and other two connected with Be and N. When a single alkali is adsorbed on a BeN DDG, the adsorption energy is calculated to be -2.48, -1.89, and -2.13 eV for Li, Na, and K, respectively. For comparison, the corresponding values on pristine graphene are -1.11, -0.67, and -1.0 eV. Consequently, the adsorption energies were greatly improved by the incorporation of BeN doping in graphene. In the next step, four alkali atoms were adsorbed around the BeN impurities which give the adsorption strength of -2.32, -1.12, -2.0 eV/atom for Li, Na, and

K, respectively. That being said, a small reduction occurred in the adsorption strength as a function of increasing alkali atoms concentration. Furthermore, BeN DDG offers an exceptional capacity of 2255, 996, and 747 mAh/g for Li, Na, and K, respectively. For comparison, the K storage capacity of $Mo_2C$, which can be regarded as an efficient anode, is 263 mAh/g [128]. This shows that our calculated storage capacity is almost 3 times to that of $Mo_2C$. The details about the storage capacity and open-circuit voltage can be found in literature [230, 232]. This paper was published in (IJQC 119, e25900, 2019) [233].

Finally, several XY DDG (X=Al, Si, P, S; Y= B, N, O) were decorated with Na and K to search for promising candidates for potential anode materials. The strength of alkali atoms is significantly increased in all the cases studied in comparison with the pristine graphene. There is a significant difference in the adsorption energy among Na and K on pure graphene. This difference, however, is largely mitigated and, furthermore, becomes meaningless (0.05 eV) in some DDG cases. Among various DDG systems, SiB and SN DDG patterns were found to be the most efficient which cause a humongous rise in the adsorption strength of alkali atoms. Having said that, the Na adsorption energy of SiB and SN DDG is -2.13 and -2.0 eV, respectively. For K, we recorded a value of -2.42 eV for both the SiB and SN isomers. It is proposed that the aforementioned systems should further be investigated to be used in alkali-based batteries. The results were published in (ACS Omega 2018, 3, 11, 15821-15828) [234] and is given in Appendix B.4.

WILEY QUANTUM CHEMISTRY

**FULL PAPER**

# Adsorption and diffusion of alkali-atoms (Li, Na, and K) on BeN dual doped graphene

**Saif Ullah**[1] ⓘ   |   **Pablo A. Denis**[2] ⓘ   |   **Fernando Sato**[1]

[1]Departamento de Física, Instituto de Ciências Exatas, Campus Universitário, Universidade Federal de Juiz de Fora, Juiz de Fora, MG, Brazil

[2]Computational Nanotechnology, DETEMA, Facultad de Química, UDELAR, Montevideo, Uruguay

**Correspondence**
Saif Ullah, Departamento de Física, Instituto de Ciências Exatas, Campus Universitário, Universidade Federal de Juiz de Fora, Juiz de Fora, MG 36036-900, Brazil.
Email: sullah@fisica.ufjf.br

**Abstract**

We employ first-principles DFT calculations to explore the potential use of BeN dual doped graphene (DDG) as an anode material for alkali-based batteries. The introduction of BeN in graphene raise the adsorption of Li, Na, and K by 1.37 eV (2.23 times), 1.23 eV (2.83 times), and 1.14 eV (2.14 times), respectively. Furthermore, BeN DDG offers a modest energy barrier for alkali atoms studied. Moreover, the alkali atoms have good chemistry with Be and the interaction strength decreases during the migration toward N. Most importantly, the exceptional storage capacity of BeN DDG for Li (~2255 mAh/g), Na (~996 mAh/g), and K (~747 mAh/g) makes it a highly desirable anode material. Additionally, the average open circuit voltage offered for Li (0.66 V), Na (0.33 V), and (K = 1.10 V) is found to be in excellent range. All these outstanding properties provide the possibility of using BeN DDG in future alkali-based batteries.

**KEYWORDS**

adsorption, alkali-based batteries, DFT, doping, electrochemical properties

## 1 | INTRODUCTION

Fossil fuels, on one hand, are the main source of energy to mankind and on another hand are the main reason for the production of greenhouse gases ($CO_2$ etc). Moreover, another issue is the nonrenewability of fossil fuels which also make the "energy storage and conversion" a sizzling topic. Subsequently, the secondary-battery technology becomes one of the best alternatives for energy storage without affecting the mothernature. The first commercialized lithium-ion battery (LIB) introduced in 1991, thanks to SONY, gained monumental attention due to its broad applications range.[1–7] However, the population growth and the scarcity of Li (22 ppm in the earth crust) are the challenges to meet the global energy demand.[8] In addition to this, the storage capacity of the well-known graphite-based anode material in LIBs is ~372 mAh/g, which is not sufficient from the practical point of view.[1,3,9] Fortunately, sodium (Na) and potassium (K) can address the former issue due to their abundance (Na = 25 670 ppm, and K = 28 650 ppm) and the same electrochemical procedure as that of LIBs.[6,7,10–15] Unfortunately, due to the bigger size of Na/K, the quest of the efficient anode material is the prime barrier. Having said that, the intercalation of Na/K to anode material(s) is a serious obstacle and, therefore, the Na storage capacity of graphite is as low as ~35 mAh/g.[16] Consequently, exploration of appropriate materials becomes critically challenging.

Graphene, by virtue of its exceptional physical and chemical properties, can be the best choice for alkali based batteries to be used as an anode material.[17] However, the likely dendrite formation will result in poor charge/discharge rate.[18–20] Fortunately, the chemistry of graphene can easily be modified by certain techniques, among which doping is regarded as the simplest and efficient way.[21–26] It is advantageous to dope graphene with the neighbors (B and N) and next neighbors (Be and O) atoms due to the relatively similar atomic radii of these atoms.[5,21,24] Additionally, the toxicity of Be is well-known but this cannot restrict the use of Be in practical applications such as in optoelectronics.[27,28] In addition to this, a safer way regarding the tackling of Be is proposed recently.[29] Furthermore, the dual doped graphene (DDG), which results in the

simultaneous integration of two dopants in graphene, is found to be relatively easier to synthesize in comparison with the mono-doped graphene. Furthermore, these DDG such as BeB, BeN, BeO, PN, SN, etc. systems possess great physic-chemical properties.[6,21,22,26,30–36] Nevertheless, BeB DDG systems have already been proven as an exceptional anode material for LIBs and SIBs.[6]

In this letter, we study the adsorption and diffusion of alkali atoms (Li, Na, and K) with BeN DDG by means of nonlocal vdW-DF DFT calculations. The main electrochemical properties, such as adsorption energy, Storage capacity, and average open circuit voltage (OCV are calculated. These remarkable properties can be useful in initiating the experiment.

## 2 | COMPUTATIONAL DETAILS

We use SIESTA[37,38] code which is based on the DFT method to perform vdW-DF1[39,40] calculations. The choice of vdW-DF1 is obvious as in recent studies, we benchmarked various DFT methods (including GGA, PBE-D, and many vdW-DF flavors) by studying the interaction of alkali atoms with benzene complex, graphene, and hexagonal boron phosphide[41] and found that the vdW-DF1 method as implemented in SIESTA code give the best interaction energies, being CCSD(T) value as the reference.[42,43] The norm-conserving (NC) Troullier-Martins pseudopotentials (PPs) were used.[44] The DZP basis set and a mesh cut-off of 200 Ry is used. We employed periodic boundary condition in a $5 \times 5$ supercell sampled with $8 \times 8 \times 1$ kpoints with a vacuum region of 20 Å. We also make use of $2 \times 2$ and $3 \times 3$ supercells to report the maximum theoretical storage capacities. The adsorption energy is calculated as:

$$E_{ads} = \frac{E_{tot} - E_{slab} - nE_{alkali}}{n}$$

where, $E_{tot}$ and $E_{slab}$ are the total and BeN DDG energies, respectively. Finally, $E_{alkali}$ and $n$ represent the energy and amount of alkali atoms, respectively.

## 3 | RESULTS AND DISCUSSION

In a recent study, it is shown that Be and N favor the ortho disposition in graphene, therefore, we started our investigation from the very same model.[6,22] This being said, there are three hexagonal rings where the initial adsorption is considered are; ring with Be and N, ring with Be, and ring with N. During optimization, the alkali atoms diffused from the BeN ring toward and beneath the Be atom, since Be atom protrudes out of graphene plane as reported in earlier studies.[5,6] This migration is due to the structural modification induced by the Be buckling which provides enough room for alkali atoms. Furthermore, this pattern is found to be the most favorable which is in agreement with the prior investigations.[5,6,23] Moreover, the least favorable site is the hexagonal ring with N. Additionally, substantial increment occurs in the adsorption by the introduction of BeN in graphene. In the second step, we adsorbed four alkali atoms around the BeN dopants and calculated the adsorption strength. Interestingly, a small reduction in the adsorption energy occurred in comparison with the single alkali adsorption. This means that BeN DDG is able to bear the load of alkali atoms and can be employed as anode material in alkali-based batteries.

Next, we study the diffusion of alkali atoms on BeN DDG. For diffusion and the calculations of energy barriers, the (climbing) nudge elastic band method ((c-) NEB) is the most sophisticated way.[45] However, it requires great computational resources. Herein, we study the diffusion of alkali atoms manually by introducing a constrained in the calculations. The alkali atoms are constrained to follow the selected path with the liberty provided along the z-axis to perceive their relaxed position. The path is divided into tiny displacement steps and the energy is calculated at each step. Two paths were selected; one going through the top of Be, BeN bridge, N and reaching the relaxed position, another is crossing the Be-C bridge, the hollow sites, the N-C bridge, and the final position. These are shown in Figure 1. The accuracy of our method is confirmed from the Li diffusion on pristine graphene where the energy barrier is calculated to be 0.28 eV which agrees well with the reported literature.[46,47] It can be seen that the energy barrier in the Li case is the highest while lowest in the K case. Furthermore, path 1 offers a bit lower energy barrier in comparison with path 2. These moderate energy barriers are comparable to that of silicon allotrope.[48] In addition to this, it is clear that, around Be atom, the interaction with alkali atoms is stronger in comparison with the N and in the vicinity of N atom. Summary of all the results is depicted in Table 1.

For the sake of maximum theoretical capacity, we use $BeNC_6$ for Li and $BeNC_{16}$ for Na and K. Moreover, the stability of the $BeNC_6$ compound is already reported.[22] Theoretical capacity, which is one of the prime electrochemical properties, can be calculated by using the following expression[5]:

$$C = \frac{nF}{M} \times \frac{1000}{3600}$$

where, $F$, $n$, and $M$ represent the Faraday constant, number of alkali ions in the electrolyte, and molar mass of the anode material. Finally, $\frac{1000}{3600}$ is for the conversion of coulomb to mAh/g. The alkali storage capacities of $XBeNC_{48}$ and $X_4BeNC_{48}$ (where X = Li, Na, and K) are calculated to be 44.703 mAh/g and 178.811 mAh/g, respectively. Furthermore, the computed maximum possible theoretical capacity in $Li_8BeNC_6$ is as high as 2254.951 mAh/g. Nevertheless, the storage capacities in $Na_8BeNC_{16}$ and $K_6BeNC_{16}$ are predicted to be 996.36 mAh/g and 747.271 mAh/g,
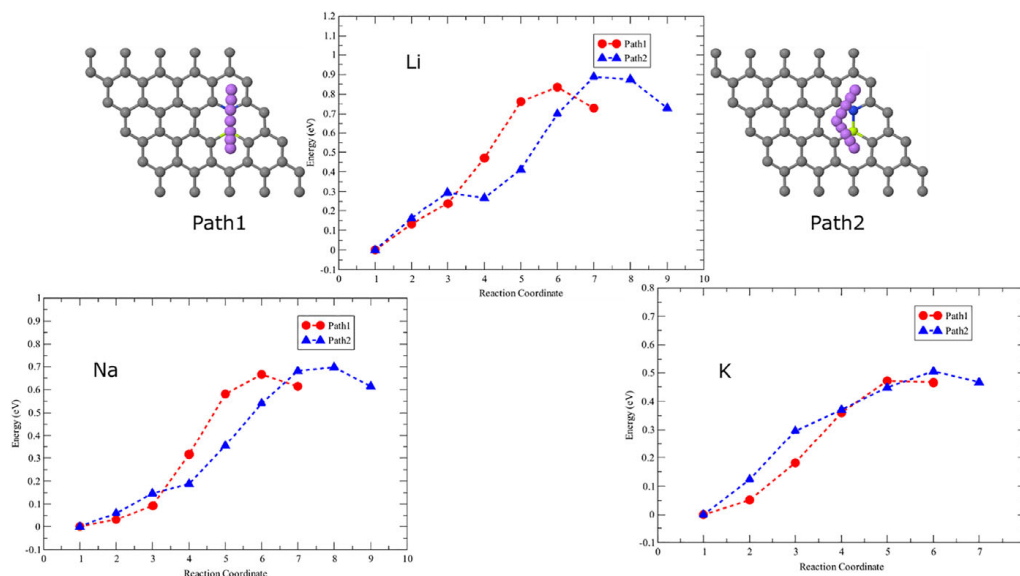
**FIGURE 1**    The alkali atoms diffusion along path 1 and path 2 is shown. It is clear that the strongest binding around Be atom goes on decreasing as the alkali atoms migrate toward N atom

respectively. The storage capacities of other versatile anode materials[43] are given for comparative purposes. The Li storage capacity of Ti3C2,[49] graphite,[1] phosphorene,[50] and Mo$_2$C[51] are 320, 372, 433, and 526 mAh/g, respectively. The Na storage capacities of graphite,[16] MoS$_2$,[52] and SnS$_2$[53] are 35, 146, and 492 mAh/g, respectively. Finally, the K storage capacities of Ti$_3$C$_2$,[54] GeS,[55] and Mo$_2$C[56] are limited to 192, 256, and 263 mAh/g, respectively. Furthermore, the Li/Na storage capacities of Be doped and Be-B DDG are 2303.3/1005.7 mAh/g and 2334/1012 mAh/g, respectively.[5–7] These exceptional storage capacities suggest that BeN DDG can compete with any of the available anode material and thus demand for its early synthesis.

Another important point is the average OCV) and, therefore, calculated by the formula given as under:

$$OCV = -\frac{(E_{tot} - E_{slab} - nE_{BCC})/n}{ze}$$

where, $E_{BCC}$ is the energy of one alkali atoms taken from their respective bulk BCC structure while $z$ is the alkali charge in the electrolyte ($z = 1$). The average OCVs in case of Li, Na, and K are computed to be 0.667 V, 0.3 V, and 1.16 V, respectively. The average OCVs vs storage capacities can be seen in Figure 2. These excellent OCVs along with the above-mentioned properties show that BeN DDG can be an exceptional anode material in alkali-based batteries.

**TABLE 1**    Summary of the results are shown. For XBeNC$_{48}$ (X = Li, Na, and K), the results of only the most favorable system are included

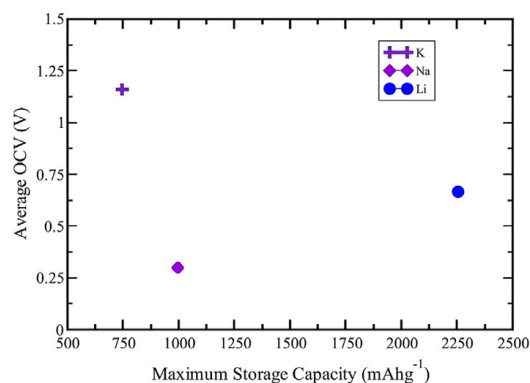| System | Adsorption energy (eV/alkali-atom) | Storage capacity (mAh/g) | OCV (V) |
|---|---|---|---|
| Graphene (LiC$_{50}$) | −1.11 | | |
| Graphene (NaC$_{50}$) | −0.67 | | |
| Graphene (KC$_{50}$) | −1.0 | | |
| LiBeNC$_{48}$ | −2.48 | 44.703 | 1.07 |
| Li$_4$BeNC$_{48}$ | −2.32 | 178.811 | 0.909 |
| Li$_8$BeNC$_6$ | −1.26 | 2254.951 | 0.023 |
| NaBeNC$_{48}$ | −1.89 | 44.703 | 0.819 |
| Na$_4$BeNC$_{48}$ | −1.12 | 178.811 | 0.046 |
| Na$_8$BeNC$_{16}$ | −1.10 | 996.36 | 0.024 |
| KBeNC$_{48}$ | −2.13 | 44.703 | 1.57 |
| K$_4$BeNC$_{48}$ | −2.0 | 178.811 | 1.54 |
| K$_6$BeNC$_{16}$ | −1.039 | 747.271 | 0.48 |

**FIGURE 2** Average OCV (V) vs maximum storage capacity (mAh/g)

## 4 | CONCLUSION

We investigated the possible use of BeN DDG as anode material in alkali-based batteries with the help of nonlocal vdW-DFT. It is shown that more than two times increment occurred in adsorption strength of alkali atoms by the introduction of BeN in graphene. Consequently, this will prevent the dendrite formation of alkali atoms. Furthermore, the lowest/highest energy barrier is found for K/Li, while an intermediate for Na. In addition to this, the excellent average OCVs of Li (0.66 V), Na (0.33 V), and K (1.16 V) ensure the safety. Finally, the exceptional storage capacities for Li (~2255 mAh/g), Na (~996 mAh/g), and K (~747 mAh/g) make BeN DDG an attractive anode material for alkali-based batteries.

## AUTHOR CONTRIBUTIONS

*Conceptualization:* Saif Ullah, Pablo A. Denis, Fernando Sato
*Methodology:* Saif Ullah, Pablo A. Denis
*Writing original draft:* Saif Ullah
*Data curation:* Saif Ullah, Pablo A. Denis
*Writing—review and editing:* Saif Ullah, Pablo A. Denis, Fernando Sato
*Funding acquisition:* Pablo A. Denis, Fernando Sato
*Resources:* Pablo A. Denis, Fernando Sato
*Supervision:* Saif Ullah, Pablo A. Denis, Fernando Sato

## ORCID

*Saif Ullah* https://orcid.org/0000-0001-8836-9862
*Pablo A. Denis* https://orcid.org/0000-0003-3739-5061

## REFERENCES

[1] J. M. Tarascon, M. Armand, *Nature* **2001**, *414*, 359.
[2] B. Scrosati, *Electrochim. Acta* **2000**, *45*, 2461.
[3] M. Armand, J. M. Tarascon, *Nature* **2008**, *451*, 652.
[4] J. B. Goodenough, Y. Kim, *Chem. Mater.* **2010**, *22*, 587.
[5] S. Ullah, P. A. Denis, F. Sato, *Appl. Mater. Today* **2017**, *9*, 333.
[6] S. Ullah, P. A. Denis, F. Sato, *New J. Chem.* **2018**, *42*, 10842.
[7] S. Ullah, P. A. Denis, F. Sato, *Science* **2018**, *2*, 1.
[8] J.-M. Tarascon, *Nat. Chem.* **2010**, *2*, 510.
[9] J. R. Dahn, T. Zheng, Y. Liu, J. S. Xue, *Science* **1995**, *270*, 590.

[10] B. L. Ellis, L. F. Nazar, *Curr. Opinion Solid State Mater. Sci.* **2012**, *16*, 168.
[11] Y. Wen, K. He, Y. Zhu, F. Han, Y. Xu, I. Matsuda, Y. Ishii, J. Cumings, C. Wang, *Nat. Commun.* **2014**, *5*, 4033.
[12] A. Samad, M. Noor-A-Alam, Y.-H. Shin, *J. Mater. Chem. A* **2016**, *4*, 14316.
[13] M. Moshkovich, Y. Gofer, D. Aurbach, *J. Electrochem. Soc.* **2001**, *148*, E155.
[14] A. Eftekhari, Z. Jian, X. Ji, *ACS Appl. Mater. Interfaces* **2017**, *9*, 4404.
[15] K. Hans Wedepohl, *Geochim. Cosmochim. Acta* **1995**, *59*, 1217.
[16] M. D. Slater, D. Kim, E. Lee, C. S. Johnson, *Adv. Funct. Mater.* **2013**, *23*, 947.
[17] K. S. Novoselov, A. K. Geim, S. V. Morozov, D. Jiang, Y. Zhang, S. V. Dubonos, I. V. Grigorieva, A. A. Firsov, *Science* **2004**, *306*, 666.
[18] J. Zhou, Q. Sun, Q. Wang, P. Jena, *Phys. Rev. B* **2014**, *90*, 205427.
[19] M. Liu, A. Kutana, Y. Liu, B. I. Yakobson, *J Phys Chem Lett* **2014**, *5*, 1225.
[20] X. Fan, W. T. Zheng, J.-L. Kuo, D. J. Singh, *ACS Appl. Mater. Interfaces* **2013**, *5*, 7793.
[21] S. Ullah, A. Hussain, W. Syed, M. A. Saqlain, I. Ahmad, O. Leenaerts, A. Karim, *RSC Adv.* **2015**, *5*, 55762.
[22] A. Hussain, S. Ullah, M. A. Farhan, *RSC Adv.* **2016**, *6*, 55990.
[23] P. A. Denis, *Chem. Phys. Lett.* **2017**, *672*, 70.
[24] S. Ullah, A. Hussain, F. Sato, *RSC Adv.* **2017**, *7*, 16064.
[25] S. Ullah, P. A. Denis, F. Sato, *ChemPhysChem* **2017**, *18*, 1864.
[26] A. Hussain, S. Ullah, M. A. Farhan, M. A. Saqlain, F. Sato, *New J. Chem.* **2017**, *41*, 10780.
[27] D. Heciri, L. Beldi, S. Drablia, H. Meradji, N. E. Derradji, H. Belkhir, B. Bouhafs, *Comput. Mater. Sci.* **2007**, *38*, 609.
[28] C. M. I. Okoye, *Eur. Phys. J B Condens. Matter.* **2004**, *39*, 5.
[29] S. A. Couchman, N. Holzmann, G. Frenking, D. J. D. Wilson, J. L. Dutton, *Dalton Trans.* **2013**, *42*, 11375.
[30] E. Cruz-Silva, F. López-Urías, E. Muñoz-Sandoval, B. G. Sumpter, H. Terrones, J.-C. Charlier, V. Meunier, M. Terrones, *ACS Nano* **2009**, *3*, 1913.
[31] Y. Zheng, Y. Jiao, L. H. Li, T. Xing, Y. Chen, M. Jaroniec, S. Z. Qiao, *ACS Nano* **2014**, *8*, 5290.
[32] P. A. Denis, C. P. Huelmo, F. Iribarne, *Comp. Theor. Chem.* **2014**, *1049*, 13.
[33] P. A. Denis, C. Pereyra Huelmo, A. S. Martins, *J. Phys. Chem. C* **2016**, *120*, 7103.
[34] P. A. Denis, C. Pereyra Huelmo, *Carbon* **2015**, *87*, 106.
[35] P. A. Denis, F. Iribarne, *Phys. Chem. Chem. Phys.* **2016**, *18*, 24693.
[36] S. Ullah, P. A. Denis, F. Sato, *ACS Omega* **2018**, *3*, 15821.
[37] P. Ordejón, E. Artacho, J. M. Soler, *Phys. Rev. B* **1996**, *53*, R10441.
[38] J. M. Soler, E. Artacho, J. D. Gale, A. Garcia, J. Junquera, P. Ordejon, D. Sanchez-Portal, *J. Phys. Condens. Matter* **2002**, *14*, 2745.
[39] M. Dion, H. Rydberg, E. Schröder, D. C. Langreth, B. I. Lundqvist, *Phys. Rev. Lett.* **2004**, *92*, 246401.
[40] G. Román-Pérez, *Phys. Rev. Lett.* **2009**, *103*, 096102.
[41] S. Ullah, P. A. Denis, F. Sato, *ACS Omega* **2018**, *3*, 16416.
[42] S. Ullah, P. A. Denis, F. Sato, *Chem. Phys. Lett.* **2018**, *706*, 343.
[43] S. Ullah, P. A. Denis, F. Sato, *Appl. Surf. Sci.* **2019**, *471*, 134.
[44] N. Troullier, J. L. Martins, *Phys. Rev. B* **1991**, *43*, 1993.
[45] G. Henkelman, B. P. Uberuaga, H. Jónsson, *J. Chem. Phys.* **2000**, *113*, 9901.
[46] X. Fan, W. Zheng, J.-L. Kuo, *ACS Appl. Mater. Interfaces* **2012**, *4*, 2432.
[47] D. Wu, Y. Li, Z. Zhou, *Theor. Chem. Accounts* **2011**, *130*, 209.
[48] A. Marzouk, F. A. Soto, J. C. Burgos, P. B. Balbuena, F. El-Mellouhi, *J. Electrochem. Soc.* **2017**, *164*, A1644.
[49] Q. Tang, Z. Zhou, P. Shen, *J. Am. Chem. Soc.* **2012**, *134*, 16909.
[50] W. Li, Y. Yang, G. Zhang, Y.-W. Zhang, *Nano Lett.* **2015**, *15*, 1691.
[51] Q. Sun, Y. Dai, Y. Ma, T. Jing, W. Wei, B. Huang, *J Phys Chem Lett* **2016**, *7*, 937.
[52] M. Mortazavi, C. Wang, J. Deng, V. B. Shenoy, N. V. Medhekar, *J. Power Sources* **2014**, *268*, 279.
[53] T. Zhou, W. K. Pang, C. Zhang, J. Yang, Z. Chen, H. K. Liu, Z. Guo, *ACS Nano* **2014**, *8*, 8323.
[54] D. Er, J. Li, M. Naguib, Y. Gogotsi, V. B. Shenoy, *ACS Appl. Mater. Interfaces* **2014**, *6*, 11173.
[55] F. Li, Y. Qu, M. Zhao, *J. Mater. Chem. A* **2016**, *4*, 8905.
[56] D. Cakr, C. Sevik, O. Gulseren, F. M. Peeters, *J. Mater. Chem. A* **2016**, *4*, 6029.

# 6 Electrochemical properties of 2D materials beyond graphene

In this chapter, 2D materials beyond graphene were investigated to design a proficient anode material. In this regard, hundreds of calculations were performed with various DFT functionals including almost every flavor of vdW-DF to study and carefully analyze the interaction of alkali atoms (Li, Na, and K) with $h$BP. For comparative purposes, the same calculations were also extended to graphene. In order to accomplish this mission, we make use of the four most famous DFT codes (VASP, SIESTA, QE, and Gaussian) which enable us to carry out semi-local GGA, DFT-D (dispersion corrected), meta GGA, and several versatile non-local vdW-DF functionals. The details can be found in Chapter 3 and in the corresponding paper [235] and the references therein. It is found that the adsorption strength has a strong dependence on the choice of functional employed. The variation in the interaction strength spans over a wide range which is quite prominent. That being said, the difference between the lowest and highest value is about 0.7 eV in almost every case. In addition, the weaker binding comes from the revPBE functional, whereas, the stronger binding is a result of using the DFT-D method. Moreover, we also observe that some of the popular vdW-DF functionals exceeded the DFT-D2 in the overestimation of the binding in a few cases. Consequently, it is crucial to handle various vdW-DF functionals with great care where the interaction between alkali metals and graphene (or related materials) is involved. Additionally, it is found that any flavor of pseudopotential can be used with various vdW-DF functionals. The use of PBE PPs requires some additional attention, whereas, revPBE works excellently with any vdW-DF flavor.

The bandgap of $h$BP is 1.1 eV which can easily be altered to a metallic one by the introduction of alkali atoms which is a requirement for good electronic conductivity. Additionally, the strength of alkali atoms on $h$BP is in quite favorable range and, furthermore, less affected by increasing the concentration of alkalis, a fact which is absent in graphene. The only exception to that is the K adsorption on a unitcell where a significant reduction in the adsorption strength was noted. This reduction can be attributed to the bigger size of K (in comparison with Na and Li) and a relatively larger space is needed for K in order to minimize the repulsion between nearest K atoms. Regarding the storage capacity, we find that $h$BP is an exceptional candidate with a large storage capacity of 1283 mAh/g for all the alkalis studied. However, the K storage capacity at the vdW-DF level as implemented in SIESTA is the only exception where the calculated value was 642 mAh/g, half of the value predicted by every other functional employed. Consequently, caution must be taken when designing an anode material for alkali-based batteries. The paper is published in (APSUS 471, 134-141 2019) [235].

We also check the relation of alkalis adsorption on $h$BAs, which is another material belonging to the same family of $h$BP and $h$BN. With the help of DFT calculations, we calculate every factor which is important in the electrochemical study. Initially, alkalis were adsorbed at various sites and found that the hollow site is the most favorable (as expected) and B site is the least. Additionally, As site is close in energy with the hollow site especially in K case. We also observe the energy change as a function of increasing the vertical height of alkali atoms from the $h$BAs plane. Interestingly, it is found that after a certain critical height, there is no energy barrier as suggested by the sharp rise in the adsorption energy. Consequently, $h$BAs can rapidly be loaded with alkalis without an energy barrier. Charge transfer is also calculated which confirms the depletion of charge around alkali atoms. This charge, in turn, was accumulated on $h$BAs. Although $h$BAs is a semiconductor with a gap of 0.89 eV, the decoration with alkalis turns the electronic behavior from semiconducting to metallic thus improving the electronic conductivity. Moreover, ionic mobility has a critical role in designing an anode material. This aspect was explored by using the SIESTA code and constrained method. The details can be seen in [233]. This method is quite reliable and much faster. It is shown that $h$BAs offers a lower energy barrier of 0.322, 0.187, and 0.095 eV for Li, Na, and K, respectively. In electrochemical properties, the most important characteristic is the storage capacity. The calculated storage capacity is 626 mAh/g for all the studied alkalis. As a comparison, we also report the storage capacities of some famous anode materials. The Li storage capacity of phosphorene is 433 mAh/g, whereas, the Na and K capacity of $SnS_2$ and $Mo_2C$ are 492 and 263 mAh/g, respectively. Finally, we also calculate the open-circuit voltage (OCV) which is found to be 0.155, 0.042, 0.39 V for Li, Na, and K, respectively. The OCV should be kept as minimum as possible and, hence, our calculated values are in the excellent range. The paper is published in (IJQC 119, e25975, 2019) [236] and is given in Appendix C.1.
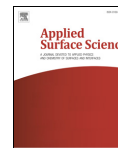
Full Length Article

# Hexagonal boron phosphide as a potential anode nominee for alkali-based batteries: A multi-flavor DFT study

Saif Ullah[a,*], Pablo A. Denis[b], Fernando Sato[a]

[a] *Departamento de Física, Instituto de Ciências Exatas, Campus Universitário, Universidade Federal de Juiz de Fora, Juiz de Fora, MG 36036-900, Brazil*
[b] *Computational Nanotechnology, DETEMA, Facultad de Química, UDELAR, CC 1157, 11800 Montevideo, Uruguay*

### A B S T R A C T

The adsorption of alkali atoms (Li, Na, and K) on graphene and hexagonal boron phosphide (h-BP) is studied by means of various density functionals including semi-local GGA, dispersion corrected DFT-D, meta-GGA, and many of the available non-local vdW-DF functionals. The accurate interaction energies are crucial for energy storage and battery applications as it is directly related to key properties in electrochemistry, such as storage capacities in general, and open circuit voltages (OCVs), in particular. A wider range of adsorption strength is predicted depending on the choice of non-local vdW-DF functionals. Furthermore, the performance of vdW-DF functionals was found to be independent of the choice of pseudopotentials used and especially if the choice is revPBE. Additionally, an excellent agreement is found between the Gaussian, VASP, and QE codes. Moreover, the h-BP is found to be an exceptional anode material for alkali batteries which can compete with any other available anode material. The small change in the adsorption energies as a function of increasing concentration of alkali atoms is a unique characteristic of h-BP. The exceptional 1283 mAh/g storage capacity not only for Li but in contrary with the previous study, also for Na in addition to the 642 mAh/g for K at vdW-DF/DZP level makes it a prominent candidate to be used as anode material. The average open circuit voltage for Li, Na, and K was also found to be in superb range. However, the values are found to be sensitive to the choice of functional, and in some cases, the storage capacity can be predicted as high as twice of the actual values. Therefore, the accurate description of the interaction is crucial and this study can be used to further refine the non-local DFT functionals. Moreover, by virtue of these properties, h-BP can be the best choice to be used as an anode material not only in LIBS but also in SIBs and KIBs.

## 1. Introduction:

The dependence on fossil fuels for energy should be reduced as they are limited and non-renewable and are the main cause of $CO_2$ production. It was already evaluated by the UN back in 2015 that the temperature of our planet-earth could rise up to 4° if we could not reduce the emission of greenhouse gases such as $CO_2$ etc [1]. In this regard, the use of secondary batteries as energy storage devices are crucial due to their broad applications range. Lithium-ion batteries (LIBs), in the past few decades, have attained much attention, ever since their first introduction back in 1991 by SONY, regarding their applications in a number of portable electronic devices, and hybrid electric cars due to their size, long cycle life, and high energy density [2–9]. However, the insufficient availability of Li will cause an exponential rise in the price, which will reduce the attraction to use Li-ion batteries [10]. Moreover, the limited storage capacity of graphite 372 mAh/g, which serves as the

anode in LIBs, limits its applications to be used in hybrid electric vehicles [2,4,6]. For this reason, sodium-ion batteries (SIBs), which is the neighbor of Li, have current interests to be used as an alternative candidate for LIBs as sodium (Na) resources are plentiful. Furthermore, the likewise electrochemical system, non-toxicity, and ample availability make SIBs a sizzling topic [8,11–16]. Additionally, potassium (K), the (next) neighbor of (Li) Na, may be another possible material that can compete in the race with Li, and Na. Moreover, the better ionic conductivity, relatively simple interfacial reactions, and much more availability make potassium-ion batteries (KIBs) even more demanding [17–19]. The elemental concentrations in part per million (ppm) are shown in Table 1 [20]. However, the bigger radii of these alkalis (Na and K) make them less fascinating as the intercalation into graphite, a successful anode for LIBs will be a difficult task. By using Na instead of Li, the storage capacity of graphite falls from 372 mAh/g to just 35 mAh/g [8,21]. In this scenario, investigation for a practicable anode

---

*S. Ullah et al.*

**Table 1**
Availability of elements in the upper earth crust in the unit of ppm is shown [20].

| Elements | Availability | Elements | Availability |
|----------|--------------|----------|--------------|
| K  | 28,650 | Y  | 20.7 |
| Na | 25,670 | B  | 17   |
| C  | 3240   | Sn | 2.5  |
| P  | 665    | Mo | 1.4  |
| Nb | 26     | Ge | 1.4  |
| Li | 22     | W  | 1.4  |

material becomes crucial.

The successful isolation of graphene revolutionized the materials science and other related fields, thanks to Geim et al., [22] and, consequently, a number of other two-dimensional (2D) materials have been synthesized experimentally and predicted theoretically [23]. Despite the exceptional properties of graphene, the ions on the surface of graphene lean to form clusters provoking the dendrite formation, thus causing a momentous degradation in the charge/discharge capability. Fortunately, many of the other 2D materials, such as nitrogen-doped defective-graphene, graphenylene, Mo$_2$C, and GeS etc, have shown their promise as anode materials for LIBS, SIBs, and KIBs [24–28]. Phosphorene is a proficient material in term of better Li/Na storage capacity (865 mAh/g) and fast diffusion of Li/Na with the energy barriers of 0.12/0.04 eV [29,30]. Transition metal dichalcogenides, such as Ti$_3$C$_2$ is proposed to be a potential nominee as anode material by virtue of its good storage capacity of Li (~ 448 mAh/g), Na (~ 352 mAh/g), and K (~ 192 mAh/g) [31]. Moreover, borophene can be regarded as an excellent anode material for LIBs having a storage capacity of 1860 mAh/g and can be an efficient anode material for SIBs and KIBs [32]. As mentioned before, after the successful exfoliation of graphene, so much have been achieved regarding the prediction and synthesis of other 2D materials and the research area is still expanding rapidly. Among the 2D hexagonal III-V binary compounds, one of the most scrutinized materials is hexagonal boron nitride (h-BN) due to its promise in nanoelectronics and related fields by virtue of its wider band-gap [33–39]. However, the imperfection also comes from its wider band-gap since electrode materials need good electronic conductivities [40]. Furthermore, the weak interaction of metals with hBN also hindered its applications in ion-batteries [41]. It is already shown that Li adsorption is not enough for altering the large band-gap of hBN to a metallic one and furthermore, the adsorption energy of Li on hBN cannot compete for even the cohesive energy of Li [40–42].

Hexagonal boron phosphide (h-BP), another III-V binary compound, has shown its worth (theoretically) even though not synthesized experimentally but predicted by DFT calculations [36,43,44]. The h-BP is a planar and graphene-like structure and a true minimum of the potential energy surface as predicted by phonons calculations. The excellent mobility compared to graphene, and the superb mechanical strength comparable to MoS2 monolayer makes the h-BP a promising and novel material [43]. All these properties along with smaller band-gap of h-BP compared to hBN worth compelling to investigate whether h-BP can serve as anode material for ion-batteries or not [36,43]?

Furthermore, the fascinating part of this work is to answer that why exceptional theoretical capacities are hard to achieve in experiments. In these kinds of studies, the interaction between slabs and adsorbed molecules/atoms are not covalently bonded and, hence, dispersion plays a key role. To this end, we used a series of versatile density functionals to study the interaction of alkali atoms with h-BP. In a recent study, we benchmarked the accuracy of different DFT functionals including the semi-local GGA, dispersion correction DFT-D, meta-GGA, and many flavors of non-local vdW-DF by taking the CCSD(T) value as a reference [45]. Consequently, it is interesting to see whether the profile of these functionals will be same in the periodic systems or not? In the

regard, the study is extended to the interaction of alkali atoms with graphene and h-BP, the latter being explored more intensively. In a recent study, PBE functional is employed to scale the interaction of Li, Na, and K with h-BP and reported excellent diffusion of these ions on h-BP [46]. The authors, however, predicted a very bad value of Na storage capacity (143 mAh/g) and even underestimated value for K storage capacity. We, on the other hand, predicted the exceptional storage capacities of 1283 mAh/g for all the three alkalis studied with any functional employed (even with revPBE) except the vdW-DF/DZP level. With the later functional, the same 1283 mAh/g is achieved for Li and Na, while ~642 mAh/g, almost half the value predicted by other functionals, was calculated for K storage. These results show that the use of a suitable functional is crucial in designing energy applications and battery technologies. Based on our calculations, we proposed that vdW-DF/DZP functionals as implemented in SIESTA code is an appropriate functional to be employed while studying the interactions of alkali atoms with carbon nanomaterials, h-BP, and other related materials. Additionally, it was found that h-BP can serve as one of the best anode materials for alkali-based batteries by virtue of its exceptional storage capacities.

## 2. Computational details

In this work, we utilized the most popular and efficient DFT codes, such as Gaussian [47], VASP [48], Quantum Espresso (QE) [49,50], and SIESTA [51,52] to study the interactions of alkalis with graphene and h-BP and to gauge the performance of different DFT functionals. For the description of electron-ion interaction, projector augmented wave (PAW) method is used both in VASP and QE [53]. Ultrasoft pseudo-potentials (US) were also used in the latter code [54]. We performed semi-local GGA [55,56], dispersion-corrected DFT (DFT-D) [57–59], meta-GGA [60,61], and several flavors of vdW-DF functionals. In the second approach, a semiempirical pair-potential correction is added which accounts for the van der Waals (vdW) forces. The expression in its simple form is as follow:

$$E_{tot} = E_{DFT} + E_{disp}$$

where, $E_{disp}$ is the dispersion part accounting for vdW forces which contains several adjustable parameters, such as s6 which is an empirical global scale factor for exchange-correlation functional and a damping factor which is useful in preventing this dispersion part from the divergence when the R is small depending on the choice of D (D2 or D3). The equation can take the form:

$$E_{disp} = -s_6 \sum_{pairs} \frac{C_6}{R_6} f_{damp}(R)$$

In the non-local functionals, the density is a pivotal variable and these functionals come within the DFT framework, fully. The vdW-DF functionals are the best alternatives to the functionals which lack the empirical input.

$$E_{nl}^c = \iint drdr' \rho(r) \Phi^c(r, r') \rho(r'),$$

where $\Phi^c(r, r')$ is a kernel function and it requires numerous approximation for its derivation from a local polarizability model.

For this reason, the vdW-DF1 (presented in 2004), vdW-DF2 (proposed in 2010), and several other versions of the vdW-DF became popular in studying the non-covalent systems. Consequently, we applied many of the available vdW-DF functionals, such as vdW-DF1 [62–67](revPBE), vdW-DF1 (PBE), vdW-DF2 [68] (PW86) [69], vdW-DF2 (revPBE), rev-vdW-DF2 [70] (PW86), rev-vdW-DF2 (revPBE), rVV10 [71] (PW86), rVV10 (revPBE), vdW-optB86b [72] (optB86) [72], vdW-optB86b (revPBE), vdW-optB88 [73] (optB88) and vdW-optB88 (revPBE) to study the interaction of alkali atoms with benzene, graphene, and h-BP. The term in parenthesis shows the type of pseudopotential used. A detailed description can be found in the electronic

135

supplementary information (ESI).

The adsorption energy is calculated to assess the relative strength of alkalis on benzene, graphene, and h-BP with the help of the following expression:

$$E_{ads} = \frac{E_{tot} - E_{sheet} - nE_{ion}}{n}$$

where, $E_{tot}$, $E_{sheet}$, $E_{ion}$ are the total energy of the system including alkalis, energy of the adsorbent, and gas-phase energy of the alkalis, respectively. Finally, $n$ is the total number of alkalis present in the system. According to this definition, the more negative value means stronger adsorption while the positive value means no adsorption (repulsion between adsorbate and adsorbent).

## 3. Results and discussions

Before investigating h-BP, we gauge the performance of different DFT functionals by studying the interaction of alkali atoms with graphene. In a recent study, it is shown that the adsorption energies predicted by various DFT functionals span over a wide range [45]. For this reason, the CCSD(T) value is taken as a reference to scale the accuracy of these employed functionals and found that the vdW-DF/DZP (without the inclusion of BSSE) as implemented in SIESTA code is the best choice to be used in term of accuracy and speed.

### 3.1. Alkalis on graphene

There are current interests in using graphene-based materials as anodes in ion batteries, and therefore a significant amount of study is dedicated to the electrochemical properties of graphene-based materials. Consequently, an accurate description of the interaction energy of alkalis with graphene becomes critical as most of the key electrochemical properties like storage capacity and open circuit voltage (OCV) are directly related to the adsorption energy. As expected, the revPBE values were the lowest amongst all. However, these values can be improved by the introduction of a dispersion term (revPBE-D2). A good agreement was found between revPBE-D2, vdW-DF1, vdW-DF2, and vdW-DF/DZP result for Na and K adsorption on graphene. However, for Li adsorption on graphene, all the three aforementioned values were a bit overestimated in comparison with the vdW-DF/DZP level. Additionally, all the other vdW-DF schemes overestimated the binding energies as compared to the vdW-DF/DZP results. Nevertheless, the various vdW-DF variants give nearly the same results. These results are plotted in Fig. 1. Moreover, the highest values come from the pawPBE-D2 with the sole exception K adsorption on graphene in which various vdW-DF functionals gave nearly the same or, in some cases, overestimated results. The adsorption of Na and K on graphene shows a similar profile as a function of supercell size, being $3 \times 3$ cell the less favorable. However, in the case of Li adsorption, a direct relation was found between adsorption energy and supercell size, being the $3 \times 3$ cell at vdW-DF/DZP level as an exception. This might be attributed to the bigger radii of Na/K where these ions are likely to interact in a smaller unit-cell, given the concentration is $NaC_8$ and $KC_8$. Additionally, it is already shown that the Li/C ratio should be kept at least 1/6 to avoid the interaction between Li-Li [74]. Nevertheless, the Li adsorption energy in the $Li_2C_2$ compound is as high as 1.40 eV/Li [75]. Consequently, the use of a bigger unit-cell ($3 \times 3$ or bigger) is crucial to obtain reliable results. The good agreement between vdW-DF/DZP, vdW-DF1, and vdW-DF2 and from the ref. [45], it is clear that the employment of these functional is critical while studying the interaction of alkali atoms with graphene and graphene-like materials. The results are summarized in Table 1 of the ESI. From Fig. 1, a wide range of variation in the adsorption energy of alkali atoms can be seen, and therefore it is necessary to use a proper functional to predict accurate electrochemical properties. Additionally, all the functionals give nearly the same profile of the adsorption energy. The (*) shows when a Na PPs
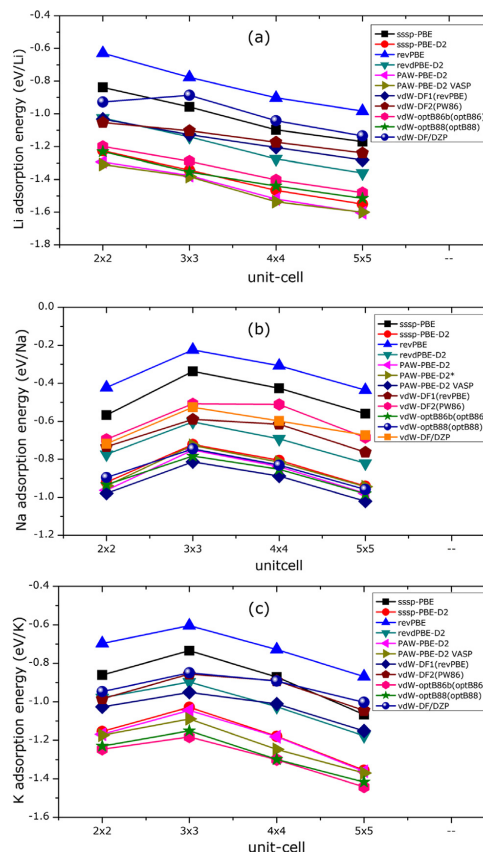


**Fig. 1.** The adsorption of (a) Li, (b) Na, and (c) K on graphene as a function of unit-cell size at various level of theories is depicted.

with a different configuration is used. The details are given in the ESI. These methods were then extended to study the interaction of alkalis with h-BP.

### 3.2. Alkalis on h-BP

Hexagonal boron phosphide has similar $sp^2$ hybridized honeycomb lattice structure as graphene with the difference that the unit-cell of h-BP consists of B and P atoms. The bond length and lattice parameters are found to be 1.9 Å and 3.28 Å, respectively, at vdW-DF/DZP level of theory. Moreover, the pawPBE-D2 level of theory gave the calculated bond length and lattice parameter of 1.85 Å and 3.21 Å, respectively. The calculated bandgap at vdW-DF/DZP level was found to be 1.1 eV, while the HSEH1PBE/6311-G* [76] level shows a bandgap opening of 1.50 eV. These outcomes are in excellent agreement with the results reported in the literature which show the precision of our employed methods [36,77]. Following this, the adsorption of alkalis on h-BP was systematically studied with various DFT functionals.

Initially, a Li/Na/K atom was kept above the hollow site, bridge site, B atom, and P atom to figure out the most stable adsorption site. Similar to graphene, the hollow site was found to be the most stable. The B and P sites were found to be less stable by 0.225 eV and 0.335 eV for Li,
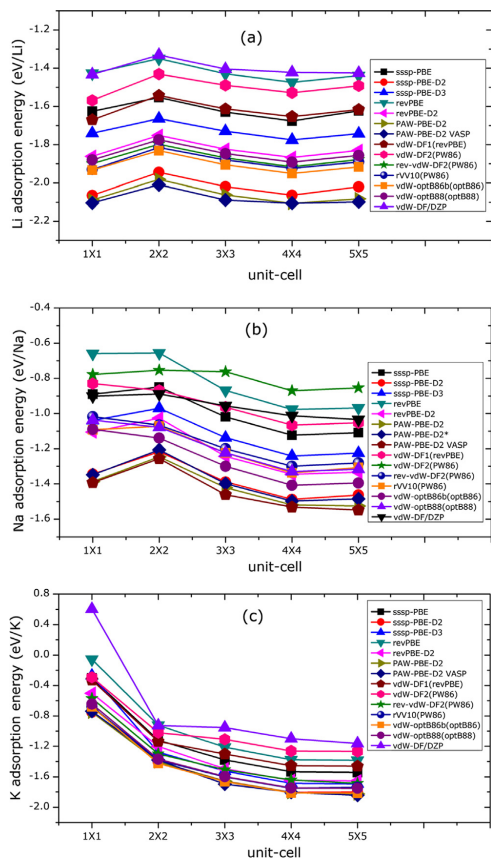
**Fig. 2.** The adsorption of (a) Li, (b) Na, and (c) K on h-BP is shown as a function of unit-cell size at various DFT levels.

0.0384 eV and 0.0137 eV for K, respectively. Furthermore, the B site is found to be less favorable by 0.15 eV for Na adsorption, while the P site bangs the Na towards the hollow site. Additionally, the Li atom was also kicked to the hollow site from the bridge position. The behavior of different alkali atoms understudy was different and consequently, a more thorough and robust investigation becomes crucial. These structures can be seen in Fig. S1 of the ESI.

For Li adsorption, as from the Fig. 2, the performance of the functionals can be categorized in nearly four groups in term of their adsorption energies. The PBE-D2 gave the highest binding energies, while revPBE and vdW-DF/DZP along with vdW-DF2 predicted the lowest binding energies in comparison with the other functionals. Additionally, the PBE-D3 values found to be the intermediate between vdW-DF/DZP and PBE-D2 values. The ssp-PBE and vdW-DF1 values are closer to the ones obtained with revPBE, vdW-DF/DZP, and especially vdW-DF2. A good agreement between the rests of the vdW-DF schemes along with the revPBE-D2 was found. Moreover, these values were in close proximity to PBE-D2 schemes than the sssp-PBE, and vdW-DF1 functionals. Additionally, the adsorption energy decreases when going from $5 \times 5$ to $2 \times 2$ supercell. However, a prominent rise in adsorption energy occurred when using $1 \times 1$ unit-cell. This rise in adsorption energy can be attributed to the structural changes appeared in the

planar structure of h-BP which then transformed into a puckered one. This rise in the adsorption energy of Li is already reported for other 2D anode materials [78].

In the case of Na adsorption, the behavior of different functionals was nearly the same as observed for the Li adsorption. However, the vdW-DF2 (PW86) functional, for larger cells ($3 \times 3$-$5 \times 5$), tends to underestimate the binding. Nevertheless, a very good agreement between vdW-DF1 and vdW-DF/DZP was observed. All the other vdW-DF functionals, as well as revPBE-D2, gave almost alike results. The PBE-D3 results were comparable with the vdW-DF/DZP and were found to be much closer to the rev-vdW-DF2 (PW86), rVV10 (PW86), and vdW-optB88 (optB88). The PBE-D2 values are overestimated as expected. However, the change in the adsorption energy of Na in a $1 \times 1$ unit-cell became eminent using the PBE-D2 method.

The case of K adsorption on h-BP is found to be different than the Li and Na. The adsorption energy increases with the increase in the cell size. Furthermore, the adsorption of K was found to be lower than Li and higher Na except for the $1 \times 1$ unit-cell in which Na adsorption was stronger than K. Once again, the good agreement between vdW-DF1, vdW-DF2, and vdW-DF/DZP along with the revPBE was noticed with the sole exception of the $1 \times 1$ cell. Besides, the PBE-D3 profile was found to be overestimated in the case of K as the values are similar to those obtained with rev-vdW-DF2 (PW86), which along with vdW-DF schemes like rVV10 (PW86), vdW-optB86b (optB86), and vdW-optB88 (optB88) give comparable results to the PBE-D2 scheme. It is important to note that every functional used (even the revPBE) gave favorable adsorption of K in a $1 \times 1$ unit-cell, while the vdW-DF/DZP level of theory suggested that this adsorption is unfavorable due to the positive adsorption energy. Moreover, the adsorption energy for a $1 \times 1$ unit-cell is significantly lower than the $2 \times 2$ cell. However, in the case of LiBP/NaBP, we see a stronger adsorption in comparison with $LiB_4P_4$/$NaB_4P_4$. As mentioned above, this is due to the structural changes appeared in the slab (h-BP). Moreover, this behavior is not new as this trend has already been reported for GeS, SnS, GeSe, and SnSe [78]. Furthermore, this tendency is also in-line with the stronger adsorption of alkali atoms adsorbed on both the sides of h-BP in a $1 \times 1$ unit-cell in comparison with the single-sided adsorption. Nevertheless, due to the larger covalent radii of K in comparison with Li and Na, the $1 \times 1$ unit-cell doesn't provide enough room for K and, hence, results in lower K strength.

For the unit-cell, the Na adsorption energy ($-0.9$ eV/Na) is pretty much higher than the K adsorption (0.6 eV/K), almost 1.5 eV, at vdW-DF/DZP level. However, for a $2 \times 2$ cell, the K adsorption energy exceeds the Na adsorption by a small value of 0.036 eV. For a $3 \times 3$ cell, both gave the same results while for a $4 \times 4$ cell, the Na adsorption is only 0.086 eV less than K adsorption. Nevertheless, the difference between Na and K adsorption on graphene is more prominent at the same level of study. To address this fully, we used the larger cells (i.e. $6 \times 6$ and $8 \times 8$). By using a $5 \times 5$ cell, the Na adsorption energy is calculated to be -1.03 eV, while that of the K is $-1.163$ eV. The difference becomes noticeable as with the use of larger cells than $4 \times 4$. It seems that the adsorption energies of Na and K reach their saturation point at this stage as the $6 \times 6$ and the $8 \times 8$ cells gave the same $-1.03$ eV and $-1.17$ eV adsorption energies for Na and K, respectively.

For a $1 \times 1$ unit-cell, the adsorption on both sides is found to be favorable than on the single side. This is due to the fact that more distortion in the h-BP slab will lead to a higher value of adsorption. The two side adsorption of Li and Na are found to be more favorable than on one side by 0.21 eV and 0.11 eV, respectively, at the vdW-DF/DZP level. Moreover, this difference becomes more distinguishable in the case of K adsorption by a value of 0.33 eV. Unfortunately, the $K_2$-h-BP has a positive adsorption energy of 0.27 eV/K at vdW-DF/DZP level, the only level of theory amongst the employed functionals which gave unfavorable adsorption. In the case of Li, the two sides' adsorption energy is found to be the same as the one side adsorption in the case of $2 \times 2$ unit-cell. However, when the cell size increased from $3 \times 3$ to $5 \times 5$,

the single side adsorption becomes favorable. Furthermore, the two Li ions can easily share the same position on the top and down of a hexagon of h-BP without inducing any change in the plane of h-BP. Conversely, a different scenario was observed for Na and K. In case of Na, the double side adsorption energy is nearly independent of the cell size, while for single side adsorption, the adsorption energy increases when going from the 2 × 2-5 × 5 cell. Subsequently, dual side adsorption energy nearly reaches the single sided one in a 3 × 3 unit-cell and becomes a little lower in 4 × 4 and 5 × 5 unit-cells. In case of K, the two sides' adsorption gave nearly the same adsorption energy as compared to the single-sided adsorption except for the 1 × 1 unit-cell, where the dual side adsorption was clearly favorable due to the substantial changes induced in the structure. Due to the larger radii of Na and K, the up and down Na/K did not share the same position on the hexagon, rather it seems that the up and down ions (Na or K) have significant repulsion. However, due to the good chemistry of h-BP towards Na/K, the ions move against each other along the surface of h-BP instead of going apart along the z-axis. These ions tend to suppress the P atoms deeper out of the plane (in opposite directions) of h-BP, hence providing more room for the ions on the hexagon. The structural changes induced by dual sided adsorption of K were larger than Na as the radius of K is bigger than Na. Furthermore, the P site was only 0.0137 eV less favorable for K, which provided enough room for two K to be adjusted in one hexagon (up and down). The Na case is different as the P site pushed the Na towards the hollow site and additionally, the B site was less favorable by 0.15 eV. Consequently, it seems that there must be a constant battle among the two Na atoms and with the P atoms as the P atoms would try to keep the Na atoms in the middle of the hexagon, while the repulsion between Na and Na will try to move apart. This might be the reason for different behaviors of dual-sided adsorption between Na and K. The geometric structures are plotted in S2 of the ESI while a comparison of single and dual-sided adsorption is plotted Fig. 3.

Finally, we also checked the dependence of different pseudopotentials on the performance (energies) of various vdW-DF functionals. It was noticed that the results of vdW-DF functionals were independent of the choice of PPs used. For Na, the vdW-DF1 (revPBE) and vdW-DF1 (PBE) yield to different energetics in 1 × 1, and 2 × 2 unit-cells. However, the results are pretty much comparable in 3 × 3-5 × 5 unit-cells. Furthermore, the very same effect was observed in the case of K when using 2 × 2 cell. This being said, every vdW-DF flavors can be used with any choice of pseudopotential(s) with some care or at least with revPBE pseudopotentials. The results are summarized in Fig. 4.

Storage capacity is an important factor to assess the capability of the anode materials. For this purpose, the storage capacities of h-BP were calculated with the help of the following expression [7]:

$$C = \frac{nF}{M} \times \frac{1000}{3600}$$

where, $n$, $F$, and $M$ are the total number of alkalis (Li, Na, and K) adsorbed, Faraday constant, and molar mass of the h-BP, respectively. The unit mAh is converted from coulomb by using $\frac{1000}{3600}$. By using this expression, the Li, and Na maximum theoretical storage capacities of h-BP are calculated to be 1283 mAh/g, which are attributed to $Li_2$-h-BP, and $Na_2$-h-BP (see Fig. S3 of the ESI). This value is pretty much larger than the commonly investigated rival anode materials for Li, such as $Ti_3C_2$ (320 mAh/g) [79], phosphorene (433 mAh/g) [29], Silicene (954 mAh/g) [80], and even Sn (994 mAh/g) [81]. For Na, the difference is even much larger in comparison with the graphite (35 mAh/g) [21], $NaBC_{31}$ (70 mAh/g) [82], $MoS_2$ (146 mAh/g) [83], and $SnS_2$ (492 mAh/g) [84]. For K, by any other level of theory employed (even with revPBE) except vdW-DF/DZP, we found the same exceptional storage capacity (1283 mAh/g) for $K_2$-h-BP. The geometric structure of $K_2$-h-BP is found to be different than the other counterparts. This being said, the structural changes in $Li_2$-h-BP and $Na_2$-h-BP are much prominent in comparison with $K_2$-h-BP, and for this reason, the vdW-DF/DZP level gave unfavorable adsorption. Consequently, the vdW-DF/DZP level (without BSSE corrections) becomes more dependable when studying the interaction of alkali atoms with graphene, h-BP, and other correlated materials. In order to find the maximum storage capacity by using the vdW-DF/DZP level of theory, we used a 2 × 2 h-BP supercell with 2 K adsorbed on one side and 2 on another side. This led to the formation of K-h-BP with a planar structure with a storage capacity of ~ 642 mAh/g, which is also much higher than that of $Ti_3C_2$ (~ 192 mAh/g) [31], GeS (256 mAh/g) [25], $Mo_2C$ (263 mAh/g) and even graphite-$KC_8$ (279 mAh/g) [85]. Nevertheless, the single K adsorption in a 1 × 1 unit-cell of h-BP leading to a structure of $K_2$-h-BP gave positive adsorption (unfavorable). Subsequently, the K adsorption on both sides are favorable as compared to the one side adsorption. These high storage capacities values indicate that h-BP can be an efficient anode material for alkalis based batteries.

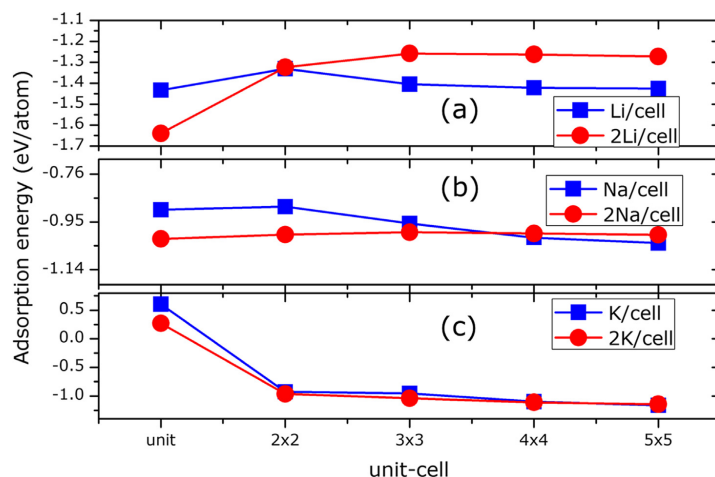Another important aspect of the good anode material is the open



**Fig. 3.** Comparison of (a) Li, (b) Na, and (c) K adsorption on the single and double side of h-BP as a function of the unit-cell size.
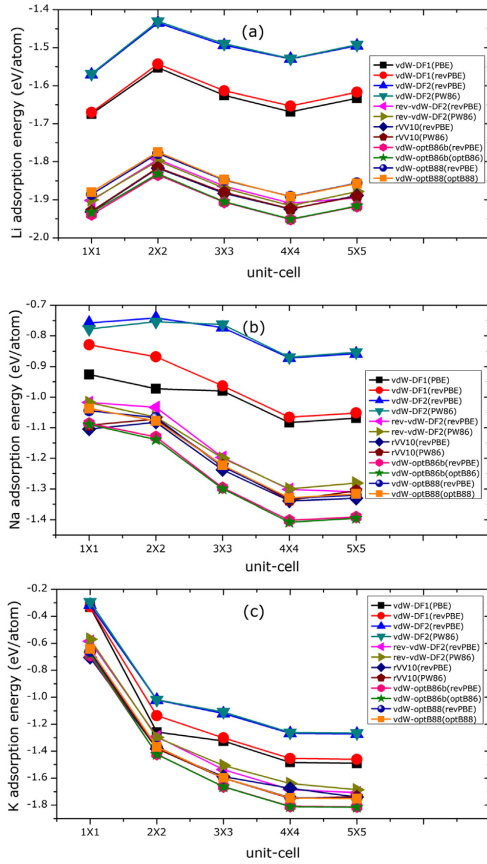
138

**Fig. 4.** The performance of various vdW-DF functionals with different PPs is plotted for (a) Li, (b) Na, and (c) K adsorption on h-BP.



**Fig. 5.** The (a) Li, (b) Na, and (c) K storage capacities are plotted vs OCVs. For the sake of clarity, the values are plotted from 0 to 642 mAh/g.

circuit voltage (OCV). The OCVs, at various DFT levels, are plotted against the storage capacities in Fig. 5. A significant variation is noted in the OCVs calculated at the different level of theories. The PBE-D3 values are intermediated among vdW-DF/DZP, vdW-DF1, vdW-DF2 and those of PBE-D2 and rest of vdW-DF functionals. The lowest values come from the vdW-DF/DZP level except for Na where these values were found to be a little higher than those calculated at vdW-DF2 level. As the values of OCVs are quite sensitive to the employed functionals, therefore, we considered the OCVs at vdW-DF/DZP level of theory. The OCVs are calculated with the following equation [8]:

$$OCV = -E_{ads}/ze$$

where, z is the charge of Li, Na, and K in the electrolyte. The calculated average OCV of h-BP for Li (1.37 V), Na (0.97 V), and K (0.93 V) are in excellent range showing that h-BP is a novel candidate to be used as the anode in ion batteries. In general, alkali-atoms storage capacity has an inverse relation with the OCVs, where an increase in storage capacity will cause a reduction in OCV [86,87]. However, there are exceptions where a higher storage capacity can have a higher OCV [78]. Same is the case for h-BP where the structural modification causes an increment in adsorption energy, thus resulting in a higher OCV for Li and Na. It is clear from Fig. 5 that OCVs are quite sensitive to the choice of DFT
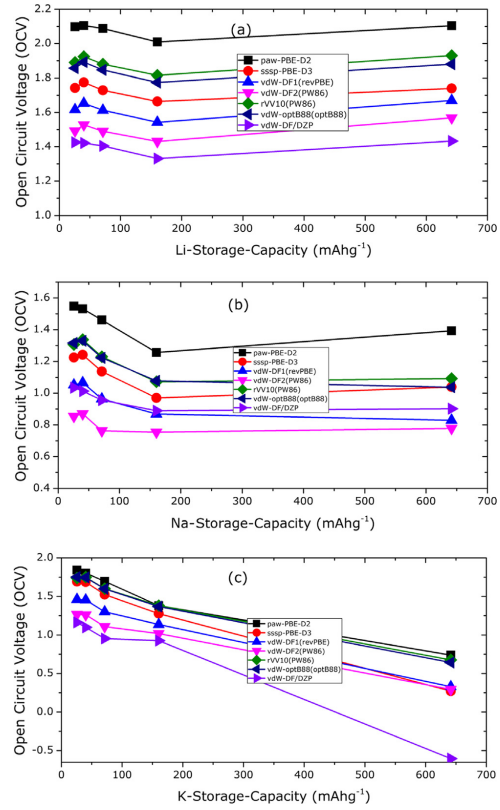
functionals. The OCVs can be categorized into three groups: The vdW-DF/DZP, vdW-DF1, vdW-DF2 which give the lowest values; the PBE-D2, the highest; and the PBE-D3, which give intermediate values. Moreover, for K adsorption, the vdW-DF/DZP value becomes negative as it crosses 450 mAh/g. Therefore, care must be taken when studying the interaction of alkali atoms with h-BP and related materials.

## 4. Conclusions

A comparative DFT study is performed to assign the role of different DFT functionals by investigating the interaction of alkali atoms (Li, Na, and K) with graphene. The wide range of adsorption energies computed at various DFT functionals suggests that the use of a proper functional is crucial in energy applications and designing better batteries. This is due to the fact that the key electrochemical properties, such as storage capacities and OCVs are directly related to the adsorption energy. Among the various flavors of non-local vdW-DF, the vdW-DF/DZP gives the lowest strength of the alkali atoms on graphene and h-BP and can be regarded as a better choice. This is evident from the excellent agreement between vdW-DF/DZP and CCSD(T) [45] and also from the K adsorption on a $1 \times 1$ unit-cell of h-BP, where all the other DFT functionals predicted favorable adsorption except vdW-DF/DZP. Furthermore, various DFT functionals can severely overestimate the value of OCVs, and therefore, care must be taken when dealing with the

aforementioned systems. Nevertheless, the variation in unit-cell size (or the alkali atoms coverage) of h-BP has a smaller impact on the adsorption strength as compared with graphene. The hollow site of h-BP is found to be the most preferable for ions adsorptions. However, the behavior of alkali atoms understudy was different at B and P sites. The P and B site is found to be the least favorable for Li and K, respectively. Though, the Na atom is pushed towards the hollow site when kept initially on the top of a P site. Finally, the performance of non-local vdW-DF functionals is found to be independent of the choice of PPs or as long as the option is revPBE.

Additionally, the h-BP is investigated to be an all-rounder anode material as it shows great chemistry with alkali atoms (Li, Na, and K). The extraordinary storage capacity of 1283 mAh/g for Li, Na, and K (at any employed level of theory except vdW-DF/DZP) were calculated. However, the vdW-DF/DZP level give a value of ~642 mAh/g for K storage capacity, which is still a remarkable value. Consequently, the use of a proper functional becomes crucial. Along with all these other properties, the excellent average open circuit voltage of 1.37 V, 0.97 V, and 0.93 V for Li, Na, and K, respectively, make the h-BP a desirable material to be used as anode material in ion batteries.

### Acknowledgments:

### Appendix A. Supplementary material

Supplementary data to this article can be found online at https:// doi.org/10.1016/j.apsusc.2018.12.020.

### References

[1] What will the weather be like in 2050?, https://www.un.org/climatechange/blog/2015/03/will-weather-like-2050/index.html, 2015.
[2] M. Armand, J.M. Tarascon, Building better batteries, Nature 451 (2008) 652–657.
[3] B. Scrosati, Recent advances in lithium ion battery materials, Electrochim. Acta 45 (2000) 2461–2466.
[4] J.M. Tarascon, M. Armand, Issues and challenges facing rechargeable lithium batteries, Nature 414 (2001) 359–367.
[5] J.B. Goodenough, Y. Kim, Challenges for rechargeable Li batteries, Chem. Mater. 22 (2010) 587–603.
[6] J.R. Dahn, T. Zheng, Y. Liu, J.S. Xue, Mechanisms for lithium insertion in carbonaceous materials, Science 270 (1995) 590.
[7] S. Ullah, P.A. Denis, F. Sato, Beryllium doped graphene as an efficient anode material for lithium-ion batteries with significantly huge capacity: a DFT study, Appl. Mater. Today 9 (2017) 333–340.
[8] S. Ullah, P.A. Denis, F. Sato, First-principles study of dual-doped graphene: towards promising anode materials for Li/Na-ion batteries, New J. Chem. 42 (2018) 10842–10851.
[9] S. Ullah, P.A. Denis, F. Sato, Adsorption of sodium on doped graphene: a vdW-DF study, Curr. Graphene Sci. 2 (2018) 1–11.
[10] J.-M. Tarascon, Is lithium the new gold? Nat. Chem. 2 (2010) 510.
[11] B.L. Ellis, L.F. Nazar, Sodium and sodium-ion energy storage batteries, Curr. Opin. Solid State Mater. Sci. 16 (2012) 168–177.
[12] Y. Cao, L. Xiao, M.L. Sushko, W. Wang, B. Schwenzer, J. Xiao, Z. Nie, L.V. Saraf, Z. Yang, J. Liu, Sodium ion insertion in hollow carbon nanowires for battery applications, Nano Lett. 12 (2012) 3783–3787.
[13] Y. Wen, K. He, Y. Zhu, F. Han, Y. Xu, I. Matsuda, Y. Ishii, J. Cumings, C. Wang, Expanded graphite as superior anode for sodium-ion batteries, Nat. Commun. 5 (2014) 4033.
[14] R. Raccichini, A. Varzi, D. Wei, S. Passerini, Critical insight into the relentless progression toward graphene and graphene-containing materials for lithium-ion battery anodes, Adv. Mater. 29 (2017) 1603421.
[15] S. Yuan, Y.-H. Zhu, W. Li, S. Wang, D. Xu, L. Li, Y. Zhang, X.-B. Zhang, Surfactant-free aqueous synthesis of pure single-crystalline snse nanosheet clusters as anode for high energy- and power-density sodium-ion batteries, Adv. Mater. 29 (2017) 1602469.
[16] A. Samad, M. Noor-A-Alam, Y.-H. Shin, First principles study of a SnS2/graphene heterostructure: a promising anode material for rechargeable Na ion batteries, J. Mater. Chem. A 4 (2016) 14316–14323.
[17] E.D. Glendening, D. Feller, M.A. Thompson, An ab initio investigation of the structure and alkali metal cation selectivity of 18-Crown-6, J. Am. Chem. Soc. 116 (1994) 10657–10669.
[18] M. Moshkovich, Y. Gofer, D. Aurbach, Investigation of the electrochemical windows of aprotic alkali metal (Li, Na, K) salt solutions, J. Electrochem. Soc. 148 (2001) E155–E167.
[19] A. Eftekhari, Z. Jian, X. Ji, Potassium secondary batteries, ACS Appl. Mater. Interf. 9 (2017) 4404–4419.
[20] K. Hans Wedepohl, The composition of the continental crust, Geochimica et Cosmochimica Acta 59 (1995) 1217–1232.
[21] M.D. Slater, D. Kim, E. Lee, C.S. Johnson, Sodium-ion batteries, Adv. Funct. Mater. 23 (2013) 947–958.
[22] K.S. Novoselov, A.K. Geim, S.V. Morozov, D. Jiang, Y. Zhang, S.V. Dubonos, I.V. Grigorieva, A.A. Firsov, Electric field effect in atomically thin carbon films, Science 306 (2004) 666–669.
[23] K.S. Novoselov, A.K. Geim, S.V. Morozov, D. Jiang, Y. Zhang, S.V. Dubonos, I.V. Gregorieve, A.A. Firsov, Science 306 (2004) 666.
[24] Q. Sun, Y. Dai, Y. Ma, T. Jing, W. Wei, B. Huang, Ab initio prediction and characterization of Mo2C monolayer as anodes for lithium-ion and sodium-ion batteries, J. Phys. Chem. Lett. 7 (2016) 937–943.
[25] F. Li, Y. Qu, M. Zhao, Germanium sulfide nanosheet: a universal anode material for alkali metal ion batteries, J. Mater. Chem. A 4 (2016) 8905–8912.
[26] D. Cakr, C. Sevik, O. Gulseren, F.M. Peeters, Mo2C as a high capacity anode material: a first-principles study, J. Mater. Chem. A 4 (2016) 6029–6035.
[27] Y.-X. Yu, Can all nitrogen-doped defects improve the performance of graphene anode materials for lithium-ion batteries? Phys. Chem. Chem. Phys. 15 (2013) 16819–16827.
[28] Y.-X. Yu, Graphenylene: a promising anode material for lithium-ion batteries with high mobility and storage, J. Mater. Chem. A 1 (2013) 13559–13566.
[29] Q.-F. Li, C.-G. Duan, X. Wan, J.-L. Kuo, Theoretical prediction of anode materials in Li-ion batteries on layered black and blue phosphorus, J. Phys. Chem. C 119 (2015) 8662–8670.
[30] V.V. Kulish, O.I. Malyi, C. Persson, P. Wu, Phosphorene as an anode material for Na-ion batteries: a first-principles study, Phys. Chem. Chem. Phys. 17 (2015) 13921–13928.
[31] D. Er, J. Li, M. Naguib, Y. Gogotsi, V.B. Shenoy, Ti3C2 MXene as a high capacity electrode material for metal (Li, Na, K, Ca) ion batteries, ACS Appl. Mater. Interf. 6 (2014) 11173–11179.
[32] H. Jiang, Z. Lu, M. Wu, F. Ciucci, T. Zhao, Borophene: a promising anode material offering high specific capacity and high rate capability for lithium-ion batteries, Nano Energy 23 (2016) 97–104.
[33] K. Watanabe, T. Taniguchi, H. Kanda, Direct-bandgap properties and evidence for ultraviolet lasing of hexagonal boron nitride single crystal, Nat. Mater. 3 (2004) 404.
[34] N. Alem, R. Erni, C. Kisielowski, M.D. Rossell, W. Gannett, A. Zettl, Atomically thin hexagonal boron nitride probed by ultrahigh-resolution transmission electron microscopy, Phys. Rev. B 80 (2009) 155425.
[35] K.K. Kim, A. Hsu, X. Jia, S.M. Kim, Y. Shi, M. Hofmann, D. Nezich, J.F. Rodriguez-Nieva, M. Dresselhaus, T. Palacios, J. Kong, Synthesis of monolayer hexagonal boron nitride on cu foil using chemical vapor deposition, Nano Lett. 12 (2012) 161–166.
[36] H. Şahin, S. Cahangirov, M. Topsakal, E. Bekaroglu, E. Akturk, R.T. Senger, S. Ciraci, Monolayer honeycomb structures of group-IV elements and III-V binary compounds: first-principles calculations, Phys. Rev. B 80 (2009) 155453.
[37] C.R. Dean, A.F. Young, I. Meric, C. Lee, L. Wang, S. Sorgenfrei, K. Watanabe, T. Taniguchi, P. Kim, K.L. Shepard, J. Hone, Boron nitride substrates for high-quality graphene electronics, Nat. Nanotechnol. 5 (2010) 722.
[38] Z. Liu, Y. Gong, W. Zhou, L. Ma, J. Yu, J.C. Idrobo, J. Jung, A.H. MacDonald, R. Vajtai, J. Lou, P.M. Ajayan, Ultrathin high-temperature oxidation-resistant coatings of hexagonal boron nitride, Nat. Commun. 4 (2013) 2541.
[39] Y. Kubota, K. Watanabe, O. Tsuda, T. Taniguchi, Deep ultraviolet light-emitting hexagonal boron nitride synthesized at atmospheric pressure, Science 317 (2007) 932–934.
[40] M. Topsakal, E. Aktürk, S. Ciraci, First-principles study of two- and one-dimensional honeycomb structures of boron nitride, Phys. Rev. B 79 (2009) 115442.
[41] Y. Hwang, Y.-C. Chung, Comparative study of metal atom adsorption on free-standing h-BN and h-BN/Ni (111) surfaces, Appl. Surface Sci. 299 (2014) 29–34.
[42] H. Yubin, C. Yong-Chae, Lithium adsorption on hexagonal boron nitride nanosheet using dispersion-corrected density functional theory calculations, Jpn. J. Appl. Phys. 52 (2013) 06GG08.
[43] D. Cakr, D. Kecik, H. Sahin, E. Durgun, F.M. Peeters, Realization of a p-n junction in a single layer boron-phosphide, Phys. Chem. Chem. Phys. 17 (2015) 13013–13020.
[44] B. Onat, L. Hallioglu, S. İpek, E. Durgun, Tuning electronic properties of monolayer hexagonal boron phosphide with group III–IV–V dopants, J. Phys. Chem. C 121 (2017) 4583–4592.
[45] S. Ullah, P.A. Denis, F. Sato, Coupled cluster and density functional investigation of the neutral sodium-benzene and potassium-benzene complexes, Chem. Phys. Lett. 706 (2018) 343–347.
[46] H.R. Jiang, W. Shyy, M. Liu, L. Wei, M.C. Wu, T.S. Zhao, Boron phosphide monolayer as a potential anode material for alkali metal-based batteries, J. Mater. Chem. A 5 (2017) 672–679.
[47] M. Frisch, G. Trucks, H. Schlegel, G. Scuseria, M. Robb, J. Cheeseman, G. Scalmani, V. Barone, B. Mennucci, G. Petersson, Gaussian 09 Revision D. 01, 2009, Gaussian Inc. Wallingford CT, (2009).

[48] G. Kresse, J. Hafner, Phys. Rev. B 49 (1994) 14251.
[49] G. Paolo, B. Stefano, B. Nicola, C. Matteo, C. Roberto, C. Carlo, C. Davide, L.C. Guido, C. Matteo, D. Ismaila, C. Andrea Dal, G. Stefano de, F. Stefano, F. Guido, G. Ralph, G. Uwe, G. Christos, K. Anton, L. Michele, M.-S. Layla, M. Nicola, M. Francesco, M. Riccardo, P. Stefano, P. Alfredo, P. Lorenzo, S. Carlo, S. Sandro, S. Gabriele, P.S. Ari, S. Alexander, U. Paolo, M.W. Renata, QUANTUM ESPRESSO: a modular and open-source software project for quantum simulations of materials, J. Phys.: Condensed Matter 21 (2009) 395502.
[50] P. Giannozzi, O. Andreussi, T. Brumme, O. Bunau, M.B. Nardelli, M. Calandra, R. Car, C. Cavazzoni, D. Ceresoli, M. Cococcioni, Advanced capabilities for materials modelling with Quantum ESPRESSO, J. Phys.: Condensed Matter 29 (2017) 465901.
[51] P. Ordejón, E. Artacho, J.M. Soler, Self-consistent order-$N$ density-functional calculations for very large systems, Phys. Rev. B 53 (1996) R10441–R10444.
[52] J.M. Soler, E. Artacho, J.D. Gale, A. Garcia, J. Junquera, P. Ordejon, D. Sanchez-Portal, The SIESTA method for ab initio order-N materials simulation, J. Phys.: Condens. Matter 14 (2002) 2745.
[53] P.E. Blochl, Phys. Rev. B 50 (1994) 17953.
[54] D. Vanderbilt, Soft self-consistent pseudopotentials in a generalized eigenvalue formalism, Phys. Rev. B 41 (1990) 7892–7895.
[55] J.P. Perdew, K. Burke, M. Ernzerhof, Generalized gradient approximation made simple, Phys. Rev. Lett. 77 (1996) 3865.
[56] Y. Zhang, W. Yang, Comment on "Generalized Gradient Approximation Made Simple", Phys. Rev. Lett. 80 (1998) 890.
[57] S. Grimme, Semiempirical GGA-type density functional constructed with a long-range dispersion correction, J. Comput. Chem. 27 (2006) 1787–1799.
[58] S. Grimme, J. Antony, S. Ehrlich, H. Krieg, A consistent and accurate ab initio parametrization of density functional dispersion correction (DFT-D) for the 94 elements H-Pu, J. Chem. Phys. 132 (2010) 154104.
[59] S. Grimme, S. Ehrlich, L. Goerigk, Effect of the damping function in dispersion corrected density functional theory, J. Comput. Chem. 32 (2011) 1456–1465.
[60] Y. Zhao, D.G. Truhlar, A new local density functional for main-group thermochemistry, transition metal bonding, thermochemical kinetics, and noncovalent interactions, J. Chem. Phys. 125 (2006) 194101.
[61] Y. Zhao, D.G. Truhlar, Density functionals with broad applicability in chemistry, Acc. Chem. Res. 41 (2008) 157–167.
[62] M. Dion, H. Rydberg, E. Schröder, D.C. Langreth, B.I. Lundqvist, Van der Waals density functional for general geometries, Phys. Rev. Lett. 92 (2004) 246401.
[63] T. Thonhauser, V.R. Cooper, S. Li, A. Puzder, P. Hyldgaard, D.C. Langreth, Van der Waals density functional: self-consistent potential and the nature of the van der Waals bond, Phys. Rev. B 76 (2007) 125112.
[64] T. Thonhauser, S. Zuluaga, C.A. Arter, K. Berland, E. Schröder, P. Hyldgaard, Spin signature of nonlocal correlation binding in metal-organic frameworks, Phys. Rev. Lett. 115 (2015) 136402.
[65] K. Berland, V.R. Cooper, K. Lee, E. Schröder, T. Thonhauser, P. Hyldgaard, B.I. Lundqvist, van der Waals forces in density functional theory: a review of the vdW-DF method, Rep. Prog. Phys. 78 (2015) 066501.
[66] D. Langreth, B.I. Lundqvist, S.D. Chakarova-Käck, V. Cooper, M. Dion, P. Hyldgaard, A. Kelkkanen, J. Kleis, L. Kong, S. Li, A density functional for sparse matter, J. Phys.: Condensed matter 21 (2009) 084203.
[67] R. Sabatini, E. Küçükbenli, B. Kolb, T. Thonhauser, S. De Gironcoli, Structural evolution of amino acid crystals under stress from a non-empirical density functional, J. Phys.: Condensed Matter 24 (2012) 424209.
[68] K. Lee, É.D. Murray, L. Kong, B.I. Lundqvist, D.C. Langreth, Higher-accuracy van der Waals density functional, Phys. Rev. B 82 (2010) 081101.
[69] J.P. Perdew, W. Yue, Accurate and simple density functional for the electronic exchange energy: generalized gradient approximation, Phys. Rev. B 33 (1986) 8800–8802.
[70] I. Hamada, van der Waals density functional made accurate, Phys. Rev. B 89 (2014) 121103.
[71] R. Sabatini, T. Gorni, S. de Gironcoli, Nonlocal van der Waals density functional made simple and efficient, Phys. Rev. B 87 (2013) 041108.
[72] J. Klimeš, D.R. Bowler, A. Michaelides, Van der Waals density functionals applied to solids, Phys. Rev. B 83 (2011) 195131.
[73] J. Klimeš, D.R. Bowler, A. Michaelides, Chemical accuracy for the van der Waals density functional, J. Phys.: Condensed matter 22 (2009) 022201.
[74] X. Fan, W. Zheng, J.-L. Kuo, Adsorption and diffusion of Li on pristine and defective graphene, ACS Appl. Mater. Interf. 4 (2012) 2432–2438.
[75] C.-K. Yang, A metallic graphene layer adsorbed with lithium, Appl. Phys. Lett. 94 (2009) 163115.
[76] J. Heyd, G.E. Scuseria, Assessment and validation of a screened Coulomb hybrid density functional, J. Chem. Phys. 120 (2004) 7274–7280.
[77] D. Çakır, D. Kecik, H. Sahin, E. Durgun, F.M. Peeters, Realization of ap–n junction in a single layer boron-phosphide, Phys. Chem. Chem. Phys. 17 (2015) 13013–13020.
[78] Y. Zhou, MX (M= Ge, Sn; X= S, Se) sheets: theoretical prediction of new promising electrode materials for Li ion batteries, J. Mater. Chem. A 4 (2016) 10906–10913.
[79] Q. Tang, Z. Zhou, P. Shen, Are MXenes promising anode materials for Li ion batteries? Computational studies on electronic properties and Li storage capability of Ti3C2 and Ti3C2X2 (X = F, OH) monolayer, J. Am. Chem. Soc. 134 (2012) 16909–16916.
[80] G.A. Tritsaris, E. Kaxiras, S. Meng, E. Wang, Adsorption and diffusion of lithium on layered silicon for Li-ion storage, Nano Lett. 13 (2013) 2258–2263.
[81] W.-J. Zhang, A review of the electrochemical performance of alloy anodes for lithium-ion batteries, J. Power Sources 196 (2011) 13–24.
[82] C. Ling, F. Mizuno, Boron-doped graphene as a promising anode for Na-ion batteries, Phys. Chem. Chem. Phys. 16 (2014) 10419–10424.
[83] M. Mortazavi, C. Wang, J. Deng, V.B. Shenoy, N.V. Medhekar, Ab initio characterization of layered MoS2 as anode for sodium-ion batteries, J. Power Sources 268 (2014) 279–286.
[84] T. Zhou, W.K. Pang, C. Zhang, J. Yang, Z. Chen, H.K. Liu, Z. Guo, Enhanced sodium-ion battery performance by structural phase transition from two-dimensional hexagonal-SnS2 to orthorhombic-SnS, Acs Nano 8 (2014) 8323–8333.
[85] K. Nobuhara, H. Nakayama, M. Nose, S. Nakanishi, H. Iba, First-principles study of alkali metal-graphite intercalation compounds, J. Power Sources 243 (2013) 585–587.
[86] Y.-X. Yu, Prediction of mobility, enhanced storage capacity, and volume change during sodiation on interlayer-expanded functionalized Ti3C2 MXene anode materials for sodium-ion batteries, J. Phys. Chem. C 120 (2016) 5288–5296.
[87] G. Lv, J. Wang, Z. Shi, L. Fan, Intercalation and delamination of two-dimensional MXene (Ti3C2Tx) and application in sodium-ion batteries, Mater. Lett. 219 (2018) 45–50.

141

83

## 7 Theoretical characterization of other 2D materials

The experimental realization of graphene opened a new door of research topic called 2D materials. The single layer of graphite (graphene) was synthesized after almost 57 years when it was first studied [6]. And now within the short period of 15 years, we have hundreds of other 2D materials already been synthesized and/or predicted/imagined theoretically [33]. These 2D materials differ significantly from each other by virtue of their electronic properties. In addition, these properties can also be altered by a number of techniques. For example, the direct sign up of graphene to FETs is prohibited due to the special electronic characteristic of graphene. To make this happen, graphene should be modified and it is already documented that these modifications come in the form of several thrilling properties. One of these modifications involves the chemical functionalization of graphene surface with H, O, or F atoms and the corresponding structures are called graphane (hydrogenated graphene), graphene oxide and fluorographene (fluorinated graphene), respectively [237–243]. The electronic properties of these patterns are quite different than the pristine graphene. Furthermore, the wide range of properties can be utilized in a broad realm of applications causing a remarkable upgrading to the present technologies. In this context, we study the hydrogenation and fluorination of monolayer boron phosphide and boron arsenide. The strength of F-BX (X=P, As) systems is found to be greater than the H-BX system as revealed by the cohesive energy calculations. In addition, the functionalization induced buckling in the structure as expected. The dynamical stability of these systems was confirmed by calculating the phonon spectra in which both the phonon band spectrum and phonon DOS were reported and discussed. The phonon spectra span over a wider range for hydrogenated systems in comparison with the fluorinated systems. This is a consequence of the different sizes of H and F. In addition, these derivatives were also tested in a high-temperature environment which can be mimic by using AIMD simulations. The structures are well retained at a temperature of 1500 K. In addition, surviving in such harsh conditions demands the use of these derivatives in high temperature operating devices. The electronic properties are quite flexible and, furthermore, direct bandgaps were observed in fluorinated systems, whereas, indirect gaps were computed for hydrogenated cases. Moreover, the wider range of the gaps (from 0.89-3.89 eV) is suitable for diverse applications. The results were published in (ACS Omega 2018, 3, 12, 16416-16423) [244] and is given in Appendix D.1.

We also predicted the stability of a new 2D monolayer of beryllium nitride family, $Be_3N_2$. It has a unique structure consisting of $sp$-$sp^2$ bonds where N atoms occupy the corners which are glued together by the Be atoms. That being said, each N atom is connected with three Be atoms making three $sp^2$ hybridized sigma bonds. However, an

unusual *sp* hybridized bond is adopted by Be. The lattice parameter is 5.24 Å which is almost two times to that of hBN. The cohesive energy is -5.075 eV/atom which is comparable to the most stable bulk beta-$Be_3N_2$ (-5.726 eV/atom) and the formation energy suggests that the experimental synthesis of monolayer $Be_3N_2$ is easier than the rival materials, $Mg_3N_2$. As the bulk beta-$Be_3N_2$ is a non-layered material so to have an idea about the possible synthesis of monolayer $Be_3N_2$, we calculate the exfoliation energy as the difference of energies of monolayer and half of the bulk phase which were then divided by the area of the monolayer. We take half of the energy of the bulk phase as the unitcell contains 10 atoms, whereas, there are 5 atoms in the unitcell of the monolayer. Furthermore, according to this formula, it is found that $Be_3N_2$ is at the interface of "high-binding" and "potentially exfoliable" materials [33]. In chemical analysis, we report a charge transfer from Be to N which is in perfect agreement with the difference in their electronegativity values. To further explore the type of bonds in monolayer $Be_3N_2$, we calculate electron localization function (ELF) [245] which reveals that a strong covalent bond is present between Be and N which is responsible for the stability and great strength. However, as new material, it is mandatory to check the dynamical stability by calculating the phonon spectrum and to analyze if the structure has some instabilities or not. All the frequencies were positive which means that $Be_3N_2$ is the local minimum over potential energy surface. In addition to this, there are only 2.34 % changes in the Be-N bonds at 900 K temperature, thus providing information about its excellent kinetic stability. In mechanical properties, we report 2D elastic constant which is calculated to be 46.5 N/m. The electronic bandgap is 2.76-4.10 eV depending on the level of employed theory. This means that $Be_3N_2$ is a wide gap semiconductor. We also check the electrochemical properties of $Be_3N_2$ which offers an exceptional storage capacity of 974 mAh/g for Li, Na, and K. In addition to this, graphite-like bulk phases of $Be_3N_2$ were also investigated. Finally, we report 1D nanoribbons that offer tunable electronic properties. These interesting results were published in (New J. Chem., 2019,43, 2933-2941) [246].

Recently, a new 2D material consisting of boron-oxygen holey framework was synthesized and the authors mentioned that some theoretical calculations will be handy to predict its potential properties [247]. In order to quench this thirst, we perform DFT calculations to explore various properties of this "newly born" 2D boroxine, $B_3O_3$. We provide a glimpse of various properties of $B_3O_3$. It has quite a unique structure in which each ring contains 3B and 3O atoms and, furthermore, each ring is connected through B-B bonds. Besides, the six rings combined together in such a way that a big hole is formed with the opposite O-O separation of 6.27 Å which is suitable to adsorb atoms or even big molecules. The cohesive energy of $B_3O_3$ is -6.72 eV/atom which is slightly lower than that of graphene (-8.07 eV/atom) but almost twice the value for phosphorene.

The phonon calculation reveals that the free-standing $B_3O_3$ is also a local minimum over the potential energy surface. Additionally, $B_3O_3$ is a wide gap semiconductor with a gap of 5.30 eV at HSEH1PBE level of theory. With the same level of theory, the gap of $h$BN is 6.1 eV. Moreover, the charge is transferred from B to O as the electronegativity of O is higher than that of B. The bonding character is revealed by the calculation of ELF [245]. It is found that two types of bonding nature are present in $B_3O_3$, ionic B-O bond and strong covalent B-B bond. Having said that, rings in $B_3O_3$ are clinched together by the strong covalent B-B bonds which seems to be the main reason for its stability. In addition, simulated scanning tunneling microscopy (STM) images are also calculated which can assist forthcoming experimental and/or theoretical studies. $B_3O_3$ has excellent kinetic and mechanical stabilities. The 2D elastic modulus is found to be greater than silicene and germanene. Besides, the stability and optoelectronic properties of the bilayer is also investigated and, furthermore, found that the introduction of an external field can seriously tune the optoelectronic properties in the bilayer. More specifically, optical properties can be tuned in the visible region when an external field is applied. Moreover, the optical properties show layer-separation which is crucial in photovoltaics for larger recombination time. Finally, a graphite-like bulk phase is also investigated and found that it is comparably robust to that of graphite. The paper is published in (RSC Adv., 2019,9, 37526-37536) [248] and is given in Appendix D.2.

## PAPER

# Theoretical characterization of hexagonal 2D Be₃N₂ monolayers†

Saif Ullah, ⓘ *[a] Pablo A. Denis, ⓘ [b] Rodrigo B. Capaz*[c] and Fernando Sato[a]

First-principles density functional theory (DFT) calculations are performed to assess the stability, and geometric, mechanical, optical and electronic properties of monolayer graphene-like Be₃N₂. We find that Be₃N₂ is a large band gap semiconductor with small electron and hole effective masses, which may promote its use in nanoelectronic devices. Furthermore, its excellent thermal, dynamical, and mechanical stability makes it a material of comparable caliber to that of graphene. In addition, the excellent electrochemical properties of Be₃N₂ make it a unique material with possible theoretical capacities of 974 mA h g⁻¹ for Li, Na, and K. Moreover, Be₃N₂ can form bulk graphite-like layered structures with two different configurations, *i.e.* N2–N1 and N2–Be1. Finally, the derivatives of Be₃N₂ (Be₃N₂ nanoribbons) also possess direct band gaps which can be finely tuned to the desired level by geometry and morphology constraints. Based on these fascinating properties, Be₃N₂ and its derivatives can find a broad range of applications in nanoelectronics and battery technologies.

## 1 Introduction

New technologies bring new materials and these materials, in turn, advance the existing technologies. A single layer of graphite, which turned out to be graphene in 2004, was studied by Wallace *et al.* as early as in 1947 by the tight-binding method.[1] This 2004 discovery appeared in the form of an almost magical material with prodigious physical, electronic, and electrical properties.[2–5] Graphene is a zero bandgap semiconductor with a Dirac cone in its band structure near the Fermi level. The electronic structure can be tuned, for instance, by confining the electronic states to 1D nanoribbons.[6,7] Depending on the width and types, the electronic and magnetic properties of these nanoribbons can be altered.[8,9] Graphene was just the beginning of the story which opened the door to the new field of 2D materials. Since then, a number of 2D materials have been investigated (experimentally/ theoretically).[10–12] For instance, h-BN has a similar hexagonal structure to graphene with a large bandgap which is due to the symmetry breaking by the presence of different species (B, and N) in its unit cell.[13] Another similar material is h-BP with an intermediate bandgap between graphene and h-BN predicted theoretically, though not synthesized experimentally.[14,15] Some materials, such as silicene and germanene, show the same Dirac-like characteristics

as graphene.[16,17] The suitable band gap of phosphorene makes it a potential nominee for its use in nanoelectronics and optoelectronics.[18,19] Comprehensive reviews on many of these 2D materials are available.[20,21] Recently, several MXenes have been investigated having exceptional electronic properties ranging from metallic to semiconducting.[22–24]

Many 2D materials have related 3D counterparts with the same composition, which can be layered or not. An obvious example is the relation between graphene and graphite (layered) or diamond (not layered). Therefore the search for novel 2D materials often begins by exploring existing 3D materials with suitable chemical bonding schemes. One such bulk material is hexagonal beryllium nitride (β-Be₃N₂) which is a non-layered, wide band gap semiconductor. In this work, we investigate the structural, mechanical, optical, and electronic properties as well as the stability of a hexagonal 2D sheet of Be₃N₂ with the help of first-principles calculations. We also study 1D nanoribbons of Be₃N₂ and a novel, graphite-like, layered structure of Be₃N₂.

In a very recent study, electronic properties of monolayer Be₃N₂ were investigated.[25] While some of our results agree with this previous publication, our study goes much beyond in the exploration of cohesive, electrochemical and optical properties. In addition, a novel graphitic-like bulk phase of Be₃N₂ is proposed.

## 2 Computational details

Calculations are performed with SIESTA,[26,27] Quantum Espresso (QE),[28,29] VASP,[30] and Gaussian codes.[31] With SIESTA, we use vdW-DF,[32] the PBE version of GGA,[33] LDA,[34] and a cocktail of GGA + LDA which we shall call the hybrid throughout the

[a] *Departamento de Física, Instituto de Ciências Exatas, Campus Universitário, Universidade Federal de Juíz de Fora, Juíz de Fora, MG 36036-900, Brazil. E-mail: sullah@fisica.ufjf.br*

[b] *Computational Nanotechnology, DETEMA, Facultad de Química, UDELAR, CC 1157, 11800 Montevideo, Uruguay*

[c] *Instituto de Física, Universidade Federal do Rio de Janeiro, Caixa Postal 68528, Rio de Janeiro, RJ 21941-972, Brazil. E-mail: capaz@if.ufrj.br*

† Electronic supplementary information (ESI) available. See DOI: 10.1039/c8nj05600e

manuscript (details are in the ESI†). The double-zeta basis set with polarization function (DZP) is selected and the norm-conserving (NC) Troullier–Martins pseudopotentials (PPs) are used in the separable form.[35] The unit-cell is sampled with $30 \times 30 \times 1$ $k$ points in the first Brillouin zone. A large vacuum space of 20 Å is created to avoid the interaction between the periodic layers along the $z$-axis. The mesh cutoff is as high as 200 Ry with the force convergence criterion of 0.01 eV Å$^{-1}$. The projector augmented wave (PAW)[36] method along with PBE PPs is used in the VASP package. As far as QE is concerned, PBE, PBE-sol,[37] LDA, and a number of different recipes of vdW-DF functionals are used. The HSEH1PBE/6-311G*[38] calculations are performed with the Gaussian code.

## 3 Results and discussion

We start our study by replicating the results of bulk β-Be$_3$N$_2$, shown in Fig. S1 of the ESI.† The calculated lattice parameters, $a = b = 2.83$ Å and $c = 9.68$ Å by QE (PBE-sol), and $a = b = 2.94$ Å and $c = 10.2$ Å by SIESTA, are in excellent agreement with the experimental $a = b = 2.841$ Å, $c = 9.693$ Å,[39] and theoretical $a = b = 2.847$ Å, $c = 9.714$ Å,[40] $a = b = 2.855$ Å, $c = 9.740$ Å,[41] $a = b = 2.851$ Å, $c = 9.726$ Å,[42] $a = b = 2.847$ Å, $c = 9.720$ Å,[43] and $a = b = 2.842$ Å, $c = 9.695$ Å[40] values. We also compare the cohesive energy of β-Be$_3$N$_2$ with the reported values in the literature. The cohesive energy is 4.21 a.u per cell with QE (PBE-sol), and 3.39 a.u per cell with SIESTA, which is also in reasonably good agreement with the values 2.115–5.010 a.u per cell[40–43] reported in the literature. This proves the reliability of our computational procedure.

### 3.1  Structural characterization

After the successful replication of β-Be$_3$N$_2$ results, we start calculations of monolayer graphene-like Be$_3$N$_2$. The geometric structure of Be$_3$N$_2$ is a 2D hexagonal honeycomb lattice as that of graphene, hexagonal boron nitride (h-BN),[44] hexagonal boron phosphide (h-BP)[15] etc. However, the atomic coordination and chemical bonding are very different. The corners of hexagons are occupied by N atoms linked together by Be atoms which act as bridges between the two N atoms. Therefore, each N atom is surrounded by three Be atoms thus forming three sp$^2$-hybridized sigma bonds. On the other hand, Be adopts a very unusual sp hybridization. This type of bonding occurs for instance in gas phase BeH$_2$ and in other molecular compounds,[45] but it is uncommon in a coordinated 2D solid. The lattice parameter ($a = b$) and Be–N bond lengths at the PBE-sol level of theory are 5.24 Å and 1.51 Å, respectively, with a bond angle of 120° as shown in Fig. 1. The nearest N–N and Be–Be distances are 3.02 Å and 2.62 Å, respectively. The structural properties calculated at the different levels of theories are given in Table S1 of the ESI.†

### 3.2  Theoretical synthesis and structural stability

The cohesive energy of Be$_3$N$_2$ is calculated and compared with its bulk counterpart β-Be$_3$N$_2$. The cohesive energy is defined as:

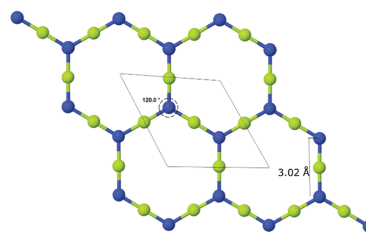$$E_{\text{coh}} = \frac{E_{\text{tot}} - n_{\text{Be}}E_{\text{Be}} - n_{\text{N}}E_{\text{N}}}{n}$$



**Fig. 1**   The geometric structure of monolayer Be$_3$N$_2$ is shown with a unit-cell highlighted. The nearest N–N bond separation is 3.02 Å at the PBE-sol level of theory.

where $E_{\text{tot}}$ is the total energy of Be$_3$N$_2$, while $E_{\text{Be}}$ and $E_{\text{N}}$ are the energies of an isolated Be atom and isolated N atom, respectively. Finally, $n$ is the number of atoms in the unit cell. Using this definition, the cohesive energy of monolayer Be$_3$N$_2$ is $-5.075$ eV per atom at the PBE-sol level of theory. In addition, the cohesive energy of β-Be$_3$N$_2$ at the same level of theory is $-5.726$ eV per atom. This shows that monolayer Be$_3$N$_2$ is metastable with respect to the bulk form. To assess the viability of experimental synthesis, the formation energy (at PBE-sol level) is calculated by using the energy of a N$_2$ molecule and bulk-Be hexagonal structure and found to be $-0.51$ eV per atom ($-2.56$ eV per formula unit). This value is lower than the one calculated for similar monolayer Mg$_3$N$_2$ (0.07 eV per atom).[46] Therefore, the formation energies suggest that monolayer Be$_3$N$_2$ is easier to synthesize experimentally than Mg$_3$N$_2$. To address the possible synthesis of monolayer Be$_3$N$_2$, the exfoliation energy is calculated. As β-Be$_3$N$_2$ is not a layered structure, we define the exfoliation energy as the total energy difference per formula (3Be + 2N) between β-Be$_3$N$_2$ and monolayer Be$_3$N$_2$, divided by the 2D unit cell area of monolayer Be$_3$N$_2$ $A_{\text{2D}}$:

$$E_{\text{exf}} = \frac{E_{\text{2D-Be}_3\text{N}_2} - \frac{1}{2}E_{\text{β-Be}_3\text{N}_2}}{A_{\text{2D}}}$$

Our calculated $E_{\text{exf}}$ at DF2-C09 and rev-vdW-DF2 functionals are 0.15 eV Å$^{-2}$ and 0.14 eV Å$^{-2}$, respectively. According to the classification of Mounet et al.,[47] Be$_3$N$_2$ would rank near the boundary between "potentially exfoliable" and "high-binding" 2D materials, which is set at 0.13 eV Å$^{-2}$. The values calculated at various vdW-DF flavors are shown in Table S2 of the ESI.†

### 3.3  Chemical analysis

In order to investigate the bonding mechanism in monolayer Be$_3$N$_2$, charge transfer analyses along with electron localization function are carried out. The Mulliken population analysis shows a charge of $-0.87e$ around the N atoms while the Hirshfeld and Voronoi population analyses reveal a charge of $-0.44e$ and $-0.6e$, respectively, around the N atoms. This can be attributed to the higher electronegativity of N in comparison with Be. The Bader charge analysis shows zero charge density around Be atoms and, consequently, all the 2$e$ valence charge of Be accumulate around N atoms. This is in-line with our previous investigations where Be
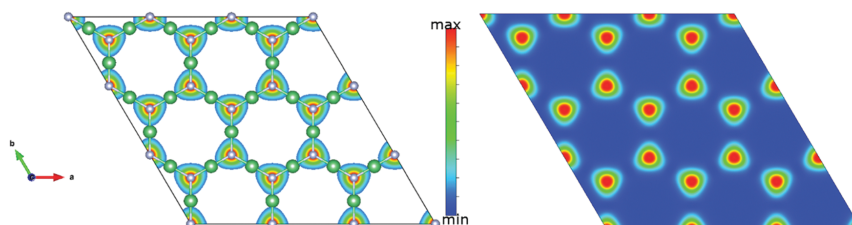
**Fig. 2** Iso-surface plot of charge density with the corresponding 2D cut is shown. Red color represents the maximum value of charge accumulation while blue shows the minimum or charge depletion. It can clearly be seen that there is no charge density around Be atoms and furthermore, the charge transfer from Be is accumulated around N atoms. This is in agreement with the Bader charge analysis.
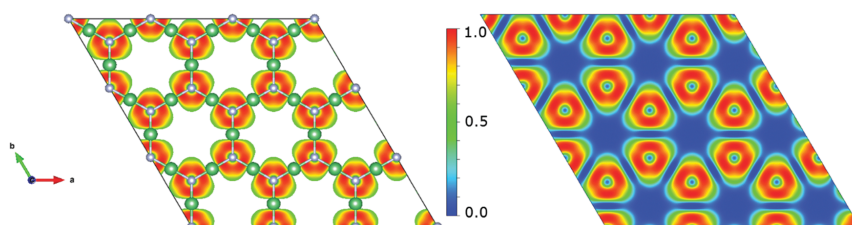


**Fig. 3** ELF along with its 2D cut is plotted. It can be seen that electrons are not localized on a specific site rather the density is spread in between N and Be atoms resulting in strong covalent bond formation. Red and blue colors represent the maximum and minimum densities, respectively. Green color shows an average uniform density.

and B are likely to transfer all their valence charge to the higher electronegative atom(s) as we see in the case of graphene, and N-doped and 3p element doped graphenes.[48–54] Although there are numerical differences, the behavior of charge transfer from Be to N is confirmed by all methods of charge population analyses. The iso-surface map of charge density along with its 2D cut is plotted in Fig. 2, where it is evident that charge is transferred from Be to N, consistently with the higher electronegativity of N than Be. The electron localization function (ELF)[55] is a handy tool to classify the nature of bonding and stability mechanism analysis which provide a picture of the electron localization in a system. The in-plane bonds between Be and N are highlighted in the iso-surface plot of ELF as can be seen in Fig. 3. Furthermore, the 2D cut of this ELF is also shown. The charge distribution region in ELF is distributed between the maximum (1) and minimum (0) values. The region where ELF takes the value 1 is regarded as the region with entirely localized electrons, while the area with 0 ELF value indicates a region with small electron density. The values around 0.5 are considered to be average where the density is regarded as the homogeneous electron gas. From the ELF plots (both the iso-surface and 2D cut), it is evident that electrons are pretty much localized around N atoms and spreading near through Be atoms thus revealing a mixed covalent and ionic (due to charge transfer) interaction, with $sp^2$ hybridization for N and sp hybridization for Be. This strong bonding is responsible for the stabilization of monolayer $Be_3N_2$.

## 3.4 Dynamical stability

In order to check the dynamical stability of the $Be_3N_2$ sheet, the phonon spectrum was calculated with the density functional perturbation theory (DFPT)[56] method using the Phonon code as implemented in QE along the high symmetry points in the first Brillouin zone. The phonon spectrum was calculated using $8 \times 8 \times 1$ $q$-points. The spectrum is shown in Fig. 4, which
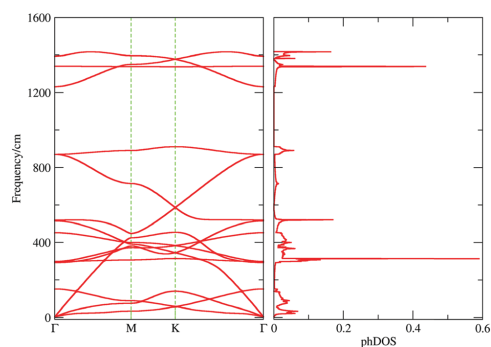


**Fig. 4** Phonon dispersion spectrum is plotted along with phonon DOS. The absence of negative frequency revealed that the $Be_3N_2$ monolayer is a true minimum of the potential energy surface.

presents no imaginary frequency thus revealing that monolayer $Be_3N_2$ is indeed a local minimum in the potential energy surface. The in-plane sound velocity is calculated to be $\sim 13.7$ km s$^{-1}$ from the phonon dispersion by taking the slope of $\omega(k)$. For comparison, the sound velocity of graphene is 22 km s$^{-1}$.

### 3.5 Kinetic stability

In order to address the kinetic stability of the monolayer $Be_3N_2$ sheet, *ab initio* molecular dynamics (AIMD) simulations as implemented in SIESTA are carried out. A $4 \times 4$ supercell was modeled to perform the simulations at 300 K, 600 K, and 900 K. It is interesting to note that the monolayer $Be_3N_2$ sheet can withstand temperatures as high as 900 K, as shown in Fig. 5. Consequently, $Be_3N_2$ monolayers can find applications even in those devices which operate at high temperatures, which include aircraft, space, oil, and gas exploration applications.[57]

### 3.6 Mechanical properties

The 2D bulk modulus or layer modulus $B_0$ of $Be_3N_2$ is calculated by observing the variations in total energy as the lattice constant varies. From the plot, $B_0$ is calculated by taking the second derivative at the minimum $B_0 = A_0 \dfrac{\partial^2 E}{\partial A^2}\Big|_{A_0} = \dfrac{\sqrt{3}}{6}\dfrac{\partial^2 E}{\partial a^2}\Big|_{a_0}$, where $a$ is the lattice constant and $A = \dfrac{\sqrt{3}a^2}{6}$ is the unit cell area for both monolayer $Be_3N_2$ and graphene (see Fig. 6). The 2D bulk modulus of $Be_3N_2$ is found to be 2.90 eV Å$^{-2}$ (46.5 N m$^{-1}$). The same level of theory is applied to calculate the bulk modulus of graphene which
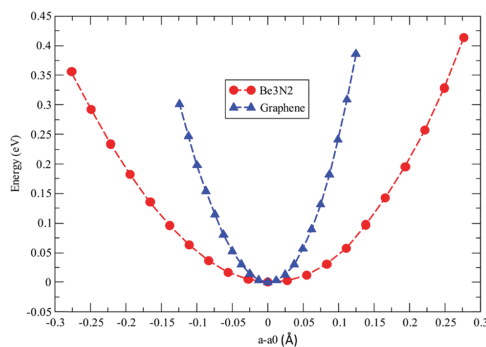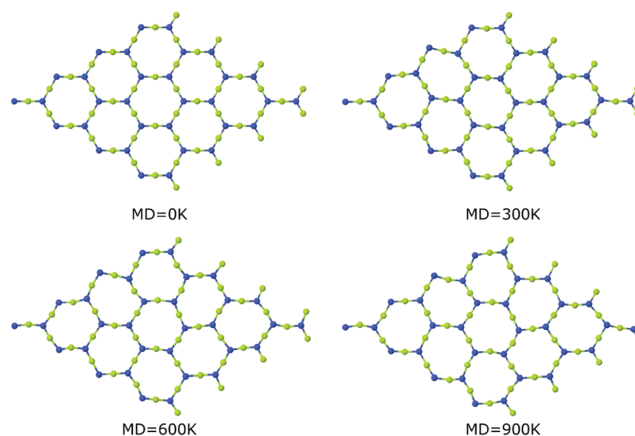


**Fig. 6** The energy (eV) *vs.* lattice constant (Å) curve of monolayer $Be_3N_2$ is plotted and compared with graphene. The second derivative gives the in-plane stiffness.

gives a value of 12.9 eV Å$^{-2}$ (206 N m$^{-1}$), in perfect agreement with the previous calculations.[58]

### 3.7 Electronic and optical properties

After ensuring the stability of monolayer $Be_3N_2$, we calculate its electronic and optical properties. The electronic band structure calculations reveal that monolayer $Be_3N_2$ is a semiconductor with a direct band-gap. The electronic band-gap occurs at the $\Gamma$ point as shown in Fig. 7. The value of band-gap opening at the hybrid GGA-LDA level as implemented in SIESTA is calculated to be 2.76 eV, while HSEH1PBE calculated with the Gaussian code



|        |          |
|--------|----------|
| MD=0K  | MD=300K  |
| MD=600K | MD=900K |

| **Bonds** | **0 K** | **300 K** | **600 K** | **900 K** |
|-----------|---------|-----------|-----------|-----------|
| Be–N      | 0       | 1.65%     | 1.72%     | 2.34%     |

**Fig. 5** Snapshots of the geometries of monolayer $Be_3N_2$ after the end of AIMD simulations treated at various temperatures are shown. The average Be–N bond increment (in %) as a function of temperature is depicted in the table.
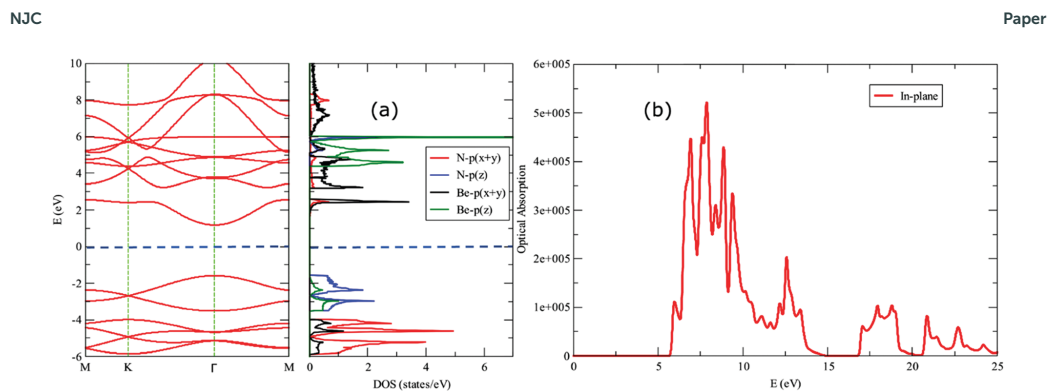
**Fig. 7** (a) Electronic band structure and the corresponding PDOS of monolayer $Be_3N_2$. The calculations show that monolayer $Be_3N_2$ is a direct gap semiconductor as the CBM and VBM lie at the gamma point. The Fermi energy is set to zero. The in-plane optical absorption is shown in (b).

revealed a gap of 4.10 eV. This 1.34 eV difference comes from the well-known underestimation of gaps in DFT using local and semilocal exchange–correlation functionals.[59,60] The HSE gap reported in ref. 25 is 3.83 eV, almost 0.27 eV lower than our calculated gap. Therefore, $Be_3N_2$ is a wide gap semiconductor. The values calculated at different levels of theory can be seen in Table S3 of the ESI.† Interestingly, the shape of the valence band resembles that of graphene, with a Dirac cone at the $K$ point but the Fermi level position is such that the whole band is occupied (both bonding and antibonding states). Indeed, partial density of states (PDOS) calculations, shown in the center and right panels of Fig. 7(a), reveal that the topmost valence band is a π-band composed of $N$-$2p_z$ and $Be$-$p_z$ orbitals. The states in deeper valence bands are σ-like, being composed of the hybridization of $N$-$2p_{x+y}$ and $Be$-$2p_{x+y}$ orbitals. On the other hand, the lowest conduction band is also σ-like, composed of the hybridized states of $Be$-$2p_{x+y}$ and $N$-$2p_{x+y}$. No contribution from the $2p_z$ orbitals was found in the conduction band.

Electron and hole effective masses are calculated from the curvature of the CBM (VBM) by the parabolic fitting of the band edges. To this end, the band structure is recalculated with a denser set of $k$ points to minimize the error in calculations. The effective mass of electrons ($m_e^\star$) is found to be 0.042 $m_e$, while the calculated effective mass of holes ($m_h^\star$) is predicted to be 0.087 $m_e$. These very small values of effective masses ensure remarkable mobilities in $Be_3N_2$ for both electron and hole transport, and by virtue of these properties, it will be interesting to see the use of $Be_3N_2$ in nanoelectronics.

We also calculate the optical absorption spectra for in-plane polarization, as shown in Fig. 7(b). Excitonic effects are not considered. Interestingly, the onset of optical absorption (optical band gap) occurs near 6 eV, much larger than the electronic band gap of 2.76 eV. This implies that, although $Be_3N_2$ is a direct-gap material, dipole selection rules forbid transitions from the first valence to the first conduction band. This result can also be understood in terms of the orbital character of band states, described above.

**3.8 Chemical reactivity**

The chemical reactivity of $Be_3N_2$ is calculated by using the hydrogen (H) reaction method as successfully reported in earlier studies.[51,61,62] An H atom is kept on the top of Be and then N and the binding energies at both sites are calculated. We find that the N site is more reactive as the H–N binding energy is calculated to be $-26.4$ kcal mol$^{-1}$ in agreement with the charge transfer analyses.[51] The binding energy of H–Be is as low as $-13.9$ kcal mol$^{-1}$. For comparison, the H–C binding energy in graphene is $-25.6$ kcal mol$^{-1}$ at the same level of theory (vdW-DF/DZP). This shows that the N site in $Be_3N_2$ is slightly more reactive to hydrogen than graphene, thus indicating that both materials should have similar properties in catalytic processes.

**3.9 Electrochemical properties**

Presently, secondary batteries are attaining enormous attention due to the energy storage and conversion issues. The biggest hurdle in designing efficient alkali-based batteries is the search for useful anode materials. Among various electrochemical properties, the storage capacity of an anode material is considered to be the most critical. To this end, $Be_3N_2$ is studied for the adsorption of alkali atoms (Li, Na, and K) above and within the hollow site as shown in Fig. S2 of the ESI.† The adsorption on top of the hollow site is found to be favorable as concluded from the adsorption energies, which are gathered in Table 1. The storage

**Table 1** Adsorption energies of alkali atoms on monolayer $Be_3N_2$ are shown. The negative adsorption energy shows favorable adsorption and *vice versa*. The maximum possible theoretical storage capacity of $Be_3N_2$ is calculated to be $\sim$974 mA h g$^{-1}$ for Li, Na, and K

| System | Adsorption energy[a] (eV per atom) | Adsorption energy[b] (eV per atom) |
|---|---|---|
| Li | $-0.008$ | $-0.42$ |
| Na | $+0.20$ | $-0.46$ |
| K | $+1.37$ | $-0.72$ |

[a] Alkali atoms within the hollow site. [b] Alkali atoms on top of the hollow site.

capacity of $Be_3N_2$ is found to be $\sim 487$ mA h g$^{-1}$ for all the alkali atoms (Li, Na, and K) tested, assuming they all adopt maximum coverage (one ion per unit cell). The storage capacity is given by $C = \dfrac{nF}{M}$, where $n$, $F$, and $M$ represent the number of ions, Faraday constant, and molar mass of the substrate, respectively, while further details can be seen in ref. 52.

This is calculated considering that ions adsorb on only one side of $Be_3N_2$. Furthermore, we decorate both the sides with alkali atoms thus resulting in a storage capacity of $\sim 974$ mA h g$^{-1}$ with enhanced adsorption strength. This is in line with our recent investigation.[63] Graphene, unfortunately, cannot be used as an anode material as these ions are likely to form clusters on it. On the other hand, the Li and Na storage capacities of graphite are limited to 370 mA h g$^{-1}$ [64,65] and 35 mA h g$^{-1}$,[66] respectively. Consequently, the use of $Be_3N_2$ can also solve the anode issue and, therefore, should be further investigated. The calculation details and procedure can be seen in ref. 52–54 and 67.

**3a Graphite-like stacked bulk-$Be_3N_2$.** A new phase of bulk $Be_3N_2$ graphite-like layered structure is also investigated. We investigate two types of stacking, as shown in Fig. 8. In the first type, nitrogen atoms on both layers are on top of each other (N2–N1 stacking) and in the second type, a N atom on layer 2 is on top of a Be on layer 1 (N2–Be1 stacking). The structures are allowed to relax. Using VASP at the PBE-D2 level of theory, both structures were found to be local minima in the total energy surface, with N2–Be1 stacking being more favorable than N2–N1. The energetics are given in Table 2. The interlayer separation for the lowest-energy N2–Be1 stacking is 2.85 Å, much smaller than that in graphite. However, the interlayer separation for the N2–N1 stacking is 3.45 Å. Notice, however, that the non-layered β-$Be_3N_2$ is still the lowest-energy bulk phase of this compound. Using $E_{exf} = \dfrac{E_{2D-Be_3N_2} - E_{g-Be_3N_2}}{A_{2D}}$, we also calculate the exfoliation energy with respect to the graphite-like structure (g-$Be_3N_2$), which is a direct measurement of the van der Waals interaction between
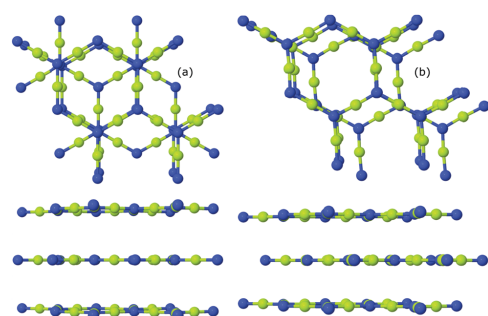
layers. We find that the exfoliation energy with respect to the N2–N1 stacking is only 4.8 meV Å$^{-2}$, whereas for the N2–Be1 stacking, the value is 9.7 meV Å$^{-2}$. Therefore, both graphite-like $Be_3N_2$ structures can be classified as "easily exfoliable" materials.[46] For comparison, the exfoliation energy of graphite at the same level of theory is 21 meV Å$^{-2}$. Therefore, graphite-like $Be_3N_2$ would be more easily exfoliable than graphite. This comparative analysis of exfoliation energy indicates the relative strength of van der Waals interactions in these different materials.

**3b $Be_3N_2$ nanoribbons.** There are four different possibilities of forming ribbons of monolayer $Be_3N_2$ nanosheets, depending on the edges or termination. These ribbons can take the form of A–Be (armchair, Be terminated), A–N (armchair, N terminated), Z–Be (zigzag, Be terminated), and Z–N (zigzag, N terminated). We passivate the edge dangling bonds using H atoms. The cohesive and formation energies are shown in Table 3. From the analysis of cohesive energies, zigzag NRs are more stable than the armchair ones. Additionally, the N-terminated NRs possess greater stabilities in comparison with their Be-terminated counterparts. The band-gaps of zigzag NRs are found to be higher than those of their armchair counterparts. Furthermore, the N-terminated NRs possess lower gaps than the Be-terminated ones. Additionally, the band gaps reduce as the width of the NRs increases, approaching the gap of 2D $Be_3N_2$ as expected from quantum confinement. Consequently, the energy band gap of $Be_3N_2$ NRs can be finely tuned by having control over morphology (Table 3). All the NR geometric structures along with their band structures are depicted in Fig. 9.

**Table 2** The energetics (eV per atom and eV per formula unit) of β-$Be_3N_2$, monolayer $Be_3N_2$, and the two graphite-like layered $Be_3N_2$ structures are depicted

| System | Energy (eV per formula unit) | Energy (eV per atom) |
|---|---|---|
| β-$Be_3N_2$ | −34.05 | −6.810 |
| Monolayer $Be_3N_2$ | −30.78 | −6.157 |
| N2–N1 | −30.90 | −6.179 |
| N2–Be1 | −31.02 | −6.203 |



**Fig. 8** The optimized geometries of bulk graphite-like layered $Be_3N_2$: (a) N2−N1 configuration and (b) N2−Be1 configuration with the corresponding side views are shown. The calculations are carried out at the PBE-D2 level as implemented in the VASP code. The N2−Be1 structure is more favorable as predicted from the total energy analysis.

**Table 3** Cohesive and formation energies calculated at the $^a$PBE-sol and hybrid level. The band-gaps shown are computed at the hybrid level

| Systems | Cohesive/formation energy$^a$ (eV per atom) | Cohesive/formation energy$^b$ (eV per atom) | Band-gap (eV) |
|---|---|---|---|
| NA5Be | −3.696/−1.929 | −4.536/−0.598 | 3.115 |
| NA6Be | −3.752/−1.928 | −4.611/−0.585 | 3.024 |
| NA7Be | −3.794/−1.927 | −4.668/−0.577 | 2.988 |
| NA5N | −3.941/−1.930 | −4.712/−0.784 | 3.042 |
| NA6N | −3.966/−1.928 | −4.769/−0.741 | 2.970 |
| NA7N | −3.984/−1.927 | −4.810/−0.710 | 2.900 |
| NZ3Be | −3.750/−1.926 | −4.612/−0.586 | 3.104 |
| NZ4Be | −3.826/−1.924 | −4.713/−0.570 | 2.979 |
| NZ5Be | −3.875/−1.923 | −4.777/−0.560 | 2.907 |
| NZ3N | −3.967/−1.929 | −4.770/−0.742 | 3.024 |
| NZ4N | −3.998/−1.926 | −4.842/−0.687 | 2.908 |
| NZ5N | −4.017/−1.924 | −4.887/−0.653 | 2.853 |

$^a$ PBE-sol. $^b$ Hybrid.
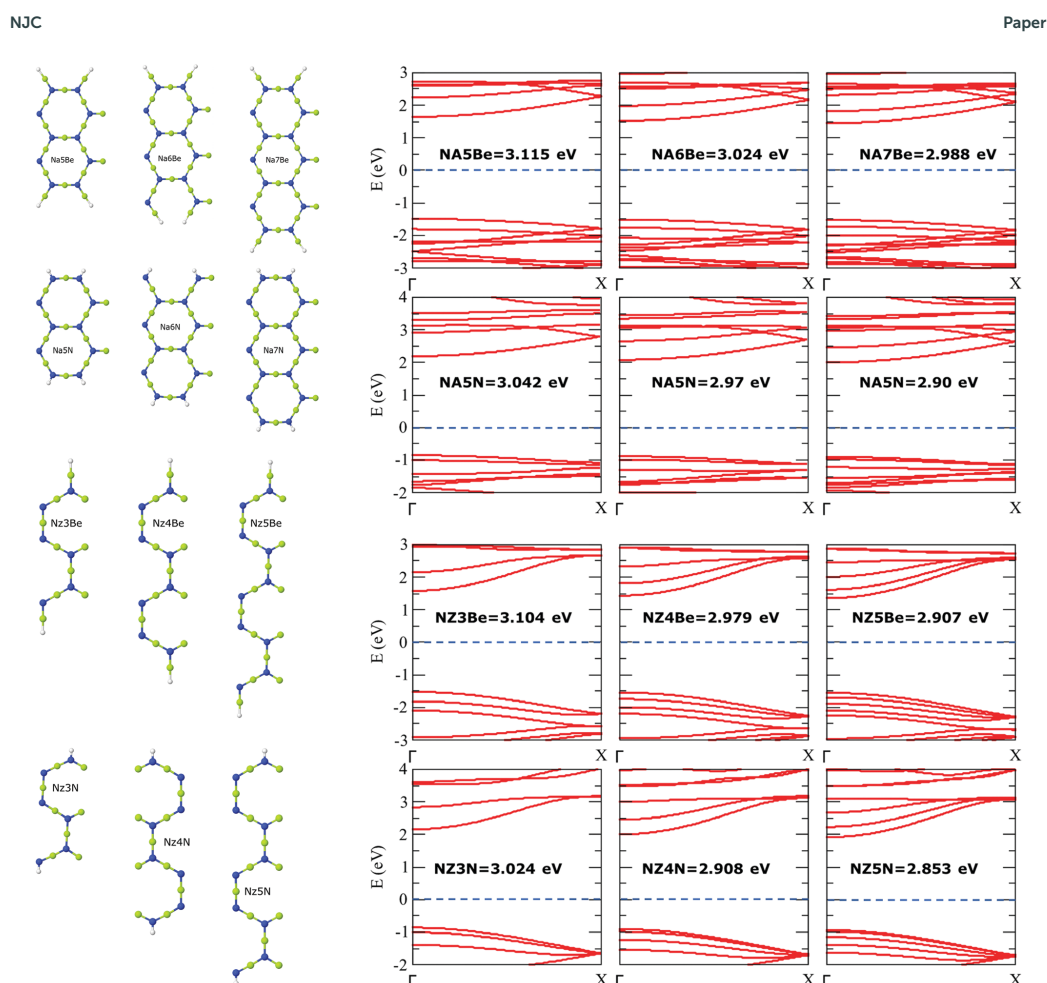
Fig. 9 Geometric and electronic structures of various $Be_3N_2$ NRs. Zero refers to the Fermi energy in each case.

## 4 Conclusion

Yet another 2D material $Be_3N_2$ is predicted through first-principles DFT calculations. It possesses the same hexagonal honeycomb lattice as that of graphene with the corner atoms consisting of N, while Be atoms act as bridges between two N atoms. $Be_3N_2$ is a 2D semiconductor with a wide band gap, which is important for applications in electronic devices. The small values of effective masses (of electrons and holes) is an attractive feature for electronic transport applications. The phonon spectrum revealed that $Be_3N_2$ is a true minimum of the potential energy surface. Furthermore, the structure is stable at temperatures as high as 900 K, as shown by AIMD simulations. Also, it can be used in catalytic processes as the reactivity is a bit greater than graphene. Most interestingly, the excellent storage capacity of $Be_3N_2$ makes it a fascinating material to be used as an anode in alkali-based batteries. In addition to that, it can be synthesized in the form of NRs and the electronic properties of these NRs can be finely tuned by control over the size and morphology. Finally, another bulk graphite-like layered phase of $Be_3N_2$ is also calculated which can take the form of N2–N1 or N2–Be1, the latter being more favorable. Based on these results, it will be fascinating to pursue $Be_3N_2$ synthesis and to see it in future nanoelectronics and alkali-based batteries.

## Conflicts of interest

There are no conflicts to declare.

## Acknowledgements

## References

1 P. R. Wallace, *Phys. Rev.*, 1947, **71**, 622–634.

2 A. K. Geim and K. S. Novoselov, *Nat. Mater.*, 2007, **6**, 183.

3 K. S. Novoselov, A. K. Geim, S. V. Morozov, D. Jiang, Y. Zhang, S. V. Dubonos, I. V. Grigorieva and A. A. Firsov, *Science*, 2004, **306**, 666–669.

4 K. S. Novoselov, A. K. Geim, S. V. Morozov, D. Jiang, M. I. Katsnelson, I. V. Grigorieva, S. Dubonos and A. A. Firsov, *Nature*, 2005, **438**, 197.

5 A. K. Geim, *Science*, 2009, **324**, 1530.

6 W. Xu and T.-W. Lee, *Mater. Horiz.*, 2016, **3**, 186–207.

7 O. V. Yazyev, *Acc. Chem. Res.*, 2013, **46**, 2319–2328.

8 Y.-W. Son, M. L. Cohen and S. G. Louie, *Phys. Rev. Lett.*, 2006, **97**, 216803.

9 Y.-W. Son, M. L. Cohen and S. G. Louie, *Nature*, 2006, **444**, 347.

10 R. Mas-Balleste, C. Gomez-Navarro, J. Gomez-Herrero and F. Zamora, *Nanoscale*, 2011, **3**, 20–30.

11 K. Novoselov, A. Mishchenko, A. Carvalho and A. C. Neto, *Science*, 2016, **353**, aac9439.

12 S. Ullah, P. A. Denis and F. Sato, *ACS Omega*, 2018, **3**, 16416–16423.

13 K. Watanabe, T. Taniguchi and H. Kanda, *Nat. Mater.*, 2004, **3**, 404.

14 D. Cakr, D. Kecik, H. Sahin, E. Durgun and F. M. Peeters, *Phys. Chem. Chem. Phys.*, 2015, **17**, 13013–13020.

15 H. Şahin, S. Cahangirov, M. Topsakal, E. Bekaroglu, E. Akturk, R. T. Senger and S. Ciraci, *Phys. Rev. B: Condens. Matter Mater. Phys.*, 2009, **80**, 155453.

16 S. Balendhran, S. Walia, H. Nili, S. Sriram and M. Bhaskaran, *Small*, 2015, **11**, 640–652.

17 S. Cahangirov, M. Topsakal, E. Aktürk, H. Şahin and S. Ciraci, *Phys. Rev. Lett.*, 2009, **102**, 236804.

18 L. Li, Y. Yu, G. J. Ye, Q. Ge, X. Ou, H. Wu, D. Feng, X. H. Chen and Y. Zhang, *Nat. Nanotechnol.*, 2014, **9**, 372.

19 X. Wang, A. M. Jones, K. L. Seyler, V. Tran, Y. Jia, H. Zhao, H. Wang, L. Yang, X. Xu and F. Xia, *Nat. Nanotechnol.*, 2015, **10**, 517.

20 Q. Tang, Z. Zhou and Z. F. Chen, *Wiley Interdisc. Rev.: Comput. Mol. Sci.*, 2015, **5**, 360–379.

21 Q. Tang and Z. Zhou, *Prog. Mater. Sci.*, 2013, **58**, 1244–1315.

22 K. F. Mak, C. Lee, J. Hone, J. Shan and T. F. Heinz, *Phys. Rev. Lett.*, 2010, **105**, 136805.

23 Y. Li, S. Tongay, Q. Yue, J. Kang, J. Wu and J. Li, *J. Appl. Phys.*, 2013, **114**, 174307.

24 J.-C. Lei, X. Zhang and Z. Zhou, *Front. Phys.*, 2015, **10**, 276–286.

25 C. Chen, B. Huang and J. Wu, *AIP Adv.*, 2018, **8**, 105105.

26 P. Ordejón, E. Artacho and J. M. Soler, *Phys. Rev. B: Condens. Matter Mater. Phys.*, 1996, **53**, R10441–R10444.

27 J. M. Soler, E. Artacho, J. D. Gale, A. Garcia, J. Junquera, P. Ordejon and D. Sanchez-Portal, *J. Phys.: Condens. Matter*, 2002, **14**, 2745.

28 P. Giannozzi, S. Baroni, N. Bonini, M. Calandra, R. Car, C. Cavazzoni, D. Ceresoli, G. L. Chiarotti, M. Cococcioni and I. Dabo, *J. Phys.: Condens. Matter*, 2009, **21**, 395502.

29 P. Giannozzi, O. Andreussi, T. Brumme, O. Bunau, M. B. Nardelli, M. Calandra, R. Car, C. Cavazzoni, D. Ceresoli and M. Cococcioni, *J. Phys.: Condens. Matter*, 2017, **29**, 465901.

30 G. Kresse and J. Hafner, *Phys. Rev. B: Condens. Matter Mater. Phys.*, 1994, **49**, 14251.

31 M. J. Frisch, G. W. Trucks, H. B. Schlegel, G. E. Scuseria, M. A. Robb, J. R. Cheeseman, G. Scalmani, V. Barone, B. Mennucci, G. A. Petersson, H. Nakatsuji, M. Caricato, X. Li, H. P. Hratchian, A. F. Izmaylov, J. Bloino, G. Zheng, J. L. Sonnenberg, M. Hada, M. Ehara, K. Toyota, R. Fukuda, J. Hasegawa, M. Ishida, T. Nakajima, Y. Honda, O. Kitao, H. Nakai, T. Vreven, J. A. Montgomery, Jr., J. E. Peralta, F. Ogliaro, M. Bearpark, J. J. Heyd, E. Brothers, K. N. Kudin, V. N. Staroverov, R. Kobayashi, J. Normand, K. Raghavachari, A. Rendell, J. C. Burant, S. S. Iyengar, J. Tomasi, M. Cossi, N. Rega, J. M. Millam, M. Klene, J. E. Knox, J. B. Cross, V. Bakken, C. Adamo, J. Jaramillo, R. Gomperts, R. E. Stratmann, O. Yazyev, A. J. Austin, R. Cammi, C. Pomelli, J. W. Ochterski, R. L. Martin, K. Morokuma, V. G. Zakrzewski, G. A. Voth, P. Salvador, J. J. Dannenberg, S. Dapprich, A. D. Daniels, O. Farkas, J. B. Foresman, J. V. Ortiz, J. Cioslowski and D. J. Fox, *Gaussian 09 (Revision A1)*, Gaussian, Inc., Wallingford, CT, 2009.

32 M. Dion, H. Rydberg, E. Schröder, D. C. Langreth and B. I. Lundqvist, *Phys. Rev. Lett.*, 2004, **92**, 246401.

33 J. P. Perdew, K. Burke and M. Ernzerhof, *Phys. Rev. Lett.*, 1996, **77**, 3865.

34 J. P. Perdew and A. Zunger, *Phys. Rev. B: Condens. Matter Mater. Phys.*, 1981, **23**, 5048–5079.

35 N. Troullier and J. L. Martins, *Phys. Rev. B: Condens. Matter Mater. Phys.*, 1991, **43**, 1993–2006.

36 P. E. Blöchl, *Phys. Rev. B: Condens. Matter Mater. Phys.*, 1994, **50**, 17953.

37 J. P. Perdew, A. Ruzsinszky, G. I. Csonka, O. A. Vydrov, G. E. Scuseria, L. A. Constantin, X. Zhou and K. Burke, *Phys. Rev. Lett.*, 2008, **100**, 136406.

38 J. Heyd and G. E. Scuseria, *J. Chem. Phys.*, 2004, **120**, 7274–7280.

39 R. W. G. Wyckoff, *Crystal structures*, R.E. Krieger Pub. Co., 1982.

40 A. Reyes-Serrato, G. Soto, A. Gamietea and M. Farias, *J. Phys. Chem. Solids*, 1998, **59**, 743–746.

41 A. Mokhtari and H. Akbarzadeh, *Phys. B*, 2003, **337**, 122–129.

42 A. Mokhtari and H. Akbarzadeh, *Phys. B*, 2002, **324**, 305–311.

**NJC**

43 M. G. M. Armenta, A. Reyes-Serrato and M. A. Borja, *Phys. Rev. B: Condens. Matter Mater. Phys.*, 2000, **62**, 4890.

44 K. Watanabe, T. Taniguchi and H. Kanda, *Nat. Mater.*, 2004, **3**, 404.

45 M. Niemeyer and P. P. Power, *Inorg. Chem.*, 1997, **36**, 4688–4696.

46 P.-F. Liu, L. Zhou, T. Frauenheim and L.-M. Wu, *Phys. Chem. Chem. Phys.*, 2016, **18**, 30379–30384.

47 N. Mounet, M. Gibertini, P. Schwaller, D. Campi, A. Merkys, A. Marrazzo, T. Sohier, I. E. Castelli, A. Cepellotti and G. Pizzi, *Nat. Nanotechnol.*, 2018, **13**, 246.

48 S. Ullah, A. Hussain, W. Syed, M. A. Saqlain, I. Ahmad, O. Leenaerts and A. Karim, *RSC Adv.*, 2015, **5**, 55762–55773.

49 A. Hussain, S. Ullah and M. A. Farhan, *RSC Adv.*, 2016, **6**, 55990–56003.

50 S. Ullah, A. Hussain and F. Sato, *RSC Adv.*, 2017, **7**, 16064–16068.

51 S. Ullah, P. A. Denis and F. Sato, *ChemPhysChem*, 2017, **18**, 1854.

52 S. Ullah, P. A. Denis and F. Sato, *Appl. Mater. Today*, 2017, **9**, 333–340.

53 S. Ullah, P. A. Denis and F. Sato, *New J. Chem.*, 2018, **42**, 10842–10851.

54 S. Ullah, P. A. Denis and F. Sato, *Curr. Graphene Sci.*, 2018, **2**, 1–11.

**Paper**

55 A. Savin, R. Nesper, S. Wengert and T. F. Fässler, *Angew. Chem., Int. Ed. Engl.*, 1997, **36**, 1808–1832.

56 S. Baroni, *Rev. Mod. Phys.*, 2001, **73**, 515.

57 C. Buttay, D. Planson, B. Allard, D. Bergogne, P. Bevilacqua, C. Joubert, M. Lazar, C. Martin, H. Morel, D. Tournier and C. Raynaud, *Mater. Sci. Eng., B*, 2011, **176**, 283–288.

58 R. C. Andrew, R. E. Mapasha, A. M. Ukpong and N. Chetty, *Phys. Rev. B: Condens. Matter Mater. Phys.*, 2012, **85**, 125428.

59 C. S. Wang and W. E. Pickett, *Phys. Rev. Lett.*, 1983, **51**, 597–600.

60 M. K. Y. Chan and G. Ceder, *Phys. Rev. Lett.*, 2010, **105**, 196403.

61 P. A. Denis, *ChemPhysChem*, 2014, **15**, 3994–4000.

62 P. A. Denis and F. Iribarne, *J. Phys. Chem. C*, 2013, **117**, 19048–19055.

63 S. Ullah, P. A. Denis and F. Sato, *Appl. Surf. Sci.*, 2019, **471**, 134–141.

64 J. M. Tarascon and M. Armand, *Nature*, 2001, **414**, 359–367.

65 M. Armand and J. M. Tarascon, *Nature*, 2008, **451**, 652–657.

66 J. R. Dahn, T. Zheng, Y. Liu and J. S. Xue, *Science*, 1995, **270**, 590.

67 S. Ullah, P. A. Denis and F. Sato, *Chem. Phys. Lett.*, 2018, **706**, 343–347.

## 8 Van der Waals heterostructures

There is a class of bulk materials made of sheets or layers held together by vdW forces. It is also interesting to see how the properties will be responding if a material is designed in such a way that every sheet is different than each other. Consequently, a new field of research, vdW heterostructures came into being. This allows the tailoring of a material by combining various layers of choice to get the desired properties. The field of 2D materials is pretty diverse and different monolayers come with very different electronic properties ranging from wide gap insulators to superconductors [3, 141, 147–153]. In this context, we investigate pristine and hybrid bilayers $h$BP and $h$BAs with the help of first-principles DFT calculations. Having said that, we have three different systems (bilayer $h$BP, bilayer $h$BAs, and bilayer $h$BP-$h$BAs) with various stacking. All the various patterns were carefully analyzed and their stability, structural and electronic properties were reported. The gap of individual $h$BP and $h$BAs is 1.09 and 0.88 eV, respectively, the gap of bilayer $h$BP and $h$BAs can be engineered down to 0.63 and 0.5 eV, in the aforementioned order. Additionally, the hybrid bilayer gap can be reduced to 0.53 eV. The stability of these bilayers is predicted from the calculation of interlayer interaction energy (IIE), which shows that these bilayers are as robust as bilayer graphene. The most stable patterns were further investigated by subjecting them to an external electric field. It is found that the optoelectronic properties show great tunability as a function of an external electric field. A sharp peak in the visible range is reported and, furthermore, a slight blue-shift is observed when an electric field is included in the calculations. Additionally, another peak starts to appear above the critical field. Most importantly, these are a consequence of the interlayer transitions, a factor critical in photovoltaics. The results were published in (APSUS 493, 308-319, 2019) [210].

By means of DFT calculations, we study Janus-like BAs bilayer to predict the stability, geometric and electronic properties. Having said that, we combine one hydrogenated and one fluorinated layer (of BAs) to make a bilayer (or a vdW heterostructure) [244]. The IIE calculations show that all the different patterns are quite close in energy. Of the interest are the electronic properties, which show a great variation as a function of the stacking pattern. That being said, the overlapping of bands around the Fermi level is observed in some cases thus giving rise to a negative bandgap. Consequently, semimetallic properties are achieved. The highest gap observed in this study at vdW-DF level is 0.33 eV. Additionally, it should be noted that the individual gap in hydrogenated and fluorinated BAs monolayer is 3.50 and 1.25 eV, respectively. Also, the gap in the hydrogenated layer was found to be indirect. This means that combining these differently functionalized layers in the bilayer form can efficiently engineer the electronic properties. In addition, charge

transfer was also discussed in detail. Since Mulliken charge analysis is strongly dependent on the basis set, we also report the Bader charge transfer mechanism. This paper was published in (CMS 170, 109186, 2019) [249] and can be found in Appendix E.1.

As discussed, there are many techniques to open a sizeable bandgap in graphene which is necessary for its utilization in FETs. However, in most of the cases, this bandgap opening does not come alone and brings some demerits with itself. The most prominent of which is the degradation of charge carrier mobility caused by the modification in Dirac cone. Fortunately, the use of $h$BN as a substrate for graphene or using $h$BN graphene vdW heterostructure can be the best solution since the charge carrier mobility is preserved up to a larger extent. However, the bandgap opening is insignificant for practical use in FETs. In addition, the gap has a weaker (or zero) tunability even with the external electric field. Another important aspect worth mentioning is that the gap disappears when graphene and $h$BN are not in a perfect Bernal stacking. In reality, it is quite difficult to achieve that perfect situation. To address this issue, we propose $SiC_3/h$BN vdW heterostructure as a potential replacement for graphene to be utilized in nanoelectronics. We select various $SiC_3$-$h$BN vdW- heterostructures, including a, hybrid $SiC_3/h$BN bilayer, a $h$BN/$SiC_3/h$BN trilayer (encapsulated monolayer $SiC_3$), and a $h$BN/$SiC_3/SiC_3/h$BN 4-layer (encapsulated bilayer $SiC_3$). Interestingly, the gap in $SiC_3/h$BN and $h$BN/$SiC_3/h$BN is of sufficient opening to be used in FETs. Additionally, the effect of the external electric field is quite strong on the evolution of gaps. A magnetic configuration is also observed in $h$BN/$SiC_3/SiC_3/h$BN and, furthermore, it is found that the gap tunability is dependent on the stacking pattern of the encapsulated bilayer. In optical properties, we see strong peaks in the visible, as well as in the deep UV region. Moreover, small peaks in the infrared region were also observed for some structures. The results are given in Appendix E.2.

Contents lists available at ScienceDirect

# Applied Surface Science
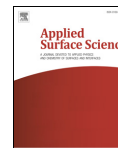
Full length article

# Tunable optoelectronic properties in h-BP/h-BAs bilayers: The effect of an external electrical field

Saif Ullah[a,*], Pablo A. Denis[b], Marcos G. Menezes[c], Fernando Sato[a]

[a] *Departamento de Física, Instituto de Ciências Exatas, Campus Universitário, Universidade Federal de Juiz de Fora, Juiz de Fora, MG 36036-900, Brazil*
[b] *Computational Nanotechnology, DETEMA, Facultad de Química, UDELAR, CC 1157, 11800 Montevideo, Uruguay*
[c] *Instituto de Física, Universidade Federal do Rio de Janeiro, Caixa Postal 68528, 21941-972 Rio de Janeiro, RJ, Brazil*

## ARTICLE INFO

## ABSTRACT

Herein, we perform DFT calculations to study the stability and the electronic and optical properties of pristine and hybrid bilayers of hexagonal boron phosphide (h-BP) and hexagonal boron arsenide (h-BAs). The electronic and optical properties of all bilayers can be modulated by the introduction of an external perpendicular electric field. Consequently, band gaps can be tuned from 0.8 eV down to zero as the field increases up to a critical value. Above this value, the gap reopens as the valence and conduction bands exhibit an anticrossing with a "Mexican-hat" shape, in a similar fashion to biased graphene bilayers. For the optical properties, we report an intense peak in the absorption spectra around 2.5–2.6 eV, with a slight blueshift as a function of electric field. Above the critical field, a new peak is observed in the infrared region which exhibits a strong field dependence. Additionally, this peak is related to the optical transitions around the "Mexican-hat" region of the band structure and the corresponding electron-hole pair shows a layer separation, which may lead to larger recombination times, a critical factor in photovoltaics. We believe that, with such tunable properties, these bilayers can find interesting applications in future devices in nanoelectronics and optoelectronics.

## 1. Introduction

Graphene is surely the first but not the only star shining on the horizon of flatland [1]. Due to its incredible properties, this material became the utmost motivation for the synthesis and prediction of other 2D materials [2–11]. The rapid growth in the electronic industry demands for the synthesis of new low dimensional materials whose electronic properties are quite flexible. The electronic structure of graphene is responsible for its unique properties but, due to the absence of a band gap, it is also a big hurdle to overcome for its use in nanoelectronics. During the past ten years, the III–V binary compounds, especially hexagonal boron nitride (h-BN), have proved their significance by virtue of their potential applications in nanoelectronics, spintronics, and optoelectronics [2,12–16]. However, the wide band gap value of h-BN (6.0–7.0 eV, as reported by GW calculations [17–19]) makes it a less compelling material for further applications in electronic devices, where a moderate and somewhat tunable band gap is required.

Among many of the III–V binary compounds, boron phosphide (BP) and boron arsenide (BAs) have also attracted considerable consideration. Furthermore, the geometric structure of bulk BP can take the form of zincblende, rocksalt, and β-Sn structures [20,21]. Besides bulk BP,

nanostructured BP has also shown its significance in terms of applications. For example, Schroten et al. reported the synthesis of nanostructured BP and its applications in photovoltaic cells [22]. The applications of BP nanotubes, their functionalization, and stability have also been documented [23]. In addition, it has been reported that BP nanoribbons have potential applications in nanoelectronics and spintronic devices [24]. The case of BAs is equally important, as there are current interests in this material due to its ultra-high thermal conductivity, which has been confirmed both theoretically and experimentally [25–28]. That being said, among the bulk materials, the thermal conductivity of BAs is second to diamond only.

Apart from that, for BP and BAs, the 2D hexagonal structures and their stabilities were also predicted with the help of DFT calculations [3,12]. Despite the fact that these structures are not synthesized yet, the enormous attention given to them by the scientific community shows their importance [3,12,29,30]. Onat et al. studied various dopants in h-BP for applications in nanoelectronics [31]. Peeters and coworkers predicted and studied the properties of a p-n junction in h-BP [32]. The fascinating characteristics of h-BP/h-BAs are the smaller band gaps of 1.1–1.36/0.89–1.14 eV in comparison with h-BN, and the remarkable charge carrier mobility [3,33]. The potential use of h-BP in alkali-based
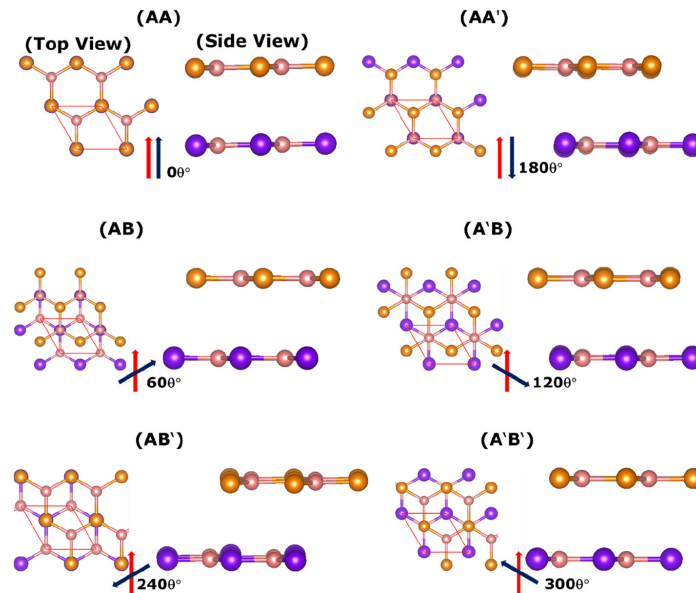
---

*S. Ullah, et al.*

**Fig. 1.** Top and side views of the relaxed geometries for all studied configurations for the hybrid bilayer.

**Table 1**

In-plane lattice constants, interlayer distances, total energies (with respect to the lowest energy configuration), and electronic band gaps for BP, BAs, and hybrid BP::BAs bilayers. For the description of each stacking, refer to Fig. 1 or see the text.

| Structure | Lattice constant a (Å) | Interlayer separation d (Å) | Relative energy (meV/atom) | Bandgap (eV) |
|---|---|---|---|---|
| h-BP | 3.28 | – | – | 1.09 |
| AA | 3.282 | 4.25 | 20.42 | 0.629 |
| AA′ | 3.284 | 4.2 | 12.73 | 1.08 |
| AB | 3.282 | 4.01 | 4.64 | 1.00 |
| A′B | 3.283 | 4.01 | 0 | 0.80 |
| AB′ | 3.283 | 4.26 | 17.38 | 0.85 |
| h-BAs | 3.45 | | | 0.88 |
| AA | 3.453 | 4.51 | 13.17 | 0.5 |
| AA′ | 3.449 | 4.49 | 7.86 | 0.88 |
| AB | 3.45 | 4.38 | 0.62 | 0.84 |
| A′B | 3.45 | 4.38 | 0 | 0.69 |
| AB′ | 3.449 | 4.49 | 5.35 | 0.65 |
| h-BP::h-Bas | | | | |
| AA | 3.369 | 4.46 | 18.72 | 0.53 |
| AA′ | 3.368 | 4.36 | 12.15 | 0.84 |
| AB | 3.367 | 4.24 | 2.56 | 0.96 |
| A′B | 3.367 | 4.13 | 0 | 0.60 |
| AB′ | 3.37 | 4.33 | 12.92 | 0.57 |
| A′B′ | 3.365 | 4.13 | 3.57 | 0.74 |

battery technology was also reported, showing that h-BP can be an efficient anode material [30,34]. Furthermore, the graphane- and fluorographene-like functionalized derivatives of h-BP and h-BAs were also predicted to be stable by means of phonon dispersion calculations [3]. Their potential use in ultrafast nanoelectronic devices is also discussed. Moreover, the electronic and thermoelectric properties of BP bilayers were also recently reported [35,36]. In addition, the electronic properties of a BP/blue phosphorene vdW-heterostructure were investigated in detail [37,38]. Finally, the optoelectronic properties of BP and gallium nitride bilayers were predicted by means of DFT

calculations by Mogulkoc et al. [39].

In this paper, we address the stability, electronic and optical properties of pristine and hybrid h-BP and h-BAs bilayers by means of first-principles calculations within the framework of Density Functional Theory (DFT). We begin by obtaining the most stable stackings for each bilayer and discussing the electronic structure for all stackings. Next, we study the effect of an external perpendicular electric field on the electronic structure and optical properties of the bilayers with lowest total energy. We find that properties such as band gaps, charge transfer, and optical excitations can be tuned by the field and that new features are introduced above a critical field value, such as new absorption peak and interlayer electron-hole pairs. Such controllable properties can lead to exciting potential applications in nanoelectronics and optoelectronics.

**2. Computational details**

All first-principles calculations within density functional theory (DFT) were performed, unless otherwise stated, using the non-local vdW-DF formalism with the aid of SIESTA code, which uses norm-conserving (NC) Troullier-Martins (TM) pseudopotentials (PPs) in utterly separable form [40–43]. The value of the mesh cutoff for real space projection is 200 Ry. The first Brillouin zone is sampled with a $30 \times 30 \times 1$ Monkhorst-Pack grid of k-points. The threshold for the total energy and forces during structural optimization is set to $10^{-6}$ eV and 0.01 eV/Å, respectively. Dipole corrections are included in all cases. Optical absorption spectra are calculated as a part of the DFT calculations and do not include electron-hole interactions (excitonic effects). For optical properties and density of states (DOS) calculations, a sufficiently dense k-point grid of $121 \times 121 \times 1$ is used.

For the most favorable structural configurations, we also use the VASP and Gaussian codes to assess the interaction energy (IE) and charge transfer [44–48]. The details can be found in the electronic supplementary material (ESI).

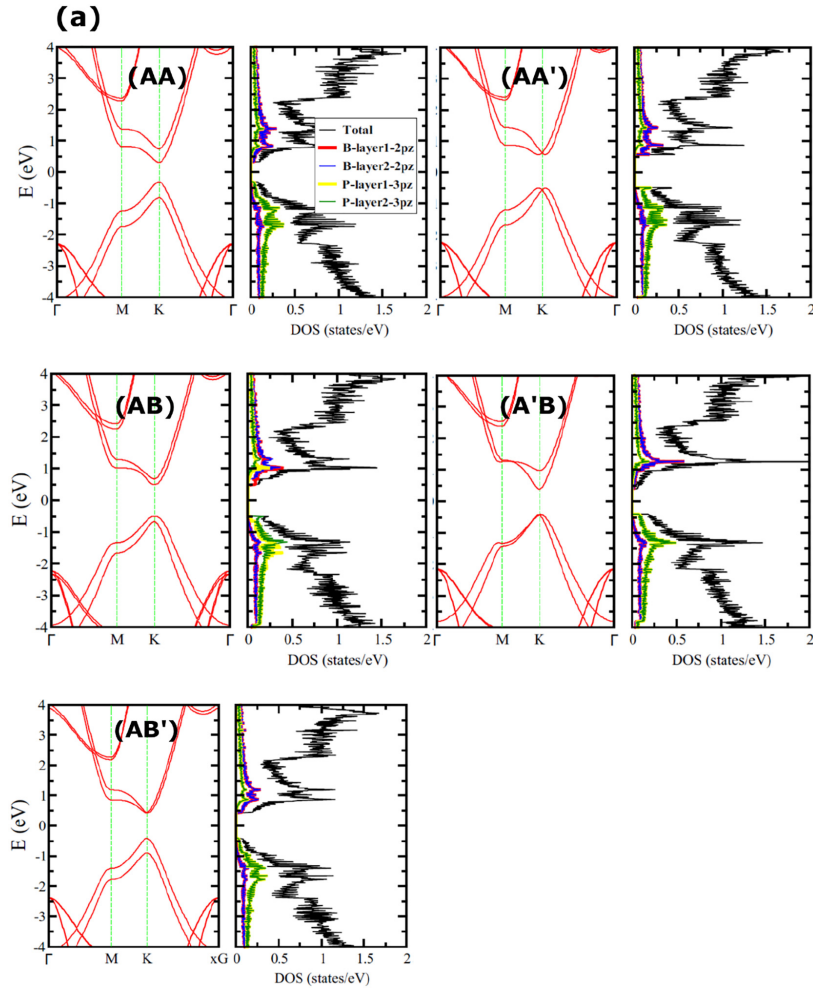The stability of these configurations is predicted by calculating the

**(a)**



**Fig. 2.** Band structures and projected density of states (PDOS) for all stackings considered in this work for (a) BP, (b) BAs, and (c) hybrid BP::BAs bilayers. In the PDOS, black lines correspond to the total DOS, red lines to the PDOS summed over the B-pz orbitals from the first layer, blue lines to B-pz orbitals from the second layer, yellow lines to X-pz orbitals from the first layer and green lines to X-pz orbitals from the second layer (X = P or As). In the hybrid system, the first layer corresponds to h-BAs. (For interpretation of the references to color in this figure legend, the reader is referred to the web version of this article.)

IE and comparing with that of bilayer graphene. The IE is calculated as [3]:

$$IE = \frac{E\_bilayer - E\_layer1 - E\_layer2}{N_{tot}}, \qquad (1)$$

where $E_{bilayer}$, $E_{layer1}$, and $E_{layer2}$ are the total energies of a bilayer and its first and second isolated monolayers, respectively. Finally, $N_{tot}$ is the total number of atoms in the simulation cell of the bilayer (4).

### 3. Results and discussion

Initially, we have performed the structural optimization on monolayer h-BP and h-BAs. The calculated lattice constants at equilibrium are 3.28 Å and 3.45 Å for h-BP and h-BAs, respectively, in perfect agreement with the previous calculations [3,30]. The electronic band gaps are also calculated and we obtain 1.09 eV for h-BP and 0.88 eV for h-BAs (both direct), again in excellent agreement with the available results in the literature (within the framework of DFT). More details regarding the monolayer calculations can be found in Fig. S1 of the ESI.

Following the same methodology, we study the pure and hybrid bilayers of these systems. We investigate both AA and AB (Bernal) stackings. All the possibilities are labeled as follows. For AA stacking, we have two possibilities. In the AA configuration, the B atoms in one layer sit right on top of B atoms in the other layer and the X atoms do the same (X = P or As). On the other hand, in the AA′ configuration, the B atoms in one layer sit on top of X atoms in the other layer. For AB stacking, we have three possibilities for the pure bilayers. In the AB configuration, the B atoms in one layer sit on top of X atoms in the other
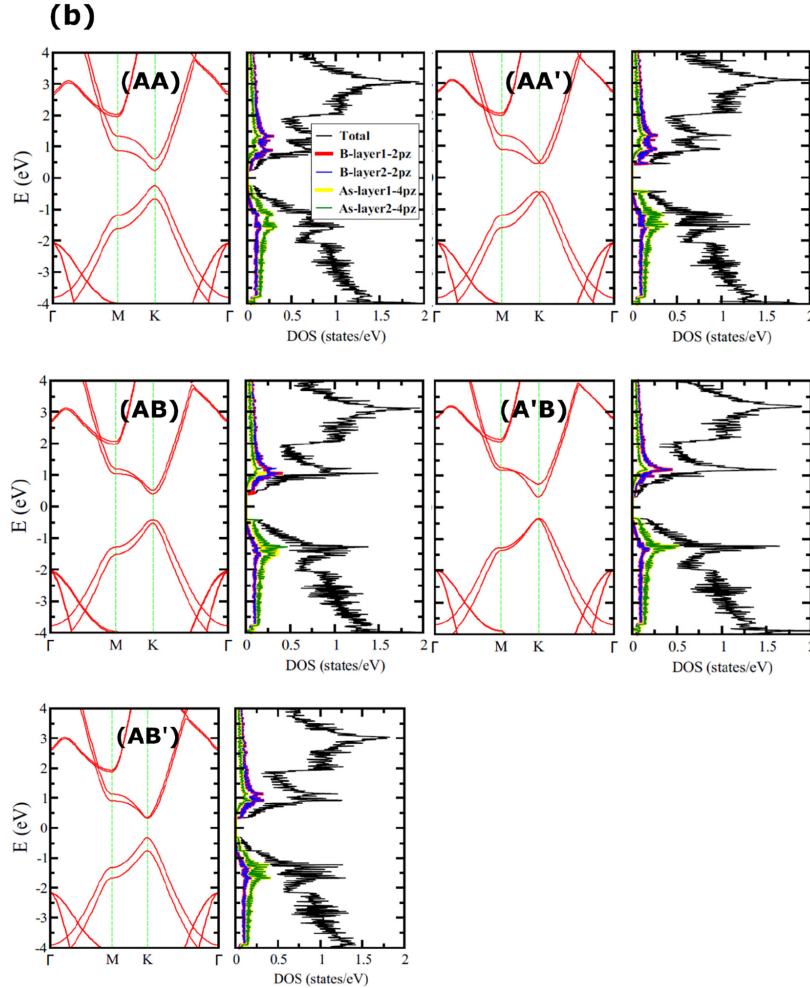
310

S. Ullah, et al.

**(b)**



**Fig. 2.** (*continued*)

layer, while the other two atoms lie on top of hollow sites. In the A′B configuration, the B atoms sit on top of each other and, in the AB′ configuration, the X atoms sit on top of each other. For the hybrid bilayer, there is an additional configuration labeled as A′B′ (B on top of P). Fig. 1 shows the optimized structures for each stacking in the case of the hybrid bilayers. The pure bilayers have similar structures and are shown in Fig. S2 in the ESI. Structural and energetic properties for all configurations are reported in Table 1. As we can see, the most favorable stacking is A′B for all bilayers, where the B atoms sit on top of each other. The total energies of all the other configurations are reported as differences with respect to this configuration.

In all cases, the in-plane lattice constant (a) of the pristine bilayers is comparable to that of their monolayer counterparts, whereas the lattice constant of the hybrid bilayers is nearly the average of those from monolayer h-BP and h-BAs. The h-BP layer expands and the h-BAs layer shrinks, with lattice constant variations between 2 and 3%. This outcome is in line with previous investigations on BP-GaN and BP-blue

phosphorene bilayers [38,39]. As mentioned above, we can see from the total energies in Table 1 that, in all bilayers, the A′B stacking is the most favorable configuration, closely followed by the AB (and A′B′) stacking. This result may be related to the lower interlayer distances found in these cases. In addition, the lowest value found for the interlayer distance is larger than the sum of the covalent radii of As and P (2.26 Å), which confirms that these layers are bonded through vdW interactions [49].

The stability of the most favorable (A′B) motifs is predicted with the calculation of the interaction energies (IE), as defined above (Eq. (1)). In SIESTA, the IEs of the pristine BP and BAs bilayers in this configuration are $-47.69$ meV/atom and $-40.1$ meV/atom, respectively, while the IE of the hybrid BP::BAs bilayer is $-13.0$ meV/atom. For comparison, the IE of graphene bilayer is $-41.0$ meV/atom with the same level of theory. Since the SIESTA results can be vulnerable to basis set superposition (BSSE) error, we employ the counterpoise corrections proposed by Boys and Bernadi [50]. Consequently, the IEs of bilayer
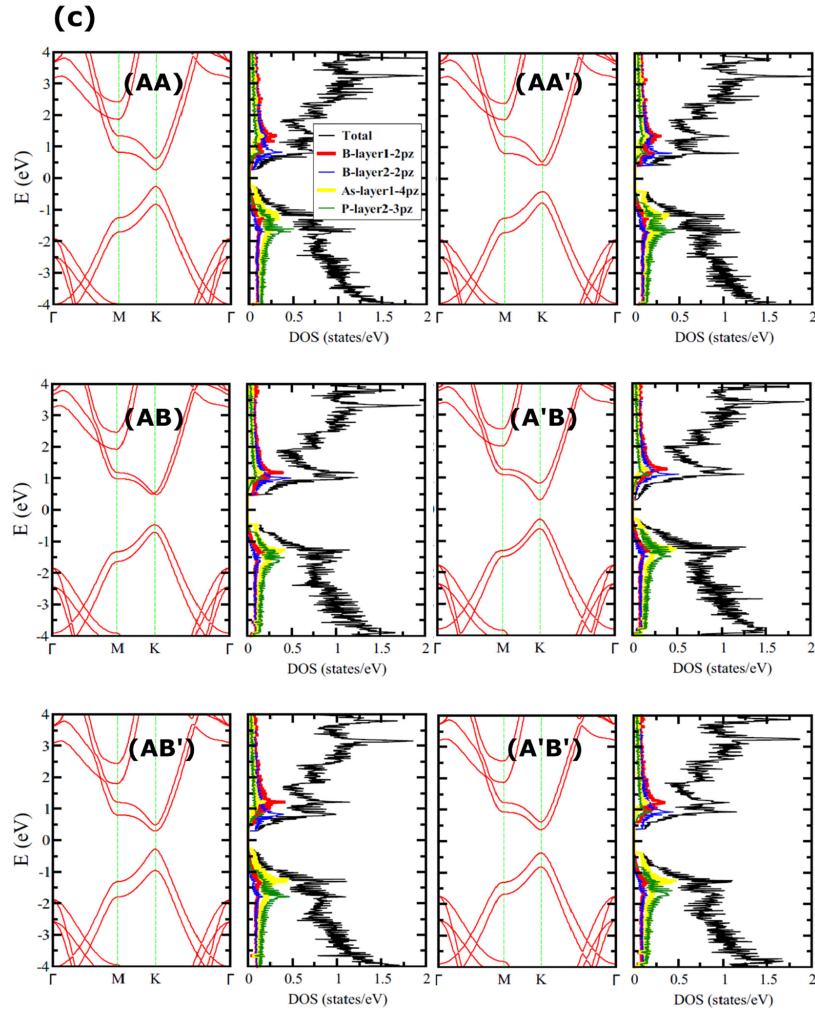
*S. Ullah, et al.*

**(c)**



**Fig. 2.** (*continued*)

**Table 2**

The interlayer charge transfer in various configurations of pristine BP, BAs, and hybrid BP::BAs bilayers. A positive (negative) value indicates electron depletion (accumulation) on the corresponding layer. For the description of each stacking, refer to Fig. 1 or see the text.

| System | Hirshfeld | System | Hirshfeld | System | Hirshfeld |
|--------|-----------|--------|-----------|--------|-----------|
| BP::BP | BP (Layer1) | BAs::BAs | BAs (Layer1) | BAs::BP | BAs (Layer1) |
| AA | 0 | AA | 0 | AA | −0.001 |
| AA′ | 0 | AA′ | 0 | AA′ | 0 |
| AB | 0.003 | AB | 0.003 | AB | 0.004 |
| A′B | 0 | A′B | 0 | A′B | 0 |
| AB′ | 0 | AB′ | 0 | AB′ | −0.001 |
| | | | | A′B′ | −0.004 |

graphene, BP, and BAs become −22.5, −20.0, and −17.7 meV/atom, respectively. For the hybrid bilayer, the IE is −3.0 meV/atom. The IEs calculated with VASP and Gaussian are given in the ESI which follow the similar trend.

Next, we calculate and report the electronic properties for all stackings. The band structures and projected density of states (PDOS) for each case are shown in Fig. 2. In most of the cases, we see a direct band gap at the K point. The notable exceptions are the AA′ configurations, in which the valence band maximum (VBM) and conduction band minimum (CBM) are slightly shifted from the K point. The AB configuration also shows a similar feature in the hybrid bilayer, but only in the conduction band. All the band gaps are reported in Table 1 where it can be seen that they are fairly stacking-dependent, with values ranging from 0.50 to 1.08 eV. Moreover, most of the band gaps of the hybrid bilayers are smaller than those of the pristine bilayers with the same configuration. The only exceptions are the AA and AB
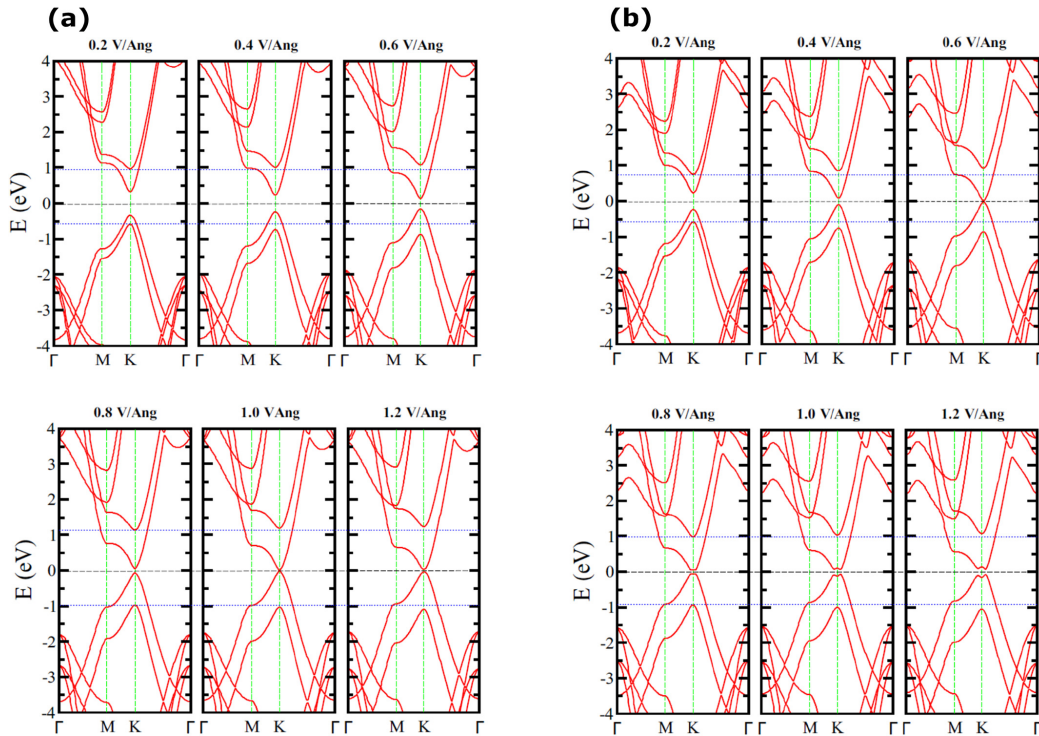
**Fig. 3.** Band structures as a function of an external electric field for the most stable (A′B) (a) BP, (b) BAs, and (c)–(d) hybrid BP::BAs bilayers. In (c), the field points from the BAs layer to the BP layer, while in (d) the direction of the field is reversed. The intensity of the field (in V/Å) is shown at the top of each plot.

configurations, which have intermediate gaps.

Another interesting feature in the band structures is that degeneracies are present in the valence or conduction bands of the pristine bilayers at the K point, depending on the stacking configuration. For AA stacking, those are seen in the AA′ configuration, where B atoms sit on top of X atoms. For Bernal stacking, the degeneracies are seen in the A′B and AB′ configurations, where the atoms that sit on top of hollow sites are identical. For A′B, the X atoms occupy the hollow sites, resulting in a degenerate valence band at the K point. On the other hand, in the AB′ configuration, the B atoms reside on the top of the hollow sites, resulting in a degenerate conduction band. As shown in the ESI, these features can easily be explained by a simple tight-binding (TB) model, in which only nearest-neighbor intra-layer and inter-layer hoppings between pz orbitals are included. In particular, for Bernal stacking, two of the band energies at the K point are simply the on-site energies of the atoms sitting on top of the hollow sites. As a result, when identical atoms occupy these sites, the energies are identical. Evidently, this result also follows from the inversion symmetry present in these configurations, which render these sites equivalent. Likewise, the degeneracies seen in the AA′ configuration are a result of the pairs of atoms that sit on top of each other being identical (B and X). Again, this also follows from the inversion symmetry present in this configuration. Note that this symmetry is actually absent in the AA configuration, where the two pairs are different (B-B and X-X) and only mirror symmetry is present. Naturally, for the hybrid bilayers, the inversion symmetry is broken in the AA′, A′B and AB′ configurations and the degeneracies are lifted, which could also explain the reduced band gaps in these cases.

As we can see in Fig. 2, the PDOS plots also show some interesting features. In all cases, the states in the vicinity of the VBM are formed mostly by pz orbitals from the X atoms (P or As), while the states in the vicinity of the CBM are formed mostly by pz orbitals from the B atoms. This is consistent with the electronic properties of monolayer III–V compounds with a honeycomb structure, where a sublattice-sensitive band structure is observed near the K point [51]. Moreover, in the hybrid bilayers, we can also see a clear layer sensitivity in the orbital composition of the low energy states in many cases. As we can see in (c), in all stackings, the VBM is composed only by As-pz states from the first layer, whereas the top of the next occupied band is composed of only P-pz states from the second layer. This effect occurs even in the most stable configuration (A′B), where the VBM is degenerate for the pristine bilayers. As discussed above, this degeneracy is lifted by the breaking of inversion symmetry and the resulting states show layer sensitivity. In addition, in the AA, AB′ and A′B′ configurations, the conduction bands also show a similar sensitivity. Their CBMs are composed only by B-pz states from the second layer, which means that these configurations are type-II heterostructures, with a VBM and a CBM associated with different layers. Similar behavior is also seen for the AB configurations in the pristine bilayers.

Finally, the low energy peaks observed in the PDOS are due to van-Hove singularities associated with the "shoulder" structures of the bands near the M point. In all cases, these peaks also show sublattice sensitivities, with the occupied (unoccupied) levels consisting mostly of X (B) atoms. A strong layer sensitivity is also observed for the hybrid bilayers. As we discuss below, such features are fundamental to the
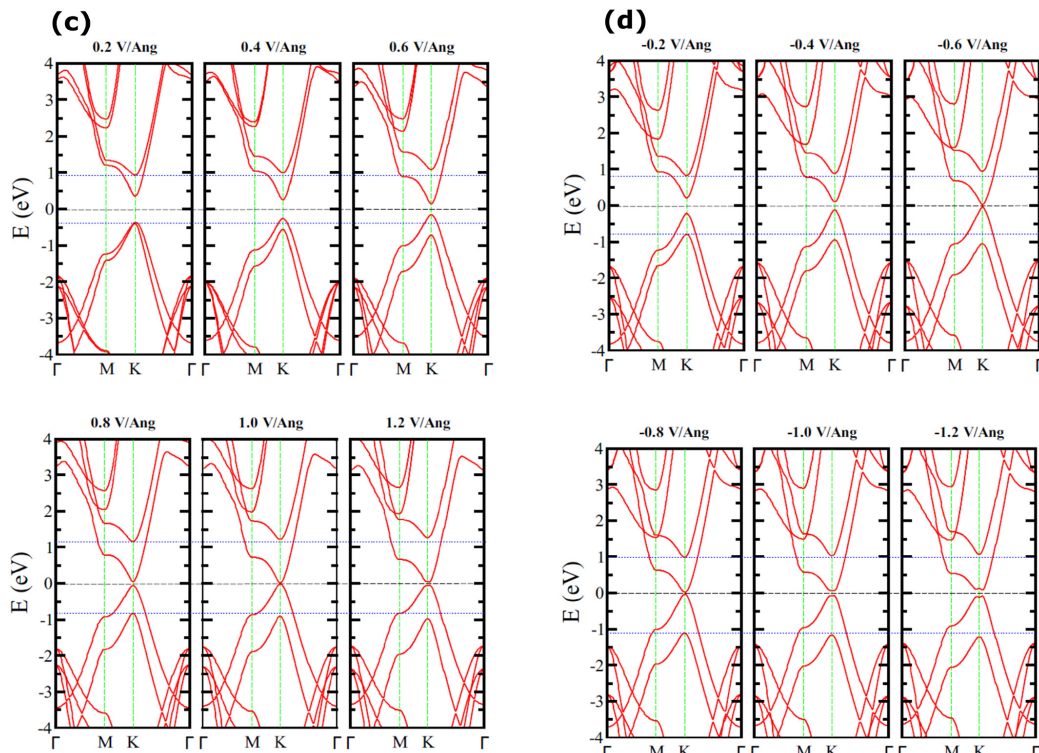
S. Ullah, et al.

**(c)**

0.2 V/Ang    0.4 V/Ang    0.6 V/Ang

0.8 V/Ang    1.0 V/Ang    1.2 V/Ang

**(d)**

-0.2 V/Ang    -0.4 V/Ang    -0.6 V/Ang

-0.8 V/Ang    -1.0 V/Ang    -1.2 V/Ang
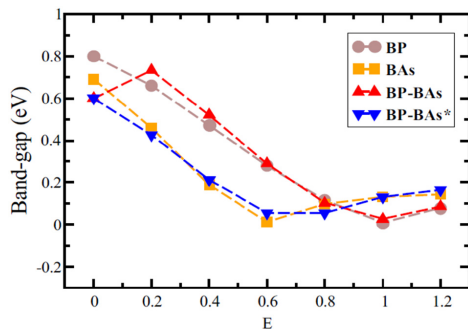
**Fig. 3.** (*continued*)



**Fig. 4.** Electronic band gaps as a function of an external electric field for the most stable (A′B) bilayers. Gray and orange lines correspond to pristine h-BP and h-BAs bilayers, respectively. For the hybrid bilayer, the red line indicates a situation in which the field points from the BAs layer to the BP layer, while the blue line indicates a situation in which the direction of the field is reversed. (For interpretation of the references to color in this figure legend, the reader is referred to the web version of this article.)

understanding of the optical properties of these systems.

We have also calculated the charge transfer between the layers. To that end, we rely on the Hirshfeld and Voronoi charge population analyses. The Mulliken analysis is exempted from our discussion, as its

values can be erroneous even with the DZP basis set [52–54]. The values for the Hirshfeld analysis are shown in Table 2 for all configurations. Voronoi values are consistent with these, so they are not reported here. As we can see, the only configuration in which charge transfer occurs in the pristine bilayers is AB, whereas the most favorable configuration, A′B, bears no charge transfer among the layers. This is consistent with the fact that the AB configuration is the only one that does not have either inversion or mirror symmetry since B and X atoms sit on top of each other. For the hybrid bilayers, these symmetries are absent in all cases and a smaller charge transfer is also observed in the AA and AB′ configurations (recall that the AB and A′B′ configurations are similar, with B and As or B and P sitting on top of each other, respectively). Still, for the lowest energy configuration, A′B, no charge transfer is observed, which may be related to the fact that identical B atoms sit on top of each other in this configuration. Finally, note that the sign of the charge transfer in the hybrid system depends on the configuration. For AB, the electrons accumulate on the BP layers, while in the AA, AB′ and A′B′ configurations, the electrons migrate towards the BAs layer.

For comparison, we also report Bader charge analysis (from the VASP results) which shows that a small interlayer charge transfer also occurs in A′B configuration. In this case, the quantity of charge transfer in the pristine BP and BAs bilayers is 0.0026 e and 0.0016e, respectively. For the hybrid bilayer, the charge transfer is more prominent, with the BAs layer transferring a charge of 0.027e to the BP layer.

Now we focus on the lowest energy configurations and study the electronic properties of the bilayers under an external electric field. The field is applied perpendicular to the layers and dipole corrections are
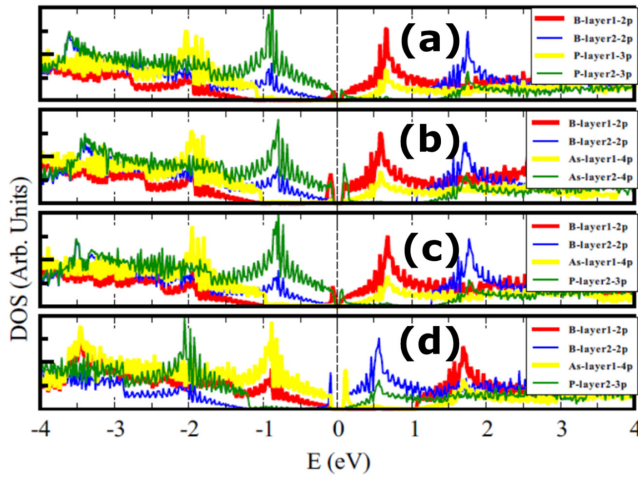
**Fig. 5.** PDOS as a function of energy for the highest electric field intensity studied (1.2 V/Å) for (a) BP, (b) BAs, and (c) BP::BAs bilayers. (d) represents the BP::BAs hybrid bilayer when the direction of the field is reversed.
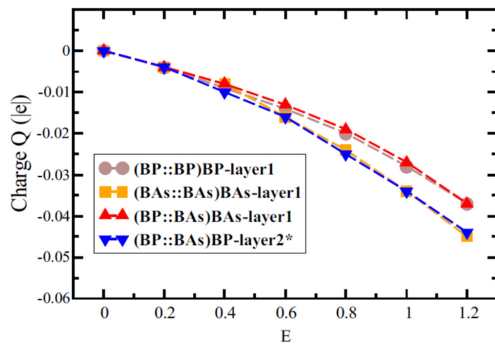


**Fig. 6.** Interlayer charge transfer as a function of the electric field for the most stable bilayers. In the gray (h-BP), orange (h-BAs) and red lines (hybrid), the field is applied from layer 1 to layer 2, while in the blue line (hybrid) the field direction is reversed. In the hybrid bilayer, layer 1 corresponds to h-BAs. (For interpretation of the references to color in this figure legend, the reader is referred to the web version of this article.)
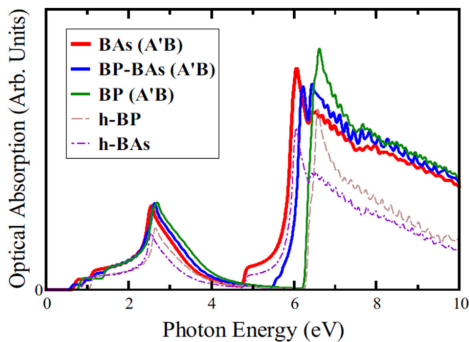


**Fig. 7.** Optical absorption of mono and bilayers calculated at zero electric field value.

included, as implemented in SIESTA. We assume that the field does not induce any significant structural modifications, so we do not perform any new relaxations. We tune the value of the external field from 0.2 to 1.2 V/Å in small intervals of 0.2 V/Å. We have also reversed the direction of the field in the hybrid bilayer in order to see its effect on the charge transfer and electronic properties. In Fig. 3, we report the band structures as a function of the field for each bilayer. As we can see, the electronic properties of these structures can be tuned by the field, as also observed in other layered vdW materials [55–59].

Note that, as shown in Fig. 4, the band gap reduces from 0.6–0.8 eV down to zero and reopens again above a critical value, which is different for each bilayer. For the pristine h-BP bilayer, the critical field is around 1.0 V/Å, while for h-BAs, the gap closes at 0.6 V/Å. For the hybrid bilayer, we see that the critical value also depends on the direction of the field, with a value around 1.0 V/Å when the field points from the BAs layer to the BP layer, and a value between 0.6 and 0.8 V/Å when this direction is reversed. Note also that the behavior of the gap closely follows that of the pure BP bilayer in the former case and that of the pure BAs bilayer in the latter. Above the critical field, the valence and conduction bands continue to move against each other, but the gap is reopened due to an avoided crossing. This results in a "Mexican-hat" shaped band structure around the K-point, similar to the one observed in biased or doped graphene bilayers [60–64]. As we discuss below, this modification induced in the electronic structure also affects the optical properties of the bilayers.

Furthermore, note that the separation between the next lowest energy bands increases as the field increases. Therefore, both the conduction band and the second valence band move downwards in energy, while the valence band and the second conduction band move upwards. This is an indication that these bands show a strong layer sensitivity, in which the bands with an orbital composition coming mostly from the same layer move in the same direction as a function of the field. As we can see in Fig. 2, this sensitivity is already verified in the hybrid bilayer even in the absence of the field but, in fact, we verify it in all cases when the field is applied. This property is further confirmed by PDOS calculations for the highest field we have considered (1.2 V/Å), as shown in Fig. 5.

We have also calculated the charge transfer as a function of the external electric field, as shown in Fig. 6. We found that the amount of charge transfer increases with the field value. No noticeable differences are observed on the behaviors below or above the critical field values. Furthermore, in the hybrid bilayer, the magnitude of the charge transfer
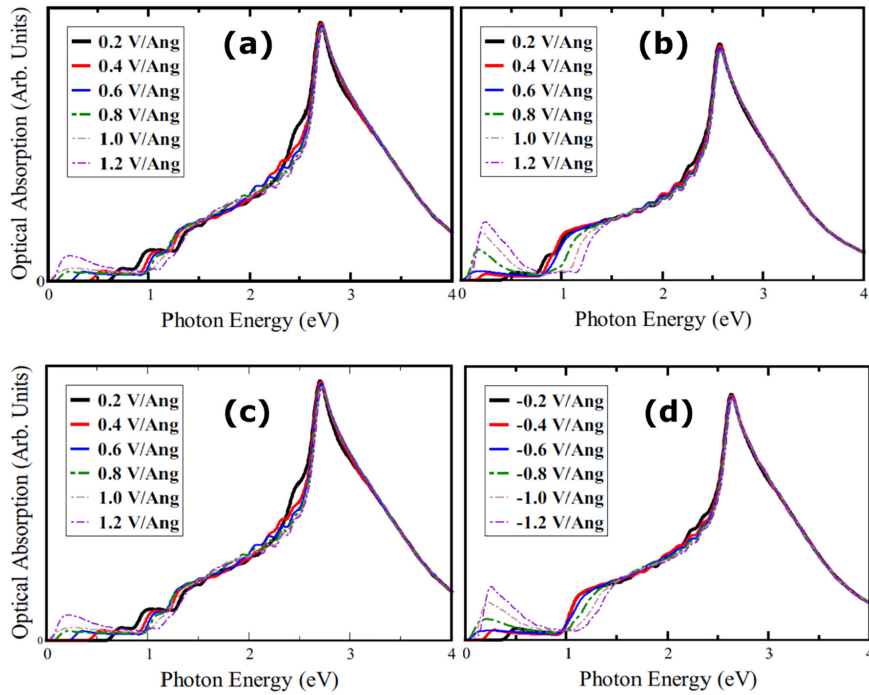
315

105

**Fig. 8.** Optical absorption spectra of (a) BP, (b) BAs, (c)–(d) hybrid BP::BAs bilayers. In (c), the electrical field points from the BP layer to the BAs layer, while in (d) the field direction is reversed. The field magnitudes are indicated in the legend of each plot.

depends on the direction of the field. In all cases, the electrons move in a direction opposite to that of the field, as expected. This polarization tends to screen the external field, so we expect that the band gap saturates at higher field values, as also observed in bilayer graphene.

Finally, we have also studied the optical properties of the most favorable (A′B) bilayers by calculating the optical absorption spectra as a function of the field. Note that, in such calculations, excitonic effects (electron-hole interaction) are not considered. As such, the value of the optical gaps (which is the onset of optical absorption) is related to the band gaps of the respective bilayers. First, we show in Fig. 7 the spectra in the absence of the field for each bilayer and we compare them with the spectra obtained from the isolated monolayers. We see that the spectra show a sharp peak around 2.5–2.6 eV, in the middle of the visible range. In the pristine bilayers, the position of this peak matches that of the corresponding monolayers, while in the hybrid bilayer it lies at an intermediate value. As we discuss below, this peak is associated with optical transitions between van-Hove singularities corresponding to the shoulder regions of the low energy bands around the M point (see Fig. 2). Note also that the onset of absorption shows a step-like structure, which is associated with optical transitions between the pairs of valence and conduction bands near the K point. The extra step found in the hybrid bilayer is a consequence of the lifting of the VBM degeneracy due to the inversion symmetry breaking, as shown in Fig. 2 and discussed above.

In Fig. 8, we show how the spectra are modified due to the presence of the external field. First, note that the sharp peak shows a slight blueshift (that is, it moves towards higher energies in the ultraviolet region) as the field increases, despite the fact that the two pairs of valence and conduction bands move considerably, as shown in Fig. 3.

To understand this weak dependence, we have plotted in Fig. 9 the first two valence and conduction bands energies at the M point as a function of the field. As we can see, the differences between the energies of the first (second) conduction band and second (first) valence band show a weak dependence with the field and match the energy of the absorption peak, which explains its structure. Moreover, our PDOS calculations for the highest field we have considered (1.2 V/Å) indicate that these bands have a strong layer sensitivity around the M point. As shown in Fig. 5, the first (second) conduction band and second (first) valence band around this point are mostly composed of pz orbitals located in the same layer. Therefore, these optical transitions induce an intra-layer electron-hole pair, where the electron and hole are found in the same layer.

Moreover, note that the electric field introduces important modifications in the infrared region of the spectra. Below the critical field, the onset of absorption (first step) roughly follows the band gap closing reported in Figs. 3 and 4. However, above the critical field, a new peak appears in this region and it is associated to optical transitions within the modified "Mexican-hat" region of the band structure around the K-point, as shown in Fig. 3. This modification of the bands is accompanied by the development of new peaks in the PDOS around this energy range, as shown in Fig. 5. These peaks also show a strong sublattice and layer sensitivity, but in this case, the occupied and unoccupied states are composed of orbitals belonging to different layers. Since the optical peak is related to a transition between these two peaks, we conclude that the transition induces an interlayer electron-hole pair, in which the electron and hole are now found in different layers. Since the recombination time of such pairs is usually longer than that of the intra-layer pairs, they may be useful for applications in photovoltaic cells,
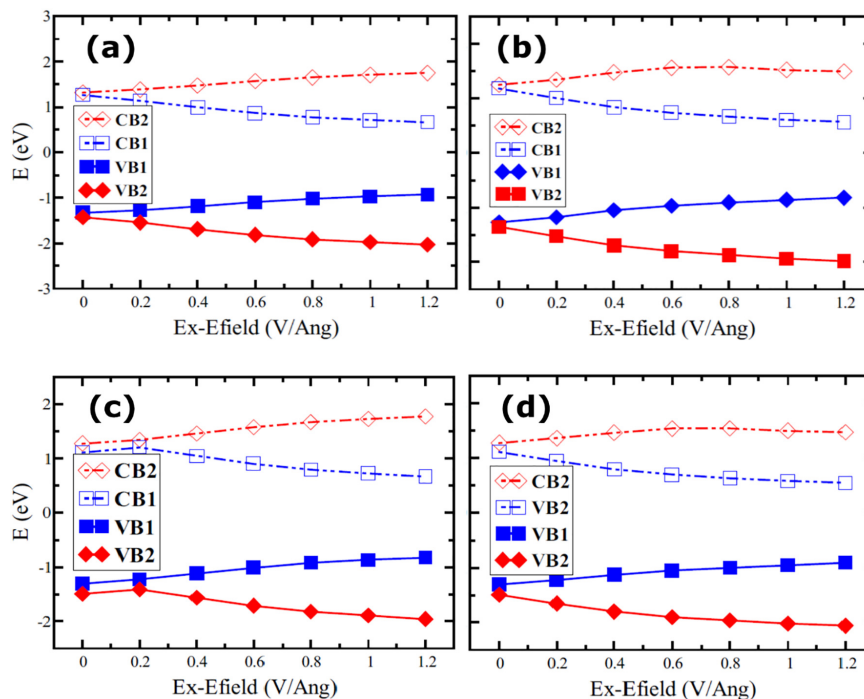
**Fig. 9.** Energies of the low energy bands at the M point as a function of the electric field for (a) BP, (b) BAs, and (c)–(d) hybrid BP::BAs bilayer. In (c), the electrical field points from the BP layer to the BAs layer, while in (d) the field direction is reversed. The field magnitudes are indicated in the legend of each plot. VB1 and VB2 (CB1 and CB2) correspond to the first and second valence (conduction) bands, as measured from the Fermi energy.

where the recombination time is a critical factor in determining the efficiency [65–67]. In addition, we can see from Fig. 8 that this absorption peak has a strong blueshift as the electrical field increases, following the band gap variation. Such a tunability in the infrared region may also be interesting for future applications in optoelectronic devices.

**4. Conclusions**

We have studied the structural, electronic, and optical properties of pristine and hybrid BP and BAs bilayers within the framework of non-local vdW-DF calculations. We have calculated and compared the stability of different stackings and various configurations of the bilayers. We found that the A′B stacking (where the B atoms sit on top of each other) is found to be the most favorable configuration in all cases. We have also investigated the effects of an external electric field applied perpendicular to the layers. We find that the electronic properties are particularly tunable, as the band gap is reduced from 0.8 eV down to zero as the field increases and then reopens again. The value of the critical field in which the gap closes depends on the bilayer type and, in the case of the hybrid bilayer, it also depends on the direction of the field. Interestingly, the band gap of the hybrid bilayer is also found to be lower than that of the pristine bilayers in most configurations. The optical properties of these systems also show great tunability. We find that the absorption spectra present a sharp peak around 2.5–2.6 eV, in the middle of the visible range, which exhibits a slight blueshift as the field strength increases. The structure of this peak is related to intra-layer optical transitions, in which the electron-hole pair resides in the

same layer. Above the critical field, the band structure develops a "Mexican-hat" shape and a new peak is observed in the infrared region of the absorption spectra. This peak shows a strong dependence with the field and it is associated with interlayer optical transitions, where now the electron and hole are found in separate layers. These properties indicate that these bilayers may find promising applications in future nano and optoelectronic devices.

**Data availability**

All the data is available from the authors on request.

**Appendix A. Supplementary data**

Supplementary data to this article can be found online at https://doi.org/10.1016/j.apsusc.2019.07.030.

## References

[1] K.S. Novoselov, A.K. Geim, S.V. Morozov, D. Jiang, Y. Zhang, S.V. Dubonos, I.V. Grigorieva, A.A. Firsov, Electric field effect in atomically thin carbon films, Science 306 (2004) 666–669.

[2] K.K. Kim, A. Hsu, X. Jia, S.M. Kim, Y. Shi, M. Hofmann, D. Nezich, J.F. Rodriguez-Nieva, M. Dresselhaus, T. Palacios, J. Kong, Synthesis of monolayer hexagonal boron nitride on Cu foil using chemical vapor deposition, Nano Lett. 12 (2012) 161–166.

[3] S. Ullah, P.A. Denis, F. Sato, Hydrogenation and fluorination of 2D boron phosphide and boron arsenide: a density functional theory investigation, ACS Omega 3 (2018) 16416–16423.

[4] S. Ullah, P.A. Denis, R.B. Capaz, F. Sato, Theoretical characterization of hexagonal 2D Be3N2 monolayers, New J. Chem. 43 (2019) 2933–2941.

[5] Q. Tang, Z. Zhou, Z. Chen, Innovation and discovery of graphene-like materials via density-functional theory computations, Wiley Interdiscip. Rev. Comput. Mol. Sci. 5 (2015) 360–379.

[6] Q. Tang, Z. Zhou, Graphene-analogous low-dimensional materials, Prog. Mater. Sci. 58 (2013) 1244–1315.

[7] J.-C. Lei, X. Zhang, Z. Zhou, Recent advances in MXene: preparation, properties, and applications, Front. Phys. 10 (2015) 276–286.

[8] Q. Zhang, K.S. Chan, J. Li, Spin-transfer torque generated in graphene based topological insulator heterostructures, Sci. Rep. 8 (2018) 4343.

[9] J. He, L. Tao, H. Zhang, B. Zhou, J. Li, Emerging 2D materials beyond graphene for ultrashort pulse generation in fiber lasers, Nanoscale 11 (2019) 2577–2593.

[10] Y. Li, B. Wu, W. Guo, L. Wang, J. Li, Y. Liu, Tailoring graphene layer-to-layer growth, Nanotechnology 28 (2017) 265101.

[11] L. Huang, Q. Yue, J. Kang, Y. Li, J. Li, Tunable band gaps in graphene/GaN van der Waals heterostructures, J. Phys. Condens. Matter 26 (2014) 295304.

[12] H. Şahin, S. Cahangirov, M. Topsakal, E. Bekaroglu, E. Akturk, R.T. Senger, S. Ciraci, Monolayer honeycomb structures of group-IV elements and III–V binary compounds: first-principles calculations, Phys. Rev. B 80 (2009) 155453.

[13] K. Watanabe, T. Taniguchi, H. Kanda, Direct-bandgap properties and evidence for ultraviolet lasing of hexagonal boron nitride single crystal, Nat. Mater. 3 (2004) 404.

[14] N. Alem, R. Erni, C. Kisielowski, M.D. Rossell, W. Gannett, A. Zettl, Atomically thin hexagonal boron nitride probed by ultrahigh-resolution transmission electron microscopy, Phys. Rev. B 80 (2009) 155425.

[15] C.R. Dean, A.F. Young, I. Meric, C. Lee, L. Wang, S. Sorgenfrei, K. Watanabe, T. Taniguchi, P. Kim, K.L. Shepard, J. Hone, Boron nitride substrates for high-quality graphene electronics, Nat. Nanotechnol. 5 (2010) 722.

[16] M.G. Menezes, R.B. Capaz, Half-metallicity induced by charge injection in hexagonal boron nitride clusters embedded in graphene, Phys. Rev. B 86 (2012) 195413.

[17] C. Attaccalite, M. Bockstedte, A. Marini, A. Rubio, L. Wirtz, Coupling of excitons and defect states in boron-nitride nanostructures, Phys. Rev. B 83 (2011) 144115.

[18] X. Blase, A. Rubio, S.G. Louie, M.L. Cohen, Quasiparticle band structure of bulk hexagonal boron nitride and related systems, Phys. Rev. B 51 (1995) 6868–6875.

[19] F. Ferreira, A.J. Chaves, N.M.R. Peres, R.M. Ribeiro, Excitons in hexagonal boron nitride single-layer: a new platform for polaritonics in the ultraviolet, J. Opt. Soc. Am. B 36 (2019) 674–683.

[20] P. Popper, T.A. Ingles, Boron phosphide, a III–V compound of zinc-blende structure, nature 179 (1957) 1075.

[21] P. Kocinski, M. Zbroszczyk, Calculated structural and electronic properties of boron phosphide under pressure, Semicond. Sci. Technol. 10 (1995) 1452–1457.

[22] E. Schroten, A. Goossens, J. Schoonman, Large-surface-area boron phosphide liquid junction solar cells, J. Electrochem. Soc. 146 (1999) 2045–2048.

[23] S.Z. Sayyad-Alangi, M.T. Baei, S. Hashemian, Adsorption and electronic structure study of thiazole on the (6,0) zigzag single-walled boron phosphide nanotube, J. Sulfur Chem. 34 (2013) 407–420.

[24] J. Dong, H. Li, L. Li, Multi-functional nano-electronics constructed using boron phosphide and silicon carbide nanoribbons, NPG Asia Mater. 5 (2013) e56.

[25] L. Lindsay, D.A. Broido, T.L. Reinecke, First-principles determination of ultrahigh thermal conductivity of boron arsenide: a competitor for diamond? Phys. Rev. Lett. 111 (2013) 025901.

[26] S. Li, Q. Zheng, Y. Lv, X. Liu, X. Wang, P.Y. Huang, D.G. Cahill, B. Lv, High thermal conductivity in cubic boron arsenide crystals, Science 361 (2018) 579.

[27] F. Tian, B. Song, X. Chen, N.K. Ravichandran, Y. Lv, K. Chen, S. Sullivan, J. Kim, Y. Zhou, T.-H. Liu, M. Goni, Z. Ding, J. Sun, G.A.G. Udalamatta Gamage, H. Sun, H. Ziyaee, L. Deng, J. Zhou, A.J. Schmidt, S. Chen, C.-W. Chu, P.Y. Huang, D. Broido, L. Shi, G. Chen, Z. Ren, Unusual high thermal conductivity in boron arsenide bulk crystals, Science 361 (2018) 582.

[28] J.S. Kang, M. Li, H. Wu, H. Nguyen, Y. Hu, Experimental observation of high thermal conductivity in boron arsenide, Science 361 (2018) 575.

[29] B. Zeng, M. Li, X. Zhang, Y. Yi, L. Fu, M. Long, First-principles prediction of the electronic structure and carrier mobility in hexagonal boron phosphide sheet and nanoribbons, J. Phys. Chem. C 120 (2016) 25037–25042.

[30] S. Ullah, P.A. Denis, F. Sato, Hexagonal boron phosphide as a potential anode nominee for alkali-based batteries: a multi-flavor DFT study, Appl. Surf. Sci. 471 (2019) 134–141.

[31] B. Onat, L. Hallioglu, S. İpek, E. Durgun, Tuning electronic properties of monolayer hexagonal boron phosphide with group III–IV–V dopants, J. Phys. Chem. C 121 (2017) 4583–4592.

[32] D. Cakr, D. Kecik, H. Sahin, E. Durgun, F.M. Peeters, Realization of a p-n junction in a single layer boron-phosphide, Phys. Chem. Chem. Phys. 17 (2015) 13013–13020.

[33] M. Xie, S. Zhang, B. Cai, Z. Zhu, Y. Zou, H. Zeng, Two-dimensional BX (X = P, As, Sb) semiconductors with mobilities approaching graphene, Nanoscale 8 (2016) 13407–13413.

[34] H.R. Jiang, W. Shyy, M. Liu, L. Wei, M.C. Wu, T.S. Zhao, Boron phosphide monolayer as a potential anode material for alkali metal-based batteries, J. Mater. Chem. A 5 (2017) 672–679.

[35] C. Tan, Q. Zhou, X. Chen, Tuning electronic properties of bilayer boron-phosphide by stacking order and electric field: a first principles investigation, 2016 17th International Conference on Electronic Packaging Technology (ICEPT), 2016, pp. 757–761.

[36] Z.Z. Zhou, H.J. Liu, D.D. Fan, G.H. Cao, C.Y. Sheng, High thermoelectric performance in the hexagonal bilayer structure consisting of light boron and phosphorus elements, Phys. Rev. B 99 (2019) 085410.

[37] J. Li, H. Duan, B. Zeng, Q. Jing, B. Cao, F. Chen, M. Long, Strain-induced band structure modulation in hexagonal boron phosphide/blue phosphene vdW heterostructure, J. Phys. Chem. C 122 (2018) 26120–26129.

[38] L. Du, K. Zheng, H. Cui, Y. Wang, L. Tao, X. Chen, Novel electronic structures and enhanced optical properties of boron phosphide/blue phosphorene and F4TCNQ/blue phosphorene heterostructures: a DFT + NEGF study, Phys. Chem. Chem. Phys. 20 (2018) 28777–28785.

[39] A. Mogulkoc, Y. Mogulkoc, M. Modarresi, B. Alkan, Electronic structure and optical properties of novel monolayer gallium nitride and boron phosphide heterobilayers, Phys. Chem. Chem. Phys. 20 (2018) 28124–28134.

[40] M. Dion, H. Rydberg, E. Schröder, D.C. Langreth, B.I. Lundqvist, Van der Waals density functional for general geometries, Phys. Rev. Lett. 92 (2004) 246401.

[41] G. Román-Pérez, J.M. Soler, Efficient implementation of a van der Waals density functional: application to double-wall carbon nanotubes, Phys. Rev. Lett. 103 (2009) 096102.

[42] P. Ordejón, E. Artacho, J.M. Soler, Self-consistent order-N density-functional calculations for very large systems, Phys. Rev. B 53 (1996) R10441.

[43] N. Troullier, J.L. Martins, Efficient pseudopotentials for plane-wave calculations, Phys. Rev. B 43 (1991) 1993–2006.

[44] G. Kresse, J. Furthmüller, Efficiency of ab-initio total energy calculations for metals and semiconductors using a plane-wave basis set, Comput. Mater. Sci. 6 (1996) 15–50.

[45] G. Kresse, J. Furthmüller, Efficient iterative schemes for ab initio total-energy calculations using a plane-wave basis set, Phys. Rev. B 54 (1996) 11169–11186.

[46] J.P. Perdew, K. Burke, M. Ernzerhof, Generalized gradient approximation made simple, Phys. Rev. Lett. 77 (1996) 3865–3868.

[47] P.E. Blöchl, Projector augmented-wave method, Phys. Rev. B 50 (1994) 17953–17979.

[48] M.J. Frisch, G.W. Trucks, H.B. Schlegel, G.E. Scuseria, M.A. Robb, J.R. Cheeseman, G. Scalmani, V. Barone, G.A. Petersson, H. Nakatsuji, X. Li, M. Caricato, A. Marenich, J. Bloino, B.G. Janesko, R. Gomperts, B. Mennucci, H.P. Hratchian, J.V. Ortiz, A.F. Izmaylov, J.L. Sonnenberg, D. Williams-Young, F. Ding, F. Lipparini, F. Egidi, J. Goings, B. Peng, A. Petrone, T. Henderson, D. Ranasinghe, V.G. Zakrzewski, J. Gao, N. Rega, G. Zheng, W. Liang, M. Hada, M. Ehara, K. Toyota, R. Fukuda, J. Hasegawa, M. Ishida, T. Nakajima, Y. Honda, O. Kitao, H. Nakai, T. Vreven, K. Throssell, J.A. Montgomery, J.E.P. Jr, F. Ogliaro, M. Bearpark, J.J. Heyd, E. Brothers, K.N. Kudin, V.N. Staroverov, T. Keith, R. Kobayashi, J. Normand, K. Raghavachari, A. Rendell, J.C. Burant, S.S. Iyengar, J. Tomasi, M. Cossi, J.M. Millam, M. Klene, C. Adamo, R. Cammi, J.W. Ochterski, R.L. Martin, K. Morokuma, O. Farkas, J.B. Foresman, D.J. Fox, Gaussian 09, Revision A1 ed, Gaussian Inc., Wallingford, CT, 2009.

[49] K. Kamiya, N. Umezawa, S. Okada, Energetics and electronic structure of graphene adsorbed on HfO₂(111): density functional theory calculations, Phys. Rev. B 83 (2011) 153413.

[50] S.F. Boys, F. Bernardi, The calculation of small molecular interactions by the differences of separate total energies. Some procedures with reduced errors, Mol. Phys. 19 (1970) 553–566.

[51] S. Ullah, M.G. Menezes, R.B. Capaz, F. Sato, Exotic hydrogenic impurity states in h-BN: the role of the structure and intervalley interactions, APS Meetings, APS, Boston, Massachusetts, 2019.

[52] S. Ullah, P.A. Denis, F. Sato, Triple-doped monolayer graphene with boron, nitrogen, aluminum, silicon, phosphorus, and sulfur, ChemPhysChem 18 (2017) 1854.

[53] S. Ullah, P.A. Denis, F. Sato, Beryllium doped graphene as an efficient anode material for lithium-ion batteries with significantly huge capacity: a DFT study, Appl. Mater. Today 9 (2017) 333–340.

[54] S. Ullah, P.A. Denis, F. Sato, First-principles study of dual-doped graphene: towards promising anode materials for Li/Na-ion batteries, New J. Chem. 42 (2018) 10842–10851.

[55] M. Sun, J.-P. Chou, J. Yu, W. Tang, Electronic properties of blue phosphorene/graphene and blue phosphorene/graphene-like gallium nitride heterostructures, Phys. Chem. Chem. Phys. 19 (2017) 17324–17330.

[56] X. Chen, C. Tan, Q. Yang, R. Meng, Q. Liang, J. Jiang, X. Sun, D.Q. Yang, T. Ren, Effect of multilayer structure, stacking order and external electric field on the electrical properties of few-layer boron-phosphide, Phys. Chem. Chem. Phys. 18 (2016) 16229–16236.

[57] X. Li, Y. Dai, Y. Ma, S. Han, B. Huang, Graphene/g-C3N4 bilayer: considerable band gap opening and effective band structure engineering, Phys. Chem. Chem. Phys. 16 (2014) 4230–4235.

[58] C. Tan, Q. Yang, R. Meng, Q. Liang, J. Jiang, X. Sun, H. Ye, X.P. Chen, An AlAs/germanene heterostructure with tunable electronic and optical properties via external electric field and strain, J. Mater. Chem. C 4 (2016) 8171–8178.

[59] X. Chen, Q. Yang, R. Meng, J. Jiang, Q. Liang, C. Tan, X. Sun, The electronic and

optical properties of novel germanene and antimonene heterostructures, J. Mater. Chem. C 4 (2016) 5434–5441.

[60] T. Ohta, A. Bostwick, T. Seyller, K. Horn, E. Rotenberg, Controlling the electronic structure of bilayer graphene, Science 313 (2006) 951.

[61] H. Min, B. Sahu, S.K. Banerjee, A.H. MacDonald, Ab initio theory of gate induced gaps in graphene bilayers, Phys. Rev. B 75 (2007) 155115.

[62] L.M. Zhang, Z.Q. Li, D.N. Basov, M.M. Fogler, Z. Hao, M.C. Martin, Determination of the electronic structure of bilayer graphene from infrared spectroscopy, Phys. Rev. B 78 (2008) 235408.

[63] Y. Zhang, T.-T. Tang, C. Girit, Z. Hao, M.C. Martin, A. Zettl, M.F. Crommie, Y.R. Shen, F. Wang, Direct observation of a widely tunable bandgap in bilayer graphene, nature 459 (2009) 820.

[64] M.G. Menezes, R.B. Capaz, J.L.B. Faria, Gap opening by asymmetric doping in graphene bilayers, Phys. Rev. B 82 (2010) 245414.

[65] S. Gélinas, O. Paré-Labrosse, C.-N. Brosseau, S. Albert-Seifried, C.R. McNeill, K.R. Kirov, I.A. Howard, R. Leonelli, R.H. Friend, C. Silva, The binding energy of charge-transfer excitons localized at polymeric semiconductor heterojunctions, J. Phys. Chem. C 115 (2011) 7114–7119.

[66] S. Gélinas, A. Rao, A. Kumar, S.L. Smith, A.W. Chin, J. Clark, T.S. van der Poll, G.C. Bazan, R.H. Friend, Ultrafast long-range charge separation in organic semiconductor photovoltaic diodes, Science 343 (2014) 512.

[67] M.M. Furchi, A. Pospischil, F. Libisch, J. Burgdörfer, T. Mueller, Photovoltaic effect in an electrically tunable van der Waals heterojunction, Nano Lett. 14 (2014) 4785–4791.

## 9  Defects

In semiconductors, defects play a key role in designing the optoelectronic properties of materials as these defects come in the form of donor and acceptors states in the bandgap of a semiconductor. These "defective materials" become suitable to be utilized in various devices, such as solar cells and light-emitting diode. Herein, we study defect levels in monolayer $h$BN, a classic and one of the most famous 2D wide gap semiconductors. We find a quite exotic behavior of the impurity structure induced inside the gap of $h$BN. The impurity level structure induced inside the gap is greatly dependent on the sublattice position and its response as an acceptor or a donor. Having said that, when a nitrogen atom is substituted with an acceptor atom, the intervalley interaction is quite strong and we only see nondegenerate levels that have strong valley and spin splitting. Conversely, when a boron atom is replaced with an acceptor, a weaker intervalley interaction is observed and, furthermore, we see near-valley-degenerate levels. Additionally, we see a similar behavior of the donor impurity. These can be attributed to the distinctive structure of $h$BN where the VBM and CBM are composed of $p_z$ orbital of N and B, respectively. We select Be(B) and C(N) for acceptor cases and C(B) and S(N) for donor cases. In the case of acceptors, when C replaces a N atom, we see a single degenerate impurity level structure composed mostly of C $p_z$ orbitals. On the contrary, when Be replaces a B atom, we observe (2+1) level structures coming mostly from N $p_z$. A similar behavior was observed for donor cases. The results were published in (Phys. Rev. B 100, 085427, 2019) [250].

# Exotic impurity-induced states in single-layer *h*-BN: The role of sublattice structure and intervalley interactions

Saif Ullah[*] and Fernando Sato

*Departamento de Física, Instituto de Ciências Exatas, Campus Universitário, Universidade Federal de Juiz de Fora,
36036-900 Juiz de Fora, MG, Brazil*

Marcos G. Menezes [†] and Rodrigo B. Capaz[‡]

*Instituto de Física, Universidade Federal do Rio de Janeiro, Caixa Postal 68528, 21941-972 Rio de Janeiro, RJ, Brazil*

By using a combination of density functional theory, tight-binding, and effective mass calculations, we explore the electronic properties of donor and acceptor states of substitutional impurities in single-layer *h*-BN. We find that the impurity level structure inside the electronic gap is quite exotic, as it strongly depends on the sublattice position of the impurity and its behavior as a donor or an acceptor. For instance, when an acceptor atom replaces a nitrogen atom, the intervalley interaction induced by the impurity potential is found to be strong and the resulting level structure consists only of nondegenerate levels with strong valley and spin splitting. On the other hand, when an acceptor replaces a boron atom, the intervalley interaction is much weaker and near-valley-degenerate levels are found. Donor impurities behave in a similar fashion. The differences between these two types of level structures can be traced to the peculiar sublattice-resolved electronic structure of pristine *h*-BN, in which the valence and conduction wave functions at the $K$ and $K'$ points are composed only of nitrogen and boron $p_z$ orbitals, respectively, and to the dependence of the intervalley interaction on them. We predict that this impurity level structure must also be present in other two-dimensional semiconductors and insulators with similar sublattice-resolved electronic states, such as other hexagonal III-V binary compounds and, consequently, offer the possibility of engineering the optical properties of these materials for potential applications in future devices.

## I. INTRODUCTION

Since the experimental discovery of graphene and its incredible properties and potential applications [1,2], a large scientific effort has been put on the search of materials with similar structural properties, the so-called two-dimensional (2D) materials. These materials form layers with thicknesses up to a few atoms and can be metallic, semiconducting, or insulating, which results in many different potential applications [3–6].

Single-layer hexagonal boron nitride (*h*-BN) was one of the first additions to this family of materials. It is formed by a one-atom-thick layer with the same honeycomb lattice of graphene, but with two different atoms in its unit cell, boron and nitrogen. However, due to the large electronegativity difference between B and N, the electronic properties of *h*-BN are significantly different than that of graphene, a zero-gap semiconductor. The quasiparticle band gaps of *h*-BN are as high as 6.0 eV for bulk and 7.0 eV for the single layer, thus revealing that *h*-BN is a wide gap insulator [7,8]. The photoluminescence spectrum of bulk *h*-BN shows a rich excitonic structure and optical gaps of 5.5–5.8 eV have been reported,

thus making it a strong candidate for applications such as ultraviolet emitters and detectors [9–14]. In fact, excitonic effects are crucial to explaining the optical properties of this material even in its bulk form, given its layered structure [15–17]. Moreover, due to its insulating properties, single-layer *h*-BN can be used to encapsulate other 2D materials and, due to its structural similarity to graphene, they can be combined into planar heterostructures with potential applications in tunneling junctions and spintronics [18–24].

In this work, we study the effects of substitutional impurities on the electronic properties of single-layer *h*-BN, with a special attention to the role of intervalley interactions. In conventional three-dimensional (3D) semiconductors and insulators, those impurities are known to introduce important changes to their optical and transport properties. For example, a carbon atom replacing a nitrogen atom is one of the most common types of defects in bulk (3D) *h*-BN. The presence of this defect is often associated with significant changes on the absorption and photoluminescence spectra, especially with the introduction of an additional peak at ∼4.0 eV due to transitions between defect levels and the conduction band [25–28]. In beryllium-implanted *h*-BN films, *p*-type conduction has also been observed, induced by the occupation of B vacancies by Be atoms [29]. Similarly, silicon-doped *h*-BN exhibits *n*-type conduction due to the replacement of B by Si atoms [30]. There are also numerous theoretical and experimental studies on the cubic phase, known as *c*-BN, in which similar

[*]sullah@fisica.ufjf.br
[†]marcosgm@if.ufrj.br
[‡]capaz@if.ufrj.br

modifications are introduced by impurities. A detailed review can be found in Ref. [31]. In bulk (3D) silicon, the impurity potential induced by group V donors is known to lift the sixfold valley degeneracy of the 1$s$ defect levels, resulting in a nondegenerate ground state [32]. In a 2D insulator such as single-layer $h$-BN, the screening is much weaker and highly nonhomogeneous, hence, the binding energies of impurity levels and valley splittings are expected to be much larger than in their 3D counterparts. Additionally, the energy ordering of these levels may be very different from predictions based on simple models such as the 2D hydrogen atom, in a similar fashion to the behavior of excitons in 2D semiconductors. However, even this model is able to describe such features when the proper behavior of screening is taken into account [33–35].

In order to address these effects, we employ a combination of different theoretical approaches, which include density functional theory (DFT), a semiempirical tight-binding (TB) model, and multivalley effective mass (EM) theory. The DFT calculations provide a more accurate picture of the effect of the impurities (in comparison with the other methods). The TB model provides a simple description of the impurity potential, which reproduces quite accurately the DFT results. Additionally, this model can also be employed in more complex calculations that cannot be tackled by DFT, such as disordered impurities on $h$-BN and similar materials. Finally, the EM calculations provide a deeper understanding of the intervalley interaction and the observed impurity levels. The paper is organized as follows. In Sec. II, we describe the methodology involved in each of these calculations. In Sec. III we present and discuss our results, and in Sec. IV we outline the main conclusions from our work.

## II. METHODS

### A. DFT calculations

We executed first-principles calculations within the framework of density functional theory (DFT) by using the SIESTA code [36–38]. Calculations with and without spin polarization were performed. The latter were used to compare with our tight-binding results, as described on the next section. Norm-conserving Troullier-Martins pseudopotentials were used to treat the ion-electron interaction [39]. For the electron-electron interaction, we have employed a fully relativistic nonlocal vdW-DF exchange-correlation functional [40,41]. We have considered supercells with sizes up to $10 \times 10$, in which the cohesive and formation energies are found to be well converged. The vacuum layer was kept as large as 20 Å in order to eliminate interactions between periodic images. The Brillouin zone of the unit cell was sampled with a $30 \times 30 \times 1$ Monkhorst-Pack $k$-point grid [42]. For the supercells, the $k$-point grids were adjusted according to their dimensions. The atomic coordinates and the supercell dimensions were relaxed until the forces were smaller than 0.02 eV/Å. A double-zeta basis set with polarization functions (DZP) was used with a mesh cutoff of 200 Ry. The equilibrium lattice constant for the pure system is calculated to be $a = 2.51$ Å, in excellent agreement with the available experimental values for single-layer and bulk $h$-BN [43,44]. The

structural properties of the defective systems are discussed in Sec. III A.

Throughout the text, we mainly discuss the results for $10 \times 10$ supercells, as they are the largest and therefore more adequate for the description of all the observed impurity states. We focus on the following substitutional impurities: Be(B), C(N), C(B), and S(N). A single impurity is placed on each supercell, replacing either a boron or a nitrogen atom, as indicated above by the parentheses. In particular, the C(N) impurity is one of the most common types of defects on $h$-BN and Be(B) doping has also been realized in $h$-BN films [29]. We also briefly discuss the results for other substitutional donor and acceptor impurities.

### B. Tight-binding calculations

In our tight-binding (TB) model, we include only a single $p_z$ orbital per atom. As we discuss in Sec. III B, the comparison between our DFT and TB results indicates that $\sigma$ orbitals do not contribute to the impurity states and are therefore unimportant to our discussion. We include only interactions between nearest neighbors with hopping $t_0 = 2.50$ eV, chosen in order to reproduce the DFT bandwidths of the $\pi$ bands. Overlaps are neglected. Onsite energies for boron and nitrogen atoms are chosen as $E_B = -6.64$ eV and $E_N = -11.47$ eV, respectively [45]. In this model, the TB band gap is simply given by $E_g^{TB} = E_B - E_N = 4.83$ eV, which reproduces quite well our DFT result ($E_g^{DFT} = 4.76$ eV). A comparison between the DFT and TB bands is shown in Fig. 1, where we see that the model provides a very good overall description of the $\pi$ bands, although electron-hole asymmetry is not reproduced. As we shall see, this simple model is enough to account for the properties of the impurity states observed in the DFT calculations.

It should be emphasized that practical implementations of DFT based in the ground state Kohn-Sham formalism are known to underestimate energy gaps. More refined calculations, such as quasiparticle calculations within the *GW*
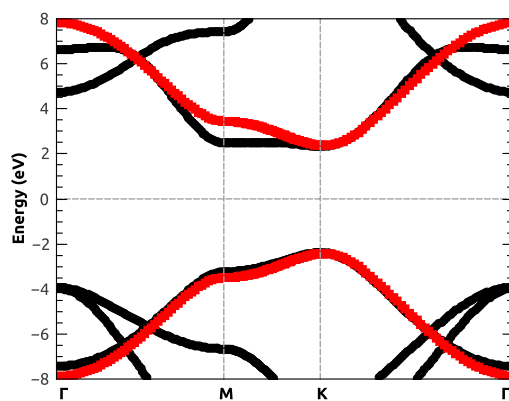


FIG. 1. Comparison between the DFT (black) and TB (red) bands in the pure system. The Fermi energy is set to zero in both cases.

112

approximation, give a quasiparticle gap of about 7.0 eV [7,46,47]. In addition, for both bulk and single-layer $h$-BN, there is a controversy in the literature whether this material has a direct or an indirect band gap [9–13,46–51]. For the single layer, the top of the valence band unmistakably lies at the $K$ point, but the position of the bottom of the conduction band depends on the choice of functional for DFT and on the level of theory in general. Some calculations report it at the $K$ point as well, resulting in a direct gap, while others report it at the $\Gamma$ point, resulting in an indirect gap. In fact, more recent $GW$ calculations favor the latter possibility [46,47]. Therefore, the properties of donor impurities in $h$-BN should, in principle, also carry the same controversy. In our DFT calculations, single-layer $h$-BN is found to be a direct gap material. The conduction band has a local minimum at the $\Gamma$ point, with an energy about 2.4 eV higher than that of the global minimum at the $K$ point. As such, we treat the properties of donor and acceptor impurities at equal footing. We believe that this controversy will not significantly change our results, as we expect that the low-energy donor levels would still be related to behavior of the conduction band near the $K$ point even if it not the global minimum, as a consequence of their $p_z$ character. Some parameters and features of our TB model and the effective mass model described in the next section may need to be adapted to fully describe these impurities, but the description of the acceptor impurities should be fairly calculation independent. We return to this point in Sec. III.

To model the substitutional impurity, we consider a different onsite energy $E_I$ to the impurity site. We also add to the onsite energies of its first and second neighbors a contribution given by a screened Coulomb potential:

$$W(r) = \frac{e^2}{4\pi K \epsilon_0 r}, \tag{1}$$

where $r$ is the distance measured from the impurity site and $K$ is the dielectric constant. For acceptors, this potential is repulsive and $K$ is positive, whereas for donors it is attractive and $K$ is chosen as negative. The impurity is placed into a $10 \times 10$ supercell, the same size used in the DFT calculations. In this model, $E_I$ and $K$ are adjustable parameters, chosen to best reproduce the DFT results for each type of impurity. Notice that this is a very crude model for the screening properties of a 2D material, whose dielectric function is known to be highly nonhomogeneous [33–35]. However, since we are only calculating $W(r)$ for first and second neighbors, we are assuming that $K$ does not change substantially for these two distances. Despite its simplicity, we find that this model reproduces quite accurately the DFT energies and wave functions of impurity levels in $h$-BN, as we discuss below. Finally, to plot the wave functions in real space, we build the Bloch wave functions using hydrogenic $p_z$ orbitals with screened atomic numbers, following the prescription of Slater [52].

### C. Multivalley effective mass calculations

In the effective mass formalism, the wave function of an impurity state is written in terms of valence (conduction) Bloch wave functions with **k** vectors in the vicinity of the valleys for acceptors (donors) [32,53,54]. For single-layer

$h$-BN, we have two inequivalent valleys at $K$ and $K'$ for both the acceptors and donors. The wave function is given by

$$\Psi(\mathbf{r}) = \sum_\mu F_\mu(\mathbf{r})\psi_\mu(\mathbf{r}), \tag{2}$$

where $\mu = K, K'$, $\psi_\mu(\mathbf{r})$ is the valence (conduction) Bloch wave function at valley $\mu$ for acceptors (donors), and $F_\mu(\mathbf{r})$ is a slowly varying function known as the envelope function.

The envelope functions satisfy a set of Schrödinger-type equations known as effective mass equations. For a system with isotropic effective mass such as $h$-BN, they are given by

$$-\frac{\hbar^2}{2m}\nabla^2 F_\mu(\mathbf{r}) + \sum_\nu \psi_\mu^*(\mathbf{r})\psi_\nu(\mathbf{r})W(r)F_\nu(\mathbf{r}) = (\epsilon - \epsilon_\mu)F_\mu(\mathbf{r}), \tag{3}$$

where $W(\mathbf{r})$ is the impurity potential. We choose for it the same form used for the TB model, given by Eq. (1). Note that the second term of this equation contains both intravalley ($\mu = \nu$) and intervalley ($\mu \neq \nu$) interactions. In both of them, the effective potential for the envelope function is a convolution of the impurity potential and valley wave functions. As we shall see, this term is central to our interpretation of the different energy level structures that we observe for impurities in $h$-BN. The effective mass is chosen to match that of our simple TB model and is given by $m = (2/3) E_g^{\mathrm{TB}} (\hbar/t_0 a)^2 \approx 0.62\, m_0$ ($m_0$ is the bare electron mass and $a = 2.51$ Å is the lattice constant of $h$-BN). For comparison, in our DFT calculations, the effective masses of the valence and conduction bands at the $K$ point along the $\Gamma$-$K$ line are 0.63 and 0.82 $m_0$, respectively. The discrepancy between the DFT and TB masses for the conduction band is expected, as our simple model does not capture electron-hole asymmetry and anisotropy, as shown in Fig. 1. On the other hand, these masses are in excellent agreement with a recent $GW$ investigation [47].

In order to solve Eq. (3), we write the envelope functions in terms of a basis of screened 2D hydrogenic orbitals for each valley [55]. Since we are only interested in the first few levels, we include only 1$s$, 2$s$, and 2$p$ envelopes in the calculations. We have verified that the mixing induced by intravalley and intervalley interactions between these envelopes and others not included is negligible. With this procedure, Eq. (3) can be transformed into a system of linear equations, which are solved for the coefficients of the expansion and the impurity energies.

### III. RESULTS

#### A. Spin-polarized DFT calculations

We begin by discussing the structural properties of all impurity configurations. In contrast to graphene, all impurities are found to settle well within the plane of $h$-BN and no out-of-plane distortions are observed [56]. In the case of the C impurity, the changes in the lattice constant are negligible (0.001 A), which is justified by the nearly comparable covalent radii of C, B, and N. The relaxed nearest-neighbor C-N and C-B bonds are found to be 1.43 and 1.51 Å, respectively, in excellent agreement with previous investigations

TABLE I. Cohesive ($E_c$) and formation ($E_f$) energies of different substitutional impurities in $h$-BN, as defined in Eqs. (4) and (5).

| Impurity | $E_c$ (eV/atom) | $E_f$ (eV) |
|---|---|---|
| Pure $h$-BN | −6.74 | |
| Be(B) | −6.70 | 5.21 |
| C(N) | −6.73 | 4.50 |
| C(B) | −6.73 | 4.20 |
| S(N) | −6.69 | 6.60 |

of impurities in graphene [57]. The rest of the B-N bonds remain nearly unchanged. For the Be(B) and S(N) impurities, more prominent changes are observed. The Be-N and S-N bonds are extended up to 1.59 and 1.73 Å, respectively, in line with previous investigations in a $Be_3N_2$ layer [58] and triple-doped graphene [59]. This results in a slight shortening of the next-neighboring B-N bonds, which are 1.43 and 1.42 Å in Be(B) and S(N), respectively. The lattice constants of Be(B) and S(N) are also a bit larger, changing by 0.004 and 0.034 Å, respectively.

In the next step, we report the stabilities of these systems by calculating the cohesive and formation energies. The cohesive energy ($E_c$) is defined by

$$E_c = \frac{E_{\text{tot}} - \sum_i n_i E_i}{N}, \tag{4}$$

where $E_{\text{tot}}$ is the total energy of the defective system, $n_i$ is the number of atoms of species $i$ present in the supercell, and $E_i$ is its corresponding energy in an isolated gas phase. Finally, $N$ is the total number of atoms in the supercell. Likewise, the formation energy ($E_f$) is defined by [60–62]

$$E_f = E_{\text{tot}} - E_{\text{pure}} + \mu_{\text{rem}} - \mu_{\text{def}}, \tag{5}$$

where $E_{\text{pure}}$ is the total energy of a pure $h$-BN supercell and $\mu_{\text{rem}}$ and $\mu_{\text{def}}$ are the chemical potentials of the removed atom (B or N) and the impurity, respectively. The chemical potentials of Be, B, C, N, and S are taken from the bulk hexagonal phase, $\alpha$-boron crystal, graphene, $N_2$, and the orthorhombic bulk phase, respectively. Both energies are reported in Table I for all impurity configurations in the 10×10 supercell. We have tested the convergence of these quantities with respect to the supercell size and we found that they are well converged within 20 meV. It can be seen from the table that C substitution at the B site is the most favorable, closely followed by C(N). Be(B) and S(N) have relatively higher formation energies, which may be related to the larger structural distortions induced by these impurities. The numerical results may change to some extent depending on the value of the chemical potential used. For that reason, we also report the cohesive energies of bulk Be, $\alpha$-boron, graphene, $N_2$, and bulk S for reference: Be = −3.22 eV/atom, B = −5.72 eV/atom, C = −7.34 eV/atom, N = −4.85 eV/atom, and S = −2.64 eV/atom [63].

Now we turn our attention to the electronic properties. In Fig. 2, we present the calculated DFT band structures for Be(B), C(N), C(B), and S(N) substitutional impurities. The first two (top row) are acceptors, while the last two (bottom row) are donors. We can clearly see an exotic behavior, with

two distinct level structures, which are related to the impurity type and the atom it replaces. For C(N) and C(B), we see a single flat impurity state for each spin channel, with a ∼1.0 eV spin-up and -down splitting. The projected density of states (PDOS) also shows that these states are mainly composed of $p_z$ states coming from the impurity itself, which is an indication of a strongly localized state. In contrast, for Be(B) and S(N), we see more complex level structures. In Be(B), we see pair of near-degenerate states followed by a nondegenerate excited state in both spin channels. In S(N), we see that the first two spin-up impurity levels show a ∼0.12 eV valley splitting, followed again by the nondegenerate excited state. In contrast, we see a single spin-down impurity level inside the gap, while the other states are hybridized into the conduction band. Moreover, the PDOS shows that the first two states have a very weak contribution from the impurity site and strong contributions from its first neighbors, while the nondegenerate excited state has similar contributions from the impurity and each neighbor. The larger dispersions observed in the bands [in comparison to the C(N) and C(B) cases] indicate that the corresponding wave functions spread more throughout the supercell, so residual interactions between the impurity and its periodic images may still be present, as we discuss below. For S(N), we also observe that each state of a near-degenerate pair has unequal PDOS amplitudes for each neighboring atom, but the sum of the amplitudes over both states is the same for the three neighbors. We also see a similar behavior in our LDOS calculations for Be(B), as discussed in the next section.

In Table II, we report the supercell magnetizations and binding energies for each impurity level. The results for the unpolarized calculations, discussed in the next section, are also included. Note that all spin-polarized cases are magnetic, with a magnetization that roughly corresponds to the electron added or removed from the system due to the impurity. From Fig. 2, we see that this behavior is related to the uneven occupation of spin-up and -down impurity levels, so the spin density is localized around the impurity. A similar behavior is experimentally observed for vacancies and hydrogen adsorbates in graphene [64–66] and theoretically predicted at the interfaces of graphene/$h$-BN heterostructures [23,24,67,68]. Note also that all binding energies are very large in comparison with those found for impurity states in bulk semiconductors, such as silicon, especially in the C(N) and C(B) cases. This is a clear manifestation of the dielectric properties of a 2D material, in which the screening is much weaker and highly nonhomogeneous. Such behavior is also seen for excitons in $h$-BN and 2D semiconductors [33–35]. Finally, note that the presence of these impurity levels may significantly change the optical properties of $h$-BN, by inducing new optical transitions between these levels and the valence/conduction bands. For instance, in the case of C(N), we may have a transition between the occupied spin-up impurity level and the conduction band with an energy of $E_g^{\text{DFT}} - E_b^0(up) = 4.49$ eV, which is compatible with the 4-eV absorption peak that is usually attributed to this impurity in bulk $h$-BN [25–28]. However, such an estimation does not take into account the quasiparticle corrections and the excitonic effects. There should also be a difference due to the confinement to a single layer. Nevertheless, part of the quasiparticle and excitonic effects usually cancel out and the
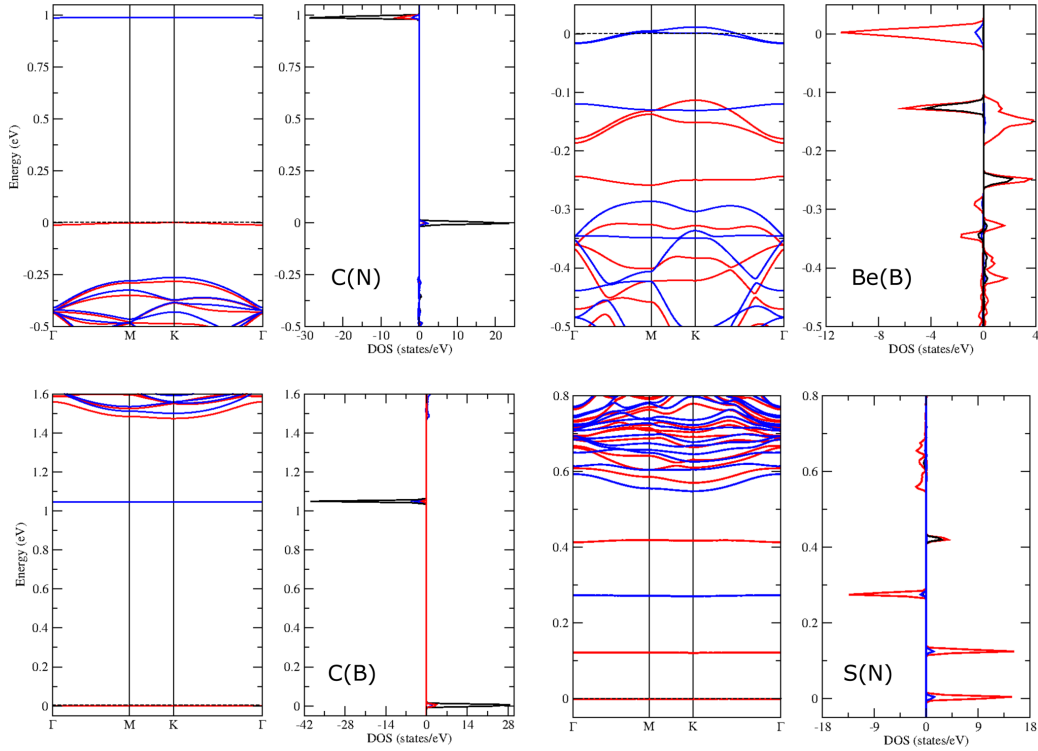
FIG. 2. Spin-polarized DFT band structures and projected density of states (PDOS) for acceptor (top) and donor (bottom) substitutional impurities. The specific impurities are indicated on each panel. For the bands, red (blue) represent spin-up (-down) states. For PDOS, the black, red, and blue lines correspond to the valence $p_z$ orbital of the impurity site, one of its first neighbors, and one of its second neighbors, respectively. Positive (negative) values represent spin-up (-down) states. The Fermi energy is set to zero in all panels (horizontal dashed lines).

difference of about 0.5 eV may provide a rough estimate of the strength of the residual excitonic effects in this system.

The differences between the two types of observed level structures shown in Fig. 2 can be traced to the sublattice-resolved band structure of pristine $h$-BN. At the $K$ and $K'$ points of the Brillouin zone, the valence and conduction band wave functions are composed of N-$p_z$ and B-$p_z$ orbitals only, respectively. We expect that the acceptor (donor) wave functions are mainly composed by combinations of valence (conduction) Bloch wave functions with **k** points in the vicinity of these valleys, so they should carry this information. This is indeed what we see in our PDOS calculations shown in Fig. 2. For Be(B) and S(N), the impurity replaces an atom that does not participate on the orbital composition of the valence and conduction band at the valleys, respectively. Correspondingly, the impurity states have weak amplitudes at the impurity site. For C(N) and C(B), the impurity replaces an atom that does participate on the orbital composition of the relevant band and the impurity states have strong amplitudes at the impurity site. These behaviors are also seen for the defect level wave functions, as we discuss below. Moreover, as we

discuss in Sec. III C, these properties lead to weak intervalley interaction in the former case and strong intervalley interaction on the latter, yielding the observed near-degenerate (small valley splitting) and nondegenerate ground states, respectively.

### B. Comparison between DFT and TB

We now discuss the results of our tight-binding (TB) model and how they compare with the DFT calculations. To that end, since our model does not include spin polarization, we have also performed unpolarized DFT calculations for the same supercells. By comparing the resulting band structures, we obtain the set of TB parameters $E_I$ and $K$ that best describe the DFT low-energy bands for each impurity. In Figs. 3 and 4, we present the DFT and optimal TB band structures and PDOS for acceptor and donor impurities, respectively. In Table II, we report the DFT binding energies and in Table III we present the optimal TB parameters. From the figures, we can see that there is an excellent agreement between the DFT and TB calculations and both of them reproduce the impurity

TABLE II. Supercell magnetizations ($M$) and binding energies for the ground ($E_b^0$) and first excited ($E_b^1$) impurity states, as given by unpolarized (unp.) and spin-polarized (up and down) DFT calculations. For each spin channel, the binding energies are defined with respect to the top (bottom) of the valence (conduction) bands for acceptor (donor) impurities.

| Imp. | $M$ ($\mu_B$) | $E_b^0$ (eV) | | | $E_b^1$ (eV) | | |
|------|------|------|------|------|------|------|------|
| | | unp. | up | down | unp. | up | down |
| Be(B) | 1.0 | 0.24 | 0.14 | 0.26 | 0.14 | 0.07 | 0.15 |
| C(N) | 1.0 | 0.79 | 0.30 | 1.30 | | | |
| C(B) | 1.0 | 1.08 | 1.49 | 0.46 | | | |
| S(N) | 0.9 | 0.38 | 0.57, 0.45 | 0.27 | 0.10 | 0.16 | |

level structures observed in the spin-polarized DFT calculations. Our simple TB model is capable of reproducing the two different types of level structures observed for all impurities, including their binding energies and orbital composition, as seen from the PDOS. The only disagreement for the PDOS lies at the energy range of the nondegenerate impurity level for Be(B) and S(N), where DFT predicts a larger participation

of the impurity $p_z$ orbital. Since our model only takes into account modifications of the onsite energies of the impurity site and its first and second neighbors, we conclude from our results that the impurity potential is indeed highly localized.

The wave functions of the impurity levels show important differences depending on the sublattice position of the impurity and its behavior as a donor or an acceptor. To study them, we compare the DFT local density of states (LDOS), integrated over the energy range of each impurity level, with the TB electronic density for the corresponding level, calculated at the $\Gamma$ point of the supercell. The TB wave functions were built from Slater-type $p_z$ orbitals with modified (screened) atomic numbers, as discussed in Sec. II B. The results for acceptors are shown in Fig. 5. Similar results were obtained for donor levels. Again, we see there is an excellent agreement between DFT and TB. Note that the wave function of the single defect level of C(N) [Figs. 5(a) and 5(d)] is more localized than those of the defect levels of Be(B) (other panels). Moreover, note that the wave function of the C(B) level is very localized at the impurity itself, while the wave functions for the Be(B) levels show a larger amplitude at its first neighbors, in agreement with the PDOS calculations reported in Fig. 3. Such features are a consequence of the



FIG. 3. Comparison between unpolarized DFT and TB band structures and projected density of states (PDOS) for acceptor impurities. The impurities and type of calculation are indicated on each panel. For PDOS, the black, red, and blue lines correspond to the valence $p_z$ orbital of the impurity site, one of its first neighbors, and one of its second neighbors, respectively. The Fermi energy is set to zero in all panels.
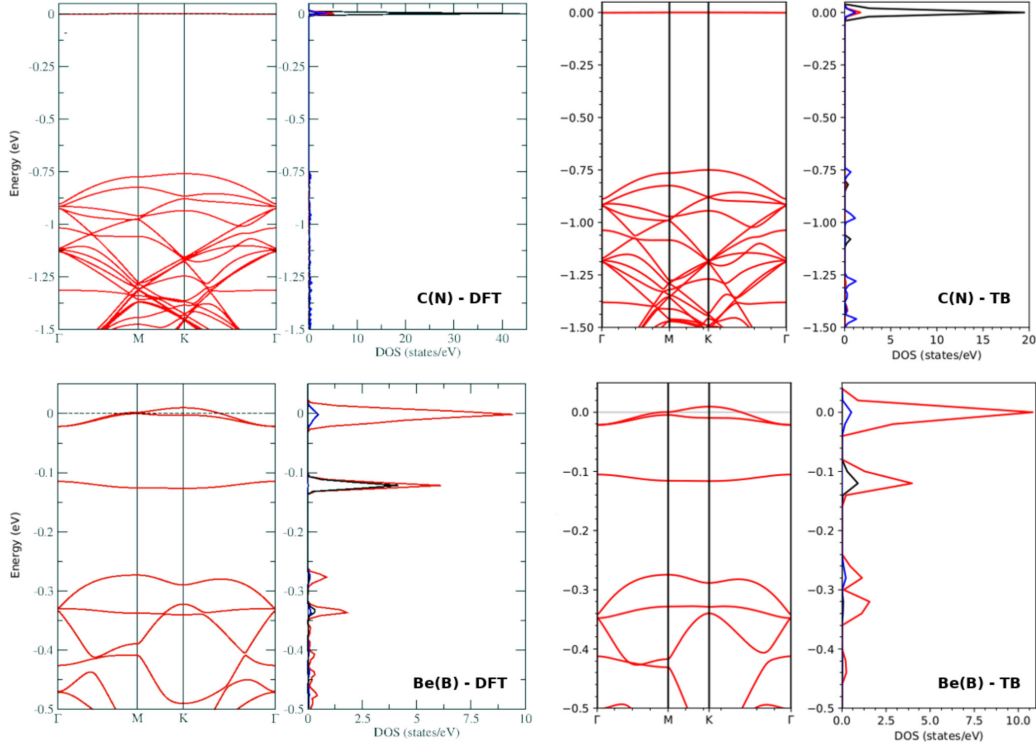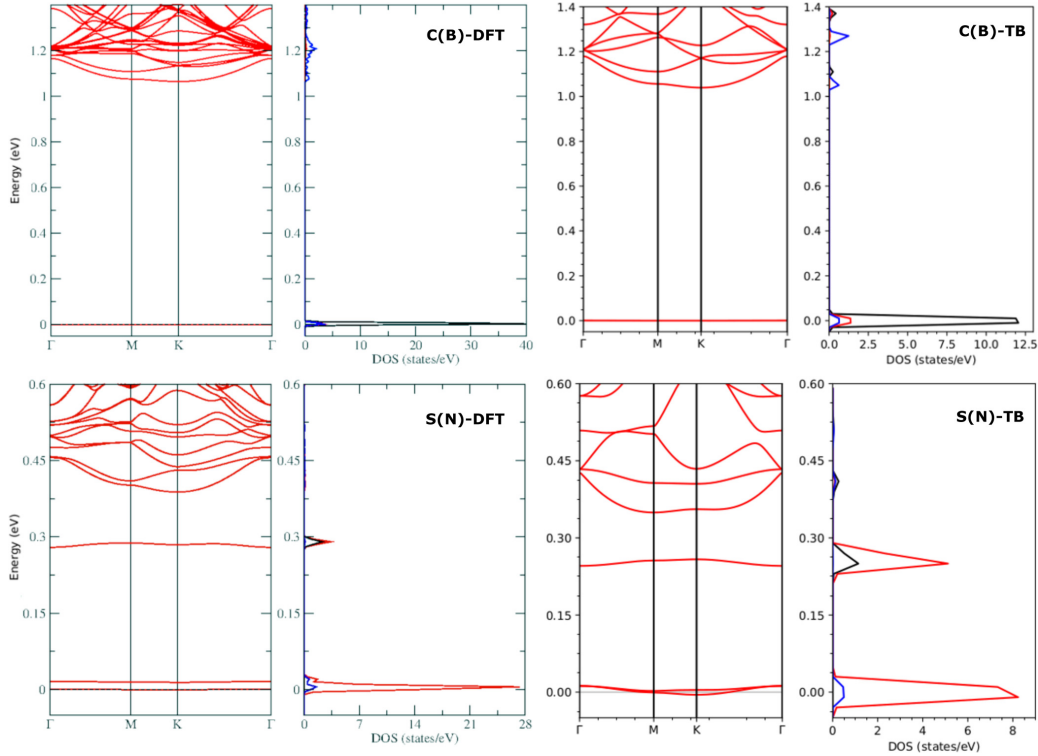
FIG. 4. Comparison between unpolarized DFT and TB band structures and projected density of states (PDOS) for donor impurities. The impurities and type of calculation are indicated on each panel. For PDOS, the black, red, and blue lines correspond to the valence $p_z$ orbital of the impurity site, one of its first neighbors, and one of its second neighbors, respectively. The Fermi energy is set to zero in all panels.

sublattice-sensitive band structure of the valence and conduction bands of pure $h$-BN at the $K$ point [14] and explain the different values obtained for the dielectric constant in Table II, as we discuss below. Finally, note that, for Be(B), the LDOS is not able to resolve the two states in the near-degenerate pair, but we can see them separately in the TB calculation. In fact, we find that those states have unequal amplitudes at each neighbor of the impurity, but the sum of their densities yields equal amplitudes, as shown in Fig. 5(f). For S(N), the small splitting of this pair in the DFT calculation allows the direct observation of each level both in DFT and TB, and a similar behavior is observed.

For C impurities, where a single defect level is seen inside the gap, we can see from Table III that the value of the screening parameter $K$ is very high. Mathematically, a very large $K$ means that the Coulomb corrections to the onsite energies of the first and second neighbors of the impurity, as given by Eq. (1), are not necessary to account for the properties of the nondegenerate level found in these cases. Therefore, the onsite energy of the impurity itself ($E_I$) is enough to reproduce the level structure in these cases. Physically, this result is related to the fact that the impurity level wave function is strongly localized at the impurity itself, with small contributions from

its neighbors, as discussed above and seen in Figs. 3, 4, and 5. The picture is quite different for the Be(B) and S(N) impurities, in which the impurity level wave functions are strongly localized at the first neighbors of the impurity and not at the impurity itself, as we can see from the same figures. As a result, the Coulomb corrections are extremely relevant in these cases, resulting in smaller values for $K$. Without these corrections, it is not possible to reproduce the $2+1$ level structure observed in these cases. We will return to this point in the next section, where we connect these properties with the sublattice-sensitive band structure of pure $h$-BN at the $K$ point

TABLE III. Tight-binding parameters that best describe the results of the unpolarized DFT calculations, as shown in Figs. 3 and 4. For a detailed description of the model, see Sec. II B.

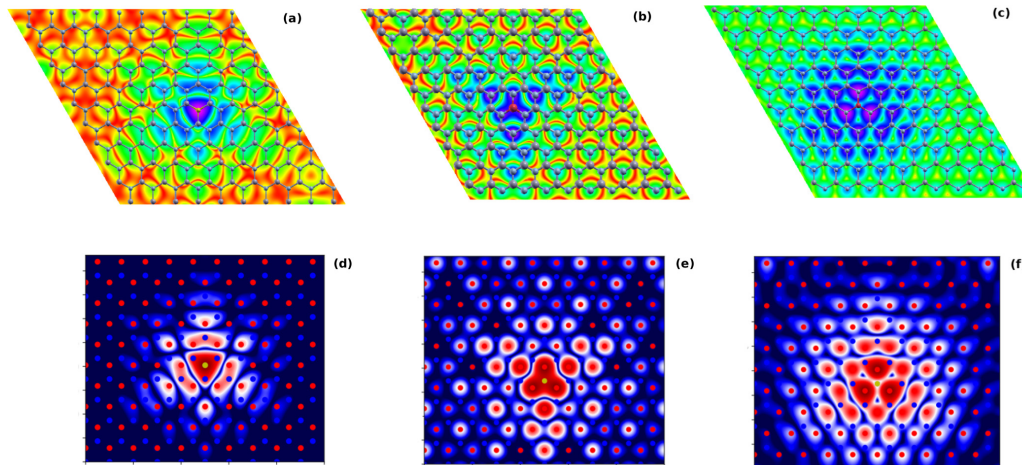| Impurity | $E_I$ (eV) | $K$ |
|---|---|---|
| Be(B) | 6.0 | 8.0 |
| C(N) | −8.5 | 50.0 |
| C(B) | −10.2 | −50.0 |
| S(N) | −20.0 | −7.0 |

FIG. 5. (a)–(c) DFT local density of states (LDOS) integrated over the energy range of the acceptor levels. (d)–(f) TB electronic densities for the corresponding acceptor levels, calculated at the $\Gamma$ point of the supercell. (a), (d) Correspond to the nondegenerate level found for the C(N) impurity; (b), (e) correspond to the nondegenerate level found for the Be(B) impurity; and (c), (f) correspond to the sum over the near-degenerate levels found for Be(B). All plots are on log scale and the color code is scaled for the minimum and maximum values on each case: Red and purple (top) and dark blue and dark red (bottom), respectively.

and the strength of the intervalley interaction, which explains these two different types of behaviors.

It is worth to mention that we also performed unpolarized DFT calculations for Mg(B), Ca(B), and Se(N) substitutional impurities, not shown here. For Mg(B) and Se(N), we also see a three-level structure with two near-degenerate levels, but the ground state is given by the nondegenerate level. For Ca(B), an even more complex level structure arises, with five levels inside the gap and a near-degenerate ground state. These level structures are an indication of stronger impurity potentials in these cases, which may induce more levels and larger valley splittings, as we discuss on the next section. They can also be explained by the TB model by using a larger difference between the onsite energies of the impurity and the replaced atom, which corresponds to the impurity potential at the position of the impurity. From these comparisons, we see that our simple TB model, including only $p_z$ orbitals and two parameters, is enough to account for the energetics and wave functions of substitutional impurity states in $h$-BN since the $\sigma$ orbitals do not play any significant role in those properties. Therefore, it can readily be adapted and employed in more complex situations where *ab initio* calculations become prohibitive, such as disordered impurities and heterostructures.

Finally, a sensitive point of supercell calculations with impurities is always their convergence with respect to the supercell size. As we mentioned above, our DFT calculations with $10\times10$ cells indicate that the cohesive and formation energies of all configurations are well converged, but one might wonder if the binding energies are also converged. This is especially true for the Be(B) and S(N) configurations, which have smaller binding energies and, correspondingly, more extended impurity states. To assess this point, we have

also performed convergence calculations with the TB model, which allows us to explore larger supercells due to its low computational cost. Supercells up to $20\times20$ were considered and the results are included as part of the Supplemental Material [69]. As discussed there, the C(N) and C(B) cases are fully converged in the $10\times10$ cell, but the Be(B) and S(N) cases are not. For instance, the binding energies for Be(B) in the $20\times20$ cell (fully converged) are 0.18 and 0.07 eV, in contrast with the values reported in Table I. Nevertheless, the level structures are identical, including the degeneracies, and the wave functions are found to have the same shape as those shown in Fig. 4, in particular their sublattice sensitivity as discussed above. Therefore, we may proceed with the DFT and TB results from the $10\times10$ supercell and use the effective mass formalism to try to understand the physical origin of these different impurity level structures, as we discuss in the next section.

### C. Effective mass calculations

In order to have a deeper understanding of the role of intervalley interaction on the observed impurity level structures, we have also performed effective mass (EM) calculations, as described in Sec. II C. We fix the effective mass to the TB value at the $K$ points, $0.60m_0$, so the only adjustable parameter in this model is the dielectric constant $K$ in Eq. (1). For simplicity, we discuss here only the case of acceptors [Be(B) and C(N)] since donors behave in a very similar fashion, as we have discussed above. The parameter $K$ is chosen in order to reproduce the DFT and TB binding energies of the impurity ground state, and we have obtained $K = 6.5$ and 10.0 for Be(B) and C(N), respectively. Note that these values are different from those reported in Table II for the TB

TABLE IV. Binding energies and envelope function amplitudes for the acceptor levels, as given by the effective mass calculations. Negative energies mean levels below the top of the valence band and negative amplitudes correspond to antisymmetrical valley combinations. Note that the absolute value of the amplitudes on each row add to one.

| Imp. | $E_b$ (eV) | K | | | | $K'$ | | | |
|---|---|---|---|---|---|---|---|---|---|
| | | $1s$ | $2s$ | $2p_x$ | $2p_y$ | $1s$ | $2s$ | $2p_x$ | $2p_y$ |
| C(N) | 0.76 | 0.50 | 0.00 | 0.00 | 0.00 | 0.49 | 0.01 | 0.00 | 0.00 |
| | 0.09 | 0.31 | 0.02 | 0.00 | 0.00 | −0.40 | 0.27 | 0.00 | 0.00 |
| | 0.04 | 0.05 | −0.89 | 0.00 | 0.00 | −0.03 | −0.03 | 0.00 | 0.00 |
| | 0.03 | 0.00 | 0.00 | −0.50 | 0.00 | 0.00 | 0.00 | 0.50 | 0.00 |
| | 0.03 | 0.00 | 0.00 | 0.50 | 0.00 | 0.00 | 0.00 | 0.50 | 0.00 |
| | 0.01 | −0.14 | −0.08 | 0.00 | 0.00 | 0.08 | 0.70 | 0.00 | 0.00 |
| | −0.04 | 0.00 | 0.00 | 0.00 | 0.50 | 0.00 | 0.00 | 0.00 | 0.50 |
| | −0.04 | 0.00 | 0.00 | 0.00 | 0.50 | 0.00 | 0.00 | 0.00 | −0.50 |
| Be(B) | 0.27 | −0.40 | 0.10 | 0.00 | 0.00 | 0.40 | −0.10 | 0.00 | 0.00 |
| | 0.27 | 0.40 | −0.10 | 0.00 | 0.00 | 0.40 | −0.10 | 0.00 | 0.00 |
| | 0.08 | 0.00 | 0.00 | −0.50 | 0.00 | 0.00 | 0.00 | 0.50 | 0.00 |
| | 0.08 | 0.00 | 0.00 | 0.50 | 0.00 | 0.00 | 0.00 | 0.50 | 0.00 |
| | 0.01 | 0.10 | 0.40 | 0.00 | 0.00 | 0.10 | 0.40 | 0.00 | 0.00 |
| | 0.01 | 0.10 | 0.40 | 0.00 | 0.00 | −0.10 | −0.40 | 0.00 | 0.00 |
| | −0.09 | 0.00 | 0.00 | 0.00 | 0.50 | 0.00 | 0.00 | 0.00 | 0.50 |
| | −0.09 | 0.00 | 0.00 | 0.00 | −0.50 | 0.00 | 0.00 | 0.00 | 0.50 |

calculations, especially for the C(N) case. This difference may be attributed to two factors. The first one is that, even though the Coulomb potential has the same form in both calculations [Eq. (1)], its implementation is a bit different. The TB model is an atomistic calculation in which the Coulomb energy is only added to the first and second neighbors of the impurity. On the other hand, the effective mass model is a continuum calculation, in which the potential is defined in all space, which naturally includes the position of the impurity. Second, the TB model has two parameters that deal with the effect of the impurity potential: The impurity onsite energy ($E_I$) and the dielectric constant $K$. The effective mass model has only one: The dielectric constant. As such, we do not expect that the values of $K$ from both models should be strictly equal. Still, we see that they are consistent. Note that the EM values of $K$ are both smaller than the TB values and the value for C(N) is larger than the value of Be(B) in both cases. Therefore, we believe that both models can be independently used and adapted to other binary 2D semiconductors and insulators and that their results should be consistent.

The binding energies and envelope amplitudes for these two impurities are shown in Table IV. The amplitudes are defined as the square modulus of the expansion coefficients of the envelope functions appearing in Eq. (2) in terms of screened 2D hydrogenic envelopes. A negative value is assigned to them whenever the full wave function is an antisymmetrical valley combination of the corresponding envelopes. Notice the striking difference between the level structures for each impurity. For C(N), a nondegenerate ground state is found with a binding energy of 0.76 eV, in good agreement with the DFT and TB results. In Fig. 6, we show the EM wave functions for the ground and first excited impurity functions for this case. By comparing with Figs. 5(a) and 5(d), we see there is a good agreement between the EM, DFT, and TB ground-state wave functions. However, the EM wave function is not able to capture the amplitudes at the B sites, which

can be readily understood by looking at Eq. (2). Note that the Bloch wave functions appearing in this equation are calculated at the $K$ and $K'$ points and, for the valence band, they have zero amplitude at these sites. Therefore, the full wave function has the same property. From Fig. 6, we can also see that the wave function of the first excited state spreads more throughout the supercell, which is an indication that this level and the other excited states, not seen in DFT and TB, may be mixed within the valence band. Moreover, from Table IV, we see that the ground and first excited states are mostly valley symmetrical and antisymmetrical combinations of 1s envelopes, respectively, with a small mixing of 2s envelopes. The large energy difference between these levels (0.67 eV) is a clear indication of a strong intervalley interaction in this case.

In contrast, the picture is quite different for Be(B). In this case, all levels are doubly degenerate, which is a clear indication of weak intervalley interaction. In fact, it can be
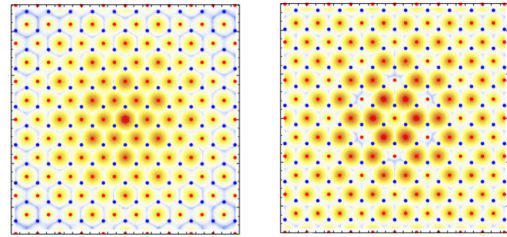


FIG. 6. EM wave functions for the ground (left) and first excited (right) impurity states of C(N). The binding energies and envelope amplitudes are shown on Table IV. Both plots are on log scale and the color code is scaled for the minimum and maximum values on each case.

shown that when one approximates the Bloch wave functions at the valleys as a Bloch sum over the nitrogen atoms that are closest to the impurity for the calculation of the intervalley interaction in Eq. (3), the result is zero. This happens because one can factor out the structure factor $f(\mathbf{K}) = 1 + e^{i2\mathbf{K}\cdot\mathbf{a}_2} + e^{i2\mathbf{K}\cdot(\mathbf{a}_1+\mathbf{a}_2)}$ from the intervalley interaction, which is zero at the $K$ point ($\mathbf{a}_1$ and $\mathbf{a}_2$ are the primitive lattice vectors of $h$-BN). Therefore, the sublattice-resolved electronic structure of $h$-BN plays a crucial role on the strength of the intervalley interaction. The combination of a zero amplitude for the valley wave functions at the impurity site and the symmetry of lattice results in the observed level structure for this case.

By comparing the level structure given by the EM calculations with the DFT and TB structures shown in Fig. 3, we see that we are able to reproduce the near doubly degenerate ground state, for which the wave functions are mostly valley symmetrical and antisymmetrical combinations of $1s$ envelopes. However, the EM approximation fails to reproduce the nondegenerate excited state. By looking at the PDOS in the same figure and the corresponding wave functions in Figs. 5(b) and 5(c), we see that this state has a nonzero amplitude at the impurity site, in contrast with the zero amplitude for the ground-state wave functions. According to our discussion above, this feature cannot be captured by the effective mass formalism, in which the valence band wave functions appearing in Eqs. (2) and (3) have zero amplitude at the boron sites for both $K$ and $K'$ points. Therefore, for an accurate description of this particular state one may need to go beyond the standard effective mass formalism, by including corrections to Eqs. (2) and (3) that contain more information about the Bloch wave functions for $\mathbf{k}$ points in the vicinity of the $K$ and $K'$ points, which have small nonzero amplitudes at the impurity site. Including these states should lead to an increased intervalley interaction and break the degeneracy of this state, in a similar fashion to the C(N) case. Note, however, that all other states found for both impurities are fully described by the standard formalism.

Finally, we must discuss how our results hold in light of the band-gap controversy mentioned in Sec. II B. First of all, as already mentioned in that section, the controversy lies only in the position of the bottom of the conduction band (CBM). The position of the top of the valence band (VBM) unmistakably lies at the $K$ point, as supported by several calculations. As a result, the electronic properties of acceptor impurities should be calculation independent, as the impurity levels are composed mostly by Bloch states near the VBM, provided they are not deep in comparison with the energy gap. Such deep states are not seen in our DFT calculations, so we believe our results for the electronic properties of acceptor levels are solid.

For donor levels, the picture is more complicated. For example, in the $GW$ calculation of Ref. [47], the authors see a $\sim$0.45 eV difference between the conduction band energies at the $K$ and $\Gamma$ points, with the latter being the CBM. Reference [46] reports a similar result. This is the opposite of what we find in our DFT calculations. Still, the closeness of these energies means that, in principle, impurity states inside the gap may be related to both minima at $K$ and $\Gamma$. However, given that the minimum at $\Gamma$ has a $\sigma$ character and the minimum at $K$ has a $p_z$ character, we expect that the sets of impurity states

related to these minima will not mix. Therefore, the properties of donor levels related to the minimum at $K$, as discussed in this work, should be solid. The sublattice sensitivity and its impact on the intervalley interaction should be the same. On the other hand, given the binding energies reported in Table II, some of these levels may not lie inside the gap, but may lie between the energies of the $K$ and $\Gamma$ minima. This may be the case of the S(N) impurity.

Finally, we mention that we see no evidence of donor levels with $\sigma$ character in our calculations, neither inside the gap nor between the $K$ and $\Gamma$ point energies. These results are confirmed by PDOS calculations in DFT. This may be related to the fact that, according to our DFT calculations, none of the impurities induce any out-of-plane distortions in the structure, so we do not see any rehybridization between and $pz$ orbitals. Moreover, given that the extra or missing electron from the impurities lies at an atomic $p_z$ orbital, we expect that these orbitals dictate the low-energy impurity level structure. We believe that higher-level $GW$ calculations should confirm these properties. Conversely, more "drastic" defects, such as vacancies, remove both $p_z$ and $\sigma$ electrons from the lattice and may induce both sets of defect levels. In fact, defect levels related to the conduction band minimum at $\Gamma$, if present, should display single-valley physics, in contrast with the two-valley physics we observe in this work.

## IV. CONCLUSIONS

We have studied the electronic and magnetic properties of substitutional impurities in $h$-BN by using a combination of different theoretical methods. We have found that these defects induce exotic levels inside the band gap, whose structure and degeneracy strongly depend on the sublattice position of the impurity and its behavior as a donor or an acceptor. In fact, such dependence can only be understood by taking into account the peculiar sublattice-resolved electronic structure of pristine $h$-BN and its impact on the strength of the intervalley interaction induced by the impurity potential. Since the valence and conduction band wave functions at the $K$ and $K'$ points consist only of N-$p_z$ and B-$p_z$ orbitals, respectively, the system will respond very differently according to the atom replaced. For instance, when a donor impurity replaces a B atom, which participates in the orbital composition of the conduction band, we find that the resulting intervalley interaction is strong, leading to a non-valley-degenerate impurity ground state, which is composed mostly of a valley-symmetrical combinations of $1s$ 2D hydrogenic envelopes. Spin degeneracy is also broken and a large split is observed. On the other hand, when a donor impurity replaces a N atom, which does not participate on the orbital composition of the same band, the resulting intervalley interaction is weaker and near-valley-degenerate levels are found, which constitute the ground state for Be(B) and S(N) impurities. These states are composed mostly of valley-symmetrical and antisymmetrical combinations of $1s$ envelopes. Excited states are also found inside the gap and spin splittings are smaller. Acceptor impurities behave in a similar fashion and respond to the orbital composition of the valence band.

Since we do not see any signatures of donor levels with $\sigma$ character, we do not expect that the band-gap controversy of

$h$-BN will strongly disrupt these results. The induced donor levels have a $p_z$ character and, as such, they are composed by Bloch states near the $K$ point of the conduction band, even if this point is not the global minimum. However, if the gap is indirect, some of the donor levels might not lie inside the gap if their binding energies are smaller than the energy difference between the conduction band energies at the $K$ and $\Gamma$ points. Even if $\sigma$ levels were present, as they might be, for example, in the case of vacancies, we expect that the mixing between $\sigma$ and $p_z$ states will be very small, if present at all. Therefore, these levels will be independent and may display different valley physics.

Our conclusions are fairly general and should apply to other systems with similar sublattice-resolved electronic states. It is important to mention that a sublattice-sensitive band structure is also found in conventional 3D binary compounds, such as cubic (zinc-blende) AlAs. However, the valley and spin splittings found in these materials are usually much smaller due to the stronger screening [70]. In that sense, binary 2D materials and their multilayers may constitute an ideal platform for the observation of these exotic level structures. Honeycomb lattices formed by III-V compounds, for which $h$-BN is the most famous example but other combinations such as BP, AlAs, and InAs are included, are potential candidates, as indicated by earlier calculations [71]. Moreover, some of them might be free from the band-gap controversy mentioned above, making it easier to consider all types of substitutional impurities on them. In all cases, the influence of the chemical imbalance between the impurity and the replaced atom on the strength of the intervalley interaction also plays an important role on the observed impurity level structures. The models and calculations developed in this work can be readily adapted and employed in such systems and may also deal with more complex situations, where *ab initio* methods become prohibitive. Moreover, such impurities can also be employed to engineer the optical properties of these materials for future devices, by inducing different optical transitions between the bands and the impurity levels and, possibly, exciton trapping, as already seen for acceptor impurities in bulk $h$-BN. Even though our calculations are not able to quantitatively predict the optical excitation energies associated with these transitions, as those need a proper description of the quasiparticle effects and the electron-hole interaction [15–17], they may serve as a guide to more refined calculations and may motivate new experiments with these materials.

[1] A. H. Castro Neto, F. Guinea, N. M. R. Peres, K. S. Novoselov, and A. K. Geim, Rev. Mod. Phys. **81**, 109 (2009).

[2] K. S. Novoselov, V. I. Falko, L. Colombo, P. R. Gellert, M. G. Schwab, and K. Kim, Nature (London) **490**, 192 (2012).

[3] A. C. Ferrari, F. Bonaccorso, V. Fal'ko, K. S. Novoselov, S. Roche, P. Boggild, S. Borini, F. H. L. Koppens, V. Palermo, N. Pugno, J. A. Garrido, R. Sordan, A. Bianco, L. Ballerini, M. Prato, E. Lidorikis, J. Kivioja, C. Marinelli, T. Ryhanen, A. Morpurgo *et al.*, Nanoscale **7**, 4598 (2015).

[4] S. Z. Butler, S. M. Hollen, L. Cao, Y. Cui, J. A. Gupta, H. R. Gutiérrez, T. F. Heinz, S. S. Hong, J. Huang, A. F. Ismach, E. Johnston-Halperin, M. Kuno, V. V. Plashnitsa, R. D. Robinson, R. S. Ruoff, S. Salahuddin, J. Shan, L. Shi, M. G. Spencer, M. Terrones *et al.*, ACS Nano **7**, 2898 (2013).

[5] A. K. Geim and I. V. Grigorieva, Nature (London) **499**, 419 (2013).

[6] K. S. Novoselov, A. Mishchenko, A. Carvalho, and A. H. Castro Neto, Science **353**, aac9439 (2016).

[7] C. Attaccalite, M. Bockstedte, A. Marini, A. Rubio, and L. Wirtz, Phys. Rev. B **83**, 144115 (2011).

[8] B. Arnaud, S. Lebègue, P. Rabiller, and M. Alouani, Phys. Rev. Lett. **96**, 026402 (2006).

[9] K. Watanabe, T. Taniguchi, and H. Kanda, Nat. Mater. **3**, 404 (2004).

[10] Y. Kubota, K. Watanabe, O. Tsuda, and T. Taniguchi, Science **317**, 932 (2007).

[11] M. G. Silly, P. Jaffrennou, J. Barjon, J.-S. Lauret, F. Ducastelle, A. Loiseau, E. Obraztsova, B. Attal-Tretout, and E. Rosencher, Phys. Rev. B **75**, 085205 (2007).

[12] G. Cassabois, P. Valvin, and B. Gil, Nat. Photon. **10**, 262 (2016).

[13] G. Cassabois, P. Valvin, and B. Gil, Phys. Rev. B **93**, 035207 (2016).

[14] T. Galvani, F. Paleari, H. P. C. Miranda, A. Molina-Sánchez, L. Wirtz, S. Latil, H. Amara, and F. Ducastelle, Phys. Rev. B **94**, 125303 (2016).

[15] J. Koskelo, G. Fugallo, M. Hakala, M. Gatti, F. Sottile, and P. Cudazzo, Phys. Rev. B **95**, 035125 (2017).

[16] L. Sponza, H. Amara, C. Attaccalite, S. Latil, T. Galvani, F. Paleari, L. Wirtz, and F. Ducastelle, Phys. Rev. B **98**, 125206 (2018).

[17] L. Schué, L. Sponza, A. Plaud, H. Bensalah, K. Watanabe, T. Taniguchi, F. Ducastelle, A. Loiseau, and J. Barjon, Phys. Rev. Lett. **122**, 067401 (2019).

[18] C. R. Dean, A. F. Young, I. Meric, C. Lee, L. Wang, S. Sorgenfrei, K. Watanabe, T. Taniguchi, P. Kim, K. L. Shepard, and J. Hone, Nat. Nanotechnol. **5**, 722 (2010).

[19] L. Ci, L. Song, C. Jin, D. Jariwala, D. Wu, Y. Li, A. Srivastava, Z. F. Wang, K. Storr, L. Balicas, F. Liu, and P. M. Ajayan, Nat. Mater. **9**, 430 (2010).

[20] M. P. Levendorf, C.-J. Kim, L. Brown, P. Y. Huang, R. W. Havener, D. A. Muller, and J. Park, Nature (London) **488**, 627 (2012).

[21] Z. Liu, L. Ma, G. Shi, W. Zhou, Y. Gong, S. Lei, X. Yang, J. Zhang, J. Yu, K. P. Hackenberg, A. Babakhani, J.-C. Idrobo, R. Vajtai, J. Lou, and P. M. Ajayan, Nat. Nanotechnol. **8**, 119 (2013).

[22] M. Kan, J. Zhou, Q. Wang, Q. Sun, and P. Jena, Phys. Rev. B **84**, 205412 (2011).

[23] Y. Liu, X. Wu, Y. Zhao, X. C. Zeng, and J. Yang, J. Phys. Chem. C **115**, 9442 (2011).

[24] M. G. Menezes and R. B. Capaz, Phys. Rev. B **86**, 195413 (2012).

[25] A. Katzir, J. T. Suss, A. Zunger, and A. Halperin, Phys. Rev. B **11**, 2370 (1975).

[26] A. W. Moore and L. S. Singer, J. Phys. Chem. Solids **33**, 343 (1972).

[27] L. Museur, E. Feldbach, and A. Kanaev, Phys. Rev. B **78**, 155204 (2008).

[28] R. Bourrellier, S. Meuret, A. Tararan, O. Stéphan, M. Kociak, L. H. G. Tizei, and A. Zobelli, Nano Lett. **16**, 4317 (2016).

[29] B. He, W. J. Zhang, Z. Q. Yao, Y. M. Chong, Y. Yang, Q. Ye, X. J. Pan, J. A. Zapien, I. Bello, S. T. Lee, I. Gerhards, H. Zutz, and H. Hofsäss, Appl. Phys. Lett. **95**, 252106 (2009).

[30] S. Majety, T. C. Doan, J. Li, J. Y. Lin, and H. X. Jiang, AIP Adv. **3**, 122116 (2013).

[31] X. Zhang, Thin Solid Films **544**, 2 (2013).

[32] W. Kohn and J. M. Luttinger, Phys. Rev. **98**, 915 (1955).

[33] K. S. Thygesen, 2D Mater. **4**, 022004 (2017).

[34] S. Latini, T. Olsen, and K. S. Thygesen, Phys. Rev. B **92**, 245123 (2015).

[35] D. Y. Qiu, F. H. da Jornada, and S. G. Louie, Phys. Rev. B **93**, 235435 (2016).

[36] P. Hohenberg and W. Kohn, Phys. Rev. **136**, B864 (1964).

[37] W. Kohn and L. J. Sham, Phys. Rev. **140**, A1133 (1965).

[38] J. M. Soler, E. Artacho, J. D. Gale, A. García, J. Junquera, P. Ordejón, and D. Sánchez-Portal, J. Phys.: Condens. Matter **14**, 2745 (2002).

[39] N. Troullier and J. L. Martins, Phys. Rev. B **43**, 1993 (1991).

[40] M. Dion, H. Rydberg, E. Schröder, D. C. Langreth, and B. I. Lundqvist, Phys. Rev. Lett. **92**, 246401 (2004).

[41] G. Roman-Perez and J. M. Soler, Phys. Rev. Lett. **103**, 096102 (2009).

[42] H. J. Monkhorst and J. D. Pack, Phys. Rev. B **13**, 5188 (1976).

[43] J. C. Meyer, A. Chuvilin, G. Algara-Siller, J. Biskupek, and U. Kaiser, Nano Lett. **9**, 2683 (2009).

[44] L. Liu, Y. P. Feng, and Z. X. Shen, Phys. Rev. B **68**, 104102 (2003).

[45] W. Harrison, *Elementary Electronic Structure* (World Scientific, Singapore, 1999).

[46] W. Xia and P. Zhang (private communication).

[47] F. Ferreira, A. J. Chaves, N. M. R. Peres, and R. M. Ribeiro, J. Opt. Soc. Am. B **36**, 674 (2019).

[48] X. Blase, A. Rubio, S. G. Louie, and M. L. Cohen, Phys. Rev. B **51**, 6868 (1995).

[49] R. M. Ribeiro and N. M. R. Peres, Phys. Rev. B **83**, 235312 (2011).

[50] D. Wickramaratne, L. Weston, and C. G. Van de Walle, J. Phys. Chem. C **122**, 25524 (2018).

[51] P. Cudazzo, L. Sponza, C. Giorgetti, L. Reining, F. Sottile, and M. Gatti, Phys. Rev. Lett. **116**, 066803 (2016).

[52] J. C. Slater, Phys. Rev. **36**, 57 (1930).

[53] K. Shindo and H. Nara, J. Phys. Soc. Jpn. **40**, 1640 (1976).

[54] J. K. Gamble, N. T. Jacobson, E. Nielsen, A. D. Baczewski, J. E. Moussa, I. Montaño, and R. P. Muller, Phys. Rev. B **91**, 235318 (2015).

[55] X. L. Yang, S. H. Guo, F. T. Chan, K. W. Wong, and W. Y. Ching, Phys. Rev. A **43**, 1186 (1991).

[56] S. Ullah, P. A Denis, and F. Sato, Appl. Mater. Today **9**, 333 (2017).

[57] S. Ullah, A. Hussain, and F. Sato, RSC Adv. **7**, 16064 (2017).

[58] S. Ullah, P. A. Denis, R. B. Capaz, and F. Sato, New J. Chem. **43**, 2933 (2019).

[59] S. Ullah, P. A. Denis, and F. Sato, Chem. Phys. Chem. **18**, 1864 (2017).

[60] N. Berseneva, A. Gulans, A. V. Krasheninnikov, and R. M. Nieminen, Phys. Rev. B **87**, 035404 (2013).

[61] Y. Fujimoto and S. Saito, Phys. Rev. B **93**, 045402 (2016).

[62] M. Gao, M. Adachi, A. Lyalin, and T. Taketsugu, J. Phys. Chem. C **120**, 15993 (2016).

[63] S. Ullah, P. A. Denis, and F. Sato, New J. Chem. **42**, 10842 (2018).

[64] M. M. Ugeda, I. Brihuega, F. Guinea, and J. M. Gómez-Rodríguez, Phys. Rev. Lett. **104**, 096804 (2010).

[65] H. González-Herrero, J. M. Gómez-Rodríguez, P. Mallet, M. Moaied, J. J. Palacios, C. Salgado, M. M. Ugeda, J.-Y. Veuillen, F. Yndurain, and I. Brihuega, Science **352**, 437 (2016).

[66] Y. Zhang, S.-Y. Li, S. Huang, W.-T. Li, J.-B. Qiao, W.-X. Wang, L.-J. Yin, K.-K. Bai, W. Duan, and L. He, Phys. Rev. Lett. **117**, 166801 (2016).

[67] J. M. Pruneda, Phys. Rev. B **81**, 161409(R) (2010).

[68] S. Bhowmick, A. K. Singh, and B. I. Yakobson, J. Phys. Chem. C **115**, 9889 (2011).

[69] See Supplemental Material at http://link.aps.org/supplemental/10.1103/PhysRevB.100.085427 for discussions of the band structure in a wide energy range and the convergence in our calculations.

[70] M. Stavola, *Identification of Defects in Semiconductors*, Semiconductors and Semimetals (Academic Press, New York, 1998).

[71] B. Onat, L. Hallioglu, S. Ipek, and E. Durgun, J. Phys. Chem. C **121**, 4583 (2017).

Part IV

Conclusions

## 10 Main conclusions

We investigate two types of doping models in graphene namely rectangular doping and hexagonal doping. In the rectangular configuration, the upper dopant sites are shifted along the positive x-axis in comparison with the upper dopant sites in the hexagonal configuration by a distance equal to the lattice constant of graphene. It is found that hexagonal doping can cause an exponential increment in the bandgap opening, whereas a linear rise is noted for rectangular doping. In addition, with hexagonal doping, the cohesive energy of graphene can be preserved up to a larger extent due to larger gaps at a lower concentration. We also propose a new family of doped graphene called triple doped graphene. Simultaneous integration of three dopants in graphene was studied and found that these systems carry interesting electronic properties. Besides, the chemical reactivity can immensely be enhanced by triple doping.Having said that, these systems can be utilized in various catalytic activities.

Several graphene-based anode materials for alkali-based batteries were designed. These include monodoped and dual doped graphene (DDG) systems. It is found that the insertion of dual doping is easier in comparison with single doping in graphene. Additionally, we note a massive rise in the storage capacity for Li, Na, and K. The storage capacity of Li, Na, and K can be uplifted to 2334, 1012, and 747 mAh/g, respectively.It should be noted that the storage Li/Na storage capacity of the graphite is just limited to 372/35 mAh/g. Nevertheless, several members of the DDG family were also investigated as potential anode materials.

We also propose possible anode materials other than graphene for metal-based batteries. These materials are $h$BP and $h$BAs which can store alkali atoms with a high concentration. The storage capacity for Li and Na can be as high as 1283 mAh/g, whereas, for K, 642 mAh/g can be achieved. Furthermore, $h$BAs offers quite a low diffusion barrier for all the studied alkali atoms which is a key factor in defining the worth of an anode material. Moreover, the performance of various DFT functionals was also compared and found that several versatile vdW-DF functionals overestimate the binding of alkali atoms. Having said that, the binding can be as different as 0.7 eV/atom. Consequently, these functionals should be used with great care.

The theoretical characterizations of several other 2D materials were performed. In the first place, we carefully analyze the hydrogenation and fluorination of monolayer BP and BAs. We find that the hydrogenated layers carry larger and indirect bandgaps, whereas fluorinated layers bear smaller and direct bandgaps. Besides, the stability of a new 2D material, $Be_3N_2$, was also proposed. Furthermore, it is a wide gap semiconductor with the optical properties in the deep UV range. Finally, various aspects of the recently

synthesized $B_3O_3$ monolayer were also explored. It has a wide bandgap and excellent kinetic stability. Furthermore, bilayers and graphite-like bulk phases were also investigated. Additionally, the introduction of an external electric field can engineer the optoelectronic properties.These theoretical investigations significantly enrich the family of 2D materials and provide a clue for the next-generation functional nanomaterials.

The optoelectronic properties of pristine and hybrid $h$BP/$h$BAs bilayer were systematically investigated. A great tunability in the optoelectronic properties as a function of an external electric field is observed. Janus-like BAs bilayer composed of one hydrogenated layer and one fluorinated layer is also explored. The wider gaps of the individual layer can significantly be reduced in bilayer formand can greatly be tuned by selecting different stacking arrangements. In addition to this, it is found that $SiC_3$-$h$BN vdW heterostructures have enough bandgap opening to be utilized in nanoelectronic devices and, furthermore, can finely be tuned with the introduction of the external electric field. In addition, strong absorption peaks were observed in the visible and UV range. These heterostructures are a potential replacement for graphene where the gap opening is not sufficient and, furthermore, weakly tunable.

The electronic properties of donor and acceptor impurity levels inside the gap of $h$BN are found to be quite exotic. These impurity levels depend on the sublattice position, as well as the behavior as an acceptor or a donor. For C(N), we observed a single impurity level inside the gap which is coming from the $p_z$ orbital of C. In addition, (2+1) level structure was observed for Be(B) which are mostly composed of $p_z$ orbitals of neighboring N.

## 10.1 Further recommendation and future prospects

*"Our imagination is the only limit to what we can hope to have in the future."*

Charles F. Kettering

In this Ph.D. thesis, several aspects of the 2D materials were studied. In chapter 4, it is shown that doping is an efficient way of introducing a sizeable gap around the Dirac point in graphene. In addition, these dopants can significantly increase the chemical reactivity of graphene which can further be utilized in catalytic processes. However, at the same time, these dopants gravely affect the carrier mobility in graphene, one of the characteristics for which graphene is famous. Having said that, the search of a certain technique or suitable dopant(s) become critical by which a finite gap can be introduced without the degradation of the carrier mobility.

In chapters 5 and 6, the electrochemical properties of doped graphene and some

other 2D materials were studied to search for a possible anode material for alkali-based batteries. Despite the fact that lots of hurdles were solved in this thesis with some great achievements, the designing of anode materials still remains an open challenge. Some of our proposed materials can achieve as large storage capacity as 2300 mAh/g but at the same time, the open-circuit voltage is also on the higher side. Moreover, with some materials, we got outstanding open circuit voltage but the storage capacities were not that phenomenal. Having said that, an efficient anode material offers large storage capacity, as low as possible open-circuit voltage, exceptional ionic mobility and electronic conductivities, and brilliant structural properties that are less affected by the loading and unloading of the alkali atoms.

In chapters 7 and 8, several other 2D materials and vdW heterostructures were designed for their potential use in optoelectronics and nanoelectronics. As graphene cannot be used in FETs due to the bandgap issue, the designing of other 2D materials becomes crucial. We propose several materials with the perfect tunable band gaps. However, it is necessary to search a 2D material not only with that perfect tunable gap but also with the superb carrier mobility. In addition, graphene can greatly restore its carrier mobility when combining in the vdW heterostructure form with $h$BN but the gap opening is not sufficient to be utilized in FETs. We addressed this issue by using SiC$_3$-$h$BN vdW heterostructures which offer sizeable gaps, great tunability in the gaps, and well-preserved carrier mobility. However, the lattice mismatch is about 10% which is somewhat larger. In this regard, a vdW heterostructure with the aforementioned properties can be an excellent candidate if the lattice mismatch is within 5%. Additionally, a higher level of theory, such as GW/BSE is required to search for the interlayer exciton.

In chapter 9, as it is mentioned that doping is an efficient technique to alter the optoelectronic properties of a semiconductor. The integration of a dopant induces an impurity level inside the gap of a semiconductor which can make the transition from the impurity level to the conduction (valence) band possible, thus designing the optical properties of the material. We studied the electronic properties of donor and acceptor impurity levels inside the gap of $h$BN which carried some exotic physics. Depending on the computational resources, GW/BSE calculations can provide further interesting insights, especially for the donor cases as there is a disagreement in the literature about the direct-indirect gap of $h$BN. Additionally, the role of donor and acceptor impurities are less investigated in transition metal dichalcogenides (TMDCs). It would be interesting to see how TMDCs will be responding to the insertion of such impurities.

# REFERENCES

1  GEIM, A. K.; NOVOSELOV, K. S. The rise of graphene. In: *Nanoscience and Technology: A Collection of Reviews from Nature Journals.* [S.l.]: World Scientific, 2010. p. 11–19.

2  YANG, G. et al. Structure of graphene and its disorders: a review. *Science and technology of advanced materials*, Taylor & Francis, v. 19, n. 1, p. 613–648, 2018.

3  NETO, A. C. et al. The electronic properties of graphene. *Reviews of modern physics*, APS, v. 81, n. 1, p. 109, 2009.

4  ERVASTI, M. M. et al. Silicon and silicon-nitrogen impurities in graphene: Structure, energetics, and effects on electronic transport. *Physical Review B*, APS, v. 92, n. 23, p. 235412, 2015.

5  PETROSKI, H. *The pencil: A history of design and circumstance.* [S.l.]: Alfred a Knopf Incorporated, 1992.

6  WALLACE, P. R. The band theory of graphite. *Physical Review*, APS, v. 71, n. 9, p. 622, 1947.

7  PEIERLS, R. Quelques propriétés typiques des corps solides. In: *Annales de l'institut Henri Poincaré.* [S.l.: s.n.], 1935. v. 5, n. 3, p. 177–222.

8  LANDAU, L. Zur theorie der phasenumwandlungen ii. *Phys. Z. Sowjetunion*, v. 11, n. 545, p. 26–35, 1937.

9  MERMIN, N. D. Crystalline order in two dimensions. *Physical Review*, APS, v. 176, n. 1, p. 250, 1968.

10  VENABLES, J.; SPILLER, G. Nucleation and growth of thin films. In: *Surface Mobilities on Solid Materials.* [S.l.]: Springer, 1983. p. 341–404.

11  EVANS, J.; THIEL, P.; BARTELT, M. C. Morphological evolution during epitaxial thin film growth: Formation of 2d islands and 3d mounds. *Surface science reports*, Elsevier, v. 61, n. 1-2, p. 1–128, 2006.

12  NOVOSELOV, K. S. et al. Electric field effect in atomically thin carbon films. *science*, American Association for the Advancement of Science, v. 306, n. 5696, p. 666–669, 2004.

13  NOVOSELOV, K. S. et al. Two-dimensional atomic crystals. *Proceedings of the National Academy of Sciences*, National Acad Sciences, v. 102, n. 30, p. 10451–10453, 2005.

14  LEE, C. et al. Measurement of the elastic properties and intrinsic strength of monolayer graphene. *science*, American Association for the Advancement of Science, v. 321, n. 5887, p. 385–388, 2008.

15  SARMA, S. D. et al. Electronic transport in two-dimensional graphene. *Reviews of modern physics*, APS, v. 83, n. 2, p. 407, 2011.

16  GEIM, A.; NOVOSELOV, K. The rise of graphene. *Nature materials*, v. 6, p. 183–191, 2007.

17  NOVOSELOV, K. S. et al. Two-dimensional gas of massless dirac fermions in graphene. *nature*, Nature Publishing Group, v. 438, n. 7065, p. 197, 2005.

18  GEIM, A. K. Graphene: status and prospects. *science*, American Association for the Advancement of Science, v. 324, n. 5934, p. 1530–1534, 2009.

19  SCHWIERZ, F. Graphene transistors. *Nature nanotechnology*, Nature Publishing Group, v. 5, n. 7, p. 487, 2010.

20  CASTRO, E. V. et al. Limits on charge carrier mobility in suspended graphene due to flexural phonons. *Physical review letters*, APS, v. 105, n. 26, p. 266601, 2010.

21  TAN, Y.-W. et al. Measurement of scattering rate and minimum conductivity in graphene. *Physical review letters*, APS, v. 99, n. 24, p. 246803, 2007.

22  KAKU, M. *Physics of the future: How science will shape human destiny and our daily lives by the year 2100.* [S.l.]: Anchor, 2012.

23  SCROSATI, B. Recent advances in lithium ion battery materials. *Electrochimica Acta*, Elsevier, v. 45, n. 15-16, p. 2461–2466, 2000.

24  TARASCON, J.-M.; ARMAND, M. Issues and challenges facing rechargeable lithium batteries. In: *Materials for Sustainable Energy: A Collection of Peer-Reviewed Research and Review Articles from Nature Publishing Group.* [S.l.]: World Scientific, 2011. p. 171–179.

25  GOODENOUGH, J. B.; KIM, Y. Challenges for rechargeable li batteries. *Chemistry of materials*, ACS Publications, v. 22, n. 3, p. 587–603, 2009.

26  OZAWA, K. Lithium-ion rechargeable batteries with licoo2 and carbon electrodes: the licoo2/c system. *Solid State Ionics*, Elsevier, v. 69, n. 3-4, p. 212–221, 1994.

27  DAHN, J. R. et al. Mechanisms for lithium insertion in carbonaceous materials. *Science*, American Association for the Advancement of Science, v. 270, n. 5236, p. 590–593, 1995.

28  TARASCON, J.-M. Is lithium the new gold? *Nature chemistry*, Nature Publishing Group, v. 2, n. 6, p. 510, 2010.

29  ELLIS, B. L.; NAZAR, L. F. Sodium and sodium-ion energy storage batteries. *Current Opinion in Solid State and Materials Science*, Elsevier, v. 16, n. 4, p. 168–177, 2012.

30  GLENDENING, E. D.; FELLER, D.; THOMPSON, M. A. An ab initio investigation of the structure and alkali metal cation selectivity of 18-crown-6. *Journal of the American Chemical Society*, ACS Publications, v. 116, n. 23, p. 10657–10669, 1994.

31  EFTEKHARI, A.; JIAN, Z.; JI, X. Potassium secondary batteries. *ACS applied materials & interfaces*, ACS Publications, v. 9, n. 5, p. 4404–4419, 2016.

32  SLATER, M. D. et al. Sodium-ion batteries. *Advanced Functional Materials*, Wiley Online Library, v. 23, n. 8, p. 947–958, 2013.

33   MOUNET, N. et al. Two-dimensional materials from high-throughput computational exfoliation of experimentally known compounds. *Nature nanotechnology*, Nature Publishing Group, v. 13, n. 3, p. 246, 2018.

34   CHHOWALLA, M. et al. The chemistry of two-dimensional layered transition metal dichalcogenide nanosheets. *Nature chemistry*, Nature Publishing Group, v. 5, n. 4, p. 263, 2013.

35   WANG, Q. H. et al. Electronics and optoelectronics of two-dimensional transition metal dichalcogenides. *Nature nanotechnology*, Nature Publishing Group, v. 7, n. 11, p. 699, 2012.

36   WATANABE, K.; TANIGUCHI, T.; KANDA, H. Direct-bandgap properties and evidence for ultraviolet lasing of hexagonal boron nitride single crystal. *Nature materials*, Nature Publishing Group, v. 3, n. 6, p. 404, 2004.

37   XIE, M. et al. Two-dimensional bx (x= p, as, sb) semiconductors with mobilities approaching graphene. *Nanoscale*, Royal Society of Chemistry, v. 8, n. 27, p. 13407–13413, 2016.

38   GEIM, A. K.; GRIGORIEVA, I. V. Van der waals heterostructures. *Nature*, Nature Publishing Group, v. 499, n. 7459, p. 419–425, 2013.

39   NOVOSELOV, K. et al. 2d materials and van der waals heterostructures. *Science*, American Association for the Advancement of Science, v. 353, n. 6298, p. aac9439, 2016.

40   ASHCROFT, N. W.; MERMIN, N. D. Solid state physics (saunders college, philadelphia, 1976). *Appendix N*, 2010.

41   KATZIR, A. et al. Point defects in hexagonal boron nitride. i. epr, thermoluminescence, and thermally-stimulated-current measurements. *Physical Review B*, APS, v. 11, n. 6, p. 2370, 1975.

42   MUSEUR, L.; FELDBACH, E.; KANAEV, A. Defect-related photoluminescence of hexagonal boron nitride. *Physical Review B*, APS, v. 78, n. 15, p. 155204, 2008.

43   HAN, M. Y. et al. Energy band-gap engineering of graphene nanoribbons. *Physical review letters*, APS, v. 98, n. 20, p. 206805, 2007.

44   LI, X. et al. Chemically derived, ultrasmooth graphene nanoribbon semiconductors. *science*, American Association for the Advancement of Science, v. 319, n. 5867, p. 1229–1232, 2008.

45   PONOMARENKO, L. et al. Chaotic dirac billiard in graphene quantum dots. *Science*, American Association for the Advancement of Science, v. 320, n. 5874, p. 356–358, 2008.

46   TRAUZETTEL, B. et al. Spin qubits in graphene quantum dots. *Nature Physics*, Nature Publishing Group, v. 3, n. 3, p. 192, 2007.

47   BAI, J. et al. Graphene nanomesh. *Nature nanotechnology*, Nature Publishing Group, v. 5, n. 3, p. 190, 2010.

48   AKHAVAN, O. Graphene nanomesh by zno nanorod photocatalysts. *ACS nano*, ACS Publications, v. 4, n. 7, p. 4174–4180, 2010.

49  BALOG, R. et al. Bandgap opening in graphene induced by patterned hydrogen adsorption. *Nature materials*, Nature Publishing Group, v. 9, n. 4, p. 315, 2010.

50  YAVARI, F. et al. Tunable bandgap in graphene by the controlled adsorption of water molecules. *small*, Wiley Online Library, v. 6, n. 22, p. 2535–2538, 2010.

51  KOZLOV, S. M.; VIÑES, F.; GÖRLING, A. Bandgap engineering of graphene by physisorbed adsorbates. *Advanced Materials*, Wiley Online Library, v. 23, n. 22-23, p. 2638–2643, 2011.

52  ZHOU, S. et al. Metal to insulator transition in epitaxial graphene induced by molecular doping. *Physical review letters*, APS, v. 101, n. 8, p. 086402, 2008.

53  PANCHAKARLA, L. et al. Synthesis, structure, and properties of boron-and nitrogen-doped graphene. *Advanced Materials*, Wiley Online Library, v. 21, n. 46, p. 4726–4730, 2009.

54  WU, M.; CAO, C.; JIANG, J. Light non-metallic atom (b, n, o and f)-doped graphene: a first-principles study. *Nanotechnology*, IOP Publishing, v. 21, n. 50, p. 505202, 2010.

55  RANI, P.; JINDAL, V. Designing band gap of graphene by b and n dopant atoms. *Rsc Advances*, Royal Society of Chemistry, v. 3, n. 3, p. 802–812, 2013.

56  ULLAH, S. et al. Band-gap tuning of graphene by be doping and be, b co-doping: a dft study. *RSC advances*, Royal Society of Chemistry, v. 5, n. 69, p. 55762–55773, 2015.

57  DENIS, P. A. Band gap opening of monolayer and bilayer graphene doped with aluminium, silicon, phosphorus, and sulfur. *Chemical Physics Letters*, Elsevier, v. 492, n. 4-6, p. 251–257, 2010.

58  DENIS, P. A. When noncovalent interactions are stronger than covalent bonds: Bilayer graphene doped with second row atoms, aluminum, silicon, phosphorus and sulfur. *Chemical Physics Letters*, Elsevier, v. 508, n. 1-3, p. 95–101, 2011.

59  ZHANG, J. et al. Low-temperature growth of large-area heteroatom-doped graphene film. *Chemistry of Materials*, ACS Publications, v. 26, n. 7, p. 2460–2466, 2014.

60  YANG, S. et al. Efficient synthesis of heteroatom (n or s)-doped graphene based on ultrathin graphene oxide-porous silica sheets for oxygen reduction reactions. *Advanced Functional Materials*, Wiley Online Library, v. 22, n. 17, p. 3634–3640, 2012.

61  GAO, H. et al. Synthesis of s-doped graphene by liquid precursor. *Nanotechnology*, IOP Publishing, v. 23, n. 27, p. 275605, 2012.

62  WANG, Z. et al. Pure thiophene–sulfur doped reduced graphene oxide: synthesis, structure, and electrical properties. *Nanoscale*, Royal Society of Chemistry, v. 6, n. 13, p. 7281–7287, 2014.

63  POH, H. L. et al. Sulfur-doped graphene via thermal exfoliation of graphite oxide in h2s, so2, or cs2 gas. *ACS nano*, ACS Publications, v. 7, n. 6, p. 5262–5272, 2013.

64  DAI, J.; YUAN, J. Modulating the electronic and magnetic structures of p-doped graphene by molecule doping. *Journal of Physics: Condensed Matter*, IOP Publishing, v. 22, n. 22, p. 225501, 2010.

65  POH, H. L. et al. Concurrent phosphorus doping and reduction of graphene oxide. *Chemistry–A European Journal*, Wiley Online Library, v. 20, n. 15, p. 4284–4291, 2014.

66  NIU, F. et al. Phosphorus doped graphene nanosheets for room temperature nh 3 sensing. *New Journal of Chemistry*, Royal Society of Chemistry, v. 38, n. 6, p. 2269–2272, 2014.

67  LARRUDE, D. G. et al. Electronic structure and ultrafast charge transfer dynamics of phosphorous doped graphene layers on a copper substrate: a combined spectroscopic study. *RSC Advances*, Royal Society of Chemistry, v. 5, n. 91, p. 74189–74197, 2015.

68  WANG, X.-Y. et al. Synthesis, structure, and chiroptical properties of a double [7] heterohelicene. *Journal of the American Chemical Society*, ACS Publications, v. 138, n. 39, p. 12783–12786, 2016.

69  WANG, X. et al. Heteroatom-doped graphene materials: syntheses, properties and applications. *Chemical Society Reviews*, Royal Society of Chemistry, v. 43, n. 20, p. 7067–7098, 2014.

70  ZHOU, W. et al. Direct determination of the chemical bonding of individual impurities in graphene. *Physical review letters*, APS, v. 109, n. 20, p. 206803, 2012.

71  RAMASSE, Q. M. et al. Probing the bonding and electronic structure of single atom dopants in graphene with electron energy loss spectroscopy. *Nano letters*, ACS Publications, v. 13, n. 10, p. 4989–4995, 2013.

72  HOUMAD, M. et al. Optical conductivity enhancement and band gap opening with silicon doped graphene. *Carbon*, Elsevier, v. 94, p. 1021–1027, 2015.

73  NAKAMURA, T.; SUZUKI, K.; YAMASHITA, M. An anionic aluminabenzene bearing aromatic and ambiphilic contributions. *Journal of the American Chemical Society*, ACS Publications, v. 136, n. 26, p. 9276–9279, 2014.

74  JIN, Z. et al. Metal-free selenium doped carbon nanotube/graphene networks as a synergistically improved cathode catalyst for oxygen reduction reaction. *Nanoscale*, Royal Society of Chemistry, v. 4, n. 20, p. 6455–6460, 2012.

75  SHE, X. et al. Creation of ge–n x–c y configures in carbon nanotubes: Origin of enhanced electrocatalytic performance for oxygen reduction reaction. *ACS applied materials & interfaces*, ACS Publications, v. 8, n. 16, p. 10383–10391, 2016.

76  DENIS, P. A. Chemical reactivity and band-gap opening of graphene doped with gallium, germanium, arsenic, and selenium atoms. *ChemPhysChem*, Wiley Online Library, v. 15, n. 18, p. 3994–4000, 2014.

77  TOH, R. J. et al. Transition metal (mn, fe, co, ni)-doped graphene hybrids for electrocatalysis. *Chemistry–An Asian Journal*, Wiley Online Library, v. 8, n. 6, p. 1295–1300, 2013.

78  ZHAO, J. et al. Free-standing single-atom-thick iron membranes suspended in graphene pores. *Science*, American Association for the Advancement of Science, v. 343, n. 6176, p. 1228–1232, 2014.

79  ROBERTSON, A. W. et al. Dynamics of single fe atoms in graphene vacancies. *Nano letters*, ACS Publications, v. 13, n. 4, p. 1468–1475, 2013.

80  SOFER, Z. et al. Uranium-and thorium-doped graphene for efficient oxygen and hydrogen peroxide reduction. *ACS nano*, ACS Publications, v. 8, n. 7, p. 7106–7114, 2014.

81  ZHENG, Y. et al. Two-step boron and nitrogen doping in graphene for enhanced synergistic catalysis. *Angewandte Chemie International Edition*, Wiley Online Library, v. 52, n. 11, p. 3110–3116, 2013.

82  WANG, S. et al. Bcn graphene as efficient metal-free electrocatalyst for the oxygen reduction reaction. *Angewandte Chemie International Edition*, Wiley Online Library, v. 51, n. 17, p. 4209–4212, 2012.

83  HUSSAIN, A.; ULLAH, S.; FARHAN, M. A. Fine tuning the band-gap of graphene by atomic and molecular doping: a density functional theory study. *RSC Advances*, Royal Society of Chemistry, v. 6, n. 61, p. 55990–56003, 2016.

84  HUSSAIN, A. et al. Structural, electronic, and magnetic properties of non-planar doping of beo in graphene: a dft study. *New Journal of Chemistry*, Royal Society of Chemistry, v. 41, n. 19, p. 10780–10789, 2017.

85  DENIS, P. A.; HUELMO, C. P. Structural characterization and chemical reactivity of dual doped graphene. *Carbon*, Elsevier, v. 87, p. 106–115, 2015.

86  DENIS, P. A.; HUELMO, C. P.; MARTINS, A. Band gap opening in dual-doped monolayer graphene. *The Journal of Physical Chemistry C*, ACS Publications, v. 120, n. 13, p. 7103–7112, 2016.

87  DENIS, P. A.; HUELMO, C. P.; IRIBARNE, F. Theoretical characterization of sulfur and nitrogen dual-doped graphene. *Computational and Theoretical Chemistry*, Elsevier, v. 1049, p. 13–19, 2014.

88  CRUZ-SILVA, E. et al. Electronic transport and mechanical properties of phosphorus-and phosphorus- nitrogen-doped carbon nanotubes. *ACS nano*, ACS Publications, v. 3, n. 7, p. 1913–1921, 2009.

89  ZHENG, Y. et al. Toward design of synergistically active carbon-based catalysts for electrocatalytic hydrogen evolution. *ACS nano*, ACS Publications, v. 8, n. 5, p. 5290–5296, 2014.

90  MA, X. et al. Phosphorus and nitrogen dual-doped few-layered porous graphene: a high-performance anode material for lithium-ion batteries. *ACS applied materials & interfaces*, ACS Publications, v. 6, n. 16, p. 14415–14422, 2014.

91  PARAKNOWITSCH, J. P. et al. Intrinsically sulfur-and nitrogen-co-doped carbons from thiazolium salts. *Chemistry–A European Journal*, Wiley Online Library, v. 18, n. 48, p. 15416–15423, 2012.

92  YOU, J.-M. et al. New approach of nitrogen and sulfur-doped graphene synthesis using dipyrrolemethane and their electrocatalytic activity for oxygen reduction in alkaline media. *Journal of Power Sources*, Elsevier, v. 275, p. 73–79, 2015.

93 KICIŃSKI, W. et al. Copolycondensation of heterocyclic aldehydes: A general approach to sulfur and nitrogen dually-doped carbon gels. *Microporous and Mesoporous Materials*, Elsevier, v. 225, p. 198–209, 2016.

94 FENG, B. et al. From graphite oxide to nitrogen and sulfur co-doped few-layered graphene by a green reduction route via chinese medicinal herbs. *RSC Advances*, Royal Society of Chemistry, v. 4, n. 34, p. 17902–17907, 2014.

95 MA, X. et al. High capacity li storage in sulfur and nitrogen dual-doped graphene networks. *Carbon*, Elsevier, v. 79, p. 310–320, 2014.

96 GOODENOUGH. *Nobel Prize in Chemistry in 2019*. Disponível em: <https://www.nobelprize.org/prizes/chemistry/2019/press-release/>.

97 ARMAND, M.; TARASCON, J.-M. Building better batteries. *nature*, Nature Publishing Group, v. 451, n. 7179, p. 652, 2008.

98 CAO, Y. et al. Sodium ion insertion in hollow carbon nanowires for battery applications. *Nano letters*, ACS Publications, v. 12, n. 7, p. 3783–3787, 2012.

99 RACCICHINI, R. et al. Critical insight into the relentless progression toward graphene and graphene-containing materials for lithium-ion battery anodes. *Advanced Materials*, Wiley Online Library, v. 29, n. 11, p. 1603421, 2017.

100 YUAN, S. et al. Surfactant-free aqueous synthesis of pure single-crystalline snse nanosheet clusters as anode for high energy-and power-density sodium-ion batteries. *Advanced Materials*, Wiley Online Library, v. 29, n. 4, p. 1602469, 2017.

101 MOSHKOVICH, M.; GOFER, Y.; AURBACH, D. Investigation of the electrochemical windows of aprotic alkali metal (li, na, k) salt solutions. *Journal of The Electrochemical Society*, The Electrochemical Society, v. 148, n. 4, p. E155–E167, 2001.

102 WU, Z.-S. et al. Doped graphene sheets as anode materials with superhigh rate and large capacity for lithium ion batteries. *ACS nano*, ACS Publications, v. 5, n. 7, p. 5463–5471, 2011.

103 GARAY-TAPIA, A.; ROMERO, A. H.; BARONE, V. Lithium adsorption on graphene: from isolated adatoms to metallic sheets. *Journal of chemical theory and computation*, ACS Publications, v. 8, n. 3, p. 1064–1071, 2012.

104 WU, D.; LI, Y.; ZHOU, Z. First-principles studies on doped graphene as anode materials in lithium-ion batteries. *Theoretical Chemistry Accounts*, Springer, v. 130, n. 2-3, p. 209–213, 2011.

105 WANG, X. et al. First-principles study on the enhancement of lithium storage capacity in boron doped graphene. *Applied Physics Letters*, AIP, v. 95, n. 18, p. 183103, 2009.

106 FAN, X.; ZHENG, W.; KUO, J.-L. Adsorption and diffusion of li on pristine and defective graphene. *ACS applied materials & interfaces*, ACS Publications, v. 4, n. 5, p. 2432–2438, 2012.

107   ZHOU, L. et al. Doped graphenes as anodes with large capacity for lithium-ion batteries. *Journal of Materials Chemistry A*, Royal Society of Chemistry, v. 4, n. 35, p. 13407–13413, 2016.

108   DENIS, P. A. Lithium adsorption on heteroatom mono and dual doped graphene. *Chemical Physics Letters*, Elsevier, v. 672, p. 70–79, 2017.

109   MOON, H. S. et al. Mechanisms of na adsorption on graphene and graphene oxide: density functional theory approach. *Carbon letters*, Korean Carbon Society, v. 16, n. 2, p. 116–120, 2015.

110   LING, C.; MIZUNO, F. Boron-doped graphene as a promising anode for na-ion batteries. *Physical Chemistry Chemical Physics*, Royal Society of Chemistry, v. 16, n. 22, p. 10419–10424, 2014.

111   WAN, W.; WANG, H. First-principles investigation of adsorption and diffusion of ions on pristine, defective and b-doped graphene. *Materials*, Multidisciplinary Digital Publishing Institute, v. 8, n. 9, p. 6163–6178, 2015.

112   YAO, L.-H. et al. Adsorption of na on intrinsic, b-doped, n-doped and vacancy graphenes: A first-principles study. *Computational Materials Science*, Elsevier, v. 85, p. 179–185, 2014.

113   PRAMUDITA, J. C. et al. Mechanisms of sodium insertion/extraction on the surface of defective graphenes. *ACS applied materials & interfaces*, ACS Publications, v. 9, n. 1, p. 431–438, 2016.

114   YANG, Y. et al. "protrusions" or "holes" in graphene: which is the better choice for sodium ion storage? *Energy & Environmental Science*, Royal Society of Chemistry, v. 10, n. 4, p. 979–986, 2017.

115   LIU, Y.; MERINOV, B. V.; GODDARD, W. A. Origin of low sodium capacity in graphite and generally weak substrate binding of na and mg among alkali and alkaline earth metals. *Proceedings of the National Academy of Sciences*, National Acad Sciences, v. 113, n. 14, p. 3735–3739, 2016.

116   YU, Y.-X. Graphenylene: a promising anode material for lithium-ion batteries with high mobility and storage. *Journal of Materials Chemistry A*, Royal Society of Chemistry, v. 1, n. 43, p. 13559–13566, 2013.

117   WANG, N. et al. Synthesis of chlorine-substituted graphdiyne and applications for lithium-ion storage. *Angewandte Chemie International Edition*, Wiley Online Library, v. 56, n. 36, p. 10740–10745, 2017.

118   WANG, X.-Q.; LI, H.-D.; WANG, J.-T. Prediction of a new two-dimensional metallic carbon allotrope. *Physical Chemistry Chemical Physics*, Royal Society of Chemistry, v. 15, n. 6, p. 2024–2030, 2013.

119   XU, L.-C. et al. Two dimensional dirac carbon allotropes from graphene. *Nanoscale*, Royal Society of Chemistry, v. 6, n. 2, p. 1113–1118, 2014.

120   YU, S. et al. Net w monolayer: A high-performance electrode material for li-ion batteries. *Applied Physics Letters*, AIP Publishing, v. 112, n. 5, p. 053903, 2018.

121  FENG, C. et al. Synthesis of molybdenum disulfide (mos2) for lithium ion battery applications. *Materials Research Bulletin*, Elsevier, v. 44, n. 9, p. 1811–1815, 2009.

122  LIU, Y. et al. A graphene-like mos 2/graphene nanocomposite as a highperformance anode for lithium ion batteries. *Journal of Materials Chemistry A*, Royal Society of Chemistry, v. 2, n. 32, p. 13109–13115, 2014.

123  XIONG, F. et al. Three-dimensional crumpled reduced graphene oxide/mos2 nanoflowers: a stable anode for lithium-ion batteries. *ACS applied materials & interfaces*, ACS Publications, v. 7, n. 23, p. 12625–12630, 2015.

124  YU, X.-Y. et al. Ultrathin mos2 nanosheets supported on n-doped carbon nanoboxes with enhanced lithium storage and electrocatalytic properties. *Angewandte Chemie International Edition*, Wiley Online Library, v. 54, n. 25, p. 7395–7398, 2015.

125  ZHENG, Y. et al. Atomic interface engineering and electric-field effect in ultrathin bi2moo6 nanosheets for superior lithium ion storage. *Advanced Materials*, Wiley Online Library, v. 29, n. 26, p. 1700396, 2017.

126  ZHOU, Y. Mx (m= ge, sn; x= s, se) sheets: Theoretical prediction of new promising electrode materials for li ion batteries. *Journal of Materials Chemistry A*, Royal Society of Chemistry, v. 4, n. 28, p. 10906–10913, 2016.

127  WAN, Q.; LI, S.; LIU, J.-B. First-principle study of li-ion storage of functionalized ti2c monolayer with vacancies. *ACS applied materials & interfaces*, ACS Publications, v. 10, n. 7, p. 6369–6377, 2018.

128  ÇAKIR, D. et al. Mo 2 c as a high capacity anode material: A first-principles study. *Journal of Materials Chemistry A*, Royal Society of Chemistry, v. 4, n. 16, p. 6029–6035, 2016.

129  MARZOUK, A. et al. Dynamics of the lithiation and sodiation of silicon allotropes: From the bulk to the surface. *Journal of The Electrochemical Society*, The Electrochemical Society, v. 164, n. 7, p. A1644–A1650, 2017.

130  ZHANG, Z. et al. First-principles computational studies on layered na2mn3o7 as a high-rate cathode material for sodium ion batteries. *Journal of Materials Chemistry A*, The Royal Society of Chemistry, v. 5, n. 25, p. 12752–12756, 2017.

131  LIU, X. et al. A first-principles study of sodium adsorption and diffusion on phosphorene. *Physical Chemistry Chemical Physics*, Royal Society of Chemistry, v. 17, n. 25, p. 16398–16404, 2015.

132  SU, J. et al. Ab initio study of graphene-like monolayer molybdenum disulfide as a promising anode material for rechargeable sodium ion batteries. *RSC Advances*, Royal Society of Chemistry, v. 4, n. 81, p. 43183–43188, 2014.

133  MORTAZAVI, M. et al. Ab initio characterization of layered mos2 as anode for sodium-ion batteries. *Journal of Power Sources*, Elsevier, v. 268, p. 279–286, 2014.

134  LI, F.; QU, Y.; ZHAO, M. Germanium sulfide nanosheet: a universal anode material for alkali metal ion batteries. *Journal of Materials Chemistry A*, Royal Society of Chemistry, v. 4, n. 22, p. 8905–8912, 2016.

135  YANG, E.; JI, H.; JUNG, Y. Two-dimensional transition metal dichalcogenide monolayers as promising sodium ion battery anodes. *The Journal of Physical Chemistry C*, ACS Publications, v. 119, n. 47, p. 26374–26380, 2015.

136  JING, Y. et al. Metallic vs2 monolayer: a promising 2d anode material for lithium ion batteries. *The Journal of Physical Chemistry C*, ACS Publications, v. 117, n. 48, p. 25409–25413, 2013.

137  BALENDHRAN, S. et al. Elemental analogues of graphene: silicene, germanene, stanene, and phosphorene. *small*, Wiley Online Library, v. 11, n. 6, p. 640–652, 2015.

138  CAHANGIROV, S. et al. Two-and one-dimensional honeycomb structures of silicon and germanium. *Physical review letters*, APS, v. 102, n. 23, p. 236804, 2009.

139  LI, L. et al. Black phosphorus field-effect transistors. *Nature nanotechnology*, Nature Publishing Group, v. 9, n. 5, p. 372, 2014.

140  WANG, X. et al. Highly anisotropic and robust excitons in monolayer black phosphorus. *Nature nanotechnology*, Nature Publishing Group, v. 10, n. 6, p. 517, 2015.

141  MAK, K. F. et al. Atomically thin mos 2: a new direct-gap semiconductor. *Physical review letters*, APS, v. 105, n. 13, p. 136805, 2010.

142  LI, Y. et al. Metal to semiconductor transition in metallic transition metal dichalcogenides. *Journal of Applied Physics*, AIP, v. 114, n. 17, p. 174307, 2013.

143  LEI, J.-C.; ZHANG, X.; ZHOU, Z. Recent advances in mxene: Preparation, properties, and applications. *Frontiers of Physics*, Springer, v. 10, n. 3, p. 276–286, 2015.

144  TANG, Q.; ZHOU, Z.; CHEN, Z. Innovation and discovery of graphene-like materials via density-functional theory computations. *Wiley Interdisciplinary Reviews: Computational Molecular Science*, Wiley Online Library, v. 5, n. 5, p. 360–379, 2015.

145  TANG, Q.; ZHOU, Z. Graphene-analogous low-dimensional materials. *Progress in materials science*, Elsevier, v. 58, n. 8, p. 1244–1315, 2013.

146  ŞAHIN, H. et al. Monolayer honeycomb structures of group-iv elements and iii-v binary compounds: First-principles calculations. *Physical Review B*, APS, v. 80, n. 15, p. 155453, 2009.

147  BRITNELL, L. et al. Electron tunneling through ultrathin boron nitride crystalline barriers. *Nano letters*, ACS Publications, v. 12, n. 3, p. 1707–1710, 2012.

148  XI, X. et al. Ising pairing in superconducting nbse 2 atomic layers. *Nature Physics*, Nature Publishing Group, v. 12, n. 2, p. 139, 2016.

149  XI, X. et al. Strongly enhanced charge-density-wave order in monolayer nbse 2. *Nature nanotechnology*, Nature Publishing Group, v. 10, n. 9, p. 765, 2015.

150  TANG, S. et al. Quantum spin hall state in monolayer 1t'-wte 2. *Nature Physics*, Nature Publishing Group, v. 13, n. 7, p. 683, 2017.

151  FEI, Z. et al. Edge conduction in monolayer wte 2. *Nature Physics*, Nature Publishing Group, v. 13, n. 7, p. 677, 2017.

152  WU, S. et al. Observation of the quantum spin hall effect up to 100 kelvin in a monolayer crystal. *Science*, American Association for the Advancement of Science, v. 359, n. 6371, p. 76–79, 2018.

153  HUANG, B. et al. Layer-dependent ferromagnetism in a van der waals crystal down to the monolayer limit. *Nature*, Nature Publishing Group, v. 546, n. 7657, p. 270, 2017.

154  RAMASUBRAMANIAM, A.; NAVEH, D.; TOWE, E. Tunable band gaps in bilayer graphene- bn heterostructures. *Nano letters*, ACS Publications, v. 11, n. 3, p. 1070–1075, 2011.

155  KHARCHE, N.; NAYAK, S. K. Quasiparticle band gap engineering of graphene and graphone on hexagonal boron nitride substrate. *Nano letters*, ACS Publications, v. 11, n. 12, p. 5274–5278, 2011.

156  QUHE, R. et al. Tunable and sizable band gap of single-layer graphene sandwiched between hexagonal boron nitride. *NPG Asia Materials*, Nature Publishing Group, v. 4, n. 2, p. e6, 2012.

157  WOESSNER, A. et al. Highly confined low-loss plasmons in graphene–boron nitride heterostructures. *Nature materials*, Nature Publishing Group, v. 14, n. 4, p. 421, 2015.

158  ZHANG, K. et al. Large scale graphene/hexagonal boron nitride heterostructure for tunable plasmonics. *Advanced Functional Materials*, Wiley Online Library, v. 24, n. 6, p. 731–738, 2014.

159  LI, L. et al. Controlling many-body states by the electric-field effect in a two-dimensional material. *Nature*, Nature Publishing Group, v. 529, n. 7585, p. 185, 2016.

160  WU, Q. et al. In situ synthesis of a large area boron nitride/graphene monolayer/boron nitride film by chemical vapor deposition. *Nanoscale*, Royal Society of Chemistry, v. 7, n. 17, p. 7574–7579, 2015.

161  YANKOWITZ, M. et al. van der waals heterostructures combining graphene and hexagonal boron nitride. *Nature Reviews Physics*, Nature Publishing Group, v. 1, n. 2, p. 112–125, 2019.

162  KRIVANEK, O. L. et al. Atom-by-atom structural and chemical analysis by annular dark-field electron microscopy. *Nature*, Nature Publishing Group, v. 464, n. 7288, p. 571, 2010.

163  CI, L. et al. Atomic layers of hybridized boron nitride and graphene domains. *Nature materials*, Nature Publishing Group, v. 9, n. 5, p. 430, 2010.

164  WEI, X. et al. Electron-beam-induced substitutional carbon doping of boron nitride nanosheets, nanoribbons, and nanotubes. *ACS nano*, ACS Publications, v. 5, n. 4, p. 2916–2922, 2011.

165  BERSENEVA, N.; KRASHENINNIKOV, A. V.; NIEMINEN, R. M. Mechanisms of postsynthesis doping of boron nitride nanostructures with carbon from first-principles simulations. *Physical review letters*, APS, v. 107, n. 3, p. 035501, 2011.

166  HUANG, B.; LEE, H. Defect and impurity properties of hexagonal boron nitride: A first-principles calculation. *Physical Review B*, APS, v. 86, n. 24, p. 245406, 2012.

167  BERSENEVA, N. et al. Electronic structure of boron nitride sheets doped with carbon from first-principles calculations. *Physical Review B*, APS, v. 87, n. 3, p. 035404, 2013.

168  ZHOU, J. et al. Electronic and magnetic properties of a bn sheet decorated with hydrogen and fluorine. *Physical Review B*, APS, v. 81, n. 8, p. 085442, 2010.

169  HE, B. et al. p-type conduction in beryllium-implanted hexagonal boron nitride films. *Applied Physics Letters*, AIP, v. 95, n. 25, p. 252106, 2009.

170  KOHN, W. *Nobel Prize in Chemistry in 1998.* Disponível em: <https://www.nobelprize.org/prizes/chemistry/1998/summary/>.

171  BORN, M.; HUANG, K. *Dynamical theory of crystal lattices.* [S.l.]: Clarendon press, 1954.

172  HARTREE, D. R. The wave mechanics of an atom with a non-coulomb central field. part ii. some results and discussion. In: CAMBRIDGE UNIVERSITY PRESS. *Mathematical Proceedings of the Cambridge Philosophical Society.* [S.l.], 1928. v. 24, n. 1, p. 111–132.

173  THOMAS, L. H. The calculation of atomic fields. In: CAMBRIDGE UNIVERSITY PRESS. *Mathematical Proceedings of the Cambridge Philosophical Society.* [S.l.], 1927. v. 23, n. 5, p. 542–548.

174  FERMI, E. Eine statistische methode zur bestimmung einiger eigenschaften des atoms und ihre anwendung auf die theorie des periodischen systems der elemente. *Zeitschrift für Physik*, Springer, v. 48, n. 1-2, p. 73–79, 1928.

175  DIRAC, P. A. Note on exchange phenomena in the thomas atom. In: CAMBRIDGE UNIVERSITY PRESS. *Mathematical Proceedings of the Cambridge Philosophical Society.* [S.l.], 1930. v. 26, n. 3, p. 376–385.

176  HOHENBERG, P.; KOHN, W. Inhomogeneous electron gas. *Physical review*, APS, v. 136, n. 3B, p. B864, 1964.

177  KOHN, W.; SHAM, L. J. Self-consistent equations including exchange and correlation effects. *Physical review*, APS, v. 140, n. 4A, p. A1133, 1965.

178  PERDEW, J. P.; YUE, W. Accurate and simple density functional for the electronic exchange energy: Generalized gradient approximation. *Physical review B*, APS, v. 33, n. 12, p. 8800, 1986.

179  PERDEW, J. P.; BURKE, K.; ERNZERHOF, M. Generalized gradient approximation made simple. *Physical review letters*, APS, v. 77, n. 18, p. 3865, 1996.

180  HUBBARD, J. Electron correlations in narrow energy bands. *Proceedings of the Royal Society of London. Series A. Mathematical and Physical Sciences*, The Royal Society London, v. 276, n. 1365, p. 238–257, 1963.

181  WAALS, J. D. Van der. *Over de Continuiteit van den Gas-en Vloeistoftoestand.* [S.l.]: Sijthoff, 1873.

182  MARGENAU, H.; KESTNER, N. R. *Theory of Intermolecular Forces: International Series of Monographs in Natural Philosophy*. [S.l.]: Elsevier, 2013.

183  BERLAND, K. et al. van der waals forces in density functional theory: a review of the vdw-df method. *Reports on Progress in Physics*, IOP Publishing, v. 78, n. 6, p. 066501, 2015.

184  GRIMME, S. Semiempirical gga-type density functional constructed with a long-range dispersion correction. *Journal of computational chemistry*, Wiley Online Library, v. 27, n. 15, p. 1787–1799, 2006.

185  GRIMME, S. et al. A consistent and accurate ab initio parametrization of density functional dispersion correction (dft-d) for the 94 elements h-pu. *The Journal of chemical physics*, AIP, v. 132, n. 15, p. 154104, 2010.

186  GRIMME, S.; EHRLICH, S.; GOERIGK, L. Effect of the damping function in dispersion corrected density functional theory. *Journal of computational chemistry*, Wiley Online Library, v. 32, n. 7, p. 1456–1465, 2011.

187  WU, Q.; YANG, W. Empirical correction to density functional theory for van der waals interactions. *The Journal of chemical physics*, AIP, v. 116, n. 2, p. 515–524, 2002.

188  DION, M. et al. Van der waals density functional for general geometries. *Physical review letters*, APS, v. 92, n. 24, p. 246401, 2004.

189  LEE, K. et al. Higher-accuracy van der waals density functional. *Physical Review B*, APS, v. 82, n. 8, p. 081101, 2010.

190  KLIMEŠ, J.; BOWLER, D. R.; MICHAELIDES, A. Van der waals density functionals applied to solids. *Physical Review B*, APS, v. 83, n. 19, p. 195131, 2011.

191  KLIMEŠ, J.; BOWLER, D. R.; MICHAELIDES, A. Chemical accuracy for the van der waals density functional. *Journal of Physics: Condensed Matter*, IOP Publishing, v. 22, n. 2, p. 022201, 2009.

192  VYDROV, O. A.; VOORHIS, T. V. Nonlocal van der waals density functional: The simpler the better. *The Journal of chemical physics*, AIP, v. 133, n. 24, p. 244103, 2010.

193  SABATINI, R.; GORNI, T.; GIRONCOLI, S. D. Nonlocal van der waals density functional made simple and efficient. *Physical Review B*, APS, v. 87, n. 4, p. 041108, 2013.

194  COOPER, V. R. Van der waals density functional: An appropriate exchange functional. *Physical Review B*, APS, v. 81, n. 16, p. 161104, 2010.

195  BERLAND, K.; HYLDGAARD, P. Exchange functional that tests the robustness of the plasmon description of the van der waals density functional. *Physical Review B*, APS, v. 89, n. 3, p. 035412, 2014.

196  MONKHORST, H. J.; PACK, J. D. Special points for brillouin-zone integrations. *Physical review B*, APS, v. 13, n. 12, p. 5188, 1976.

197  BACHELET, G.; HAMANN, D.; SCHLÜTER, M. Pseudopotentials that work: From h to pu. *Physical Review B*, APS, v. 26, n. 8, p. 4199, 1982.

198  PAYNE, M. C. et al. Iterative minimization techniques for ab initio total-energy calculations: molecular dynamics and conjugate gradients. *Reviews of modern physics*, APS, v. 64, n. 4, p. 1045, 1992.

199  BLÖCHL, P. E. Projector augmented-wave method. *Physical review B*, APS, v. 50, n. 24, p. 17953, 1994.

200  HERRING, C. A new method for calculating wave functions in crystals. *Physical Review*, APS, v. 57, n. 12, p. 1169, 1940.

201  SCHWARZ, K.; BLAHA, P.; MADSEN, G. K. Electronic structure calculations of solids using the wien2k package for material sciences. *Computer Physics Communications*, Elsevier, v. 147, n. 1-2, p. 71–76, 2002.

202  WILLIAMS, A.; KÜBLER, J.; JR, C. G. Cohesive properties of metallic compounds: Augmented-spherical-wave calculations. *Physical Review B*, APS, v. 19, n. 12, p. 6094, 1979.

203  ANDERSEN, O. K. Linear methods in band theory. *Physical Review B*, APS, v. 12, n. 8, p. 3060, 1975.

204  MARTIN, R. M.; MARTIN, R. M. *Electronic structure: basic theory and practical methods.* [S.l.]: Cambridge university press, 2004.

205  ARTACHO, E. *Nobel Prize in Chemistry in 2019.* Disponível em: <https://departments.icmab.es/leem/siesta/Documentation/Manuals/siesta-4.0.pdf>.

206  ORDEJÓN, P.; ARTACHO, E.; SOLER, J. M. Self-consistent order-n density-functional calculations for very large systems. *Physical Review B*, APS, v. 53, n. 16, p. R10441, 1996.

207  SOLER, J. M. et al. The siesta method for ab initio order-n materials simulation. *Journal of Physics: Condensed Matter*, IOP Publishing, v. 14, n. 11, p. 2745, 2002.

208  TROULLIER, N.; MARTINS, J. L. Efficient pseudopotentials for plane-wave calculations. *Physical review B*, APS, v. 43, n. 3, p. 1993, 1991.

209  BOYS, S. F.; BERNARDI, F. The calculation of small molecular interactions by the differences of separate total energies. some procedures with reduced errors. *Molecular Physics*, Taylor & Francis, v. 19, n. 4, p. 553–566, 1970.

210  ULLAH, S. et al. Tunable optoelectronic properties in h-bp/h-bas bilayers: The effect of an external electrical field. *Applied Surface Science*, Elsevier, v. 493, p. 308–319, 2019.

211  GARCIA, A. *ATOM user manual.* [S.l.]: ICMAB-CSIC, Bilbao, 2008.

212  KRESSE, G.; HAFNER, J. Ab initio molecular dynamics for liquid metals. *Physical Review B*, APS, v. 47, n. 1, p. 558, 1993.

213  KRESSE, G.; FURTHMÜLLER, J. Efficiency of ab-initio total energy calculations for metals and semiconductors using a plane-wave basis set. *Computational materials science*, Elsevier, v. 6, n. 1, p. 15–50, 1996.

214  KRESSE, G.; FURTHMÜLLER, J. Efficient iterative schemes for ab initio total-energy calculations using a plane-wave basis set. *Physical review B*, APS, v. 54, n. 16, p. 11169, 1996.

215  FRISCH, M. et al. Gaussian 09, revision a. 02, gaussian. *Inc., Wallingford, CT*, v. 200, p. 28, 2009.

216  GIANNOZZI, P. et al. Quantum espresso: a modular and open-source software project for quantum simulations of materials. *Journal of physics: Condensed matter*, IOP Publishing, v. 21, n. 39, p. 395502, 2009.

217  GIANNOZZI, P. et al. Advanced capabilities for materials modelling with quantum espresso. *Journal of Physics: Condensed Matter*, IOP Publishing, v. 29, n. 46, p. 465901, 2017.

218  VANDERBILT, D. Optimally smooth norm-conserving pseudopotentials. *Physical Review B*, APS, v. 32, n. 12, p. 8412, 1985.

219  SCHLIPF, M.; GYGI, F. Optimization algorithm for the generation of oncv pseudopotentials. *Computer Physics Communications*, Elsevier, v. 196, p. 36–44, 2015.

220  GARRITY, K. et al. Gbrv high-throughput pseudopotentials. *see https://www. physics. rutgers. edu/gbrv*, 2017.

221  GARRITY, K. F. et al. Pseudopotentials for high-throughput dft calculations. *Computational Materials Science*, Elsevier, v. 81, p. 446–452, 2014.

222  PRANDINI, G. et al. Precision and efficiency in solid-state pseudopotential calculations. *npj Computational Materials*, Nature Publishing Group, v. 4, n. 1, p. 72, 2018.

223  CASTELLI, I. et al. Standard solid state pseudopotentials (sssp). *preparation," http://www. materialscloud. ch/sssp*, 2018.

224  CORSO, A. D. Pseudopotentials periodic table: From h to pu. *Computational Materials Science*, Elsevier, v. 95, p. 337–350, 2014.

225  MARZARI, N. *Nobel Prize in Chemistry in 2019*. Disponível em: <https: //www.quantum-espresso.org/pseudopotentials>.

226  ULLAH, S.; HUSSAIN, A.; SATO, F. Rectangular and hexagonal doping of graphene with b, n, and o: a dft study. *RSC advances*, Royal Society of Chemistry, v. 7, n. 26, p. 16064–16068, 2017.

227  ULLAH, S.; DENIS, P. A.; SATO, F. Triple-doped monolayer graphene with boron, nitrogen, aluminum, silicon, phosphorus, and sulfur. *ChemPhysChem*, Wiley Online Library, v. 18, n. 14, p. 1864–1873, 2017.

228  ULLAH, S.; DENIS, P. A.; SATO, F. Coupled cluster and density functional investigation of the neutral sodium-benzene and potassium-benzene complexes. *Chemical Physics Letters*, Elsevier, v. 706, p. 343–347, 2018.

229   ULLAH, S.; DENIS, P. A.; SATO, F. Coupled cluster investigation of the interaction of beryllium, magnesium, and calcium with pyridine: Implications for the adsorption on nitrogen-doped graphene. *Computational and Theoretical Chemistry*, Elsevier, v. 1150, p. 57–62, 2019.

230   ULLAH, S.; DENIS, P. A.; SATO, F. Beryllium doped graphene as an efficient anode material for lithium-ion batteries with significantly huge capacity: A dft study. *Applied Materials Today*, Elsevier, v. 9, p. 333–340, 2017.

231   ULLAH, S.; DENIS, P. A.; SATO, F. Adsorption of sodium on doped graphene: A vdw-df study. *Current Graphene Science*, v. 2, n. 1, p. 35–44, 2018. ISSN 2452-2732/2452-2740.

232   ULLAH, S.; DENIS, P. A.; SATO, F. First-principles study of dual-doped graphene: towards promising anode materials for li/na-ion batteries. *New Journal of Chemistry*, Royal Society of Chemistry, v. 42, n. 13, p. 10842–10851, 2018.

233   ULLAH, S.; DENIS, P. A.; SATO, F. Adsorption and diffusion of alkali-atoms (li, na, and k) on ben dual doped graphene. *International Journal of Quantum Chemistry*, Wiley Online Library, v. 119, n. 11, p. e25900, 2019.

234   ULLAH, S.; DENIS, P. A.; SATO, F. Unusual enhancement of the adsorption energies of sodium and potassium in sulfur- nitrogen and silicon- boron codoped graphene. *ACS Omega*, ACS Publications, v. 3, n. 11, p. 15821–15828, 2018.

235   ULLAH, S.; DENIS, P. A.; SATO, F. Hexagonal boron phosphide as a potential anode nominee for alkali-based batteries: A multi-flavor dft study. *Applied Surface Science*, Elsevier, v. 471, p. 134–141, 2019.

236   ULLAH, S.; DENIS, P. A.; SATO, F. Monolayer boron-arsenide as a perfect anode for alkali-based batteries with large storage capacities and fast mobilities. *International Journal of Quantum Chemistry*, Wiley Online Library, v. 119, n. 18, p. e25975, 2019.

237   SLUITER, M. H.; KAWAZOE, Y. Cluster expansion method for adsorption: Application to hydrogen chemisorption on graphene. *Physical Review B*, APS, v. 68, n. 8, p. 085410, 2003.

238   SOFO, J. O.; CHAUDHARI, A. S.; BARBER, G. D. Graphane: A two-dimensional hydrocarbon. *Physical Review B*, APS, v. 75, n. 15, p. 153401, 2007.

239   DENIS, P. A.; IRIBARNE, F. On the hydrogen addition to graphene. *Journal of Molecular Structure: THEOCHEM*, Elsevier, v. 907, n. 1-3, p. 93–103, 2009.

240   CHARLIER, J.-C.; GONZE, X.; MICHENAUD, J.-P. First-principles study of graphite monofluoride (cf) n. *Physical Review B*, APS, v. 47, n. 24, p. 16162, 1993.

241   LEENAERTS, O. et al. First-principles investigation of graphene fluoride and graphane. *Physical Review B*, APS, v. 82, n. 19, p. 195436, 2010.

242   CHENG, S.-H. et al. Reversible fluorination of graphene: Evidence of a two-dimensional wide bandgap semiconductor. *Physical Review B*, APS, v. 81, n. 20, p. 205435, 2010.

243   FREIRE, E. B. et al. Exploring the effect of substitutional doping on the electronic properties of graphene oxide. *Journal of materials science*, Springer, v. 53, n. 10, p. 7516–7526, 2018.

244   ULLAH, S.; DENIS, P. A.; SATO, F. Hydrogenation and fluorination of 2d boron phosphide and boron arsenide: A density functional theory investigation. *ACS Omega*, ACS Publications, v. 3, n. 12, p. 16416–16423, 2018.

245   SAVIN, A. et al. Elf: The electron localization function. *Angewandte Chemie International Edition in English*, Wiley Online Library, v. 36, n. 17, p. 1808–1832, 1997.

246   ULLAH, S. et al. Theoretical characterization of hexagonal 2d be 3 n 2 monolayers. *New Journal of Chemistry*, Royal Society of Chemistry, v. 43, n. 7, p. 2933–2941, 2019.

247   STREDANSKY, M. et al. On-surface synthesis of a 2d boroxine framework: a route to a novel 2d material? *Chemical communications*, Royal Society of Chemistry, v. 54, n. 32, p. 3971–3973, 2018.

248   ULLAH, S.; DENIS, P. A.; SATO, F. Theoretical investigation of various aspects of two dimensional holey boroxine, b 3 o 3. *RSC Advances*, Royal Society of Chemistry, v. 9, n. 64, p. 37526–37536, 2019.

249   ULLAH, S.; DENIS, P. A.; SATO, F. Non-trivial band gaps and charge transfer in janus-like functionalized bilayer boron arsenide. *Computational Materials Science*, Elsevier, v. 170, p. 109186, 2019.

250   ULLAH, S. et al. Exotic impurity-induced states in single-layer h-bn: The role of sublattice structure and intervalley interactions. *Physical Review B*, APS, v. 100, n. 8, p. 085427, 2019.

### APPENDIX  A  –  Electronic properties of doped graphene

A.1   Additional paper 1: Rectangular and hexagonal doping of graphene with B, N, and O: a DFT study

# RSC Advances

## PAPER

# Rectangular and hexagonal doping of graphene with B, N, and O: a DFT study†

Saif Ullah,[*a] Akhtar Hussain[b] and Fernando Sato[a]

First-principles density functional theory (DFT) calculations were carried out to investigate the rectangular and hexagonal doping of graphene with B, N, and O. In both of these configurations, though the dopants are incorporated at the same sublattices sites (A or B), the calculated values of the band gaps are very different with nearly the same amount of cohesive energies. In this study, the highest value of the band gap (1.68 eV) is achieved when a maximum of 4 O atoms are substituted at hexagonal positions, resulting in a lower cohesive energy relative to that of the other studied systems. Hexagonal doping with 3 O atoms is significantly more efficient in terms of opening the band gap and improving the structural stability than the rectangular doping with 4 O atoms. Our results show the opportunity to induce a higher band gap values having a smaller concentration of dopants, with better structural stabilities.

## Introduction

Graphene is a single layer of $sp^2$ hybridized carbon atoms arranged in a honeycomb lattice, and is the basic building block of all graphitic materials of every dimension (0D, 1D, and 3D).[1–4] The extraordinary physical, electrical, and optical properties of graphene nominate it as a potential candidate for use in semiconductor electronic devices.[3,5–7] The exceptional charge carrier mobility of graphene ($10^6$ $cm^2$ V $s^{-1}$) makes it very much desirable for use in semiconductor electronic devices.[8]

Besides these distinctive properties, the one big hurdle is the zero gap character of graphene, which restricts its use in nanoelectronics. In this regard, the band gap engineering of graphene is necessary.[9] Fortunately, we can overcome this issue in a number of ways. Graphene superstructures such as quantum dots,[10,11] nanoribbons,[12,13] and nanomeshes[14] can address this problem by inducing a quantum confinement effect, which leads to the opening of a band gap around the Dirac point. Furthermore, one of the simple and efficient techniques to alter the electronic structure of graphene is substitutional doping where C atoms are replaced by impurity atoms. Graphene can be doped with Al, B, $NO_2$, $H_2O$, and F4-TCNQ to achieve p-type doping, while for n-type doping N and alkali metals are used as dopants.[15–20] Graphene is usually doped with B and N atoms because these dopants are the neighbors of C. Moreover, by using B and N dopants, the 2D geometry of graphene is retained

due to the nearly equal covalent radii of these atoms. Additionally, graphene can be doped with Be, co-doped with Be–B and Be–N, and molecular doping with BeO to change the electronic structure, significantly.[21,22] Graphene has been doped with B, N, O, and F, in a previous study, to investigate the electronic properties of graphene, but this study was limited to one dopant atom only.[17] A systematic study on the doping of graphene with B and N can be found in ref. 23. These authors studied different sites with varying concentrations of the dopants and found that, for maximum band gap opening in graphene, the dopants must be integrated at the same sublattices positions (A or B). In our recent study, we investigated two types of doping configuration of Be in graphene, namely rectangular and hexagonal.[21] In that study, we discovered that, after the selection of a suitable dopant, in order to induce higher band gaps it is important not only to employ the dopants at the same sublattices sites (A or B), but also to choose specific sites (i.e. hexagonal configurations). To the best of our knowledge, these rectangular and hexagonal configurations are not reported in the literature for any atom(s) other than Be.

In this study, the doping of graphene with B, N, and O is investigated using a DFT study. We have chosen previously investigated rectangular and hexagonal configurations for our doped graphene systems to check the response of the electronic structures. The main theme of this study is to check the validity of our configurations for other atoms (B, N and O) except Be, and to obtain the optimum value of the band gap of graphene with the minimum number of dopants.

## Computational details

First-principles density functional theory (DFT) calculations were performed using the SIESTA code.[24] For electron–ion interactions, we used Troullier–Martins norm conserving

[a]Departamento de Física, Instituto de Ciências Exatas, Campus Universitário, Universidade Federal de Juiz de Fora, Juiz de Fora, MG 36036-900, Brazil. E-mail: sullah@fisica.ufjf.br

[b]TPD, Pakistan Institute of Nuclear Science and Technology (PINSTECH), P.O. Nilore, Islamabad, Pakistan

pseudopotentials.[25] The GGA = PBE level of theory was used for electron–electron interactions.[26] The double zeta (DZ) basis set was selected and the orbital confining cut-off was set to 0.01 Ry. For higher doping concentrations (9.375–12.5%), we have performed VDW-DF[27] calculations complemented by the double zeta basis set with polarization (DZP) to investigate the magnetic moment, if any. The mesh cut-off value was fixed to 200 Ry for our 4 × 4 graphene supercell with periodic boundary conditions. The z-axis was set to 14 Å to avoid interactions between the layers. The Brillouin zone was sampled with 30 × 30 × 1 Monkhorst–Pack k-points. The optimization procedure was done using a conjugate gradient algorithm until all of the forces were less than 0.01 eV Å⁻¹. For the cohesive energy calculations, we used the following formula:

$$E_{coh} = [E_{tot} - n_i E_i]/n, (i = C, B, N, and O)$$

$E_{coh}$ is the cohesive energy per atom. $E_i$ and $E_{tot}$ correspond to the energy of an individual element (the gas phase energy) in the same supercell and the total energy of the system, respectively. $n$ represents the total number of atoms in the supercell.

## Results and discussion

Primarily, we optimized our 4 × 4 graphene sheet to get a relaxed structure. The relaxed C–C bonds were found to be 1.44 Å in length, in agreement with prior studies.[21–23,28] This relaxed geometry with the corresponding band structure is shown in Fig. S1 in the ESI.† This optimized graphene sheet was doped with B, N, and O atoms in rectangular and hexagonal configurations with increasing concentration, ranging from 3.125% to 12.5% (1–4 C atoms replaced by impurity atoms). In the rectangular configuration, the C atom(s) replaced by dopant(s) is (are) denoted by RD1–RD4 (hollow spheres) and in the hexagonal configuration these dopants are denoted by HD1–HD4, as can be seen from Fig. 1. The upper two dopants (R-D2, R-D4) in the rectangular configuration are shifted along the positive x-axis by 2.46 Å (which is the lattice constant of graphene) relative to H-D2 and H-D4 of the hexagonal configuration. The results so obtained are presented below.

### B-doping

Initially, one C atom is replaced with one B atom making the B concentration 3.125% in the host graphene. The geometry was
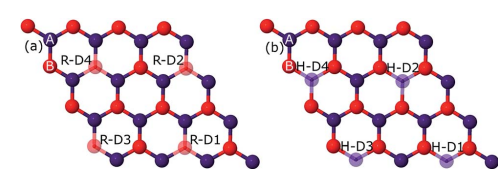


Fig. 1 The red hollow spheres, denoted by RD1–RD4, corresponding to rectangular doping are presented in (a). The hexagonal configuration is shown by the blue hollow spheres (HD1–HD4) pictured in (b). A and B indicate the sublattice sites A and B.

fully relaxed to the required accuracy. The C–B bonds were enlarged to a value of 1.50 Å due to the larger covalent radius of B (85 pm) compared to that of C (75 pm). Due to the electron deficit character of B, the Fermi level underwent a downward shift of 0.78 eV from the Dirac point. The electronic band structure calculations show a band gap opening of 0.21 eV as can be seen in Fig. 2. All of these values were found to be in good agreement with the earlier findings.[17,23]

After the satisfactory replication of these results, we started doping graphene with B at varying concentrations at the rectangular and hexagonal sites (Fig. 1). Their geometries, along with their band structures, can be seen in Fig. S2–S7 in the ESI.†

The C atoms in a graphene sheet consisting of 32 atoms are substituted with 1 to 4 B atoms in the rectangular configuration, which caused a linear increase in the band gap values, ranging from 0.21 to 0.55 eV (Fig. 3). This linear increase in the band gap with an increasing percentage of B-atoms can be achieved when all of the B-atoms are employed in the graphene sheet at the same sublattice sites (A or B).[23] Moreover, the band gap values can be increased significantly if the B dopants are integrated at the hexagonal sites. By doping with 4 B atoms hexagonally, an abrupt increase in the value of the band gap can be seen as compared to rectangular doping with 4 B atoms. This is due to the fact that the B dopants actually make a 2 × 2 superlattice in
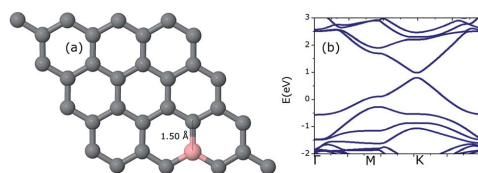


Fig. 2 Optimized geometry of a 4 × 4 graphene sheet doped with a single B atom (a) along with the corresponding band structure graph (b). The Fermi level is set to a zero energy scale.
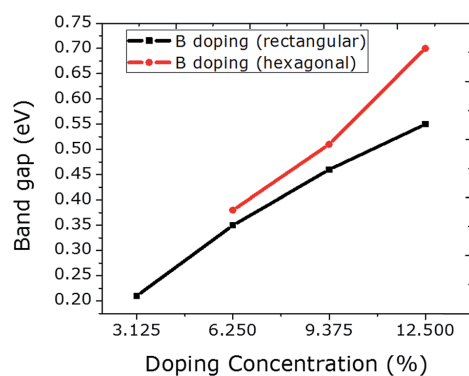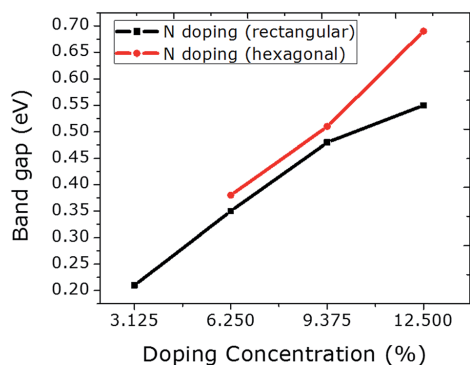


Fig. 3 The relationship between B doping with increasing concentration at rectangular and hexagonal sites and the respective band gap values is plotted.

graphene, which can be regarded as ideal hexagonal doping. Furthermore, these configurations (rectangular and hexagonal) led to the same geometry and structural stability, yet different band gap values are observed. Due to the larger covalent radius of B than of C, an expansion in the unit cell is observed for B doping. Spin polarized calculations reveal that only 4 B atom-doping of graphene at hexagonal sites induced a magnetic moment of 0.7 $\mu_B$. These indicate the proficiency of hexagonal doping.

### N-doping

A N atom was doped into a graphene sheet and the C–N bonds were found to be 1.42 Å in length after structural optimization. As the N atom is electron-rich relative to the C atom, the Fermi level is raised by 0.78 eV. The same band gap value of 0.21 eV is observed as in the case of the single B atom. Fig. S7–S14 in the ESI† correspond to the N doping of graphene.

The number of N atoms is increased in the graphene sheet from 1 to 4 in rectangular configurations. A linear rise in the band gap value is achieved (Fig. 4), which is similar to the B



**Fig. 4** The relationship between N doping with increasing concentration at rectangular and hexagonal sites and the band gap values is plotted.

doping presented above. This linear rise was reported by Rani and Jindal[23] when N atoms were doped into graphene at the same sublattices sites (A or B). The band gap values can be enhanced significantly by incorporating the N atoms at hexagonal sites, which is comparable to the result of hexagonal doping with B discussed above. Similar to B doping, a higher value for the band gap can be achieved by N doping hexagonally, which also tended to the same stability as that of rectangular doping. Furthermore, a negligibly small reduction in unit cell size is observed due to the smaller covalent radius of N than that of C. No magnetic moment was calculated for rectangular doping. However, hexagonal doping with 3 and 4 N atoms induced magnetic moments of 0.8 and 1.3 $\mu_B$, respectively. The magnetic moment that arose from the 3 N atom hexagonal doping is greater than that from the 4 B atom hexagonal doping.

### O-doping

It is interesting to investigate the rectangular and hexagonal doping of graphene with O as O atom has two electrons more than C, which could be compared to the results obtained previously from Be doping (having two electrons less than C).[21] Additionally, there is no such study regarding oxygen doping at specific sites in graphene. For this purpose, we doped graphene with a single atom of O initially. The optimized C–O bonds were found to be 1.49 Å in length, which is comparable to the value of 1.50 Å obtained before.[17] The Fermi level is moved upward by 0.58 eV. This insertion of O in graphene induced a band gap opening of 0.57 eV, which is a bit higher than the value of 0.50 eV calculated by Wu *et al.*[17]

The doping concentration of O in graphene is increased from 3.125 to 12.5% (1–4 O) in the rectangular configuration. A linear rise in band gap is observed with rectangular doping. However, an exponential rise in the band gap can be seen from the hexagonal doping of graphene with O. The value of the band gap is increased enormously from 1.03 to 1.68 eV just by choosing specific dopant sites (hexagonal). This huge increase occurs because the dopants form a 2 × 2 superlattice in the graphene, which can be considered as the ideal hexagonal doping configuration. This tendency of increasing the band gap linearly and exponentially is in agreement with Be doping with
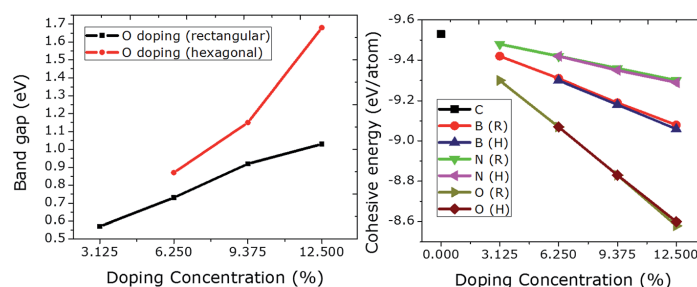


**Fig. 5** The relationship between O doping with increasing concentration at rectangular and hexagonal sites and their respective band gap values. The rectangular doping causes a linear increase in the band gap, while hexagonal doping leads to an exponential rise.

**Table 1** Summary of the calculations performed for B, N, and O doping in graphene[a]

| Dopants | Concentration (%) | Configuration | Cohesive energy (eV per atom) | Band gap (eV) |
|---|---|---|---|---|
| 1B | 3.125 | Rectangular | −9.42 | 0.21 |
| 2B | 6.25 | Rectangular | −9.31 | 0.35 |
| 2B | 6.25 | Hexagonal | −9.30 | 0.38 |
| 3B | 9.375 | Rectangular | −9.19 | 0.46 |
| 3B | 9.375 | Hexagonal | −9.18 | 0.51 |
| 4B | 12.5 | Rectangular | −9.08 | 0.55 |
| 4B | 12.5 | Hexagonal | −9.06 | 0.70 |
| 1N | 3.125 | Rectangular | −9.48 | 0.21 |
| 2N | 6.25 | Rectangular | −9.42 | 0.35 |
| 2N | 6.25 | Hexagonal | −9.42 | 0.38 |
| 3N | 9.375 | Rectangular | −9.36 | 0.48 |
| 3N | 9.375 | Hexagonal | −9.35 | 0.51 |
| 4N | 12.5 | Rectangular | −9.30 | 0.55 |
| 4N | 12.5 | Hexagonal | −9.29 | 0.69 |
| 1O | 3.125 | Rectangular | −9.30 | 0.57 |
| 2O | 6.25 | Rectangular | −9.07 | 0.73 |
| 2O | 6.25 | Hexagonal | −9.07 | 0.87 |
| 3O | 9.375 | Rectangular | −8.83 | 0.92 |
| 3O | 9.375 | Hexagonal | −8.83 | 1.15 |
| 4O | 12.5 | Rectangular | −8.58 | 1.03 |
| 4O | 12.5 | Hexagonal | −8.60 | 1.68 |

[a] The calculated value of the cohesive energy of graphene is −9.53 eV per atom.

increasing doping concentration.[21] Moreover, the size of the unit cell is found to be the same as that in pristine graphene even at a high dopant concentration (12.5%). No magnetic moment was observed for any case (rectangular or hexagonal) at any level of dopant concentration.

The effect of doping concentration on the structural stability is shown in Fig. 5 (right panel). The cohesive energies of N doped graphene are higher than those of B and O doped graphene. The lowest cohesive energies are plotted for O doping which at the same time give rise to higher values for the band gaps (max. value = 1.68 eV) when compared to B and N doping. An increase in the dopant concentration gives rise to a higher value of the band gap, and at the same time leads to a linear decrease in the cohesive energy. All of the results are summarized in Table 1.

## Conclusions

Electronic structure calculations for graphene doped with B, N, and O at rectangular and hexagonal sites are carried out using first-principles density functional theory (DFT). The dopant number is increased from 1–4 in a 4 × 4 graphene sheet. A linear increase in band gap values occurred due to the rectangular doping while an exponential rise in band gaps can be seen due to the hexagonal configuration of the dopants in the graphene. This difference in the band gaps obtained for different configurations is more prominent for O doping, which is comparable to Be doping[21] as these atoms have two electrons more and fewer, respectively, than the C atom. The value of the band gap obtained from 3 O atoms doped at the hexagonal site

is substantially greater than that when 4 O atoms are doped at the rectangular site, hence, providing the opportunity to induce a higher value of the band gap with better structural stability. Furthermore, for hexagonal doping with 4 B, 3 N, and 4 N atoms, we have observed magnetic moments at the VDW-DF/DZP level of theory. No magnetic moment was observed for O doping. This shows the supremacy of hexagonal site doping over rectangular site doping. Our results offer the possibility of getting a higher value of the band gap with a higher structural stability, due to a lower amount of dopants.

## Acknowledgements

## References

1 P. R. Wallace, *Phys. Rev.*, 1947, **71**, 622.

2 R. Saito, G. Dresselhaus and M. S. Dresselhaus, *Physical Properties of Carbon Nanotubes*, Imperial College Press, London, UK, 1998.

3 A. K. Geim and K. S. Novoselov, *Nat. Mater.*, 2007, **6**, 183.

4 A. H. C. Neto, F. Guinea, N. M. R. Peres, K. S. Novoselov and A. K. Geim, *Rev. Mod. Phys.*, 2009, **81**, 109.

5 K. S. Novoselov, A. K. Geim, S. V. Morozov, D. Jiang, Y. Zhang, S. V. Dubonos, I. V. Gregorieve and A. A. Firsov, *Science*, 2004, **306**, 666.

6 K. S. Novoselov, A. K. Geim, S. V. Morozov, D. Jiang, M. I. Katsnelson, I. V. Grigorieva, S. V. Dubonos and A. A. Firsov, *Nature*, 2005, **197**, 438.

7 A. K. Geim, *Science*, 2009, **324**, 1530.

8 E. V. Castro, H. Ochoa, M. I. Katsnelson, R. V. Gorbachev, D. C. Elias, K. S. Novoselov, A. K. Geim and F. Guinea, *Phys. Rev. Lett.*, 2010, **105**, 266601.

9 K. S. Novoselov, *Nat. Mater.*, 2007, **6**, 720.

10 L. A. Ponomarenko, F. Schedin, M. I. Katsnelson, R. Yang, E. W. Hill, K. S. Novoselov and A. K. Geim, *Science*, 2008, **320**, 356.

11 B. Trauzettel, D. V. Bulaev, D. Loss and G. Burkard, *Nat. Phys.*, 2007, **3**, 192.

12 M. Y. Han, B. Ozyilmaz, Y. Zhang and P. Kim, *Phys. Rev. Lett.*, 2007, **98**, 206805.

13 X. Li, X. Wang, L. zhang, S. Lee and H. Dai, *Science*, 2008, **319**, 1229.

14 J. Bai, X. Zhong, S. Jiang, Y. Huang and X. Duan, *Nat. Nanotechnol.*, 2010, **5**, 190.

15 P. A. Denis, *Chem. Phys. Lett.*, 2010, **492**, 251.

16 A. Lherbier, X. Blasé, Y.-M. Niquet, F. Triozon and S. Roche, *Phys. Rev. Lett.*, 2008, **101**, 036808.

17 M. Wu, C. Cao and J. Z. Jiang, *Nanotechnology*, 2010, **21**, 505202.

18 E. H. Hwang, S. Adam and S. D. Sarma, *Phys. Rev. B: Condens. Matter Mater. Phys.*, 2007, **76**, 195421.

19 O. Leenaerts, B. Partoens and F. M. Peeters, *Phys. Rev. B: Condens. Matter Mater. Phys.*, 2008, **77**, 125416.

20 H. Pinto, R. Jones, J. P. Goss and P. R. Briddon, *J. Phys.: Condens. Matter*, 2009, **21**, 402001.

21 S. Ullah, A. Hussain, W. A. Syed, M. A. Saqlain, I. Ahmad, O. Leenaerts and A. Karim, *RSC Adv.*, 2015, **5**, 55762.

22 A. Hussain, S. Ullah and M. A. Farhan, *RSC Adv.*, 2016, **6**, 55990.

23 P. Rani and V. K. Jindal, *RSC Adv.*, 2013, **3**, 802.

24 J. M. Soler, E. Artacho, J. D. Gale, A. García, J. Junquera, P. Ordejón and D. Sánchez-Portal, *J. Phys.: Condens. Matter*, 2002, **14**, 2745.

25 N. Troullier and J. L. Martins, *Phys. Rev. B: Condens. Matter Mater. Phys.*, 1991, **43**, 1993.

26 J. P. Perdew, K. Burke and M. Ernzerhof, *Phys. Rev. Lett.*, 1996, 77, 3865.

27 M. Dion, H. Rydberg, E. Schröder, D. C. Langreth and B. I. Lundqvist, *Phys. Rev. Lett.*, 2004, **92**, 246401.

28 D. R. Cooper, B. D'Anjou, N. Ghattamaneni, B. Harack, M. Hilke, A. Horth, N. Majlis, M. Massicotte, L. Vandsburger, E. Whiteway and V. Yu, *ISRN Condens. Matter Phys.*, 2012, **2012**, 56.

149

**APPENDIX B – Electrochemical properties of doped graphene**

B.1 Additional paper 1: Beryllium doped graphene as an efficient anode material for lithium-ion batteries with significantly huge capacity: A DFT study
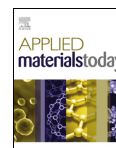
# Beryllium doped graphene as an efficient anode material for lithium-ion batteries with significantly huge capacity: A DFT study

Saif Ullah [a,*], Pablo A. Denis [b], Fernando Sato [a]

[a] *Departamento de Física, Instituto de Ciências Exatas, Campus Universitário, Universidade Federal de Juiz de Fora, 36036-900 Juiz de Fora, MG, Brazil*
[b] *Computational Nanotechnology, DETEMA, Facultad de Química, UDELAR, CC 1157, 11800 Montevideo, Uruguay*

## ARTICLE INFO

## ABSTRACT

First-principles density functional theory (DFT) calculations were performed to investigate the lithium (Li) adsorption upon beryllium (Be) doped graphene. Be acts as hole doping in graphene leaving the structure as electron deficient, offering a greater tendency for Li adsorption than in pristine and boron (B) doped graphene. The introduction of Be augments the adsorption energy of Li from $-1.11$ to $-2.53$ eV/Li. Furthermore, 12, and 16 Li ions can easily be captured by one Be center in the single and double vacancy case, respectively, with the adsorption energies of $-1.33$ eV/Li (for both the cases), showing that Be doped graphene is an excellent anode material for lithium ion batteries (LIBs). Consequently, the presence of structural defects, in particular, a divacancy is found to be more efficient in terms of Li storage capacity. A huge Li storage capacity (2303.295 mAh/g) is calculated for $Li_8BeC_7$ having reasonable adsorption energy ($-1.47$ eV/Li). Our calculated capacity is 6.19 times greater than that of the graphite.

© 2017 Elsevier Ltd. All rights reserved.

## 1. Introduction

Lithium ion batteries (LIBs), which have been extensively used in cellular phones, camcorders, laptop computers and wearable devices, and are also a prospective nominee for hybrid electric cars by virtue of their size and exceptional performance [1]. The most commonly used anode material for LIBs is graphite [2,3]. Unfortunately, the limited lithium (Li) storage capacity of graphite (372 mAh/g) makes it a less desirable candidate for LIBs. A suitable anode material is the one, which offers the higher adsorption capacity and easily diffusion of Li on anode material. Carbon nanotubes (CNTs) have the possibilities to adsorb the Li, both inside and on the outside surfaces. For this reason, single-walled CNTs (SWCNTs) have been investigated experimentally, which revealed a higher reversible capacity (as compared to graphite) of 500 mAh/g [4]. Moreover, the chemical etching [5], and ball-milling [6] techniques offer the possibility of synthesizing $Li_{2.7}C_6$ CNTs, exhibiting a much higher Li capacity of up to 1000 mAh/g. Due to the exceptional properties of graphene, such as high thermal and electrical conductivities, large surface area, outstanding mechanical strength and wide-ranging electrochemical window, makes it a potential and alternative candidate for its use as anode material in LIBs [7–12].

Unfortunately, there are some issues related to the use of graphene as an anode material. Regardless of the Li concentration upon graphene, the Li atoms are likely to form clusters which can lead to the dendrite formation, resulting in a serious reduction in the charge/discharge capacity of the battery/batteries [13–15]. The Li adsorption energy upon graphene is weaker than the Li–Li interaction, which is the main reason for Li-clusters formation. To avoid Li-clusters formation, the adsorption energy of Li on graphene should exceed the cohesive energy of the bulk Li.

Fortunately, there are certain techniques which can address these issues. Few of them include the modification of the graphene surface [16], edge [17], point defects [18], grain boundary [19], doping and complimentary synergy effects [20–26]. However, substitutional doping is the easier and efficient way to enhance the Li adsorption on graphene. The dopants can seriously alter the magnetic [27,28], thermal [29], electronic [30–32], mechanical [30] and transport properties [30,33] as well as the chemical reactivity of graphene [23,34–41], thus increasing the novelty of these graphene systems regarding to their applications.

The most frequently studied dopants are B and N in graphene, which are the neighbors of C atom. B acts as hole doping (p-type) while N as electron doping (n-type) in graphene. These dopants can alter the electronic structure of graphene by lifting (N) or lowering (B) the Fermi level in the conduction and valence bands, respectively. Regarding the concentration of N doping in graphene and its applications in oxygen reduction reaction and fuel cell

---

materials, a very meticulous information can be found in the literature [42,43]. These authors explicitly reported the formation energies of N doped graphene as a function of N concentration, and also marked the maximum possible N concentration in graphene. The high concentration of B dopants in graphene ($BC_3$) hinders the formation of clusters of the adsorbates [44], and hence, it can be regarded as a good anode material for battery applications. In a recent study, a very high reversible capacity of 1549 mAh/g with a low charge/discharge rate of 50 mA/g was reported for B doped graphene [45]. Wang et al. predicted a much higher Li capacity of 2271 mAh/g for $Li_6BC_5$ (B doped graphene) using DFT calculations[46]. B doped graphene is found to be much more efficient than N doped graphene in terms of the good adsorption of Li. It is due to the fact that B transfers a big portion of its valence charge to graphene, leaving graphene as a p-type doped, and the Li which can be regarded as electron doping in graphene, and therefore, favors the B doped graphene to be adsorbed on.

Beryllium (Be) is the next neighbor to C (having two electrons less than C) and can be doped in graphene [47,48]. Graphene can be doped with Be by means of chemical vapor deposition (CVD) techniques. The theoretical capacity of Be adsorbed fullerene for H storage was investigated by Lee et al. [49]. In our recent study, we have investigated that Be is far more efficient than B in terms of charge transfer (p-type doping) and engineering the electronic structure of graphene [47,48], and hence one can expect the better chemistry of Li with Be doped graphene. Furthermore, the interaction of Be with different kinds of nanotubes and fullerenes are well described in the literature [50–52].

This study is an attempt to test the adsorption and storage capacity of Li on Be doped graphene. We hope that these interesting results will surely motivate experimentalists to synthesize and fabricate Be doped graphene anode for Li adsorption.

## 2. Computational details

We have performed first-principles VDW-DF [53] calculations to investigate the interaction of Li with Be doped graphene with the help of SIESTA code [54,55], which is based on the density functional theory (DFT). The electrons-ions interaction is described by the Troullier–Martins pseudopotentials [56]. A $5 \times 5$ supercell consisting of 50 atoms, with the periodic boundary condition in all directions, is sampled with $8 \times 8 \times 1$ Monkhorst–Pack k-points scheme. The unit cell is allowed to relax in $xy$ directions while the $z$-axis is kept frozen at 20 Å, so in order to avoid the interactions between replicas. In order to predict the maximum possible Li storage capacity of Be doped graphene, we used a $2 \times 2$ supercell sampled with $60 \times 60 \times 1$ k-points grid. Spin polarization is taken into account (for all the calculations) using a double-zeta basis set with polarization functions (DZP). The split norm is set to 0.15. The orbital confining cut-off is set to 0.01 Ry, and the mesh cut-off is fixed to 200 Ry. The geometry optimization procedure was followed by conjugate gradient algorithm until the Hellman–Feynman forces were smaller than 0.02 eV/Å. In order to calculate the adsorption energies of Li on Be doped graphene, we use the following formula:

$$E_{ads} = \frac{E_{tot} - E_{sheet} - nE_{Li}}{n}$$

where $E_{tot}$, $E_{sheet}$ and $E_{Li}$ represents the total energy of the system, energy of Be doped graphene slab and energy of isolated Li. Finally, $n$ shows the number of Li ion(s).

We also performed M06-L and M06-2X calculations [57] as implemented in Gaussian 2009 [58] to shed light into the charge distribution of Be doped graphene. The basis sets selected were the 6-31G* and 6-311G* [59]. The ultrafine grid was employed in all calculations and the unit cells were sampled using 1000 k-points. We

employed $N \times N$ unit cell $N = 2$–10 to perform periodic M06-L calculations and a circumcoronene model ($C_{54}H_{18}$) to mimic graphene in the M06-2X experiments. A well described benchmarking of the M06-2X functional for the interaction between benzene and Li can be found in Ref. [60], which shows a good performance against the coupled cluster calculations.

## 3. Results and discussions

Primarily, graphene sheet consisting of 50C atoms is doped with single Be atom (on a mono-vacancy) making the Be concentration 2% in the host graphene. We have considered both the in-plane doping and with buckling height of Be in graphene. The latter is found 3.31 eV more stable with a buckling height of 0.78 Å. The electronic band structure calculations reveal a downward shift of 0.82 eV in Fermi level, which shows p-type doping. Band gaps of 0.49 eV (indirect) and 0.40 eV (direct) are induced at Fermi level and around Dirac point, respectively. For cohesive energy calculations, the following expression has been used: $E_{coh} = (E_{tot} - n_iE_i)/n$ ($i =$ C, and Be). The $E_i$ is the energy of isolated atom (C, and Be), while $n_i$ is the number of $i$th specie. Finally, the $n$ represents the total number of atoms in a supercell. The cohesive energies of graphene and Be doped graphene are computed to be $-7.335$ and $-7.129$ eV/atom, respectively. All these outcomes are in good agreement with our previous findings [47]. The formation energy is calculated with the help of the following equation: $E_{for} = E_{tot} - (n)\mu_c - \mu_{Be}$, where $E_{for}$, and $E_{tot}$ correspond to the formation and total energy, respectively. The chemical potential of C ($\mu_c$) is calculated as the cohesive energy per C atom of the pristine graphene, while for the $\mu_{Be}$, the energy of isolated Be atom is used. According to this equation, the formation energy of Be doped graphene is found to be 2.91 eV. Furthermore, the formation energies at different Be concentration are also calculated by using $7 \times 7$ (2.63 eV), $6 \times 6$ (2.80 eV), $4 \times 4$ (2.96 eV), and $2 \times 2$ (3.08 eV) supercells, which shows that Be concentration has a strong impact on the formation energies. The introduction of Be dopant alters the charge distribution in graphene. In order to obtain an adequate description of the charge transfer, we have used different basis sets as we have shown in our very recent study that Mulliken charges are strongly dependent on the type of basis sets [61]. In effect, at the M06-l/6-31G* level, the Mulliken charge of Be is $-0.34\ e^-$, obviously looks very weird as the electronegativity of C is higher than Be. This
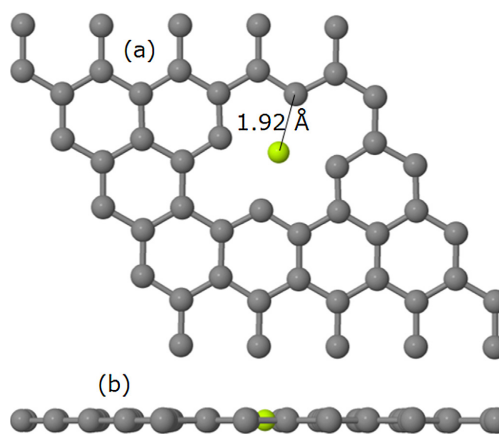


**Fig. 1.** Top (a) and side view (b) of a 585 divacancy graphene doped with Be.

being said, that the charge must be transferred from Be to graphene as we have already reported this in our past study [47]. However, if the basis set is increased to 6-311G*, the Mulliken analysis is completely different as the charge of Be is +0.25. The latter value does not change when the unit cell is increased, being similar for a 10 × 10 unit cell. The M06-2X/6-311G* calculations, supported the results obtained at the M06-L/6-311G* level. We found that the Mulliken charge of Be, when it is introduced in the circumcoronene model, is +0.18. The Natural Bond Order analysis of this Be doped graphene flake also indicated a positive charge for Be but the value was larger, as $0.83e^-$ were transferred to the carbon atoms. In spite of the fact that the NBO and Mulliken analysis gave different values, the important point is that both the studies predict a positive charge for Be.

For the comparative purposes, a 585 divacancy graphene doped with Be atom is also taken into account. In this case, the Be stays within the graphene plane and can be compared to the behavior of

3p and 4p elements (see Fig. 1) [62]. The calculated formation and cohesive energies were 3.96 eV, and −7.103 eV/atom, respectively.

The next step was to find the adsorption energy of Li on pristine graphene, to compare with the results obtained for Be doped graphene. As it is an established fact that Li atoms favor the hollow sites in graphene and also in CNTs, so we just considered the hollow site for the Li adsorption on graphene [63–67]. The adsorption energy is found to be −1.13 eV/Li, which is pretty much comparable with the available data [66,68]. After these successful replications of results, we were in a position to study the interaction of Li with Be doped graphene.

Initially, one Li atom is adsorbed on the hollow site of the hexagon in which Be is a part, and on the same side on which Be is protruded of the graphene plane. The separation between Li from graphene plane and Be atom is found to be 2.1 and 2.37 Å, respectively. The adsorption energy is calculated to be −2.37 eV/Li-atom. Furthermore, the opposite side of Be doped graphene is also
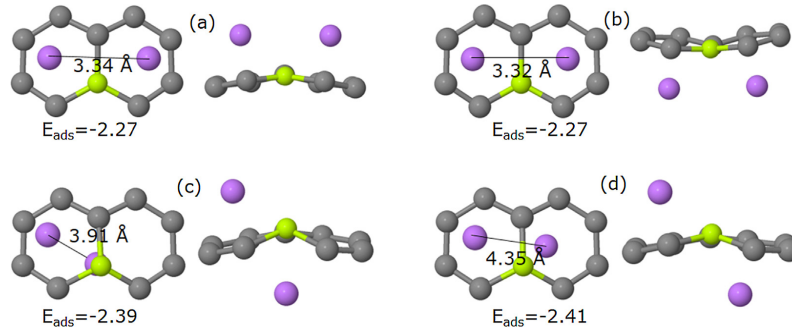


**Fig. 2.** Top and side view of the adsorption of two Li upon Be doped graphene (part of 5 × 5 supercell) with different configurations (a) 2-up, (b) 2-down, (c) 1up1down same hexagon, (d) 1up1down different hexagons is depicted.

**Table 1**
Adsorption energies (eV), charges ($e$), and magnetic moments ($\mu_B$) calculated for Li adsorption on Be doped graphene.[a]

| Configuration | Number of Li ions | Adsorption energy ($E_{ads}$) = eV/Li | Charges/Li Mulliken/Hirshfeld/Voronoi ($e$) | Magnetic moment ($\mu_B$) |
|---|---|---|---|---|
| **Be doping on mono-vacancy** | | | | |
| 1down | 1 | −2.53 | 0.496/0.395 | 0 |
| 1up | 1 | −2.38 | 0.448 | 0 |
| 1up1down-different hexagon | 2 | −2.41 | 0.465 | 0 |
| 1up1down | 2 | −2.39 | 0.476 | 0 |
| 2down | 2 | −2.27 | 0.418 | 0 |
| 2up | 2 | −2.27 | 0.418 | 0 |
| 3up | 3 | −2.05 | 0.314 | 0.8 |
| 2up1down | 3 | −2.03 | 0.436 | 0 |
| 3down | 3 | −2.02 | 0.314 | 0.8 |
| 3up1down | 4 | −1.89 | 0.434 | 0 |
| 2up2down | 4 | −1.80 | 0.319 | 1.12 |
| 3up2down | 5 | −1.75 | 0.264 | 0 |
| 3up3down | 6 | −1.68 | 0.26/0.151 | 0 |
| 4up3down | 7 | −1.60 | 0.253 | 0.87 |
| 4up4down | 8 | −1.52 | 0.234 | 0 |
| 5up4down | 9 | −1.47 | 0.21 | 0.9 |
| 5up5down | 10 | −1.40 | 0.21 | 0 |
| 6up5down | 11 | −1.37 | 0.212 | 0 |
| 6up6down | 12 | −1.33 | 0.192/0.104 | 0 |
| | | | | |
| **Be doping on divacancy** | | | | |
| 1up | 1 | −2.38 | 0.472/0.386/0.406 | 0.94 |
| 3up3down | 6 | −1.846 | 0.29/0.186/0.207 | 1.40 |
| 4up4down | 8 | −1.754 | 0.26/142/0.164 | 0 |
| 6up6down | 12 | −1.475 | 0.196/0.098/0.118 | 0 |
| 8up8down | 16 | −1.33 | 0.184/0.091/0.11 | 0 |

[a] Eads on pristine graphene is −1.13 eV/Li.
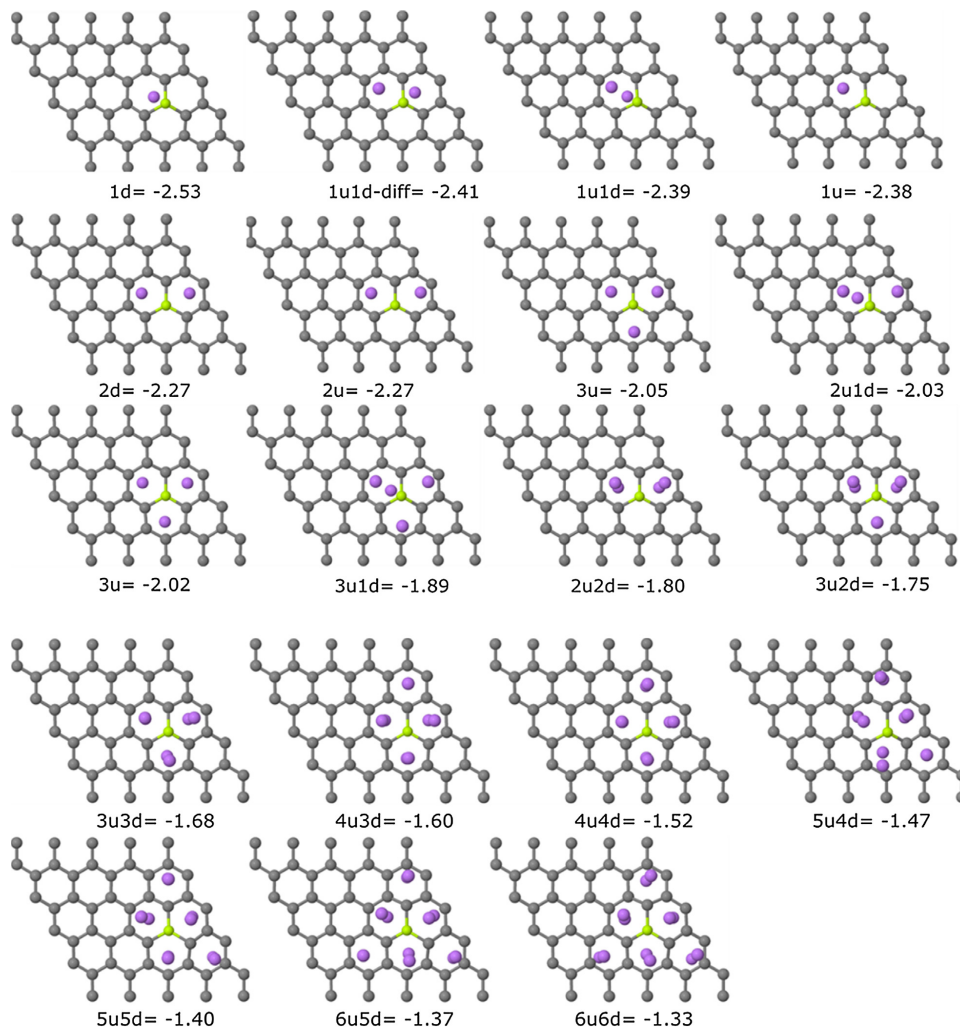
**Fig. 3.** Increasing concentration of Li ions on Be doped graphene (5 × 5 supercell) is shown along with their respective adsorption energies. The adsorption energies are in the unit of eV/Li.

considered for Li interaction, and we found that Li atom migrated towards Be impurity. This migration of Li towards bigger dopants (Al, Si, P, and S) is recently reported by Denis et al. [69]. The height of Li from the graphene plane is reduced to 1.32 Å and the Li–Be distance is found to be 2.41 Å. The adsorption energy is interestingly increased to −2.53 eV/Li. The introduction of Be impurity enhanced the adsorption energy of Li by 1.24 and 1.4 eV/Li for top and down configurations, respectively. With regards to charge transfer, the Mulliken analysis indicated that when Li is adsorbed on a Be-doped circumcoronene model, the charge of Be is +0.34 while Li has a positive charge of +0.67. The NBO analysis indicated a similar trend, with a positive charge of 0.73 and 0.87 for Be and Li, respectively, at the M06-2X/6-311G* level.

The Li concentration is increased to two ions (per 5 × 5 supercell) for which we have different conformations. We considered the Li configuration as 2up, 2down, 1up1down on the same hexagon, and 1up1down on different hexagons around the Be impurity. The Li–Li distance has a strong impact on the adsorption energies. Higher the Li–Li separation, greater will be the value of adsorption energy with the lone exception of 2down for which the Li–Li separation is minimum but led to the same energy as that of 2up. The Li–Li distance and the corresponding adsorption energies can be seen in Fig. 2.

As there are three hexagons around the Be impurity which can accommodate 3–3 Li ions on both sides. The studied configurations are 2up1down, 3up, 3down, 2up2down, 3up1down, 3up2down and

154

3up3down. The results are presented in Table 1. For 6 Li ion, the adsorption energy is calculated to be as high as −1.68 eV/Li. These interesting findings strive us to investigate that whether more Li ions can be attached to the Be atom in the Be doped graphene or not? For this purpose, we have considered the next nearest neighbor hexagons for Li ions attachment. These arrangements are 4up3down, 4up4down, 5up4down, 5up5down, 6up5down, and 6up6down (see Fig. 3). For the extreme case viz 6up6down, fascinatingly, we obtained a very good adsorption energy of −1.33 eV/Li. This adsorption energy is still 0.20 eV/Li greater than that of calculated for single Li adsorption on pristine graphene. In this configuration, the Li ions made 2-D (2-dimensional) tetrahedron on both the sides of Be doped graphene see Fig. SM1. The adsorption capacity as a function of adsorption energy is depicted in Fig. 4.

The pDOS calculations for 1Li (up/down) show that the Be atom is largely contributing along with the C atoms to the total DOS only in the valence band. The Li contribute to the DOS in the conduction band in the region around 2 eV energy scale. This can be seen in Fig. 5(b) and (c) in the form of a high sharp peak in the total DOS. It is interesting to note that increasing concentration of Li gave rise to many intense peaks in the DOS with increasing the range of Li contribution. For 3up3down, all the high-intensity peaks in the total DOS comes from the Li atoms ranging from −0.4 to 3.0 eV, showing that Li atoms are contributing in the valence band as well. Additionally, for 6up6down, the DOS is dominated by Li atoms over an energy range of −1.0–3.0 eV. Moreover, the discrete peaks of Li now taken the form of continuous states in this range mentioned before. Furthermore, there are many states from Li in the valence band and these states are shifting deep into valence band.

The Be doped 585 divacancy graphene is also decorated with Li. The studied configurations are 1up, 3up3down, 4up4down, 6up6down, and 8up8down as depicted in Fig. 6. For 1up isomer, the adsorption energy is −2.38 eV/Li, which is just the same as calculated for 1up configuration on Be doped graphene (mono-vacancy). However, for 3up3down, a better adsorption energy (−1.846 eV/Li) was calculated compared to the Be doping on mono-vacancy (−1.68 eV/Li). As there are four dangling bonds around Be atom, so it offers the space for 4Li atoms. At this moment, the difference between adsorption energies of Li on single and double vacancy graphene doped with Be is much more prominent.
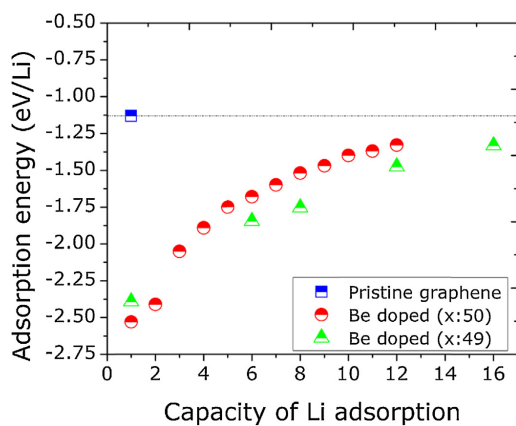


**Fig. 4.** The adsorption energies of Li on pristine (half-filled blue square), Be doped in mono-vacancy (half-filled red sphere), and Be doped in divacancy graphene (half-filled green triangle) are depicted. Patterns with higher adsorption energies are plotted for the mono-vacancy case. (For interpretation of the references to color in this figure legend, the reader is referred to the web version of this article.)
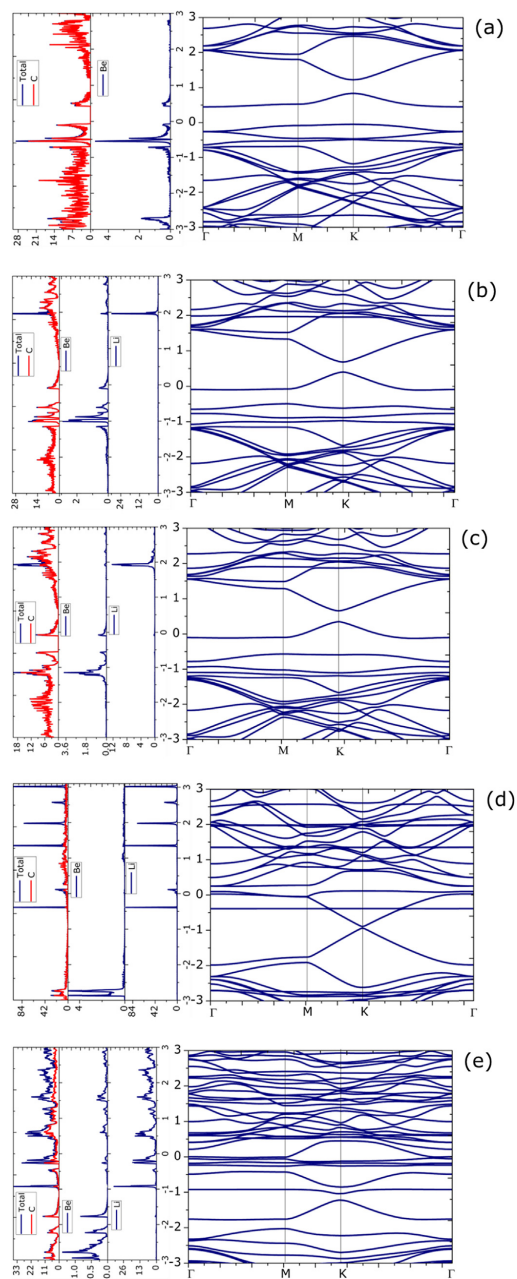


**Fig. 5.** Band structures (left side) along with their respective pDOS graphs (right side) of (a) Be doped graphene, (b) 1Li-down, (c) 1Li-up, (d) 3Liup-3down, and (e) 6Liup-6down are depicted.
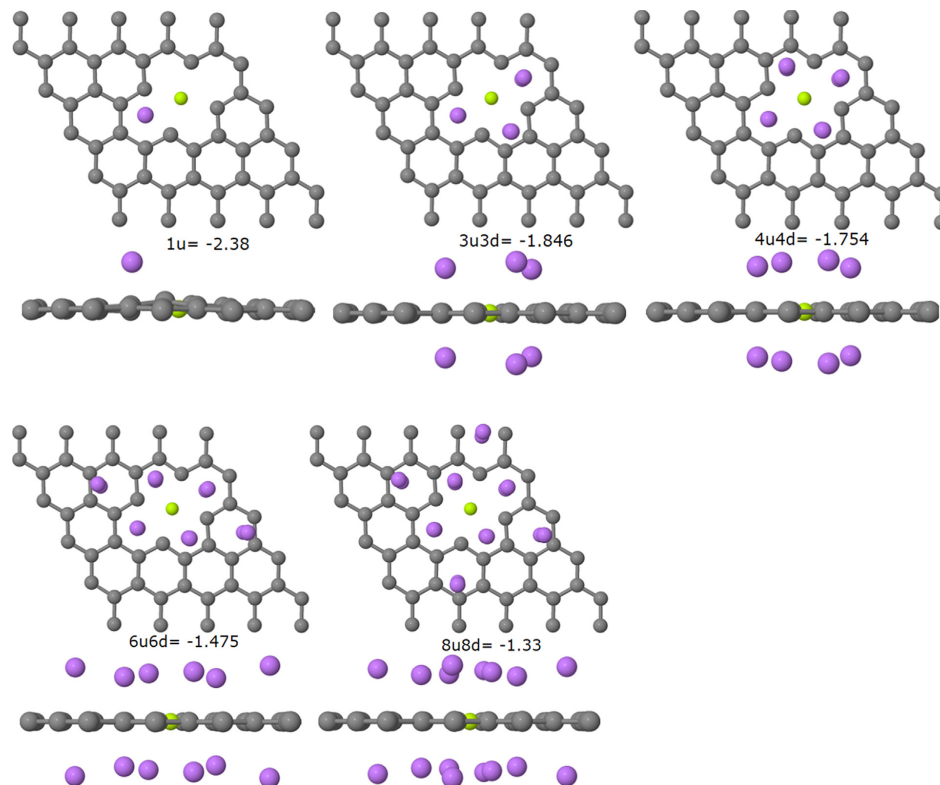
**Fig. 6.** Increasing concentration of Li ions on a 585 divacancy graphene doped with Be (5 × 5 supercell) is shown along with their respective adsorption energies. The adsorption energies are in the unit of eV/Li.

This difference is 0.3 eV/Li as the calculated adsorption energy is −1.754 eV/Li. The 6up6down pattern has an adsorption energy of −1.475 eV/Li. Finally, the 8up8down configuration was calculated as there are 4 nearest and 4 next nearest positions for Li adsorption around Be atom. This arrangement has the same adsorption energy (−1.33 eV/Li) as calculated for 6up6down (mono-vacancy case). This shows the efficacy of Be doping in graphene with divacancy. A summary of the results is given in Table 1. The Li charge has a strong dependence on the Li coverage as the Li concentration increases, the charge transfer from Li to Be doped graphene decreases.

It is, indeed, worthy to calculate the storage capacity (electrochemical performance) of Be doped graphene and compare it with other anode materials. The following expression is used for the calculation of the storage capacity of Be doped graphene:

$$C = \frac{nF}{M} \times \frac{1000}{3600}$$

where $n$ shows the number of charge(s) (Li-ions) adsorbed, $F$ is the Faraday constant, $M$ is the molar mass of graphene with impurity/impurities (Be doped graphene), and finally, 1000/3600 is used for the conversion of coulomb to mAh. With the help of this equation, the theoretical specific capacities of the $Li_{12}BeC_{49}$, $Li_{12}BeC_{48}$, and $Li_{16}BeC_{48}$ systems are found to be 538.226, 549.266, and 732.355 mAh/g, respectively, which are sufficiently larger

than the recently reported value (212.6 mAh/g) [70] evaluated for $Li_{6.84}B_2C_{70}$. In Ref. [70], 2B dopants were used. These values are higher than that of $Ti_3C_2$ (320 mAh/g) [71], graphite (372 mAh/g) [3], phosphorene (433 mAh/g) [72] and even higher than $Mo_2C$ (526 mAh/g) [73].

In order to evaluate the maximum possible Li storage capacity of Be doped graphene, we considered a 2 × 2 graphene supercell (consisting of 8 atoms) doped with one Be atom. The dopant concentration in graphene is 12.5%. In our recent study, we have studied the same Be concentration in graphene i.e. 4Be in a 4 × 4 supercell. The computed formation energy is 3.08 eV. We adsorbed 6 Li ions (3up3down) upon this system to form $Li_6BeC_7$ (see Fig. 7). The adsorption energy is calculated to be −1.59 eV/Li, slightly lower than that of $Li_6BeC_{49}$ (−1.68 eV/Li). Surprisingly, a very high theoretical Li storage capacity of 1727.471278 mAh/g is calculated for $Li_6BeC_7$. This interesting adsorption energy compels us to take all the hexagons into account for Li adsorption. For this purpose, we calculated the adsorption of 8Li ions giving rise to $Li_8BeC_7$ as shown in Fig. 7. The distance between Li–Li on the same surface (2.76–2.82 Å) and between the two layers of Li (3.60–3.62 Å) is quite larger than that of pristine graphene and $Li_6BC_5$ [46]. The band structure and pDOS graphs calculated for $BeC_7$, $Li_6BeC_7$, and $Li_8BeC_7$ is presented in SM 2 of the Supplementary material. For $Li_6BeC_7$, the same value of energy gap is induced at K and Γ point, while for $Li_8BeC_7$, the band gap is shifted from K to Γ'. The
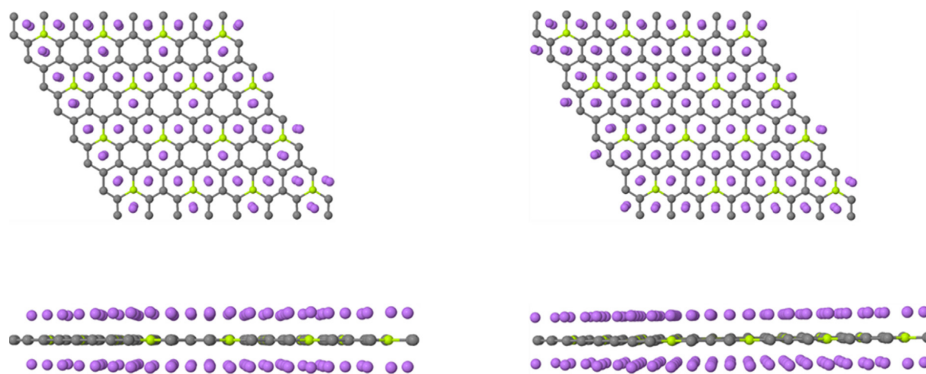
**Fig. 7.** Top and side view of $Li_6BeC_7$ (left side) and $Li_8BeC_7$ (right side) is depicted.

adsorption energy is as high as −1.475 eV/Li, leading to a theoretical capacity of 2303.295 mAh/g. This enormous storage capacity is higher than the experimental 1549 mAh/g [45] as well as the theoretical capacity (2271 mAh/g) [46] of Li on B doped graphene.

In order to have further insights of the Be doped graphene as anode materials for LIBs, the lithiation potential ($V_{Li}$) is calculated by using the following equation:

$$V_{Li} = -\frac{E_{tot} - E_{sheet} - nE_{Li}}{nzF}$$

where, $z$ represents the electronic charge of Li ions ($z$=1) in the electrolyte. An increase in the Li concentration causes a reduction in the $V_{Li}$. The $V_{Li}$ decreases from 2.53 to 1.33 V, and 2.38 to 1.33 V as the Li concentration increases from 1 to 12 atoms on monovacancy (Be doped), and from 1 to 16 atoms on divacancy (Be doped) graphene, respectively. These values are sufficiently larger than those reported for B doping (1.52 to 0.10 V for 1 to 6 atoms) [70]. The $V_{Li}$ for $Li_6BeC_7$, and $Li_8BeC_7$ are predicted to be 1.59, and 1.47 V, respectively.

## 4. Conclusions

The adsorption of Li ions upon Be doped graphene has been investigated with the help of DFT simulations. After the introduction of Be, the graphene turns out to be an electron deficient system. The Be can augments the adsorption energy of Li up to −2.53 eV/Li, which is 2.24 times that of Li adsorption on pristine graphene. Li ions can be stored not only on the top of hexagons centered with Be but on the nearest neighboring hexagons also. Around one Be center in graphene, 12 Li ions (mono-vacancy case), and 16 Li ions (divacancy case) can be attached easily. This shows that greater number of Li ions can be stored with the lesser number of doping in graphene, thus preserving the extraordinary properties of graphene up to a great extent. A dramatic increase in the storage capacity for Li (2303.295 mAh/g) is occurred by Be doping giving rise to $Li_8BeC_7$. Our interesting results offer the possibility of using Be doped graphene as anode materials for LIBs.

## Acknowledgments

## Appendix A. Supplementary data

Supplementary data associated with this article can be found, in the online version, at doi:10.1016/j.apmt.2017.08.013.

## References

[1] M. Armand, J.M. Tarascon, Building better batteries, Nature 451 (2008) 652–657.
[2] J.R. Dahn, T. Zheng, Y. Liu, J.S. Xue, Mechanisms for lithium insertion in carbonaceous materials, Science 270 (1995) 590.
[3] J.M. Tarascon, M. Armand, Issues and challenges facing rechargeable lithium batteries, Nature 414 (2001) 359–367.
[4] A.S. Claye, J.E. Fischer, C.B. Huffman, A.G. Rinzler, R.E. Smalley, Solid-state electrochemistry of the Li single wall carbon nanotube system, J. Electrochem. Soc. 147 (2000) 2845–2852.
[5] H. Shimoda, B. Gao, X.P. Tang, A. Kleinhammes, L. Fleming, Y. Wu, O. Zhou, Lithium intercalation into opened single-wall carbon nanotubes: storage capacity and electronic properties, Phys. Rev. Lett. 88 (2001) 015502.
[6] B. Gao, C. Bower, J.D. Lorentzen, L. Fleming, A. Kleinhammes, X.P. Tang, L.E. McNeil, Y. Wu, O. Zhou, Enhanced saturation lithium composition in ball-milled single-walled carbon nanotubes, Chem. Phys. Lett. 327 (2000) 69–75.
[7] A.K. Geim, K.S. Novoselov, The rise of graphene, Nat. Mater. 6 (2007) 183–191.
[8] A.A. Balandin, S. Ghosh, W. Bao, I. Calizo, D. Teweldebrhan, F. Miao, C.N. Lau, Superior thermal conductivity of single-layer graphene, Nano Lett. 8 (2008) 902–907.
[9] K.S. Novoselov, V.I. Falko, L. Colombo, P.R. Gellert, M.G. Schwab, K. Kim, A roadmap for graphene, Nature 490 (2012) 192–200.
[10] K.S. Novoselov, A.K. Geim, S.V. Morozov, D. Jiang, Y. Zhang, S.V. Dubonos, I.V. Grigorieva, A.A. Firsov, Electric field effect in atomically thin carbon films, Science 306 (2004) 666.
[11] M.D. Stoller, S. Park, Y. Zhu, J. An, R.S. Ruoff, Graphene-based ultracapacitors, Nano Lett. 8 (2008) 3498–3502.
[12] M. Xu, T. Liang, M. Shi, H. Chen, Graphene-like two-dimensional materials, Chem. Rev. 113 (2013) 3766–3798.
[13] J. Zhou, Q. Sun, Q. Wang, P. Jena, Tailoring Li adsorption on graphene, Phys. Rev. B: Condens. Matter 90 (2014) 205427.
[14] M. Liu, A. Kutana, Y. Liu, B.I. Yakobson, First-principles studies of Li nucleation on graphene, J. Phys. Chem. Lett. 5 (2014) 1225–1229.
[15] X. Fan, W.T. Zheng, J.-L. Kuo, D.J. Singh, Adsorption of single Li and the formation of small Li clusters on graphene for the anode of lithium-ion batteries, ACS Appl. Mater. Interfaces 5 (2013) 7793–7797.
[16] G. Kim, S.-H. Jhi, N. Park, S.G. Louie, M.L. Cohen, Optimization of metal dispersion in doped graphitic materials for hydrogen storage, Phys. Rev. B: Condens. Matter 78 (2008) 085408.
[17] C. Uthaisar, V. Barone, Edge effects on the characteristics of Li diffusion in graphene, Nano Lett. 10 (2010) 2838–2842.
[18] L.-J. Zhou, Z.F. Hou, L.-M. Wu, First-principles study of lithium adsorption and diffusion on graphene with point defects, J. Phys. Chem. C 116 (2012) 21780–21787.

[19] L.-J. Zhou, Z.F. Hou, L.-M. Wu, Y.-F. Zhang, First-principles studies of lithium adsorption and diffusion on graphene with grain boundaries, J. Phys. Chem. C 118 (2014) 28055–28062.

[20] R.P. Hardikar, D. Das, S.S. Han, K.-R. Lee, A.K. Singh, Boron doped defective graphene as a potential anode material for Li-ion batteries, Phys. Chem. Chem. Phys. 16 (2014) 16502–16508.

[21] Y.-X. Yu, Can all nitrogen-doped defects improve the performance of graphene anode materials for lithium-ion batteries? Phys. Chem. Chem. Phys. 15 (2013) 16819–16827.

[22] L. Wang, Z. Sofer, J. Luxa, M. Pumera, Nitrogen doped graphene: influence of precursors and conditions of the synthesis, J. Mater. Chem. C 2 (2014) 2887–2893.

[23] H. Tian, Z. Sofer, M. Pumera, A. Bonanni, Investigation on the ability of heteroatom-doped graphene for biorecognition, Nanoscale 9 (2017) 3530–3536.

[24] C.E. Chng, Z. Sofer, M. Pumera, A. Bonanni, Doped and undoped graphene platforms: the influence of structural properties on the detection of polyphenols, Sci. Rep. 6 (2016) 20673.

[25] S.M. Tan, H.L. Poh, Z. Sofer, M. Pumera, Boron-doped graphene and boron-doped diamond electrodes: detection of biomarkers and resistance to fouling, Analyst 138 (2013) 4885–4891.

[26] H.L. Poh, P. Šimek, Z. Sofer, M. Pumera, Halogenation of graphene with chlorine, bromine, or iodine by exfoliation in a halogen atmosphere, Chem. Eur. J. 19 (2013) 2655–2662.

[27] P.A. Denis, Band gap opening of monolayer and bilayer graphene doped with aluminium, silicon, phosphorus, and sulfur, Chem. Phys. Lett. 492 (2010) 251–257.

[28] D. Xiao, W. Yao, Q. Niu, Valley-contrasting physics in graphene: magnetic moment and topological transport, Phys. Rev. Lett. 99 (2007) 236809.

[29] E.K. Goharshadi, S.J. Mahdizadeh, Thermal conductivity and heat transport properties of nitrogen-doped graphene, J. Mol. Graphics Modell. 62 (2015) 74–80.

[30] P. Willke, J.A. Amani, A. Sinterhauf, S. Thakur, T. Kotzott, T. Druga, S. Weikert, K. Maiti, H. Hofsäss, M. Wenderoth, Doping of graphene by low-energy ion beam implantation: structural, electronic, and transport properties, Nano Lett. 15 (2015) 5110–5115.

[31] G. Giovannetti, P.A. Khomyakov, G. Brocks, V.M. Karpan, J. van den Brink, P.J. Kelly, Doping graphene with metal contacts, Phys. Rev. Lett. 101 (2008) 026803.

[32] F. Wang, G. Liu, S. Rothwell, M. Nevius, A. Tejeda, A. Taleb-Ibrahimi, L.C. Feldman, P.I. Cohen, E.H. Conrad, Wide-gap semiconducting graphene from nitrogen-seeded SiC, Nano Lett. 13 (2013) 4827–4832.

[33] Y.-C. Lin, C.-Y. Lin, P.-W. Chiu, Controllable graphene N-doping with ammonia plasma, Appl. Phys. Lett. 96 (2010) 133110.

[34] S. Kawai, S. Saito, S. Osumi, S. Yamaguchi, A.S. Foster, P. Spijker, E. Meyer, Atomically controlled substitutional boron-doping of graphene nanoribbons, Nat. Commun. 6 (2015) 8098.

[35] H. Wang, T. Maiyalagan, X. Wang, Review on recent progress in nitrogen-doped graphene: synthesis, characterization, and its potential applications, ACS Catal. 2 (2012) 781–794.

[36] C.H.A. Wong, Z. Sofer, K. Klímová, M. Pumera, Microwave exfoliation of graphite oxides in H2S plasma for the synthesis of sulfur-doped graphenes as oxygen reduction catalysts, ACS Appl. Mater. Interfaces 8 (2016) 31849–31855.

[37] C.K. Chua, Z. Sofer, B. Khezri, R.D. Webster, M. Pumera, Ball-milled sulfur-doped graphene materials contain metallic impurities originating from ball-milling apparatus: their influence on the catalytic properties, Phys. Chem. Chem. Phys. 18 (2016) 17875–17880.

[38] K. Klímová, M. Pumera, J. Luxa, O. Jankovský, D. Sedmidubský, S. Matějková, Z. Sofer, Graphene oxide sorption capacity toward elements over the whole periodic table: a comparative study, J. Phys. Chem. C 120 (2016) 24203–24212.

[39] H. Tian, L. Wang, Z. Sofer, M. Pumera, A. Bonanni, Doped graphene for DNA analysis: the electrochemical signal is strongly influenced by the kind of dopant and the nucleobase structure, Sci. Rep. 6 (2016) 33046.

[40] A. Ambrosi, A. Bonanni, Z. Sofer, J.S. Cross, M. Pumera, Electrochemistry at chemically modified graphenes, Chem. Eur. J. 17 (2011) 10763–10770.

[41] M. Giovanni, H.L. Poh, A. Ambrosi, G. Zhao, Z. Sofer, F. Sanek, B. Khezri, R.D. Webster, M. Pumera, Noble metal (Pd, Ru, Rh, Pt, Au, Ag) doped graphene hybrids for electrocatalysis, Nanoscale 4 (2012) 5002–5008.

[42] D. Kwak, A. Khetan, S. Noh, H. Pitsch, B. Han, First principles study of morphology, doping level, and water solvation effects on the catalytic mechanism of nitrogen-doped graphene in the oxygen reduction reaction, ChemCatChem 6 (2014) 2662–2670.

[43] M.H. Seo, S.M. Choi, E.J. Lim, I.H. Kwon, J.K. Seo, S.H. Noh, W.B. Kim, B. Han, Toward new fuel cell support materials: a theoretical and experimental study of nitrogen-doped graphene, ChemSusChem 7 (2014) 2609–2620.

[44] M. Endo, C. Kim, K. Nishimura, T. Fujino, K. Miyashita, Recent development of carbon materials for Li ion batteries, Carbon 38 (2000) 183–197.

[45] Z.-S. Wu, Z. Ren, L. Xu, F. Li, H.-M. Cheng, Doped graphene sheets as anode materials with superhigh rate and large capacity for lithium ion batteries, ACS Nano 5 (2011) 5463–5471.

[46] X. Wang, Z. Zeng, H. Ahn, G. Wang, First-principles study on the enhancement of lithium storage capacity in boron doped graphene, Appl. Phys. Lett. 95 (2009) 183103.

[47] S. Ullah, A. Hussain, W. Syed, M.A. Saqlain, I. Ahmad, O. Leenaerts, A. Karim, Band-gap tuning of graphene by Be doping and Be, B co-doping: a DFT study, RSC Adv. 5 (2015) 55762–55773.

[48] A. Hussain, S. Ullah, M.A. Farhan, Fine tuning the band-gap of graphene by atomic and molecular doping: a density functional theory study, RSC Adv. 6 (2016) 55990–56003.

[49] H. Lee, B. Huang, W. Duan, J. Ihm, Ab initio study of beryllium-decorated fullerenes for hydrogen storage, J. Appl. Phys. 107 (2010) 084304.

[50] J. Beheshtian, M.T. Baei, Z. Bagheri, A.A. Peyghan, Carbon nitride nanotube as a sensor for alkali and alkaline earth cations, Appl. Surf. Sci. 264 (2013) 699–706.

[51] M. Moradi, A.A. Peyghan, Z. Bagheri, Tuning the electronic properties of C 30 B 15N 15 fullerene via encapsulation of alkali and alkali earth metals, Synth. Met. 177 (2013) 94–99.

[52] A.A. Peyghan, M. Noei, The alkali and alkaline earth metal doped ZnO nanotubes: DFT studies, Physica B 432 (2014) 105–110.

[53] M. Dion, H. Rydberg, E. Schröder, D.C. Langreth, B.I. Lundqvist, Van der Waals density functional for general geometries, Phys. Rev. Lett. 92 (2004) 246401.

[54] J.M. Soler, E. Artacho, J.D. Gale, A. Garcia, J. Junquera, P. Ordejon, D. Sanchez-Portal, The SIESTA method for ab initio order-N materials simulation, J. Phys.: Condens. Matter 14 (2002) 2745.

[55] P. Ordejón, E. Artacho, J.M. Soler, Self-consistent order-$N$ density-functional calculations for very large systems, Phys. Rev. B: Condens. Matter 53 (1996) R10441–R10444.

[56] N. Troullier, J.L. Martins, Efficient pseudopotentials for plane-wave calculations, Phys. Rev. B: Condens. Matter 43 (1991) 1993–2006.

[57] Y. Zhao, D.G. Truhlar, A new local density functional for main-group thermochemistry, transition metal bonding, thermochemical kinetics, and noncovalent interactions, J. Chem. Phys. 125 (2006) 194101.

[58] W.J. Hehre, L. Radom, P.v.R. Schleyer, J. Pople, AB INITIO Molecular Orbital Theory, Wiley, New York, 1986.

[59] M. Frisch, G. Trucks, H. Schlegel, G. Scuseria, M. Robb, J. Cheeseman, G. Scalmani, V. Barone, B. Mennucci, G. Petersson, Gaussian 09 Revision A. 1, 2009, Vol. 139, Gaussian Inc., Wallingford, CT, 2009.

[60] P.A. Denis, F. Iribarne, C2V or C6V: which is the most stable structure of the benzene–lithium complex? Chem. Phys. Lett. 573 (2013) 15–18.

[61] S. Ullah, P.A. Denis, F. Sato, Triple-doped monolayer graphene with boron, nitrogen, aluminum, silicon, phosphorus, and sulfur, ChemPhysChem 18 (2017) 1864–1873.

[62] L. Tsetseris, B. Wang, S.T. Pantelides, Substitutional doping of graphene: the role of carbon divacancies, Phys. Rev. B: Condens. Matter 89 (2014) 035411.

[63] Z. Zhou, J. Zhao, X. Gao, Z. Chen, J. Yan, P. von Ragué Schleyer, M. Morinaga, Do composite single-walled nanotubes have enhanced capability for lithium storage? Chem. Mater. 17 (2005) 992–1000.

[64] M. Khantha, N.A. Cordero, L.M. Molina, J.A. Alonso, L.A. Girifalco, Interaction of lithium with graphene: an ab initio study, Phys. Rev. B: Condens. Matter 70 (2004) 125422.

[65] M. Khantha, N.A. Cordero, J.A. Alonso, M. Cawkwell, L.A. Girifalco, Interaction and concerted diffusion of lithium in a (5, 5) carbon nanotube, Phys. Rev. B: Condens. Matter 78 (2008) 115430.

[66] L. Chen, Y. Zhang, N. Koratkar, P. Jena, S.K. Nayak, First-principles study of interaction of molecular hydrogen with Li-doped carbon nanotube peapod structures, Phys. Rev. B: Condens. Matter 77 (2008) 033405.

[67] M. Farjam, H. Rafii-Tabar, Energy gap opening in submonolayer lithium on graphene: local density functional and tight-binding calculations, Phys. Rev. B: Condens. Matter 79 (2009) 045417.

[68] P.A. Denis, Chemical reactivity of lithium doped monolayer and bilayer graphene, J. Phys. Chem. C 115 (2011) 13392–13398.

[69] P.A. Denis, Lithium adsorption on heteroatom mono and dual doped graphene, Chem. Phys. Lett. 672 (2017) 70–79.

[70] L. Zhou, Z.F. Hou, B. Gao, T. Frauenheim, Doped graphenes as anodes with large capacity for lithium-ion batteries, J. Mater. Chem. A 4 (2016) 13407–13413.

[71] Q. Tang, Z. Zhou, Z. Chen, Single-layer [Cu2Br(IN)2]$n$ coordination polymer (CP): electronic and magnetic properties, and implication for molecular sensors, J. Phys. Chem. C 116 (2012) 4119–4125.

[72] W. Li, Y. Yang, G. Zhang, Y.-W. Zhang, Ultrafast and directional diffusion of lithium in phosphorene for high-performance lithium-ion battery, Nano Lett. 15 (2015) 1691–1697.

[73] Q. Sun, Y. Dai, Y. Ma, T. Jing, W. Wei, B. Huang, Ab initio prediction and characterization of Mo2C monolayer as anodes for lithium-ion and sodium-ion batteries, J. Phys. Chem. Lett. 7 (2016) 937–943.

B.2   Additional paper 2: Adsorption of Sodium on Doped Graphene: A vdW-DF Study

**RESEARCH ARTICLE**

# Adsorption of Sodium on Doped Graphene: A vdW-DF Study
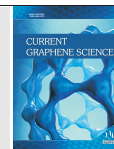
Saif Ullah[a,*], Pablo A. Denis[b] and Fernando Sato[a]

[a]*Departamento de Física, Instituto de Ciências Exatas, Campus Universitário, Universidade Federal de Juiz de Fora, Juiz de Fora, MG 36036-900, Brazil;* [b]*Computational Nanotechnology, DETEMA, Facultad de Química, UDELAR, CC 1157, 11800 Montevideo, Uruguay*

**Abstract:** **Background**: Due to its very low cost and availability of sodium, the sodium ion batteries (SIBs) can be the best alternative to the existing lithium-ion batteries (LIBs). The search for a novel anode candidate is the key hurdle associated with SIBs.

**Objective and Method**: A novel anode contender, Be-doped graphene, is proposed for the SIBs through our first-principles calculations.

**Results**: The integration of Be can cause a 6 times increment in the adsorption of Na as revealed by M06-2X calculations. The sodiation potential is in a good range in order to evade the security concerns caused by the dendrite formation. A total of 10 Na ions are attached easily around on beryllium (Be) centre in graphene sheet causing an enhancement in the Na storage capacity. The value of storage capacity calculated for $Na_8BeC_{17}$ is 2.7 times that of graphitic carbon in LIBs (~370 mAh/g), and 3.35 times that of hard carbon in SIBs (300 mAh/g).

**Conclusion**: These results show the novelty and promising potential of the Be-doped graphene to be used as anode material for SIBs.

## 1. INTRODUCTION

The cellular phones, laptop computers, camcorders, and hybrid electric vehicles are becoming an essential part of our life, which is giving birth to the key issues related to the energy conversion and storage. By virtue of their high energy densities, long lifetime and as replacements for fossil fuels, lithium-ion batteries (LIBs) are the main preference for the expansion of renewable energy technology [1-4]. However, due to the limited availability and exponential rise in the price of Li make it a less demanding material to be used in batteries. Fortunately, sodium ion batteries (SIBs) can be the best alternative to the LIBs due to the similar electrochemical system, non-toxicity, greater availability and lower cost [4-13]. However, selecting a proper anode material for SIBs is a hard task. As the Na atom has bigger radius than Li, so it is difficult to intercalate the Na into graphite [14-16]. Moreover, the limited storage capacity of graphite (35 mAh/g) hinders its use as anode material in SIBs [17]. Therefore, a proper and efficient anode material plays a key role in the advancement of LIB and SIB technologies [17].

Graphene, by virtue of its excellent adsorption, dielectric and transport properties, can possibly be a potential anode material as Na can be adsorbed on both sides [18-23]. Moreover, a report on SIBs with rGO as anode material can be found in reference [24]. Unfortunately, ions adsorbed on graphene form clusters resulting in dendrite formation, which can cause a serious degradation in the charge/discharge capacity. However, there are certain methods which can cope with this issue. Some of them are the alteration of graphene surface [25], point defects [26], edge [27], grain boundary [28], doping and commendatory synergistic effects [29-35]. Among these, substitutional doping is the easier technique as many of the properties such as electronic [36-49], thermal [50], magnetic [39, 51], mechanical [36], transport [36, 52], and reactivity [53-65] can easily be modified with doping. These modifications result in the better novelty of graphene-based systems concerning to their applications. Moon *et al*. [66] discussed the mechanism of Na adsorption on graphene and rGO. Wan *et al*. [67] reported the Na adsorption upon pristine, defective, and boron doped graphene. Yao *et al*. [68] argued that the adsorption of Na on vacancy and boron doped graphene is favorable with an adsorption energy of 3.4 and 2.7 times greater than that of pristine graphene, respectively. Ling and Muzino [7] proposed a very efficient B doped graphene ($BC_3$) as anode material for SIBs.

*Address correspondence to this autor at the Departamento de Física, Instituto de Ciências Exatas, Campus Universitário, Universidade Federal de Juiz de Fora, Juiz de Fora, MG 36036-900, Brazil;
E-mail: sullah@fisica.ufjf.br

In this work, we have used the Be-doped graphene to investigate the adsorption of Na atoms. The good (poor) adsorption of Na upon B (N) doped graphene compelled us to test the interaction of Na with Be-doped graphene as Be is far more efficient than B in terms of charge transfer (p-type doping) in graphene [45]. According to our interesting results, the practical use of Be-doped graphene as the anode material is just a matter of time.

## 2. DETAILS OF COMPUTATION

First-principles vdW-DF [69] spin-polarized calculations were performed with the help of SIESTA code [70, 71] to study the Na interaction with Be-doped graphene. The double zeta basis set with polarization function (DZP) was selected. The split norm was set to 0.15, while the orbital confining-cutoff was fixed to 0.01 Ry. The interaction between valence electrons and ionic cores were described by Troullier-Martins norm-conserving pseudopotentials [72]. A 5 x 5 supercell was sampled with 8 x 8 x 1 k points. The periodic boundary condition was applied in all the directions with allowing the cell to relax in xy-axes, while the z-axis was kept frozen at 20 Å. A denser kpoints grid (40 x 40 x 1) was selected for the density of states (DOS) calculation. The conjugate gradient algorithm (CG) was used for the geometry optimization with convergence criteria of 0.02 eV/Å.

For comparative purpose, we carried out M06-2X calculations [73] as implemented in Gaussian 2009 [74] to shed light into the charge distribution when Na is adsorbed onto Be-doped graphene. The basis sets selected were 6-311G* [75] because smaller basis sets gave incorrect charge distributions as reported by us [61]. The advantage of M06-2X is that the exact exchange is included in it, which is difficult in the periodic calculations. We selected a circumcoronene model ($C_{54}H_{18}$) to mimic graphene in the M06-2X experiment. Na was adsorbed on the central part of perfect and Be-doped circumcoronene. Vibrational frequencies were calculated for all the calculations performed with M06-2X which confirmed that they are minima in the potential energy surface.

## 3. RESULTS AND DISCUSSION

### 3.1. Na and its Interaction with Pristine Graphene

The adsorption energy calculation is a useful method to study the stability of adsorbate on the surfaces. We used the following expression to give an account on the adsorption of Na upon graphene systems:

$$E_{ads} = \frac{E_{tot} - E_{sheet} - nE_{Na}}{n}$$

where, $E_{tot}$, $E_{sheet}$, and $E_{Na}$ are the energies of graphene systems (doped/undoped/defective) with Na ions, pristine/doped/defective graphene systems, and isolated Na, respectively.

Initially, one Na ion is adsorbed on the hollow site of a 5 x 5 graphene unit cell. The adsorption energy of Na is calculated to be -0.672 eV/Na, which is consistent with the values calculated with different level of theories (-0.71 [68], -0.507

[66], -0.88, -0.63, -0.70 [76]. The stable adsorption means that the adsorption energy of Na on graphene must exceed the cohesive energy of bulk Na to prevent the dendrite formation of the ions. For this purpose, we calculated the cohesive energy of bulk Na (body-centered cubic) using the following formula:

$$E_{coh} = \frac{E_{tot} - n_i E_i}{n}$$

where, $E_i$, and $n_i$ are the energy and total number of ith specie(s). The cohesive energy of bulk Na was calculated to be -1.078 eV/Na, agreeing well with reported values (-1.07eV/Na [77], -1.08 eV/Na [76], and -1.13 eV/Na [78]. The lattice constant *a* was found to be 4.225 Å, which is inline with the experimental (4.22-4.29 Å) [79, 80] and theoretical (4.05-4.24 Å) [77, 81, 82] values. This shows that Na ions will form clusters, and therefore, the adsorption of Na on graphene is unlikely.

### 3.2. Interaction of Na with Be-doped Graphene

As the adsorption of Na on pristine graphene suggests that it will not be a stable anode material, and therefore, we moved towards Be-doped graphene. We studied the adsorption of Na on both the sides of Be-doped graphene, as the protrusion of Be from the plane of graphene makes the two sides of graphene unequal. The distance between Na and Be in the up and down configurations was observed to be 2.66 Å, and 2.58 Å, correspondingly. Furthermore, the Na stays on the hexagon in the up configuration, while in the down configuration, the Na migrated towards the Be and relaxed just underneath Be. This behavior was the same as reported for Li [83]. The adsorption energy of Na on the same (up) and opposite (down) sides of the protrusion was -1.783 eV/Na, and -2.045 eV/Na, respectively. This shows more than 3 times increment in the adsorption energy of Na compared to the pristine case. As for the M06-2X/6-311G* calculations performed with the circumcoronene model, we observed a similar trend. In effect, the adsorption energy of Na onto circumcoronene was 0.45 eV, while for Na adsorption below Be in Be-doped circumcoronene, it was 2.86 eV, more than six times larger than for pristine circumcoronene. Therefore, in the presence of Be, we can confirm a dramatic increase in the interaction between Na and graphene. We have confirmed that the Be-doped circumcoronene model with and without Na adsorbed underneath have all real vibrational frequencies, thus confirming the stability of the structures.

For the adsorption of two Na ions, we covered almost every possibility. The selected patterns are both the Na up, Na down, one Na up and one down in the same ring, and one Na up and one down in the different rings. The latter two cases show a clear preference over the former two cases as suggested by their adsorption energies. This means that greater the separation between Na-Na ions, the higher will be the adsorption energy. Around one Be center, there are three hexagons, which can accommodate three Na ions on either side (a total of six). For the adsorption of six Na ions, the adsorption energy was -1.479 to -1.544 eV/Na, for different configurations. For the extreme case studied *i.e.* ten Na ions,
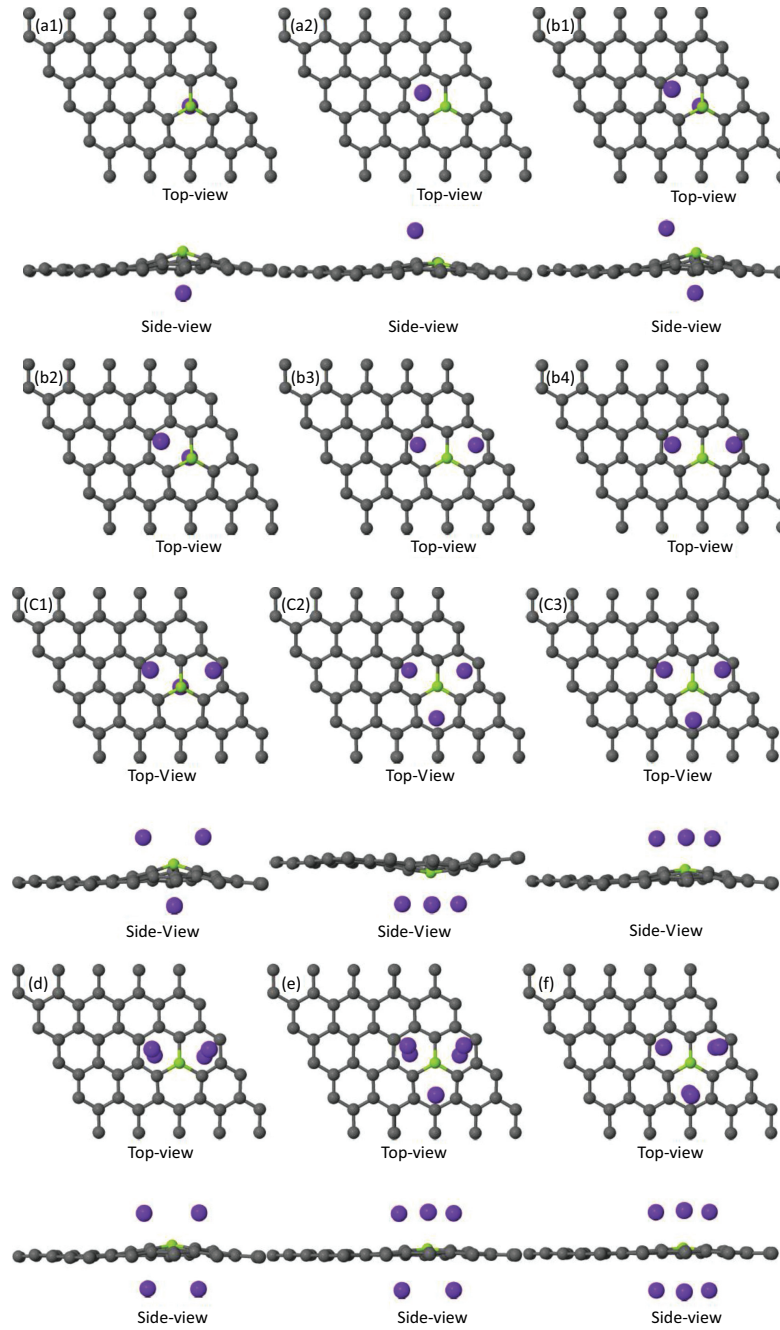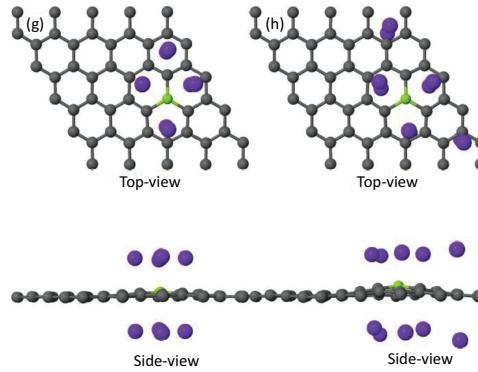
**Fig. (1). contd...**

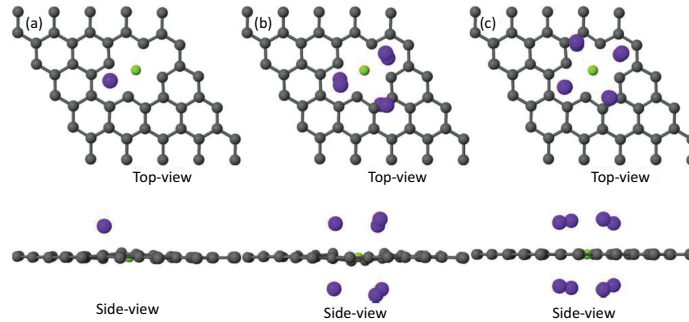**Fig. (1).** Top and side view of Na adsorption on Be doped graphene.



**Fig. (2).** Top and side view of Na adsorption on a divacancy graphene doped with Be.
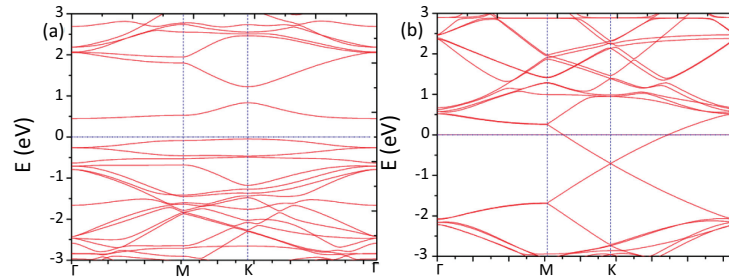


**Fig. (3).** Electronic bands structures of (**a**) Be doped graphene and (**b**) Na adsorbed graphene.

the adsorption energy was as good as -1.06 eV/Na. We didn't go beyond this level as the adsorption energy reached the cohesive energy of bulk Na. However, further adsorption of Na ions was possible but this can severely affect the charge/discharge rate. These geometric structures can be seen in Fig. (**1**).

To investigate how Na storage is influenced by the presence of defects, we studied the adsorption of Na on a double vacancy Be-doped graphene as can be seen in Fig. (**2**). As Be stays in the plane of a divacancy graphene, the separation

between Na and Be is as large as 2.91 Å. The adsorption energy (-1.78 eV/Na) is the same as calculated for Be-doped mono-vacancy graphene (up case), while lower than the down case. However, with increasing concentration of Na, the adsorption energies were found to be better than their mono-vacancy counterparts. Additionally, the four dangling bonds around Be atoms provide a room for four Na ions on either side (a total of 8 Na ions). The adsorption energy for this case is as high as -1.163 eV/Na. The Na adsorption capacity *vs* the adsorption energy is plotted in Fig. (**7**).
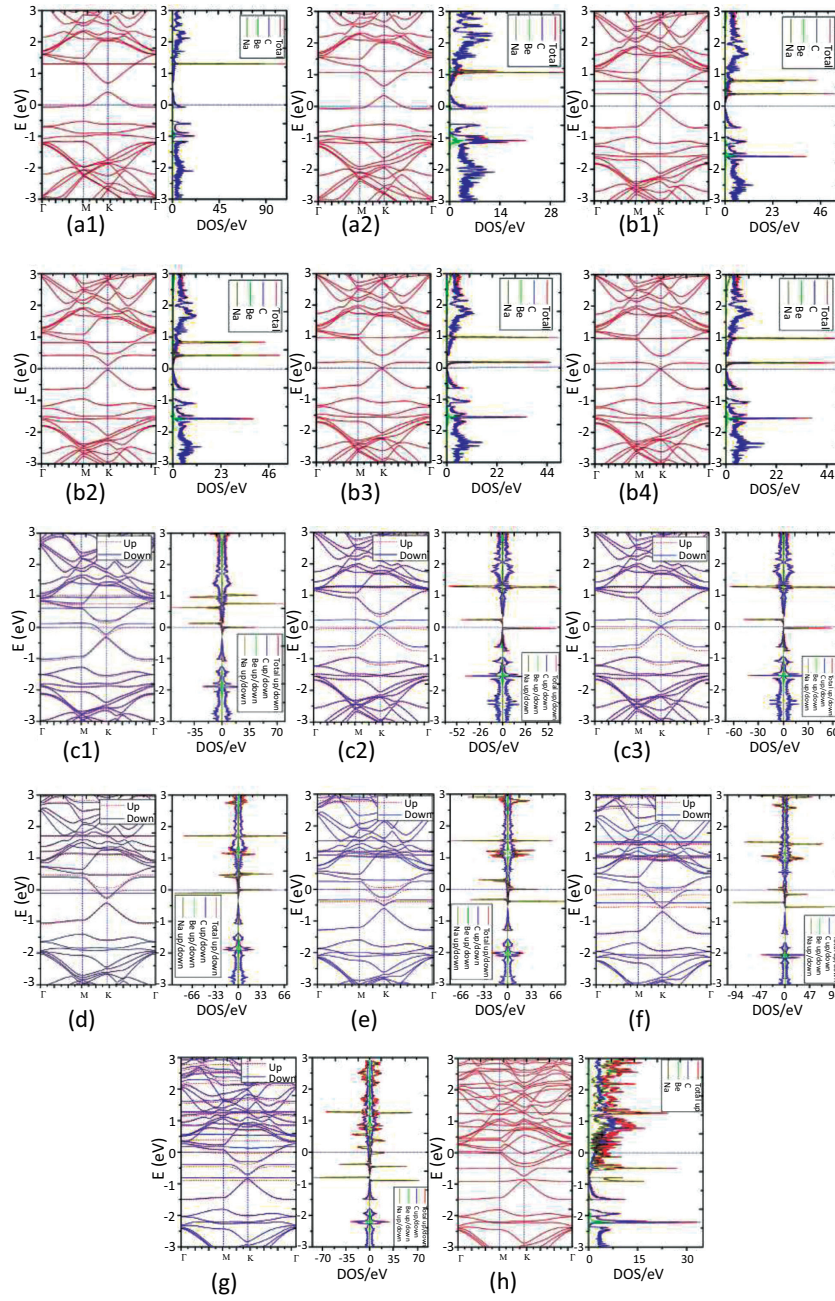
**Fig. (4).** Electronic bands structures with their corresponding PDOS graphs for different concentration of Na adsorbed on Be doped graphene are shown.
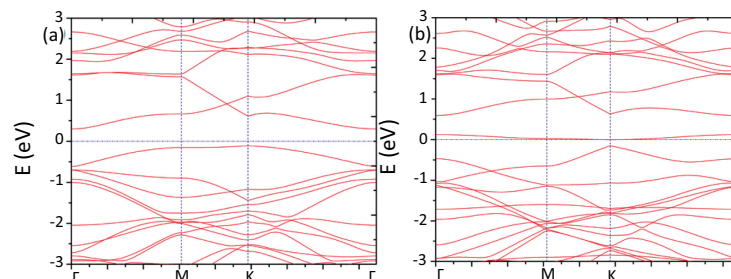
**Fig. (5).** Electronic bands structures of (**a**) divacancy defective graphene and (**b**) Be doped defective graphene.

### 3.3. Chemical Analysis (Charge Transfer)

For the charge transfer between Na and graphene sheet (pristine/doped/defective), we calculated the Mulliken, Hirshfeld, and Voronoi charges. For Na adsorption on pristine graphene, the Mulliken charge analysis showed a charge transfer of 0.504e from Na to graphene. The Hirshfeld charge of Na is also positive with a bit lower value of 0.431e. The introduction of Be in graphene caused the redistribution of charges [45, 46]. The Mulliken and Hirshfeld charges of Na, when adsorbed on Be-doped graphene (down case), were +0.633e, and +0.480e, respectively. In the case of the circumcoronene model, the M06-2X/6-311G* calculations indicated that the Mulliken charges of Na and Be were +0.94 and +0.32e. The Natural Bond Order analysis indicated a similar charge for Na but for Be, it increased to +0.75e. Additionally, to support these results, we also calculated the Voronoi charges, which revealed that a charge of 0.487e is transferred from Na to graphene system. For Na adsorption on divacancy graphene doped with Be, the charge of Na was found to be a bit higher than their mono-vacancy co-equal parts. Moreover, all of these charge analyses showed that a significant amount of charge shifted from Na to Be-doped graphene. However, with increasing concentration of Na, a reduction in the charge transfer occurred from Na to the slab. Furthermore, Hirshfeld and Voronoi charges gave nearly the same results, where the values of Mulliken and NBO charges were a bit higher than both the former analysis.

### 3.4. Electronic Properties

The introduction of Be in graphene sheet caused an indirect band-gap opening of 0.49 eV at Fermi level and a direct gap opening of 0.41 eV around Dirac point. Moreover, the Fermi level also shifted downward by almost 1 eV from Dirac point (see Fig. **3a**), These results are in a good accordance with our prior investigations [45]. In addition to this, we calculated the electronic band structure of Na adsorbed graphene and found that Na did not induce significant changes in the band structure of graphene except for an upward shift of 1eV of the Fermi level as shown in Fig. (**3b**), a value which is similar to that observed for Li-doped graphene [84], at the same level of theory. This upward shift of the Fermi level is in accordance with the charge transfer from Na to graphene. However, an extra energy band was induced at Fermi level. The adsorption of Na changed the semiconducting behavior of Be doped graphene to metallic one. Furthermore, the gap around Dirac point reduced to 0.33 eV, and 0.30 eV for up and down configuration, respectively. For two Na ions, small values of the band-gaps opening (0.017-0.163 eV) were observed at Fermi level. Furthermore, the PDOS calculations disclosed that the conduction band minimum (CBM) comes from the DOS of Na atoms. The increasing concentration of Na ions induced some extra energy bands and caused the Fermi level to shift upward. From the PDOS calculations, it is clear that for lower concentration, the Na ion(s) contribute to the total DOS only in the conduction band. As the Na concentration increases, the range of discrete peaks of Na in the total DOS also increases with some contribution in the valence band as well. For ten Na ions, the PDOS of Na takes the form of continuous peaks spreading over a wide range of up to -1 eV in the valence band. All these band structures and PDOS graphs are depicted in Fig. (**4**).

We also calculated the electronic structures of Na adsorbed on a divacancy graphene doped with Be. Initially, we compared the band structures of an undoped divacancy graphene with the doped (Be) one. The undoped structure has a large band-gap (indirect) opening of 0.467 eV as shown in Fig. (**5a**). The introduction of Be reduced the band-gap opening to 0.156 eV (see Fig. (**5b**)). Moreover, the band-gap opening was calculated to be a direct one. For one Na adsorption, the band structure is half-metallic as a gap (indirect) of 0.494 eV is observed for spin down channel only. The Na atom is contributing to the total DOS in the conduction band near the 1 eV energy range as can be seen from the pDOS graph. By increasing the Na concentration, the peaks of Na spread in the conduction band and start shifting towards the valence band. For 8 Na ions, there is a very high peak from the Na atom in the valence band at an energy range of 0.9 eV. All these graphs are plotted in Fig. (**6**). A summary of the results is shown in Table **1**.

### 3.5. Electrochemical Analysis

In order to give an account of the electrochemical performance of our anode material, the storage capacity is calculated with the following expression:

$$C = \frac{nF}{M} \times \frac{1000}{3600}$$

**Table 1.** Adsorption energies (eV), charges (e), magnetic moments and band gaps calculated for the adsorption of Na onto Be-doped graphene.

| Configuration | Total Number of Na Ions | Adsorption Energy (eV/Na) | Charge/Na (e)[a/b/c] | Magnetic Moment ($\mu_B$) | Band-gap (eV)[x/y] |
|---|---|---|---|---|---|
| **Mono-vacancy graphene doped with Be** | | | | | |
| **a1** | 1 | -2.045 | 0.633/0.480/0.487 | 0.03 | M |
| **a2** | 1 | -1.783 | 0.586/0.495/0.515 | 0.00 | M |
| **b1** | 2 | -1.833 | 0.603/0.480/0.496 | 0.00 | 0.163 |
| **b2** | 2 | -1.832 | 0.604/0.480/0.495 | 0.00 | 0.163 |
| **b3** | 2 | -1.62 | 0.485/0.395/0.415 | 0.00 | 0.017 |
| **b4** | 2 | -1.619 | 0.486/0.396/0.416 | 0.00 | 0.027 |
| **c1** | 3 | -1.544 | 0.431/0.326/0.338 | 0.82 | 0.14*/M |
| **c2** | 3 | -1.48 | 0.358/0.257/0.272 | 1.00 | 0.348/M |
| **c3** | 3 | -1.479 | 0.359/0.257/0.272 | 1.00 | 0.38/M |
| **d** | 4 | -1.335 | 0.301/0.223/0.231 | 0.22 | 0.06*/M |
| **e** | 5 | -1.3 | 0.274/0.196/0.201 | 0.51 | 0.06*/M |
| **f** | 6 | -1.261 | 0.241/0.138/0.170 | 0.51 | M/M |
| **g** | 8 | -1.123 | 0.204/0.143/0.144 | 0.88 | M/M |
| **h** | 10 | -1.059 | 0.153/0.110/0.109 | 0.02 | M |
| **Divacancy Graphene Doped with Be** | | | | | |
| **a** | 1 | -1.78 | 0.6/0.490/0.500 | 0.81 | M/0.49* |
| **b** | 6 | -1.312 | 0.268/0.186/0.190 | 0.75 | M/M |
| **c** | 8 | -1.163 | 0.269/0.18/0.19 | 0.00 | M |
| **Be Doped Graphene (3 x 3 supercell)** | | | | | |
| **$Na_6BeC_{17}$** | 6 | -1.31 | 0.176/0.11/0.11 | 0.19 | - |
| **$Na_8BeC_{17}$** | 8 | -1.261 | 0.12/0.07/0.07 | 0.00 | - |

Eads on pristine graphene is -0.67 eV/Na
a/b/c Mulliken/Hirshfeld/Voronoi
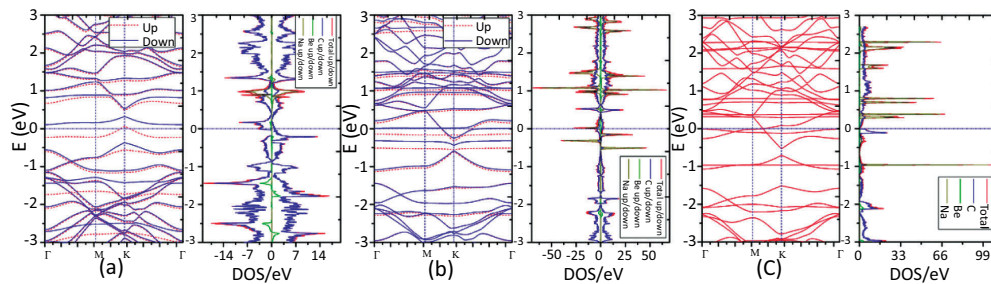x/y Spin-up/down
* Indirect gap



**Fig. (6).** Electronic bands structures with their corresponding PDOS graphs for different concentration of Na adsorbed on Be doped defective graphene are depicted.
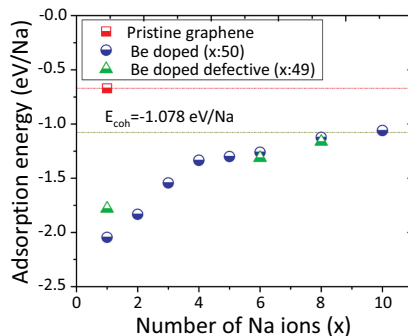
**Fig. (7).** The adsorption energies of Na on Be doped graphene (half-filled blue sphere), and Be doped defective graphene (half-filled green triangles) are plotted with a reference value of adsorption energy of Na on pristine graphene (half-filled red square) and cohesive energy of bulk Na. Isomers with higher stability are plotted. *(The color version of the figure is available in the electronic copy of the article).*

where, $n$ is the adsorbed charge(s) (Na ions), $F$ and $M$ is the Faraday constant and the molar mass of the Be doped graphene, respectively. The term $\frac{1000}{3600}$ is used for the unit conversion (from coulomb to mAh). The theoretical Na storage capacity of $Na_{10}BeC_{49}$, $Na_8BeC_{48}$, $Na_6BeC_{17}$, and $Na_8BeC_{17}$ was calculated to be 448.522 mAh/g, 366.178 mAh/g, 754.266 mAh/g, and 1005.688 mAh/g, respectively. The value 1005.688 mAh/g is far more better than that of graphitic carbon (~35 mAh/g) [17], hard carbon (~300 mAh/g)[85], $NaBC_{31}$ (~70 mAh/g) (7), and even highly B doped graphene, $NaBC_3$ (~762 mAh/g) [7]. Our maximum calculated capacity was nearly 2.7 times that of the graphite anode (in LIBs), and 3.35 times that of the hard carbon (in SIBs).

The following formula is used to calculate the sodiation potential ($V_{Na}$):

$$V_{Na=-\frac{E_{tot}-E_{sheet}-nE_{Na}}{nzF}}$$

According to this equation, $V_{Na}$ of Be doped graphene decreased from 2.045-1.06 V as the concentration of Na ions increased from 1 to 10. For $Na_8BeC_{17}$; $V_{Na}$ was calculated to be 1.26 V. These values are better than that calculated for $BC_3$ [7] structure. It should be noted that when the Be concentration increased from 2 to 5.55 %, an enhancement occurred in the efficiency of the anode.

**CONCLUSION**

We proposed a promising material, Be-doped graphene, as an efficient anode contender for SIBs. The M06-2X calculations show that the adsorption of Na can be enhanced 6 times by the introduction of Be. One Be center in graphene sheet can provide a room for up to 10 Na ions. For $Na_8BeC_{17}$, the calculated storage capacity was found to be 1005.688 mAh/g with a $V_{Na}$ potential of 1.26 V. This value of storage capacity is 2.7 times that of graphitic carbon in LIBs (~370 mAh/g), and 3.35 times that of hard carbon in SIBs (300 mAh/g). The $V_{Na}$ is in good range in order to evade the security concerns caused by the dendrite formation. Moreover, the addition of Na did not induce any significant change in the lattice of Be doped graphene, which

may be favorable for better cyclability. All these interesting properties propose that Be-doped graphene can be a better choice for the anode material in SIBs, and demand for its early synthesis. With the terrific advancement in the experimentation, we hope that Be-doped graphene will soon be a practical anode for SIBs.

**DATA AVAILABILITY**

Any kind of input/output file can be provided on request.

**CONSENT FOR PUBLICATION**

Not applicable.

**CONFLICT OF INTEREST**

The authors declare no conflict of interest, financial or otherwise.

**REFERENCES**

[1] Scrosati B. Recent advances in lithium-ion battery materials. Electrochimica Acta 2000; 45(15): 2461-6.
[2] Tarascon JM, Armand M. Issues and challenges facing rechargeable lithium batteries. Nature 2001; 414(6861): 359-67.
[3] Goodenough JB, Kim Y. Challenges for rechargeable li batteries. Chem Mater 2010; 22(3): 587-603.
[4] Ellis BL, Nazar LF. Sodium and sodium-ion energy storage batteries. Curr Opin Solid State Mater Sci 2012; 16(4): 168-77.
[5] Cao Y, Xiao L, Sushko ML, *et al.* Sodium ion insertion in hollow carbon nanowires for battery applications. Nano Lett 2012; 12(7): 3783-7.

[6]     Wen Y, He K, Zhu Y, *et al*. Expanded graphite as superior anode for sodium-ion batteries. Nat Commun 2014; 5: 4033.

[7]     Ling C, Mizuno F. Boron-doped graphene as a promising anode for Na-ion batteries. Phys Chem Chem Phys 2014; 16(22): 10419-24.

[8]     Kim SW, Seo DH, Ma X, Ceder G, Kang K. Electrode materials for rechargeable sodium-ion batteries: Potential alternatives to current lithium-ion batteries. Adv Energ Mater 2012; 2(7): 710-21.

[9]     Zhang J, Wang D-W, Lv W, *et al*. Achieving superb sodium storage performance on carbon anodes through an ether-derived solid electrolyte interphase. Energ Environ Sci 2017; 10(1): 370-6.

[10]    Raccichini R, Varzi A, Wei D, Passerini S. Critical insight into the relentless progression toward graphene and graphene-containing materials for lithium-ion battery anodes. Adv Mater 2017; 29(11): 1603421.

[11]    Yuan S, Zhu Y-H, Li W, *et al*. Surfactant-free aqueous synthesis of pure single-crystalline SnSe nanosheet clusters as anode for high energy- and power-density sodium-ion batteries. Adv Mater 2017; 29(4): 1602469.

[12]    Wang F, Wu X, Li C, *et al*. Nanostructured positive electrode materials for post-lithium ion batteries. Energ Environ Sci 2016; 9(12): 3570-611.

[13]    Huang Y, Zhu M, Huang Y, *et al*. Multifunctional energy storage and conversion devices. Adv Mater 2016; 28(38): 8344-64.

[14]    Asher R. A lamellar compound of sodium and graphite. J Inorg Nuclear Chem 1959; 10(3-4): 238-49.

[15]    Ge P, Fouletier M. Electrochemical intercalation of sodium in graphite. Solid State Ionics 1988; 28: 1172-5.

[16]    Stevens D, Dahn J. The mechanisms of lithium and sodium insertion in carbon materials. J Electrochem Soc 2001; 148(8): A803-A11.

[17]    Slater MD, Kim D, Lee E, Johnson CS. Sodium-ion batteries. Adv Funct Mater 2013; 23(8): 947-58.

[18]    Wang V, Mizuseki H, He H, Chen G, Zhang S, Kawazoe Y. Calcium-decorated graphene for hydrogen storage: A van der Waals density functional study. Compu Mater Sci 2012; 55: 180-5.

[19]    Chi M, Zhao YP. Adsorption of formaldehyde molecule on the intrinsic and Al-doped graphene: A first principle study. Compu Mater Sci 2009; 46(4): 1085-90.

[20]    Park HL, Chung YC. Hydrogen storage in Al and Ti dispersed on graphene with boron substitution: First-principles calculations. Compu Mater Sci 2010; 49(4): S297-S301.

[21]    Lherbier A, Botello-Mendez AR, Charlier JC. Electronic and transport properties of unbalanced sublattice N-doping in graphene. Nano Lett 2013; 13(4): 1446-50.

[22]    Song WL, Wang W, Veca LM, *et al*. Polymer/carbon nanocomposites for enhanced thermal transport properties–carbon nanotubes versus graphene sheets as nanoscale fillers. J Mater Chem 2012; 22(33): 17133-9.

[23]    Song WL, Cao MS, Lu MM, Liu J, Yuan J, Fan LZ. Improved dielectric properties and highly efficient and broadened bandwidth electromagnetic attenuation of thickness-decreased carbon nanosheet/wax composites. J Mater Chem C 2013; 1(9): 1846-54.

[24]    Wang YX, Chou SL, Liu HK, Dou SX. Reduced graphene oxide with superior cycling stability and rate capability for sodium storage. Carbon 2013; 57: 202-8.

[25]    Kim G, Jhi S-H, Park N, Louie SG, Cohen ML. Optimization of metal dispersion in doped graphitic materials for hydrogen storage. Phys Rev B 2008; 78(8): 085408.

[26]    Zhou LJ, Hou ZF, Wu LM. First-principles study of lithium adsorption and diffusion on graphene with point defects. J Phys Chem C 2012; 116(41): 21780-7.

[27]    Uthaisar C, Barone V. Edge effects on the characteristics of li diffusion in graphene. Nano Lett 2010; 10(8): 2838-42.

[28]    Zhou LJ, Hou ZF, Wu LM, Zhang YF. First-principles studies of lithium adsorption and diffusion on graphene with grain boundaries. J Phys Chem C 2014; 118(48): 28055-62.

[29]    Hardikar RP, Das D, Han SS, Lee K-R, Singh AK. Boron doped defective graphene as a potential anode material for Li-ion batteries. Phys Chem Chem Phys 2014; 16(31): 16502-8.

[30]    Yu Y-X. Can all nitrogen-doped defects improve the performance of graphene anode materials for lithium-ion batteries? Phys Chem Chem Phys 2013; 15(39): 16819-27.

[31]    Wang L, Sofer Z, Luxa J, Pumera M. Nitrogen doped graphene: Influence of precursors and conditions of the synthesis. J Mater Chem C 2014; 2(16): 2887-93.

[32]    Tian H, Sofer Z, Pumera M, Bonanni A. Investigation on the ability of heteroatom-doped graphene for biorecognition. Nanoscale 2017; 9(10): 3530-6.

[33]    Chng CE, Sofer Z, Pumera M, Bonanni A. Doped and undoped graphene platforms: the influence of structural properties on the detection of polyphenols. Sci Reports 2016; 6: 20673.

[34]    Tan SM, Poh HL, Sofer Z, Pumera M. Boron-doped graphene and boron-doped diamond electrodes: detection of biomarkers and resistance to fouling. Analyst 2013; 138(17): 4885-91.

[35]    Poh HL, Šimek P, Sofer Z, Pumera M. Sulfur-doped graphene *via* thermal exfoliation of graphite oxide in H2S, SO2, or CS2 Gas. ACS Nano 2013; 7(6): 5262-72.

[36]    Willke P, Amani JA, Sinterhauf A, *et al*. Doping of graphene by low-energy ion beam implantation: structural, electronic, and transport properties. Nano Lett 2015; 15(8): 5110-5.

[37]    Giovannetti G, Khomyakov PA, Brocks G, Karpan VM, van den Brink J, Kelly PJ. Doping graphene with metal contacts. Phys Rev Lett 2008; 101(2): 026803.

[38]    Wang F, Liu G, Rothwell S, *et al*. Wide-gap semiconducting graphene from nitrogen-seeded SiC. Nano Lett 2013; 13(10): 4827-32.

[39]    Denis PA. Band gap opening of monolayer and bilayer graphene doped with aluminium, silicon, phosphorus, and sulfur. Chem Phys Lett 2010; 492(4-6): 251-7.

[40]    Denis PA. When noncovalent interactions are stronger than covalent bonds: Bilayer graphene doped with second row atoms, aluminum, silicon, phosphorus and sulfur. Chem Phys Lett 2011; 508(1-3): 95-101.

[41]    Denis PA. Mono and dual doped monolayer graphene with aluminum, silicon, phosphorus and sulfur. Compu Theor Chem 2016; 1097: 40-7.

[42]    Denis PA, Huelmo CP, Iribarne F. Theoretical characterization of sulfur and nitrogen dual-doped graphene. Compu Theor Chem 2014; 1049: 13-9.

[43]    Denis PA, Iribarne F. Dual doped monolayer and bilayer graphene: The case of 4p and 2p elements. Chem Phys Lett 2016; 658: 152-7.

[44]    Denis PA, Pereyra Huelmo C, Martins AS. Band Gap Opening in Dual-Doped Monolayer Graphene. J Phys Chem C 2016; 120(13): 7103-12.

[45]    Ullah S, Hussain A, Syed W, *et al*. Band-gap tuning of graphene by Be doping and Be, B co-doping: A DFT study. RSC Adv 2015; 5(69): 55762-73.

[46]    Hussain A, Ullah S, Farhan MA. Fine tuning the band-gap of graphene by atomic and molecular doping: a density functional theory study. RSC Adv 2016; 6(61): 55990-6003.

[47]    Ullah S, Hussain A, Sato F. Rectangular and hexagonal doping of graphene with B, N, and O: A DFT study. RSC Adv 2017; 7(26): 16064-8.

[48]    Paulo VCM, Mota FdB, Artur JSM, Caio MCdC. Adsorption of monovalent metal atoms on graphene: A theoretical approach. Nanotechnol 2010; 21(11): 115701.

[49]    Anota EC, Escobedo-Morales A, Villanueva MS, Vázquez-Cuchillo O, Rosas ER. On the influence of point defects on the structural and electronic properties of graphene-like sheets: A molecular simulation study. J Molecular Model 2013; 19(2): 839-46.

[50]    Goharshadi EK, Mahdizadeh SJ. Thermal conductivity and heat transport properties of nitrogen-doped graphene. J Mol Graph Model 2015; 62: 74-80.

[51]    Xiao D, Yao W, Niu Q. Valley-contrasting physics in graphene: magnetic moment and topological transport. Phys Rev Lett 2007; 99(23): 236809.

[52]    Lin YC, Lin CY, Chiu PW. Controllable graphene N-doping with ammonia plasma. Appl Phys Lett 2010; 96(13): 133110.

[53]    Kawai S, Saito S, Osumi S, *et al*. Atomically controlled substitutional boron-doping of graphene nanoribbons. Nat Commun 2015; 6: 8098.

[54]    Wang H, Maiyalagan T, Wang X. Review on recent progress in nitrogen-doped graphene: synthesis, characterization, and its potential applications. ACS Catalysis 2012; 2(5): 781-94.

[55]    Wong CHA, Sofer Z, Klímová K, Pumera M. Microwave exfoliation of graphite oxides in H2S plasma for the synthesis of sulfur-doped graphenes as oxygen reduction catalysts. ACS Appl Mater Inter 2016; 8(46): 31849-55.

[56]    Chua CK, Sofer Z, Khezri B, Webster RD, Pumera M. Ball-milled sulfur-doped graphene materials contain metallic impurities

originating from ball-milling apparatus: Their influence on the catalytic properties. Phys Chem Chem Phys 2016; 18(27): 17875-80.

[57]   Klímová K, Pumera M, Luxa J, *et al*. Graphene oxide sorption capacity toward elements over the whole periodic table: A comparative study. J Phys Chem C 2016; 120(42): 24203-12.

[58]   Tian H, Wang L, Sofer Z, Pumera M, Bonanni A. Doped graphene for DNA analysis: The electrochemical signal is strongly influenced by the kind of dopant and the nucleobase structure. Sci Reports 2016; 6: 33046.

[59]   Ambrosi A, Bonanni A, Sofer Z, Cross JS, Pumera M. Electrochemistry at chemically modified graphenes. Chem Eur J 2011; 17(38): 10763-70.

[60]   Denis PA. Chemical reactivity and band-gap opening of graphene doped with gallium, germanium, arsenic, and selenium atoms. Chem Phys Chem 2014; 15(18): 3994-4000.

[61]   Ullah S, Denis PA, Sato F. Triple-doped monolayer graphene with boron, nitrogen, aluminum, silicon, phosphorus, and sulfur. Chem Phys Chem 2017; 18(14): 1864-73.

[62]   Denis PA, Iribarne F. The effect of the dopant nature on the reactivity, interlayer bonding and electronic properties of dual doped bilayer graphene. Phys Chem Chem Phys 2016; 18(35): 24693-703.

[63]   Denis PA, Pereyra Huelmo C. Structural characterization and chemical reactivity of dual doped graphene. Carbon 2015; 87: 106-15.

[64]   Denis PA, Ullah S, Sato F. Triple doped monolayer graphene with boron, nitrogen, aluminum, silicon, phosphorus and sulfur. Chem Phys Chem 2017; 18(4): 1854.

[65]   Rosas JH, Gutiérrez RR, Escobedo-Morales A, Anota EC. First principles calculations of the electronic and chemical properties of graphene, graphane, and graphene oxide. J Molecular Model 2011; 17(5): 1133-9.

[66]   Moon HS, Lee JH, Kwon S, Kim IT, Lee SG. Mechanisms of Na adsorption on graphene and graphene oxide: Density functional theory approach. Carbon Lett 2015; 16(2): 116-20.

[67]   Wan W, Wang H. First-principles investigation of adsorption and diffusion of ions on pristine, defective and B-doped graphene. Materials 2015; 8(9): 6163-78.

[68]   Yao LH, Cao MS, Yang HJ, Liu XJ, Fang XY, Yuan J. Adsorption of Na on intrinsic, B-doped, N-doped and vacancy graphenes: A first-principles study. Comp Mater Sci 2014; 85: 179-85.

[69]   Dion M, Rydberg H, Schröder E, Langreth DC, Lundqvist BI. Van der waals density functional for general geometries. Phys Rev Lett 2004; 92(24): 246401.

[70]   Ordejón P, Artacho E, Soler JM. Self-consistent order-$N$ density-functional calculations for very large systems. Phys Rev B 1996; 53(16): R10441-4.

[71]   Soler JM, Artacho E, Gale JD, *et al*. The SIESTA method for ab initio order-N materials simulation. J Phys: Condens Matter 2002; 14: 2745.

[72]   Troullier N, Martins JL. Efficient pseudopotentials for plane-wave calculations. Phys Rev B 1991; 43(3): 1993-2006.

[73]   Zhao Y, Truhlar DG. A new local density functional for main-group thermochemistry, transition metal bonding, thermochemical kinetics, and noncovalent interactions. J Chem Phys 2006; 125(19): 194101.

[74]   Frisch M, Trucks G, Schlegel H, *et al*. Electronic supplementary material (ESI) for chemical science, gaussian 09; revision D.01. Wallingford CT USA: Gaussian Inc; 2009.

[75]   Hehre WJ, Radom L, Schleyer PvR, Pople J. AB INITIO Molecular Orbital Theory. New York: Wiley; 1986.

[76]   Liang Z, Fan X, Zheng W, Singh DJ. Adsorption and formation of small Na clusters on pristine and double-vacancy graphene for anodes of Na-Ion batteries. ACS Appl Mater Inter 2017; 9(20): 17076-84.

[77]   Malyi OI, Sopiha K, Kulish VV, Tan TL, Manzhos S, Persson C. A computational study of Na behavior on graphene. Appl Surface Sci 2015; 333: 235-43.

[78]   Maezono R, Towler M, Lee Y, Needs R. Quantum Monte Carlo study of sodium. Phys Rev B 2003; 68(16): 165103.

[79]   Böhm B, Klemm W. Zur kenntnis des verhaltens der alkalimetalle zueinander. Zeitschrift für anorganische und allgemeine Chemie 1939; 243(1): 69-85.

[80]   Berliner R, Fajen O, Smith H, Hitterman R. Neutron powder-diffraction studies of lithium, sodium, and potassium metal. Phys Rev B 1989; 40(18): 12086.

[81]   Haas P, Tran F, Blaha P. Calculation of the lattice constant of solids with semilocal functionals. Phys Rev B 2009; 79(8): 085104.

[82]   Malyi O, Kulish VV, Tan TL, Manzhos SA. Computational study of the insertion of Li, Na, and Mg atoms into Si (111) nanosheets. Nano Energy 2013; 2(6): 1149-57.

[83]   Denis PA. Lithium adsorption on heteroatom mono and dual doped graphene. Chem Phys Lett 2017; 672: 70-9.

[84]   Denis PA. Chemical reactivity of lithium doped monolayer and bilayer graphene. J Phys Chem C 2011; 115(27): 13392-8.

[85]   Komaba S, Murata W, Ishikawa T, *et al*. Electrochemical Na insertion and solid electrolyte interphase for hard-carbon electrodes and application to Na-Ion batteries. Adv Funct Mater 2011; 21(20): 3859-67.

## PAPER

Check for updates

# First-principles study of dual-doped graphene: towards promising anode materials for Li/Na-ion batteries†

Saif Ullah, [ID] *[a] Pablo A. Denis [ID] [b] and Fernando Sato[a]

Two-dimensional materials as electrodes have significant potential in energy storage and conversion and can address the issues related to battery technologies. Accordingly, first-principles calculations were executed to search for the best possible anode material for Li/Na ion batteries. Three families of dual-doped graphene (DDG) including Be−B, BeN, and BeO were studied because it is easier to synthesize DDG instead of its mono-doped counterpart. Among them, Be−B DDG was found to be the most promising since it can cause a massive increase in the adsorption of Li (2.33 eV, by 3.1 times) and Na (2.24 eV, by 4.3 times) at the vdW-DF/DZP level of theory. The integration of these ions caused the structures to become metallic, resulting in good electronic conductivity, which is essential for anode materials. Furthermore, Be−B DDG exhibited an average open circuit voltage of 2.34 V (1.3* V) and 1.82 V (1.02* V) for Li and Na, respectively, when the energy of the isolated gas-phase (* represents the energy of one atom taken from the bulk) is used for Li and Na. This modest average open circuit voltage of 1.3* V for Li is in the range of that of the most commonly used graphite-Li (0.11 V) and $TiO_2$-Li (1.5–1.8 V). Moreover, the negligible percentage change in the plane of Be−B DDG during the intercalation of Li/Na ensured good cyclic stability. Additionally, the exceptional storage capacities of 2334 mA h $g^{-1}$ for Li and 1012 mA h $g^{-1}$ for Na with an open circuit voltage of 0.23* V and 0.25* V, respectively, shows that Be−B DDG has potential as a remarkable anode material for LIBs and SIBs.

## Introduction

Currently, one of the key issues for mankind is energy storage and conversion due to the rapid development in the manufacturing of cellular phones, camcorders, laptop computers, *etc.* Consequently, one of the promising alternatives is secondary batteries, which can power the world. Due to their exceptional performance and size, lithium ion batteries (LIBs) are widely used in numerous electronic equipment and are an eventual candidate for hybrid electric cars.[1–5] Graphite, which serves as an anode material for LIBs, is a less efficient material for anodes due to its limited storage capacity of 372 mA h $g^{-1}$.[3,6] Another key issue related to LIBs is the availability of Li because Li reservoirs are limited. The world is

based on the demand and supply principle, thus the increase in the demand for Li has resulted in an exponential increase in its cost, and due to this demand, Tarascon has argued that Li is the next gold.[7] An alternative to the LIBs is sodium ion batteries (SIBs), which involve a similar electrochemical system to that of LIBs.[5,8–16] Furthermore, the non-toxicity and abundance of Na (23 000 parts per million) compared to Li (20 ppm) in the earth crust makes it an interesting and desirable candidate to be employed in SIBs.[17] However, since the world is imperfect, Na is less suitable as a proper anode material. This is because the covalent radius of Na is much bigger than that of Li, and hence, it cannot be intercalated into graphite despite the fact that graphite is a successful anode for LIBs.[18–20] Furthermore, the Li and Na storage capacities of graphite are limited to ∼372 mA h $g^{-1}$ and ∼35 mA h $g^{-1}$, respectively.[3,21] Therefore, the search for proper anode materials is crucial, especially, for the more desirable SIBs.

The remarkable properties of graphene such as large surface area, superb adsorption on both sides, excellent transport, electrical, thermal and mechanical properties and wide-ranging electrochemical window, make it an appealing material as an anode in LIBs/SIBs.[22–34] However, there is an issue with the storage of ions on graphene, where ions adsorbed on graphene can easily form clusters, thus causing the formation of dendrites.[35–37] Consequently, the charge/discharge capacity is seriously affected.

[a] *Departamento de Física, Instituto de Ciências Exatas, Campus Universitário, Universidade Federal de Juiz de Fora, Juiz de Fora, MG 36036-900, Brazil. E-mail: sullah@fisica.ufjf.br*

[b] *Computational Nanotechnology, DETEMA, Facultad de Química, UDELAR, CC 1157, 11800 Montevideo, Uruguay*

† Electronic supplementary information (ESI) available: Fig. S1 for the MD results. The bands structures calculated for BeO, BeN, and Be−B DDG are depicted in Fig. S2. The adsorption of Li/Na on BeN, BeO, and Be−B DDG with an increase in concentration is shown in Fig. S3. The calculated bands structures for Li/Na adsorption on Be−B DDG are plotted in Fig. S4 and S5. Finally, $Li_8BeBC_6$ and $Na_8BeBC_{16}$ are depicted in Fig. S6. See DOI: 10.1039/c8nj01098f

Fortunately, there are some convenient techniques that can decrease the impact of/resolve this issue, namely modulation of the graphene surface with transition-metals, grain boundaries, edges, point defects, and doping.[38-54] Moreover, substitutional doping has the advantage of being an easy technique that can efficiently refine the electronic, magnetic, optical, thermal, mechanical, and transport properties, and chemical reactivity of graphene, which extend the applications of graphene.[44-46,48-50,55-79]

Boron (B) and nitrogen (N), which are neighbors to C, can be doped easily in the plane of graphene.[46] The incorporation of beryllium (Be) and oxygen (O) (which are also neighbors to C) in graphene is studied systematically with the help of DFT.[44-46,48,49] All these dopants can effectively modify the properties of graphene. Among them, Be and B act as hole (p-type) dopants, whereas N and O behave as electron (n-type) dopants. The adsorption of Li/Na ions is favorable on hole-doped graphene, where it is suggested in many studies that their adsorption on B-doped graphene is much more favorable than on N-doped graphene.[80,81] In this regard, B-doped graphene shows an excellent Li storage capacity of 1549 mA h g$^{-1}$ (experimentally)[82] and 2271 mA h g$^{-1}$ (theoretically).[83] In a recent study, we reported that Be-doped graphene has a maximum theoretical Li capacity of $\sim$2303.3 mA h g$^{-1}$ with a lithiation potential of $\sim$1.48 V.[49]

Two heterogeneous species can be integrated into graphene simultaneously with great ease compared to monodoping. Dual-doped graphene (DDG) is found to be much more efficient than mono-doped graphene to alter the physicochemical properties of graphene. It has been shown that PN,[84-86] SN,[61,64,85-91] BeB,[44] BeN,[45] and BeO[45,48] DDG have exciting catalytic and electronic properties. Therefore, in this study, we report the interactions of Li/Na with BeB, BeN, and BeO DDG by means of density functional theory (DFT). Among them, BeB is of particular interest because Be and B cause the structure of graphene to be electron deficient, which in turn, offers better chemistry with the ions.

## Computational details

The vdW-DF[92] calculations were carried out using the ab-initio DFT based SIESTA code[93,94] to study the chemistry between ions (Li/Na) and our DDG systems. We used the norm-conserving Troullier–Martins pseudopotentials (PPs)[95] for the electron–ion interactions. For our calculations, we adopted a 5 × 5 supercell with the periodic boundary condition using 8 × 8 × 1 k-points sampling. The z-axis was kept fixed at 20 Å to avoid interactions between the periodic replicas if any. All the geometries were fully relaxed along the xy orientations. To search for magnetism, all the calculations were performed with the inclusion of spin polarization and by employing the double-zeta basis sets with polarization functions (DZP). The mesh cut-off and orbital confining cut-off were set to 200 Ry and 0.01 Ry, respectively, while the split-norm employed was 0.15. The conjugate gradient (CG) scheme was adopted for the geometry optimization and the convergence criteria for the forces and energies were set to 0.02 eV Å$^{-1}$ and 10$^{-6}$ eV, respectively. For the molecular dynamics simulations (MD), the same DZP basis set was employed. We imposed the (NVT) canonical ensemble conditions and the target temperature was selected to be 300 K and 600 K, which was controlled by the Nose–Hoover method. We set the time frame to 1.0 fs.

For the different configurations of Be–B doped graphene, we also used the quantum espresso code, which is a plane-wave DFT package.[96] The projector augmented wave (PAW) was used to describe the electron–ion interaction.[97] The generalized gradient approximation (GGA) was adopted with the Perdew–Burke–Ernzerhof (PBE) exchange–correlation functional.[98] For the expansion of the wavefunctions and charge densities, the cutoff energies of 40 Ry, and 320 Ry were used, respectively.

## Results and discussions

Initially, we studied the integration of dual doping in graphene with different configurations, i.e. the ortho, meta, and para configurations. For Be–O, the ortho configuration shows a clear preference of $\sim$5.14 and $\sim$3.82 eV over the meta and para configurations, respectively. This is expected because Be and O favor the formation of BeO. For Be–N, the ortho configuration is favored by 2.2 to 2.14 eV over the other two configurations. These results are in accordance with our previous investigations.[45,90,99] In the case of the Be–B-doped graphene, the difference in energetics between the various configurations was not as high compared to the other two combinations (Be–N and Be–O). Additionally, the ortho configuration of Be–B is found to be more favorable than meta and para configurations by 0.26 and 0.36 eV, respectively, using the vdW-DF/DZP level of theory. However, the paw/PBE level of theory suggests that the ortho configuration is favored by 0.356 and 0.22 eV over the meta and para configurations, respectively. This being said, the difference between the energetics of the ortho and para configurations is $\sim$0.2 eV. To report the stabilities, we calculated the cohesive and formation energies. For the cohesive energy calculations, there is a very good explanation with the equation found in the literature,[100,101] but we used the following expression, which we successfully applied in our previous works:[44-46,48,49,99]

$$E_{coh} = \frac{E_{tot} - n_i E_i}{n} \quad (i = C, Be, B, N \text{ or } O)$$

where, $E_{tot}$ is the total energy of the slab including dopants (Be, B, N, or O) and $n_i$ is ith species present in the system. The term $E_i$ is the gas phase energy of the individual atoms and $n$ is the total number of atoms in the configurations. The cohesive energies of BeO, BeN, and Be–B are calculated to be −7.048 eV per atom, −7.061 eV per atom, and −7.024 eV per atom, respectively. The cohesive energies of the pristine and individual Be-doped graphene are −7.335 eV per atom and −7.129 eV per atom, respectively.[49] It should be noted that the introduction of a second species causes a minor reduction in the cohesive energy. For the calculation of formation energies, we used the following formula:

$$E_{for} = E_{tot} - (n)\mu_c - \mu_{Be} - \mu_x$$

where, $\mu_c$ is the chemical potential of C and can be calculated as the cohesive energy per atom of graphene. The atomic forms of all the dopants were used as the chemical potentials, except C.

Here, $n$ is 48 and $x$ represents B, N, or O. The calculated formation energies are −0.3 eV, −0.94 eV, and 0.9 eV for the BeO, BeN, and Be–B substituted graphene, respectively. The calculated formation energy of Be-doped graphene is 2.91 eV.[49] According to the comparison of the cohesive and formation energies, it is found that the integration of BeN in graphene is relatively easier than BeO or Be–B doping. Additionally, the stability of the BeN DDG is higher than that of both the BeO and Be–B DDG systems. However, the difference in cohesive energy between BeO and Be–B DDG is only 0.024 eV per atom. Nevertheless, the synthesis of our DDG is much easier than that for the individual Be-doped graphene.

Furthermore, MD simulations were performed (using the method discussed in the computational detail section) for the *ortho* and *para* configurations at 300 and 600 K. Both structures were found to be thermally stable even at 600 K, and the results are depicted in S1 of the ESI.†

In the second step, bands structure calculations were executed using the classic G–M–K–G and a special G–M–K–G–M′–K′–G–M″–K″–G k-path. The BeO-doped graphene shows a band gap opening of 0.36 and 0.23 eV at the classic and special k-path, respectively. For the BeB- and BeN-doped graphene, a downward shift of the Fermi level is observed, which alters the semi-metallic behavior of graphene to conducting. The Fermi level shift for the BeN-doped graphene is noted to be 0.53 eV, while an energy gap opening of 0.34 eV around the Dirac point is also observed. For the Be–B *ortho* (*para*) case, the downward shift in the Fermi level is as high as 0.5 eV (0.58 eV for the classic and 0.44 eV for the special k-paths). Furthermore, the gap around the Dirac point is calculated to be 0.22 eV and 0.11 eV following the classic and special k-path, respectively, for the Be–B *ortho* case. The gap computed at the special path is half of the gap calculated at the classic path. For the case of Be–B *para*, this difference is even more prominent as the classic path calculations show a gap of about 0.65 eV around the Dirac point, while by following the special k-path, this gap is as low as 0.25 eV. The band structures plots are shown in S2 of the ESI.† The good agreement of these outcomes with our previous investigations validates our computational methodology.[44,45,48]

Different charge transfer techniques such as Mulliken, Hirshfeld, and Voronoi charge analyses were calculated and compared. In the case of Be–B, the Mulliken analysis at the vDW-DF/DZP level shows that some portion of the charge of C atoms is accumulated around the Be and B atoms. However, the Hirshfeld and Voronoi analyses illustrate that Be and B both are positive, meaning that charge is transferred from these heterogeneous species to the C atoms. According to the higher electronegativity of C compared to Be and B, the charge should be given to the C atoms, as reported in our earlier articles.[44,45,48] In the case of BeN, the N atom is found to be negative according to the Hirshfeld and Voronoi analyses, which are in accordance with our prior studies.[45,99] However, the Mulliken analysis revealed that N is positive at the vDW-DF/DZP level, which is peculiar due to the higher electronegativity of N than C. Conversely, the O atom (in Be–O) is found to be positive, as shown by the Hirshfeld and Voronoi population analyses, despite the fact that O is more electronegative than the rest of the atoms in the Be–O-doped graphene. Nevertheless, the Mulliken analysis indicates a very small charge gain (0.03 $e$) around the O atom. The discrepancy in the Mullikan analysis is due to the basis sets since we have shown that considerably larger basis sets are required for accurate Mulliken charge transfer.[49,99] To have a better idea about the charge transfer, we calculated the Bader analysis and found that Be and B transferred all their valence charge to the C atoms. In the case of BeN, N gained a charge of 2.85 $e$, while the O atom in the BeO-doped system was found to be −1.54 $e$. All these Bader analysis results are in excellent agreement with our earlier findings.[44,45,48] To accurately describe the Mulliken analysis, the M06-l/6-311G* level[102] calculations were performed with the Gaussian 2009 code.[103] Be and B are found to be much positive, while N and O are found to be −0.91 $e$ and −0.68 $e$, respectively. The Mulliken analysis at the M06-l/6-311G* level of theory gave similar trends of charge transfer to the Bader, Hirshfeld, and Voronoi analyses.

To gauge the adsorption of ions (Li/Na) on the pristine/doped graphene systems, we used the following formula:

$$E_{ads} = \frac{E_{tot} - E_{sheet} - nE_{ion}}{n}$$

where, $E_{tot}$ is the total energy of the system (ion adsorbed undoped/doped graphene) and $E_{sheet}$ represents the energy of the undoped/doped graphene sheet. Also, $n$ and $E_{ion}$ are the total number of ions adsorbed and gas phase energy of the ions (or energy of a single ion in the bulk), respectively. The values are distinguished by *, where the energies of the ions are taken from their bulk bcc structures.

Initially, the hollow site of the pristine graphene was chosen for the ion adsorption since ions prefer the hollow sites in graphene. The adsorption energies are −1.11 eV per Li and −0.68 eV per Na, which agree with the previous results.[49,104] These results confirm the accuracy of our vdW-DF/DZP level of theory. Turning our focus to the doped graphene, three hexagon sites were primarily marked for ion adsorption. The selected sites were the hexagon with both dopants, the hexagon with one type of impurity (Be), and the hexagon with another type of impurity (B, N, or O). The two surfaces of graphene are not equal due to the protrusion of Be in Be–B systems, therefore, we considered both surfaces for ion adsorption. The opposite surface to the Be protrusion and below Be was found to be more suitable, as shown by the adsorption energy.[49] As expected, the BeN- and BeO-doped graphene were found to be less favorable compared to the Be–B-doped graphene. For Be–B *ortho*, the highest adsorption energies are −2.41 (−1.00*) eV per Li and −2.02 (−0.94*) eV per Na. For Be–B *para*, the Li adsorption energy is as high as −3.44 (−2.03*) eV per Li and for Na it is computed to be −2.92 (−1.84*) eV per Na. This means that a huge increase of 2.33 eV and 2.24 eV in adsorption energy occurred for the Li and Na ions, respectively. Consequently, the Be–B-doped graphene was further investigated. The most favorable BeN, BeO, and Be–B products are presented in Fig. 1, while the others are grouped in Fig. S3 in the ESI.† For Be–B *ortho*, all the Be and B contributing hexagons were enhanced with the ions on one side. This shows that a total of four Li/Na
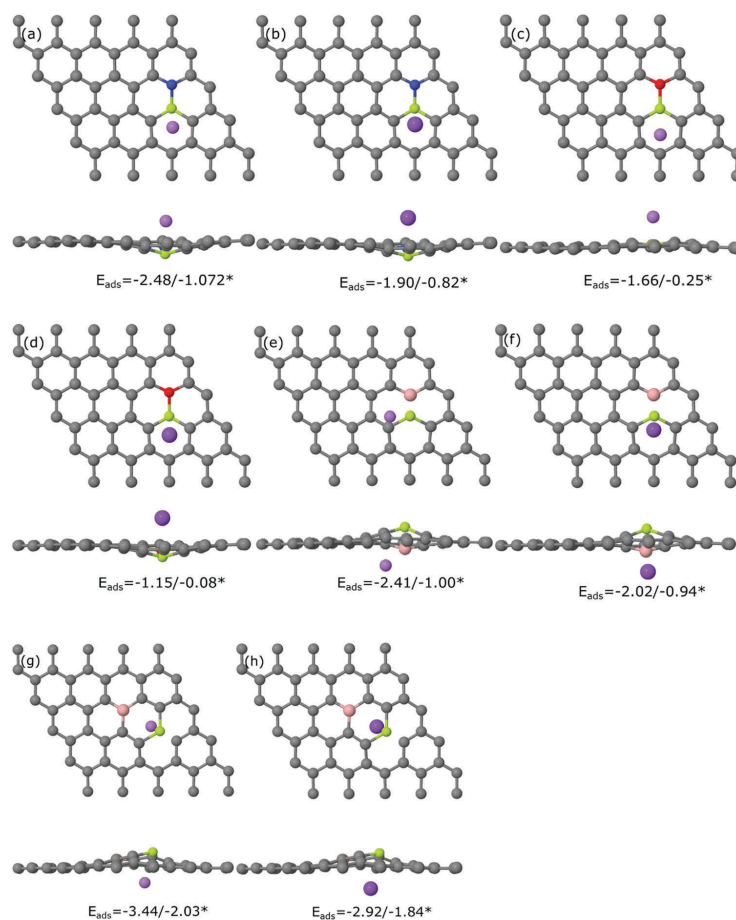
Fig. 1  Top- and side-view of (a) Li adsorption on BeN DDG, (b) Na adsorption on BeN DDG, (c) Li adsorption on BeO DDG, (d) Na adsorption on BeO DDG, and (e and f) Li and Na adsorption on Be–B *ortho* and (g and h) Li and Na adsorption on Be–B *para* DDG, respectively, together with their corresponding adsorption energies. * Represents the energies of Li/Na taken from the bulk bcc.

ions were adsorbed. The Li and Na adsorption energies are calculated to be $-1.74$ ($-0.33*$) eV per Li and $-1.15$ ($-0.07*$) eV per Na, respectively. Finally, the nearest neighboring hexagons were taken into account, resulting in the adsorption of 8 ions. The calculated adsorption energies were $-1.41$ ($-0.001*$) eV per Li and $-1.08$ ($-0.003*$) eV per Na. The same calculation was executed for the Be–B *para* conformation. The *para* disposition offers a total of nine sites for ions around the dopants and nearest hexagons. Additionally, with greater storage, the adsorption is still found to be more favorable than Be–B *ortho*. The adsorption energies of Li and Na are as high as $-1.60$ ($-0.18*$) eV per Li and $-1.25$ ($-0.17*$) eV per Na, respectively.

The tendency of better adsorption for Be–B *para* in comparison with Be–B *ortho* was also confirmed by the charge transfer

analyses. For one Li adsorbed on a Be–B hexagon, the charge transferred from the Li atom to Be–B *ortho* DDG is computed to be $0.43/0.33/0.35$ *e* according to the Mulliken/Hirshfeld/Voronoi charge analyses. However, if the Be–B *para* configuration is considered, the charge transferred from Li is calculated to be $-0.42/0.38/0.42$ *e*. Nevertheless, it can be noted that the increment in charge transfer is seen only in the Hirshfeld and Voronoi analyses. The corresponding Na charge is $0.54/0.41/0.42$ *e* and $0.57/0.49/0.52$ *e* for the Be–B *ortho* and Be–B *para* configurations, respectively. All these charge analyses show that charge is transferred from the ions to the doped graphene systems. Moreover, an increase in the adsorption of ions causes a reduction in the charge transfer and adsorption energies. The data is collected in Table 1.

**Table 1** Summary of the results obtained for Li/Na adsorption on DDG

| Configuration | Adsorption energy $E_{ads}$ = eV per Li | Adsorption energy $E_{ads}$ = eV per Na | Charge (Li) Mulliken/ Hirshfeld/Voronoi | Charge (Na) Mulliken/ Hirshfeld/Voronoi |
|---|---|---|---|---|
| Be–B, *ortho* | | | | |
| Be–B, dn | −2.41/−1.00[a] | −2.02/−0.94[a] | 0.41/0.36/0.37 | 0.53/42/42 |
| Be–B | −2.14/−0.73[a] | −1.62/−0.54[a] | 0.43/0.33/0.35 | 0.54/0.41/0.42 |
| Be | −1.93/−0.52[a] | −1.40/−0.33[a] | 0.46/0.38/0.41 | 0.57/0.47/0.48 |
| B | −2.20/−0.78[a] | −1.67/−0.6[a] | 0.45/0.35/0.37 | 0.54/0.42/0.43 |
| 4-Ions | −1.74/−0.33[a] | −1.15/−0.07[a] | 0.31/0.26/0.29 | 0.31/0.23/0.24 |
| 7-Ions | — | −1.09/−0.01[a] | | 0.20/0.14/0.15 |
| 8-Ions | −1.41/−0.001[a] | −1.08/−0.003[a] | 0.18/0.11/0.14 | 0.17/0.12/0.13 |
| | | | | |
| Be–B, *para* | | | | |
| Be–B, dn | −3.44/−2.03[a] | −2.92/−1.84[a] | 0.48/0.37/0.39 | 0.62/0.47/0.48 |
| Be–B | −3.44/−2.03[a] | −2.82/−1.75[a] | 0.42/0.38/0.42 | 0.57/0.49/0.52 |
| Be | −3.44/−2.03[a] | −2.57/−1.5[a] | 0.48/0.37/0.39 | 0.61/0.51/0.53 |
| B | −3.07/−1.66[a] | −2.54/−1.46[a] | 0.46/0.42/0.45 | 0.61/0.54/0.55 |
| 3-Ions | −2.32/−0.90[a] | −1.62/−0.54[a] | 0.38/0.32/0.36 | 0.38/0.30/0.31 |
| 3-Ions, dn | −2.32/−0.90[a] | −1.60/−0.52[a] | 0.38/0.32/— | 0.36/0.27/— |
| 5-Ions | −2.02/−0.60[a] | −1.50/−0.42[a] | 0.26/0.16/0.20 | 0.28/0.19/0.20 |
| 9-Ions | −1.60/−0.18[a] | −1.25/−0.17[a] | 0.18/0.10/0.12 | 0.14/0.10/—0.11 |
| | | | | |
| BeN | | | | |
| Be–N | −2.48/−1.07[a] | −1.90/−0.82[a] | 0.52/—/— | 0.65/—/— |
| Be | −2.43/−1.01[a] | −1.82/−0.75[a] | 0.45/—/— | 0.60/—/— |
| N | −1.75/−0.34[a] | −1.28/−0.21[a] | 0.56/—/— | 0.62/—/— |
| | | | | |
| BeO | | | | |
| Be–O | −1.20/+0.22[a] | −1.15/−0.07[a] | 0.54/—/— | 0.63/—/— |
| Be | −1.66/−0.25[a] | −1.08/−0.005[a] | 0.47/—/— | 0.58/—/— |
| O | −0.91/+0.50[a] | 0.51/+0.57[a] | 0.57/—/— | 0.55/—/— |

[a] Refers to the energies from the bulk bcc of Li and Na.

The insertion of these ions causes the Be–B-doped graphene to become metallic, thus providing better electronic transport, which is crucial for a good anode material. The band structures of the Li-adsorbed and Na-adsorbed Be–B are presented in Fig. S4 and S5 in the ESI,† respectively. In addition to band structure calculations, projected density of states (PDOS) calculations were also performed. When the concentration of Li/Na is limited to one ion, its contribution to the total DOS (TDOS) is only in the conduction band region. An increase in the concentration of these ions induce many states in the conduction band, which start migrating towards the valence band. For the extreme cases, these ions contribute to the TDOS in the valence band over a reasonable region, and the valence band maximum (VBM) consists mostly of the PDOS of Li/Na. Moreover, the conduction band is greatly dominated by these ions. The PDOS are plotted in Fig. 2 and 3 for the *ortho* and *para* configurations, respectively.

Another aspect of a good anode material is related to its storage capacity, where the great the storage capacity, the better the anode. The storage capacity is predicted using the same formula reported in our previous investigation as follows:

$$C = \frac{nF}{M} \times \frac{1000}{3600}$$

where, $n$ is the total number of adsorbed Li/Na ions, $M$ is the molar mass of doped graphene, and $F$ is the Faraday constant. Additionally, the coulomb value is converted to mA h by simply multiplying the expression by 1000/3600. According to this expression, the ion (Li/Na) storage capacity of Be–B *ortho* and

Be–B *para* is theoretically predicted to be ∼360 mA h g⁻¹ and ∼405 mA h g⁻¹, respectively. Nevertheless, it should be noted that we selected only one side of the doped graphene systems although both surfaces of graphene can be decorated with Li/Na. Consequently, by using both sides of the doped graphene, it can be predicted that the theoretical storage capacity of Li/Na can reach up to ∼710 mA h g⁻¹ and ∼810 mA h g⁻¹ for Be–B *ortho* and Be–B *para*, respectively. In search of the maximum possible theoretical storage capacity, we computed $Li_8BeBC_6$ and $Na_8BeBC_{16}$ (see S6, ESI†) and predicted their storage capacity to be ∼2334 mA h g⁻¹ and ∼1012 mA h g⁻¹, respectively. These values were compared with other famous anode materials. For Li, our evaluated storage capacity was exceptionally higher than that of phosphorene (433 mA h g⁻¹),[105] $Ti_3C_2$ (320 mA h g⁻¹),[106] graphite (372 mA h g⁻¹),[3] and $Mo_2C$ (526 mA h g⁻¹).[107] For the case of Na, its storage capacity is also extremely higher than the $MoS_2$ (146 mA h g⁻¹)[108] and $SnS_2$ (492 mA h g⁻¹).[109] It is noteworthy that we obtained the same exceptional capacities (∼2334 mA h g⁻¹ for Li and ∼1012 mA h g⁻¹ for Na) even when we used the energies of Li and Na in their bulk form. These remarkably high Li/Na storage capacities make Be–B-doped graphene a suitable choice as an anode material in LIBs/SIBs.

Finally, we also calculated the open circuit voltage (OCV), which determines the novelty of an anode material. The expression used for OCV is as follows:
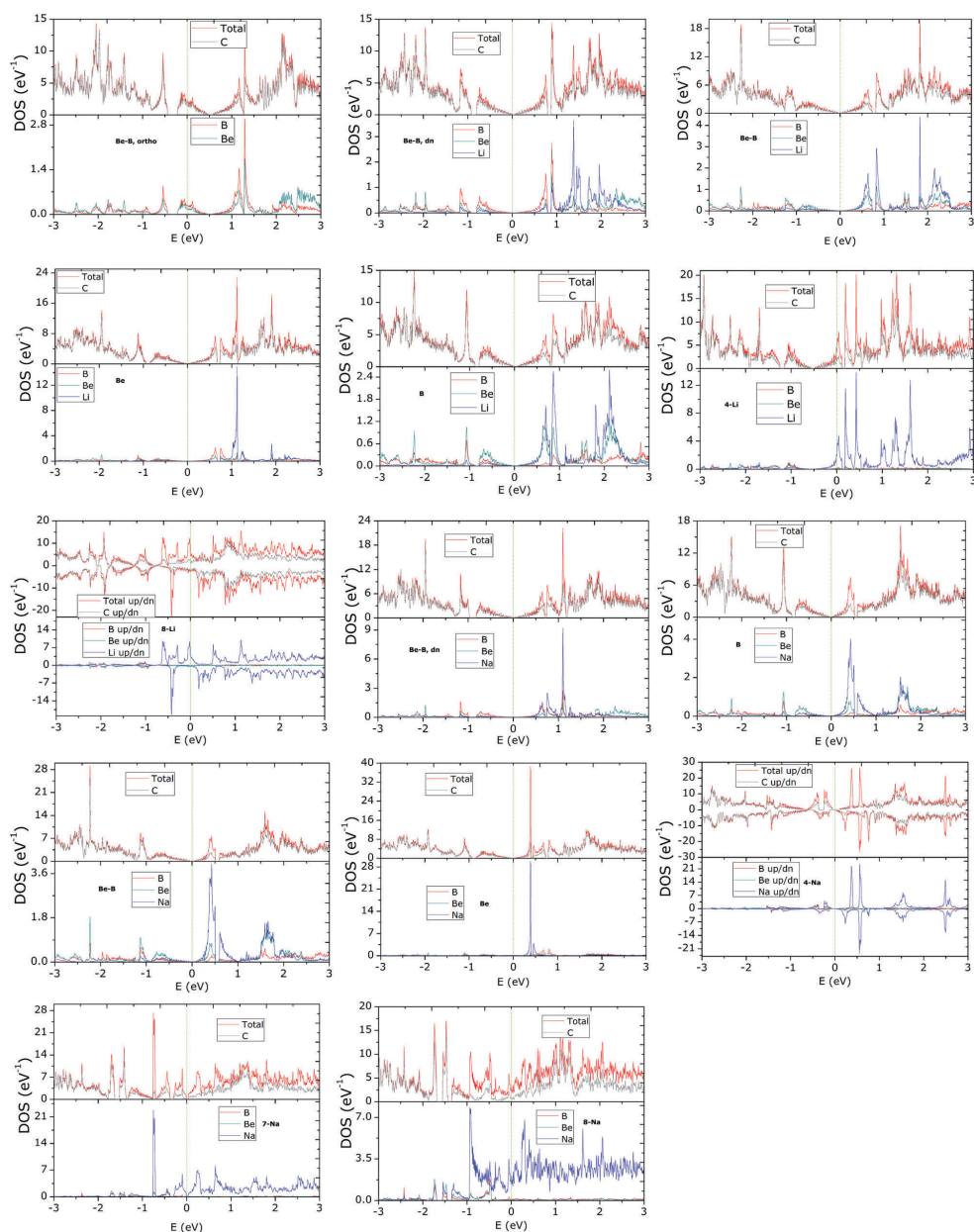
$$OCV = -\frac{E_{ads}}{ze}$$

**Fig. 2** PDOS plotted for Li/Na adsorbed Be–B *ortho* DDG. The doping of Be and B causes a downward shift in the Fermi level and a Dirac point exists in the conduction band. The introduction of Li/Na rearranges the Dirac point at the Fermi level. Additionally, an increase in the concentration of Li/Na makes the structures metallic and induces many states around the Fermi level, confirming the good electronic conductivity. The configuration 8-Li has a magnetic moment of 1.65 $\mu_B$, while a magnetic moment of 1 $\mu_B$ is calculated for 4-Na.
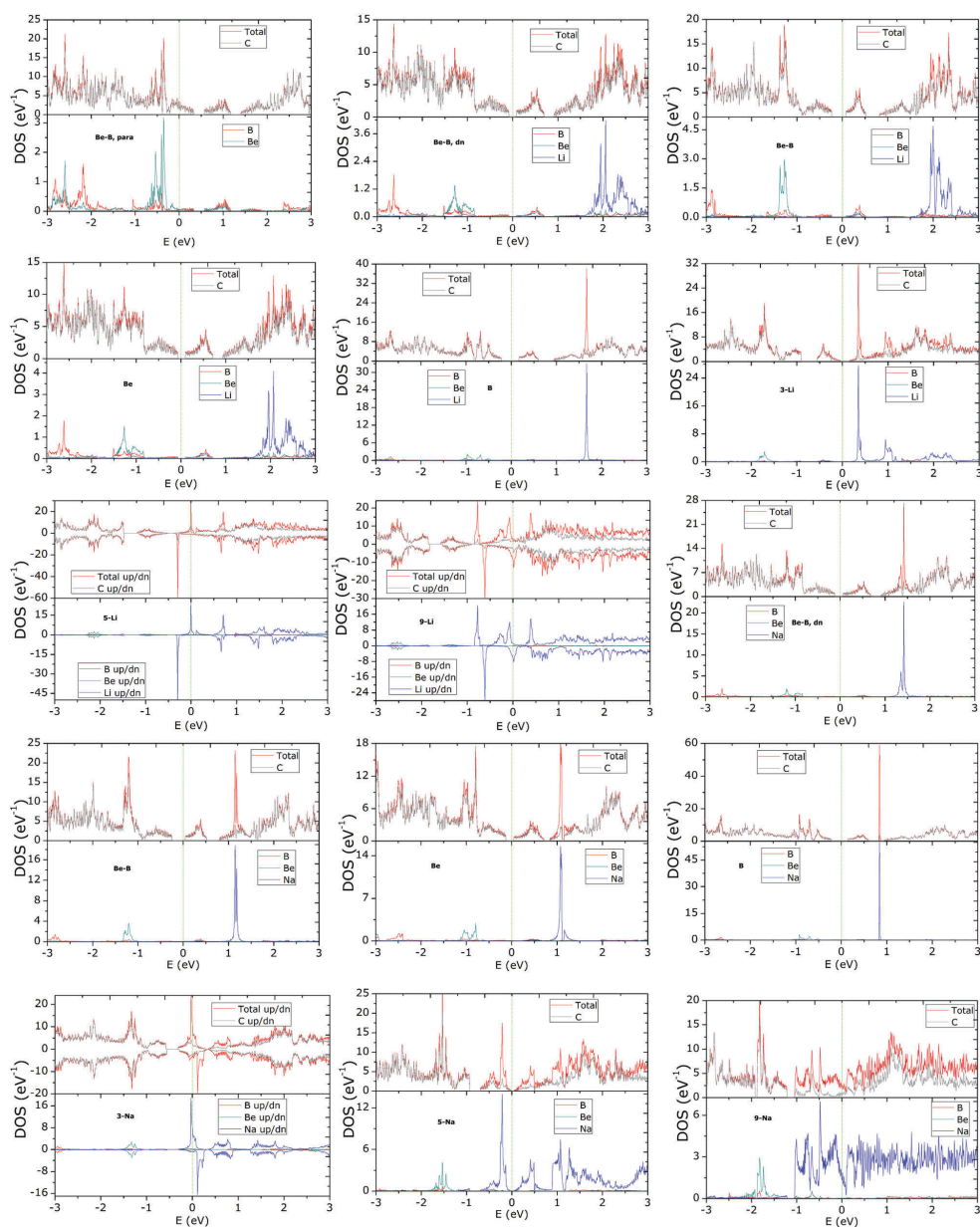
**Fig. 3** PDOS plots are shown for the Li/Na adsorption on the Be–B *para* configurations. The 5-Li, 9-Li, and 3-Na configurations induce a magnetic moment of 0.33 $\mu_B$, 1.5 $\mu_B$, and 0.93 $\mu_B$, respectively. Here, conducting behavior is also noted with an increase in the Li/Na concentration.

where, $z$ is the electronic charge of the Li/Na ions ($z = 1$) in the electrolyte. The OCVs for Be–B *ortho* are in the range of 2.41–1.41 V for Li and 2.02–1.08 V for Na. However, for Be–B *para*, these values are 3.44–1.60 V for Li and 2.92–1.25 V for Na.

177
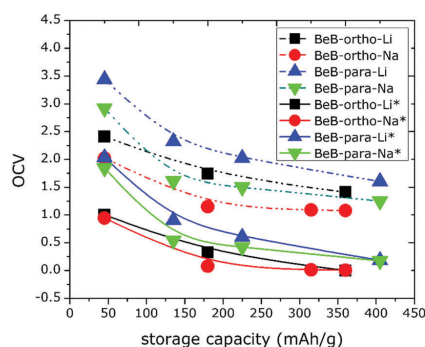
Fig. 4 OCV (in V) *vs.* storage capacity (in mA h g⁻¹). The energies of Li and Na are used from both the isolated gas phase and bulk bcc. The latter is represented by *. The range of the OCVs is excellent.
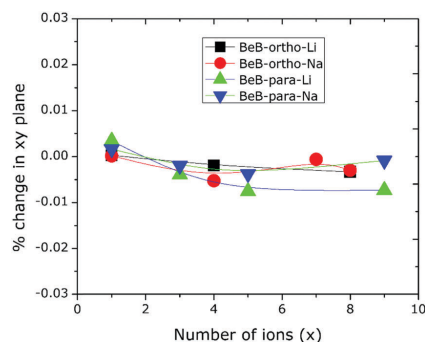


Fig. 5 Percentage area change *vs.* Li/Na content. A negligible change occurred in the area of Be–B DDG during the loading of Li/Na.

Furthermore, we used both forms of energies of Li and Na (isolated gas-phase and from the bulk). The OCVs *vs.* storage capacities plots are shown in Fig. 4. For Li, graphite and TiO$_2$ have OCVs of 0.11 V and 1.5–1.8 V, respectively.[110,111] The atypical OCV values show that Be–B-doped graphene is a suitable choice as a functional LIB/SIB anode. Additionally, the percentage change in the area of Be–B DDG with an increase in Li/Na ions is plotted in Fig. 5, which shows a very minute change in the area of Be–B DDG with an increase in Li/Na content.

## Conclusions

By means of first-principles density functional theory (DFT) calculations, Be–B, BeN, and BeO DDG were studied since it easier to achieve dual doping instead of monodoping in graphene. Due to its excellent electrochemical properties, the Be–B DDG is found to be an efficient anode material for both LIBs and SIBs. Due to the electron deficient character of Be and B compared to

C, the graphene sheet is considered to be hole-doped, turning the graphene sheet into a perfect material for Li/Na adsorption.[49] The simultaneous integration of Be and B can intensify the adsorption of Li and Na by up to ∼3.1 and ∼4.3 times, respectively. An increase in the concentration of Li/Na causes a reduction in the charge transfer to the Be–B DDG sheet and, consequently, a decline in the adsorption energy. However, it is found that an increase in the concentration of adsorbed ions caused the structures to become metallic, ensuring better electronic conductivity. Another important aspect is the minor change in the plane of Be–B DDG during the intercalation of Li/Na, thus ensuring good cycling stability. Moreover, its outstanding OCVs makes Be–B DDG distinguishable from other rival materials. Furthermore, the storage capacities are as high as ∼810 mA h g⁻¹ for both Li$_9$BeBC$_{48}$ and Na$_9$BeBC$_{48}$. For the maximum possible theoretical storage capacities, Li$_8$BeBC$_6$ and Na$_8$BeBC$_{16}$ were calculated and it was found that these systems exhibit phenomenal storage capacities of ∼2334 mA h g⁻¹ and 1012 mA h g⁻¹, respectively. All these outstanding properties reveal that Be–B DDG is a potential exceptional anode material for both the LIBs/SIBs.

## Conflicts of interest

There are no conflicts of interest.

## Acknowledgements

## References

1 M. Armand and J. M. Tarascon, *Nature*, 2008, **451**, 652–657.

2 B. Scrosati, *Electrochim. Acta*, 2000, **45**, 2461–2466.

3 J. M. Tarascon and M. Armand, *Nature*, 2001, **414**, 359–367.

4 J. B. Goodenough and Y. Kim, *Chem. Mater.*, 2010, **22**, 587–603.

5 B. L. Ellis and L. F. Nazar, *Curr. Opin. Solid State Mater. Sci.*, 2012, **16**, 168–177.

6 J. R. Dahn, T. Zheng, Y. Liu and J. S. Xue, *Science*, 1995, **270**, 590.

7 J.-M. Tarascon, *Nat. Chem.*, 2010, **2**, 510.

8 Y. Cao, L. Xiao, M. L. Sushko, W. Wang, B. Schwenzer, J. Xiao, Z. Nie, L. V. Saraf, Z. Yang and J. Liu, *Nano Lett.*, 2012, **12**, 3783–3787.

9 Y. Wen, K. He, Y. Zhu, F. Han, Y. Xu, I. Matsuda, Y. Ishii, J. Cumings and C. Wang, *Nat. Commun.*, 2014, **5**, 4033.

10 C. Ling and F. Mizuno, *Phys. Chem. Chem. Phys.*, 2014, **16**, 10419–10424.

11 S.-W. Kim, D.-H. Seo, X. Ma, G. Ceder and K. Kang, *Adv. Energy Mater.*, 2012, **2**, 710–721.

12 J. Zhang, D.-W. Wang, W. Lv, S. Zhang, Q. Liang, D. Zheng, F. Kang and Q.-H. Yang, *Energy Environ. Sci.*, 2017, **10**, 370–376.

13 R. Raccichini, A. Varzi, D. Wei and S. Passerini, *Adv. Mater.*, 2017, **29**, 1603421.

14 S. Yuan, Y.-H. Zhu, W. Li, S. Wang, D. Xu, L. Li, Y. Zhang and X.-B. Zhang, *Adv. Mater.*, 2017, **29**, 1602469.

15 F. Wang, X. Wu, C. Li, Y. Zhu, L. Fu, Y. Wu and X. Liu, *Energy Environ. Sci.*, 2016, **9**, 3570–3611.

16 Y. Huang, M. Zhu, Y. Huang, Z. Pei, H. Li, Z. Wang, Q. Xue and C. Zhi, *Adv. Mater.*, 2016, **28**, 8344–8364.

17 D. Larcher and J.-M. Tarascon, *Nat. Chem.*, 2015, **7**, 19–29.

18 R. Asher, *J. Inorg. Nucl. Chem.*, 1959, **10**, 238–249.

19 P. Ge and M. Fouletier, *Solid State Ionics*, 1988, **28**, 1172–1175.

20 D. Stevens and J. Dahn, *J. Electrochem. Soc.*, 2001, **148**, A803–A811.

21 M. D. Slater, D. Kim, E. Lee and C. S. Johnson, *Adv. Funct. Mater.*, 2013, **23**, 947–958.

22 A. K. Geim and K. S. Novoselov, *Nat. Mater.*, 2007, **6**, 183–191.

23 A. A. Balandin, S. Ghosh, W. Bao, I. Calizo, D. Teweldebrhan, F. Miao and C. N. Lau, *Nano Lett.*, 2008, **8**, 902–907.

24 K. S. Novoselov, V. I. Falko, L. Colombo, P. R. Gellert, M. G. Schwab and K. Kim, *Nature*, 2012, **490**, 192–200.

25 K. S. Novoselov, A. K. Geim, S. V. Morozov, D. Jiang, Y. Zhang, S. V. Dubonos, I. V. Grigorieva and A. A. Firsov, *Science*, 2004, **306**, 666.

26 M. D. Stoller, S. Park, Y. Zhu, J. An and R. S. Ruoff, *Nano Lett.*, 2008, **8**, 3498–3502.

27 M. Xu, T. Liang, M. Shi and H. Chen, *Chem. Rev.*, 2013, **113**, 3766–3798.

28 V. Wang, H. Mizuseki, H. He, G. Chen, S. Zhang and Y. Kawazoe, *Comput. Mater. Sci.*, 2012, **55**, 180–185.

29 M. Chi and Y.-P. Zhao, *Comput. Mater. Sci.*, 2009, **46**, 1085–1090.

30 H.-L. Park and Y.-C. Chung, *Comput. Mater. Sci.*, 2010, **49**, S297–S301.

31 A. Lherbier, A. R. Botello-Mendez and J.-C. Charlier, *Nano Lett.*, 2013, **13**, 1446–1450.

32 W.-L. Song, W. Wang, L. M. Veca, C. Y. Kong, M.-S. Cao, P. Wang, M. J. Meziani, H. Qian, G. E. LeCroy and L. Cao, *J. Mater. Chem.*, 2012, **22**, 17133–17139.

33 W.-L. Song, M.-S. Cao, M.-M. Lu, J. Liu, J. Yuan and L.-Z. Fan, *J. Mater. Chem. C*, 2013, **1**, 1846–1854.

34 L. Wang and M. Pumera, *Appl. Mater. Today*, 2016, **5**, 134–141.

35 J. Zhou, Q. Sun, Q. Wang and P. Jena, *Phys. Rev. B: Condens. Matter Mater. Phys.*, 2014, **90**, 205427.

36 M. Liu, A. Kutana, Y. Liu and B. I. Yakobson, *J. Phys. Lett.*, 2014, **5**, 1225–1229.

37 X. Fan, W. T. Zheng, J.-L. Kuo and D. J. Singh, *ACS Appl. Mater. Interfaces*, 2013, **5**, 7793–7797.

38 G. Kim, S.-H. Jhi, N. Park, S. G. Louie and M. L. Cohen, *Phys. Rev. B: Condens. Matter Mater. Phys.*, 2008, **78**, 085408.

39 L.-J. Zhou, Z. F. Hou and L.-M. Wu, *J. Phys. Chem. C*, 2012, **116**, 21780–21787.

40 C. Uthaisar and V. Barone, *Nano Lett.*, 2010, **10**, 2838–2842.

41 L.-J. Zhou, Z. F. Hou, L.-M. Wu and Y.-F. Zhang, *J. Phys. Chem. C*, 2014, **118**, 28055–28062.

42 R. P. Hardikar, D. Das, S. S. Han, K.-R. Lee and A. K. Singh, *Phys. Chem. Chem. Phys.*, 2014, **16**, 16502–16508.

43 S. M. Tan, H. L. Poh, Z. Sofer and M. Pumera, *Analyst*, 2013, **138**, 4885–4891.

44 S. Ullah, A. Hussain, W. Syed, M. A. Saqlain, I. Ahmad, O. Leenaerts and A. Karim, *RSC Adv.*, 2015, **5**, 55762–55773.

45 A. Hussain, S. Ullah and M. A. Farhan, *RSC Adv.*, 2016, **6**, 55990–56003.

46 S. Ullah, A. Hussain and F. Sato, *RSC Adv.*, 2017, **7**, 16064–16068.

47 P. A. Denis, S. Ullah and F. Sato, *ChemPhysChem*, 2017, **18**, 1864.

48 A. Hussain, S. Ullah, M. A. Farhan, M. A. Saqlain and F. Sato, *New J. Chem.*, 2017, **41**, 10780–10789.

49 S. Ullah, P. A. Denis and F. Sato, *Appl. Mater. Today*, 2017, **9**, 333–340.

50 T. V. Vineesh, M. A. Nazrulla, S. Krishnamoorthy, T. N. Narayanan and S. Alwarappan, *Appl. Mater. Today*, 2015, **1**, 74–79.

51 N. Saikia and R. C. Deka, *New J. Chem.*, 2014, **38**, 1116–1128.

52 H. Lin, L. Chu, X. Wang, Z. Yao, F. Liu, Y. Ai, X. Zhuang and S. Han, *New J. Chem.*, 2016, **40**, 6022–6029.

53 F. Niu, L.-M. Tao, Y.-C. Deng, Q.-H. Wang and W.-G. Song, *New J. Chem.*, 2014, **38**, 2269–2272.

54 T. Wu, H. Shen, L. Sun, B. Cheng, B. Liu and J. Shen, *New J. Chem.*, 2012, **36**, 1385–1391.

55 P. Willke, J. A. Amani, A. Sinterhauf, S. Thakur, T. Kotzott, T. Druga, S. Weikert, K. Maiti, H. Hofsäss and M. Wenderoth, *Nano Lett.*, 2015, **15**, 5110–5115.

56 G. Giovannetti, P. A. Khomyakov, G. Brocks, V. M. Karpan, J. van den Brink and P. J. Kelly, *Phys. Rev. Lett.*, 2008, **101**, 026803.

57 F. Wang, G. Liu, S. Rothwell, M. Nevius, A. Tejeda, A. Taleb-Ibrahimi, L. C. Feldman, P. I. Cohen and E. H. Conrad, *Nano Lett.*, 2013, **13**, 4827–4832.

58 P. A. Denis, *Chem. Phys. Lett.*, 2010, **492**, 251–257.

59 P. A. Denis, *Comput. Theor. Chem.*, 2016, **1097**, 40–47.

60 P. A. Denis, *Chem. Phys. Lett.*, 2011, **508**, 95–101.

61 P. A. Denis, C. P. Huelmo and F. Iribarne, *Comput. Theor. Chem.*, 2014, **1049**, 13–19.

62 P. A. Denis, *ChemPhysChem*, 2014, **15**, 3994–4000.

63 P. A. Denis and F. Iribarne, *Chem. Phys. Lett.*, 2016, **658**, 152–157.

64 P. A. Denis, C. Pereyra Huelmo and A. S. Martins, *J. Phys. Chem. C*, 2016, **120**, 7103–7112.

65 S. Ullah, P. A. Denis and F. Sato, *ChemPhysChem*, 2017, **18**, 1864–1873.

66 E. K. Goharshadi and S. J. Mahdizadeh, *J. Mol. Graphics Modell.*, 2015, **62**, 74–80.

179

67 D. Xiao, W. Yao and Q. Niu, *Phys. Rev. Lett.*, 2007, **99**, 236809.

68 S. Kawai, S. Saito, S. Osumi, S. Yamaguchi, A. S. Foster, P. Spijker and E. Meyer, *Nat. Commun.*, 2015, **6**, 8098.

69 Y.-C. Lin, C.-Y. Lin and P.-W. Chiu, *Appl. Phys. Lett.*, 2010, **96**, 133110.

70 H. Wang, T. Maiyalagan and X. Wang, *ACS Catal.*, 2012, **2**, 781–794.

71 C. H. A. Wong, Z. K. Sofer, K. I. Klímova and M. Pumera, *ACS Appl. Mater. Interfaces*, 2016, **8**, 31849–31855.

72 C. K. Chua, Z. Sofer, B. Khezri, R. D. Webster and M. Pumera, *Phys. Chem. Chem. Phys.*, 2016, **18**, 17875–17880.

73 K. Klímová, M. Pumera, J. Luxa, O. Jankovský, D. Sedmidubský, S. Matějková and Z. Sofer, *J. Phys. Chem. C*, 2016, **120**, 24203–24212.

74 H. Tian, L. Wang, Z. Sofer, M. Pumera and A. Bonanni, *Sci. Rep.*, 2016, **6**, 33046.

75 A. Ambrosi, A. Bonanni, Z. Sofer, J. S. Cross and M. Pumera, *Chem. – Eur. J.*, 2011, **17**, 10763–10770.

76 L. K. Putri, L.-L. Tan, W.-J. Ong, W. S. Chang and S.-P. Chai, *Appl. Mater. Today*, 2016, **4**, 9–16.

77 O. Jankovský, P. Marvan, M. Nováček, J. Luxa, V. Mazánek, K. Klímová, D. Sedmidubský and Z. Sofer, *Appl. Mater. Today*, 2016, **4**, 45–53.

78 X.-X. Ma and X.-Q. He, *Appl. Mater. Today*, 2016, **4**, 1–8.

79 R. Giardi, S. Porro, T. Topuria, L. Thompson, C. F. Pirri and H.-C. Kim, *Appl. Mater. Today*, 2015, **1**, 27–32.

80 L. Zhou, Z. F. Hou, B. Gao and T. Frauenheim, *J. Mater. Chem. A*, 2016, **4**, 13407–13413.

81 L.-H. Yao, M.-S. Cao, H.-J. Yang, X.-J. Liu, X.-Y. Fang and J. Yuan, *Comput. Mater. Sci.*, 2014, **85**, 179–185.

82 Z.-S. Wu, W. Ren, L. Xu, F. Li and H.-M. Cheng, *ACS Nano*, 2011, **5**, 5463–5471.

83 X. Wang, Z. Zeng, H. Ahn and G. Wang, *Appl. Phys. Lett.*, 2009, **95**, 183103.

84 E. Cruz-Silva, F. López-Urías, E. Muñoz-Sandoval, B. G. Sumpter, H. Terrones, J.-C. Charlier, V. Meunier and M. Terrones, *ACS Nano*, 2009, **3**, 1913–1921.

85 Y. Zheng, Y. Jiao, L. H. Li, T. Xing, Y. Chen, M. Jaroniec and S. Z. Qiao, *ACS Nano*, 2014, **8**, 5290–5296.

86 X. Ma, G. Ning, C. Qi, C. Xu and J. Gao, *ACS Appl. Mater. Interfaces*, 2014, **6**, 14415–14422.

87 J. P. Paraknowitsch, B. Wienert, Y. Zhang and A. Thomas, *Chem. – Eur. J.*, 2012, **18**, 15416–15423.

88 J.-M. You, M. S. Ahmed, H. S. Han, J. E. Choe, Z. Üstündağ and S. Jeon, *J. Power Sources*, 2015, **275**, 73–79.

89 W. Kiciński, M. Norek, A. Dziura and M. Polański, *Microporous Mesoporous Mater.*, 2016, **225**, 198–209.

90 P. A. Denis and C. Pereyra Huelmo, *Carbon*, 2015, **87**, 106–115.

91 P. A. Denis and F. Iribarne, *Phys. Chem. Chem. Phys.*, 2016, **18**, 24693–24703.

92 M. Dion, H. Rydberg, E. Schröder, D. C. Langreth and B. I. Lundqvist, *Phys. Rev. Lett.*, 2004, **92**, 246401.

93 P. Ordejón, E. Artacho and J. M. Soler, *Phys. Rev. B: Condens. Matter Mater. Phys.*, 1996, **53**, R10441–R10444.

94 J. M. Soler, E. Artacho, J. D. Gale, A. Garcia, J. Junquera, P. Ordejon and D. Sanchez-Portal, *J. Phys.: Condens. Matter*, 2002, **14**, 2745.

95 N. Troullier and J. L. Martins, *Phys. Rev. B: Condens. Matter Mater. Phys.*, 1991, **43**, 1993–2006.

96 P. Giannozzi, S. Baroni, N. Bonini, M. Calandra, R. Car, C. Cavazzoni, D. Ceresoli, G. L. Chiarotti, M. Cococcioni and I. Dabo, *J. Phys.: Condens. Matter*, 2009, **21**, 395502.

97 P. E. Blöchl, *Phys. Rev. B: Condens. Matter Mater. Phys.*, 1994, **50**, 17953.

98 J. P. Perdew, K. Burke and M. Ernzerhof, *Phys. Rev. Lett.*, 1996, **77**, 3865.

99 S. Ullah, P. A. Denis and F. Sato, *ChemPhysChem*, 2017, **18**, 1854.

100 E. Perim, R. Paupitz, P. A. S. Autreto and D. S. Galvao, *J. Phys. Chem. C*, 2014, **118**, 23670–23674.

101 J. Du, C. Xia, T. Wang, W. Xiong and J. Li, *J. Mater. Chem. C*, 2016, **4**, 9294–9302.

102 W. Hehre, L. Radom, P. v. R. Schleyer and J. A. Pople, *Ab Initio Molecular Orbital Theory*, Wiley, New York, 1986.

103 M. J. Frisch, G. W. Trucks, H. B. Schlegel, G. E. Scuseria, M. A. Robb, J. R. Cheeseman, G. Scalmani, V. Barone, B. Mennucci, G. A. Petersson, H. Nakatsuji, M. Caricato, X. Li, H. P. Hratchian, A. F. Izmaylov, J. Bloino, G. Zheng, J. L. Sonnenberg, M. Hada, M. Ehara, K. Toyota, R. Fukuda, J. Hasegawa, M. Ishida, T. Nakajima, Y. Honda, O. Kitao, H. Nakai, T. Vreven, J. A. Montgomery, Jr., J. E. Peralta, F. Ogliaro, M. Bearpark, J. J. Heyd, E. Brothers, K. N. Kudin, V. N. Staroverov, R. Kobayashi, J. Normand, K. Raghavachari, A. Rendell, J. C. Burant, S. S. Iyengar, J. Tomasi, M. Cossi, N. Rega, J. M. Millam, M. Klene, J. E. Knox, J. B. Cross, V. Bakken, C. Adamo, J. Jaramillo, R. Gomperts, R. E. Stratmann, O. Yazyev, A. J. Austin, R. Cammi, C. Pomelli, J. W. Ochterski, R. L. Martin, K. Morokuma, V. G. Zakrzewski, G. A. Voth, P. Salvador, J. J. Dannenberg, S. Dapprich, A. D. Daniels, O. Farkas, J. B. Foresman, J. V. Ortiz, J. Cioslowski and D. J. Fox, *Gaussian 09 (Revision A1)*, Gaussian, Inc., Wallingford, CT, 2009.

104 P. A. Denis, *J. Phys. Chem. C*, 2011, **115**, 13392–13398.

105 W. Li, Y. Yang, G. Zhang and Y.-W. Zhang, *Nano Lett.*, 2015, **15**, 1691–1697.

106 Q. Tang, Z. Zhou and P. Shen, *J. Am. Chem. Soc.*, 2012, **134**, 16909–16916.

107 Q. Sun, Y. Dai, Y. Ma, T. Jing, W. Wei and B. Huang, *J. Phys. Lett.*, 2016, **7**, 937–943.

108 M. Mortazavi, C. Wang, J. Deng, V. B. Shenoy and N. V. Medhekar, *J. Power Sources*, 2014, **268**, 279–286.

109 T. Zhou, W. K. Pang, C. Zhang, J. Yang, Z. Chen, H. K. Liu and Z. Guo, *ACS Nano*, 2014, **8**, 8323–8333.

110 M. Winter, J. O. Besenhard, M. E. Spahr and P. Novak, *Adv. Mater.*, 1998, **10**, 725–763.

111 Z. Yang, D. Choi, S. Kerisit, K. M. Rosso, D. Wang, J. Zhang, G. Graff and J. Liu, *J. Power Sources*, 2009, **192**, 588–598.

180

B.4   Additional paper 4: Unusual Enhancement of the Adsorption Energies of Sodium and Potassium in Sulfur-Nitrogen and Silicon-Boron Codoped Graphene

# Unusual Enhancement of the Adsorption Energies of Sodium and Potassium in Sulfur−Nitrogen and Silicon−Boron Codoped Graphene

Saif Ullah,*[,‡] Pablo A. Denis,*[,†] and Fernando Sato[‡]

[†]Computational Nanotechnology, DETEMA, Facultad de Química, UDELAR, CC 1157, Montevideo 11800, Uruguay

[‡]Departamento de Física, Instituto de Ciências Exatas, Campus Universitário, Universidade Federal de Juiz de Fora, Juiz de Fora, MG 36036-900, Brazil

**ABSTRACT:** Herein, we have employed first-principles calculations to investigate the interaction between XY dual-doped graphene (DDG) (X = AL, Si, P, S; Y = B, N, O) and sodium/potassium. The introduction of two dopants alters the adsorption energy (AE) of sodium and potassium with respect to perfect graphene by an average of 0.88 and 0.66 eV, respectively. The systems that display the strongest interactions with the two alkalies assayed are SN and SiB DDG. Although the adsorption energy of sodium on graphene is weaker in comparison to that of potassium, the introduction of these dopants significantly reduces this difference. In effect, in some cases, the AE-K and AE-NA differ by less than 0.05 eV. The protrusion of the 3p dopants out of the graphene plane creates a hole where sodium and potassium can easily be intercalated between two layers of dual-doped graphene. The interlayer distances are reduced by less than 0.4 Å after K intercalation, making the process very favorable. Finally, most importantly, this eminent rise in adsorption energies guarantees exceptional storage capacities at the cost of low doping concentration.



A = Na, K

Opps I did it again,
SN codoped graphene
binds Na and
K with high affinity
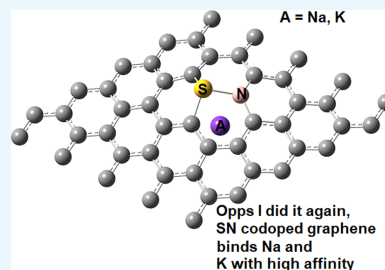
## 1. INTRODUCTION

In 2020, the Protocol of Kyoto[1] comes to an end and the Paris[2] agreement will be implemented to limit the temperature rise of the planet by less than 1.5 °C, with respect to preindustrial levels. The achievement of this goal requires a significant reduction in greenhouse gas emissions. For this reason, major automobile companies are planning to use solely battery-powered engines in their near future, as the famous Rolls Royce Company has recently announced.[3] In fact, countries like France are planning to prohibit the commercialization of fossil fuel-based cars by 2040.[4] Over the last few decades, lithium has been extensively used to design the best rechargeable batteries. In particular, graphene has been considered to be the most promising material to improve the performance of lithium-based batteries.[5−9] A large number of theoretical investigations have been devoted to understanding the interaction between lithium and graphene,[10−18] as well as with sulfur,[19] fullerenes,[20] transition-metal dichalgogenides,[21] or two-dimensional boron materials.[22] And this task has not been easy because the interaction between carbon materials and alkalies is affected by the self-interaction error when using density functional theory.[23−27] For example, it is difficult to obtain a reasonable picture with the most popular density functionals even for the benzene-alkali systems.[22,23] Nevertheless, theoretical calculations have been very useful to shed light into the chemistry behind alkali-based secondary batteries.[10−18] Recently, we studied the effect of dual doping

on the adsorption of lithium onto mono (X) and dual-doped (XY) graphene, where X = B, N, O; Y = Al, Si, P, S.[28] Interestingly, we found that for all dual-doped graphene (DDG) systems, the clustering of lithium is inhibited. In the particular case of nitrogen-doped graphene, the adsorption energy (AE) of lithium is lower than that computed for pristine graphene. However, when nitrogen is combined with aluminum, silicon, phosphorus, or sulfur, the AE is tremendously improved. The most paradigmatic case is that of SN DDG, which presents the strongest AE with Li: −2.99 eV, at the van der Waals density functional (vdW-DF)/double-ζ plus polarization (DZP) level. This value is almost three times the AE of Li over pristine graphene. This result is not entirely surprising because, among dual-doped graphene systems, the SN-doped flavor seems to display unique properties.[29−38] Although lithium is the best choice for alkali-based rechargeable batteries, the problem is that it would be impossible to meet the global demand if it is supposed to replace gasoline. Sodium and potassium are much more abundant than lithium in the Earth's crust. For this reason, they are good candidates to surrogate lithium. However, important challenges must be faced to design useful sodium or potassium rechargeable batteries with reasonable life-

**Table 1. Sodium Adsorption Energies onto Graphene 5 × 5 and Circumcoronene Dual-Doped**

| dopant | vdW-DF/DZP G5 × 5[a] | M06-2X/6-311G* circumcoronene[b] | PBE-D2/VASP G5 × 5 | PBE-D2/6-311G* circumcoronene |
|---|---|---|---|---|
| AlB | −1.58 | −1.81 | −2.44 | −2.10 |
| AlN | −1.55 | −1.98 | −2.44 | −2.05 |
| AlO | −1.63 | −1.64 | −2.43 | −1.99 |
| SiB | **−2.13** | **−2.90** | **−2.72** | **−2.94** |
| SiN | −1.63 | −2.11 | −2.42 | −2.09 |
| SiO | −1.42 | −1.34 | −2.21 | −1.62 |
| PB | −1.47 | −1.75 | −2.36 | −1.91 |
| PN | −0.96 | −1.15 | −1.92 | −1.37 |
| PO | −1.71 | −1.97 | −2.51 | −2.18 |
| SB | −1.10 | −1.96 | −2.35 | −2.03 |
| SN | **−2.00** | **−3.35** | **−2.91** | **−2.92** |
| SO | −0.97 | −1.30 | −2.13 | −1.49 |
| G5 × 5 | −0.67 | −0.45 | −1.08 | −0.71 |

[a]Calculations were performed using periodic conditions and a 5 × 5 unit cell of graphene. [b]Calculations were performed using a graphene flake (circumcoronene).

**Table 2. Potassium Adsorption Energies onto Graphene 5 × 5 and Circumcoronene Dual Doped**

| dopant | vdW-DF/DZP G5 × 5[a,c] | M06-2X/6-311G* circumcoronene[b,c] | PBE-D2/VASP G5 × 5[c] | PBE-D2/6-311G* circumcoronene[c] |
|---|---|---|---|---|
| AlB | −1.81 | −2.22 | −2.55 | −2.33 |
| AlN | −1.75 | −2.35 | −2.51 | −2.27 |
| AlO | −1.78 | −1.95 | −2.47 | −2.18 |
| SiB | **−2.42** | **−3.36** | **−3.06** | **−3.24** |
| SiN | −1.84 | −2.47 | −2.51 | −2.32 |
| SiO | −1.64 | −1.75 | −2.31 | −1.88 |
| PB | −1.81 | −2.20 | −2.51 | −1.93 |
| PN | −1.40 | −1.57 | −2.05 | −1.65 |
| PO | −1.95 | −2.32 | −2.58 | −1.39 |
| SB | −1.08 | −2.36 | −2.47 | −2.31 |
| SN | **−2.42** | **−3.64** | **−3.03** | **−3.05** |
| SO | −1.20 | −1.69 | −2.22 | −1.73 |
| G5 × 5 | −1.1 | −0.96 | −1.40 | −1.10 |

[a]Calculations were performed using periodic conditions and a 5 × 5 unit cell of graphene. [b]Calculations were performed using a graphene flake (circumcoronene). [c]Lowest values are in bold.

times.[39−43] Bearing in mind the impressive results that we obtained when lithium interacts with DDG,[28] we considered that a study that investigates the adsorption of sodium and potassium on these doped graphene systems can help to pave the way toward the development of useful lithium-free rechargeable batteries.

## 2. RESULTS AND DISCUSSION

**2.1. Sodium Adsorption on Dual-Doped Graphene.** The adsorption energy (AE) of sodium on graphene is −0.67 eV, at the vdW-DF/DZP level. This value is 0.44 eV higher than the one computed for lithium (−1.11 eV), using the same methodology. Also, it is significantly smaller than the cohesive energy of bulk sodium, which is −1.078 eV/atom. Therefore, graphene should be modified to inhibit the agglomeration of sodium atoms. In Table 1, we gathered the AE of sodium on 12 DDG systems when sodium is adsorbed below the 3p dopant. At the vdW-DF/DZP level, for 9 cases, studied the adsorption of sodium is stronger than the cohesive energy of bulk sodium. The three DDG systems for which the AE is higher are PN, SO, and SB DDG, but it is worth mentioning that all dopants decrease the AE with respect to that of graphene. The variation of the AE upon doping strongly depends on the choice of heteroatoms introduced. According to the vdW-DF/DZP results, the lowest AE was determined for SiB DDG (−2.13 eV), being closely followed by SN DDG (−2.00 eV). This trend is different than that observed for the adsorption of lithium on DDG,[28] because SN DDG exhibited the lowest AE, and SiB DDG exhibited the second lowest. The net effect of introducing a pair of SiB/SN dopants is a 3.2/3.0 time decrease of the AE of sodium with respect to that of graphene. The results obtained employing the PBE-D2 method and plane waves also point to a significant decrease of the AE when two dopants are introduced. However, SN DDG presents the lowest AE, closely followed by SiB DDG. Thus, it seems to be clear that SN and SiB DDG are the best candidates for increasing the affinity of graphene toward sodium.

Finally, to support the outcome of the vdW-DF and PBE-D2 calculations, we determined the AE onto a hydrogen-terminated graphene cluster. The AE obtained employing the circumcoronene model also indicated a significant increase in the affinity toward sodium adsorption. In line with the PBE-D2 results, SN DDG presents the lowest AE at the M06-2X/6-311G* level of theory, and SiB DDG the second lowest. For SN/SiB DDG, the AE of sodium decreases 7.4/6.4 times with

respect to that of graphene. In light of these results, we can confirm that there is a remarkable decrease in the AE of sodium upon doping. Also, this effect is larger than the one observed for lithium. In effect, the AE of Li onto SN DDG is 2.9 times lower than that computed for graphene.[28]

**2.2. Potassium Adsorption on Dual-Doped Graphene.** The lower cohesive energy of bulk potassium with respect to that of lithium and sodium is an advantage to develop potassium-anode materials, but its large size is a problem. The cohesive energy of bulk potassium is −0.934 eV/atom, about 0.18 eV higher than that for sodium. Interestingly, the AE of potassium on graphene is lower than the cohesive energy of bulk potassium by 0.144 eV. In Table 2, the AE of potassium onto DDG are presented. In line with the results obtained for sodium, all dopants decrease the AE, but in the case of potassium, all of the AE are lower than the cohesive energy of bulk potassium. In fact, when considering the 12 DDG systems, the average AE for potassium is −1.76 eV whereas that of sodium is −1.55 eV, at the vdW-DF/DZP level. This trend is not surprising because the AE of potassium on graphene is lower by 0.33 eV, with respect to that of sodium. The lowest AE is observed for SN and SiB DDG. At the vdW-DF/DZP level, the AE is −2.43 eV in both cases. This value is 2.2 times lower than the value determined for graphene. This finding is fully supported by the PBE-D2 calculations performed with VASP. Indeed, the AE determined for SN and SiB DDG are −3.03 and −3.06 eV, respectively. In agreement with the vdW-DF results, the AE is 2.2 times lower after co-doping.

The variations observed for the AE of potassium on DDG systems were reproduced by the M06-2X calculations carried out for dual-doped circumcoronene. However, again SN DDG is the best system if we are interested in obtaining record-breaking AE. At the M06-2X/6-311G* level, the AE of potassium on SN DDG is 3.8 times lower than that for graphene. This enhancement is almost a half of that observed for sodium at the same level of theory. This result is likely to be linked to the fact that the bonding of sodium on graphene is weaker than for potassium.

**2.3. Comparison between Sodium and Potassium.** Inspection of the results presented in Tables 1 and 2 clearly indicates that the AE can be finely tuned if the adequate combination of dopants is selected. Also, it is clear that for the 12 cases assayed, the dual doping is an effective method to increase the adhesion of these two alkalies onto graphene. For sodium and potassium, the differences between the largest and lowest AEs are very similar. For example, at the vdW-DF/DZP level, it is 1.17 eV for sodium, whereas the value computed for potassium is 1.34 eV. However, the M06-2X method suggests a value that is twice larger. This deviation is likely to be related to the fact that for the latter functional, we used a circumcoronene model. This statement is supported by the results obtained when the cluster models are studied using the PBE-D2/6-311G* method. For example, in the case of potassium, the difference between the largest and lowest AE is 1.58 eV, significantly larger than the value obtained using the PBE-D2 method and periodic conditions, namely, 1.1 eV.

The four methods employed suggested stronger adsorption for potassium as compared to that of sodium. In the case of pristine graphene, the AEs of potassium are lower than those computed for sodium by 0.43, 0.51, 0.32, and 0.39 eV, at the vdW-DF/DZP, M06-2X/6-311G*, PBE-D2, and PBE-D2/6-311G* levels of theory, respectively. However, after doping,

these values become smaller. In effect, the average difference between the AE-K and AE-Na is 0.25, 0.39, 0.14, and 0.23 eV, at the vdW-DF/DZP, M06-2X/6-311G*, PBE-D2, and PBE-D2/6-311G* levels of theory, respectively. Therefore, doping is an effective method to equilibrate the AE of sodium and potassium on graphene. It is difficult to identify a method that can predict when the AE of sodium and potassium are more similar. For example, at the PBE-D2 level, the difference AE-K − AE-Na is 0.04 eV for AlO DDG, about 0.1 eV smaller than the average value. A similar trend is observed if the vdW-DF method is employed. However, discrepancies occur for SB and PO DDG. Inspection of the M06-2X results seems to indicate that AlO DDG is the system for which sodium and potassium display more similar AE. Finally, the PBE-D2/6-311G* results are not in line with those obtained with the same functional and periodic conditions. Indeed, the cluster model calculations performed at the PBE-D2/6-311G* level of theory indicated that for PB DDG, the AE of potassium is only 0.02 eV lower than that computed for sodium.

**2.4. Why is Co-Doping So Useful?** In the introduction, we mentioned that the adsorption of Li on N-doped graphene (N in graphitic configuration) is weaker than that on undoped graphene. This is not strange since nitrogen has one more electron than carbon and thus induces an n-type doping. In contrast, boron, which is a p-type dopant, significantly increases the adsorption of Li on graphene. Given that boron has one electron less than carbon, it facilitates the charge transfer from lithium to graphene. The AE of Li on B-doped graphene is −2.41 eV, more than twice the value computed for graphene. On the same lines, Al also improves the interaction since the AE of Li on Al-doped graphene is −2.71 eV. This value is 0.3 eV larger than that computed for B-doped graphene. In the case of Al, there is another fact, besides having one electron less than carbon, which contributes to lowering the AE: the introduction of a 3p dopant induces significant structural modifications, as can be appreciated in Figure 1. In effect, a hole is created around the dopant, which facilitates the interaction of the alkali with the carbon atoms. This finding is
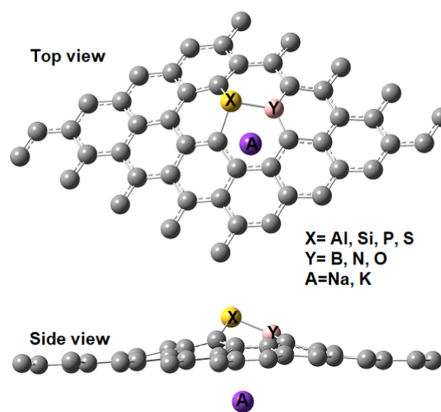


**Figure 1.** Optimized structure for dual-doped graphene with an ortho disposition of dopants and an alkali atom adsorbed below the 3p dopant.
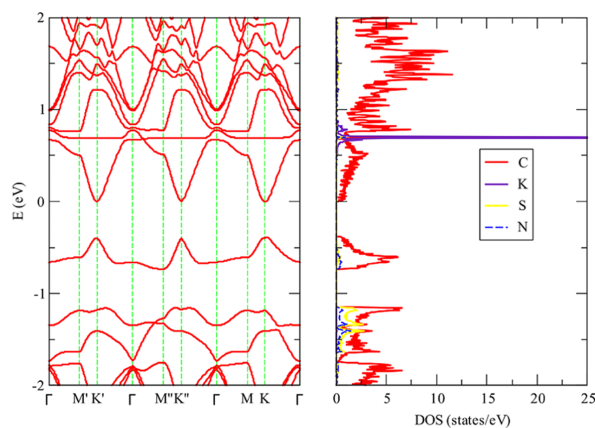
184

**Figure 2.** Band structure and partial density of states determined for potassium adsorbed onto 5 × 5 SN dual-doped graphene, at the vdW-DF/DZP level of theory. (The Fermi level is located at 0.0 eV.)
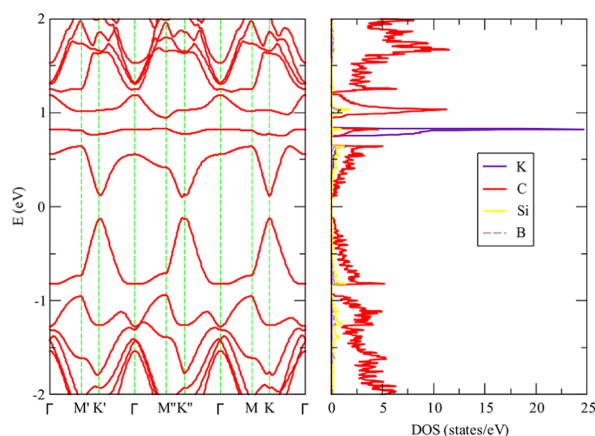


**Figure 3.** Band structure and partial density of states determined for potassium adsorbed onto 5 × 5 SiB dual-doped graphene, at the vdW-DF/DZP level of theory. (The Fermi level is located at 0.0 eV.)

not new; it has been documented before that the adsorption on curved $\pi$ surfaces is stronger than that on planar ones.[59] Also, this is the reason why the adsorption below the 3p dopant is much stronger than that above it.[28] In the particular base of SiB DDG, the two factors are maximized. On one hand, we have the p-type doping of graphene. On the other hand, silicon creates the structural distortion that creates a hole where sodium or potassium can be adsorbed. Finally, in the case of SN DDG, the peculiar structure of this system is the reason behind the strong affinity toward alkalies. As we have explained in our previous investigation of SN DDG,[29−31] the S and N dopants replace a CC bond but are not bonded. Therefore, nitrogen adopts a pyridinic configuration, which facilitates the interaction with alkalies. We note that the interaction between alkalies and pyridinic nitrogen is markedly different than that observed for graphitic nitrogen. This is not surprising since it is

well documented that in the Li:::pyridine complex, the Li atom prefers a $\sigma$ bonding mode, i.e., Li near the nitrogen and in the pyridine plane, instead of a $\pi$ complexation.[60] Thus, to make the N doping of graphene useful, the pyridinic configuration of the nitrogen dopant should be favored during the synthetic procedure.

**2.5. Electronic Structure of SN and SiB Dual-Doped Graphene with Adsorbed Alkalies.** In our previous work about lithium adsorption on DDG, we found that when lithium is adsorbed on SN DDG the system is not a metal but a semiconductor with a gap of 0.2 eV for an 8 × 8 unit cell. This results in a contrast with the electronic structure determined when lithium is adsorbed on pristine graphene since this system has a metallic character. In Figure 2, we present the band structure and density of states determined when potassium is adsorbed on SN DDG. In line with the results
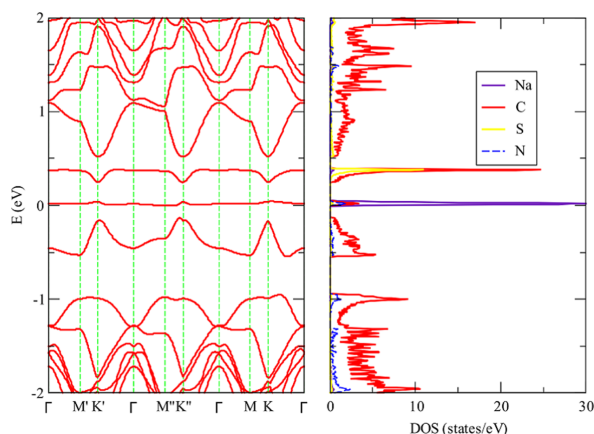
**Figure 4.** Band structure and partial density of states determined for sodium adsorbed onto 5 × 5 SiN dual-doped graphene, at the vdW-DF/DZP level of theory. (The Fermi level is located at 0.0 eV.)

obtained for lithium, a gap of 0.42 eV is opened. In the same vein, when potassium is adsorbed on SiB DDG, we can observe in Figure 3 that the system is a semiconductor. In this case, the gap is smaller, that is, 0.21 eV. The partial density of states clearly shows that the empty potassium states are located far from the Fermi level. For the sake of completeness, we plotted the band structure and density of states for SN DDG with a sodium atom adsorbed. As we can appreciate in Figure 4, the system is also a small band gap semiconductor.

**2.6. Are the Cluster Model Calculations Useful?** The use of polycyclic aromatic hydrocarbon instead of graphene is useful to identify which combination of dopants is more useful if one is interested in increasing the strength of the alkali–graphene interaction. SN and SiB DDG have been indicated by the four methods as the most promising materials to develop alkali-based rechargeable batteries. Also, the four methods point to PN DDG as the system displaying less affinity toward sodium. However, for potassium, the picture is different as the DFT methods suggest three different systems to have the highest AE with K: SB, PN, and PO DDG. Thus, the differences cannot be attributed to the use of a finite graphene model.

In the case of the PBE-D2/6-311G* method, the AEs computed using cluster models are higher (less negative) than those obtained when using that same functional and periodic conditions. On average, they are 0.35 and 0.45 eV higher than those computed for sodium and potassium, respectively. This difference is expected to be increased if the basis set superposition error (BSSE) is included for the PBE-D2/6-311G* calculations (Note: PBE-D2 periodic calculations with VASP are BSSE free). On the contrary, the AEs computed using the M06-2X/6-311G* method are among significantly lower than those computed using the other methods. Although the doping level is very similar, the hydrogen atoms of the cluster induce a different charge distribution. For example, according to the Mulliken analysis at the M06-L/6-311G* level, the 18 carbon atoms of circumcoronene bonded to the hydrogen atoms bear a negative charge of $-0.2e$. However, in graphene, the carbon atoms located at the same distance from

the dopants are not charged. This difference, for sure, will alter the long-range interactions.

**2.7. Intercalation in SN Dual-Doped Graphene.** Due to their high affinity toward alkalies, we investigated their intercalation between two layers of SN DDG when both sulfur atoms protrude out forming a hole, as shown in Figure 5.
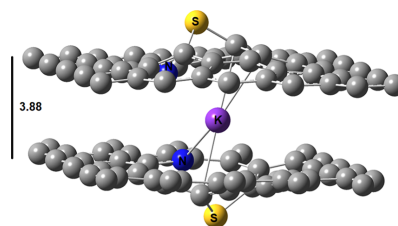


**Figure 5.** Optimized structure for S, N dual-doped bilayer graphene with a potassium atom intercalated.

At the PBE-D2 level and using VASP, the interaction energy between sodium and the two SN DDG layers is $-6.32$ eV. This value is larger (in absolute terms) than twice the Eads of sodium on one layer of SN DDG by 0.50 eV. On the contrary, the interaction is weaker than the sum of interlayer interaction energy of two layers of SN DDG plus twice the AE of sodium on SN DDG by 2.03 eV. Thus, some energy is clearly lost during the intercalation process. Yet, it is not too much because of the hole created by the protrusion of the sulfur atoms out of the graphene plane.

Interestingly, the intercalation of potassium does not significantly affect the interlayer distance of bilayer SN DDG. At the vdW-DF/DZP level, the two layers of SN DDG are separated by an average distance of 3.59 Å, when sulfur atoms protrude out. This value is increased to 3.88 Å when one potassium atom is placed in the hole created by the S and N dopants introduced in both layers. The structures are shown in Figure 2. In the same line, for potassium, the interaction with

the two SN DDG layers plus the interlayer interaction energy of two layers of SN DDG is −8.59 eV. This value is 2.85 eV lower than the intercalation energy of potassium between two layers of SN DDG. The energy forfeited to intercalate potassium is 0.84 eV larger than that of sodium because potassium has a larger atomic radius. Alkali intercalation is a possible process from a thermodynamic standpoint since energy is gained when these alkalies are inside the hole created by the dopants. For example, when the sulfur atoms protrude out of the interlayer region, the two layers of SN DDG are held by −2.53 eV, but after potassium intercalation, this value decreases to −5.74 eV.

## 3. CONCLUSIONS

We have studied the interaction between XY dual-doped graphene (X = AL, Si, P, S; Y = B, N, O) and sodium/potassium by employing periodic and finite models. The introduction of two dopants decreases the adsorption energy of sodium and potassium with respect to that of perfect graphene by 0.88 and 0.66 eV on average. The systems that display the strongest interactions with the two alkalies assayed are SN and SiB DDG. Although the adsorption energy of sodium on graphene is weaker than that for potassium, the introduction of dopants reduces the difference. In effect, in some cases, the AE-K and AE-NA differed by less than 0.05 eV. The protrusion of the 3p dopants out of the graphene plane creates a hole where sodium and potassium can be easily intercalated between two layers of dual-doped graphene. The interlayer distances are reduced by less than 0.4 Å after K intercalation, making the process very favorable. The monumental rise in AE guarantees the remarkable storage capacities at the cost of lower doping concentration, thus preserving the extraordinary properties of graphene up to a large extent.

## 4. METHODS

We studied the adsorption of sodium and potassium onto dual-doped graphene (DDG) using two approaches. In the first place, we carried out periodic calculations using a 5 × 5 unit cell of graphene. Second, we performed simulations employing a graphene flake terminated with hydrogen atoms. The molecule selected was circumcoronene ($C_{54}H_{18}$). The disposition of the dopants is the same that employed in our previous studies for the DDG systems.[28−32] In general, the 2p and 3p dopants prefer to replace a CC bond, except in the case of SiB, which prefers a para disposition of the dopants, as has been documented by us in ref 25. The structure is shown in Figure 1.

For the periodic calculations, we selected the vdW-DF functional developed by Dion et al.,[44] as implemented in SIESTA.[45,46] We utilized the double-$\zeta$ basis set (DZP) with polarization functions and fixed the orbital confining cutoff to 0.01 Ry. The split norm used was 0.15. For all systems, the calculations were performed with the inclusion of spin polarization. The interaction between ionic cores and valence electrons was described by the Troullier−Martins norm-conserving pseudopotentials.[47] Optimizations were carried out using the conjugate gradient algorithm until all residual forces were smaller than 0.01 eV/Å. The unit cells were optimized, and they were sampled using a 40 × 40 × 1 (about 900 k-points $\gamma$ centered) Monkhorst−Pack sampling.

For comparative purposes, we performed PBE-D2[48−50] calculations, as implemented in VASP.[51−54] The projector-

augmented plane wave approach (PAW) was selected, and the plane wave cutoff was 450Ry. The Brillouin zone was sampled with a 7 × 7 × 1 $\gamma$ centered k-point grid. For sodium and potassium, the PV PAW potentials were utilized, which include 7 valence electrons.

The calculations that involved the circumcoronene model were performed using the M06-2X[55,56] and PBE-D2 methods. The basis set selected was the 6-311G*,[57] and the ultrafine grid was utilized. All systems were confirmed to be minima by the calculations of vibrational frequencies. These calculations were carried out with Gaussian 2009.[58] We determined the adsorption energy as follows: AE = $E$(graphene + X) − $E$(X) − $E$(graphene). The $E$(graphene + X), $E$(X), and $E$(graphene) represent the energy of the total system, energy of Na/K, and the energy of the slab, respectively. Zero-point energy corrections were not considered for computing AE. According to this definition, the negative value is for favorable interaction; a more negative value means stronger the interaction. Hereafter, PBE-D2 refers to the results obtained using VASP and a 5 × 5 unit cell, whereas the notation PBE-D2/6-311G* is utilized to discuss the results obtained using the circumcoronene model.

## ■ AUTHOR INFORMATION

**Corresponding Authors**
*E-mail: sullah@fisica.ufjf.br (S.U.).
*E-mail: pablod@fq.edu.uy. Tel: 0059899714280. Fax: 00589229241906 (P.A.D.).

**ORCID** ⊙
Saif Ullah: 0000-0001-8836-9862
Pablo A. Denis: 0000-0003-3739-5061

**Notes**
The authors declare no competing financial interest.

## ■ REFERENCES

(1) https://unfccc.int/process/the-kyoto-protocol.
(2) https://unfccc.int/sites/default/files/english_paris_agreement. pdf.
(3) https://driving.ca/auto-news/news/rolls-royce-will-gradually-switch-to-fully-electric-cars-by-2040.
(4) https://www.theguardian.com/business/2017/jul/06/france-ban-petrol-diesel-cars-2040-emmanuel-macron-volvo.
(5) Zhang, C.; Mahmood, N.; Yin, H.; Liu, F.; Hou, Y. Synthesis of Phosphorus-Doped Graphene and its Multifunctional Applications for Oxygen Reduction Reaction and Lithium Ion Batteries. *Adv. Mater.* **2013**, *25*, 4932−4937.
(6) Reddy, A. L. M.; Srivastava, A.; Gowda, S. R.; Gullapalli, H.; Dubey, M.; Ajayan, P. M. Synthesis Of Nitrogen-Doped Graphene Films For Lithium Battery Application. *ACS Nano* **2010**, *4*, 6337−6342.
(7) Ning, G.; Ma, X.; Zhu, X.; Cao, Y.; Sun, Y.; Qi, C.; Fan, Z.; Li, Y.; Zhang, X.; Lan, X.; Gao, J. Enhancing the Li Storage Capacity and

Initial Coulombic Efficiency for Porous Carbons by Sulfur Doping. *ACS Appl. Mater. Interfaces* **2014**, *6*, 15950−15958.

(8) Zhang, M.; Lei, D.; Yu, X.; Chen, L.; Li, Q.; Wang, Y.; Wang, T.; Cao, G. Graphene oxide oxidizes stannous ions to synthesize tin sulfide−graphene nanocomposites with small crystal size for high performance lithium ion batteries. *J. Mater. Chem.* **2012**, *22*, 23091−23097.

(9) Ma, X.; Ning, G.; Sun, Y.; Pu, Y.; Gao, J. High Capacity Li Storage in Sulfur and Nitrogen Dual-doped Graphene Networks. *Carbon* **2014**, *79*, 310−320.

(10) Kamphaus, E. P.; Balbuena, P. B. Long-Chain Polysulfide Retention at the Cathode of Li−S Batteries. *J. Phys. Chem. C* **2016**, *120*, 4296−4305.

(11) Denis, P. A. Chemical Reactivity of Lithium Doped Monolayer and Bilayer Graphene. *J. Phys. Chem. C* **2011**, *115*, 13392−13398.

(12) Jalbout, A. F.; Ortiz, Y. P.; Seligman, T. H. Spontaneous symmetry breaking and strong deformations in metal adsorbed graphene sheets. *Chem. Phys. Lett.* **2013**, *564*, 69−72.

(13) Valencia, F.; Romero, A. H.; Ancilotto, F.; Silvestri, P. L. Lithium Adsorption on Graphite from Density Functional Theory Calculations. *J. Phys. Chem. B* **2006**, *110*, 14832−14841.

(14) Lu, M.; Zhang, M.; Liu, H. Predicted two-dimensional electrides: Lithium−carbon monolayer sheet. *Phys. Lett. A* **2015**, *379*, 2511−2514.

(15) Deng, X.; Wu, Y.; Dai, J.; Kang, D.; Zhang, D. Electronic structure tuning and band gap opening of graphene by hole/electron codoping. *Phys. Lett. A* **2011**, *375*, 3890−3894.

(16) Rani, P.; Bhandari, R.; Jindal, V. K. Band Gap Modulation of Graphene with Increasing Concentration of Li/B Doping. *Adv. Sci. Lett.* **2015**, *21*, 2826−2829.

(17) Rani, B.; Jindal, V. K.; Dharamvir, K. Energetics of a Li Atom adsorbed on B/N doped graphene with monovacancy. *J. Solid. State Chem.* **2016**, *240*, 67−75.

(18) Ullah, S.; Denis, P. A.; Sato, F. Beryllium doped graphene as an efficient anode material for lithium-ion batteries with significantly huge capacity: A DFT study. *Appl. Mater. Today* **2017**, *9*, 333−340.

(19) Chen, X.; Hou, T.; Persson, K. A.; Zhang, Q. Combining theory and experiment in lithium−sulfur batteries: Current progress and future perspectives. *Mater. Today* **2018**, DOI: 10.1016/j.mattod.2018.04.007.

(20) Sood, P.; Kim, K. C.; Jang, S. S. Electrochemical and electronic properties of nitrogen doped fullerene and its derivatives for lithium-ion battery applications. *J. Energy Chem.* **2018**, *27*, 528−534.

(21) Fan, S.; Zou, X.; Du, H.; Gan, L.; Xu, C.; Lv, W.; He, Y. B.; Yang, Q. H.; Kang, F.; Li, J. Theoretical Investigation of the Intercalation Chemistry of Lithium/Sodium Ions in Transition Metal Dichalcogenides. *J. Phys. Chem. C* **2017**, *121*, 13599−13605.

(22) Jiang, N.; Li, B.; Ning, F.; Xia, D. All boron-based 2D material as anode material in Li-ion batteries. *J. Energy Chem.* **2018**, *27*, 1651−1654.

(23) Ferre-Vilaplana, A. Storage of Hydrogen Adsorbed on Alkali Metal Doped Single-Layer All-Carbon Materials. *J. Phys. Chem. C* **2008**, *112*, 3998−4004.

(24) Martínez, J. I.; Cabria, I.; López, M. J.; Alonso, J. A. Adsorption of Lithium on Finite Graphitic Clusters. *J. Phys. Chem. C* **2009**, *113*, 939−941.

(25) Baker, T. A.; Head-Gordon, M. Modeling the Charge Transfer between Alkali Metals and Polycyclic Aromatic Hydrocarbons Using Electronic Structure Methods. *J. Phys. Chem. A* **2010**, *114*, 10326−10333.

(26) Denis, P. A.; Iribarne, F. C2V or C6V: Which is the most stable structure of the benzene−lithium complex? *Chem. Phys. Lett.* **2013**, *573*, 15−18.

(27) Ullah, S.; Denis, P. A.; Sato, F. Coupled Cluster and Density Functional Investigation of the Neutral Sodium-Benzene and Potassium-Benzene Complexes. *Chem. Phys. Lett.* **2018**, *706*, 343−347.

(28) Denis, P. A. Lithium adsorption on heteroatom mono and dual doped graphene. *Chem. Phys. Lett.* **2017**, *672*, 70−79.

(29) Denis, P. A.; Pereyra, C. P. Structural Characterization and Chemical Reactivity of Dual Doped Graphene. *Carbon* **2015**, *87*, 106−115.

(30) Denis, P. A.; Pereyra Huelmo, C.; Martins, A. S. Band Gap Opening in Dual-Doped Monolayer Graphene. *J. Phys. Chem. C* **2016**, *120*, 7103−7112.

(31) Denis, P. A.; Pereyra Huelmo, C.; Iribarne, F. Theoretical Characterization of Sulfur and Nitrogen Dual-doped Graphene. *Comput. Theor. Chem.* **2014**, *1049*, 13−19.

(32) Denis, P. A.; Iribarne, F. The effect of the dopant nature on the reactivity, interlayer bonding and electronic properties of dual doped bilayer graphene. *Phys. Chem. Chem. Phys.* **2016**, *18*, 24693−24703.

(33) You, J. M.; Ahmed, M. S.; Han, H. S.; Choe, J.; Ustundag, Z.; Jeon, S. New approach of nitrogen and sulfur-doped graphene synthesis using dipyrrolemethane and their electrocatalytic activity for oxygen reduction in alkaline media. *J. Power Sources* **2015**, *275*, 73−79.

(34) Feng, B.; Xie, J.; Dong, C.; Zhang, S.; Cao, G.; Zhao, X. From graphite oxide to nitrogen and sulfur co-doped few-layered graphene by a green reduction route via Chinese medicinal herbs. *RSC Adv.* **2014**, *4*, 17902−17907.

(35) Wohlgemuth, S.-A.; Vilela, F.; Titirici, M.-M.; Antonietti, M. A One-pot Hydrothermal Synthesis of Tunable Dual Heteroatom-doped Carbon Microspheres. *Green Chem.* **2012**, *14*, 741−749.

(36) Wohlgemuth, S.-A.; White, R. J.; Willinger, M.-G.; Titirici, M.-M.; Antonietti, M. A One-pot Hydrothermal Synthesis of Sulfur and Nitrogen Doped Carbon Aerogels with Enhanced Electrocatalytic Activity in the Oxygen Reduction Reaction. *Green Chem.* **2012**, *14*, 1515−1523.

(37) Xu, J.; Dong, G.; Jin, C.; Huan, M.; Guan, L. Sulfur and Nitrogen Co-Doped, Few-Layered Graphene Oxide as a Highly Efficient Electrocatalyst for the Oxygen-Reduction Reaction. *ChemSusChem* **2013**, *6*, 493−499.

(38) Ma, X.; Ning, G.; Sun, Y.; Pu, Y.; Gao, J. High Ccapacity Li Storage in Sulfur and Nitrogen Dual-doped Graphene Networks. *Carbon* **2014**, *79*, 310−320.

(39) Ullah, S.; Denis, P. A.; Sato, F. First-principles study of dual-doped graphene: toward promising anode materials for Li/Na-ion batteries. *New. J. Chem.* **2018**, *42*, 10842−10851.

(40) Wang, X.; Li, G.; Hassan, F. M.; Li, J.; Fan, X.; Batmaz, R.; Xiao, X.; Chei, Z. Sulfur covalently bonded graphene with large capacity and high rate for high-performance sodium-ion batteries anodes. *Nano Energy* **2015**, *15*, 746−754.

(41) Yang, S.; Li, S.; Tang, S.; Dong, W.; Sun, W.; Shen, D.; Wang, M. Sodium adsorption and intercalation in bilayer graphene from density functional theory calculations. *Theor. Chem. Acc.* **2016**, *135*, No. 164.

(42) Luo, X. F.; Wang, S. Y.; Tseng, C. M.; Lee, S. W.; Chiang, W. H.; Chang, J. K. Microplasma-assisted bottom-up synthesis of graphene nanosheets with superior sodium-ion storage performance. *J. Mater. Chem. A* **2016**, *4*, 7624−7631.

(43) Zhou, Q.; Liu, L.; Guo, G.; Yan, Z.; Tan, J.; Huang, Z.; Chen, X.; Wang, X. Sandwich-like cobalt sulfide−graphene composite—an anode material with excellent electrochemical performance for sodium ion batteries. *RSC Adv.* **2015**, *5*, 71644−71651.

(44) Dion, M.; Rydberg, H.; Schroder, E.; Langreth, D. C.; Lundqvist, B. I. Van der Waals density functional for general geometries. *Phys. Rev. Lett.* **2004**, *92*, No. 246401.

(45) Soler, J. M.; Artacho, E.; Gale, J. D.; Garcia, A.; Junquera, J.; Ordejon, P.; Sanchez-Portal, D. The SIESTA Method for Ab Initio Order-N Materials Simulation. *J. Phys.: Condens. Matter* **2002**, *14*, 2745−2779.

(46) Ordejón, P.; Artacho, E.; Soler, J. M. Self-consistent order-N Density-functional Calculations for Very Large Systems. *Phys. Rev. B* **1996**, *53*, R10441−R10444.

(47) Troullier, N.; Martins, J. L. Efficient Pseudopotentials for Plane-Wave Calculations. *Phys. Rev. B* **1991**, *43*, 1993−2006.

(48) Perdew, J. P.; Burke, K.; Ernzerhof, M. Generalized Gradient Approximation Made Simple. *Phys. Rev. Lett.* **1996**, *77*, No. 3865.

(49) Grimme, S. Semiempirical GGA-type density functional constructed with a long-range dispersion correction. *J. Comput. Chem.* **2006**, *27*, 1787−1799.

(50) Grimme, S.; Ehrlich, S.; Goerigk, L. Effect of the damping function in dispersion corrected density functional theory. *J. Comput. Chem.* **2011**, *32*, 1456−1465.

(51) Kresse, G.; Hafner, J. Ab initio molecular dynamics for liquid metals. *Phys. Rev. B* **1993**, *47*, 558−561.

(52) Kresse, G.; Furthmüller, J. Efficiency of ab-initio total energy calculations for metals and semiconductors using a plane-wave basis set. *J. Comput. Mater. Sci.* **1996**, *6*, 15−50.

(53) Kresse, G.; Furthmüller, J. Efficient iterative schemes for ab initio total-energy calculations using a plane-wave basis set. *Phys. Rev. B* **1996**, *54*, No. 11169.

(54) Kresse, G.; Joubert, D. From ultrasoft pseudopotentials to the projector augmented-wave method. *Phys. Rev. B* **1999**, *59*, No. 1758.

(55) Zhao, Y.; Truhlar, D. G. A New Local Density Functional for Main-group Thermochemistry, Transition Metal Bonding, Thermo-chemical Kinetics, and Noncovalent Interactions. *J. Chem. Phys.* **2006**, *125*, No. 194101.

(56) Zhao, Y.; Truhlar, D. G. Density Functionals with Broad Applicability in Chemistry. *Acc. Chem. Res.* **2008**, *41*, 157−167.

(57) Hehre, W.; Radom, L.; Schleyer, P. v. R.; Pople, J. A. *Ab Initio Molecular Orbital Theory*; Wiley: NY, 1986.

(58) Frisch, M. J.; Trucks, G. W.; Schlegel, H. B.; Scuseria, G. E.; Robb, M. A.; Cheeseman, J. R.; Scalmani, G.; Barone, V.; Mennucci, B.; Petersson, G. A.et al. *Gaussian 09*, revision D.01; Gaussian, Inc.: Wallingford, CT, 2009.

(59) Denis, P. A. Methane adsorption inside and outside pristine and N-doped single wall carbon nanotubes. *Chem. Phys.* **2008**, *353*, 79−86.

(60) Krasnokutski, S. A.; Yang, D. S. High-resolution electron spectroscopy and $\sigma/\pi$ structures of M(pyridine) and M+(pyridine) (M = Li, Ca, and Sc) complexes. *J. Chem. Phys.* **2009**, *130*, No. 134313.

189

## APPENDIX C – Electrochemical properties of 2D materials beyond graphene

### C.1  Additional paper 1:Monolayer boron-arsenide as a perfect anode for alkali-based batteries with large storage capacities and fast mobilities

**FULL PAPER**

# Monolayer boron-arsenide as a perfect anode for alkali-based batteries with large storage capacities and fast mobilities

Saif Ullah[1] 🔶 | Pablo A. Denis[2] 🔶 | Fernando Sato[1]

[1]Departamento de Física, Instituto de Ciências Exatas, Campus Universitário, Universidade Federal de Juiz de Fora, Juiz de Fora, Brazil

[2]Computational Nanotechnology, DETEMA, Facultad de Química, UDELAR, Montevideo, Uruguay

**Correspondence**
Saif Ullah, Departamento de Física, Instituto de Ciências Exatas, Campus Universitário, Universidade Federal de Juiz de Fora, Juiz de Fora, MG 36036-900, Brazil.
Email: sullah@fisica.ufjf.br

**Funding information**
Agencia Nacional de Investigación e Innovación; Conselho Nacional de Desenvolvimento Científico e Tecnológico; Coordenação de Aperfeiçoamento de Pessoal de Nível Superior; Financiadora de Estudos e Projetos; Fundação de Amparo à Pesquisa do Estado de Minas Gerais; ANII; Comisión Sectorial de Investigación Científica (CSIC); PEDECIBA Quimica

**Abstract**

We investigate, by means of first-principles density functional theory (DFT) calculation, the possibility of using hexagonal boron-arsenide (h-BAs) as an anode material for alkali-based batteries. We show that the adsorption strength of alkali atoms (Li, Na, and K) on h-BAs in comparison with graphene and other related materials changes a little as a function of alkali atom concentration. When the separation between alkali atoms and h-BAs is less than the critical distance of ~5 Å, the adsorption energy abruptly increases showing fast adsorption without an energy barrier. Furthermore, the low energy barriers of 0.322, 0.187, and 0.0.095 eV for Li, Na, and K, respectively, ensure the fast ionic diffusivities for all the three alkali atoms. Additionally, the addition of these alkali atoms transforms the electronic properties of h-BAs from semiconducting to metallic, resulting in improved electronic conductivities. Most interestingly, the excellent storage capacities of h-BAs (~626 mAh/g) for alkali atoms make it a material of similar caliber to that of other popular anode materials. Finally, the average open circuit voltages are calculated and found to be in the desired range. In short, h-BAs possess every quality that is crucial for an anode material and thus it is interesting to see h-BAs in alkali-based battery technologies.

**KEYWORDS**
alkali-based batteries, DFT, h-BAs, OCVs, storage capacities

## 1 | INTRODUCTION

The World population growth as well as the finite resources and non-renewability of fossil fuels, our dependence on fossil fuels and, consequently, the emission of $CO_2$, etc, are a danger alarm to mankind.[1] For this reason, the investigation of other energy resources, which are renewable and environmentally friendly, becomes crucial. Subsequently, the first thing that catches the attention is the use of secondary batteries as energy storage and conversion. In the past couple of decades, the secondary batteries became much more popular due to the variety of possible applications and their high energy density. One example is the first commercial lithium-ion battery (LIB) presented by SONY in 1991 whose fame is no more a secret.[2–8] However, the storage capacity of graphite, which serves as an anode in LIBs, is around 372 mAh/g.[2,4,5] This low storage capacity does not meet the requirements to be of the practical use, let us say in the rechargeable-electric cars.[9] Another fear is that Li will become priceless in the near future due to its non-abundant resources.[10] Luckily, Li can be replaced with the more abundant sodium (Na) and potassium (K) due to the matching electrochemical setup.[11–17] These pleasant alternatives, however, become impractical due to the larger radii of Na and K when it comes to the choice of anode material. For this reason, the Na storage capacity of graphite is no more than 35 mAh/g.[11,18] In this regard, the practical applications of alkali-based batteries strongly depend on the efficient anode material and, consequently, the exploration of an appropriate anode material becomes a hot subject.

Despite the exceptional properties and various applications of graphene, the utilization of graphene as anode material in alkali-based batteries is restricted by the dendrite formation of the alkali atoms.[19,20] However, the first-ever isolation of graphene is a milestone in the subject of 2D materials which unravel the investigation of other 2D materials. In the short time of 14 years, at the time of writing these words, more than a thousand of other 2D materials have been experimentally synthesized or theoretically predicted.[21,22] Among these, many have the (possible) potential to be used as anodes in alkali-based batteries. Just to name a few, phosphorene, borophene, graphenylene, $Be_3N_2$, $Mo_2C$, $Ti_3C_2$, GeS, $Sc_2C$, $VS_2$, SiC, and $VC_2$, can be regarded as efficient anode materials by virtue of their good storage capacities and ions diffusivities.[22–34]

Regardless of what has been achieved, the quest for innovative 2D anode materials for alkali-based batteries is still demanding. Among the various 2D networks, the III-V binary compounds are of eminent interests due to their remarkable physical and chemical properties.[35–37] The most popular of which is hexagonal boron-nitride (h-BN) with a wide bandgap and, for this reason, the adsorption of alkali atoms would not alter this wider gap to a metallic one since good electronic conductivities are crucial for a worthy anode material.[38–41] Additionally, the weaker chemistry between Li and h-BN is also a serious hurdle.[42,43] Another similar compound is hexagonal boron-phosphide (h-BP) with a good adsorption of alkali atoms and with a narrower bandgap in comparison with h-BN, and it is proposed to be a potential anode material for alkali-based batteries.[37,44–47] The theoretically predicted hexagonal boron-arsenide (h-BAs) has the same structural properties as that of h-BN/h-BP with the only difference that a N/P is replaced by As atom.[37] Furthermore, the smaller bandgap in comparison with h-BP and the excellent mobilities (touching to that of graphene) makes it a hot candidate as anode material for alkali-based batteries.[48] Very recently, we studied the hydrogenation and fluorination of h-BAs (along with h-BP) which turned out in interesting physical, vibrational, and electronic properties.[49] Nevertheless, to the best of our knowledge, the interaction of alkali atoms with h-BAs has not been articulated.

In order to fill this discrepancy, we investigate, in this paper, the potential use of h-BAs as an anode for alkali-based batteries. To this end, first-principles density functional theory (DFT) calculations were performed to study the interaction of alkali atoms (Li, Na, and K) with h-BAs. We calculated the main electrochemical properties, such as adsorption energies, chemical analysis, electronic conductivities, ionic mobilities, storage capacities, and, finally, the open circuit voltages (OCVs). The results were compared with the popular anode materials.

## 2 | COMPUTATIONAL DETAILS

We use quantum espresso package (QE)[50,51] and Spanish Initiative for Electronic Simulations with Thousands of Atoms (SIESTA)[52,53] codes which are based on Kohn-Sham DFT. In QE, we use projector-augmented-wave method to describe the electron-ion interactions.[54] For electron-electron interactions, the Perdew-Burke-Ernzerhof (PBE) flavor of the generalized gradient approximation was implemented.[55,56] We use pseudopotentials (PPs) with the valence configuration of $2s^1$ for Li, $2s^2 2p^1$ for B, $3s^1 2p^6$ for Na, $3s^2 4s^1 3p^6$ for K, and $4s^2 4p^3$ for As.[57] In order to take the long-range van der Waals interactions into account, the dispersion corrected scheme of Grimme, PBE-D2, is utilized.[58] We select a kinetic energy cutoff of 60 and 480 Ry for the expansion of wave functions and charge density, respectively. The unit cell is sampled with a $16 \times 16 \times 1$ Monkhorst-Pack grid in the first Brillouin zone. The energy convergence criterion between each cycle is set to $10^{-6}$ eV. Structural relaxation is done until the forces on each atom were less than 0.015 eV/Å.

We also carry vdW-DF1[59,60] calculations with the aid of SIESTA code. We make use of norm-conserving Troullier-Martins PPs to describe the interactions of valence electrons with the ionic cores.[61] The mesh cutoff and the orbital confining cutoff are set to 200 and 0.01 Ry, respectively. Spin polarization is taken into account for each and every case. We employ double zeta basis set with polarization function. For relaxation, we adopted the conjugate-gradient scheme and used a denser kpoints grid of $30 \times 30 \times 1$ for unit cell sampling in the first Brillouin zone. Since the unit cell is repeating in all the directions, a 20 Å vacuum space is created along the nonperiodic direction between the pseudo-images. We use various cell sizes ranging from $1 \times 1$ to $5 \times 5$ supercell.

The adsorption energy is given as:

$E_{ads} = \frac{E_{tot} - E_{anode} - nE_{alkali}}{n}$, where $E_{tot}$ and $E_{anode}$ is the total energy of the system including alkali atoms and energy of the h-BAs slab, respectively. $E_{alkali}$ is the energy of alkali atoms (Li, Na, and K), taken from the bulk body-centered-cubic structures. Based on our recent investigations,[47,62] we stick to both the aforementioned methods.

## 3 | RESULTS AND DISCUSSION

The geometric structure of h-BAs along with the illustrative high symmetry adsorption sites are shown in Figure 1. The B-As bond length 1.96 Å/1.99 Å and lattice parameter 3.39 Å/3.45 Å, at the PBE-D2/vdW-DF level, are in excellent agreement with the previous results.[37,49]

We adsorb alkali atoms on the hollow, B, and As sites and found that the hollow site is the most favorable for all the three alkali atoms at both the levels. Moreover, it is found that As site has better adsorption strength than B site. This can be attributed to the slightly higher electronegativity of As in comparison with B. At vdW-DF level, for Li, the As and B sites have energies of 0.21 and 0.36 eV, respectively, when taking the hollow

**FIGURE 1**  A, Top and B, side views of geometric structure of hexagonal boron-arsenide (h-BAs) is shown along with the possible adsorption sites
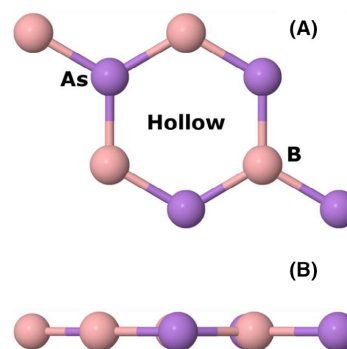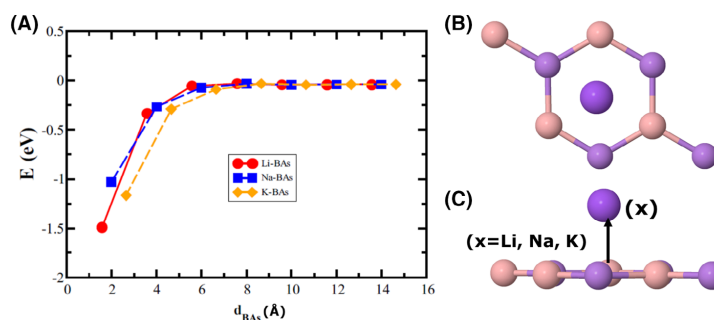


**FIGURE 2**  A, The difference in potential energy with respect to the change in the height of alkali atoms from the hexagonal boron-arsenide (h-BAs) plane. B, Top and C, side views of the most stable site of alkali adsorption on h-BAs. The results are from the vdW-DF calculations



site as a reference. In a similar way, the energy differences at As and B sites for Na adsorption are 0.022 and 0.024 eV, respectively. Interestingly, the As site, for K adsorption, is just 0.008 eV favorable than the B site. As far as the PBE-D2 level is concerned, the energy of As site is 0.43 eV, whereas that of B is 0.51 eV, for Li case. For Na, these differences reduce to 0.21 and 0.31 eV. Nevertheless, for K case, the energies of As and B sites are 0.09 and 0.20 eV, respectively. Nonetheless, hollow site is the most favorable in each case and taken as a reference. Furthermore, the adsorption of Li on As and B sites as well as the adsorption of Na on B site has an unfavorable adsorption. Besides, the adsorption energy of K at both the As and B sites is found to be favorable.

The adsorption of Li/K is found to be stronger than that of Na in all the cases. The adsorption strength of K is weaker than that of Li in higher concentration cases, whereas, we see stronger adsorption of K as compared to that of Li in the low concentration. The very same behavior is already reported for alkali adsorption on the h-BP.[46] At the vdW-DF level, the height of Li, Na, and K on hollow sites from the h-BAs plane is around 1.56, 1.99, and 2.42 Å, respectively. The PBE-D2 values are 1.55, 2.08, and 2.55 Å for Li, Na, and K, respectively. These different heights can be assigned to the different covalent radii of these alkali atoms. In the next step, the alkali atom's height is gradually increased from the surface of h-BAs by 12 Å in the 2 Å interval. This means that Li, Na, and K are elevated to a distance of 13.56, 13.99, and 14.42 Å from the plane of h-BAs. It is quite clear from the potential energy vs alkali atoms distance graph as shown in Figure 2 that beyond 7 Å, no change in the energies is observed. This means that beyond this distance, alkali atoms will not interact with h-BAs. However, more interestingly, an abrupt rise in the energies can be seen when the distance is less than 5 Å. Consequently, a fast loading without an energy barrier is expected when the alkali atoms reach this critical height.

We also calculate the adsorption energies for various concentrations of alkali atoms. The adsorption energies are gathered in Table S1 and plotted in Figure 3. It is evident from the figure that, however, both the employed methods give different numerical results but they exhibit the same profile. For Li and Na, the adsorption strength decreases as a function of Li/Na concentration to a certain extent, that is, $2 \times 2$ unit cell. Beyond this limit, the adsorption strength starts increasing again. This is due to the tug-of-war kind of situation between the repulsive interactions among adjacent Li/Na and the attractive interaction induced due to the structural modifications in the h-BAs plane. The structural modifications in n-hBAs and $n_2$-hBAs (n = La, and Na) become more notable and, therefore, cause an increment in the adsorption strength. These high concentration geometric structures can be seen in Figure S1 where it is clear that h-BAs transformed from the planar to a puckered structure. For K, the adsorption strength smoothly decreases as the K concentration increases. The reason for this is the larger covalent radius of K, which needs more
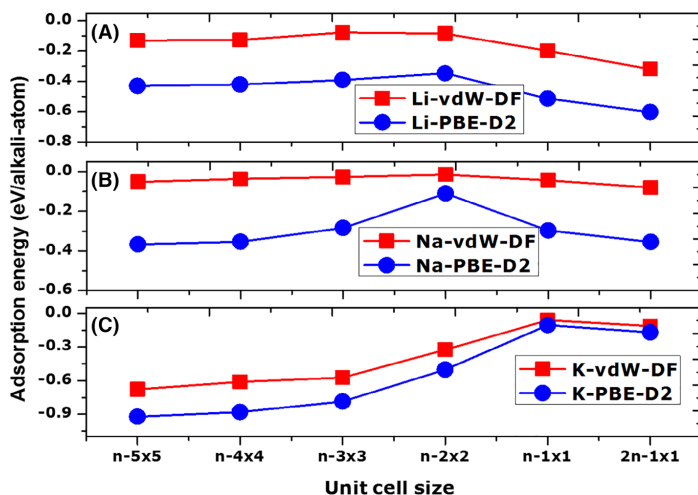
**FIGURE 3** Change in adsorption energy as a function of alkali atoms concentration for A, Li; B, Na; and C, K

space, in comparison with Li and Na. Similar kind of results have already been reported for GeS, SnS, GeSe, SnSe,[63] and h-BP,[46,47] and a detailed explanation can be found in ref. [47].

In chemical analysis, we report different charge transfer mechanisms namely, Bader, Mulliken, Hirshfeld, and Voronoi. In the case of $5 \times 5$ unit cell, the Bader charge analysis shows that 0.99e, 0.87e, and 0.86e charge is transferred from Li, Na, and K, respectively, to h-BAs. The Mulliken charge of Li, Na, and K is +0.18e, +0.40e, and + 0.75e, respectively. Additionally, the Hirshfeld (Voronoi) charge is found to be +305e (+337e), +417e (+452e), and +0.606e (+0.611e) for Li, Na, and K, respectively. Although the charges are numerically different, they show the same trend of transferring the charge from alkali atoms to h-BAs. The charges are gathered in Table S2.

The electronic conductivities play a vital role in determining the quality of an anode material. The h-BAs is a semiconductor with a gap of 0.89/2.17 eV at vdW-DF/HSEH1PBE level.[49] We calculate the electronic properties of alkali atoms adsorbed on a $5 \times 5$ unit cell of h-BAs. After alkali atom adsorption, it can be seen that the electronic band structures show metallic behavior as the conduction band minima is crossing the Fermi level. Consequently, the electronic conductivities can significantly be modified which is crucial for an anode to be used in battery applications. Furthermore, from the projected density of states (PDOS), the contribution of alkali atoms can be seen in the conduction band in the shape of narrow sharp peaks. The electronic band structures with their corresponding PDOS are given in Figure 4.

Another important aspect of the anode material is its ionic mobility and, therefore, the diffusion of alkali atoms alongside the energy barriers is calculated. We make use of the constrained method using SIESTA code by restricting the alkali atoms to move in a specific direction. Having said that, the xy position of alkali atoms was selected manually, whereas the height from h-BAs is relaxed to reach the optimized position. The details can be seen in ref. [64,65]. We select four paths, as the number of paths changes from structure to structure,[66] for alkali diffusion; path1 passing through the bridge and extended to the next hollow site; path2 passing through the B, bridge, As, and reaching the hollow site; path3 and path4 attain the next nearest hollow sites by passing through the B and As sites, respectively. The diffusion paths are given in Figure 5. It should be noted that for all the alkali atoms studied, path4 provides smaller energy barrier in comparison with other paths, whereas path1 and path2 being the second and most unfavorable, respectively. For Li, the path4 (path1) offers a barrier of 0.322 (0.35) eV, whereas the barrier along the path2 is 0.404 eV. In the similar fashion, the energy barrier along path4 (path1) and path2 is 0.187 (0.208) eV/0.095 (0.113) eV and 0.245/0.133 eV for Na/K, respectively.

By utilizing the Arrhenius equation, we compared the difference between path4 (path1) and path2, and is given as:

$$k \sim e^{\frac{-E_a}{k_B T}}$$

where $k$ is the rate constant or temperature-dependent molecular transition, $E_a$ is the activation energy or diffusion barrier, $k_B$ is Boltzmann's constant, and $T$ is the temperature in kelvin. We found that the ion diffusivity along path4 (path1) is 24 (8), 9 (4), and 4 (2) times larger for Li, Na, and K, respectively, in comparison with that of path2. However, the calculated values of diffusion barriers of h-BAs are better than those of h-BP, but the profile of energy barriers and speed of ions diffusivities along path1 in comparison with path2 is in the perfect agreement with ref. [46]. Nevertheless, the authors did not report path3 or path4. This also shows the effectiveness of our employed method. As a comparison, the
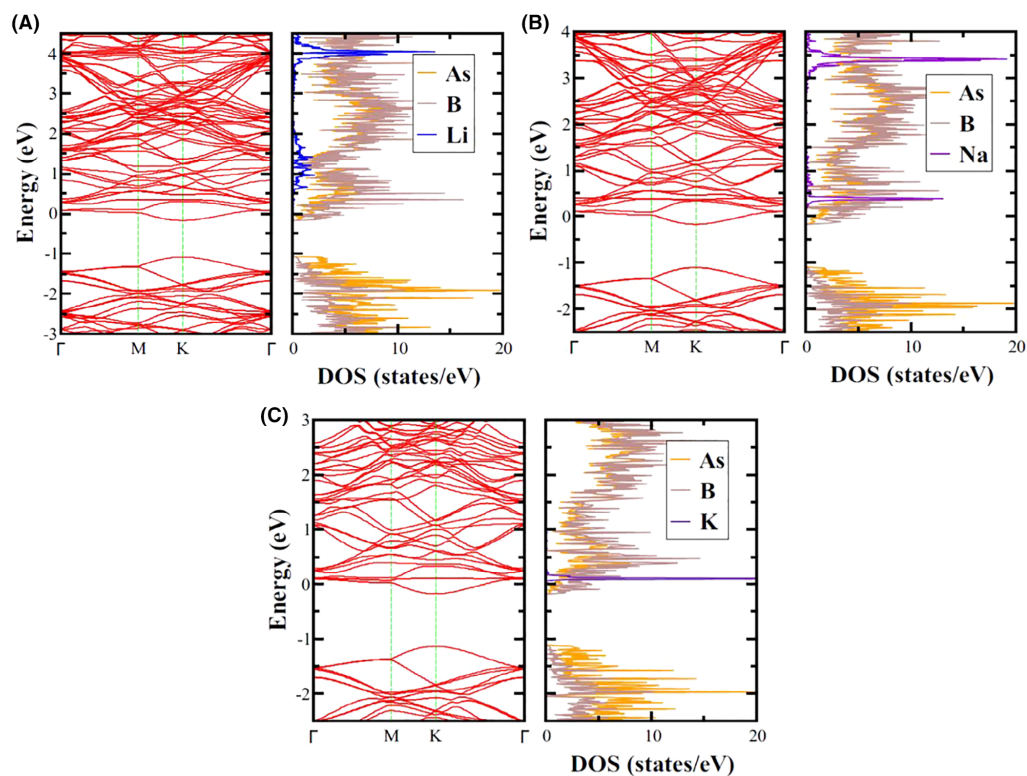
**FIGURE 4** The electronic band structures along with their corresponding PDOS of A, Li-; B, Na-; and C, K-adsorbed hexagonal boron-arsenide (h-BAs) at vdW-DF level. The Fermi energy is set to zero
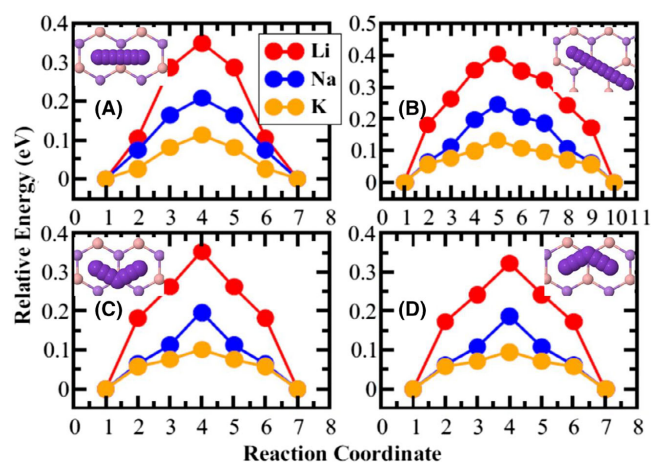


**FIGURE 5** Energy profile of alkali atoms (Li, Na, and K) diffusion along A, path1; B, path2; C, path3; and D, path4. In the inset, the corresponding geometric representation of all the path is given
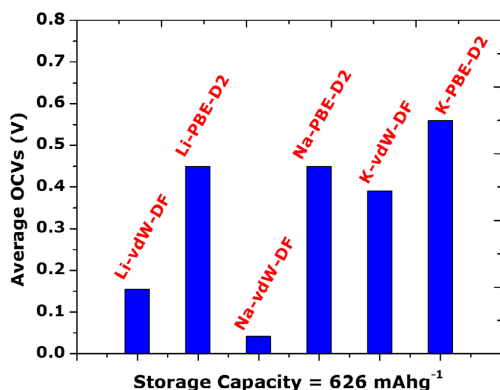
**FIGURE 6** Average open circuit voltages (OCVs) vs the maximum storage capacities at both levels of theory

Li diffusion barriers of the efficient anode materials, such as Si (0.58 eV)[67] and Sn (0.39 eV),[68] are larger than those of h-BAs. These small values of energy barriers for all the three alkali atoms (Li, Na, and K) suggest that h-BAs can be an efficient anode material for alkali-based batteries.

The heart of electrochemical properties is the storage capacity which can show the class of an anode material. In this regard, we calculate the Li, Na, and K storage capacity of h-BAs. We use the following equation:

$$C = \frac{n_{\text{alkali}} F}{M_{\text{anode}}} \gamma$$

where $n_{\text{alkali}}$, $F$, and $M_{\text{anode}}$ are the number of alkali atom(s), Faraday constant, and the molar mass of the anode (h-BAs), respectively. The term $\gamma$, which is equal to 1000/3600, is used to get the units in mAh. We evaluate the storage capacities at various concentration, that is, n-$B_{25}As_{25}$, n-$B_{16}As_{16}$, n-$B_9As_9$, n-$B_4As_4$, n-BAs, and $n_2$-BAs (n = Li, Na, and K). Interestingly, it is found that, at both the employed levels, the maximum storage capacity of h-BAs for every ion studied is around 626 mAh/g. Additionally, a comparison with the popular anode materials is done to show the promise of h-BAs as an anode. For Li, the storage capacities of $Ti_3C_2$,[69] graphite,[2,4] and phosphorene[24] are 320, 372, and 433 mAh/g, respectively. Furthermore, the Na storage capacities of graphite,[18] $NaBC_{31}$,[70] $MoS_2$,[71] and even $SnS_2$[72] are limited to 35, 70, 146, and 492 mAh/g, respectively. Moreover, it can be seen that the K storage capacity of h-BAs (626 mAh/g) is extremely higher than the 192, 256, and 263 mAh/g for $Ti_3C_2$,[29] GeS,[30] and $Mo_2C$,[27] respectively. In addition to this, there exists some efficient anode materials for Li/Na among which a few are: $Sc_2C$ (462/362 mAh/g),[31] $VS_2$ (466 mAh/g),[32] $VC_2$ (1430 mAh/g),[34] $SiC_3$ (2090 mAh/g),[33] Be-N doped graphene (2255/996 mAh/g),[65] Be doped graphene (2303/1005 mAh/g),[7] and Be-B doped graphene (2334/1012 mAh/g).[8] This shows that h-BAs has extremely high storage capacities for all the alkali atoms studied and thus can be regarded as an exceptional anode material in alkali-based batteries.

Finally, we report the average OCV for h-BAs. The equation used to calculate the OCV in its simplest form is given as:

$$OCV = -\frac{E_{\text{ads}}}{ze}$$

where $z$ signify the alkali atom (Li, Na, and K) charge present in the electrolyte. The average OCVs, at PBE-D2 level, for Li, Na, and K are found to be 0.45, 0.30, and 0.56 V, respectively. However, at vdW-DF level, the average OCVs are 0.155, 0.042, and 0.39 V for Li, Na, and K, respectively. The average OCVs along with the maximum storage capacities are plotted in Figure 6. The remarkable average OCVs along with every other aspects show that h-BAs can compete with any of the available anode material.

## 4 | CONCLUSIONS

The potential use of h-BAs as anode material in alkali-based batteries is investigated with the help of DFT calculations. Based on our previous experience, we select PBE-D2 (in QE) and vdW-DF (in SIESTA) methods to explore almost every aspect that is crucial in electrochemical properties. We found a favorable adsorption of alkali atoms on h-BAs in comparison with graphene and other related materials. Furthermore, the unique characteristic of h-BAs is that the adsorption energies undergo a minute change with respect to the various concentrations of alkali atoms except

for K, where the high concentrations induce a significant reduction in the adsorption strength. Unlike to h-BP, where B site is the second most favorable in many cases, the As site is found to be the second most favorable for all the cases. All the charge transfer analyses revealed a substantial amount of charge transfer from alkali atoms to h-BAs, revealing a stronger chemistry between them. A fast loading without an energy barrier is expected when the distance between alkali atoms and h-BAs is less than 5 Å. Additionally, the desirable metallic properties after alkali intercalation and the fast diffusivity with an energy barrier of 0.322, 0.187, 0.0.095 eV for Li, Na, and K, respectively, make h-BAs a desirable anode material. What makes h-BAs so attractive is the exceptional storage capacity of ~626 mAh/g, achieved at both levels of theory, for all the alkali atoms studied. Finally, the average OCVs are in the desirable range where high energy density is required. By virtue of these properties, it is expected that h-BAs can be potentially a high-class anode material for alkali-based batteries.

## DATA ACCESSIBILITY

All the data are available from the authors on request.

## ORCID

*Saif Ullah* https://orcid.org/0000-0001-8836-9862
*Pablo A. Denis* https://orcid.org/0000-0003-3739-5061

## REFERENCES

[1] What will the weather be like in 2050? https://www.un.org/sustainabledevelopment/blog/2015/03/what-will-the-weather-be-like-in-2050/ (accessed: December **2016**).
[2] J. R. Dahn, T. Zheng, Y. Liu, J. S. Xue, *Science* **1995**, *270*, 590.
[3] B. Scrosati, *Electrochim. Acta* **2000**, *45*, 2461.
[4] J. M. Tarascon, M. Armand, *Nature* **2001**, *414*, 359.
[5] M. Armand, J. M. Tarascon, *Nature* **2008**, *451*, 652.
[6] J. B. Goodenough, Y. Kim, *Chem. Mater.* **2010**, *22*, 587.
[7] S. Ullah, P. A. Denis, F. Sato, *Appl. Mater. Today* **2017**, *9*, 333.
[8] S. Ullah, P. A. Denis, F. Sato, *New J. Chem.* **2018**, *42*, 10842.
[9] B. Scrosati, K. M. Abraham, W. A. van Schalkwijk, J. Hassoun, *Lithium Batteries: Advanced Technologies and Applications*, John Wiley & Sons, Hoboken, New Jersey **2013**.
[10] J.-M. Tarascon, *Nat. Chem.* **2010**, *2*, 510.
[11] S. Ullah, P. A. Denis, F. Sato, *Curr. Graphene Sci.* **2018**, *2*, 1.
[12] B. L. Ellis, L. F. Nazar, *Curr. Opin. Solid State Mater. Sci.* **2012**, *16*, 168.
[13] Y. Cao, L. Xiao, M. L. Sushko, W. Wang, B. Schwenzer, J. Xiao, Z. Nie, L. V. Saraf, Z. Yang, J. Liu, *Nano Lett.* **2012**, *12*, 3783.
[14] A. Samad, M. Noor-A-Alam, Y.-H. Shin, *J. Mater. Chem. A* **2016**, *4*, 14316.
[15] E. D. Glendening, D. Feller, M. A. Thompson, *J. Am. Chem. Soc.* **1994**, *116*, 10657.
[16] M. Moshkovich, Y. Gofer, D. Aurbach, *J. Electrochem. Soc.* **2001**, *148*, E155.
[17] A. Eftekhari, Z. Jian, X. Ji, *ACS Appl. Mater. Interfaces* **2017**, *9*, 4404.
[18] M. D. Slater, D. Kim, E. Lee, C. S. Johnson, *Adv. Funct. Mater.* **2013**, *23*, 947.
[19] K. S. Novoselov, A. K. Geim, S. V. Morozov, D. Jiang, Y. Zhang, S. V. Dubonos, I. V. Grigorieva, A. A. Firsov, *Science* **2004**, *306*, 666.
[20] M. Liu, A. Kutana, Y. Liu, B. I. Yakobson, *J. Phys. Chem. Lett.* **2014**, *5*, 1225.
[21] N. Mounet, M. Gibertini, P. Schwaller, D. Campi, A. Merkys, A. Marrazzo, T. Sohier, I. E. Castelli, A. Cepellotti, G. Pizzi, *Nat. Nanotechnol.* **2018**, *13*, 246.
[22] S. Ullah, P. A. Denis, R. B. Capaz, F. Sato, *New J. Chem.* **2019**, *43*, 2933.
[23] V. V. Kulish, O. I. Malyi, C. Persson, P. Wu, *Phys. Chem. Chem. Phys.* **2015**, *17*, 13921.
[24] Q.-F. Li, C.-G. Duan, X. Wan, J.-L. Kuo, *J. Phys. Chem. C* **2015**, *119*, 8662.
[25] H. Jiang, Z. Lu, M. Wu, F. Ciucci, T. Zhao, *Nano Energy* **2016**, *23*, 97.
[26] Y.-X. Yu, *J. Mater. Chem. A* **2013**, *1*, 13559.
[27] D. Cakr, C. Sevik, O. Gulseren, F. M. Peeters, *J. Mater. Chem. A* **2016**, *4*, 6029.
[28] Q. Sun, Y. Dai, Y. Ma, T. Jing, W. Wei, B. Huang, *J. Physi. Chem. Lett.* **2016**, *7*, 937.

[29]  D. Er, J. Li, M. Naguib, Y. Gogotsi, V. B. Shenoy, *ACS Appl. Mater. Interfaces* **2014**, *6*, 11173.

[30]  F. Li, Y. Qu, M. Zhao, *J. Mater. Chem. A* **2016**, *4*, 8905.

[31]  X. Lv, W. Wei, Q. Sun, L. Yu, B. Huang, Y. Dai, *ChemPhysChem* **2017**, *18*, 1627.

[32]  Y. Jing, Z. Zhou, C. R. Cabrera, Z. Chen, *J. Phys. Chem. C* **2013**, *117*, 25409.

[33]  X. Lv, W. Wei, B. Huang, Y. Dai, *J. Mater. Chem. A* **2019**, *7*, 2165.

[34]  J. Xu, D. Wang, R. Lian, X. Gao, Y. Liu, G. Yury, G. Chen, Y. Wei, *J. Mater. Chem. A* **2019**, *7*, 8873.

[35]  K. Watanabe, T. Taniguchi, H. Kanda, *Nat. Mater.* **2004**, *3*, 404.

[36]  N. Alem, R. Erni, C. Kisielowski, M. D. Rossell, W. Gannett, A. Zettl, *Phys. Rev. B* **2009**, *80*, 155425.

[37]  H. Şahin, S. Cahangirov, M. Topsakal, E. Bekaroglu, E. Akturk, R. T. Senger, S. Ciraci, *Phys. Rev. B* **2009**, *80*, 155453.

[38]  K. K. Kim, A. Hsu, X. Jia, S. M. Kim, Y. Shi, M. Hofmann, D. Nezich, J. F. Rodriguez-Nieva, M. Dresselhaus, T. Palacios, J. Kong, *Nano Lett.* **2012**, *12*, 161.

[39]  C. R. Dean, A. F. Young, I. Meric, C. Lee, L. Wang, S. Sorgenfrei, K. Watanabe, T. Taniguchi, P. Kim, K. L. Shepard, J. Hone, *Nat. Nanotechnol.* **2010**, *5*, 722.

[40]  Z. Liu, Y. Gong, W. Zhou, L. Ma, J. Yu, J. C. Idrobo, J. Jung, A. H. MacDonald, R. Vajtai, J. Lou, P. M. Ajayan, *Nat. Commun.* **2013**, *4*, 2541.

[41]  M. Topsakal, E. Aktürk, S. Ciraci, *Phys. Rev. B* **2009**, *79*, 115442.

[42]  Y. Hwang, Y.-C. Chung, *Appl. Surf. Sci.* **2014**, *299*, 29.

[43]  H. Yubin, C. Yong-Chae, *Jpn. J. Appl. Phys.* **2013**, *52*, 06GG08.

[44]  D. Cakr, D. Kecik, H. Sahin, E. Durgun, F. M. Peeters, *Phys. Chem. Chem. Phys.* **2015**, *17*, 13013.

[45]  B. Onat, L. Hallioglu, S. İpek, E. Durgun, *J. Phys. Chem. C* **2017**, *121*, 4583.

[46]  H. R. Jiang, W. Shyy, M. Liu, L. Wei, M. C. Wu, T. S. Zhao, *J. Mater. Chem. A* **2017**, *5*, 672.

[47]  S. Ullah, P. A. Denis, F. Sato, *Appl. Surf. Sci.* **2019**, *471*, 134.

[48]  M. Xie, S. Zhang, B. Cai, Z. Zhu, Y. Zou, H. Zeng, *Nanoscale* **2016**, *8*, 13407.

[49]  S. Ullah, P. A. Denis, F. Sato, *ACS Omega* **2018**, *3*, 16416.

[50]  P. Giannozzi, S. Baroni, N. Bonini, M. Calandra, R. Car, C. Cavazzoni, D. Ceresoli, G. L. Chiarotti, M. Cococcioni, I. Dabo, *J. Phys. Condens. Matter* **2009**, *21*, 395502.

[51]  P. Giannozzi, O. Andreussi, T. Brumme, O. Bunau, M. B. Nardelli, M. Calandra, R. Car, C. Cavazzoni, D. Ceresoli, M. Cococcioni, *J. Phys. Condens. Matter* **2017**, *29*, 465901.

[52]  P. Ordejón, E. Artacho, J. M. Soler, *Phys. Rev. B* **1996**, *53*, R10441.

[53]  J. M. Soler, E. Artacho, J. D. Gale, A. García, J. Junquera, P. Ordejón, D. Sánchez-Portal, *J. Phys. Condens. Matter* **2002**, *14*, 2745.

[54]  P. E. Blöchl, *Phys. Rev. B* **1994**, *50*, 17953.

[55]  J. P. Perdew, K. Burke, M. Ernzerhof, *Phys. Rev. Lett.* **1996**, *77*, 3865.

[56]  J. P. Perdew, K. Burke, M. Ernzerhof, *Phys. Rev. Lett.* **1997**, *78*, 1396.

[57]  A. Dal Corso, *Comput. Mater. Sci.* **2014**, *95*, 337.

[58]  S. Grimme, *J. Comput. Chem.* **2006**, *27*, 1787.

[59]  M. Dion, H. Rydberg, E. Schröder, D. C. Langreth, B. I. Lundqvist, *Phys. Rev. Lett.* **2004**, *92*, 246401.

[60]  G. Román-Pérez, J. M. Soler, *Phys. Rev. Lett.* **2009**, *103*, 096102.

[61]  N. Troullier, J. L. Martins, *Phys. Rev. B* **1991**, *43*, 1993.

[62]  S. Ullah, P. A. Denis, F. Sato, *Chem. Phys. Lett.* **2018**, *706*, 343.

[63]  Y. Zhou, *J. Mater. Chem. A* **2016**, *4*, 10906.

[64]  X. Sun, Z. Wang, Y. Q. Fu, *Sci. Rep.* **2015**, *5*, 18712.

[65]  S. Ullah, P. A. Denis, F. Sato, *Int. J. Quantum Chem.* **2019**, *119*, e25900.

[66]  X. Lv, W. Wei, Q. Sun, B. Huang, Y. Dai, *J. Phys. D Appl. Phys.* **2017**, *50*, 235501.

[67]  W. Wan, Q. Zhang, Y. Cui, E. Wang, *J. Phys. Condens. Matter* **2010**, *22*, 415501.

[68]  C.-Y. Chou, H. Kim, G. S. Hwang, *J. Phys. Chem. C* **2011**, *115*, 20018.

[69]  Q. Tang, Z. Zhou, P. Shen, *J. Am. Chem. Soc.* **2012**, *134*, 16909.

[70]  C. Ling, F. Mizuno, *Phys. Chem. Chem. Phys.* **2014**, *16*, 10419.

[71]  M. Mortazavi, C. Wang, J. Deng, V. B. Shenoy, N. V. Medhekar, *J. Power Sources* **2014**, *268*, 279.

[72]  T. Zhou, W. K. Pang, C. Zhang, J. Yang, Z. Chen, H. K. Liu, Z. Guo, *ACS Nano* **2014**, *8*, 8323.

## SUPPORTING INFORMATION

Additional supporting information may be found online in the Supporting Information section at the end of this article.

# APPENDIX  D  –  Theoretical characterization of other 2D materials

## D.1   Additional paper 1: Hydrogenation and Fluorination of 2D Boron Phosphide and Boron Arsenide: A Density Functional Theory Investigation

Article

# Hydrogenation and Fluorination of 2D Boron Phosphide and Boron Arsenide: A Density Functional Theory Investigation

Saif Ullah,*,[†] Pablo A. Denis,*,[‡] and Fernando Sato[†]

[†]Departamento de Física, Instituto de Ciências Exatas, Universidade Federal de Juiz de Fora, Campus Universitário, Juiz de Fora, Minas Gerais 36036-900, Brazil

[‡]Computational Nanotechnology, DETEMA, Facultad de Química, UDELAR, CC 1157, Montevideo 11800, Uruguay

Ⓢ Supporting Information

**ABSTRACT:** First-principles density functional theory calculations are performed to study the stability and electronic properties of hydrogenated and fluorinated two-dimensional $sp^3$ boron phosphide (BP) and boron arsenide (BAs). As expected, the phonon dispersion spectrum and phonon density of states of hydrogenated and fluorinated BX (X = P, As) systems are found to be different, which can be attributed to the different masses of hydrogen and fluorine. Hydrogenated BX systems bear larger and indirect band gaps and are found to be different from fluorinated BX systems. These derivatives can be utilized in hydrogen storage applications and ultrafast electronic devices. Finally, we investigated the stability and electronic properties of stacked bilayers of functionalized BP. Interestingly, we found that these systems display strong interlayer interactions, which impart strong stability. In contrast with the electronic properties determined for the fluorinated/hydrogenated monolayers, we found that the electronic properties of these bilayers can finely be tuned to a narrow gap semiconductor, metallic or nearly semimetallic one by selecting a suitable arrangement of layers. Moreover, the nearly linear dispersion of the conduction band edge and the heavy-, light-hole bands are the interesting characteristics. Furthermore, the exceptional values of effective masses assure the fast electronic transport, making this material very attractive to construct electronic devices.
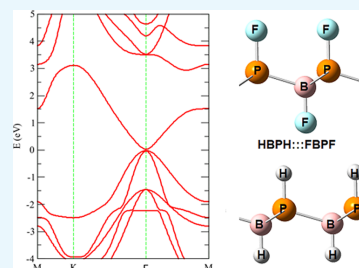
## 1. INTRODUCTION

The groundbreaking scotch tape experiment of successful isolation of graphene opened a new research area of two-dimensional (2D) materials.[1] Since then, many 2D materials are predicted by density functional theory (DFT) calculations followed by their experimental synthesis. Furthermore, modification of the existing materials can lead to some exciting properties, especially in the case of graphene.[2−5] The chemical modification of graphene is a common practice for which radicals such as hydrogen (H),[6−8] oxygen (O),[9] fluorine,[10−12] and so forth are adsorbed on graphene. These adsorbates can take the form of an irregular pattern in graphene oxide[2] or systematic motifs in hydrogenated graphene (graphane)[3,7,8] and fluorinated graphene[10−12] (fluorographene).[5] Moreover, these modifications can significantly alter the electronic properties of graphene as both graphane and fluorographene are considered to be wide band gap semiconductors. However, the list is not limited to that because new/modified materials come with a number of applications, thus causing the advancement of the present technologies.[13−16] Some of these materials with exceptional properties include (but are not limited to) stanene,[17,18] $Nb_2O_3$,[19] plumbene,[20] arsenene,[21] and silicene.[22,23]

Soon after the exfoliation of graphene, the synthesis of monolayer III−V binary compounds became a sizzling area of research with a particular interest toward the hexagonal boron nitride (h-BN).[24−32] By virtue of its wide band gap, h-BN has lots of potential applications in nanoelectronics to be used as a dielectric material, ultraviolet light emitter, and oxidation-resistant coating.[13−21]

Another III−V binary compound that joined the league is hexagonal boron phosphide (h-BP).[24,33] Despite the fact that it is not yet synthesized experimentally, it is already in the focus of theoretical studies. The geometric structure of h-BP is identical to that of graphene and h-BN, whereas two heterogeneous species (B and P) share the unit cell causing the breaking of symmetry and resulting in a band gap opening of 0.82−1.81 eV depending on the employed level of theory. Another material that is analogous to h-BP is hexagonal boron arsenide (h-BAs)[34] having a band gap opening of 0.71 eV at local density approximation and 1.24 eV at $GW_0$ levels of theory. Both these systems are found to be stable as predicted by the phonon dispersion spectrum. In this paper, we study the hydrogenation and fluorination of 2D BP and BAs, their effects on stability, and structural and electronic properties with the help of DFT calculations. To the best of our knowledge, the
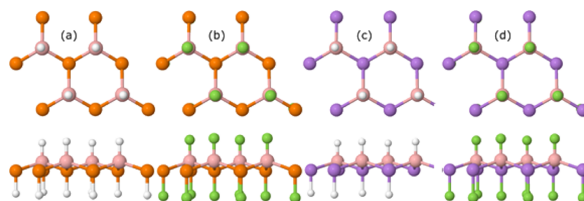
**Figure 1.** Top and side view of (a) H−BP, (b) F−BP, (c) H−BAs, and (d) F−BAs derivatives.

literature lacks such an investigation. In the following, we demonstrate that these systems display unique stability and electronic properties, which can be fine-tuned when fluorinated and hydrogenated BX layers are stacked, X = P, As.

## 2. RESULTS AND DISCUSSION

Initially, we optimized h-BP and h-BAs to check the validity of our computational procedure. The bond lengths and lattice parameters were in good agreement with the previous studies.[24,33] We also reproduced the band structures by employing the $\Gamma-M-K-\Gamma$ path showing excellent agreement with the reported literature. In the next step, we studied the hydrogenation and fluorination of BX in chair conformation as this is the most favorable configuration in the case of graphane and fluorographene.[11] After the introduction of these radicals, the planar BX structures are altered to the puckered ones. The very same happens to graphene by the addition of these radicals.

**2.1. Structural Properties.** In the case of H−BP/F−BP, the lattice parameters and B−P bond lengths are found to be 3.199 Å/3.272 Å and 1.93 Å/1.99 Å, respectively. The distances of H from B and P are found to be 1.22 and 1.43 Å, respectively. The F−B bond length is found to be 1.39 Å, whereas the F−P bond length is as large as 1.61 Å. The H/F−P distance is almost 0.21 Å larger than the H/F−B distance. As discussed above, these structures are no longer planar and, therefore, we calculated the buckling height difference and found that B−P is 0.56 and 0.628 Å apart, in the case of H−BP and F−BP, respectively. Additionally, the lattice parameters and B−As bond lengths are calculated to be 3.414 Å/3.499 Å and 2.06 Å/2.12 Å for H−BAs and F−BAs, respectively. These larger lattice parameters (in comparison with the BP ones) can be attributed to the bigger covalent radius of As. The difference in the lattice parameters of H−BP and F−BP is 0.073 Å, whereas in the case of H−BAs and F−BAs, this difference is a bit larger (0.085 Å). Furthermore, the H−B (1.21 Å) and H−As (1.53 Å) bonds are smaller than the F−B (1.39 Å) and F−As (1.77 Å) bonds. In addition to this, the height between B and As is found to be 0.6 and 0.636 Å in H−BAs and F−BAs, respectively. It should be noted that both the sides of BX were functionalized, so there is no need to introduce a substrate. However, in the case where the use of a substrate is necessary, help can be taken from a very nice literature reported recently.[35] All these geometric structures can be seen in Figure 1.

**2.2. Cohesive Strength.** In order to assess the strength of these derivatives, cohesive energies are calculated and compared with the pristine BX cases. The expression used is given as

$$E_{coh} = \frac{E_{tot} - \sum n_x E_x}{N}$$

where $n_x$ and $E_x$ are the number and gas-phase energy of the atom type $x$, whereas $N$ is the total number of atoms in the simulation box. Finally, $E_{tot}$ is the total energy of the system under study. It is found that fluorination causes a minor reduction in the cohesive energy (CE) of BP in comparison with the pristine cases, whereas for BAs, fluorination increases the CE. On the contrary, hydrogenation significantly reduces the CE by 0.86 and 0.60 eV for BP and BAs, respectively. The CE analysis shows that the fluorinated derivatives can be equally stable as compared to their parent compounds. The summary of cohesive energies and formation energies (FEs) is shown in Table 1.

**Table 1. Cohesive Strength (eV/atom), Formation Energies (eV), and Band Gaps (eV) Calculated at Different Levels of Theory**

| system | CE vdW-DF | CE M06-L | formation energy M06-L | gap (vdW-DF) | gap (HSEH1PBE) |
|---|---|---|---|---|---|
| BP | −4.58 | −4.74 | −9.50 | 1.1 | 1.49 |
| H−BP | −3.74 | −3.75 | −15.0 | 3.89[a] | 4.80[a] |
|  |  |  |  |  | (5.60 direct) |
| F−BP | −4.40 | −4.45 | −17.8 | 1.53 | 2.17 |
| BAs | −4.14 | −4.67 | −9.3 | 0.89 | 2.17 |
| H−BAs | −3.54 | −3.82 | −15.3 | 3.50[a] | 4.43[a] |
|  |  |  |  |  | (5.15 direct) |
| F−BAs | −4.26 | −4.53 | −18.1 | 1.25 | 2.21 |
| HBPF |  | −4.10 | −17.0 |  | 4.28 |
| FBPH |  | −4.15 | −16.5 |  | 3.71 |
| HBAsF |  | −4.14 | −16.6 |  | 3.82 |
| FBAsH |  | −4.26 | −16.4 |  | 3.27 |

[a]Indirect gap.

**2.3. Dynamical Stability.** In order to check whether these derivatives are dynamically stable or not, the phonon spectrum is calculated within the density functional perturbation theory[36] with $8 \times 8 \times 1$ $q$-points. The presence of a negative frequency is the sign of instability, and in this regard, all the calculated derivatives are stable as they all lack negative frequencies as can be seen from the phonon band spectrum along with the corresponding phonon density of states (PhDOS). The high-frequency modes in hydrogenated systems are sufficiently higher in frequency as compared to the fluorinated counterparts. The higher-frequency modes in H−BP and H−BAs are in the frequency range of around 2500 cm$^{-1}$, the latter being a bit higher. This higher-frequency degenerate mode in pristine h-BP/h-BAs appears at a frequency around 1000 cm$^{-1}$/840 cm$^{-1}$. Furthermore, this
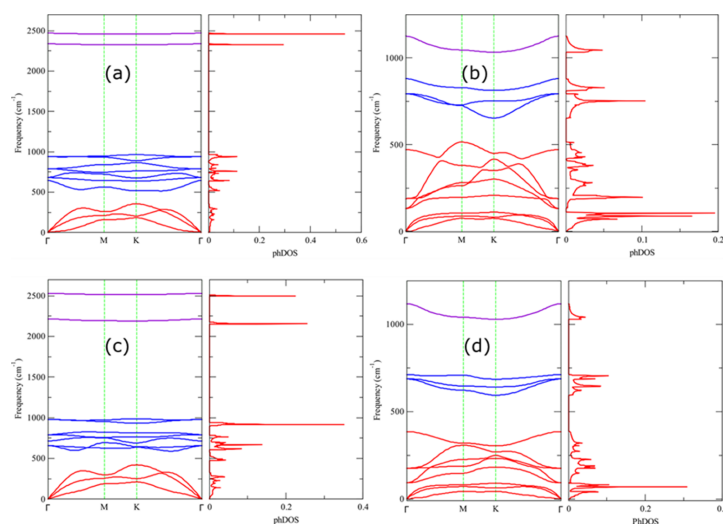
**Figure 2.** Phonon band spectrum along with respective PhDOS plots for (a) H−BP, (b) F−BP, (c) H−BAs, and (d) F−BAs. The absence of negative frequencies guarantees the stability of these derivatives.
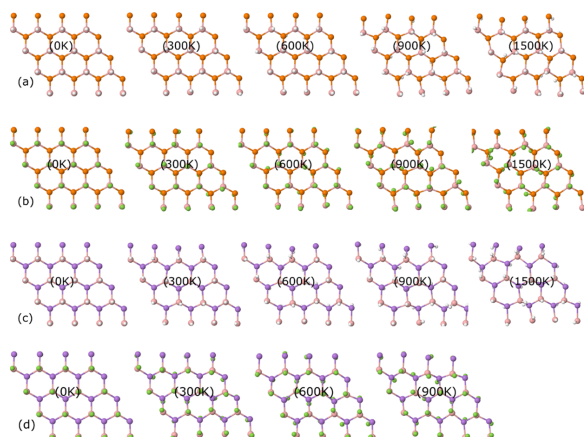


**Figure 3.** Molecular dynamics snapshots after the end of 1 fs simulations steps treated at various temperatures for (a) H−BP, (b) F−BP, (c) H−BAs, and (d) F−BAs.

degenerate mode splits into two modes in H−BP, and even more prominently in H−BAs. The phonon spectrum of hydrogenated and fluorinated systems differs from each other, which can be attributed to the different atomic masses of H and F. Additionally, the intensities of hydrogenated systems are higher than those of fluorinated counterparts as can be seen from PhDOS. It is evident from the phonon spectrum/DOS that the phonon can be bifurcated into high-, intermediate-, and low-frequency groups not only for hydrogenated cases but also for fluorinated cases. This characteristic is missing in fluorographene[37] where the clear separated groups are absent.

Consequently, the H−BX and F−BX systems can be as stable as derivatives just like graphane and fluorographene. The phonon plots can be seen in Figure 2 where these low-, intermediate-, and high-frequency groups are in the range of ~500, ~1000, and ~2500, respectively, for the HBX system. However, these groups span over a (bit) wider range for HBP in comparison with FBAs. For the sack of brevity, the low-, intermediate-, and high-frequency groups are colored as red, blue, and violet, respectively, in phonon bands.

**2.4. Kinetic Stability.** Ab initio molecular dynamic (AIMD) simulations are carried out to assess the thermal
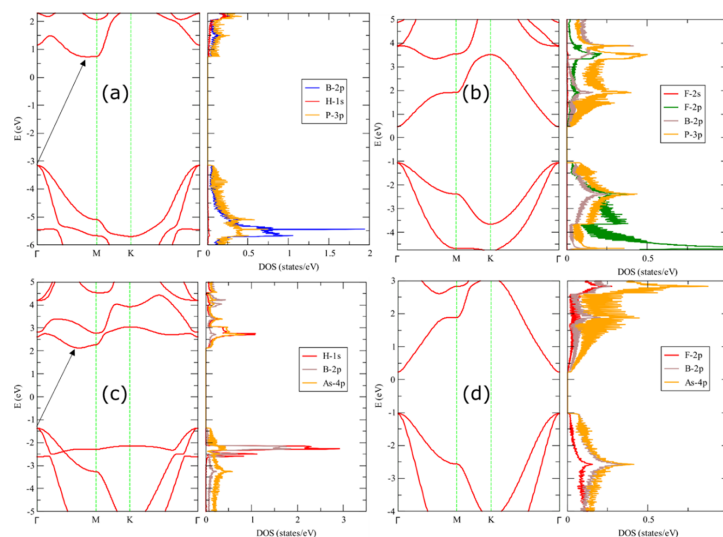
202

**Figure 4.** Electronic band structures determined at the vdW-DF/double zeta plus polarization (DZP) level, along with the respective PDOS plots for (a) H−BP, (b) F−BP, (c) H−BAs, and (d) F−BAs. The Fermi energy is set to zero.
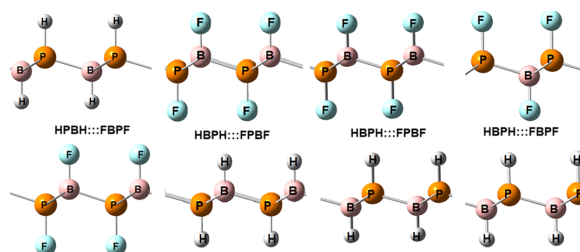


**Figure 5.** Optimized unit cells for the bilayer systems formed by the stacking of one H−BP layer onto F−BP.

stability of these derivatives. We constructed a 4 × 4 unit cell to perform MD at 300, 600, 900, and 1500 K. We use the SIESTA code and the vdW-DF level of theory. The simulations last for 1 fs and are divided into 1000 steps. The *NVT* ensemble is used with a Nose−Hoover thermostat.[41] Snapshots of the final steps at various temperatures are shown in Figure 3. The excellent high-temperature stabilities of these derivatives except the F−BAs at 1500 K guarantee their applications in high-temperature operating devices. Furthermore, the average changes in bonds and angles are depicted in Table S1. Moreover, the stability of some structures was also confirmed by examining them for 2 ps at 1500 K.

**2.5Electronic Properties of F−BX and H−BX (X = P, As).** The electronic band structures and projected density of states (PDOS) are calculated, and it is found that these derivatives possess different electronic properties in comparison with each other and also with the pristine case.[24] The calculated band gaps of h-BP and h-BAs are found to be 1.10 and 0.89 eV, respectively. These band gaps appear at K and are of direct nature. However, the band gaps of H−BX are of

indirect nature, being the valence band maximum (VBM) at Γ and conduction band minimum (CBM) at Γ−M. The computed band gaps of H−BP and H−BAs are 3.89 and 3.50 eV, respectively. Furthermore, PDOS shows that there is a negligible contribution of H to the DOS at VBM or CBM in H−BP. However, in H−BAs, a significant contribution of H to the DOS can be seen, which hybridized mostly with B 2p in valence and with As 4p in the conduction band. F−BP and F−BAs show a band gap opening of 1.53 and 1.25 eV, respectively. Nevertheless, these are direct gaps induced at the Γ point. Moreover, the VBM in both the cases has twofold degeneracy. The P 3p orbitals hybridized with B 2p and F 4p at VBM and CBM, being the P 3p contribution a bit more at CBM. Nearly, the same picture can be seen in the case of F−BAs, where more contribution comes from the As 4p orbitals. Besides, the curvature at CBM and VBM in F−BP and especially in F−BAs is likely to have exceptional mobilities. These show that F−BX systems can be utilized in ultrafast electronic devices. The band structures along with corresponding PDOS are plotted as shown in Figure 4. For the sake of
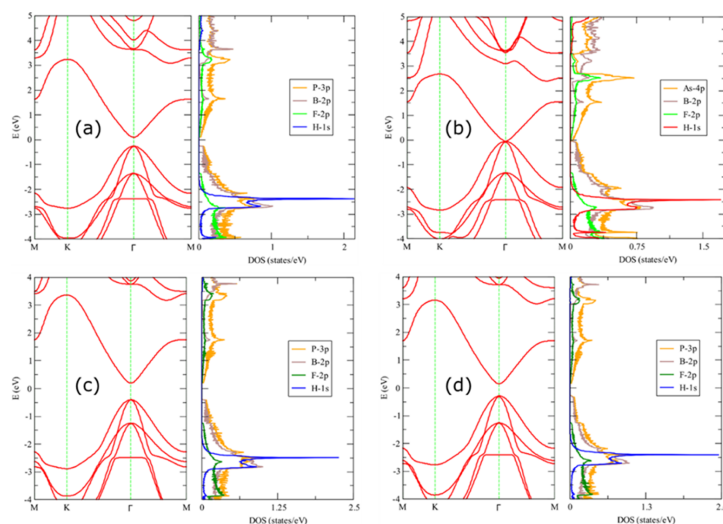
203

**Figure 6.** Electronic band structures along with the respective PDOS plots for (a) HPBH:::FPBF, (b) HPBH:::FBPF, (c) HBPH:::FBPF, and (d) HBPH:::FPBF at the vdW-DF/DZP level of theory.

completeness, we also studied the mixed monolayers: HBPF, FBPH, FBAsF, and FBAsH. Interestingly, these systems present band gaps which are bracketed by the ones computed for F−BX and H−BX. Therefore, using Janus-type functionalization, it is possible to obtain a finer tuning of the band gap.

**2.6 Stability and Electronic Properties of Mixed Bilayers.** In a recent work, we showed that it is possible to adjust the band gap of functionalized silicene if two layers are stacked.[23] In this line, we have considered the case of stacking one layer of H−BP onto F−BP. There are four possible stacking possibilities for these systems which are shown in Figure 5.

In the case of BP, we found that the four combinations have very similar energy, the most stable one being that which combines HBPH:::FBPF (see Figure 6). This structure is only 0.002 eV/atom more stable than HPBH:::FBPF. The remaining two of structures are in the same range of stability. Interestingly, these systems are expected to be very stable because the fluorine and hydrogen atoms of different layers are expected to interact through F:::H hydrogen bonds because the fluorine atoms are negatively charged while the hydrogen atoms bear a positive charge. For example, in the case of HBPH:::FBPF, according to Mulliken analysis, the H atom bonded to P has a positive charge of +0.1 e while the F atom bonded to B bears a negative charge equal to −0.3 e⁻, at the M06-L/6-311G* level of theory. Additionally, these outcomes are in accordance with the lower (higher) electronegativity of H (F). Thus, we can expect a strong interaction between monolayers. The interlayer interaction energy (IE) of HBPH:::FBPF is 0.015 eV/atom, at the M06-L/6-31G* level of theory. This value is only 0.06 eV/atom smaller than the stacking interaction computed for bilayer graphene using the same methodology. With regard to the electronic properties, we have found that the band gaps of monolayers were significantly reduced when stacked. For example,

HBPH:::FBPF and HBPH:::FPBF are metals, while the HPBH:::FPBF has a band gap of 0.38 eV. Perhaps the most interesting case is HPBH:::FBPF, which is a small band gap semiconductor (0.04 eV) featuring somewhat linear dispersion at the CBM. Furthermore, the VBM is composed of heavy-hole and light-hole bands. To further gain insights, we calculated the effective masses of electrons and holes from the curvature of conduction and valence bands. The calculated value of the effective mass of electrons is $0.027m_0$. Furthermore, the effective mass of the heavy-hole band is computed to be $0.045m_0$, while that of the light-hole band is as low as $0.014m_0$. These exceptional values are the surety of remarkable electronic transport in these bilayers. Consequently, these materials become critically attractive to develop BP-based fast nanoelectronic materials.

## 3. CONCLUSIONS

The hydrogenation and fluorination of h-BP and h-BAs are studied by means of DFT calculations. The vibrational properties are found to be different from their parent compounds. The hydrogenated and fluorinated BX (X = P, As) systems are likely to have the comparable stabilities as compared to graphane and fluorographene, respectively. The AIMD simulations suggest that these derivatives can be stable at temperatures as high as 1500 K with the sole exception of F−BAs. Just like the vibrational properties, their electronic properties are also different from h-BP/h-BAs and from each other. The H−BX systems show larger and indirect band gaps in comparison with the F−BX counterparts. The former can have applications in hydrogen storage devices, while the latter can be utilized in ultrafast electronic devices. Finally, we investigated the stability and electronic properties of stacked bilayers of functionalized BP. Interestingly, we found that these systems display strong interlayer interactions, which turn them very stable. In contrast with the electronic properties

204

determined for the fluorinated/hydrogenated monolayers, we found that the bilayers have some exciting characteristics, such as nearly linear dispersion of the conduction band and heavy- and light-hole bands. By virtue of these interesting properties, these bilayers can find applications in fast nanoelectronic devices.

## 4. METHODS

All the calculations are performed with quantum espresso (QE),[38,39] SIESTA,[40,41] and Gaussian[42] codes which are based on DFT methods. We use the projector-augmented wave[43] method and Perdew−Burke−Ernzerhof (PBE)[44] flavor of the generalized gradient approximation to describe the exchange and correlation in QE. The dispersion-corrected PBE-D2[45] scheme is used. The kinetic energy cutoff for the expansion of wave function is set to 60 Ry and 8 times of this value is set for charge densities. The force-convergence criterion is set to $10^{-5}$ Ry/bohr with the energy criteria of $10^{-12}$ Ry. We utilized the PBEsol[46] and PBE pseudopotentials (PPs) for BP and BAs, respectively, from the Standard Solid-State Pseudopotentials library.[47] The vdW-DF[48,49] calculations are carried out as implemented in the SIESTA code. The norm-conserving Troullier−Martins PPs were utilized in their complete separable form.[50] The basis set selected was the DZP polarization functions. The mesh cutoff is 200 Ry in all the calculations. In the case of the calculations performed with SIESTA, geometry optimization is followed until the forces were less than 0.01 eV/Å. The unit cell is sampled with a 30 × 30 × 1 grid of $k$-points. The vacuum region along the $z$-axis is fixed to 20 Å. The M06-L/6-31G*[51] and HSEH1PBE/6-31G*[52] geometry optimizations are carried out with Gaussian 09 using the default convergence criteria.[28] The ultrafine grid was selected, and 3000 $k$-points were used to sample the unit cell. From now and onward, H−BX and F−BX will be used for monolayer hydrogenated and fluorinated BX, respectively, and X being P and As. Interlayer IEs were calculated as IE = $[E(\text{bilayer}) - E(\text{monolayer 1}) - E(\text{monolayer 2})]/N_{\text{atoms}}$, where $E(\text{bilayer})$ is the energy of the bilayered system and $E(\text{monolayer})$ corresponds to the energy of the isolated monolayers which form the bilayer. FEs were calculated as[53] FE = $E(\text{Z}-\text{BX}-\text{Y}) \mu\text{B} - \mu\text{X} - \mu\text{Z} - \mu\text{Y}$, where $E(\text{Z}-\text{BX}-\text{Y})$ is the energy of the monolayer and $\mu\text{B}$, $\mu\text{X}$, $\mu\text{Z}$, and $\mu\text{Y}$ are the chemical potentials of the atoms involved. In all cases, we selected the energies of the isolated atoms as a reference.

## ■ ASSOCIATED CONTENT

### ⓢ Supporting Information

The Supporting Information is available free of charge on the ACS Publications website at DOI: 10.1021/acsome-ga.8b02605.

Average changes in bonds and angles at different temperatures (PDF)

## ■ AUTHOR INFORMATION

### Corresponding Authors
*E-mail: sullah@fisica.ufjf.br (S.U.).
*E-mail: pablod@fq.edu.uy (P.A.D.).
### ORCID ⓘ
Saif Ullah: 0000-0001-8836-9862
Pablo A. Denis: 0000-0003-3739-5061

## ■ REFERENCES

(1) Novoselov, K. S.; Geim, A. K.; Morozov, S. V.; Jiang, D.; Zhang, Y.; Dubonos, S. V.; Grigorieva, I. V.; Firsov, A. A. Electric Field Effect in Atomically Thin Carbon Films. *Science* **2004**, *306*, 666−669.

(2) Dikin, D. A.; Stankovich, S.; Zimney, E. J.; Piner, R. D.; Dommett, G. H. B.; Evmenenko, G.; Nguyen, S. T.; Ruoff, R. S. Preparation and characterization of graphene oxide paper. *Nature* **2007**, *448*, 457−460.

(3) Elias, D. C.; Nair, R. R.; Mohiuddin, T. M. G.; Morozov, S. V.; Blake, P.; Halsall, M. P.; Ferrari, A. C.; Boukhvalov, D. W.; Katsnelson, M. I.; Geim, A. K.; Novoselov, K. S. Control of graphene's properties by reversible hydrogenation: evidence for graphane. *Science* **2009**, *323*, 610−613.

(4) Withers, F.; Dubois, M.; Savchenko, A. K. Electron properties of fluorinated single-layer graphene transistors. *Phys. Rev. B: Condens. Matter Mater. Phys.* **2010**, *82*, 073403.

(5) Nair, R. R.; Ren, W.; Jalil, R.; Riaz, I.; Kravets, V. G.; Britnell, L.; Blake, P.; Schedin, F.; Mayorov, A. S.; Yuan, S.; Katsnelson, M. I.; Cheng, H.-M.; Strupinski, W.; Bulusheva, L. G.; Okotrub, A. V.; Grigorieva, I. V.; Grigorenko, A. N.; Novoselov, K. S.; Geim, A. K. Fluorographene: a two-dimensional counterpart of Teflon. *Small* **2010**, *6*, 2877−2884.

(6) Sluiter, M. H. F.; Kawazoe, Y. Cluster expansion method for adsorption: Application to hydrogen chemisorption on graphene. *Phys. Rev. B: Condens. Matter Mater. Phys.* **2003**, *68*, 085410.

(7) Sofo, J. O.; Chaudhari, A. S.; Barber, G. D. Graphane: A two-dimensional hydrocarbon. *Phys. Rev. B: Condens. Matter Mater. Phys.* **2007**, *75*, 153401.

(8) Denis, P. A.; Iribarne, F. On the hydrogen addition to graphene. *J. Mol. Struct.: THEOCHEM* **2009**, *907*, 93−103.

(9) Denis, P. A. Density functional investigation of thioepoxidated and thiolated graphene. *J. Phys. Chem. C* **2009**, *113*, 5612−5619.

(10) Charlier, J.-C.; Gonze, X.; Michenaud, J.-P. First-principles study of graphite monofluoride (CF) n. *Phys. Rev. B: Condens. Matter Mater. Phys.* **1993**, *47*, 16162−16168.

(11) Leenaerts, O.; Peelaers, H.; Hernández-Nieves, A.; Partoens, B.; Peeters, F.M. First-principles investigation of graphene fluoride and graphane. *Phys. Rev. B: Condens. Matter Mater. Phys.* **2010**, *82*, 195436.

(12) Cheng, S.-H.; Zou, K.; Okino, F.; Gutierrez, H. R.; Gupta, A.; Shen, N.; Eklund, P. C.; Sofo, J. O.; Zhu, J. Reversible fluorination of graphene: Evidence of a two-dimensional wide bandgap semiconductor. *Phys. Rev. B: Condens. Matter Mater. Phys.* **2010**, *81*, 205435.

(13) Kuklin, A. V.; Baryshnikov, G. V.; Minaev, B. F.; Ignatova, N.; Ågren, H. Strong Topological States and High Charge Carrier Mobility in Tetraoxa[8]circulene Nanosheets. *J. Phys. Chem. C* **2018**, *122*, 22216−22222.

(14) Baryshnikov, G. V.; Minaev, B. F.; Karaush, N. N.; Minaeva, V. A. Design of nanoscaled materials based on tetraoxa[8]circulene. *Phys. Chem. Chem. Phys.* **2014**, *16*, 6555−6559.

(15) Baryshnikov, G. V.; Minaev, B. F.; Karaush, N. N.; Minaeva, V. A. The art of the possible: computational design of the 1D and 2D

materials based on the tetraoxa[8]circulene monomer. *RSC Adv.* **2014**, *4*, 25843−25851.

(16) Karaush, N. N.; Baryshnikov, G. V.; Minaev, B. F. DFT characterization of a new possible graphene allotrope. *Chem. Phys. Lett.* **2014**, *612*, 229−233.

(17) Zhang, R.-W.; Zhang, C.-W.; Ji, W.-X.; Li, S.-S.; Hu, S.-J.; Yan, S.-S.; Li, P.; Wang, P.-J.; Li, F. Ethynyl-functionalized stanene film: a promising candidate as large-gap quantum spin Hall insulator. *New J. Phys.* **2015**, *17*, 083036.

(18) Zhang, M.-h.; Zhang, C.-w.; Wang, P.-j.; Li, S.-s. Prediction of high-temperature Chern insulator with half-metallic edge states in asymmetry-functionalized stanene. *Nanoscale* **2018**, *10*, 20226−20233.

(19) Zhang, S.-J.; Zhang, C.-W.; Zhang, S.-F.; Ji, W.-X.; Li, P.; Wang, P.-J.; Yan, S.-S. Intrinsic Dirac half-metal and quantum anomalous Hall phase in a hexagonal metal-oxide lattice. *Phys. Rev. B: Condens. Matter Mater. Phys.* **2017**, *96*, 205433.

(20) Zhao, H.; Zhang, C.-w.; Ji, W.-x.; Zhang, R.-w.; Li, S.-s.; Yan, S.-s.; Zhang, B.-m.; Li, P.; Wang, P.-j. Unexpected Giant-Gap Quantum Spin Hall Insulator in Chemically Decorated Plumbene Monolayer. *Sci. Rep.* **2016**, *6*, 20152.

(21) Wang, Y.-p.; Ji, W.-x.; Zhang, C.-w.; Li, P.; Zhang, S.-f.; Wang, P.-j.; Li, S.-s.; Yan, S.-s. Two-dimensional arsenene oxide: A realistic large-gap quantum spin Hall insulator. *Appl. Phys. Lett.* **2017**, *110*, 213101.

(22) Zhang, C.-w.; Yan, S.-s. First-Principles Study of Ferromagnetism in Two-Dimensional Silicene with Hydrogenation. *J. Phys. Chem. C* **2012**, *116*, 4163−4166.

(23) Denis, P. A. Stacked functionalized silicene: a powerful system to adjust the electronic structure of silicene. *Phys. Chem. Chem. Phys.* **2015**, *17*, 5393−5402.

(24) Şahin, H.; Cahangirov, S.; Topsakal, M.; Bekaroglu, E.; Akturk, E.; Senger, R. T.; Ciraci, S. Monolayer honeycomb structures of group-IV elements and III-V binary compounds: First-principles calculations. *Phys. Rev. B: Condens. Matter Mater. Phys.* **2009**, *80*, 155453.

(25) Kim, K. K.; Hsu, A.; Jia, X.; Kim, S. M.; Shi, Y.; Hofmann, M.; Nezich, D.; Rodriguez-Nieva, J. F.; Dresselhaus, M.; Palacios, T.; Kong, J. Synthesis of monolayer hexagonal boron nitride on Cu foil using chemical vapor deposition. *Nano Lett.* **2011**, *12*, 161−166.

(26) Watanabe, K.; Taniguchi, T.; Kanda, H. Direct-bandgap properties and evidence for ultraviolet lasing of hexagonal boron nitride single crystal. *Nat. Mater.* **2004**, *3*, 404−409.

(27) Alem, N.; Erni, R.; Kisielowski, C.; Rossell, M. D.; Gannett, W.; Zettl, A. Atomically thin hexagonal boron nitride probed by ultrahigh-resolution transmission electron microscopy. *Phys. Rev. B: Condens. Matter Mater. Phys.* **2009**, *80*, 155425.

(28) Denis, P. A.; Iribarne, F. New Approach to Accomplish the Covalent Functionalization of Boron Nitride Nanosheets: Cyclo-addition Reactions. *J. Phys. Chem. C* **2018**, *122*, 18583−18587.

(29) Kim, K. K.; Hsu, A.; Jia, X.; Kim, S. M.; Shi, Y.; Hofmann, M.; Nezich, D.; Rodriguez-Nieva, J. F.; Dresselhaus, M.; Palacios, T.; Kong, J. Synthesis of Monolayer Hexagonal Boron Nitride on Cu Foil Using Chemical Vapor Deposition. *Nano Lett.* **2012**, *12*, 161−166.

(30) Dean, C. R.; Young, A. F.; Meric, I.; Lee, C.; Wang, L.; Sorgenfrei, S.; Watanabe, K.; Taniguchi, T.; Kim, P.; Shepard, K. L.; Hone, J. Boron nitride substrates for high-quality graphene electronics. *Nat. Nanotechnol.* **2010**, *5*, 722−726.

(31) Liu, Z.; Gong, Y.; Zhou, W.; Ma, L.; Yu, J.; Idrobo, J. C.; Jung, J.; MacDonald, A. H.; Vajtai, R.; Lou, J.; Ajayan, P. M. Ultrathin high-temperature oxidation-resistant coatings of hexagonal boron nitride. *Nat. Commun.* **2013**, *4*, 2541.

(32) Karaush, N. N.; Bondarchuk, S. V.; Baryshnikov, G. V.; Minaeva, V. A.; Sun, W.-H.; Minaev, B. F. Computational study of the structure, UV-vis absorption spectra and conductivity of biphenylene-based polymers and their boron nitride analogues. *RSC Adv.* **2016**, *6*, 49505−49516.

(33) Çakr, D.; Kecik, D.; Sahin, H.; Durgun, E.; Peeters, F. M. Realization of a p-n junction in a single layer boron-phosphide. *Phys. Chem. Chem. Phys.* **2015**, *17*, 13013−13020.

(34) Zhang, R.-w.; Zhang, C.-w.; Ji, W.-x.; Li, S.-s.; Wang, P.-j.; Hu, S.-j.; Yan, S.-s. Hydrogenated boron arsenide nanosheet: a promising candidate for bipolar magnetic semiconductor. *Appl. Phys. Express* **2015**, *8*, 113001.

(35) Li, S.-s.; Ji, W.-x.; Hu, S.-j.; Zhang, C.-w.; Yan, S.-s. Effect of Amidogen Functionalization on Quantum Spin Hall Effect in Bi/Sb(111) Films. *ACS Appl. Mater. Interfaces* **2017**, *9*, 41443−41453.

(36) Baroni, S.; de Gironcoli, S.; Dal Corso, A.; Giannozzi, P. Phonons and related crystal properties from density-functional perturbation theory. *Rev. Mod. Phys.* **2001**, *73*, 515−562.

(37) Peelaers, H.; Hernández-Nieves, A. D.; Leenaerts, O.; Partoens, B.; Peeters, F. M. Vibrational properties of graphene fluoride and graphane. *Appl. Phys. Lett.* **2011**, *98*, 051914.

(38) Giannozzi, P.; Baroni, S.; Bonini, N.; Calandra, M.; Car, R.; Cavazzoni, C.; Ceresoli, D.; Chiarotti, G. L.; Cococcioni, M.; Dabo, I.; Dal Corso, A.; de Gironcoli, S.; Fabris, S.; Fratesi, G.; Gebauer, R.; Gerstmann, U.; Gougoussis, C.; Kokalj, A.; Lazzeri, M.; Martin-Samos, L.; Marzari, N.; Mauri, F.; Mazzarello, R.; Paolini, S.; Pasquarello, A.; Paulatto, L.; Sbraccia, C.; Scandolo, S.; Sclauzero, G.; Seitsonen, A. P.; Smogunov, A.; Umari, P.; Wentzcovitch, R. M. QUANTUM ESPRESSO: a modular and open-source software project for quantum simulations of materials. *J. Phys.: Condens. Matter* **2009**, *21*, 395502.

(39) Giannozzi, P.; Andreussi, O.; Brumme, T.; Bunau, O.; Buongiorno Nardelli, M.; Calandra, M.; Car, R.; Cavazzoni, C.; Ceresoli, D.; Cococcioni, M.; Colonna, N.; Carnimeo, I.; Dal Corso, A.; de Gironcoli, S.; Delugas, P.; DiStasio, R. A.; Ferretti, A.; Floris, A.; Fratesi, G.; Fugallo, G.; Gebauer, R.; Gerstmann, U.; Giustino, F.; Gorni, T.; Jia, J.; Kawamura, M.; Ko, H.-Y.; Kokalj, A.; Küçükbenli, E.; Lazzeri, M.; Marsili, M.; Marzari, N.; Mauri, F.; Nguyen, N. L.; Nguyen, H.-V.; Otero-de-la-Roza, A.; Paulatto, L.; Poncé, S.; Rocca, D.; Sabatini, R.; Santra, B.; Schlipf, M.; Seitsonen, A. P.; Smogunov, A.; Timrov, I.; Thonhauser, T.; Umari, P.; Vast, N.; Wu, X.; Baroni, S. Advanced capabilities for materials modelling with Quantum ESPRESSO. *J. Phys.: Condens. Matter* **2017**, *29*, 465901.

(40) Soler, J. M.; Artacho, E.; Gale, J. D.; García, A.; Junquera, J.; Ordejón, P.; Sánchez-Portal, D. The SIESTA Method for Ab Initio Order-N Materials Simulation. *J. Phys.: Condens. Matter* **2002**, *14*, 2745−2779.

(41) Ordejón, P.; Artacho, E.; Soler, J. M. Self-consistent order-N Density-functional Calculations for Very Large Systems. *Phys. Rev. B: Condens. Matter Mater. Phys.* **1996**, *53*, R10441−R10444.

(42) Frisch, M. J.; Trucks, G. W.; Schlegel, H. B.; Scuseria, G. E.; Robb, M. A.; Cheeseman, J. R.; Scalmani, G.; Barone, V.; Mennucci, B.; Petersson, G. A.; et al. *Gaussian 09*, Revision D; Gaussian, Inc.: Wallingford CT, 2009.

(43) Blöchl, P. E. Projector augmented-wave method. *Phys. Rev. B: Condens. Matter Mater. Phys.* **1994**, *50*, 17953−17979.

(44) Perdew, J. P.; Burke, K.; Ernzerhof, M. Generalized Gradient Approximation Made Simple. *Phys. Rev. Lett.* **1996**, *77*, 3865−3868.

(45) Grimme, S. Semiempirical GGA-type density functional constructed with a long-range dispersion correction. *J. Comput. Chem.* **2006**, *27*, 1787−1799.

(46) Perdew, J. P.; Ruzsinszky, A.; Csonka, G. I.; Vydrov, O. A.; Scuseria, G. E.; Constantin, L. A.; Zhou, X.; Burke, K. Restoring the density-gradient expansion for exchange in solids and surfaces. *Phys. Rev. Lett.* **2008**, *100*, 136406.

(47) Prandini, G.; Marrazzo, A.; Castelli, I. E.; Mounet, N.; Marzari, N. Precision and efficiency in solid-state pseudopotential calculations. arXiv:1806.05609, **2018**.

(48) Dion, M.; Rydberg, H.; Schröder, E.; Langreth, D. C.; Lundqvist, B. I. Van der Waals density functional for general geometries. *Phys. Rev. Lett.* **2004**, *92*, 246401.

(49) Román-Pérez, G.; Soler, J. M. Efficient Implementation of a van der Waals Density Functional: Application to Double-Wall Carbon Nanotubes. *Phys. Rev. Lett.* **2009**, *103*, 096102.

206

(50) Troullier, N.; Martins, J. L. Efficient Pseudopotentials for Plane-Wave Calculations. *Phys. Rev. B: Condens. Matter Mater. Phys.* **1991**, *43*, 1993−2006.

(51) Zhao, Y.; Truhlar, D. G. A New Local Density Functional for Main-group Thermochemistry, Transition Metal Bonding, Thermochemical Kinetics, and Noncovalent Interactions. *J. Chem. Phys.* **2006**, *125*, 194101.

(52) Heyd, J.; Scuseria, G. E. Assessment and validation of a screened Coulomb hybrid density functional. *J. Chem. Phys.* **2004**, *120*, 7274−7280.

(53) Ullah, S.; Denis, P. A.; Sato, F. Beryllium doped graphene as an efficient anode material for lithium-ion batteries with significantly huge capacity: A DFT study. *Appl. Mater. Today* **2017**, *9*, 333−340.

207

# Theoretical investigation of various aspects of two dimensional holey boroxine, B₃O₃†

Saif Ullah, [iD] *[b] Pablo A. Denis [iD] *[a] and Fernando Sato[b]

By means of first-principles calculations, we study the structural, electronic and mechanical properties of the newly synthesized boron–oxygen holey framework (*Chem. Comm.* 2018, **54**, 3971). It has a planar structure formed by $B_3O_3$ hexagons, which are joined *via* strong covalent boron–boron bonds. The six $B_3O_3$ units are connected with six-fold symmetry exhibiting a large hole with a surface area of 23 Å², which is ideal for the adsorption of alkalis. For neutral alkalis, we found that the adsorption energy of potassium is 14 and 12 kcal mol⁻¹ larger than those determined for sodium and lithium, respectively. In contrast, for alkali cations, there is a clear preference for lithium over sodium and potassium. With regard to its electronic properties, it is an insulator with an electronic band gap of 5.3 eV, at the HSE level of theory. We further investigate the effect of strain on the band gap and find it a less efficient technique to tune the electronic properties. The wide optical gap of $B_3O_3$ can be utilized in ultraviolet (UV) applications, such as UV photodetectors, *etc.* Additionally, the 2D elastic modulus of $B_3O_3$ (53.9 N m⁻¹) is larger than that of $Be_3N_2$, silicene, and germanene. Besides, we also report bilayer and graphite-like bulk $B_3O_3$ and furthermore, find that the optoelectronic properties of the bilayer can be tuned with an external electric field. The great tunability of optical properties from UV to the visible range offers a vast range of applications in optoelectronics.

## 1. Introduction

The preparation of graphene in 2004 opened new research directions in all branches of science.[1] It is difficult to make a full list of the two dimensional (2D) materials available. Without trying to be exhaustive, we can mention the transition metal chalcogenides[2,3] $MoS_2$, $WS_2$, $MoSe_2$, $WSe_2$, $MoTe_2$, the MXenes,[4] which are layered compounds formed by transition metal nitrides or carbides, the p-block based 2D materials like silicene,[5,6] germanene,[7] antimonene,[8] bismuthene,[9] black[10] and blue phosphorene[11] as well as graphdyne[12] and the isoelectronic analog of graphene, boron nitride[13,14] among many others. Upon reading the latter list it is possible to postulate that 2D materials can only exist when their bulk materials are layered. However, it has been shown that it is possible to synthesize an atomic single layer material when the bulk is not layered, being silicene a clear example. Recently, Stredansky *et al.*[15] reported the synthesis of a novel 2D material based on the boronic acid condensation. Using three tetrahydroxyboron ($H_2B_2O_4$) molecules, a six-membered boroxine ring molecule was formed along with three molecules of water. Although the boroxine layers could readily be identified in the STM studies, the authors suggested that further improvements in the synthetic procedure should be made in order to reduce the occurrence of non-six-fold symmetry motifs. Concomitantly, Lin *et al.*[16] proposed a porous boron oxide monolayer with a robust band gap, which is similar to the one synthesized by Stredansky *et al.*[15] They showed that boroxine is perfectly planar with uniform pores with a 6.27 Å diameter and exhibit an indirect wide band gap with the possible applications in optoelectronics This work is the extension to the previous predicted (theoretical) and synthesized (experimentally) boroxine by exploring the microscopic science and including new interesting capabilities such as the high affinity for alkalis and the study of bilayer boroxine as well as the bulk layered material. As by-product, we have found a minor discrepancy in the electronic structure of boroxine. In effect, our HSEH1PBE calculations indicated that the gap is direct, in contrast with the results reported by Lin *et al.*[16] In the text, the only "$B_3O_3$" will refer to the monolayer $B_3O_3$ unless it is followed by "ring" or "hexagon".

## 2. Methods

We study boroxine ($B_3O_3$) by means of spin-polarized vdW-DF,[17] M06-L,[18] and HSEH1PBE[19] density functional theory (DFT) calculation. We use SIESTA[20,21] code to perform vdW-DF calculations. We select the double-zeta basis set with polarization

*[a]Computational Nanotechnology, DETEMA, Facultad de Química, UDELAR, CC 1157, 11800 Montevideo, Uruguay. E-mail: pablod@fq.edu.uy*

*[b]Departamento de Física, Instituto de Ciências Exatas, Campus Universitário, Universidade Federal de Juiz de Fora, Juiz de Fora, MG 36036-900, Brazil. Fax: +55 589229241906; Tel: +55 59899714280*

† Electronic supplementary information (ESI) available. See DOI: 10.1039/c9ra07338h

209

functions and fixed the orbital confining cut-off to 0.01 Ry with the default value (0.15) of split-norm. The interaction between ionic cores and valence electrons is described by the Troullier–Martins norm-conserving (NC) pseudopotentials.[22] Geometry optimizations were carried out using the conjugate gradient algorithm until all the residual forces were smaller than 0.01 eV Å$^{-1}$. The unit cells were optimized and they were sampled using a $50 \times 50 \times 1$ (about 900 $k$-points gamma centered) Monkhorst–Pack sampling, the periodic M06-L and HSEH1PBE calculations were carried out with Gaussian 09.[23] The basis set selected were Pople's 6-31G* and 6-311G*.[24] In general, we did not observe significant differences in the results obtained using both basis sets. 1000 $k$-points were used to sample the unit cell and the ultrafine grid was employed. For comparative calculations, we also investigate the adsorption of alkalis employing a boroxine ($B_3O_3$) cluster formed by six $B_3O_3$ units and terminated with hydrogen atoms. In general, the results indicate the same trend as that obtained employing infinite models.

We also perform PBE-D2 (ref. 25) and PBE-D3 (ref. 26) calculations with the help of VASP code.[27] We use generalized gradient approximation (GGA) with the flavor proposed by Perdew, Burke, and Ernzerhof (PBE)[28,29] assisted with the projector augmented wave (PAW).[30]

Finally, we also use a hybrid functional (not in a true sense) which is a mixture of LDA-GGA[28,29,31] as implemented in SIESTA, especially for the calculation of in-plane elastic modulus to compare our results with our previous work on graphene and Be$_3$N$_2$.[32] The details are in ref. 31. Throughout the manuscript, the hybrid is referring to the aforementioned method. Finally, we also report *ab initio* molecular dynamics (AIMD) simulations at 300–600 K with the aid of SIESTA code. Further details regarding the computational methods can be seen in the ESI.†

# 3. Results and discussion

### 3.1 Structural properties of 2D boroxine

As suggested by the experimental study[15] and the theoretical study by Lin *et al.*,[16] we find that 2D boroxine can adopt six-fold symmetry. The unit cell employed in our calculations is shown in Fig. 1.

The six-fold symmetry structure is obtained by joining the B$_3$O$_3$ hexagons obtained after the condensation of three tetra-hydrodiboron molecules. The B–B bonds are 1.71–1.72 Å long, a value which is bracketed by the B1–B1 and B1–B2 bond distances found in *Pmmn* borophene, namely, 1.613 and 1.879 Å, respectively, which are in excellent agreement with the PBE results previously reported.[16] The B–O bond length 1.38–1.39 Å is among the highest values of which B–O can adopt in molecular forms. As suggested by Coulson,[32] this may indicate a moderate to weak participation of the π orbitals of boron and oxygen. A fact that seems to be corroborated by the partial density of states presented in Fig. 2. When the six B$_3$O$_3$ molecules are joined, they leave a hole in which the distance between the opposite O atoms is 6.21–6.28 Å (depending on the level of theory) and the surface is close to 23 Å$^2$, ideal for the adsorption of large atoms or molecules, as observed for crown ethers. For example, the 18-crown-6 ether has a high affinity for the

hydronium ion H$_3$O$^+$. In addition to this, it allows the dissolution of KMnO$_4$ in benzene thanks to the complexation of the potassium ion. We show in Section 3.8 that 2D boroxine has also a strong affinity towards alkalis, especially to potassium.

To report the structural stability, we calculate the formation energy and since we use the atomic form of B and O as the chemical potential, the formation energy here is equal to the cohesive energy. We make use of the following expression: $E_{\text{coh}} = \dfrac{E_{B_3O_3} - 6E_B - 6E_O}{12}$, where $E_{B_3O_3}$ is the total energy of the unit cell containing 6B and 6O atoms. $E_B$ and $E_O$ are taken as the gas-phase energies of B and O, respectively. The cohesive energy of B$_3$O$_3$ PBE-D3 level is −6.72 eV per atom, just 0.04 lower than the value reported by Lin *et al.*[16] For the comparison, the cohesive energy of graphene at the same level of theory is −8.07 eV per atom. This means that B$_3$O$_3$ has a comparable strength to that of graphene. At the M06-L level, the cohesive energy of B$_3$O$_3$ −6.3 eV per atom which is twice the value calculated for phosphorene (−3.1 eV per atom) at the same level. Further information is given in ESI.† The data regarding structural properties and stability at various levels of theory is shown in Table S1.†

### 3.2 Dynamical stability

In the experiment, 2D boroxine (B$_3$O$_3$) was grown on Au (111) surface and, therefore, it is necessary to check the dynamical stability of free-standing boroxine (B$_3$O$_3$). To that end, we calculate phonon spectrum by supercell approach as implemented in SIESTA code along the G–M–K–G high symmetry points. We use a $2 \times 2 \times 1$ supercell to calculate the phonon band spectrum, whereas, a $1 \times 1 \times 1$ cell also give converged result, keeping in mind that the unit cell size is already large enough. The phonon spectrum graph is shown in Fig. 2 where it is clear that 2D boroxine is certainly a local minimum in the potential energy surface due to the absence of any negative frequency. The highest frequency of B$_3$O$_3$ is ∼1450 cm$^{-1}$.

### 3.3 Electronic properties

The electronic properties of 2D boroxine are predicted by calculating the electronic band structure and for additional comprehension, the orbital projected density of states (PDOS) is also computed. With SIESTA (both the levels employed), 2D boroxine (B$_3$O$_3$) is a wide and indirect band gap material with conduction band minima (CBM) lie at M point, while valence band maxima (VBM) at gamma point. However, the energy difference between gamma and M points is quite low (55 meV). This indirect gap nature is also confirmed by VASP code with a slight disagreement as the CBM appears at the $K$ point which is in line with the previous findings by Lin *et al.*[16] The calculated value of band gap, at vdW-DF level is 3.80 eV. However, the M06-L level of theory revealed a direct gap with a value of 3.9 eV. As expected, the band gap was significantly underestimated by the vdW-DF method and also by the M06-L functional. In effect, HSEH1PBE calculations indicated that the band gap of boroxine is direct, namely 5.30 eV which is a bit higher than the previously reported value of 5.23 eV. The latter value is smaller than
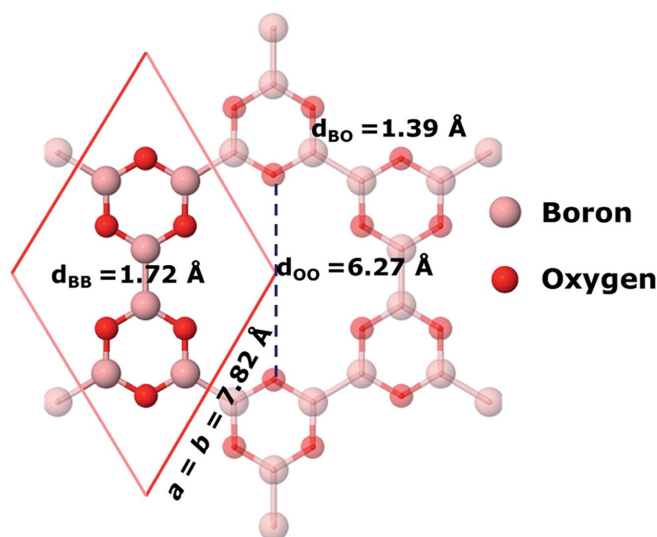
**Fig. 1** The unit cell and bond lengths of 2D boroxine (B₃O₃) at PBE-D3 level of theory. Periodically repeated atoms are made translucent.
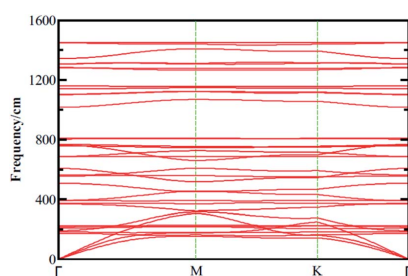


**Fig. 2** Phonon dispersion curves calculated for boroxine (B₃O₃) calculated at vdW-DF/DZP level of theory with SIESTA code.

the gap computed for boron nitride at the HSEH1PBE level, namely, 6.1 eV. Moreover, B₃O₃ bears the same direct-indirect band gap controversy as that of boron nitride.

From the PDOS, the CBM has a $\pi$ character and mostly composed of B-p$_z$ with a slight involvement from O-p$_z$. However, the O-p$_{(x+y)}$ strongly hybridized with B-p$_{(x+y)}$ to form the VBM and, therefore, has a $\sigma$-like character. Furthermore, the valence and conduction bands are mostly governed by O and B, respectively. Additionally, this outcome also reflects in LDOS plots shown in Fig. 3 where the density around O atoms can be seen in VB case, whereas, for CB, the density can be spotted around B and O with a larger LDOS amplitude on B in comparison with O. Besides, we also check the effect of strain on the electronic structure of B₃O₃ and find that it is a less efficient technique to alter the electronic properties. The band structures are given in Fig. S1 in ESI.†

## 3.4 Chemical analysis and bonding character

We calculate the charge transfer with the help of various charge transfer mechanisms namely Hirshfeld and Voronoi as in SIESTA, Mulliken as in Gaussian, and Bader as in VASP. Each of these methods reveals qualitatively the same results of charge transfer from B to O as in the spirit of their electronegativity values. The total charge density calculated at PBE-D3 level is plotted in Fig. 4(a), where charge accumulation on O atoms can be seen quite vividly. The quantitative results are given in Table S1.† Furthermore, to picture the electron localization in B₃O₃, we calculate electron localization function (ELF) which is quite useful in predicting the bonding character, as well as the stability mechanism. The details regarding the interpretation of ELF plots can be seen in ref. 31 and 33. In B₃O₃ rings, we see electron localization on O atoms broadens towards B atoms and a complete charge delocalization in the vicinity of B atoms. This is in perfect agreement with the previous experimental + DFT study on B₃O₃ rings held together by phenyl molecules where the authors reported the ultra-fast charge delocalization with the charge localization on O atoms[34] Such an analysis, however, is absent for phenyl-free B₃O₃ rings which are bonded *via* B atoms. Consequently, the ELF becomes crucial and much more meaningful. Interestingly, we find a strong charge localization between B–B atoms, the region between two B₃O₃ rings. This indicates that the B₃O₃ rings are held together by strong covalent bonds with the ionic bonds (by virtue of charge transfer) present between B–O. This strong covalent bond might be responsible for the stability of B₃O₃ monolayer consisting of B₃O₃ rings. Moreover, we also calculate simulated scanning tunneling microscopy (STM) image (based on Tersoff–Hamann
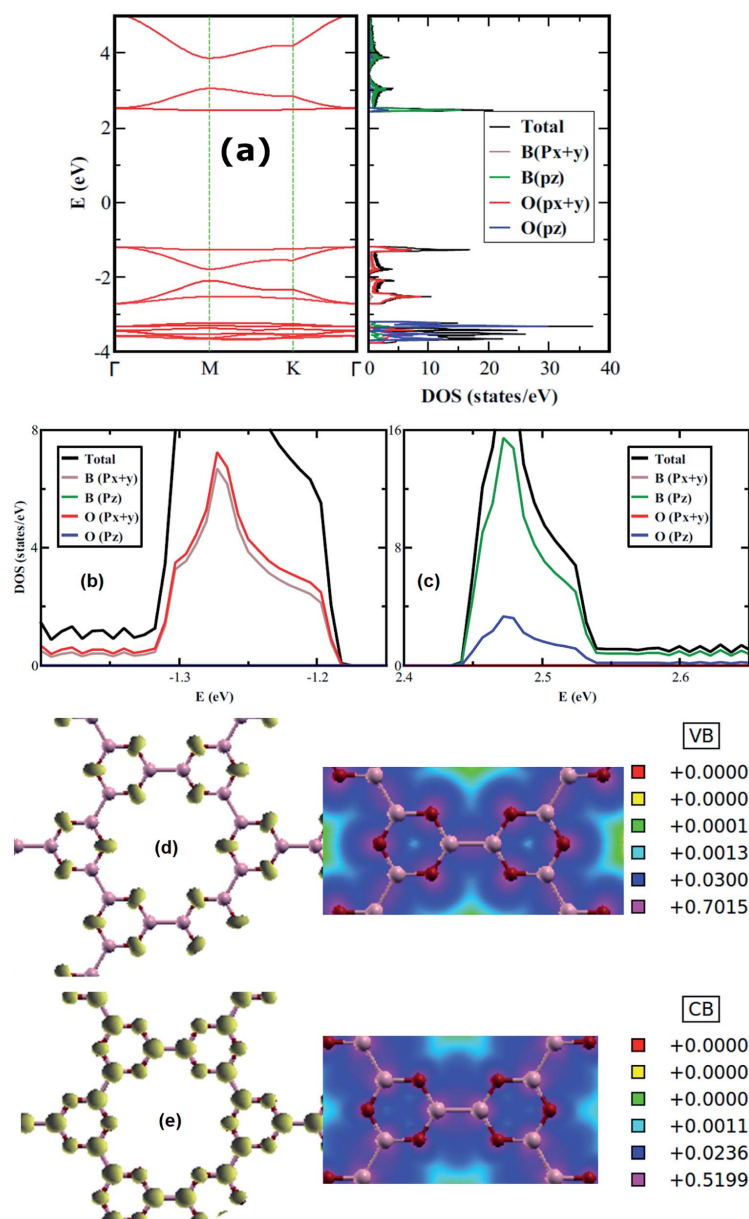
**Fig. 3** Electronic band structure along with (total and projected) density of states (a); projected density of states near the (b) valence band maximum and (c) the conduction band minimum; 3D plots along with their 2D cuts of LDOS of filled (d) and empty states (e) of boroxine calculated at the hybrid level of theory.
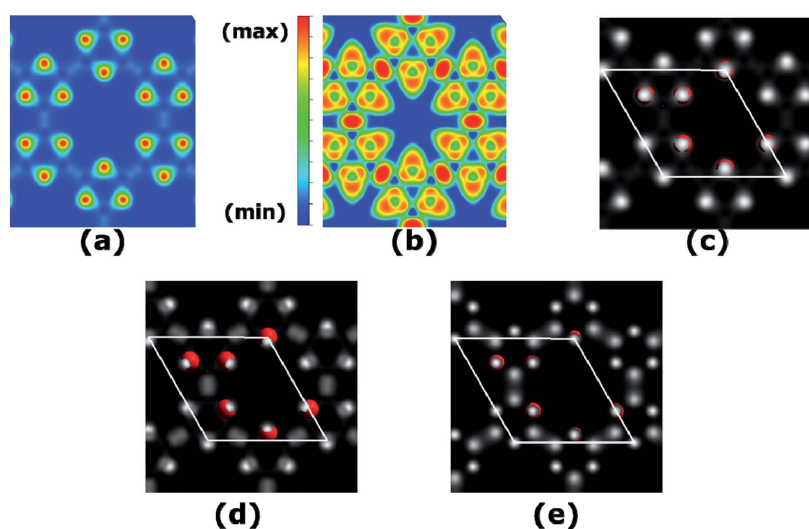
212

**Fig. 4** (a) Total charge density, (b) ELF, where red means strong electron localization and blue means the opposite, whereas, the green represents a region with a homogenous electron density, (c) STM image of $B_3O_3$, (d) STM image of filled and (e) empty states.

approximations)[35] of $B_3O_3$ monolayer which is given in (c) and is in agreement with the experimental result. O atoms in the unit cell are shown for the sake of brevity. In addition, we also calculate STM images of the filled and empty states which are in agreement with the PDOS (and LDOS) calculations.

**3.5 Kinetic stability**

We also test boroxine with high temperatures (300 and 600 K) to see the response. The initial and final structures treated at 600 K are shown in Fig. 5. The negligible structural modifications suggest that $B_3O_3$ is quite stable at high temperatures. This point has already been proved experimentally. In addition, we also calculate the average change appeared in the B–O and B–B

bond lengths at a temperature of 600 K. We find a slight variation of 0.986% and 0.602% in B–O and B–B bonds, respectively. That being said, boroxine can be used in high temperatures environment, such as space, aircraft, oil, and gas research applications.[36] Nevertheless, it will be interesting to see the highest temperature range that $B_3O_3$ can withstand and, therefore, propose a separate investigation to find the melting point of $B_3O_3$.

**3.6 Mechanical properties**

In Fig. 6, we present the stress curve employed to calculate the in-plane elastic modulus ($Y_{2D}$) of 2D boroxine. We vary the lattice constant in small steps and observe the energy change as
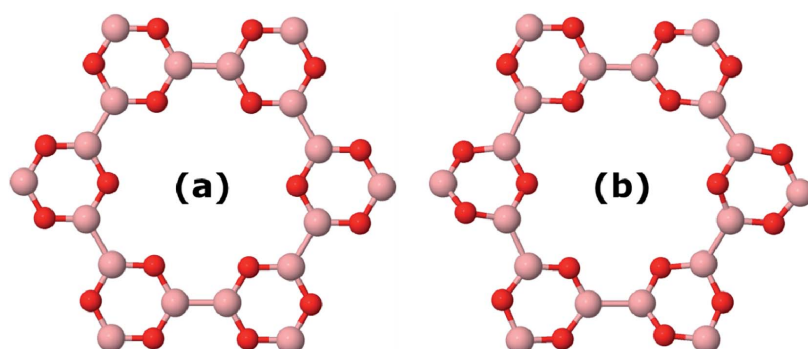


**Fig. 5** Snapshots of the results of AIMD of boroxine at (a) 0 K, and (b) 600 K. The negligible distortion in the structure reflects its robustness.
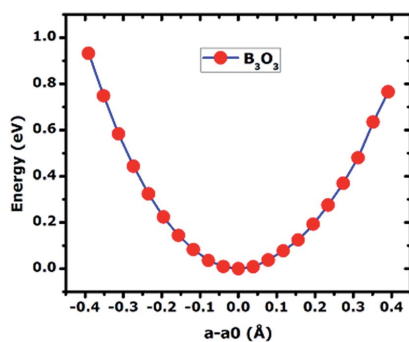
**Fig. 6** The curve of total energy (in eV) *vs.* change in lattice constant (in Å) calculated of 2D $B_3O_3$ at the hybrid level of theory. The in-plane stiffness is calculated by taking the second derivative at the minimum.
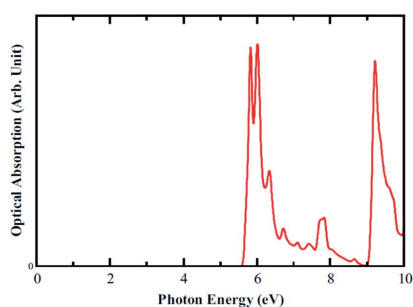


**Fig. 7** Optical Absorption spectra calculated for $B_3O_3$, at the hybrid level of theory.

**Table 1** Adsorption energies for lithium, sodium, and potassium at the M06-L/6-31G* level of theory

|        | Infinite boroxine | $(B_3O_3)_6H_6$ flake |
|--------|-------------------|------------------------|
| Li     | −52.0             | −55.2                  |
| Na     | −50.6             | −54.2                  |
| K      | −64.1             | −67.8                  |
| Li$^+$ |                   | −60.7                  |
| Na$^+$ |                   | −51.63                 |
| K$^+$  |                   | −47.3                  |

a function of lattice parameter. The second derivative from the plot gives the $Y_{2D}$ and is given by: $Y_{2D} = A_0 \frac{\partial^2 E}{\partial A^2}\Big|_{A_0} = \frac{\sqrt{3}}{6} \frac{\partial^2 E}{\partial a^2}\Big|_{a_0}$, $A = \frac{\sqrt{3}a^2}{6}$, represents the 2D area of $B_3O_3$ and $a$ is the lattice constant. At the hybrid level, the 2D bulk modulus of $B_3O_3$ is 53.9 N m$^{-1}$, about 17.93 N m$^{-1}$ smaller than the values reported by Lin *et al.*[16] The latter values are significantly smaller than the one determined for graphene

(206 N m$^{-1}$) in our earlier study at the same level of theory.[31] The earlier reported value of $Y_{2D}$ of graphene (206.6 N m$^{-1}$), hBN (177 N m$^{-1}$), SiC (116.5 N m$^{-1}$), and GeC (101 N m$^{-1}$) are higher than that of $B_3O_3$. However, this value is slightly higher than that of $Be_3N_2$ (46.5 N m$^{-1}$),[31] silicene (44.5 N m$^{-1}$), and germanene (29.6 N m$^{-1}$).[37]

### 3.7 Optical properties

Optical absorption spectra are also calculated for parallel polarization without taking into account the excitonic effect. The onset of optical absorption, which is the optical gap, appears around 5.7 eV as can be seen in Fig. 7. This value is sufficiently larger than the electronic band gap of 3.66 eV, meaning that the optical transition from first valence to first conduction band is forbidden as per dipole selection rules. This can be understood by looking at the orbital character shown in PDOS plot. The first transition occurs from the blue peak to the green peak ($p_z$–$p_z$). Moreover, the separation between these two pi bands is around 5.7 eV, thus agreeing well the optical gap. Additionally, the optical gap is in the deep UV range.

### 3.8 Adsorption of alkalis

As expressed in the first section, based on the chemistry displayed by the 18-crown-6 ether, we expect a strong affinity of 2D boroxine towards potassium. In Table 1, we list the adsorption energies computed for lithium, sodium, and potassium using finite and infinite models. The calculations were performed at the M06-L/6-31G* level of theory and we used a larger unit cell composed of six $B_3O_3$ rings so that the unit cell contains a complete hole (as shown in Fig. 1, but including the translucent atoms). The adsorption energies of lithium, sodium, and potassium on the hexagonal hole of boroxine are −52.0, −50.6 and −64.1 kcal mol$^{-1}$, respectively. Large differences, which may indicate that it is possible to separate selectively adsorb the latter alkali. However, for the adsorption of cations, the situation is reversed and lithium becomes clearly favored. In addition to this, it will also be interesting to integrate a metal atom in the hole of $B_3O_3$ and utilize it as a $B_3O_3$-supported metal single-atom catalyst, just like $C_2N$.[38,39] With regard to the electronic properties, in Fig. 8 we present the band structure and total and projected density of states for boroxine with a potassium atom adsorbed in the hole. The band gap determined for boroxine with a Li, Na and K atoms adsorbed in the hole are: 0.16/3.86, 0.03/3.79 and 0.08/3.93 eV, respectively, at the M06-L/ 6-31G* level of theory (spin-up/spin-down notation). Thus, alkali atom adsorption dramatically changes the gap for one spin channel while the other is minimally affected. Therefore, it may be possible to attain selective pins polarized transport using these elements.

### 3.9 Bilayer boroxine

We also calculate $B_3O_3$ bilayers in AA, AB, and AB2 stacking as shown in Fig. 9. In AA stacking, the interlayer distance is about 3.57 Å. In AB stacking, the second layer is translated about 1.39 Å (the B–O bond length) along the *x*-axis, whereas, in AB2 stacking, this translation is about 2.78 Å (the next neighboring
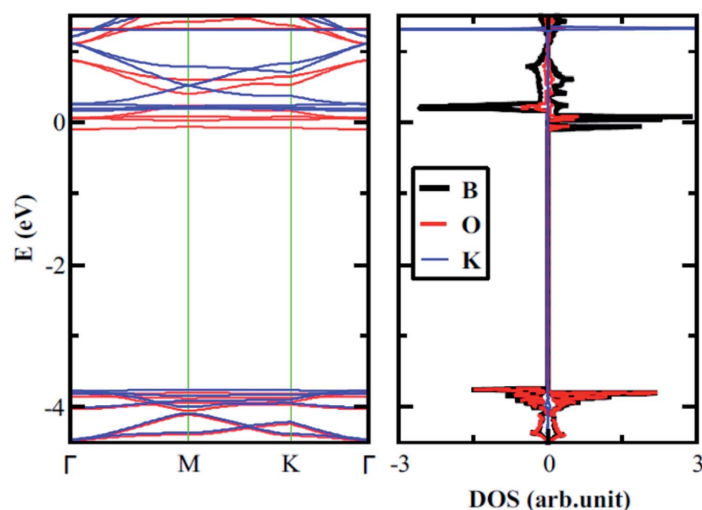
**Fig. 8** Band structure and density of states determined for boroxine with a potassium atom adsorbed in the central hole, at the VDW-DF/DZP level of theory.

B–O bond length) at PBE-D3 level. The interlayer separation in AB ($h_1 = 3.18$, $h_2 = 3.3$ Å) is larger than that of AB2 ($h_1 = 3.02$, $h_2 = 3.28$ Å). Here, $h_1$ is the interlayer separation between B–O (or O–B), whereas, $h_2$ refers to the separation between B–B (O–O) in AB (AB2) bilayer. We show the periodic structures of these bilayers in Fig. S2 bilayer in ESI.† For comparison, the interlayer

distance in bilayer graphene at PBE-D3 level is 3.33 Å, which is larger than that of AB2 stacking. Furthermore, the interlayer separation has a direct impact on the stability of the bilayers, AB2 being the most favorable, whereas, AA is the least. We also calculate the interlayer interaction energy (IIE) as:

$$IIE = \frac{2E_1 - E_{tot}}{N},$$ where $E_1$ and $E_{tot}$ are the energies of
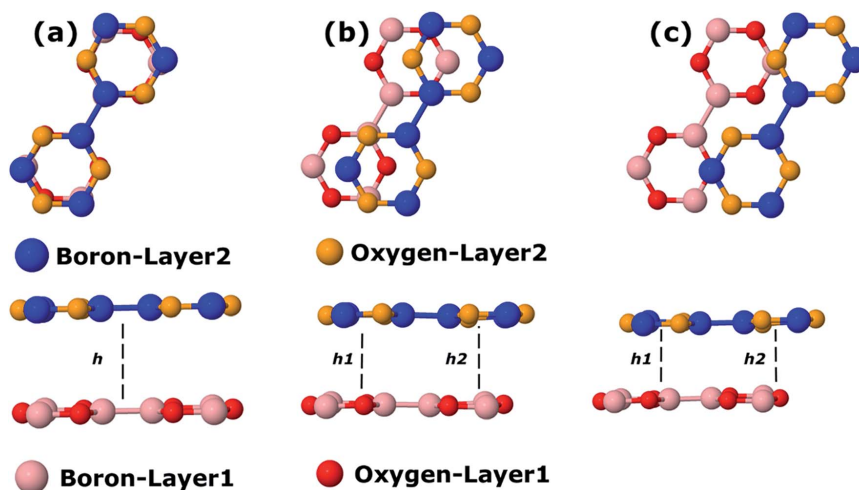


**Fig. 9** Top and side view bilayer B3O3 with (a) AA, (b) AB, and (c) AB2 stacking. In the AA pattern, $h$ represents the interlayer distance. In the other two stackings, $h_1$ and $h_2$ correspond to the separation between B–O (O–B) and B–B (O–B), respectively.

**Table 2** Relative energy (in meV), interlayer interaction energy (IIE) (in meV per atom), exfoliation energy ($E_{exf}$) (in meV Å$^{-2}$), and interlayer separation at PBE–D3 level in $B_3O_3$ patterns. The $h$ represents interlayer distance in the AA pattern, whereas, $h_1/h_2$ represents B–O/B–B (or O–O) separation in different layers of other patterns

|  | Relative energy (meV) | IIE (meV per atom) | $E_{exf}$ (meV Å$^{-2}$) | Interlayer separation, $h$, $h_1/h_2$ (Å) |
|---|---|---|---|---|
| $B_3O_3$ | 743.71 |  |  |  |
| AA-bilayer | 589 | 6.45 |  | 3.57 |
| AB-bilayer | 443 | 12.5 |  | 3.18/3.3 |
| AB2-bilayer | 358 | 16.05 |  | 3.02/3.28 |
| AA-bulk | 447 | 12.4 | 2.8 | 3.48 |
| AB-bulk | 150 | 24.7 | 5.6 | 3.15/3.15 |
| AB2-bulk | 0 | 31 | 7 | 3.09/3.11 |
| Graphene-bilayer |  | 24 |  | 3.33 |
| Graphite |  | 52.7 | 20 | 3.34 |

monolayer and bilayer, respectively. In addition, we compare the outcome with bilayer graphene. Interestingly, we find that IIE in AB2 stacking is comparable to that of bilayer graphene. Table 2 is decorated with relevant data at the PBE-D3 level. The results obtained using other methods are gathered in Table S2.† The electronic band structures are given in Fig. 10. Furthermore, the bilayer gaps are found to be lower than that of the single layer.

We also consider the effect of an external electric field on the electronic structure of AB2 stacked bilayer $B_3O_3$. We keep on increasing the field until we reach a limit where the gap becomes zero. The band structure plots are shown in Fig. S3 in ESI† and the band gap values as a function of the increasing field are shown in Fig. 11. We divide the plot into three parts where green, orange, and red colors represent reasonably-high, very-high, and extremely-high external electric field range. It is not known how much external electric field can be applied to
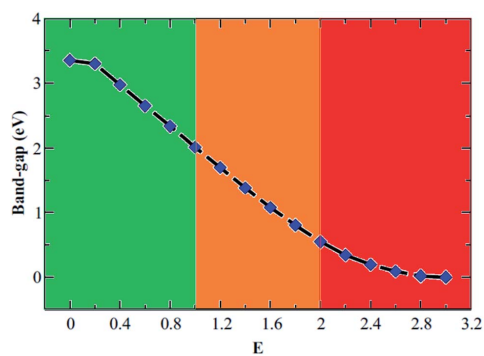


**Fig. 11** Band gap (in eV) variation as a function of external electric field (in V Å$^{-1}$) for AB2 stacked bilayer boroxine.
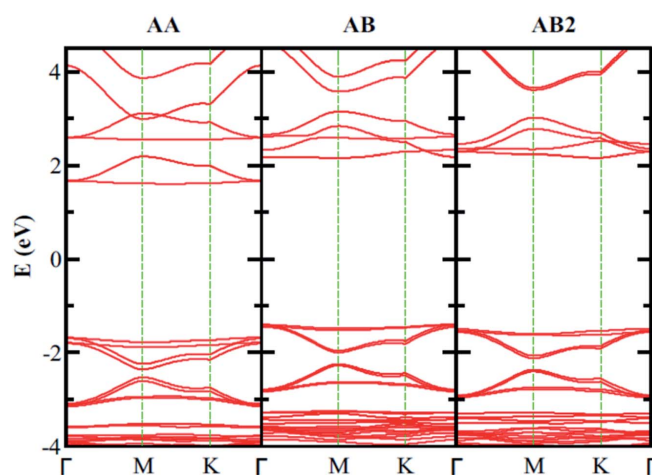


**Fig. 10** Electronic band structure of bilayer $B_3O_3$ with different stacking at vdW-DF level. The band gaps in AA, AB, and AB2 stacking are 3.28 eV, 3.56, and 3.65 eV, respectively, at the vdW-DF level.
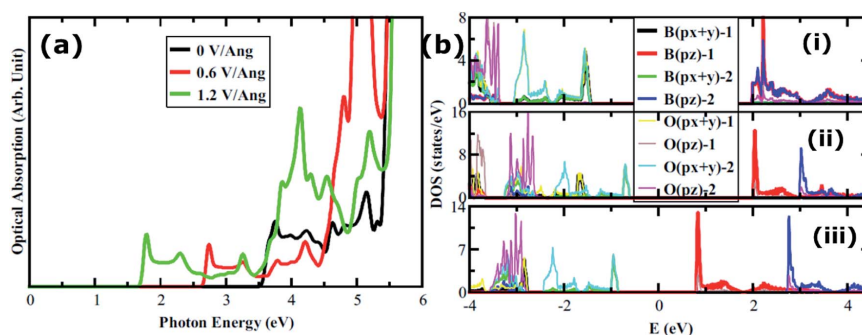
Fig. 12 (a) Optical absorption spectra of AB2 bilayer at various values of the external electric field. (b) Layer-resolved PDOS of AB2 bilayer (i) at 0, (ii) 0.6, and (iii) 1.2 V Å$^{-1}$.

$B_3O_3$ until it reaches its breakdown region. However, this study can motivate both theoreticians and experimentalists to initiate such an investigation. Moreover, it can be noted that the external electric field can significantly alter the electronic properties. The gap reaches a value of 1.7 eV at a field of 1.2 V Å$^{-1}$ from 3.47 eV (at 0 V Å$^{-1}$). In addition to this, we also calculate the optical properties of AB2 bilayer with and without the external electric field. Here, we consider the structure at 0, 0.6, and 1.2 V Å$^{-1}$ external electric field. The layer-resolved PDOS along with the optical absorption spectra is given in Fig. 12. Unlike the monolayer, it seems that the σ to π transition becomes allowed by the dipole selection rule in bilayer. Furthermore, there induce some extra peaks which seem to be coming from the transition between the broad B–O-σ band and the narrow B–O-π band. Most interestingly, these peaks correspond to interlayer transition and, furthermore, can be tuned

right in the visible range. Nevertheless, those intense peaks in the deep UV range also look like the result of an interlayer transition. In photovoltaics, such transitions have an edge over the intralayer ones.[40–44] However, we propose that more accurate calculations, such as GW/BSE are required to confirm these outcomes.

### 3.10 Graphite-like bulk B3O3

Finally, we consider graphite-like $B_3O_3$ in bulk form which is a new phase of $B_3O_3$ at PBE-D3 level. We consider the same patterns as that of the bilayers. From the total energy calculations, it is evident that these patterns are local minima in the total energy surface, again AB2 pattern being the most favorable. The same outcome is confirmed by all the employed levels of theory. In bulk form, they exhibit the same band gaps like
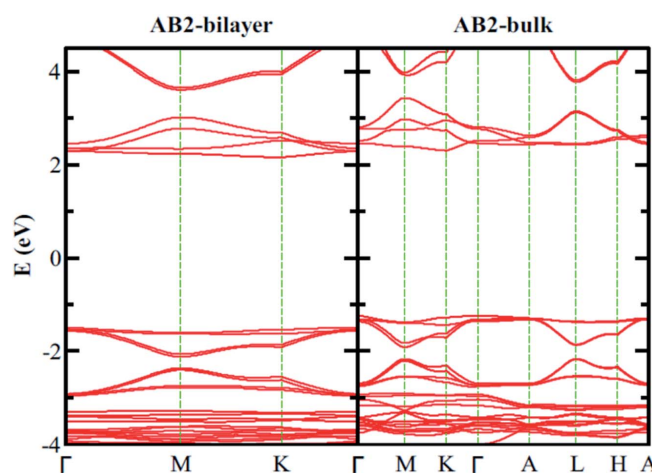


Fig. 13 Comparison of the electronic band structure of AB2 stacking of $B_3O_3$ in bilayer and bulk form at vdW-DF level.
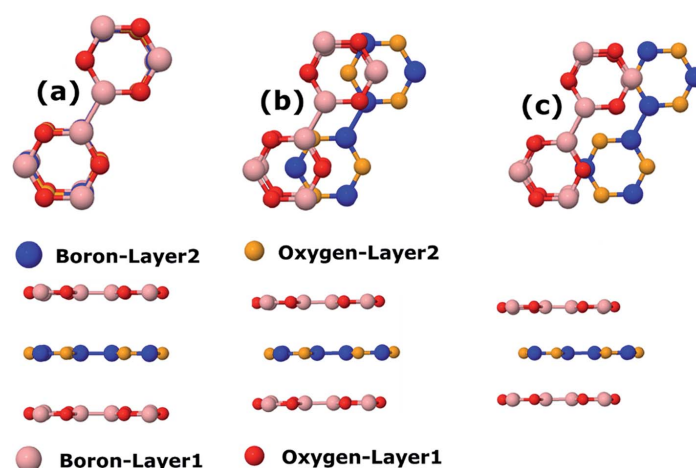
**Fig. 14** Top and side view of (a) AA, (b) AB, and (c) AB2 patterns of $B_3O_3$ in bulk form at PBE–D3 level.

that in the bilayer-form and as a comparison, the bilayer and bulk band structures of AB2 stacking are given in Fig. 13. We also calculate the exfoliation energy as reported elsewhere using the following equation:[31] $E_{exf} = \dfrac{E_{B_3O_3} - E_{g-B_3O_3}}{A_{B_3O_3}}$, where the energy difference between monolayer $B_3O_3$ and graphite-like bulk $B_3O_3$ is divided by the monolayer area. From Table 2, it is evident that $B_3O_3$ in bulk form is not only comparably robust to that of graphite but the monolayer can be exfoliated with a lot ease as well. The geometries are given in Fig. 14.

## 4. Conclusions

We employed first-principles calculations to perform a thorough theoretical characterization of the various aspects of the recently synthesized boroxine $B_3O_3$ monolayer. In agreement with previous theoretical investigations by Lin *et al.*,[16] we found that the structure is perfectly planar formed by $B_3O_3$ hexagons with hexagonal symmetry, joined by a strong covalent bond between BB as reveal by ELF. The six $B_3O_3$ units joined with sixfold symmetry exhibiting a large hole with a surface of 23 $\text{Å}^2$, which is ideal for the adsorption of potassium and the hydronium ion. In effect, we found that boroxine preferentially binds potassium over sodium. In contrast with previous works, we found that the band gap is direct. In effect, HSE calculations indicate that it is an insulator with a direct electronic band gap equal to 5.3 eV. Based on the cohesive energy calculations, $B_3O_3$ monolayer is comparably strong as that of graphene and remains negligibly distorted even at 600 K as from AIMD simulations. The elastic modulus is higher than that of $Be_3N_2$, silicene, and germanene. Besides, we also explore the bilayer and bulk form of $B_3O_3$ and find that those phases are equally robust in comparison to bilayer graphene and graphite. Furthermore, the exfoliation energy calculations suggest that

the exfoliation of monolayer $B_3O_3$ from the bulk phase is quite easier than that of graphene-graphite. In addition, we find a great tenability of the optoelectronic properties in the presence of external electric field. That being said, the optical properties can be tuned from deep UV to the visible range thus offering a vast range of applications in optoelectronics.

## Conflicts of interest

The authors declare no conflicts of interest.

## References

1 K. S. Novoselov, A. K. Geim, S. V. Morozov, D. Jiang, Y. Zhang, S. V. Dubonos, I. V. Grigorieva and A. A. Firsov, *Science*, 2004, **306**, 666–669.

2 Z. Zeng, Z. Yin, X. Huang, H. Li, Q. He, G. Lu, F. Boey and H. Zhang, *Angew. Chem., Int. Ed.*, 2011, **50**, 11093–11097.

3 G. Ye, Y. Gong, J. Lin, B. Li, Y. He, S. T. Pantelides, W. Zhou, R. Vajtai and P. M. Ajayan, *Nano Lett.*, 2016, **16**, 1097–1103.

4 Y. Gogosti and B. Anasori, *ACS Nano*, 2019, **13**, 8491–8494.

5 P. Vogt, P. De Padova, C. Quaresima, J. Avila, E. Frantzeskakis, M. C. Asensio, A. Resta, B. Ealet and G. Le Lay, *Phys. Rev. Lett.*, 2012, **108**, 155501.

6 P. A. Denis, *Phys. Chem. Chem. Phys.*, 2015, **17**, 5393–5402.

7 M. E. Davila, L. Xian, S. Cahangirov, A. Rubio and G. Le Lay, *New J. Phys.*, 2014, **16**, 095002.

8 J. Ji, X. Song, J. Liu, Z. Yan, C. Huo, S. Zhang, M. Su, L. Liao, W. Wang, Z. Ni, Y. Hao and H. Zeng, *Nat. Commun.*, 2016, **7**, 13352.

9 F. Reis, G. Li, L. Dudy, M. Bauernfeind, S. Glass, W. Hanke, R. Thomale, J. Schäfer and R. Claessen, *Science*, 2017, **357**, 287–290.

10 H. Liu, A. T. Neal, Z. Zhu, D. Tomanek and P. D. Ye, *ACS Nano*, 2014, **8**, 4033.

11 Z. Zhu and D. Tomanek, *Phys. Rev. Lett.*, 2012, **112**, 176802.

12 M. Zhang, H. Sun, X. Wang, H. Du, J. He, Y. Long, Y. Zhang and C. Huang, *J. Phys. Chem. C*, 2019, **123**, 5010–5016.

13 J. Wang, F. Ma and M. Sun, *RSC Adv.*, 2017, **7**, 16801–16822.

14 P. A. Denis and F. Iribarne, *J. Phys. Chem. C*, 2018, **122**, 18583–18587.

15 M. Stredansky, A. Sala, T. Fontanot, R. Costantini, C. Africh, G. Comelli, L. Floreano, A. Morgante and A. Cossaro, *Chem. Commun.*, 2018, **54**, 3971.

16 S. Lin, J. Gu, H. Zhang, Y. Wang and Z. Chen, *FlatChem*, 2018, **9**, 27–32.

17 M. Dion, H. Rydberg, E. Schroder, D. C. Langreth and B. I. Lundqvist, *Phys. Rev. Lett.*, 2004, **92**, 246401.

18 Y. Zhao and D. G. Truhlar, *J. Chem. Phys.*, 2006, **125**, 194101.

19 J. Heyd and G. E. Scuseria, *J. Chem. Phys.*, 2004, **120**, 7274–7280.

20 J. M. Soler, E. Aratacho, J. D. Gale, A. Garcia, J. Junquera, P. Ordejon and S.-D. Portal, The SIESTA Method for *Ab Initio* Order-N Materials Simulation, *J. Phys.: Condens. Matter*, 2002, **14**, 2745–2779.

21 P. Ordejon, E. Artacho and J. M. Soler, *Phys. Rev. B: Condens. Matter Mater. Phys.*, 1996, **53**, R10441–R10444.

22 N. Troullier and J. L. Martins, *Phys. Rev. B: Condens. Matter Mater. Phys.*, 1991, **43**, 1993–2006.

23 M. J. Frisch, G. W. Trucks, H. B. Schlegel, G. E. Scuseria, M. A. Robb, J. R. Cheeseman, G. Scalmani, V. Barone, B. Mennucci, G. A. Petersson, H. Nakatsuji, M. Caricato, X. Li, H. P. Hratchian, A. F. Izmaylov, J. Bloino, G. Zheng, J. L. Sonnenberg, M. Hada, M. Ehara, K. Toyota, R. Fukuda, J. Hasegawa, M. Ishida, T. Nakajima, Y. Honda, O. Kitao, H. Nakai, T. Vreven, J. A. Montgomery, Jr., J. E. Peralta, F. Ogliaro, M. Bearpark, J. J. Heyd, E. Brothers, K. N. Kudin, V. N. Staroverov, R. Kobayashi, J. Normand, K. Raghavachari, A. Rendell, J. C. Burant, S. S. Iyengar, J. Tomasi, M. Cossi, N. Rega, J. M. Millam, M. Klene, J. E. Knox, J. B. Cross, V. Bakken, C. Adamo, J. Jaramillo, R. Gomperts, R. E. Stratmann, O. Yazyev, A. J. Austin, R. Cammi, C. Pomelli, J. W. Ochterski, R. L. Martin, K. Morokuma, V. G. Zakrzewski, G. A. Voth, P. Salvador, J. J. Dannenberg, S. Dapprich, A. D. Daniels, Ö. Farkas, J. B. Foresman, J. V. Ortiz, J. Cioslowski and D. J. Fox, *Gaussian 09, Revision D.01*, Gaussian, Inc., Wallingford CT, 2009.

24 W. Hehre, L. Radom, P. v. R. Schleyer, and J. A. Pople, *Ab initio Molecular Orbital Theory*, Wiley, New Work, 1986.

25 S. Grimme, *J. Comput. Chem.*, 2006, **27**, 1787–1799.

26 S. Grimme, S. Ehrlich and L. Goerigk, *J. Comput. Chem.*, 2011, **32**, 1456–1465.

27 G. Kresse and J. Hafner, *Phys. Rev. B: Condens. Matter Mater. Phys.*, 1994, **49**, 14251–14269.

28 J. P. Perdew, K. Burke and M. Ernzerhof, *Phys. Rev. Lett.*, 1996, **77**, 3865–3868.

29 J. P. Perdew, K. Burke and M. Ernzerhof, *Phys. Rev. Lett.*, 1997, **78**, 1396.

30 P. E. Blöchl, *Phys. Rev. B: Condens. Matter Mater. Phys.*, 1994, **50**, 17953–17979.

31 G. Kresse and J. Furthmuller, *Comput. Mater. Sci.*, 1996, **6**, 15.

32 S. Ullah, P. A. Denis, R. B. Capaz and F. Sato, *New J. Chem.*, 2019, **43**, 2933–2941.

33 C. A. Coulson and T. W. Dingle, *Acta Crystallogr., Sect. B: Struct. Crystallogr. Cryst. Chem.*, 1968, **24**, 153.

34 A. Savin, R. Nesper, S. Wengert and T. F. Fässler, *Angew. Chem., Int. Ed.*, 1997, **36**, 1808–1832.

35 D. Toffoli, M. Stredansky, Z. Feng, G. Balducci, S. Furlan, M. Stener, H. Ustunel, D. Cvetko, G. Kladnik, A. Morgante, A. Verdini, C. Dri, G. Comelli, G. Fronzoni and A. Cossaro, *Chem. Sci.*, 2017, **8**, 3789–3798.

36 J. Tersoff and D. R. Hamann, *Phys. Rev. B: Condens. Matter Mater. Phys.*, 1985, **31**, 805–813.

37 C. Buttay, D. Planson, B. Allard, D. Bergogne, P. Bevilacqua, C. Joubert, M. Lazar, C. Martin, H. Morel, D. Tournier and C. Raynaud, *J. Mater. Sci. Eng. B*, 2011, **176**, 283–288.

38 R. C. Andrew, R. E. Mapasha, A. M. Ukpong and N. Chetty, *Phys. Rev. B: Condens. Matter Mater. Phys.*, 2012, **85**, 125428.

39 L. Liu and A. Corma, *Chem. Rev.*, 2018, **118**, 4981–5079.

40 J. Mahmood, F. Li, C. Kim, H.-J. Choi, O. Gwon, S.-M. Jung, J.-M. Seo, S.-J. Cho, Y.-W. Ju, H. Y. Jeong, G. Kim and J.-B. Baek, *Nano Energy*, 2018, **44**, 304–310.

41 S. Ullah, P. A. Denis, M. G. Menezes and F. Sato, *Appl. Surf. Sci.*, 2019, **493**, 308–319.

42 S. Gélinas, O. Paré-Labrosse, C.-N. Brosseau, S. Albert-Seifried, C. R. McNeill, K. R. Kirov, I. A. Howard, R. Leonelli, R. H. Friend and C. Silva, *J. Phys. Chem. C*, 2011, **115**, 7114–7119.

43 S. Gélinas, A. Rao, A. Kumar, S. L. Smith, A. W. Chin, J. Clark, T. S. van der Poll, G. C. Bazan and R. H. Friend, *Science*, 2014, **343**, 512.

44 M. M. Furchi, A. Pospischil, F. Libisch, J. Burgdörfer and T. Mueller, *Nano Lett.*, 2014, **14**, 4785–4791.

## APPENDIX  E  –   Van der Waals heterostructures

E.1  Additional paper 1: Non-trivial band gaps and charge transfer in Janus-like functionalized bilayer boron arsenide

# Non-trivial band gaps and charge transfer in Janus-like functionalized bilayer boron arsenide

Saif Ullah[a,*], Pablo A. Denis[b,*], Fernando Sato[a]

[a] *Departamento de Física, Instituto de Ciências Exatas, Campus Universitário, Universidade Federal de Juiz de Fora, Juiz de Fora, MG 36036-900, Brazil*
[b] *Computational Nanotechnology, DETEMA, Facultad de Química, UDELAR, CC 1157, 11800 Montevideo, Uruguay*

ABSTRACT

Herein, we predict the stability, structural and electronic properties of Janus-like boron arsenide (BAs) bilayer with the help of DFT calculations. We combine one hydrogenated and one fluorinated BAs layers in different stacking and arrangements. The interlayer charge transfer is also calculated and discussed with the help of various charge population mechanism. In addition to this, the choice of basis set is critical in determining the interlayer distances and consequently, the energy gaps. Additionally, the layer-resolved PDOS, at vdW-DF level, revealed that these bilayers are type-II semiconductors as the valence and conduction bands are composed of different layers. Furthermore, the band gap of these bilayers can efficiently be engineered from 0 to 0.54 eV by controlling the arrangement of the layers. That being said, the electronic properties can optionally be tuned from semiconducting to semimetallic. Additionally, the shape of the conduction band minima and the heavy-, light-hole bands provides the opportunity of utilization of these bilayers in ultrafast nanoelectronics.

## 1. Introduction

2D materials have become a separate area of research ever since the first successful attempt of isolation of graphene from its parent material, graphite [1]. The various interesting properties along with the atom-size thickness of graphene make it utterly demanding in nanoelectronics [2,3]. However, the use of pristine graphene as semiconductor devices is restricted by the absence of an energy gap. This hurdle can be overcome by various methods, such as the chemical modification of graphene [4,5] by introducing hydrogen (H) [5–8], oxygen (O) [4,9], and fluorine (F) [10–14], etc and by using bilayer of graphene [15,16]. These adaptations change not only the physical but also the chemical properties by virtue of charge redistribution as in the case of graphene [5], graphene-oxide [4], and fluorographene [12,13]. Moreover, graphene is the first but not the only 2D material. There are hundreds of 2D materials already synthesized or theoretically predicted among which a few are boron nitride [17], boron phosphide [18,19], boron arsenide [18], phosphorene [20], and Be3N2 [21], etc.

Another material which got nearly the same fame is a binary compound consisting of boron (B) and nitrogen (N) with the similar hexagonal honeycomb lattice, h-BN [17]. Despite the fact that both graphene and h-BN have a number of potential applications, the wide band gap of h-BN is not suitable for transistors applications. Fortunately, there are other members of the same family (as that of h-BN) which

exhibit smaller band gaps. Among them, monolayer boron phosphide (BP) [18,19] and boron arsenide (BAs) [18] are already in the limelight despite the fact that they are yet to be synthesized. The calculated band gaps, at van der Waals density functional (vdW-DF) level, are direct and 1.1 eV and 0.89 eV for BP and BAs, respectively [19,22]. However, in bulk form, BAs possesses an indirect gap which can be modified by the introduction of defects [23–25]. Moreover, in monolayer form, hBP and hBAs can serve as one the efficient anode materials for alkali-based rechargeable batteries [19,26]. Nevertheless, the possible synthesis of these monolayers might be a question mark as their parent materials (in bulk form) are non-layered. Fortunately, with the help of certain techniques, it is possible to synthesize monolayers from the non-layered bulk parent materials [27–30]. In addition to this, the theory suggests the possibility of these monolayers. Furthermore, hBP and hBAs bilayers (pristine and hybrid) were recently investigated with the help of DFT studies and proposed for applications in optoelectronic devices [31]. Apart from that, the interlayer interaction energy calculations suggested that the strength of these bilayers are comparable to bilayer graphene. Besides, in a recent study, it is shown that both the monolayer BP and BAs can be hydrogenated (fluorinated) just like graphane (fluorographene) [22,32]. Furthermore, it is predicted, by means of density functional perturbation theory and *ab initio* molecular dynamics simulations, that these derivatives are as stable and efficient as that of hydrogenated-, fluorinated-graphene. That being said, the experimental
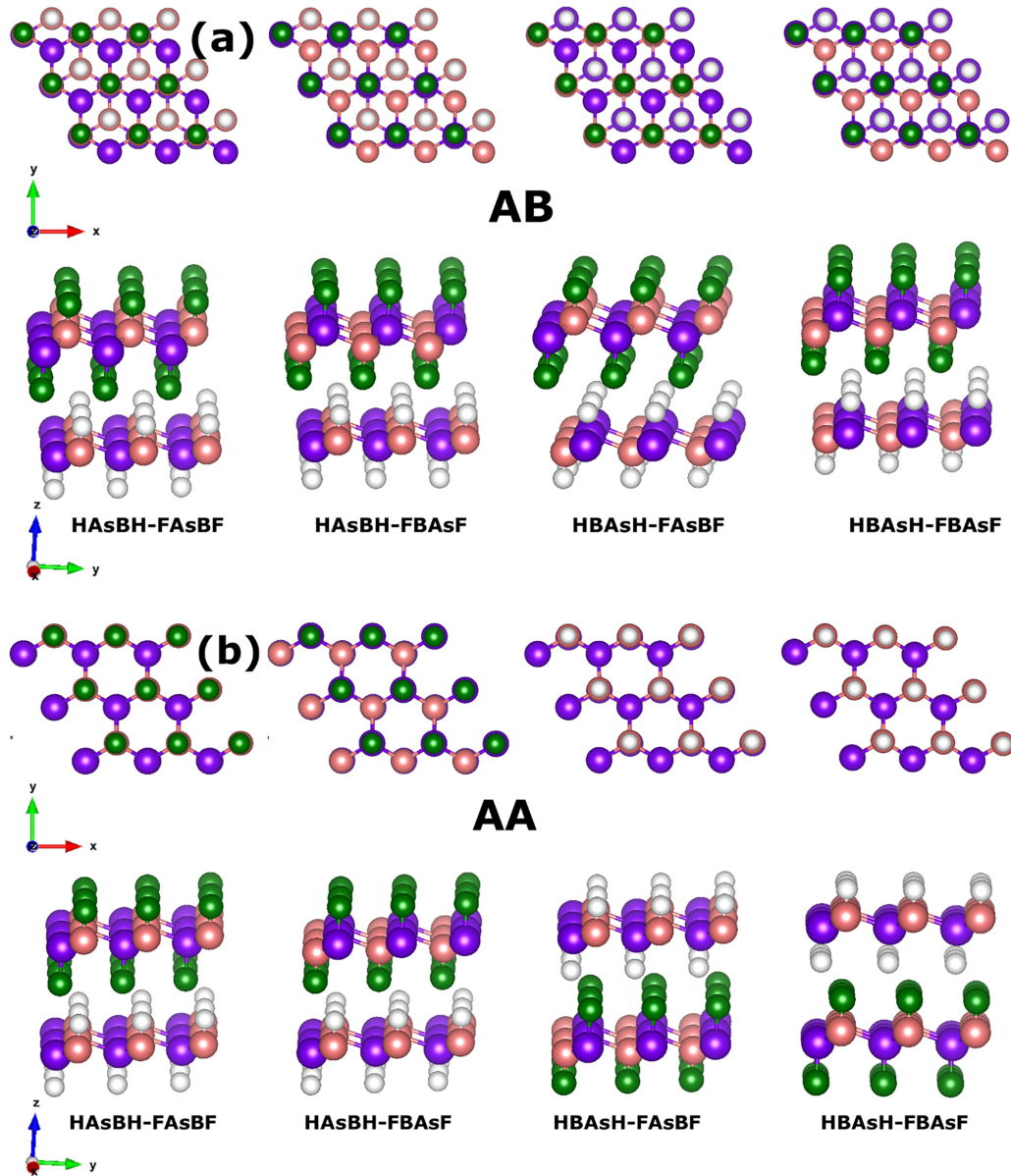
---

**Fig. 1.** Various configurations of different stacking (a) AB and (b) AA of bilayer HAsBH-FAsBF. White, pink, green, and purple spheres represent H, B, F, and As atoms, respectively.

synthesis of these monolayers is not forbidden. Furthermore, the possibility of tuning the electronic properties of functionalized silicene, when stacked, is already reported [33].

In this study, we predict the electronic properties of mixed bilayer BAs functionalized with H and F. To that end, first-principles density functional theory (DFT) calculations are performed within the non-local vdW-DF approximation. In addition to this, several other methodologies, such as PBE-D2, M06-L, and HSEH1PBE were also employed to get the optimum knowledge related to these bilayers. We calculate the relative stability, interlayer interaction energy, layer separation, charge transfer among the layers, and electronic properties of these mixed systems.

**Table 1**
Relative energies (meV/atom) determined for the HAsBH-FAsBF bilayers.

| System | PBE-D2 | M06-L |
|---|---|---|
| *AB stacked* | | |
| HAsBH-FAsBF | 2.950 | 2.140 |
| HAsBH-FBAsF | 3.116 | 2.14 |
| HBAsH-FAsBF | 0.00 | 0.00 |
| HBAsH-FBAsF | 1.940 | 1.94 |
| *AA stacked* | | |
| HAsBH-FAsBF | 3.186 | 2.17 |
| HAsBH-FBAsF | 3.006 | 1.36 |
| FBAsF-HAsBH | 1.347 | 2.38 |
| FAsBF-HAsBH | 2.827 | 1.73 |

**Table 2**
Interlayer H::F distance (Å) determined for the HAsBH-FAsBF bilayers at various levels of theory.

| Interlayer H::F distance | | PBE-D2 | vdW-DF | M06-L 6-311G* |
|---|---|---|---|---|
| HAsBH-FAsBF | AB | 2.51 | 2.49 | 2.84 |
| HAsBH-FBAsF | AB | 2.53 | 2.6 | 2.84 |
| HBAsH-FAsBF | AB | 2.48 | 2.42 | 2.83 |
| HBAsH-FBAsF | AB | 2.52 | 2.55 | 2.87 |
| HAsBH-FAsBF | AA | 2.56 | 2.53 | 2.80 |
| HAsBH-FBAsF | AA | 2.56 | 2.53 | 2.91 |
| HBAsH-FAsBF | AA | 2.5 | 2.4 | 2.86 |
| HBAsH-FBAsF | AA | 2.51 | 2.48 | 2.91 |

## 2. Computational details

Based on our previous experience, we use three of the most versatile DFT codes namely, VASP [34,35], GAUSSIAN [36], and SIESTA [37,38]. In VASP, projector augmented wave (PAW) [39] method along with the Perdew-Burke-Ernzerhof [40,41] flavor of the generalized gradient approximations is used. The DFT energies were corrected by the addition of a dispersion term known as Grimme's correction (DFT-D2) [42,43]. We use 500 eV kinetic energy cut off and adopt a first-order Methfessel-Paxton [44] smearing method with a lower smearing width (0.01). We also execute M06-L/6-311G* [35,36] calculations with the aid of Gaussian-09 code. We also perform HSEH1PBE [45,46] calculations for the estimation of band gaps. Finally, the non-local vdW-DF [47,48] calculations are performed with SIESTA code where norm-conserving (NC) Troullier-Martins pseudopotentails [49] (PPs) are used. We adopt a mesh cut off of 200 Ry in real space projection. We select $30 \times 30 \times 1$ kpoint grid with the energy and force tolerance of $10^{-6}$ eV and 0.02 eV/Å, respectively. For the calculations of PDOS, we use denser kpoints of $121 \times 121 \times 1$.

In order to have an idea of the strength and experimental feasibility, we calculate interlayer-layer interaction energy (IIE) and formation energy described elsewhere [22,50]:

$$IIE = \frac{E\_bilayer - E\_layerH - E\_layerF}{N_{tot}}$$

where $E\_bilayer$, $E\_layerH$, and $E\_layerF$ correspond to total energy of the system, energy of hydrogenated layer, and energy of fluorinated layer, respectively. Finally, $N_{tot}$ represents the number of atoms considered in the simulation.

$$FE = E_{XBAsY} - \mu_H - \mu_B - \mu_F - \mu_{As},$$

where $E_{XBAsY}$ represents the total energy whereas, $\mu_H$, $\mu_B$, $\mu_F$, and $\mu_{As}$ are the chemical potentials of individual specie involved. We use the energy of isolated atoms as a reference in all cases.

The results are explained in the following section.

## 3. Results

### 3.1. Structural properties

In order to create one hydrogenated and one fluorinated layer in the bilayer conformation, there exist four possibilities. For AB isomers, these four arrangements are; F-B on the top of As-H, F-B on the top of B-H, F-As above the As-H, and F-As above the B-H. All the geometries investigated in this study can be spotted in Fig. 1. The HBAsH-FAsBF in the AB stacking (F-B on top of B-H) is found to be the most favorable which is only 1.347 meV lower than the HBAsH-FAsBF in the AA stacking. That being said, all these motifs are quite close in energy. This may be due to the fact that F (H) atom is more electronegative (electropositive) in comparison with H (F), resulting in stronger electrostatic interaction between the layers. At the PBE-D2 level of theory, we determined that the interlayer interaction energy (IIE) in HBAsH-FAsBF is −14.885 meV/atom. The same level of theory, when applied to bilayer graphene, gives a value of −24.96 meV/atom. This means that the binding in bilayer graphene is only 10.07 meV/atom more favorable in comparison with the HBAsH-FAsBF bilayer. The M06-L/6-311G* values are in excellent agreement with that of PBE-D2 as the IIE in HBAsH-FAsBF is −13.764 meV/atom. For the same system, the B-B separation is 6.06 Å at vdW-DF/DZP level, in good accordance with PBE-D2 value (6.04 Å). We also report the interlayer H::F separations. An excellent agreement is found among the vdW-DF/DZP and PBE-D2. However, the M06-L/6-311G* values are found to be a bit overestimated. We also calculate the formation energy and compare with the individual (H and F) layer. The formation energy of the most favorable pattern, at M06-L level, is −31.84 eV (−3.98 eV/atom. The formation energy of monolayer BAs, hydrogenated BAs, and fluorinated BAs were reported to be −4.65 eV/atom, −3.825 eV/atom, and −4.525 eV/atom, respectively. For comparison, the formation energy of black phosphorene is −3.09 eV/atom and is already been synthesized. Having said that, the formation of these bilayers is experimentally achievable.

It is worth noting that the choice of basis set in Gaussian code is crucial as the M06-L/6-31G* basis set is found to be insufficient in describing these structures. For example, when using the 6-311G* basis set instead of 6-31G*, the interlayer F-H distances are increased by 0.7 Å. At the M06-L/6-311G* level of theory, the interlayer F-H distances are in the range of 2.80–2.91 Å, an indication of the presence of weak electrostatic interaction between the F and H atoms, F being more electronegative than H. The data related to the relative energies and the interlayer H-F bond lengths can be seen in Tables 1 and 2, respectively.

### 3.2. Electronic properties

We calculate the electronic properties of different arrangements of bilayers BAs as discussed in the above section. As can be seen in Fig. 2, at vdW-DF/DZP level, the band gap is strongly dependent on the type of stacking and geometry arrangements. In some cases, we see the bands overlapping around the Fermi level resulting in a negative band gap, thus altering the electronic character to semimetallic. This negative band gap can be as high as −0.9 eV or as low as −0.03 eV. As for as the positive band gap is concerned, it can also be engineered effectively depending on the geometry and stacking. The band gap opening can be modulated up to 0.33 eV at vdW-DF/DZP level. Consequently, the electronic properties of these systems can be modified from negative-gap (semimetallic) to positive-gap (semiconducting), which is a critical factor for applications in nanoelectronics, and quantum computing [51]. However, the band structures calculated with VASP (PBE-D2) show no positive band gap opening in any case. Furthermore, the PBE-D2 results suggest that all these systems are negative band gap (semimetallic) materials. The band structures are given in Fig. S1 in ESI. Additionally, the bands crossing around the Fermi level, at PBE-D2 level, are consistent with the one observed at vdW-DF level, however, the PBE-D2 fails to predict the positive band gap. This inconsistency can
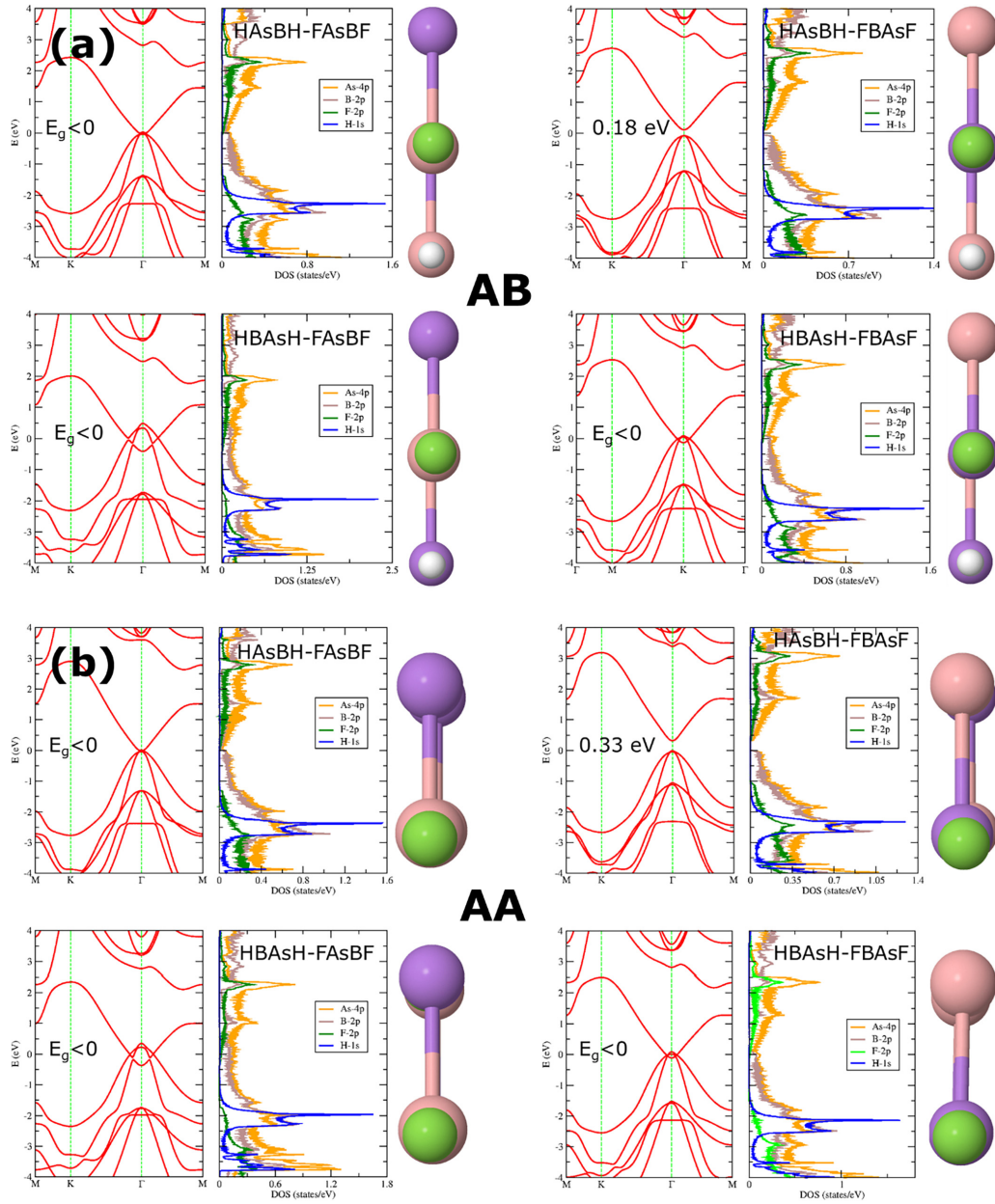
**Fig. 2.** Electronic band structures along with the corresponding PDOS, at vdW-DF/DZP level, of (a) AB and (b) AA HAsBH-FAsBF.

be attributed to the underestimation of gaps in DFT by employing local and semi-local functionals [21,52,53]. Nearly the same behavior of the gaps is observed at M06-L/6-311G* level. On the other hand, HSEH1PBE/6-311G* method reveals that the band gaps of AA stacked motifs can either be semimetallic or semiconducting (0.54 eV being the maximum) depending on the arrangements. Furthermore, the valence band consists of heavy-hole and light-hole bands and the shape of the bands around the Fermi level is somewhat in between the linear and

4

**Table 3**
Cohesive energies (eV) and band gaps (eV) determined for the HAsBH-FAsBF bilayers.

| System | Cohesive energy PBE-D2 | Gap PBE-D2 | Gap vdW-DF | Gap M06-L 6-311G* | Gap HSE 6-311G* |
|---|---|---|---|---|---|
| BAs | | | 0.89 | | |
| HAsBH | | | 3.50* | | |
| FAsBF | | | 1.25 | | |
| *AB stacked* | | | | | |
| HAsBH-FAsBF | −4.0635 | −0.33 | −0.07 | Semimetal | 0.00 |
| HAsBH-FBAsF | −4.0634 | −0.14 | 0.18 | Semimetal | 0.00 |
| HBAsH-FAsBF | −4.0665 | −0.47 | −0.90 | Semimetal | −0.09 |
| HBAsH-FBAsF | −4.0645 | −0.44 | −0.22 | Semimetal | −0.03 |
| *AA stacked* | | | | | |
| HAsBH-FAsBF | −4.0633 | −0.31 | −0.03 | Semimetal | 0.00 |
| HAsBH-FBAsF | −4.0635 | −0.08 | 0.33 | 0.16 | 0.54 |
| HBAsH-FAsBF | −4.066 | −0.45 | −0.72 | Semimetal | −0.10 |
| HBAsH-FBAsF | −4.0636 | −0.44 | −0.20 | Semimetal | −0.03 |
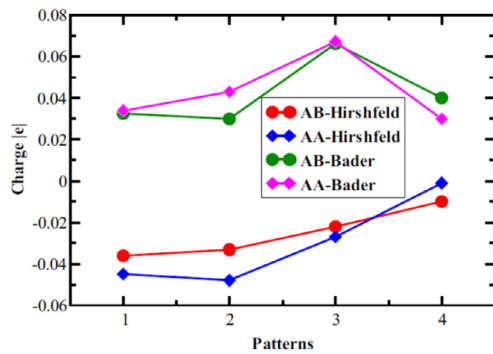


**Fig. 3.** Average Hirshfeld and Bader charges of the hydrogenated layers. The former suggests that charge is accumulated whereas, the latter shows that charge is depleted around the hydrogenated layers. The sequence of the patterns is the same as given in Fig. 1.

parabolic, resulting into smaller values of the effective mass of electron and hole. That being said, these systems provide the opportunity to be exploited in ultrafast nanoelectronics (Table 3).

We also calculate the projected density of states (PDOS) for the whole system and for the layers as well. It can be seen that the DOS near the valence band maxima (VBM) comes from the hybridization of B-2p and As-4p orbitals. However, the conduction band minima (CBM) is mostly consisting of the As-4p orbitals. We also resolve the layer-PDOS which reveal that the hydrogenated and fluorinated layers are

contributing to the VBM and CBM, respectively. That being said, these bilayers are of type-II semiconductors as the conduction and valence bands are composed of different layers. The plots are given in S2 of the ESI. This can be understood in the light of charge transfer (discussed below) among the layers. Furthermore, the energy range for the H-1s levels is quite narrower in comparison with the other which can also justify the charge transfer to the H atoms. Since in favorable conditions, the electrons occupy the narrower and lowest possible energy bands and therefore, we see that the VBM is composed of the hydrogenated layer in all the cases.

### 3.3. Charge transfer

For the charge transfer at vdW-DF/DZP level, we observe that in all the cases studied, charge is transferred from the fluorinated layer to the hydrogenated one as suggested by the Hirshfeld analysis. The Voronoi analysis shows similar results both qualitatively and quantitatively. Additionally, the amount of charge transfer depends on the stacking and configuration and plotted in Fig. 3.

However, the Mulliken population analysis, at M06-L/6-311G* level, shows a mixed trend of the charge transfer where the hydrogenated (fluorinated) layer can be positive (negative) or otherwise. Nevertheless, we also calculate Mulliken charges, at vdW-DF/DZP level, with the help of SIESTA code, the results of which are in perfect agreement with the Hirshfeld and Voronoi analyses. Having said that, the same method (Mulliken) gives unlike trend of charge transfer in different codes. Since Mulliken charges are strongly dependent on the choice of the basis set and are therefore prone to the charge population inversion [50,54–56]. At this stage, it is important to cross-check the results with a code which is independent of the size of the basis set and for this reason, we report Bader charge analysis using VASP package. Here, we find that in each and every case, the charge is accumulated on the fluorinated layers, especially on F atoms. Nevertheless, H atoms also attain a significant amount of charge from the attached B and As. All these outcomes are in perfect agreement with the electronegativity values, F (H) being the most (second-most) electronegative in comparison with B and As atoms. The charge depletion on hydrogenated layers accumulates on the fluorinated ones. Furthermore, in all patterns, the population around both B and As in fluorinated layer is larger than their counterparts in the hydrogenated layer as their charge is transferred to the attached H atoms, as well as the fluorinated layer. In a similar fashion, the H (F) attached to B is found to be more populated than the H (F) coupled with As. The numerical values of Bader charges can be seen in Table 4. Additionally, the amount of charge transfer among the layers is related to the stability of the patterns except HBAsH-FBAsF in AA stacking. We also show charge density plots in Fig. S3. The charges are gathered in Table S1 of the ESI.

### 4. Conclusions

By means of first-principles density functional theory (DFT)

**Table 4**
Numerical results from the Bader charge analysis calculated at DFT-D2 level of theory with the help of VASP code.

| | H-B | B | As | H-As | F-B | B | As | F-As |
|---|---|---|---|---|---|---|---|---|
| *AB stacked* | | | | | | | | |
| HAsBH-FAsBF | 2.0921 | 1.9029 | 3.9689 | 2.0036 | 8.01 | 2.0417 | 3.9999 | 7.981 |
| HAsBH-FBAsF | 2.0961 | 1.9054 | 3.9648 | 2.0038 | 8.0258 | 2.0097 | 4.0289 | 7.9654 |
| HBAsH-FAsBF | 2.1109 | 1.9053 | 3.9176 | 1.9999 | 8.0142 | 2.0542 | 4.0164 | 7.9815 |
| HBAsH-FBAsF | 2.1177 | 1.875 | 3.9706 | 1.9932 | 8.0269 | 2.0322 | 4.0204 | 7.9641 |
| *AA stacked* | | | | | | | | |
| HAsBH-FAsBF | 2.1073 | 1.8856 | 3.9567 | 2.017 | 8.0136 | 2.0115 | 4.0267 | 7.9817 |
| HAsBH-FBAsF | 2.1177 | 1.9208 | 3.9235 | 1.9952 | 8.0247 | 2.0399 | 4.0112 | 7.9669 |
| HBAsH-FAsBF | 2.1151 | 1.9089 | 3.9071 | 2.0016 | 8.0133 | 1.984 | 4.0837 | 7.9862 |
| HBAsH-FBAsF | 2.1098 | 1.8852 | 3.9664 | 2.0088 | 8.0276 | 2.0093 | 4.0322 | 7.9607 |

calculations, we predict the stability and electronic properties of mixed functionalized BAs bilayers. We combine one hydrogenated and one fluorinated BAs bilayers in various stacking and arrangements. A minute change in the relative energies as a function of stacking and arrangement shows the robustness of these bilayers. The interlayer interaction energy is calculated and compared with the bilayer graphene. Furthermore, the choice of the basis set has a strong influence on the interlayer H-F distances and so on the band gaps. We also calculate the charge transfer among the layers which is found to be strongly dependent on the arrangements of the layers. As per Bader charge analysis, we see a charge accumulation around F and H atoms which is in accordance with their electronegativity values. In addition to this, the layer-resolved Bader analysis reveals the accumulation of charge population around fluorinated layers. Furthermore, these bilayers are of type-II nature semiconductors as revealed by the layer resolved PDOS at vdW-DF level, in which the valence and conduction bands are composed of different layers. Finally, the flexibility in the electronic properties demands the use of these bilayers in nanoelectronic devices.

## 5. Data availability

All the data is available from the authors on request.

## CRediT authorship contribution statement

**Saif Ullah:** Conceptualization, Methodology, Writing - original draft, Data curation, Writing - review & editing, Funding acquisition, Resources, Supervision. **Pablo A. Denis:** Conceptualization, Methodology, Data curation, Writing - review & editing, Funding acquisition, Resources, Supervision. **Fernando Sato:** Conceptualization, Writing - review & editing, Funding acquisition, Resources, Supervision.

## Conflict of interest

There is no conflict of interest.

## Acknowledgments

## Appendix A. Supplementary data

Supplementary data to this article can be found online at https://doi.org/10.1016/j.commatsci.2019.109186.

## References

[1] K.S. Novoselov, A.K. Geim, S.V. Morozov, D. Jiang, Y. Zhang, S.V. Dubonos, I.V. Grigorieva, A.A. Firsov, Electric field effect in atomically thin carbon films, Science 306 (2004) 666–669.
[2] K.S. Novoselov, A.K. Geim, S. Morozov, D. Jiang, M. Katsnelson, I. Grigorieva, S. Dubonos, A. Firsov, Two-dimensional gas of massless Dirac fermions in graphene, Nature 438 (2005) 197.
[3] A.K. Geim, K.S. Novoselov, The rise of graphene, Nat. Mater. 6 (2007) 183.
[4] D.A. Dikin, S. Stankovich, E.J. Zimney, R.D. Piner, G.H.B. Dommett, G. Evmenenko, S.T. Nguyen, R.S. Ruoff, Preparation and characterization of graphene oxide paper, Nature 448 (2007) 457.
[5] D.C. Elias, R.R. Nair, T. Mohiuddin, S. Morozov, P. Blake, M. Halsall, A. Ferrari, D. Boukhvalov, M. Katsnelson, A. Geim, Control of graphene's properties by reversible hydrogenation: evidence for graphane, Science 323 (2009) 610–613.
[6] M.H. Sluiter, Y. Kawazoe, Cluster expansion method for adsorption: Application to

[7] hydrogen chemisorption on graphene, Phys. Rev. B 68 (2003) 085410.
[7] J.O. Sofo, A.S. Chaudhari, G.D. Barber, Graphane: a two-dimensional hydrocarbon, Phys. Rev. B 75 (2007) 153401.
[8] P.A. Denis, F. Iribarne, On the hydrogen addition to graphene, J. Mol. Struct. (Thoechem.) 907 (2009) 93–103.
[9] P.A. Denis, Density functional investigation of thioepoxidated and thiolated graphene, J. Phys. Chem. C 113 (2009) 5612–5619.
[10] F. Withers, M. Dubois, A.K. Savchenko, Electron properties of fluorinated single-layer graphene transistors, Phys. Rev. B 82 (2010) 073403.
[11] R.R. Nair, W. Ren, R. Jalil, I. Riaz, V.G. Kravets, L. Britnell, P. Blake, F. Schedin, A.S. Mayorov, S. Yuan, Fluorographene: a two-dimensional counterpart of Teflon, Small 6 (2010,) 2877–2884.
[12] J.-C. Charlier, X. Gonze, J.-P. Michenaud, First-principles study of graphite monofluoride (CF) n, Phys. Rev. B 47 (1993) 16162.
[13] O. Leenaerts, H. Peelaers, A. Hernández-Nieves, B. Partoens, F. Peeters, First-principles investigation of graphene fluoride and graphane, Phys. Rev. B 82 (2010) 195436.
[14] S.-H. Cheng, K. Zou, F. Okino, H.R. Gutierrez, A. Gupta, N. Shen, P. Eklund, J. Sofo, J. Zhu, Reversible fluorination of graphene: evidence of a two-dimensional wide bandgap semiconductor, Phys. Rev. B 81 (2010) 205435.
[15] A.C. Ferrari, J.C. Meyer, V. Scardaci, C. Casiraghi, M. Lazzeri, F. Mauri, S. Piscanec, D. Jiang, K.S. Novoselov, S. Roth, A.K. Geim, Raman spectrum of graphene and graphene layers, Phys. Rev. Lett. 97 (2006) 187401.
[16] T. Ohta, A. Bostwick, T. Seyller, K. Horn, E. Rotenberg, Controlling the electronic structure of bilayer graphene, Science 313 (2006) 951.
[17] K. Watanabe, T. Taniguchi, H. Kanda, Direct-bandgap properties and evidence for ultraviolet lasing of hexagonal boron nitride single crystal, Nat. Mater. 3 (2004) 404.
[18] H. Şahin, S. Cahangirov, M. Topsakal, E. Bekaroglu, E. Akturk, R.T. Senger, S. Ciraci, Monolayer honeycomb structures of group-IV elements and III-V binary compounds: first-principles calculations, Phys. Rev. B 80 (2009) 155453.
[19] S. Ullah, P.A. Denis, F. Sato, Hexagonal boron phosphide as a potential anode nominee for alkali-based batteries: a multi-flavor DFT study, Appl. Surf. Sci. 471 (2019) 134–141.
[20] H. Liu, A.T. Neal, Z. Zhu, Z. Luo, X. Xu, D. Tománek, P.D. Ye, Phosphorene: an unexplored 2D semiconductor with a high hole mobility, ACS Nano 8 (2014) 4033–4041.
[21] S. Ullah, P.A. Denis, R.B. Capaz, F. Sato, Theoretical characterization of hexagonal 2D Be3N2 monolayers, New J. Chem. 43 (2019) 2933–2941.
[22] S. Ullah, P.A. Denis, F. Sato, Hydrogenation and fluorination of 2D boron phosphide and boron arsenide: a density functional theory investigation, ACS Omega 3 (2018) 16416–16423.
[23] S. Chae, K. Mengle, J.T. Heron, E. Kioupakis, Point defects and dopants of boron arsenide from first-principles calculations: Donor compensation and doping asymmetry, Appl. Phys. Lett. 113 (2018) 212101.
[24] K. Bushick, K. Mengle, N. Sanders, E. Kioupakis, Band structure and carrier effective masses of boron arsenide: effects of quasiparticle and spin-orbit coupling corrections, Appl. Phys. Lett. 114 (2019) 022101.
[25] J. Buckeridge, D.O. Scanlon, Electronic band structure and optical properties of boron arsenide, Phys. Rev. Mater. 3 (2019) 051601.
[26] S. Ullah, P.A. Denis, F. Sato, Monolayer boron-arsenide as a perfect anode for alkali-based batteries with large storage capacities and fast mobilities, Int. J. Quantum Chem. 119 (2019) e25975.
[27] Q. Wang, K. Xu, Z. Wang, F. Wang, Y. Huang, M. Safdar, X. Zhan, F. Wang, Z. Cheng, J. He, van der Waals epitaxial ultrathin two-dimensional nonlayered semiconductor for highly efficient flexible optoelectronic devices, Nano Lett. 15 (2015) 1183–1189.
[28] F. Wang, Z. Wang, T.A. Shifa, Y. Wen, F. Wang, X. Zhan, Q. Wang, K. Xu, Y. Huang, L. Yin, C. Jiang, J. He, Two-dimensional non-layered materials: synthesis, properties and applications, Adv. Funct. Mater. 27 (2017) 1603254.
[29] Z. Xie, C. Xing, W. Huang, T. Fan, Z. Li, J. Zhao, Y. Xiang, Z. Guo, J. Li, Z. Yang, B. Dong, J. Qu, D. Fan, H. Zhang, Nonlayered 2D materials: ultrathin 2D nonlayered tellurium nanosheets: facile liquid-phase exfoliation, characterization, and photoresponse with high performance and enhanced stability, Adv. Funct. Mater. 28 (2018) 1870107.
[30] K. Yao, P. Chen, Z. Zhang, J. Li, R. Ai, H. Ma, B. Zhao, G. Sun, R. Wu, X. Tang, B. Li, J. Hu, X. Duan, X. Duan, Synthesis of ultrathin two-dimensional nanosheets and van der Waals heterostructures from non-layered γ-CuI, NPJ 2 (2018) 16.
[31] S. Ullah, P.A. Denis, M.G. Menezes, F. Sato, Tunable optoelectronic properties in h-BP/h-BAs bilayers: the effect of an external electrical field, Appl. Surf. Sci. 493 (2019) 308–319.
[32] R.-W. Zhang, C.-W. Zhang, W.-X. Ji, S.-S. Li, P.-J. Wang, S.-J. Hu, S.-S. Yan, Hydrogenated boron arsenide nanosheet: a promising candidate for bipolar magnetic semiconductor, Appl. Phys. Express 8 (2015) 113001.
[33] P.A. Denis, Stacked functionalized silicene: a powerful system to adjust the electronic structure of silicene, Phys. Chem. Chem. Phys. 17 (2015) 5393–5402.
[34] G. Kresse, J. Furthmüller, Efficiency of ab-initio total energy calculations for metals and semiconductors using a plane-wave basis set, Comput. Mater. Sci. 6 (1996) 15–50.
[35] G. Kresse, J. Furthmüller, Efficient iterative schemes for ab initio total-energy calculations using a plane-wave basis set, Phys. Rev. B 54 (1996) 11169–11186.
[36] M.J. Frisch, G.W. Trucks, H.B. Schlegel, G.E. Scuseria, M.A. Robb, J.R. Cheeseman, G. Scalmani, V. Barone, G.A. Petersson, H. Nakatsuji, X. Li, M. Caricato, A. Marenich, J. Bloino, B.G. Janesko, R. Gomperts, B. Mennucci, H.P. Hratchian, J.V. Ortiz, A.F. Izmaylov, J.L. Sonnenberg, D. Williams-Young, F. Ding, F. Lipparini, F. Egidi, J. Goings, B. Peng, A. Petrone, T. Henderson, D. Ranasinghe, V.G.

Zakrzewski, J. Gao, N. Rega, G. Zheng, W. Liang, M. Hada, M. Ehara, K. Toyata, R. Fukuda, J. Hasegawa, M. Ishida, T. Nakajima, Y. Honda, O. Kitao, H. Nakai, T. Vreven, K. Throssell, J.A. Montgomery, J.E.P,. Jr., F. Ogliaro, M. Bearpark, J.J. Heyd, E. Brothers, K.N. Kudin, V.N. Staroverov, T. Keith, R. Kobayashi, J. Normand, K. Raghavachari, A. Rendell, J.C. Burant, S.S. Iyengar, J. Tomasi, M. Cossi, J.M. Millam, M. Klene, C. Adamo, R. Cammi, J.W. Ochterski, R.L. Martin, K. Morokuma, O. Farkas, J.B. Foresman, D.J. Fox, Gaussian 09, revision A1 ed., Gaussian Inc., Wallingford, CT, 2009.

[37] P. Ordejón, E. Artacho, J.M. Soler, Self-consistent order-N density-functional calculations for very large systems, Phys. Rev. B 53 (1996) R10441.

[38] J.M. Soler, E. Artacho, J.D. Gale, A. García, J. Junquera, P. Ordejón, D. Sánchez-Portal, The SIESTA method for ab initio order-N materials simulation, J. Phys.: Condens. Matter 14 (2002) 2745.

[39] G. Kresse, D. Joubert, From ultrasoft pseudopotentials to the projector augmented-wave method, Phys. Rev. B 59 (1999) 1758–1775.

[40] J.P. Perdew, K. Burke, M. Ernzerhof, Generalized gradient approximation made simple, Phys. Rev. Lett. 77 (1996) 3865–3868.

[41] J.P. Perdew, K. Burke, M. Ernzerhof, Generalized gradient approximation made simple [Phys. Rev. Lett. 77, 3865 (1996)], Phys. Rev. Lett. 78 (1997) 1396–1396.

[42] S. Grimme, Semiempirical GGA-type density functional constructed with a long-range dispersion correction, J. Comput. Chem. 27 (2006) 1787–1799.

[43] S. Grimme, J. Antony, S. Ehrlich, H. Krieg, A consistent and accurate ab initio parametrization of density functional dispersion correction (DFT-D) for the 94 elements H-Pu, J. Chem. Phys. 132 (2010) 154104.

[44] M. Methfessel, A.T. Paxton, High-precision sampling for Brillouin-zone integration in metals, Phys. Rev. B 40 (1989) 3616–3621.

[45] J. Heyd, G.E. Scuseria, Assessment and validation of a screened Coulomb hybrid density functional, J. Chem. Phys. 120 (2004) 7274–7280.

[46] V. Barone, G.E. Scuseria, Theoretical study of the electronic properties of narrow single-walled carbon nanotubes: beyond the local density approximation, J. Chem. Phys. 121 (2004) 10376–10379.

[47] M. Dion, H. Rydberg, E. Schröder, D.C. Langreth, B.I. Lundqvist, Van der Waals density functional for general geometries, Phys. Rev. Lett. 92 (2004) 246401.

[48] G. Román-Pérez, J.M. Soler, Efficient implementation of a van der Waals density functional: application to double-wall carbon nanotubes, Phys. Rev. Lett. 103 (2009) 096102.

[49] N. Troullier, J.L. Martins, Efficient pseudopotentials for plane-wave calculations, Phys. Rev. B 43 (1991) 1993–2006.

[50] S. Ullah, P.A. Denis, F. Sato, Beryllium doped graphene as an efficient anode material for lithium-ion batteries with significantly huge capacity: a DFT study, Appl. Mater. Today 9 (2017) 333–340.

[51] N. Malkoval, G.W. Bryant, Surface states in negative-band-gap semiconductor films: intrinsic or topological? Physica B 410 (2013) 147–156.

[52] C.S. Wang, W.E. Pickett, Density-functional theory of excitation spectra of semiconductors: application to Si, Phys. Rev. Lett. 51 (1983) 597–600.

[53] M.K.Y. Chan, G. Ceder, Efficient band gap prediction for solids, Phys. Rev. Lett. 105 (2010) 196403.

[54] K.B. Wiberg, P.R. Rablen, Comparison of atomic charges derived via different procedures, J. Comput. Chem. 14 (1993) 1504–1518.

[55] S. Ullah, P.A. Denis, F. Sato, Triple-doped monolayer graphene with boron, nitrogen, aluminum, silicon, phosphorus, and sulfur, ChemPhysChem 18 (2017) 1854–1854.

[56] S. Ullah, P.A. Denis, F. Sato, First-principles study of dual-doped graphene: towards promising anode materials for Li/Na-ion batteries, New J. Chem. 42 (2018) 10842–10851.

# Tunable and sizeable band gaps in SiC₃/hBN vdW heterostructures: A potential replacement for graphene in future nanoelectronics

Saif Ullah,[a,*] Pablo A. Denis,[b] Marcos G. Menezes,[c] and Fernando Sato[a]

a- Departamento de Física, Instituto de Ciências Exatas, Campus Universitário, Universidade Federal de Juiz de Fora, Juiz de Fora, MG 36036-900, Brazil

b- Computational Nanotechnology, DETEMA, Facultad de Química, UDELAR, CC 1157, 11800 Montevideo, Uruguay

c- Instituto de Física, Universidade Federal do Rio de Janeiro, Caixa Postal 68528, 21941-972, Rio de Janeiro, RJ, Brazil

*email:sullah@fisica.ufjf.br

**Abstract**

Benefitting from the exceptional carrier mobility of graphene in nanoelectronics is a great challenge by virtue of the band gap issue. In this context, we perform first-principles calculations based on density functional theory on siligraphene ($SiC_3$)/hexagonal boron nitride (hBN) vdW-heterostructures as a potential replacement for graphene. $SiC_3$ is a material composed of a 2x2 graphene cell doped with two Si atoms at *para* positions and it has comparable electronic properties to that of graphene, including the presence of a Dirac-like cone. We consider different $SiC_3$-hBN vdW-heterostructures, including a hybrid $SiC_3$/hBN bilayer, a h-BN/$SiC_3$/h-BN trilayer (encapsulated monolayer $SiC_3$), and a h-BN/$SiC_3$/$SiC_3$/h-BN 4-layer (encapsulated bilayer $SiC_3$). While the gap for single-layer graphene encapsulated in hBN is about 0.03 eV, the gap in the $SiC_3$-hBN heterostructures can be as high as 0.11 eV and can further be fine-tuned by an external electric field and strain. Such tunability is (much) weaker in the graphene/hBN system. In contrast, for the encapsulated $SiC_3$ bilayer, the gap tunability is strongly stacking dependent and a magnetic configuration is found depending on the width of the low-energy bands. The optical properties of these structures are also quite attractive, with strong absorption peaks in both visible and deep UV regions. Some of the structures also display small peaks at the infrared region. These peaks show a stacking sensibility, but are rather insensitive to the external field. In light of these results, we believe that these heterostructures can be potential candidates for future applications in nanoelectronic and optoelectronic devices, thus triggering new experimental investigations.

**Introduction:**

Once considered impossible, graphene is one of the most studied materials since the groundbreaking yet simple discovery of the isolation of monolayer form graphite dated back to 2004 [1]. This first-ever synthesized 2D material with a hexagonal honeycomb lattice brought some exceptional properties and exotic physics [1-4]. For example, the excellent charge carrier mobility, which is about $2\times10^5$ cm$^2$V$^{-1}$s$^{-1}$, is one of the outstanding properties of graphene [5]. This along with several other interesting properties including the atom-size thickness make the utilization of graphene highly desirable in nanoelectronics. However, pure graphene cannot be used in devices such as field-effect transistors due to the absence of an energy gap. This issue can be tackled in many ways and the most popular and easier approach is the injection of a foreign impurity atom in graphene or the decoration of graphene with certain atoms/molecules. Substitutional doping choices include the group III boron (B) and group V nitrogen (N) atoms, as well as the group II beryllium (Be) and group VI oxygen (O) or the codoping of these light impurity atoms [6-8]. In addition, the simultaneous integration of three types of impurity atoms is also reported [9]. The functionalization of graphene can be done with the introduction of hydrogen (H), fluorine (F), F4TCNQ, DMBI, TCNE, etc [10-13]. These methods can open up a sizeable energy gap around the Dirac point and, apparently, seem to be the best solutions. However, these methods gravely affect the Dirac cones and the carrier mobility. On the other hand, the introduction of an appropriate substrate can preserve the exceptional carrier mobility in graphene [14, 15], but the gaps induced as a consequence of its presence are not tunable. As an example, the charge carrier mobility and electronic characteristics are gravely degraded in graphene grown on the SiO2 substrate [3]. On the other hand, hexagonal boron nitride (hBN), which is a wide gap insulator, can be graphene's best companion as its carrier mobility is almost preserved [16, 17]. However, the gap opening is very tiny (in the most favorable systems) to be of any practical use in the diverse field of nanoelectronics [18].

In this regard, the search for another material having similar electronic characteristics to that of graphene with a somewhat tunable band gap is crucial. In fact, the platter of 2D materials have a wide range of options but only a few of which exhibits the Dirac-like characteristics including silicene, various graphynes, FeB2, Be5C2, and some other 2D materials [19-27]. In addition,

various SiC compounds with adjustable electronic properties have been proposed [28-30] and, among them, $SiC_3$ possesses a similar Dirac cone [28]. The structure of $SiC_3$ can be thought as a Si doping of graphene at para positions and, despite the fact that Si doping (by virtue of its larger radius) makes a protrusion in the graphene plane, this material has a perfectly planar structure [31]. Moreover, the Fermi velocities are of the order of $7.34X10^5$ m/s, a bit lower than that of graphene $(9.92X10^5$ m/s). In bilayer graphene, the gaps can efficiently be engineered by applying an external electric field or through a symmetry-breaking doping, reaching values up to 0.25 eV [32-35]. The effect of strain is analogous to the aforementioned techniques [36]. Since the external electric field does not lead to gap tuning in single-layer graphene, it is critical to develop a method in which a sizeable gap can be introduced around the Dirac point without compromising its charge carrier mobility.

In this work, we perform first-principles calculations based on density functional theory (DFT) to study the electronic properties of different $SiC_3$-hBN vdW-heterostructures, including a hybrid $SiC_3$/hBN bilayer, a h-BN/$SiC_3$/h-BN trilayer (encapsulated monolayer $SiC_3$), and a h-BN/$SiC_3$/$SiC_3$/h-BN 4-layer (encapsulated bilayer $SiC_3$). The most favorable patterns are further analyzed by subjecting them to an external electric field (in all cases) and strain (for the hybrid bilayer only) in order to study the tunability in the optoelectronic properties. Contrary to the case of single-layer graphene, we find that the band gap opening is sufficiently higher and, additionally, tunable to these external parameters. As we discuss below, such tunability gives an edge to $SiC_3$ over graphene, especially for future applications in FETs. Additionally, for the encapsulated bilayer $SiC_3$, we find a magnetic ground state for the most stable configuration with quite larger gap in the both the spin up and down channels. Therefore, we expect this work to spark new experimental investigations.

**Methods:**

All the calculations in this work were carried out, unless otherwise stated, within the framework of the van der Waals density functional (vdW-DF1) as implemented in the SIESTA code, which is based on first-principles density functional theory (DFT) [37-39]. We use norm-conserving (NC) Troullier-Martins (TM) pseudopotentials (PPs) in fully separable form to treat the electron-ion interaction [40]. The kpoint sampling in the first Brillouin zone is 17X17X1 with a mesh cutoff of 200 Ry in the real space projection. The structures are considered optimized when the forces on

each atom are less than 0.02 eV/Å with the energy convergence criteria of $10^{-6}$ eV between each electronic step. The calculations of density of states and optical properties were carried out with sufficiently denser kpoint grids (61X61X1). The optical properties do not include excitonic effects, which can be very important in low-dimensional systems[41, 42]. Still, the general trends should be qualitatively reproduced, such as the tunability with an external field and the stacking dependence. We take all bands into account in all the optical calculations. We make use of a large vacuum region (more than 20 Å wide in all calculations) and dipole corrections are taken into account. We also make use of vdW-DF2, optB88-vdW, vdW-DF-c09, vdW-DF-cx, and VV10 functionals as implemented in SIESTA [43-48]. In addition, M06-L and HSEH1PBE calculations are also performed with the help of Gaussian code [49-51]. To cross-check some of the results, VASP and Quantum Espresso (QE) codes were also utilized [52-59].

**Results and discussion:**

Primarily, we start our investigation by calculating the band gap of single layer graphene on hBN as a benchmark. We select two configurations with AB stacking, namely AB (when B lies on top of a C atom and N lies at a hollow site) and AB2 (when N lies on top of a C atom and B lies at a hollow site). The band gaps at vdW-DF1 level for these configurations are 0.02 and 0.03 eV, respectively. The M06-L and HSEH1PBE calculations yield gaps of 0.06 and 0.05 eV, respectively. Nevertheless, a HSEH1PBE calculation with the M06-L optimized geometry gives a band gap of 0.10 eV. This value is in good agreement with the many-body GW value [60]. For hBN/graphene/hBN trilayer, the gap is 0.078 eV at vdW-DF1/DZP level.

Next, we calculate the structural and electronic properties of monolayer hBN and $SiC_3$. The lattice parameters of hBN (in a 2x2 supercell) and $SiC_3$ are 5.04 (2.52 for a unit cell) and 5.64 Å, respectively. The geometric structure of $SiC_3$ is simply a 2x2 graphene unitcell with the Si doping at the para position without the protrusion of Si atoms. Additionally, the band gap of hBN is found to be 5.76 eV, whereas a Dirac cone is observed for $SiC_3$. The computed results are in excellent agreement with those reported in the literature and are given in Fig. S1 in the electronic supplementary information (ESI) [28, 61]. Following this, a systematic investigation of the different hBN-$SiC_3$ vdW-heterostructures is carried out and discussed in the following sections.

**Hybrid SiC₃/hBN bilayers:**

We consider five possible configurations, AA, AB, AB2, AB3, and AB4 as given in Fig. 1.
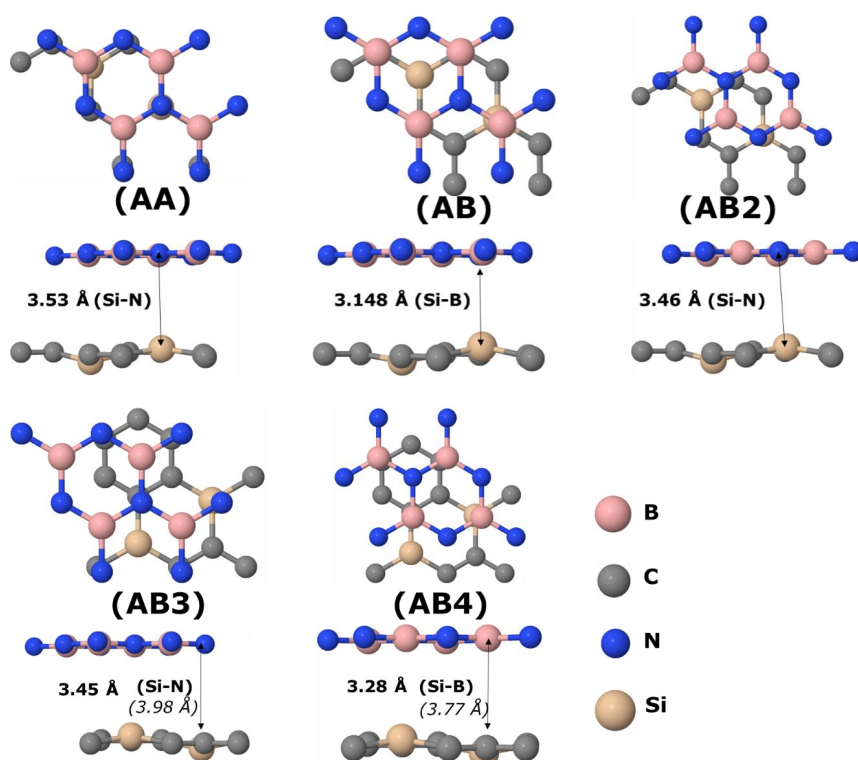


**Fig. 1:** Various relaxed configurations of a hybrid $SiC_3$/hBN bilayer. Values in bold show the minimum interlayer separation computed as the difference between the highest atom in $SiC_3$ layer and lowest atom in hBN layer. Values in italic represent the actual distance between mentioned atoms.

Note that there is only one possible configuration with AA stacking, as in this case one Si atom in the unit cell sits on top of a B atom and the other on top of a N atom. In the AB configuration, one Si atom sits on top of a hollow site and the other on top of a B atom. The rest of the B atoms sit on

top of the C atoms, whereas all the N atoms sit on top of hollow sites. In AB2, the positions of the B and N atoms are interchanged with respect to the AB configuration. The AB3 and AB4 configurations have similar stackings to those of AB2 and AB, respectively. While monolayer $SiC_3$ has a planar structure in its isolated form, a small buckling is introduced in the presence of the h-BN layer. This might be attributed to the shrinkage of the $SiC_3$ layer as the lattice constants of the hybrid bilayer are about 5.37 Å in all configurations, which is in the middle of the values for isolated $SiC_3$ and hBN. Moreover, we also check the use of a larger cell (144 atoms) and find the same energetics (eV/atom), structural (lattice constant and buckling) and electronic properties. In the AB (AB2) configuration, the Si atom on top of B (N) moves towards the hBN layer, while the opposite happens in AB3 and AB4. Among those configurations, AB is found to be the most favorable, as shown by the total energy differences reported in Table 1. Regarding the electronic properties, the AA, AB, and AB2 configurations have relatively higher band gaps (0.193, 0.110, and 0.145 eV, respectively) in comparison with AB3 (0.018 eV) and AB4 (0.082 eV). This 0.11 eV gap in $SiC_3$/hBN is larger than that of graphene/hBN (0.022 eV at the same level of theory) and is sufficient for practical applications in electronic devices [60]. In addition, the M06-L and HSEH1PBE gap is 0.17 and 0.22 eV, respectively, for the most stable (AB) configuration. Moreover, it should be noted that quasiparticle corrections can enhance this band gap value. This is a clear indication of the advantage of $SiC_3$ over graphene in that aspect. Since the lattice mismatch in SiC/hBN is larger than that of graphene/hBN, it is important to check whether this gap is due to the introduction of hBN or just due to the in-plane strain. In this context, we take the monolayer $SiC_3$ from the vdW-heterostructure and calculate the electronic structure with that geometry and find a minute gap of 0.06 eV.

| Configuration | Lattice constant $a$ | Relative energy | Band gap |
|---|---|---|---|
| AA | 5.372 | 81.5 | 0.193 |
| AB | 5.375 | 0.0 | 0.110 |
| AB2 | 5.373 | 80.5 | 0.145 |
| AB3 | 5.374 | 90.5 | 0.018 |
| AB4 | 5.377 | 21.5 | 0.082 |

**Table 1:** Lattice constant (Å), relative energy (meV), and band gaps (eV) for the hybrid SiC3/h-BN bilayer configurations shown in Fig. 1.

Consequently, the sizeable gap in the vdW-heterostructure is a result of the introduction of the hBN layer. The electronic band structures for each configuration are shown in Fig. 2, where we can see that the structure of the Dirac cones from $SiC_3$ is well preserved away from the K point despite the presence of the gaps.
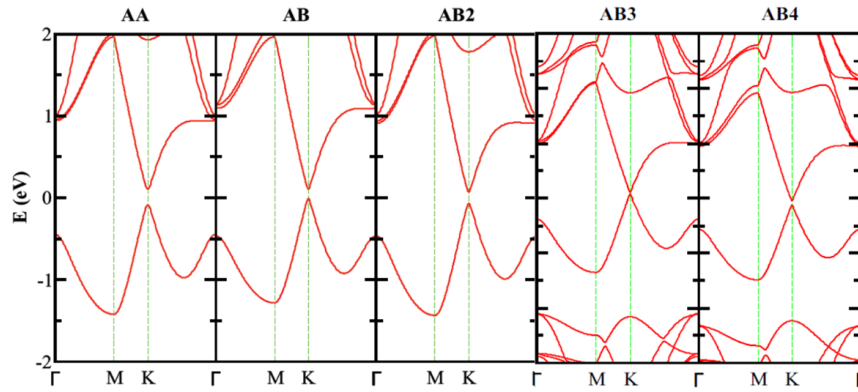


**Fig. 2:** Electronic band structure for the hybrid $SiC_3$/h-BN bilayer configurations shown in Fig. 1.

We also check the effects of a biaxial strain (lattice constant modification) and an external electric field in the most favorable configuration (AB). For strain, we compress the structure to the limit of pure hBN (5.04 Å and 12% strain) and expand it to the limit of $SiC_3$ (5.64 Å and 10%). The evolution of the band gap with strain is shown in Fig. 3. As we can see, the gap can be regarded as insensitive to large expansions (>1%), as gap variations are smaller than 0.03 eV. On the other hand, large contractions have a great impact on the value of the gap, as it can be increased up to 1.5 eV in the hBN limit. We also show in Fig. 3 the evolution of the gaps with an external electric field applied perpendicular to the layers. In these plots, positive (negative) field values represent the field direction from $SiC_3$ towards hBN (hBN towards $SiC_3$). As we can see, for the field in the foward direction, the gap decreases down to zero at 0.8 V/Ang and then starts to increase above this magnitude, which is a sign of band inversion. In contrast, for the reversed direction, the gap

increases almost linearly with the field magnitude, reaching about 0.3 eV at 1.2 V/Ang. The band structures for selected field values can be found in Fig. S3 of the ESI. These results indicate that the hybrid SiC$_3$/hBN bilayer offers a great gap tunability that can be explored in future FET devices.
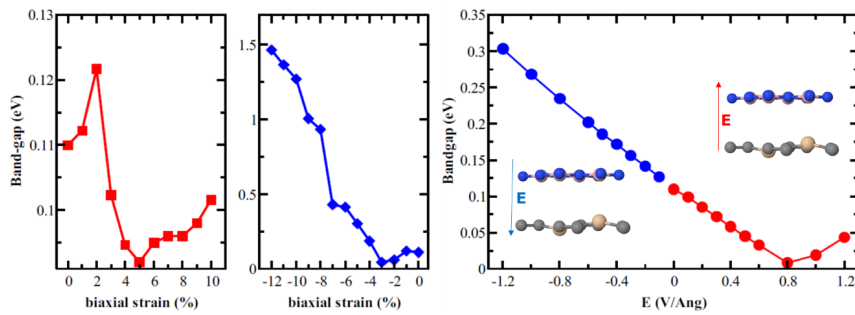


**Fig. 3:** Band gap of the SiC$_3$/h-BN bilayer (most favorable configuration) as a function of a biaxial strain (left) and an external electric field applied perpendicular to the layers (right). The field direction is indicated in the panels.

We have also calculated the optical absorption spectrum of the hybrid bilayer and compared it with those from the isolated hBN and SiC$_3$ monolayers. The plot is shown in Fig. 4. We can see that, in the hybrid structure, the position of the first sharp peak in the visible region is slightly blueshifted. Our PDOS calculations (reported in the ESI) indicate that this peak is associated to optical transitions between the first valence and conduction bands at k-points around the middle of the $\Gamma$-K line. These bands retain a dominant SiC$_3$ character, but the gap opening leads to a rigid shift of these bands and to the observed blueshift. The second sharp absorption peak is also pushed deep in the ultraviolet region and, additionally, the third peak at 5.2 eV corresponds to the redshifted h-BN peak. Finally, we can also see that the spectrum acquires an additional structure in the 3.0 - 4.0 eV range. These peaks and the additional structure result from a strong rehybridization between SiC$_3$ and hBN occupied bands in the deep energy range and the corresponding transitions between these bands and unoccupied bands.
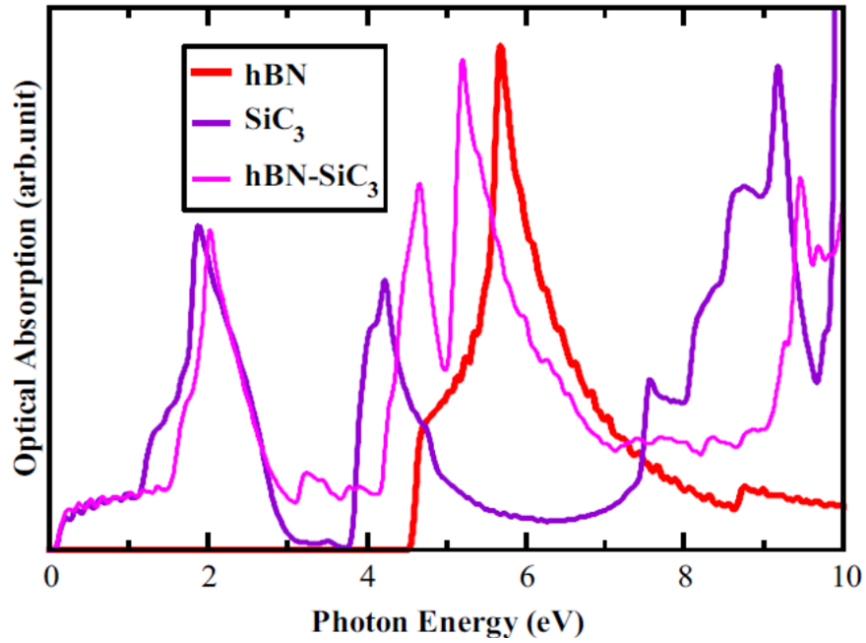
**Fig. 4:** Optical absorption spectra of isolated monolayer hBN, monolayer SiC$_3$, and the hybrid hBN/SiC$_3$ bilayer in the most favorable configuration.

The effect of the external electric field on the optical properties is also considered, as shown in Fig. 5. We can see that the structure of the infrared and visible ranges is rather insenstive to the field strength except for a modulation of the absorption edge, following that of the band gap, and a weak dispersion of the first peak, especially for the reversed field direction. In the deep UV range we see a richer structure, in which the second peak may redshift or blueshift and display additional structure depending on the field direction, while the third peak is less sensitive.
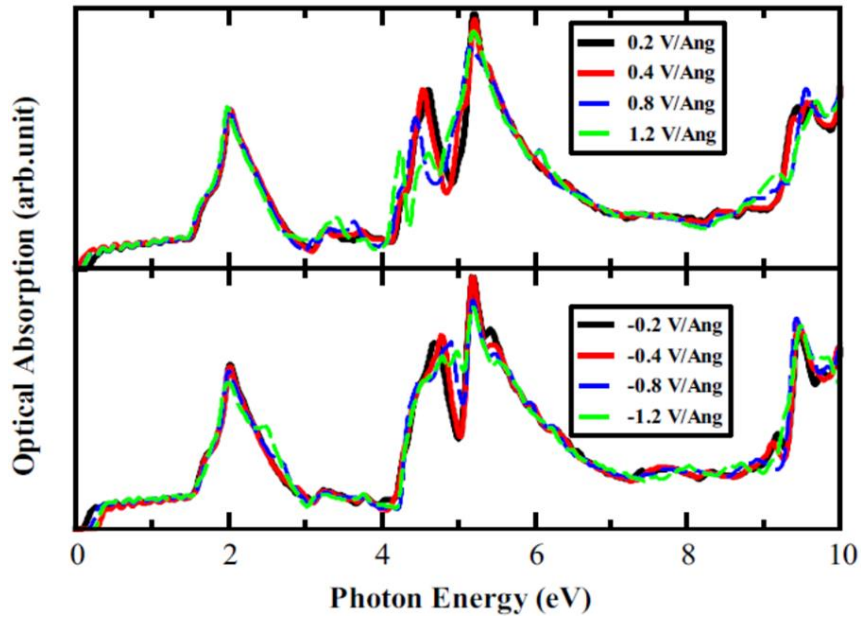
**Fig. 5:** Optical properties of the hybrid SiC$_3$/hBN bilayer as a function of an external electric field applied perpendicular to the layers. Positive (negative) values indicate the field direction (see text).

**hBN/SiC$_3$/hBN trilayers (encapsulated SiC$_3$):**

Here we explore two types of stacking: ABA, and ABC. The relaxed structures are shown in Fig. 6. The ABA configuration is slightly more favorable, with a 0.02 eV total energy difference. This may be a result of a favorable AB stacking for the SiC$_3$/hBN bilayer and the AA stacking found in bulk hBN. The lattice constant is found to be the same for both configurations: 5.256 Å. It is smaller than that of the hybrid bilayers we discussed above, which is a consequence of the presence of the additional hBN layer.
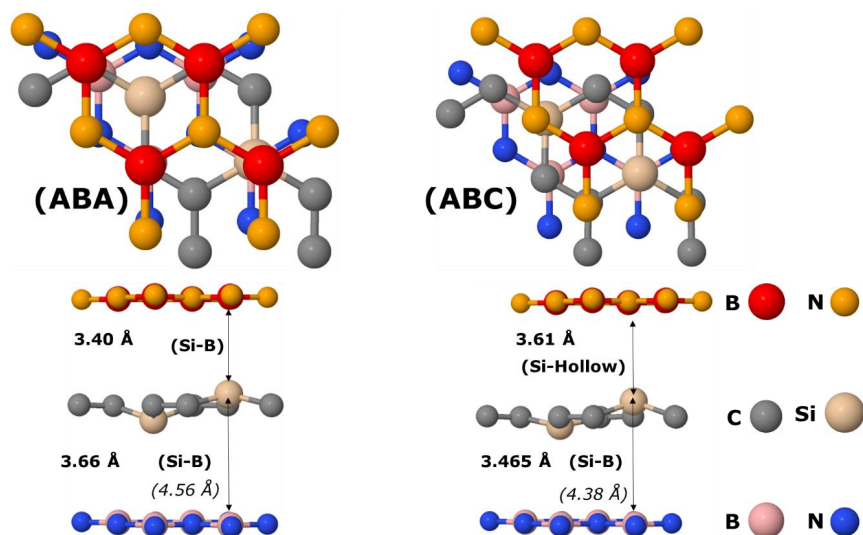
**Fig. 6:** Geometric structures of SiC₃ monolayer encapsulated in hBN. B and N atoms from different layers are shown in different colors.

The electronic band gaps in the ABA and ABC configurations are 0.235 and 0.272 eV, respectively. It should be noted that we used vdW-DF2 for ABA trilayer. Further details are given in Additional information section. The electronic band structures are shown in Fig. 7.
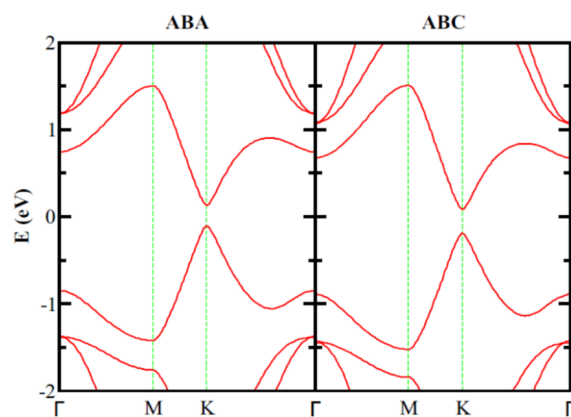
**Fig. 7:** Electronic band structures of the ABA and ABC configurations of encapsulated $SiC_3$.

For comparison, single-layer graphene encapsulated in hBN has a band gap of 0.078 eV which is in good agreement with the previous studies [18, 62]. The gaps, however, were as large as 0.40 and 0.50 eV at M06-L and HSEH1PBE levels, respectively. To further verify this, the gap at vdW-DF2 level (in QE and VASP) is 0.27 eV. Moreover, we have also investigated the effects of an external perpendicular electric field on the electronic and optical properties of these stackings. We consider a single direction for the field in ABA and two directions in ABC (direct and reversed). We find that the introduction of an external electric field is an efficient technique to fine-tune the electronic properties of encapsulated $SiC_3$, as shown in Fig. 8. For both stackings, we can see that the gap can be either increased or decreased depending on the field direction, as in the hybrid bilayer. For high field intensities, the gap can reach 0.378 eV in the ABA structure and 0.43 eV in ABC, both higher values than those found in the hybrid bilayer. In contrast, the band gap of single-layer graphene encapsulated in hBN is already reported to be rather insensitive to the introduction of an external electric field. In a previous study, it is shown that at a field intensity of 1 V/Å, the gap is increased only by 0.02 eV[18, 62]. Consequently, encapsulated $SiC_3$ has a clear advantage in tunability, which is a fundamental property for applications in nanoelectronic devices.
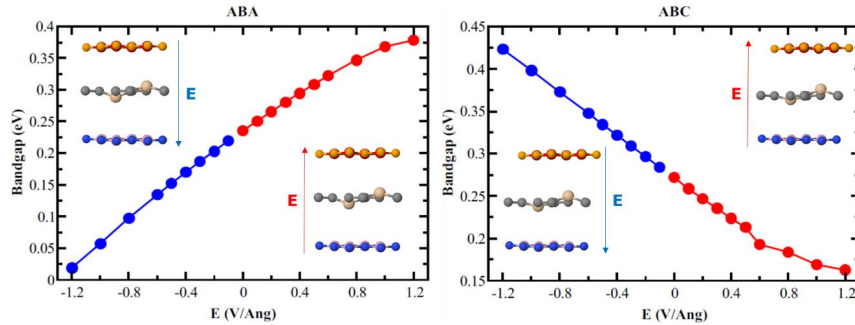


**Fig. 8:** Band gap as a function of an external electric field for (a) ABA and (b,c) ABC stacking. Negative field values indicate a reversed direction.

The optical absorption spectra of the ABA and ABC trilayers as a function of the external field is shown in Fig. 8. By comparing the zero-field values with those from the AB hybrid bilayer in Fig.

9(e), we see that the introduction of the additional hBN layer leads to small blueshifts of the first three sharp peaks. This result implies that the encapsulation of SiC$_3$ with hBN can be an efficient way to tune to optical properties of the system in both visible and deep UV ranges. In contrast, we can also see that the spectra are less sensitive to the electric field strength, in a similar fashion to the hybrid bilayer (see Fig. S4 and S5 in ESI). Still, the peak at the visible range shows an interesting dispersion at high field intensities, in which it splits into two peaks for ABA and ABC stacking with reversed field direction. The second and third peaks follow a similar behavior to that of the hybrid bilayer. The band structures as a function of the external electric field is given in Fig. S6 in ESI.
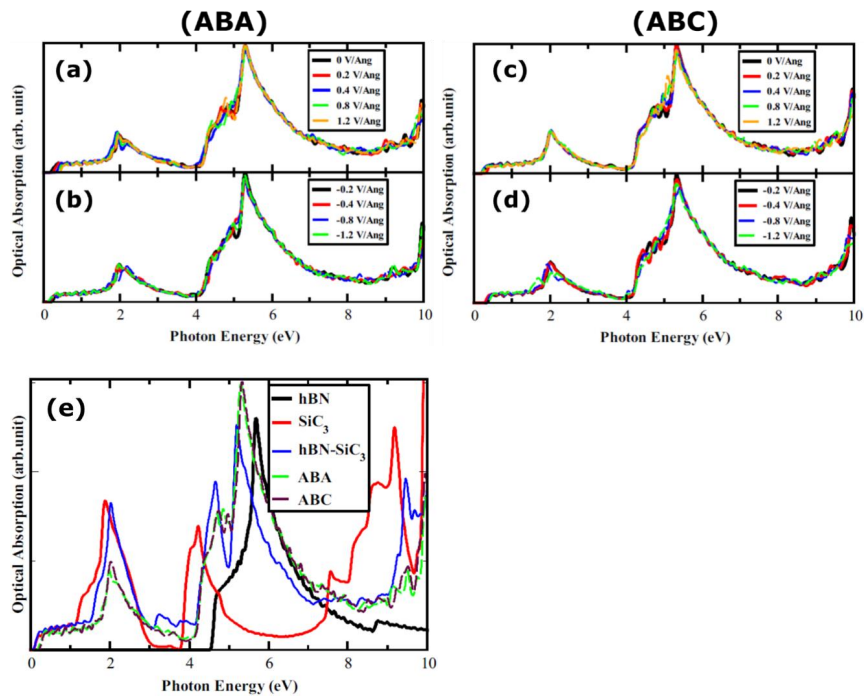
**Fig. 9:** Absorption spectra of (a,b) ABA and (c,d) ABC stacked trilayers as a function of an external electric field. Negative field values indicate a reversed direction Panel (e) shows a comparison between the spectra of single-layer hBN, $SiC_3$, hybrid $SiC_3$/hBN and the two trilayers.

**hBN/SiC₃/SiC₃/hBN 4-layer (encapsulated SiC₃ bilayer):**

Before diving into the encapsulated bilayer $SiC_3$, we first study the properties of the isolated $SiC_3$ bilayer. We select three different stackings: AA, AB, and AB2, as shown in Fig. 10. In AB stacking, half of the Si atoms sit on top of C atoms, while the other half sit on top of hollow sites. In AB2, one third of the Si atoms sit on top of each other, while the rest sit on top of hollow sites. The AB2 configuration is about 0.415 and 0.541 eV/cell more favorable than the AB and AA configurations, respectively. This could be attributed to the larger number of Si atoms sitting on top of hollow sites in this configuration. The lattice constants are 5.647, 5.646, and 5.640 Å for AA, AB, and AB2 patterns, respectively, which are quite close to the monolayer value. The AA and AB patterns are perfectly planar, whereas some buckling is introduced in the AB2 case as the Si atoms on top of each other move towards each other. This Si-Si distance is about 2.57 Å. As we can see in the band structures from Fig. 10, the AA configuration has semimetallic behavior and displays a diamond shaped band structure near the K point, in a similar fashion to AA-stacked bilayer graphene. In contrast, the AB and AB2 configurations have near-zero gaps as a result of the avoided crossing between the valence and conduction bands.
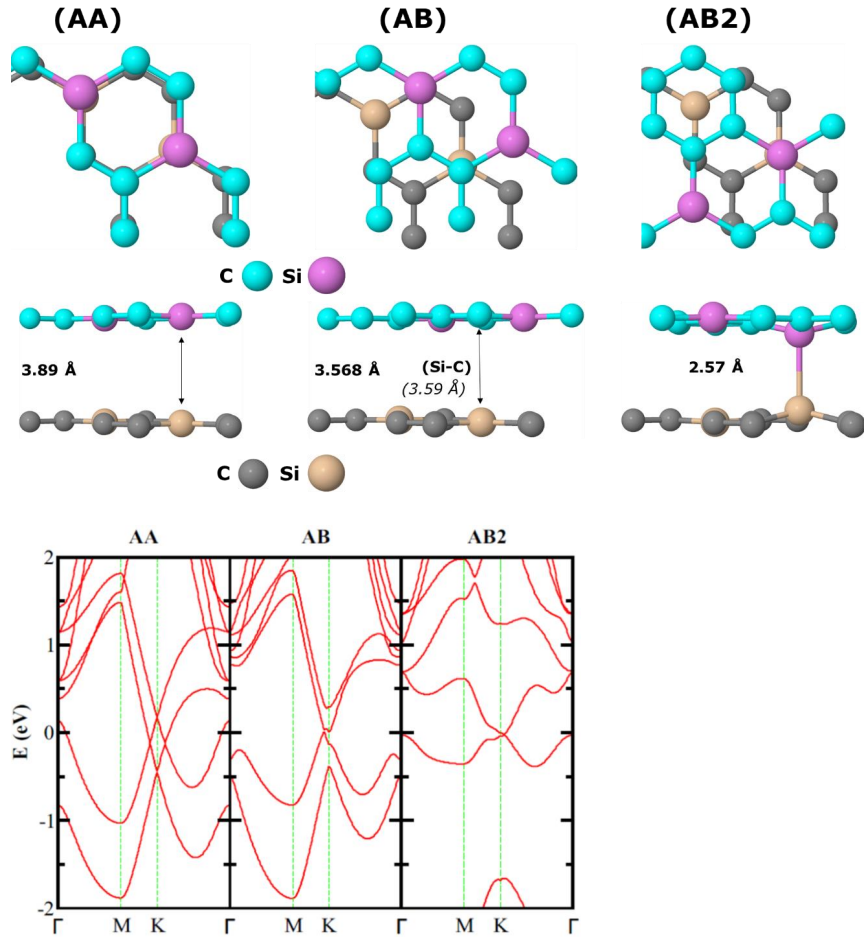
**Fig. 10:** Relaxed structures of different isolated SiC$_3$ bilayers along with the corresponding electronic band structures.

With these results in mind, now we investigate the encapsulated SiC$_3$ bilayer. We consider five different types of stacking, namely ABAA, ABBA, ABCA, ABC2A' and ABC2A. The optimized geometries for the first four are shown in Fig. 11, while the ABC2A structure is discussed separately below. The lattice constants, total energies and band gaps are shown in Table 2 and the

band structures are shown in Fig. 12. We can see that, for the first four stackings, the low energy bands resemble those of the corresponding isolated bilayers, with readjusted bandwidths and small gap openings. In particular, for the ABBA configuration, we can see that the semimetallic character is lost as the valence band states near Gamma move away from the Fermi energy. The diamond shape near the K point is retained, but a small gap is opened at the crossings. For ABAA, the anti-crossing between the valence and conduction bands is reduced and the bands resemble more those of isolated bilayer graphene. For ABCA and ABC2A', the low energy bands shrink and slightly overlap in the vicinity of the Fermi energy, leading to a semimetallic behavior. Among these four structures, we have verified that an external electric field does not lead to gap opening, except for the ABAA case. In that case, we find a tunable band gap, as depicted in Fig. 13. The gap initially increases with field and then decreases as a different pair of bands moves towards the Fermi energy. Moreover, at high field intensities, the bands around the Fermi level display a Mexican-hat shape, in a similar fashion to biased isolated bilayer graphene and bilayer hBP/hBAs [33, 35, 63-66]. The band structures for all cases can be found in Fig. S7 of the ESI.
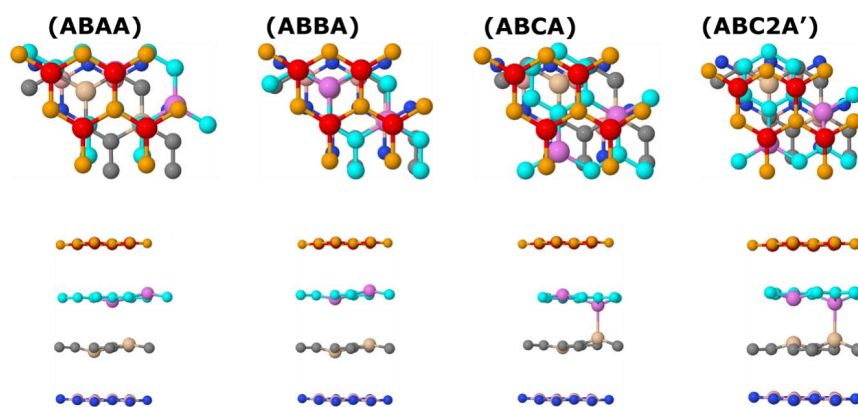


**Fig. 11:** Optimized structures for four different stackings of bilayer $SiC_3$ encapsulated in hBN.

| Pattern | Lattice constant $a$ | Relative energy | Band gap |
|---------|---------------------|-----------------|----------|
| ABAA | 5.374 | 922 | 0.060 |
| ABBA | 5.372 | 955 | 0.05 |

| | | | |
|---|---|---|---|
| ABCA | 5.36 | 199 | -0.045 |
| ABC2A' | 5.348 | 118 | -0.1016 |
| ABC2A | 5.34 | 0 | 0.86/1.60* |

**Table 2:** Lattice constant (Å), relative energy (meV), and band gaps (eV) for various configurations of bilayer SiC$_3$ encapsulated in hBN. * represents spin up and down band gaps.
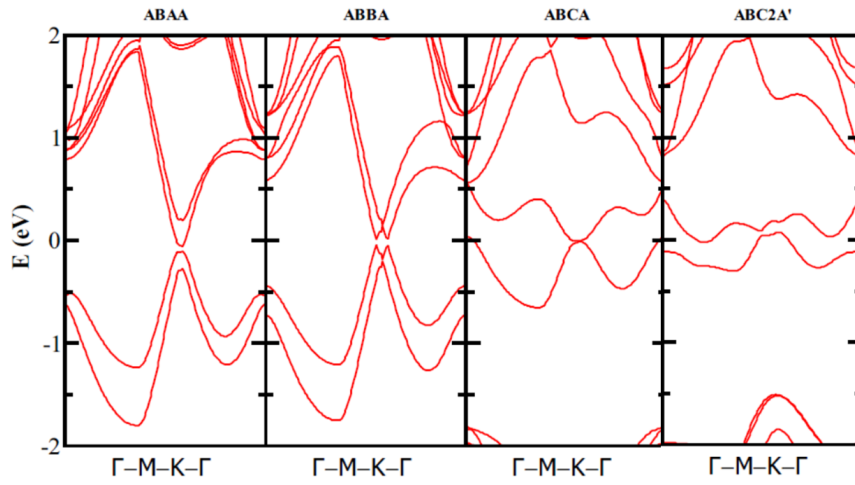


**Fig. 12:** Band structures of different configurations of bilayer SiC$_3$ encapsulated in hBN.
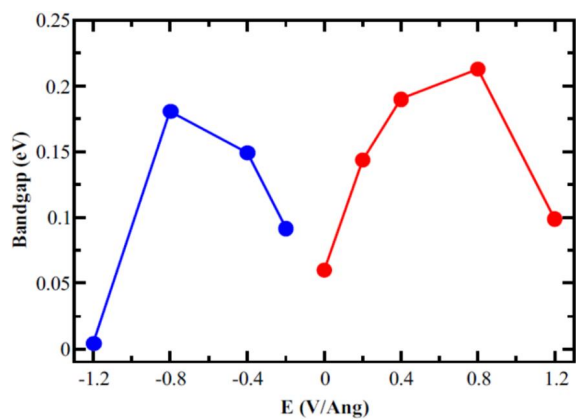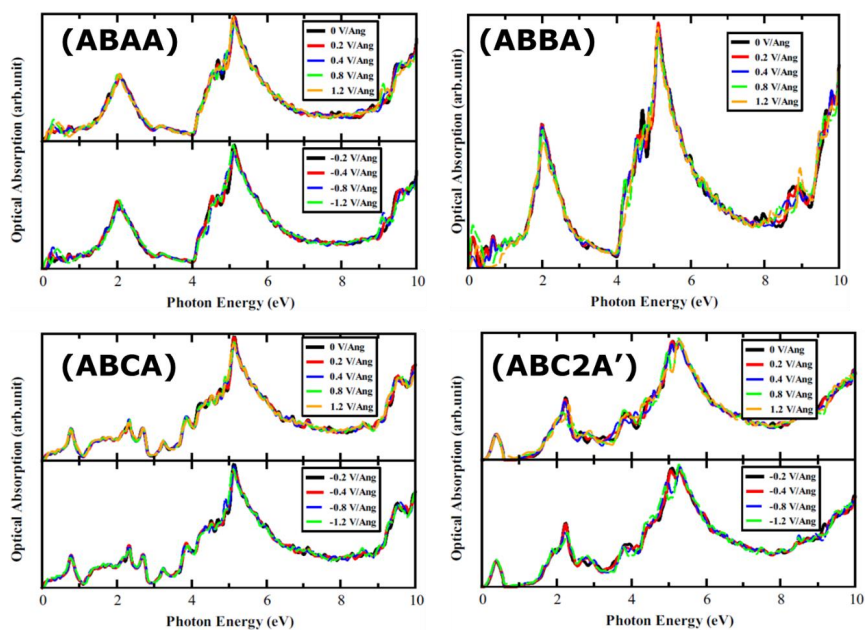
**Fig. 13:** Band gap as a function of an external electric field for the ABAA configuration.
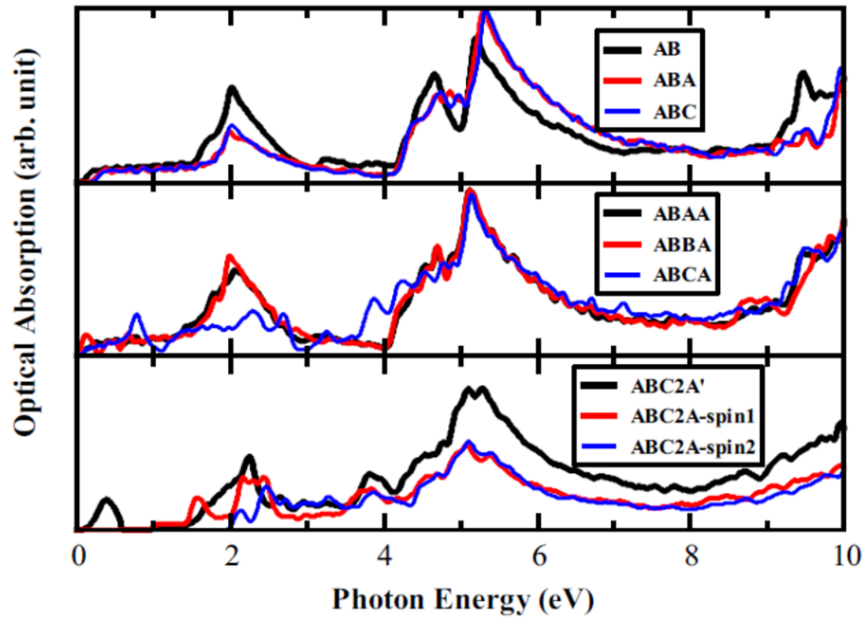
**Fig. 14:** Optical absorption spectra of different configurations of bilayer SiC$_3$ encapsulated in hBN as a function of an external electric field. Absorption spectra of various stacking at zero field value is also given.

In Fig. 12, we show the optical absorption spectra of the same four configurations as a function of an external electric field. As we can see, the ABAA and ABBA configurations have very similar profiles to those we found in the hybrid bilayer and encapsulated monolayer. Interestingly, the first peak at the visible range looks more broad and symmetric for these encapsulated bilayers, which may be related to new optical transitions between the two pairs of low-energy bands. The infrared region of the spectra also display more structure and tunability with the field, following the evolution of these bands. In contrast, the low-energy absorption profiles of the ABCA and ABC2A' structures are very different. Both exhibit a peak in the infrared region, which is related to optical transitions between the weakly-dispersive valence and conduction bands. This peak is also rather insensitive to the external field, as a result of the low tunability of these bands. In ABCA, there are now two peaks in the visible range, which are related to transitions between the

valence band and a deeper unnocupied band. The same happens for the peak in the ABC2A' configuration.

Finally, we discuss the ABC2A configuration, which comes with some interesting electronic properties. As shown in Fig. 15, this structure is very similar to the ABC2A' structure, but there is no relative displacement between the external hBN layers. In an unpolarized calculation, this structure displays low-energy bands with weak dispersion, very similar to those found in the ABCA and ABC2A' structures discussed above. The small bandwidths lead to an increased density of states near the Fermi energy, which result in instability and favor a magnetic state in a spin-polarized calculation for this case. As such, the low-energy bands exhibit large spin splittings, as shown in the band structure plots of Fig. 15. We find band gaps of 0.86 and 1.60 eV in the spin up and down channels, respectively. As both spin up low-energy bands are fully occupied, the resulting magnetization for this configuration is $2\mu\beta$. From the spin density, this magnetic moment comes mostly from the N and C atoms.
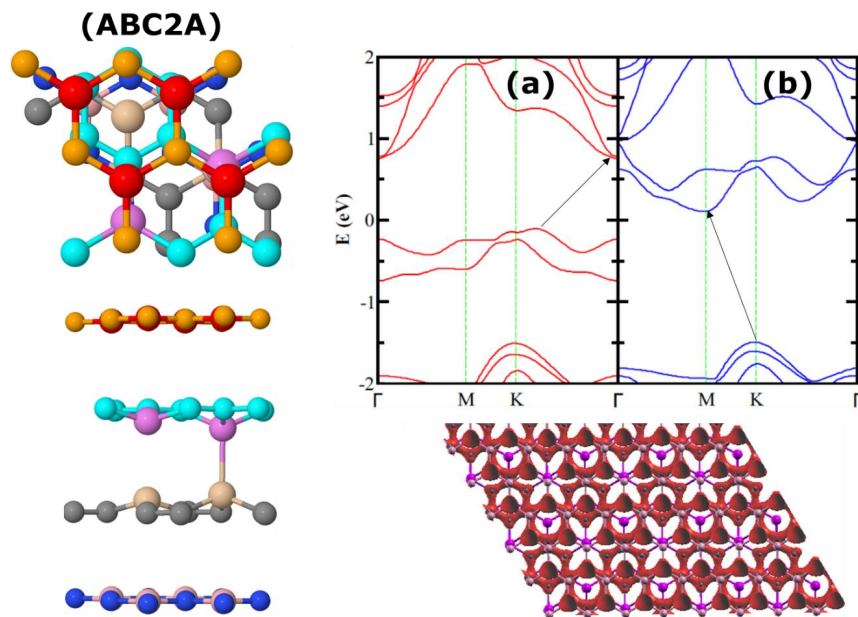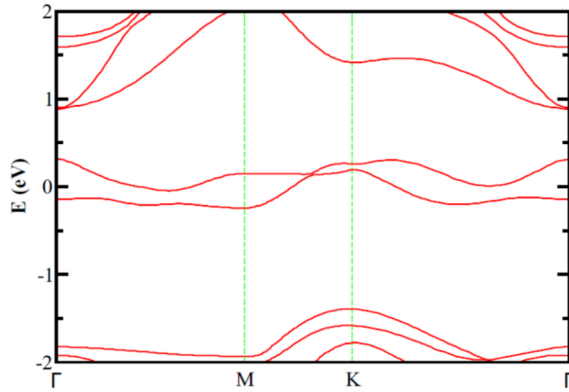
**Fig. 15:** Optimized geometry, spin polarized band structure and spin density profile for the ABC2A configuration.

In addition, we find that these gaps show significant tunability in both channels when subjected to an external electric field, as shown in Fig. 16. An increasing electric field causes a decrease in the gaps down to 0.4 and 0.2 eV for the reversed field direction. These gaps are, however, of indirect nature. Moreover, as the field intensity is increased, the gap between the spin up and down low energy bands decreases, until they eventually cross the Fermi energy. After this point, the system starts to lose magnetization and becomes metallic. The evolution of the band structure with the field is shown in Fig. S7 of the ESI.
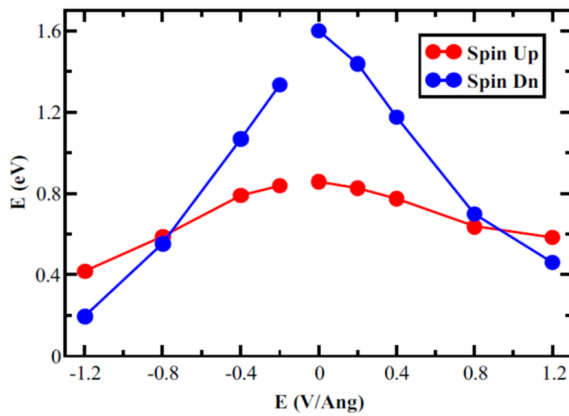
**Fig. 16:** Band gap as a function of an external electric field for the ABC2A configuration. Negative values indicate a reverse field direction.

The optical absorption spectrum of this structure for each spin channel is shown in Fig. 17. Note that, for low field intensities, there is no structure below 1 eV, as both spin up (down) low-energy bands are fully occupied (unoccupied). At higher intensities, these bands cross the Fermi energy and are now partially occupied, allowing for new optical transitions and a small structure in this range. Above 1eV, the spectrum shows a very rich structure and high tunability, as a result of the displacement of the low energy bands towards the Fermi energy.
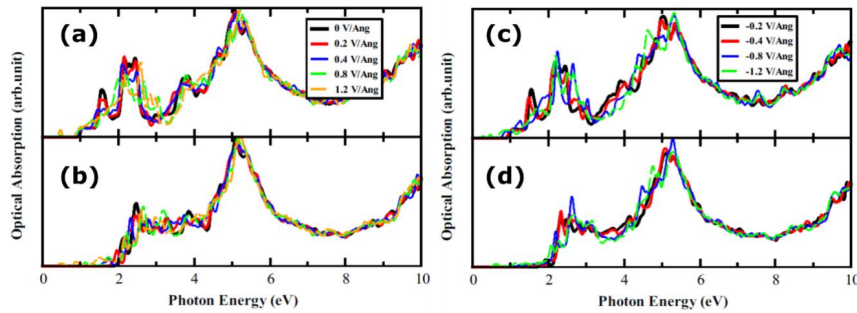


**Fig. 17:** Optical absorption spectra as a function of an external electric field for the ABC2A configuration calculated from (a)(c) spin up and (b) (d) and spin down channels. Negative values indicate a reverse field direction.

**Conclusions:**

In summary, we have combined $SiC_3$ with hBN in various stackings and configurations and calculated the resulting electronic and optical properties. The gaps in the $SiC_3$/h-BN hybrid bilayers are quite larger than those of its graphene-hBN counterpart and are found to be sufficient for practical applications in future nanoelectronic devices without compromising the linear-like character of the valence and conduction bands in the vicinity of the K point. Furthermore, the gaps are found to be highly responsive to both biaxial strain and an external perpendicular electric field. For encapsulated single-layer $SiC_3$, the gaps are not only larger than those reported for encapsulated graphene, but also show a great tunability with the introduction of the electric field,

a property that is much weaker in encapsulated graphene. Finally, in the case of encapsulated bilayer $SiC_3$, we find that the tunability of the band gap is strongly dependent on the stacking configuration. In particular, three of them display low-energy bands with weak dispersion and one of them favors a magnetic state. The low-energy bands in this state have a large spin splitting, leading to band gaps of 0.86 and 1.6 eV in spin up and down channel, respectively, along with a total magnetic moment of $2\mu\beta$. These interesting results provide the possibility of using $SiC_3$ heterostructures in future nanoelectronic devices by virtue of its flexible band gaps.

The optical properties of these systems are also very attractive, with the absorption spectra of all structures displaying prominent peaks at both visible and deep UV ranges, as a result of the combined features from $SiC_3$ and hBN. These position of these peaks are stacking-dependent, but show a rather weak dispersion with the application of an external electric field. Moreover, a new peak is introduced in the infrared region for some configurations of encapsulated bilayer $SiC_3$, as a result of new optical transitions between the modified low-energy bands. Therefore, these heterostructures may also be useful for future optoelectronic devices in a wide range of the electromagnetic spectrum. As such, we hope these results will spark new theoretical and experimental investigations.

### Acknowledgments:

### Additional information:

Using vdW-DF1 (in SIESTA), we find that the ABA trilayer gap is pretty much underestimated. To address this issue, we employ DZDP, TZP, and even TZDP basis set. However, we find no effect on the band gap. Furthermore, several other vdW-DF flavors as mentioned earlier were utilized. It is found that bandgap are sensitive to the choice of vdW-DF flavor. Among them, vdW-DF2 gave reasonable results. The gap at vdW-DF2 level is 0.235 eV, whereas the gap at vdW-DF1

level is ~0.13 eV. For ABC trilayer, this difference in gaps at vdW-DF1 (0.272 eV) and vdW-DF2 (0.31 eV) levels is quite small.

In addition to this, PBE-D2 calculations were also performed with the aid of VASP code which reveal quite larger gaps. The calculated values of band gap are 0.54 and 1.74 eV for bilayer and trilayer, respectively. We also check the same geometries with QE (vdW-DF2 and single point calculations) and that the gaps are 0.56 (bilayer) and 1.21 eV (trilayer). Nevertheless, the full relaxation of the ABA structure with vdW-DF2 (QE and VASP) reveal a gap of 0.27 eV. Additionally, we find a minor difference in the buckling of Si atoms in PBE-D2 and vdW-DF2 geometries. That being said, the gap is highly sensitive to changes in geometry and, furthermore, requires much caution when handling such systems.

The Gaussian data is given in Table 3.

| | Band gap M06-L | Band gap HSE | Lattice constant | Formation Energy |
|---|---|---|---|---|
| hBN | 5.29 | 6.06 | 5.00 | -8.28 |
| SiC3 | - | - | 5.62 | -6.36 |
| hBN/SiC3 (AB) | 0.17 | 0.22 | 5.34 | -7.14 |
| hBN/SiC3/hBN (ABA) | 0.40 | 0.50 | 5.22 | -7.49 |
| hBN/SiC3/SiC3/hBN (ABC2A) | $1.26/1.73^{*}$ $1.59/2.12^{\#}$ | $1.62/2.36^{*}$ $1.91/2.76^{\#}$ | 5.29 | -7.67 |

**Table 3:** Bandgap (in eV), lattice constant (in Å), and formation energy in (eV/atom). The direct and indirect gaps are represented by $^{\#}$ and $^{*}$, respectively.

**Data Availability:**

All the data is available from the authors on request.

**References:**

[1]    K. S. Novoselov, A. K. Geim, S. V. Morozov, D. Jiang, Y. Zhang, S. V. Dubonos, I. V. Grigorieva, and A. A. Firsov, "Electric field effect in atomically thin carbon films," *Science,* vol. 306, pp. 666-669, 2004.
[2]    A. K. Geim and K. S. Novoselov, "The rise of graphene," *Nature Materials,* vol. 6, p. 183, 2007.

[3]     K. S. Novoselov, A. K. Geim, S. Morozov, D. Jiang, M. Katsnelson, I. Grigorieva, S. Dubonos, and A. Firsov, "Two-dimensional gas of massless Dirac fermions in graphene," *nature,* vol. 438, p. 197, 2005.

[4]     A. K. Geim, "Graphene: Status and Prospects," *Science,* vol. 324, p. 1530, 2009.

[5]     E. V. Castro, H. Ochoa, M. I. Katsnelson, R. V. Gorbachev, D. C. Elias, K. S. Novoselov, A. K. Geim, and F. Guinea, "Limits on Charge Carrier Mobility in Suspended Graphene due to Flexural Phonons," *Physical review letters,* vol. 105, p. 266601, 2010.

[6]     S. Ullah, A. Hussain, W. Syed, M. A. Saqlain, I. Ahmad, O. Leenaerts, and A. Karim, "Band-gap tuning of graphene by Be doping and Be, B co-doping: a DFT study," *RSC Advances,* vol. 5, pp. 55762-55773, 2015.

[7]     A. Hussain, S. Ullah, and M. A. Farhan, "Fine tuning the band-gap of graphene by atomic and molecular doping: a density functional theory study," *RSC Advances,* vol. 6, pp. 55990-56003, 2016.

[8]     S. Ullah, P. A. Denis, and F. Sato, "First-principles study of dual-doped graphene: towards promising anode materials for Li/Na-ion batteries," *New Journal of Chemistry,* vol. 42, pp. 10842-10851, 2018.

[9]     S. Ullah, P. A. Denis, and F. Sato, "Triple-Doped Monolayer Graphene with Boron, Nitrogen, Aluminum, Silicon, Phosphorus, and Sulfur," *ChemPhysChem,* vol. 18, pp. 1864-1873, 2017/07/19 2017.

[10]    O. Leenaerts, H. Peelaers, A. Hernández-Nieves, B. Partoens, and F. Peeters, "First-principles investigation of graphene fluoride and graphane," *Physical Review B,* vol. 82, p. 195436, 2010.

[11]    H. Peelaers, A. Hernandez-Nieves, O. Leenaerts, B. Partoens, and F. Peeters, "Vibrational properties of graphene fluoride and graphane," *Applied Physics Letters,* vol. 98, p. 051914, 2011.

[12]    P. A. Denis, "Chemical Reactivity of Electron-Doped and Hole-Doped Graphene," *The Journal of Physical Chemistry C,* vol. 117, pp. 3895-3902, 2013/02/28 2013.

[13]    P. A. Denis and F. Iribarne, "Strong N-Doped Graphene: The Case of 4-(1,3-Dimethyl-2,3-dihydro-1H-benzoimidazol-2-yl)phenyl)dimethylamine (N-DMBI)," *The Journal of Physical Chemistry C,* vol. 119, pp. 15103-15111, 2015/07/09 2015.

[14]    S. Y. Zhou, G. H. Gweon, A. V. Fedorov, P. N. First, W. A. de Heer, D. H. Lee, F. Guinea, A. H. Castro Neto, and A. Lanzara, "Substrate-induced bandgap opening in epitaxial graphene," *Nature Materials,* vol. 6, pp. 770-775, 2007/10/01 2007.

[15]    G. Giovannetti, P. A. Khomyakov, G. Brocks, P. J. Kelly, and J. van den Brink, "Substrate-induced band gap in graphene on hexagonal boron nitride: Ab initio density functional calculations," *Physical Review B,* vol. 76, p. 073103, 2007.

[16]    C. R. Dean, A. F. Young, I. Meric, C. Lee, L. Wang, S. Sorgenfrei, K. Watanabe, T. Taniguchi, P. Kim, K. L. Shepard, and J. Hone, "Boron nitride substrates for high-quality graphene electronics," *Nature Nanotechnology,* vol. 5, pp. 722-726, 2010/10/01 2010.

[17]    D. Usachov, V. K. Adamchuk, D. Haberer, A. Grüneis, H. Sachdev, A. B. Preobrajenski, C. Laubschat, and D. V. Vyalikh, "Quasifreestanding single-layer hexagonal boron nitride as a substrate for graphene synthesis," *Physical Review B,* vol. 82, p. 075415, 2010.

[18]    A. Ramasubramaniam, D. Naveh, and E. Towe, "Tunable Band Gaps in Bilayer Graphene–BN Heterostructures," *Nano Letters,* vol. 11, pp. 1070-1075, 2011/03/09 2011.

[19]    S. Cahangirov, M. Topsakal, E. Aktürk, H. Şahin, and S. Ciraci, "Two- and One-Dimensional Honeycomb Structures of Silicon and Germanium," *Physical review letters,* vol. 102, p. 236804, 2009.

[20]    D. Malko, C. Neiss, F. Viñes, and A. Görling, "Competition for Graphene: Graphynes with Direction-Dependent Dirac Cones," *Physical review letters,* vol. 108, p. 086804, 2012.

[21] H. Huang, W. Duan, and Z. Liu, "The existence/absence of Dirac cones in graphynes," *New Journal of Physics,* vol. 15, p. 023004, 2013/02/04 2013.

[22] H. Zhang, Y. Li, J. Hou, A. Du, and Z. Chen, "Dirac State in the FeB2 Monolayer with Graphene-Like Boron Sheet," *Nano Letters,* vol. 16, pp. 6124-6129, 2016/10/12 2016.

[23] Y. Wang, F. Li, Y. Li, and Z. Chen, "Semi-metallic Be5C2 monolayer global minimum with quasi-planar pentacoordinate carbons and negative Poisson's ratio," *Nature communications,* vol. 7, p. 11488, 2016/05/03 2016.

[24] F. Ma, Y. Jiao, G. Gao, Y. Gu, A. Bilic, Z. Chen, and A. Du, "Graphene-like Two-Dimensional Ionic Boron with Double Dirac Cones at Ambient Condition," *Nano Letters,* vol. 16, pp. 3022-3028, 2016/05/11 2016.

[25] L.-C. Xu, R.-Z. Wang, M.-S. Miao, X.-L. Wei, Y.-P. Chen, H. Yan, W.-M. Lau, L.-M. Liu, and Y.-M. Ma, "Two dimensional Dirac carbon allotropes from graphene," *Nanoscale,* vol. 6, pp. 1113-1118, 2014.

[26] X.-F. Zhou, X. Dong, A. R. Oganov, Q. Zhu, Y. Tian, and H.-T. Wang, "Semimetallic Two-Dimensional Boron Allotrope with Massless Dirac Fermions," *Physical review letters,* vol. 112, p. 085502, 2014.

[27] Y. Ma, Y. Dai, X. Li, Q. Sun, and B. Huang, "Prediction of two-dimensional materials with half-metallic Dirac cones: Ni2C18H12 and Co2C18H12," *Carbon,* vol. 73, pp. 382-388, 2014/07/01/ 2014.

[28] Y. Ding and Y. Wang, "Geometric and Electronic Structures of Two-Dimensional SiC3 Compound," *The Journal of Physical Chemistry C,* vol. 118, pp. 4509-4515, 2014/02/27 2014.

[29] P. Li, R. Zhou, and X. C. Zeng, "The search for the most stable structures of silicon–carbon monolayer compounds," *Nanoscale,* vol. 6, pp. 11685-11691, 2014.

[30] Z. Shi, Z. Zhang, A. Kutana, and B. I. Yakobson, "Predicting Two-Dimensional Silicon Carbide Monolayers," *Acs Nano,* vol. 9, pp. 9802-9809, 2015/10/27 2015.

[31] P. A. Denis, S. Ullah, and F. Sato, "Triple Doped Monolayer Graphene with Boron, Nitrogen, Aluminum, Silicon, Phosphorus and Sulfur," *ChemPhysChem,* 2017.

[32] F. Xia, D. B. Farmer, Y.-m. Lin, and P. Avouris, "Graphene Field-Effect Transistors with High On/Off Current Ratio and Large Transport Band Gap at Room Temperature," *Nano Letters,* vol. 10, pp. 715-718, 2010/02/10 2010.

[33] Y. Zhang, T.-T. Tang, C. Girit, Z. Hao, M. C. Martin, A. Zettl, M. F. Crommie, Y. R. Shen, and F. Wang, "Direct observation of a widely tunable bandgap in bilayer graphene," *nature,* vol. 459, pp. 820-823, 2009/06/01 2009.

[34] J. B. Oostinga, H. B. Heersche, X. Liu, A. F. Morpurgo, and L. M. K. Vandersypen, "Gate-induced insulating state in bilayer graphene devices," *Nature Materials,* vol. 7, pp. 151-157, 2008/02/01 2008.

[35] M. G. Menezes, R. B. Capaz, and J. L. B. Faria, "Gap opening by asymmetric doping in graphene bilayers," *Physical Review B,* vol. 82, p. 245414, 2010.

[36] S.-M. Choi, S.-H. Jhi, and Y.-W. Son, "Effects of strain on electronic properties of graphene," *Physical Review B,* vol. 81, p. 081407, 2010.

[37] M. Dion, H. Rydberg, E. Schröder, D. C. Langreth, and B. I. Lundqvist, "Van der Waals Density Functional for General Geometries," *Physical review letters,* vol. 92, p. 246401, 2004.

[38] G. Román-Pérez and J. M. Soler, "Efficient Implementation of a van der Waals Density Functional: Application to Double-Wall Carbon Nanotubes," *Physical review letters,* vol. 103, p. 096102, 2009.

[39] P. Ordejón, E. Artacho, and J. M. Soler, "Self-consistent order-N density-functional calculations for very large systems," *Physical Review B,* vol. 53, p. R10441, 1996.

[40] N. Troullier and J. L. Martins, "Efficient pseudopotentials for plane-wave calculations," *Physical Review B,* vol. 43, pp. 1993-2006, 1991.

[41]     K. S. Thygesen, "Calculating excitons, plasmons, and quasiparticles in 2D materials and van der Waals heterostructures," *2D Materials,* vol. 4, p. 022004, 2017.

[42]     D. Y. Qiu, F. H. da Jornada, and S. G. Louie, "Screening and many-body effects in two-dimensional crystals: Monolayer ${\mathrm{MoS}}_{2}$," *Physical Review B,* vol. 93, p. 235435, 2016.

[43]     K. Lee, É. D. Murray, L. Kong, B. I. Lundqvist, and D. C. Langreth, "Higher-accuracy van der Waals density functional," *Physical Review B,* vol. 82, p. 081101, 2010.

[44]     J. Klimeš, D. R. Bowler, and A. Michaelides, "Chemical accuracy for the van der Waals density functional," *Journal of physics: Condensed matter,* vol. 22, p. 022201, 2009.

[45]     J. Klimeš, D. R. Bowler, and A. Michaelides, "Van der Waals density functionals applied to solids," *Physical Review B,* vol. 83, p. 195131, 2011.

[46]     V. R. Cooper, "Van der Waals density functional: An appropriate exchange functional," *Physical Review B,* vol. 81, p. 161104, 2010.

[47]     K. Berland and P. Hyldgaard, "Exchange functional that tests the robustness of the plasmon description of the van der Waals density functional," *Physical Review B,* vol. 89, p. 035412, 2014.

[48]     O. A. Vydrov and T. Van Voorhis, "Nonlocal van der Waals density functional made simple," *Physical review letters,* vol. 103, p. 063004, 2009.

[49]     M. J. Frisch, G. W. Trucks, H. B. Schlegel, G. E. Scuseria, M. A. Robb, J. R. Cheeseman, G. Scalmani, V. Barone, G. A. Petersson, H. Nakatsuji, X. Li, M. Caricato, A. Marenich, J. Bloino, B. G. Janesko, R. Gomperts, B. Mennucci, H. P. Hratchian, J. V. Ortiz, A. F. Izmaylov, J. L. Sonnenberg, D. Williams-Young, F. Ding, F. Lipparini, F. Egidi, J. Goings, B. Peng, A. Petrone, T. Henderson, D. Ranasinghe, V. G. Zakrzewski, J. Gao, N. Rega, G. Zheng, W. Liang, M. Hada, M. Ehara, K. Toyota, R. Fukuda, J. Hasegawa, M. Ishida, T. Nakajima, Y. Honda, O. Kitao, H. Nakai, T. Vreven, K. Throssell, J. A. Montgomery, J. E. P. Jr., F. Ogliaro, M. Bearpark, J. J. Heyd, E. Brothers, K. N. Kudin, V. N. Staroverov, T. Keith, R. Kobayashi, J. Normand, K. Raghavachari, A. Rendell, J. C. Burant, S. S. Iyengar, J. Tomasi, M. Cossi, J. M. Millam, M. Klene, C. Adamo, R. Cammi, J. W. Ochterski, R. L. Martin, K. Morokuma, O. Farkas, J. B. Foresman, and D. J. Fox, "Gaussian 09, revision A1 ed," *Gaussian Inc.: Wallingford, CT,* 2009.

[50]     J. Heyd and G. E. Scuseria, "Assessment and validation of a screened Coulomb hybrid density functional," *The Journal of chemical physics,* vol. 120, pp. 7274-7280, 2004.

[51]     V. Barone and G. E. Scuseria, "Theoretical study of the electronic properties of narrow single-walled carbon nanotubes: Beyond the local density approximation," *The Journal of chemical physics,* vol. 121, pp. 10376-10379, 2004.

[52]     G. Kresse and J. Furthmüller, "Efficiency of ab-initio total energy calculations for metals and semiconductors using a plane-wave basis set," *Computational Materials Science,* vol. 6, pp. 15-50, 1996/07/01/ 1996.

[53]     G. Kresse and J. Furthmüller, "Efficient iterative schemes for ab initio total-energy calculations using a plane-wave basis set," *Physical Review B,* vol. 54, pp. 11169-11186, 1996.

[54]     G. Kresse and D. Joubert, "From ultrasoft pseudopotentials to the projector augmented-wave method," *Physical Review B,* vol. 59, pp. 1758-1775, 1999.

[55]     J. P. Perdew, K. Burke, and M. Ernzerhof, "Generalized Gradient Approximation Made Simple," *Physical review letters,* vol. 77, pp. 3865-3868, 1996.

[56]     J. P. Perdew, K. Burke, and M. Ernzerhof, "Generalized Gradient Approximation Made Simple [Phys. Rev. Lett. 77, 3865 (1996)]," *Physical review letters,* vol. 78, pp. 1396-1396, 1997.

[57]     S. Grimme, "Semiempirical GGA-type density functional constructed with a long-range dispersion correction," *Journal of computational chemistry,* vol. 27, pp. 1787-1799, 2006.

[58]     P. Giannozzi, S. Baroni, N. Bonini, M. Calandra, R. Car, C. Cavazzoni, D. Ceresoli, G. L. Chiarotti, M. Cococcioni, and I. Dabo, "QUANTUM ESPRESSO: a modular and open-source software project for

quantum simulations of materials," *Journal of physics: Condensed matter,* vol. 21, p. 395502, 2009.

[59] P. Giannozzi, O. Andreussi, T. Brumme, O. Bunau, M. Buongiorno Nardelli, M. Calandra, R. Car, C. Cavazzoni, D. Ceresoli, M. Cococcioni, N. Colonna, I. Carnimeo, A. Dal Corso, S. de Gironcoli, P. Delugas, R. A. DiStasio, A. Ferretti, A. Floris, G. Fratesi, G. Fugallo, R. Gebauer, U. Gerstmann, F. Giustino, T. Gorni, J. Jia, M. Kawamura, H. Y. Ko, A. Kokalj, E. Küçükbenli, M. Lazzeri, M. Marsili, N. Marzari, F. Mauri, N. L. Nguyen, H. V. Nguyen, A. Otero-de-la-Roza, L. Paulatto, S. Poncé, D. Rocca, R. Sabatini, B. Santra, M. Schlipf, A. P. Seitsonen, A. Smogunov, I. Timrov, T. Thonhauser, P. Umari, N. Vast, X. Wu, and S. Baroni, "Advanced capabilities for materials modelling with Quantum ESPRESSO," *Journal of physics: Condensed matter,* vol. 29, p. 465901, 2017/10/24 2017.

[60] N. Kharche and S. K. Nayak, "Quasiparticle Band Gap Engineering of Graphene and Graphone on Hexagonal Boron Nitride Substrate," *Nano Letters,* vol. 11, pp. 5274-5278, 2011/12/14 2011.

[61] S. Ullah, F. Sato, M. G. Menezes, and R. B. Capaz, "Exotic impurity-induced states in single-layer $h$-BN: The role of sublattice structure and intervalley interactions," *Physical Review B,* vol. 100, p. 085427, 2019.

[62] R. Quhe, J. Zheng, G. Luo, Q. Liu, R. Qin, J. Zhou, D. Yu, S. Nagase, W.-N. Mei, Z. Gao, and J. Lu, "Tunable and sizable band gap of single-layer graphene sandwiched between hexagonal boron nitride," *Npg Asia Materials,* vol. 4, pp. e6-e6, 2012/02/01 2012.

[63] T. Ohta, A. Bostwick, T. Seyller, K. Horn, and E. Rotenberg, "Controlling the Electronic Structure of Bilayer Graphene," *Science,* vol. 313, p. 951, 2006.

[64] H. Min, B. Sahu, S. K. Banerjee, and A. H. MacDonald, "Ab initio theory of gate induced gaps in graphene bilayers," *Physical Review B,* vol. 75, p. 155115, 2007.

[65] L. M. Zhang, Z. Q. Li, D. N. Basov, M. M. Fogler, Z. Hao, and M. C. Martin, "Determination of the electronic structure of bilayer graphene from infrared spectroscopy," *Physical Review B,* vol. 78, p. 235408, 2008.

[66] S. Ullah, P. A. Denis, M. G. Menezes, and F. Sato, "Tunable optoelectronic properties in h-BP/h-BAs bilayers: The effect of an external electrical field," *Applied Surface Science,* vol. 493, pp. 308-319, 2019/11/01/ 2019.